UNIVERSITAT POLITÈCNICA DE CATALUNYA
BARCELONATECH
Departament de Teoria del Senyal
i Comunicacions

Contributions to Land, Sea, and Sea-Ice Remote Sensing Using GNSS-Reflectometry

Author

Alberto Alonso Arroyo

Thesis Advisor

Prof. Adriano José Camps Carmona

A Thesis submitted to the Universitat Politècnica de Catalunya (UPC) in partial fulfillment of the requirements for the degree of DOCTOR OF PHILOSOPHY

Ph.D. program on Signal Theory and Communications
Remote Sensing Laboratory (RSLAB) Group
Barcelona, September 2016

Thesis written by Alberto Alonso Arroyo

Contributions to Land, Sea, and Ice remote sensing using GNSS-Reflectometry

Ph.D. Program on Signal Theory and Communications

The work presented in this PhD Thesis has been supported in part by EU Feder and Spanish grants from the MICINN with project refs. AYA2008-05906-C02-01/ESP and AYA2011-29183-C02-01/ESP. Also, part of the instruments and field campaigns performed were financed by ACROSS (Advanced Remote Sensing Ground-Truth Demo and Test Facilities), TERENO (Terrestrial Environmental Observatories) funded by the German Helmholtz-Association, a Monash University Faculty of Engineering Seed grant 2013, and the Australian GRDC (Grains Research & Development Corporation) with project UMO-0004, and involved the Birchip Cropping Group. Finally, and with even more importance, the author received financial support along all the PhD thesis through a FI-AGAUR grant from the Generalitat de Catalunya, and a Fulbright grant for a 10-month visiting research stay at NOAA (National Oceanic and Atmospheric Administration).

To my parents Emilio and Marce.
To Laura, for being always there.

Abstract

This work is the result of 5 years of work devoted to the analysis of GNSS scattered signals over different surfaces (land, coastal sea, sea, and sea ice), and under different geometries (ground-based, airborne, and spaceborne). It presents the analysis of two different GNSS-R techniques for the retrieval of geophysical parameters.

This work starts introducing the state of the art in GNSS-R in order to settle down the signal model for GNSS signals that has been used. Subsequently, the theoretical basis of one of the GNSS-R techniques is presented, which is the Interference Pattern Technique (IPT). The theoretical effect of different surface parameters such as dielectric constant, polarization, antenna height, topography, and roughness on the IPT is presented. Dielectric constant and roughness affects its amplitude, topography and antenna height affects its oscillation frequency, and polarization affects its phase. Polarization in this case is really important since it is the base of one of the retrieval algorithms derived during this PhD thesis. All the works performed by other authors prior to this PhD Thesis dissertation are also detailed. Two different field experiments conducted during this PhD thesis using the IPT technique and the dual-polarization SMIGOL instrument are described in order to prove the theoretical concepts derived and presented. One of the experiments describes two novel soil moisture retrieval algorithms: one based on the amplitude of the horizontal polarization interference pattern, and the other one based on looking to the phase difference between horizontal and vertical interference patterns. The other experiment that used the IPT helped to derive a novel retrieval algorithm to estimate SWH based on detecting the angle up to were the coherent model works. It also helped to test new estimators to measure the sea surface level from the coherent region of the interference pattern more accurately. The interference pattern oscillation frequency, which can be measured only in the coherent region, is related to the sea surface level.

The other technique used and described in this PhD Thesis dissertation is GNSS-scatterometry. First, a theoretical overview of the technique including the reflected field statistics are presented, continuing the different SNRs defined and different algorithms to estimate the coherent and incoherent scattered components are presented. Those last points are new in the GNSS-R field. After that, all the works from other authors performed before and while this PhD Thesis dissertation was conducted are also described. Later, different field experiments performed under different conditions are described to prove the theoretical concepts presented. Those experiments were conducted under different geometries and with platforms both still and moving. First, two ground-based field campaigns using still platforms are described. One on them used linear (H-Pol and V-Pol) and the other one circular (LHCP) polarization for the reflected signals. A novel

soil moisture retrieval algorithm for the linear polarization case is derived. Some problems occurred with the (LHCP) field campaign that prevented the derivation a retrieval algorithm. Second, two ground-based experiments with moving platforms are described but its data is still under analysis by other research groups. After that, four airborne field experiments are presented. The first two field experiments use the LARGO receiver. The first one is dedicated to determine the relationship between the GNSS-R LHCP coherent scattered power and L-Band brightness temperature. For the first time, a quantitative evaluation of this relationship appears in this dissertation. The final goal of that study is to obtain more accurate soil moisture estimations for the radiometry data with enhanced spatial resolution. The second one analyzes the correlation between the GNSS-R LHCP coherent scattered power and multi-spectral indexes. The final goal of that study is to evaluate the potential synergies between those kind of data. The other two airborne experiments are performed with a different kind of receiver in order to determine the amount of coherent and incoherent scattered power was in the GNSS-R LHCP data. Those experiments are also used to prove experimentally the reflected field statistics presented in the theoretical sections. Different algorithms proposed to estimate the coherent and incoherent scattered components are applied to the experimental data. The relationship between the coherent scattered component and the incoherent one is also related to the surfaces' nature. Also, relationships between those components and the thermal SNR are presented to assess the use of different retrieval algorithms depending on which scattering component is dominating.

An independent analysis of spaceborne GNSS-R scattered signals using data from the recently launched UK TDS-1 is presented, proposing different algorithms for sea ice detection and evaluating its performance. These algorithms are based on estimating how coherent is the reflection to relate it to sea ice. They are different from previous algorithms due to the different properties of the UK TDS-1 data (DDMs using 1 ms of coherent integration time and 1 s of incoherent one). Therefore, they are more based on detecting particular DDM parameters and features rather than looking into the reflected field statistics due to the absence of that data.

Finally, a technique to measure vegetation canopy parameters based on the attenuation induced by vegetation on the GNSS signals that pass through the vegetation layer is presented. This technique is supported by a 1-year experimental field campaign which tries to demonstrate the potential of the proposed technique. Also, the GNSS-R RHCP received power is correlated against different indexes such are greenness, redness, blueness, sky cover, Normalized Difference Vegetation Index (NDVI), and Leaf Area Index (LAI). This experiment provides novel results analyzing the vegetation transmissivity in the GNSS-R field, and specially relating it to the NDVI parameter.

Acknowledgements

Sometimes we are not aware about the support we receive in our achievements, which is why I would like to devote this section to express my gratitude to all those that contributed in more or less extent to the development of this work. This is the result of five years of hard work that without you I could not have completed.

First and above all, I would like to express my gratitude to professor Adriano Camps, who is my PhD Thesis advisor. You introduced me the remote sensing world in 2011, and you gave me the opportunity to develop my first research activities with the final degree project. While I was performing it you invited me to join your research team and start my PhD. Even though my first answer was not positive, here I am, five years later writing my PhD Thesis dissertation. You have taught me the beauty of research, which I intend to continue along my career. You have always dedicated me the time I needed, even postponing your own work to untimely hours, and I would really like to thank you for all mentioned above.

Second, I would like to thank Dr. Valery Zavorotny from NOAA. You invited me as a guest researcher at NOAA, and you have dedicated large part of your time to deep and highly interesting discussions, very often about science and sometimes about topics I could have not even imagined before. I could not have asked for more dedication from your side, and I have really enjoyed and taken profit of my time at NOAA. I would also like to express my gratitude to you for your kindness in other matters, such as the priceless help you provide in my year spent on the USA, specially on my first month when I was out of my comfort zone.

Besides Adriano and Valery, I would like to thank other professors at UPC, who have helped me without interest in particular fields of my Thesis. Among them, I would like to highlight first Dr. Albert Aguasca, who has helped me in several hardware problems I faced along my thesis. I know that without your help I would probably have spend 1 more year trying to understand and solve some problems you already solved in the past, specially all those implementation issues that only people who deal with hardware can understand. Second, I would like to thank Dr. Carlos López whose support and understanding of some theoretical matters has been extremely important in some parts of the developed work. From you Carlos, I think that I also will have a friend for the future.

Apart from the professors, I would like to express my gratitude to all the co-workers I have had at UPC along this years, who have deeply and disinterestedly helped me in the development of this work. When I started my PhD Thesis I was highly encouraged by the

PAU team: Xavi, Isaac, Enric, and specially Neri who guided me during the final degree project. Apart from the PAU team, I would also like to thank my current co-workers: Hyuk, Dani, Raul, Roger, and Jorge, with whom I have shared the good and bad moments of performing a PhD, and in the bad moments, we have helped each other to stand up and keep on fighting. Roger we tried to start a company with some of the developments made on this PhD Thesis, and even though I withdrawn my participation after a year, I believe in you and I hope you the best on that. I would also like to thank other PhD students at UPC with whom I have shared this trip. Those are Ruben, Edu, Dani, Alberto, Marcs (Imbert and Lort), Israel and Alba. We will remember our 8 am coffees. I would also like to include here Joaquim, Josep, Ruben, and Albert, the UPC technicians that have given advice and carried out some of the work that nobody sees, but without their contribution things would not advance as they should. Furthermore, during this PhD thesis I have had the possibility of advising three different Master Thesis, and I would like to thank Pol, Sandra, and Tommaso for their dedication and for the confidence the put on me for being their advisor. I would like to highlight that some of the people I have mentioned in this paragraph started being co-workers, but along the trip that is a PhD Thesis they have turned into real friends.

Moreover, as it is sometimes said, a PhD is long-run endurance race, in which you have to push hard and be constant along the whole period, without losing entirely all the energy. For keeping me always up and with a smile no matter what trouble I had faced I would like to thank my girlfriend Laura. You have listened when you had to, you have supported me when you had to, and you have discussed me when you had to. I was used to work hard, but you showed me not to surrender and not to give up until your goals have been achieved. After a bad day you wake up every morning with all the energy to overcome any problem you faced the day before and you have passed that energy to me. Apart from Laura, I would also like to thank my parents, Emilio and Marce, for their lifelong support since I was born until now. You have been always there, in the good and in the bad moments. You have always believed in me, and helped me to believe even more in myself. You have probably been the highest influence in my life and helped me become what I have become. What I achieved and what I have yet to achieve could not be understood without you.

Finally, I would like to thank the funding agencies from which I have received funding while I was performing this PhD Thesis. In this regard, I would like to particularly thank AGAUR for providing me a three-year FI-AGAUR grant to perform this thesis, and the Fulbright commission in Spain, who supported my research project providing me a grant under the Fulbright program sponsorship for my stay at NOAA.

Contents

List of Acronyms

ACF Auto-Correlation Function

ADDMV Allan Delay-Doppler Map (DDM) Variance

AGC Automatic Gain Control

AM Amplitude Modulation

ARTIST Arctic Radiation and Turbulence Interaction STudy

ASI Arctic Radiation and Turbulence Interaction STudy (ARTIST) Sea Ice

AWGN Additive White Gaussian Noise

BB Base-Band

BOC Binary Offset Carrier

BPSK Binary Phase Shift Keying

BRCS Bistatic Radar Cross-Section

C/N0 Carrier-to-Noise density Ratio [dB/Hz]

CAP CAPON

CDMA Code Division Multiple Access

CF Correlation Function

cGNSS-R conventional Global Navigation Satellite Systems (GNSS)-Reflectometry (GNSS-R)

CNSA China National Space Administration

CORS Continuously Operating Reference Station

COTS commercial Off The Shelf

CRP Cosmic Ray Probe

CU University of Colorado

CW Continuous Wave

CWFM Continuous Wave (CW) Frequency Modulation

CYGNSS CYclone Global Navigation Satellite System

DBF Digital Beam Forming

DDM Delay-Doppler Map

DDMs Delay-Doppler Maps
DDMA DDM Average
DDMV DDM Variance
DEM Digital Elevation Model
DFT Discrete Fourier Transform
D-GPS Differential Global Positioning System (GPS)
DIW Doppler Integrated Waveform
DLL Delay Locked Loop
DMC Disaster Monitoring Constellation
DMR Delay Mapping Receiver
DoD Department of Defense
DODEREC DOppler-DElay RECeiver
DORIS Doppler Orbitography and Repositioning Integrated by Satellite
DPU Digital Processing Unit
DSM Digital Surface Model
DSSS Direct Sequence Spread Spectrum
DUO Down and Up Observations
ECEF Earth-Centered, Earth-Fixed
EGEM European GNSS-R Environmental Monitoring
EGNOS European Geostationary Navigation Overlay Service
EIRP Equivalent Isotropically Radiated Power
EM Electro-Magnetic
EO Earth Observation
ESA European Space Agency
EU European Union
EURYI European Young Investigator
FAA Federal Aviation Administration
FDMA Frequency Division Multiple Access
FDR Frequency Domain Reflectometry
FFT Fast Fourier Transform
FLL Frequency Locked Loop
FM Frequency Modulation
FOC Fully Operational Capability
FOV Field of View
FP Fourier Periodogram

FPGA Field Programmable Gate Array

GAGAN GPS-aided Geostationaty Earth Orbit (GEO)-Augmentated Navigation System

GB Ground-Based

GBAS Ground Based Augmentation System

GC Gold Codes

GCS Global Cartesian System

GE Google Earth

GELOz GNSS-R Experiments over Land in Australia

GEO Geostationaty Earth Orbit

GEROS GNSS rEflectometry, Radio Occultation and Scatterometry

GEROS-ISS GNSS rEflectometry, Radio Occultation and Scatterometry (GEROS) on board the International Space Station (ISS)

GGA Global Positioning System System Fixed Data

GLONASS GLObalnaya NAvigatsionnaya Sputnikovaya Sistema

GNSS Global Navigation Satellite Systems

GNSS-R GNSS-Reflectometry

GNSS-RO GNSS-Radio Occultations

GNSS-T GNSS-Transmitted

GO Geometric Optics

GOLD-RTR GPS Open Loop Differential Real-Time Receiver

GPS Global Positioning System

GRDC Grains Research & Development Corporation

GriPAU GPS Receiver Instrument for Passive Avanced Unit (PAU)

GRVI Green-Red Vegetation Index

GSO Geostationary Sun-synchronous Orbit

GSV GPS Satellites in View

H Horizontal

HW Hardware

I/Q In-phase and Quadrature

ICAO International Civil Aviation Organization

ICD Interface Control Document

ICF Interferometric Complex Field

IEEC Institut d'Estudis Espacials de Catalunya

IF Intermediate Frequency

IFFT Inverse Fast Fourier Transform (FFT)

iGNSS-R interferometric GNSS-R

IMU Inertial Measurement Unit

INTA Instituto Nacional de Técnicas Aeroespaciales

IP Interference Pattern

IPCC Intergovernmental Panel on Climate Change

IPT Interference Pattern Technique

IOD In Orbit Demonstrator

IOV In Orbit Validation

IR InfraRed

ISS International Space Station

IRNSS Indian Regional Navigation Satellite System

KA Kirchhoff Approximation

L-MEB L-band Microwave Emission of the Biosphere

LAI Leaf Area Index

LARGO Light Airborne Reflectometer for GNSS Observations

LCS Local Cartesian System

LEO Low Earth Orbit

LES Leading Edge Slope

LHCP Left Hand Circular Polarization

LIDAR LIght Detection And Ranging

LNA Low Noise Amplifier

LORAN LOng RAnge Navigation

LOS Line Of Sight

LS Least-Squares Periodogram

LSP Lomb-Scargle Periodogram

LST Land Surface Temperature

LWC Leave Water Content

McGiver Monitoring of the Canopy using a GNSS-Transmitted (GNSS-T) Instrument for VEgetation Research

MEO Medium Earth Orbit

MERITXELL Multifrequency Experimental Radiometer with Interference Tracking for EXperiments over Land and Littoral

MERRByS Measurement of Earth Reflected Radio-navigation Signals By Satellite

MF Matched Filter

MIR Microwave Interferometric Reflectometer

ML Maximal Length

MSAS Multi-functional transport Satellite-based Augmentation System

MSSL Mean Sea Surface Level

NASA National Aeronautics and Space Administration

NAVSAT Navy Navigation Satellite System

NAVSTAR NAVigation STAR

NBRCS Normalized Bistatic Radar Cross-Section (BRCS)

NBCS Normalized Bistatic Cross Section

NDVI Normalized Difference Vegetation Index

NDWI Normalized Difference Water Index

NF Noise Figure

NIR Near InfraRed

NMEA National Marine Electronics Association

NMRI Normalized Microwave Reflection Index

NOAA National Oceanic Atmospheric Administration

NSIDC National Sea & Ice Data Center

OBDH On Board Data Handling

OSISAF Ocean and Sea Ice SAF

P-SMIGOL Polarimetric SMIGOL

PARIS PAssive Reflectometry and Interferometry System

PARIS-IOD PAssive Reflectometry and Interferometry System (PARIS)-In Orbit Demonstrator

PAU Passive Avanced Unit

PAU-ORA PAU-One Receiver Airborne

PAU-RAD PAU-RADiometer

PAU-SA PAU-Synthetic Aperture

PBO Plate Boundary Observatory

PI Microwave Polarization Difference Index

PIPT Polarimetric Interference Pattern Technique (IPT)

PIR PARIS Interferometric Receiver

PIRA PARIS Interferometric Receiver (PIR) Aircraft

PLL Phase Locked Loop

PLMR Polarimetric L-Band Microwave Radiometer

PNT Positioning Navigation and Timing

PO Physical Optics
PP Pulse Peakiness
PR Pseudo-Range
PRN Pseudo-Random Noise
PYCARO P(Y) and C/A ReflectOmeter
QPSK Quadrature Phase Shift Keying
QZSS Quasi-Zenith Satellite System
RADAR RAdio Detection And Ranging
RAR Real Aperture RAdio Detection And Ranging (RADAR)
RF Radio Frequency
RFI Radio Frequency Interference
RHCP Right Hand Circular Polarization
RIAA Real-value Iterative Adaptive Approach
RMC Recommended Minimum sentence C
RMSE Root Mean Square Error
RNSS Regional Navigation Satellite Systems
ROI Region Of Interest
ROSCOSMOS Russian Federal Space Agency
RSLab Remote Sensing Laboratory
RWGN Random White Gaussian Noise
Rx Receiver
SAR Synthetic Aperture RADAR
SAW Surface Acoustic Wave
SBAS Satellite Based Augmentation System
SDCM System for Differential Corrections and Monitoring
SDR Software Defined Radio
SIC Sea Ice Concentration
SM Soil Moisture
SMAP Soil Moisture Active and Passive
SMIGOL Soil Moisture (SM) IPT GNSS Observations at L-band
SMOS Soil Moisture Ocean Salinity
SNAS Satellite Navigation Augmentation System
SNR Signal-to-Noise Ratio
SONAR SOund Navigation And Ranging
SSO Sun Synchronous Orbit

SSS Sea Surface Salinity

SST Sea Surface Temperature

SV Space Vehicle

SVN Space Vehicle (SV) Number

SWH Significant Wave Height

SWIR Short-Wave InfraRed

$\mathbf{T}_B$ Brightness Temperature

$\mathbf{T}_{BH}$ H-Pol Brightness Temperature

$\mathbf{T}_{BV}$ V-Pol Brightness Temperature

TC Time Chip

TDR Time Domain Reflectometry

TEC Total Electron Content

TES Trailing Edge Slope

TFSR Tapped Feedback Shift Register

TIR Thermal InfraRed

TOA Time Of Arrival

TPR Total Power Radiometer

Tx Transmitter

UAV Unnamed Aerial Vehicle

UK United Kingdom

UK-DMC United Kingdom - Disaster Monitoring Constellation

UK TDS-1 United Kingdom (UK) TechDemoSat-1

UPC Univesitat Politècnica de Catalunya - BarcelonaTech

USA United States of America

USRP Universal Software Radio Peripheral

UTM Universal Transverse Mercator

V Vertical

VOR VHF Omnidirectional Range

VSWR Voltage Standard Wave Ratio

VWC Vegetation Water Content

WAAS Wide Area Augmentation System

WAF Woodward Ambiguity Function

WAGE Wide Area GPS Enhancement

WGS84 World Geodetic System 84

WP Waveform Peak

WS Wind speed

List of Figures

List of Tables

1

Chapter 1
Introduction

This chapter is the first and introductory chapter of this PhD Thesis dissertation. It expresses a general overview of remote sensing. It also talks briefly about soil moisture monitoring, which is one of the main topics of this dissertation, and also about coastal sea and sea ice monitoring, which are topics that are also tackled. Apart from introducing those topics, it also describes the goals of this dissertation highlighting specially the innovative part. There is a special section dedicated to introduce the research group and how it got involved with GNSS-R technology. A section stating the motivation of the entire PhD Thesis is also included. The chapter ends with a short summary about how the dissertation is structured and the contents of each chapter.

1.1 Remote Sensing

Remote sensing is defined as the ability to measure the properties of a target without touching it. This last part is very important, because by not touching the target, its properties are not modified and therefore the measurement obtained can be more accurate. In other words, it is a non-disturbing measurement. Even though remote sensing seems a very particular application, if we open our mind we will see that remote sensing is everywhere, from taking a picture with a camera, where the picture is the result of the light photons that reach the camera sensor during a period of time, to the estimation of the Universe expansion speed by measuring the Doppler signature of all Astral objects surrounding the Earth (astronomy). Remote sensing is based on measuring one parameter which is directly or indirectly related to the parameter of interest. In the first example, the number of photons reaching the camera sensor at each spectral band is translated into an RGB picture that we can look, understand, and interpret. In the second one, a frequency measurement is translated into a speed measurement, which is a concept that, for instance, is also applied in one of the radar types to measure our speed while we are driving.

This PhD Thesis is mainly related to Electro-Magnetic (EM) remote sensing, which is based on measuring a signal that has been scattered off a target in order to infer its properties from the scattering signature. In EM remote sensing there are several frequency bands that are interesting to measure target parameters. The decision of whether to use one band or another one depends on the target's properties aimed to be measured, and its scattering signature at that particular spectral band. Figure 1.1 shows a summary of the entire EM spectrum detailing the spectral bands.

This PhD Thesis dissertation focuses on one small part of the entire EM spectrum, which is called L-band, belonging to the microwave region of the spectrum [1]. L-band spans from 1–2 GHz, which is translated into a wavelength from 30–15 cm respectively [1]. There are two main reasons for the use of L-band in this dissertation. The main one is that the source of energy used comes from GNSS satellites which are centered at L-band since the atmosphere at that particular frequency band is nearly transparent. The second one is that one of the main parameters targeted is soil moisture, and L-band has proven to be the EM frequency band with larger sensitivity to that parameter.

In the microwave remote sensing field there are different techniques that can be used, which are generally classified into two groups: active and passive. Active techniques are based on emitting a signal and measuring the scattered echo produced. Systems using active techniques are known as RADARs, which have different modes of operation depending on how the signal is processed. The Real Aperture RADAR (RAR) and the Synthetic Aperture RADAR (SAR) are two examples of them. In the passive group it is possible to identify two different techniques: microwave radiometry and "passive" RADARs, among which GNSS-R is one kind. Microwave radiometry is based on sensing the spontaneous energy emitted by any object at a temperature above 0 K. GNSS-R is based on sensing the forward scattered GNSS signals.

Microwave remote sensing can be used to measure different properties of different targets at different scales. Generally speaking, the platform used to set the payload determines the scale of the parameter under measurement (either global or local). For

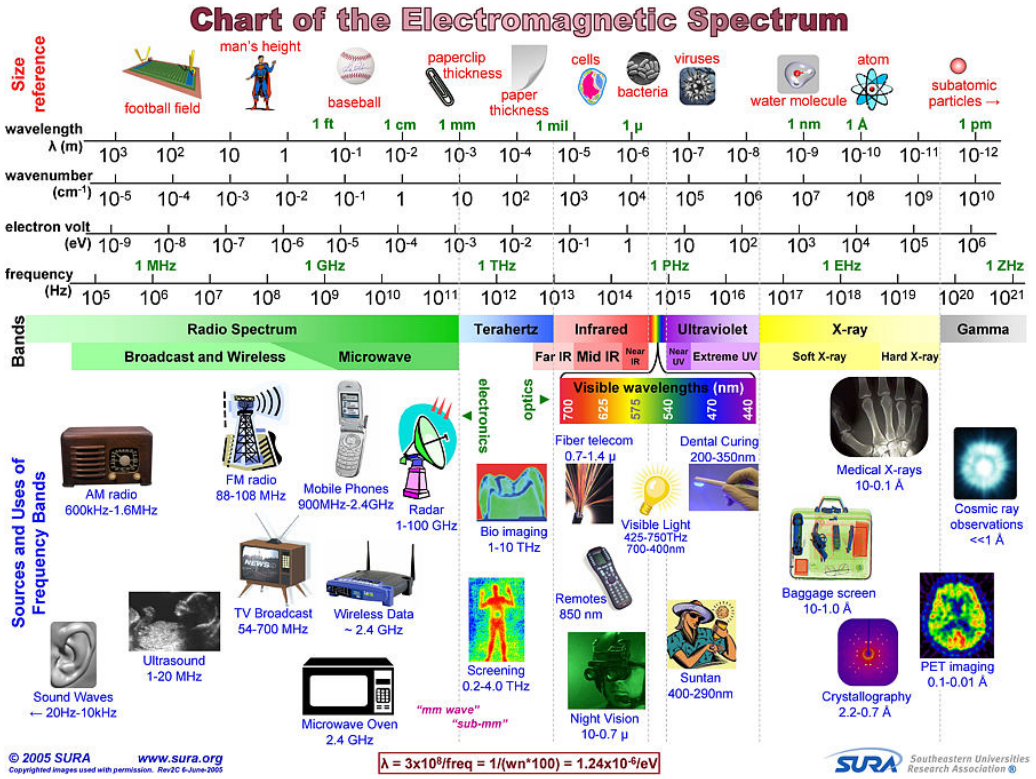

Figure 1.1: Summary of the EM spectrum. [Source: `http://www.sura.org/commercialization/docs/SURA_EMS_chart_full.jpg`]

instance, a global scale can only be achieved using satellite data. Local measurements can be obtained from satellite data, airborne data, and/or ground-based data. The technique used, together with some platform parameters, such as speed or height, determines the final measurement resolution, the measurement accuracy, and the total area covered.

1.2 Earth Observation and Climate Monitoring

Global Warming is a trending topic and it is becoming more and more important to the scientific community. It has mainly two different consequences: the average temperature of the Earth is rising, and its standard deviation is rising too. In other words, the Earth is becoming a warmer planet, and the weather more unpredictable. According to the National Oceanic Atmospheric Administration (NOAA) a change in the average temperature and in its standard deviation will have consequences in ten different climate indicators. Those indicators and their relationship to Climate Change are depicted in Fig. 1.2. Summarizing, it is predicted that Climate Change will rise the sea level, increase both land and sea surface temperature, increase the atmosphere's humidity, the troposphere's air temperature, and increase both ocean's temperature and heat content.

Conversely, it is predicted to decrease the Earth's snow cover, the glaciers, and to reduce sea ice content.

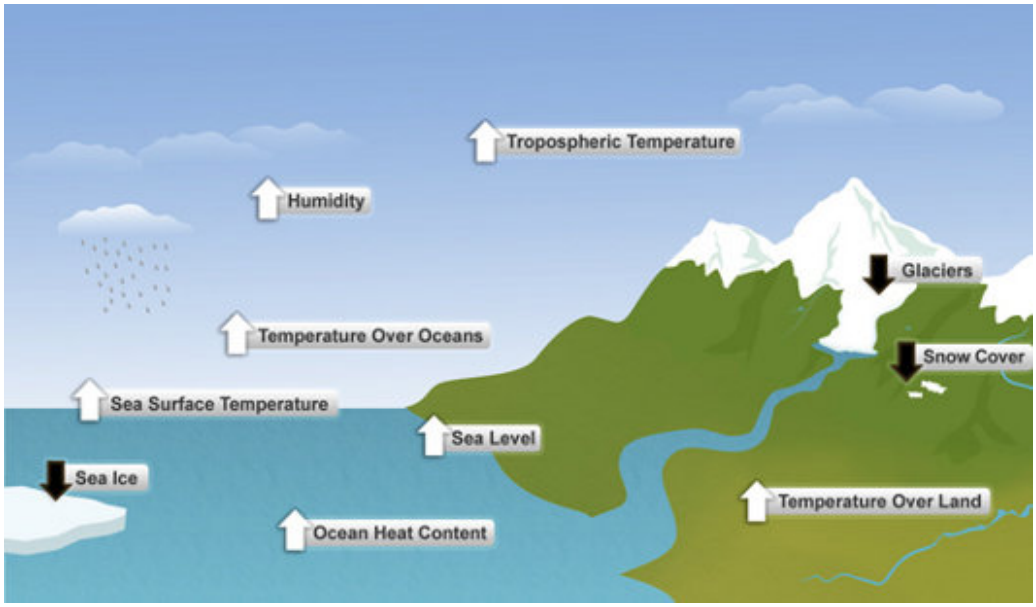

Figure 1.2: Ten climate indicators and its behavior due to global warming. [Source: `http://www.noaanews.noaa.gov/stories2010/images/warmingindicators.jpg`]

The first step to understand all those parameters is to monitor them, and remote sensing is the best way to do it. One key point of remote sensing is that can be performed from satellites at both global and local scales. The first satellite ever successfully launched was the Russian Sputnik-1 in 1957. This test satellite triggered the space race, and probably it is one of the causes for the cutting-edge technology that humanity has developed along time. Since 1957, hundreds/thousands of satellites and missions have been conducted, most of them with scientific purposes in order to monitor Earth geophysical parameters. Initially, satellites carried optical payloads due to the high resolution they can provide, and the fact that the optical field had quickly evolved due to its application in photography. Also, the fact that the atmosphere is nearly transparent at the optical frequency band of the EM spectrum was an add-on. However, optical systems cannot penetrate through clouds, a limitation that triggered the evolution of microwave technology, which is able to penetrate through them. Nowadays, microwave technology can provide images much less sensitive to the presence of clouds with a spatial resolution on the order of optical systems (see for instance TerraSAR satellite parameters which provide images with 0.5 m spatial resolution from spaceborne observations [2]). Summarizing, there are a wide set of tools available at different frequency bands to monitor different Earth's geophysical parameters at a global scale in order to start understanding the changes in our planet, and therefore try to stop or mitigate them.

Among those ten indicators of Climate Change, this PhD Thesis dissertation deals with the measurement of sea ice (mainly detection), and sea surface level [3]. There is another parameter involved in the Climate Change phenomena that is also monitored

in this PhD Thesis dissertation which is soil moisture. Soil moisture is highly related to the Earth's Water cycle which is being affected severely by Climate Change [4]. The measurement of soil moisture has lately become extremely important for the scientific community, and has led to the development and launch of three different satellite missions based on microwave radiometry at L-band: the Soil Moisture Ocean Salinity (SMOS) mission [5–7], the AQUARIUS mission [8], and the Soil Moisture Active and Passive (SMAP) missio [9–11]. All those references show that the aforementioned missions are relatively recent in time, highlighting the importance of soil moisture monitoring to the scientific community. Both SMOS and SMAP are still active missions at the time of writing this PhD Thesis dissertation.

It is also important to take into account that all those parameters measured at a global scale from satellite observations need some validation at field level (local scale). Different techniques using different technologies have been used to validate them via direct destructive measurements or via remote sensing measurements based or not on EM emission or scattering. The mean sea surface level is generally measured at a local scale by buoys deployed along the entire planet (see `http://www.ndbc.noaa.gov/`) or by a global network of tide gauges (see `http://www.oco.noaa.gov/tideGauges.html`), which are owned and/or managed by NOAA. The mean surface level is also monitored at a global scale by radar altimeters such as the ones from the Jason-X and Sentinel-3 missions [12, 13]. In this PhD Thesis the concept of the GPS tide gauge is cited, explained, and used. Different signal processing algorithms over GNSS-R data are proposed to measure sea surface level as an alternative to conventional buoys or traditional tide gauges. The sea ice is normally monitored at a global scale by measuring the microwave radiometry polarimetric signature difference of sea ice and ocean open water at 89 GHz. It is extremely difficult to obtain local sea ice data, and generally the only data available are the satellite observations. The largest variety of methodologies is found when the parameter aimed to be measured is soil moisture. It is possible to find both direct and indirect techniques. Direct methods are destructive methods based on taking terrain samples, weight them, dry them, and weight them again to compute the soil water content by relating it to the weight loss. This methodology is known as gravimetric method. The other local methodologies are more indirect. One type is based on measuring the electrical capacitance of a terrain sample which is directly related to its soil moisture content. Those techniques include both the Time Domain Reflectometry (TDR) and Frequency Domain Reflectometry (FDR) strategies [14]. Another type is based on neutron probes, which has the drawback of being a radioactive technique. This PhD Thesis also shows several alternatives to measure soil moisture at a local scale from both small fields ($\sim$ m) and large ones ($\sim$ km) using different approaches.

This PhD Thesis dissertation describes and validates different remote sensing alternatives to measure the aforementioned geophysical parameters using the opportunity signals emitted by the navigation signals. The methodologies proposed are alternatives to conventional techniques which might be of interest to the scientific community.

1.3 GNSS-R at the UPC Research Lab

GNSS-R starts at Univesitat Politècnica de Catalunya - BarcelonaTech (UPC) with the development of the DOppler-DElay RECeiver (DODEREC) in 2001 and presented to the scientific community in 2003 [15]. This is followed by the European Young Investigator (EURYI) proposal made by Prof. Camps in 2003 and awarded in 2004 with the project entitled "Passive Adanced Unit (PAU): A Hybrid L-band Radiometer, GNSS-Reflectometer and IR-radiometer for Passive Remote Sensing of the Ocean". As it can be deduced from its title, it consisted of a family of instruments for remote sensing of the ocean surface. The L-band microwave radiometer was intended to measure the Sea Surface Salinity (SSS) of the ocean. The InfraRed (IR) radiometer was intended to measure the ocean's Sea Surface Temperature (SST) and therefore obtain the emissivity from the T_B measurements performed using the L-band microwave radiometer. The GNSS-R reflectometer goal was to correct the bias induced by the sea state/roughness on the measured sea surface T_B, and therefore, on both sea surface emissivity and SSS measurements. The PAU project triggered the GNSS-R research at UPC and it is the main cause of more than 10 years of cutting-edge GNSS-R research developing different theoretical advances and instruments. Subsequently, a brief summary of the most relevant developments is provided.

The PAU project started with the design and development of two different L-band microwave radiometers based on two different concepts. The first one was the PAU-Synthetic Aperture (PAU-SA) which is a microwave radiometer based on a synthetic aperture approach [16], which is the concept in which the SMOS satellite is based [7]. The second one was the PAU-RADiometer (PAU-RAD) which is also a microwave radiometer based on a real aperture approach [17]. The PAU-RAD adds Digital Beam Forming (DBF) capabilities in order to steer the antenna beam electronically.

Together with these two different L-band microwave radiometers, different GNSS-R instruments were developed. The first one was the GPS Receiver Instrument for PAU (GriPAU) [18], which is a hybrid instrument based on the combination of a microwave radiometer and a GNSS-R reflectometer. The L-band microwave radiometer of the GriPAU works as a Total Power Radiometer (TPR) in order to measure the T_B of the surface under observation. The reflectometer computes Delay-Doppler Maps (DDMs) in real-time in order to estimate the sea state. This instrument was the first ground-based instrument that aimed at implementing the PAU concept. The second instrument was the Multifrequency Experimental Radiometer with Interference Tracking for EXperiments over Land and Littoral (MERITXELL) [19], which is a multi-spectral radiometer designed to measure the T_B at different frequency bands and includes a GNSS-R reflectometer payload based on the SiGe instrument [20]. The third one was the PAU-One Receiver Airborne (PAU-ORA) which was a GNSS-R-only instrument based on the SiGe receiver too. The data processing was performed off-line in a computer after the GNSS reflected signals were sampled and stored. The fourth one was the SM IPT GNSS Observations at L-band (SMIGOL) reflectometer [21], which is based on the use of GNSS technology as back-end receivers. The last one was the PAU instrument, which is the implementation of the GriPAU for a space-borne platform [22–25]. All those instruments helped to demonstrate the first GNSS-R theoretical developments introduced by the research group. An overview of all the instruments developed can be found in [26, 27].

It is remarkable that the experimental tests of the SMIGOL instrument helped to derive several applications such as [28]:

- Soil moisture monitoring using the Brewster angle position observed at V-Pol interference pattern.
- Vegetation height estimation measuring the position of the different notches on the interference pattern.
- Snow depth monitoring by measuring the interference pattern oscillation period.
- Water level estimation of a reservoir measuring the interference pattern oscillation period too.
- Vegetation water content estimation using GNSS transmitted signals.

which are extremely important since they were one of the triggers of this dissertation.

During the development PhD Thesis different instruments have been conceived by the research group. The first one is the P(Y) and C/A ReflectOmeter (PYCARO) instrument [29], which uses both the P(Y) and C/A code to perform GNSS-R measurements. The second one is the Microwave Interferometric Reflectometer (MIR) [30–33], which is an airborne version of a dual-band multi-beam interferometric reflectometer based on the PARIS concept. The MIR uses analog beam-forming in order to steer the beam. Finally, the author of this PhD Thesis has entirely designed and built the dual-polarization SMIGOL instrument [34, 35], the Light Airborne Reflectometer for GNSS Observations (LARGO) instrument [36, 37], and the Monitoring of the Canopy using a GNSS-T Instrument for VEgetation Research (McGiver) instrument. He has also contributed to the development and manufacturing of the two versions of Down and Up Observations (DUO) instrument [38, 39], specially to the second one, and to the initial tests of the PAU instrument. All the instruments in which the author has collaborated, directly or indirectly, are presented in this PhD Thesis dissertation starting from Chapter 5 until the end.

1.4 Goals

This PhD Thesis dissertation is in part the natural continuation of the one defended by Ph.D. Nereida Rodriguez-Alvarez in December 2011 entitled "Contributions to Earth Observation Using GNSS-R Opportunity Signals" [28]. Therefore, the initial goals settled to be covered in the PhD were driven by the future research lines specified in [28], which were:

- Extend the IPT to dual-polarization.
- Design, develop, and manufacture an instrument to perform dual-polarization IPT field measurements.
- Assess the soil moisture estimation using the dual-polarization interference patterns.
- Water level estimation over coastal sea, a surface with larger dynamics.
- Simplify the vegetation water content estimation algorithm to one receiver.
- Design, develop, and manufacture an instrument to test the simplified concept, and

perform a field experiment to demonstrate it.

The fulfillment of the first three points is shown in Chapter 6, of the fourth point is shown in Chapter 7, and of the last two points are shown in Chapter 11.

However, while performing the PhD Thesis a new goal came out:

- enhancing the soil moisture coverage by using a GNSS-based scatterometric approach, which came together with the development of a low-cost instrument to perform those GNSS measurements.

This goal had a direct consequence which was to determine and measure both the coherent and the incoherent scattering components, and to assess their validity in the retrieval of geophysical parameters. This part became later a strong part of the entire PhD Thesis dissertation as it was also directly related to the initially specified goals, which is shown in Chapter 7. Chapter 4, one part of Chapter 6, and Chapters 8–10 are devoted to the scatterometric work.

1.5 Motivation

The first contact I had with remote sensing field was in 2010–2011, while I attended a microwave remote sensing course and I was performing the final project of the Telecommunications engineering degree. The more I discovered about remote sensing applications, the more fascinating was becoming that field to me. Apart from that, the opportunity of performing a final degree project based on research, and not on a mass market application, helped me find a desire for learning more about remote sensing applications and its benefits to Earth Observation. Since my final project degree project was partially based on hardware enhancement of the first SMIGOL version, after the hardware was finished, my first direction was to keep on the research lines settled by PhD. Nereida Rodriguez-Alvarez. Therefore, to analyze further scientific applications of the same instrument. One of the problems faced in [28] was that depending on the surface roughness conditions it was difficult to detect the Brewster angle position. To solve this, a more in-depth analysis of the IPT had to be performed. The dual-polarization interference pattern technique became a solution to improve the Brewster angle position detection.

Apart from that, GNSS-R measurements using the IPT were too local and required long exposure times to retrieve a soil moisture value. Currently, there are two well-known microwave remote sensing methods to estimate soil moisture at relatively large scale. One kind of them are techniques based on RARs or SARs which relate the back-scattered power to the soil moisture content. The main drawback of these techniques is that the back-scattered power correlation with soil moisture decreases with the presence of vegetation and surface roughness. Surface roughness is a special issue since its effect is sometimes even more important than the dielectric constant/soil moisture. The other method is microwave radiometry, which measures the microwave radiation emitted spontaneously by a surface at a temperature above 0 K, and links it to the soil moisture content. The spatial resolution of this technique depends on the antenna directivity, which is directly related to the antenna size. This results in very large antennas for the desired spatial resolution, which makes the technique sometimes not operational. A GNSS-scatterometric based approach would benefit from two different things. The first one is a forward-scattering

geometry, and therefore the presence of a coherent component. Due to this component, the forward-scattered power should correlate more with the soil moisture than the back-scattered power, and be less affected by noise. The second one is that the presence of a coherent component makes the spatial resolution much finer than the one achievable with microwave radiometers. However, the relatively low-power of the received GNSS reflected signals may limit the sensitivity range. A third point that may emerge in favor of a GNSS-R-based technique is its cost and power consumption, since only a receiver is needed which does not require the highly stabilized thermal control necessary in a microwave radiometer. Therefore, the payload would be much simpler than the other alternative techniques, and its cost lower. Apart from that, GNSS-R may benefit from the continuous and cutting-edge technological evolution that is leading the GNSS field, because a GNSS-R payload can be seen as a slightly modified GNSS receiver, justifying altogether the lower cost of this technology.

Another parameter to be measured in this PhD Thesis dissertation is the coastal sea surface level. This was arised as the validation of the initial water level retrieval concept, which appeared in [28], but over a surface with waves. Local coastal sea surface level measurements are performed either via buoys or via tide gauges. Buoys are expensive instruments because, in spite of their complexity, they have to be designed to resist the highly corrosive sea water conditions. Tide gauges are normally instruments based on short-range radar measurements (CW Frequency Modulation (CWFM) radars), and they can be cheaper since they do not need to experience such a corrosive medium. However, they need more maintenance due to the large amount of data they generate. GNSS-R has its place here because it can reach a precision similar to the short-range radars [40] with a similar or even lower cost. Furthermore, due to the positioning capabilities, it is able to automatize all measurements, referencing them to a predefined reference level (mean sea level, ellipsoid, geoid, etc...).

The time-line of this PhD Thesis was also more than suitable, when different GNSS-R-based space missions are planned, being planned, or scheduled to be launched. The UK TechDemoSat-1 (UK TDS-1) satellite with a GNSS-R payload was launched in 2014. At the time of starting this PhD Thesis, the PARIS mission was in phase A. Also, the PAU instrument on-board the Instituto Nacional de Técnicas Aeroespaciales (INTA) MicroSAT-1 was in phase D. The ^{3}Cat-2 mission was being defined (phase A) at the UPC NanoSat Lab premises. The CYclone Global Navigation Satellite System (CYGNSS) mission was also in phase A with its launch planned for November, 2016. While this PhD Thesis was being conducted, the PARIS mission was not considered for phase B, and the GEROS on board the ISS (GEROS-ISS) mission analysis started using many of the PARIS mission concepts. The increase of GNSS-R satellite missions requires that the scientific community develop several geophysical parameters retrieval algorithms prior to exploitation of the satellite data. Theoretical scattering models to analyze reflected signals already exist, but their validation using experimental data is not so well expanded. The move performed in this PhD Thesis dissertation towards the analysis of scatterometric techniques aims at filling that gap, and consequently analyze the potential applications of scatterometric GNSS-R measurements at a smaller scale, but based on experimental data. This also aims at improving the scientific applicability and/or commercial exploitation of GNSS-R data and deriving new retrieval algorithms that could be used in the forthcoming missions.

1.6 PhD Thesis Dissertation Structure

This PhD Thesis dissertation is divided in 12 Chapters with several appendices that complement all the information provided in each chapter. The entire structure is the following:

- Chapter 1 makes a simple and brief introduction to remote sensing, and in particular to the parameters that have been measured in this PhD Thesis. Apart from that, it states the main goals of the entire Thesis, it describes and introduces the research group, it describes what motivated the Thesis, and it concludes with a detailed structure of the entire dissertation.
- Chapter 2 settles the state of the art of GNSS and GNSS-R. It starts with a brief introduction to navigation and what motivated the development of the navigation field. Subsequently, GNSS systems and their signals are introduced which are the ones used for remote sensing applications. Next, GNSS-R techniques are introduced together with the theoretical signal model used and the observation geometry. It also presents an overview of the past, current, and forthcoming GNSS-R spaceborne missions which are currently five [United Kingdom - Disaster Monitoring Constellation (UK-DMC), UK TDS-1, ^{3}Cat-2, CYGNSS, and GEROS-ISS].
- Chapter 3 is the first theoretical chapter of this dissertation. It develops the theoretical model for the dual-polarization IPT, and shows how every parameter of the model affects the interference pattern shape. The main interest is in the polarization behavior where, for the first time, the phase difference between horizontal and vertical polarization interference patterns is shown. Subsequently, all previous works related to that technique are described including a summary of Rodriguez-Alvarez PhD Thesis dissertation. Also, a detailed description of a similar technique developed at University of Colorado (CU) known as the SNR-analysis is included.
- Chapter 4 is the second and last theoretical chapter of this dissertation. It uses the signal model presented in Chapter 2 and adapts it to the scatterometric application. It also shows the reflected field statistics from a theoretical point of view. Subsequently, it presents different techniques to extract the coherent and incoherent scattered components from both real-valued and complex-valued samples. It also defines the different SNRs that are faced in GNSS-R with the novelty of adding a coherent component. The chapter ends with a detailed description of the GNSS-R scatterometric developments performed by other authors before and meanwhile this PhD Thesis was being conducted.
- Chapter 5 is the only chapter dedicated to the hardware developed, manufactured, and used in the entire dissertation. Four different instruments are described. The dual-polarization SMIGOL, the LARGO, and the McGiver were entirely designed, manufactured, and tested at the UPC Remote Sensing Lab premises. Special interest is made on the antenna design, which is a key point on both the dual-polarization SMIGOL and LARGO instruments. The design and manufacturing of the initial stages of the PAU instrument were supervised during this dissertation.
- Chapter 6 is the first chapter dedicated to the experimental part of this PhD Thesis dissertation. It describes the different ground-based experiments dedicated to land and soil moisture monitoring using both the IPT approach (Australia) and the scat-

terometric approach (*Tarragona*, *Viladecans*, and Yanco, Australia). This Chapter presents the first results published using the dual polarization IPT together with the new retrieval algorithms developed. In the scatterometric approach different instrument configurations (antennas and polarization states) and platforms were tested, some of them involving still platforms and others moving ones.

- Chapter 7 is the second chapter dedicated to the experimental part and it is also based on a ground-based approach. However, the main goal of this chapter is to show the performance of the IPT for the retrieval of significant wave height (novel application) and sea surface level measurements (improved results). A three-month field campaign performed at the *Pont del Petroli, Badalona*, Spain is described and analyzed in detail. This is the first experiment performed over a dynamic surface using the IPT geometrical configuration.
- Chapter 8, like Chapter 6, focuses on land monitoring, using the scatterometric approach and the LARGO instrument, but from airborne platforms. It shows two different field campaigns performed. The first is the GELOz flights performed in Australia, with the goal of studying the relationship between GNSS-R data and microwave radiometry data. The second is the one performed over a vineyard in *Salamanca*, Spain using a paramotor. That collaborative field campaign led to assess the synergy capabilities of GNSS-R and other sensors, which is also a consequence of the developments made during the data analysis of the GELOz flights.
- Chapter 9 focuses on the experimental characterization of the different surface scattering properties. It is performed by experimentally computing the amount of coherent and non-coherent scattered power from different surfaces such as land, vegetated covered land, sea, rivers, and water reservoirs. In this case, instead of using pre-processed data like it was done with the LARGO instrument, it uses raw data that is processed by an appropriate software developed. It shows the data from two different field campaigns, one performed along the Catalan coast, and another one along the South-Eastern part of the USA.
- Chapter 10 shows one spaceborne application of GNSS-R data developed during the author's stay at NOAA using the available data from the recently launched UK TDS-1 mission. It shows how sea ice can be detected in comparison with open water by means of measuring the degree of coherence of the received signal. Different estimators are proposed, tested, and characterized. Sea ice maps obtained using this methodology are shown.
- Chapter 11 shows the simplification of the Vegetation Water Content (VWC) retrieval algorithm proposed as one of the goals of this PhD Thesis. The relationship between the GPS received signal power and different vegetation indicators such as Normalized Difference Vegetation Index (NDVI) or Leaf Area Index (LAI) is studied. An algorithm to estimate vegetation opacity at L-band using multi-angular observations is proposed. The field campaign conducted to analyze those parameters was conducted at *La Fageda d'en Jordà, Catalunya*, Spain.
- Chapter 12 is the final chapter of this PhD Thesis dissertation. It starts with an overview of the entire dissertation. It continues with the main conclusions obtained from the theoretical and experimental works developed. It highlights the novel points of this dissertation. Finally, it ends proposing some future research lines.

The Appendices provide extra information such as mathematical developments or extra explanations to better support the contents of each chapter.

As it has been seen this PhD Thesis dissertation is structured in three different parts without taking into account the introduction and the conclusions. Chapters 3–4 contain the theoretical part, describing clearly the two techniques that are exploited. Chapter 5 contains a description all the hardware designed, manufactured, and/or used during this dissertation, and it is an overview of the instrumentation part. Chapters 6–11 contain the experimental part.

2

Chapter 2
Theoretical Background

This chapter aims at providing an overview of the origins of GNSS remote sensing and establish the theoretical background for the developments and field experiments performed in this PhD Thesis dissertation. It starts with a brief introduction to GNSS systems, and in particular the GPS, which is the one that has been used in this dissertation. It introduces the origins of GNSS-R. The theoretical background and signal models for the different GNSS-R techniques are presented too. Finally, it shows an overview of past, current, and forthcoming GNSS-R space missions.

2.1 Global Navigation Satellite Systems

The need of positioning and navigation comes from ancient times, when the angular measurements of the stars on the sky were used to infer the position and determine the navigation route. However, it was not until the Second World War, with developments in radio receivers, that another class of navigation arised based on the measurement of radio wave propagation, such as the VHF Omnidirectional Range (VOR), LOng RAnge Navigation (LORAN), Decca, and OMEGA, which is the first truly global-range radio navigation system [41–43]. Subsequently, the first satellite navigation system was launched, known as TRANSIT or Navy Navigation Satellite System (NAVSAT), which was used to determine the user's position and then start an inertial navigation with enough accuracy. However, the revolution in navigation had not yet come. It was in 1973 when a constellation of artificial "stars" or satellites, initially known as NAVigation STAR (NAVSTAR), was proposed to be used for global positioning [44]. This was the trigger that revolutionized radio navigation, and the father of all GNSS currently used.

Nowadays, there are two fully operational GNSS systems used, the American GPS and the Russian GLONASS. Furthermore, there are two other coming systems such as the European Galileo and the Chinese BeiDou, which means that by 2020 there will be more than 120 GNSS satellites for global positioning and navigation purposes. However, not all the systems have the same properties as they have to share the same frequency bands without interfering each other, a fact that is successfully achieved.

All GNSS systems are based on a Time Of Arrival (TOA) measurement. GNSS satellites have atomic clocks synchronized among them. A GNSS receiver locks to the satellites' clock. It interprets the ephemeris and almanac data in order to determine the satellites' position and the signal's time of emission. It measures the time of reception and computes the time the signal has used to travel from the satellite to the receiver. This last time measurement is converted into a distance measurement called Pseudo-Range (PR) using the speed of the light ($c \approx 3 \cdot 10^8$ m/s). For each satellite the geometric figure of all points satisfying the measured PR is a sphere centered at the GNSS satellite position, and with the PR as its radius. The intersection between three spheres provides generally two points, but one is discarded, as it is far away from the Earth's surface. Consequently, the 3-D position is determined. Figure 2.1 shows an example of the 3-D triangulation performed using the spheres from the PR information. Despite not depicted in the figure, it is worth mentioning that at least a fourth satellite is necessary to compensate for clock errors.

Since current GNSS systems are based on PR measurements, which are determined estimating the EM delay path of the transmitted EM wave from the GNSS satellites to the GNSS receivers, all GNSS signals must accomplish 4 very important properties:

1. $\mathrm{ACF}_{i,i}(\Delta t) \approx 0$ for $\Delta t \neq 0$, where i stands for the code identifier. This means that for any range that is not the true range, the Auto-Correlation Function (ACF) of the signal must be 0, to avoid ambiguity problems. However, since the satellites repeat their code, there is an inherent ambiguity of a certain distance. For instance, for the GPS system and the C/A code, this ambiguity is of 300 km because the code is repeated every 1 ms.
2. $\mathrm{ACF}_{i,i}(\Delta t) = maximum$ for $\Delta t = 0$. In other words, the normalized $\mathrm{ACF}_{i,i}(0) = 1$.

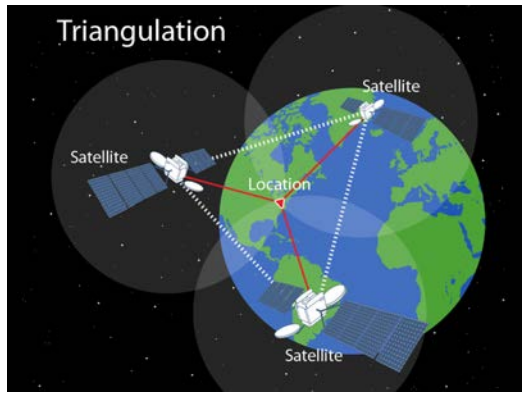

Figure 2.1: GNSS triangulation example. [Source: `http://www.howtechnologywork.com/how-does-a-gps-work/`]

This means that for the true range, the ACF of the signal must be maximum and detectable by the receiver. This last part means that a minimum SNR is required.

3. $\mathrm{CF}_{i,k} \approx 0$ for $i \neq k$ and for all values of Δt, where i and k are code identifiers. This means that the Correlation Function (CF) between the signals transmitted from different satellites ($i \neq k$) has to be very close to 0 to avoid cross-talk.
4. $\mathrm{CF}_{sys1,sys2} \approx 0$ for all values of Δt. This means that the CF between signals from different systems has to be very close to 0 to avoid interference among systems.

The first three properties are normally achieved by the use of Pseudo-Random Noise (PRN) sequences or Direct Sequence Spread Spectrum (DSSS) techniques [44, 45]. Also, as it will be seen later, in the GPS system the third property is achieved using the so called Gold Codes [44, 45]. The last required property is accomplished by the technique used to access to the propagating medium. GPS, Galileo, GLONASS, and BeiDou-2 are located at different frequency bands, which basically means than a Frequency Division Multiple Access (FDMA) technique to access to the medium is used to avoid interference between system. However, for instance, GPS and Galileo share the L1/E1-Band and some part of the L5/E5ab. In order to avoid cross-talk between GPS and Galileo, Galileo uses a Binary Offset Carrier (BOC) modulation, which concentrates a large part of the power on the outer parts of the frequency bands, whereas in the GPS system it is concentrated on the central part of the frequency band. This is extremely important in those cases that the spectral band is shared. Also the codes used add an extra rejection (Code Division Multiple Access (CDMA)). Figures 2.2 and 2.3 show an overview of all GNSS systems, signals and frequency allocation bands. It is possible to identify the shared bands which need a high rejection and the separated bands, in which the receiver's Radio Frequency (RF) filter already attenuates the out-of-band codes to avoid the cross-talk effect. Appendix A shows in detail a description of all the main signal parameters for the four different GNSS systems. Information about the carrier frequency, bandwidth, modulation, In-phase and Quadrature (I/Q) components, and code properties is also shown.

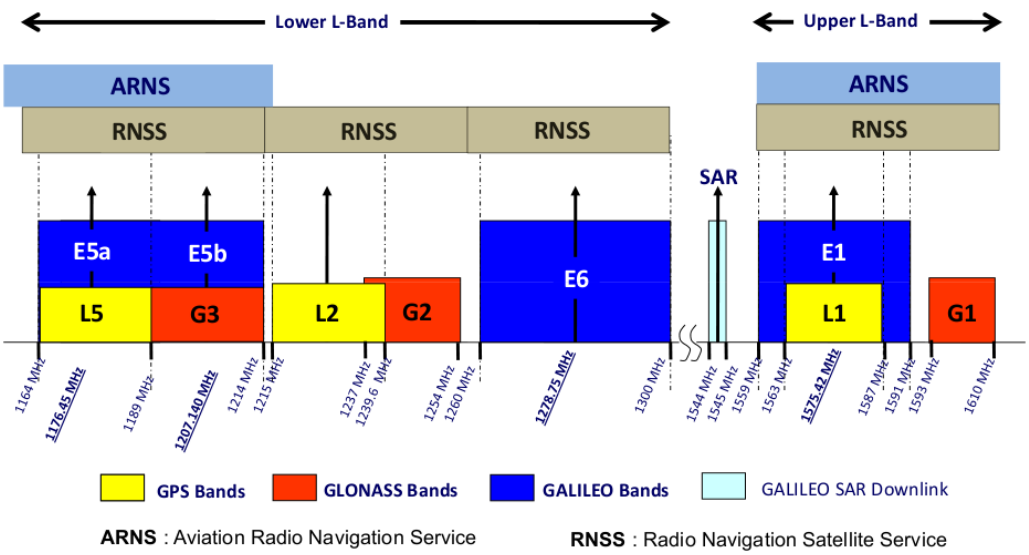

Figure 2.2: Frequency allocation of the different GNSS systems. [Source: `http://www.navipedia.net/index.php/GNSS_signal`]

2.1.1 GPS Constellation and Signals

GPS was designed to provide location, navigation, and timing everywhere in the world, independently from time and weather conditions. It is composed of 30 different satellites orbiting in 6 different orbital planes, each plane having at least 4 operational satellites. There is always a back-up satellite in each orbital plane to replace one of the main satellites in case of failure. GPS satellites are not equally spaced along their orbital plane. The six orbital planes have a 55° inclination and a separation of 60° among them in the ascending node. The satellites' orbit altitude is 20163 km, a nearly circular Medium Earth Orbit (MEO), corresponding to a period of 12 sideral hours. In other words, the same satellite will be seen at the same exact position the day after, but 4 minutes before. This satellite constellation helps to have at least always the four minimum necessary satellites in view. The coverage depends on the latitude where the receiver is located, but 80% of the time there are at least 7 satellites in view. In most populated places it is common to find up to 12 satellites in view. This fact helps to improve the system's accuracy, availability and reliability. Figure 2.4 shows an artist view of the GPS constellation.

The GPS signal is emitted in three different frequency bands: L1 (1.57542 GHz), L2 (1.2276 GHz), and L5 (1.17645 GHz). In those bands, GNSS signals are transmitted in the in-phase and quadrature components. GPS satellites transmit a minimum of three different codes: the Coarse/Acquisition (C/A) code, the P(Y) code, and the M code. The (C/A) code is an open/public code for civilian applications while both P(Y) and M codes are encrypted codes for military ones. The C/A code is only transmitted at L1-band, while the encrypted codes are transmitted in at least two different frequency bands to improve the position accuracy. Nowadays, apart from those codes, GPS satellites transmit other new designed codes shown in Fig. 2.3.

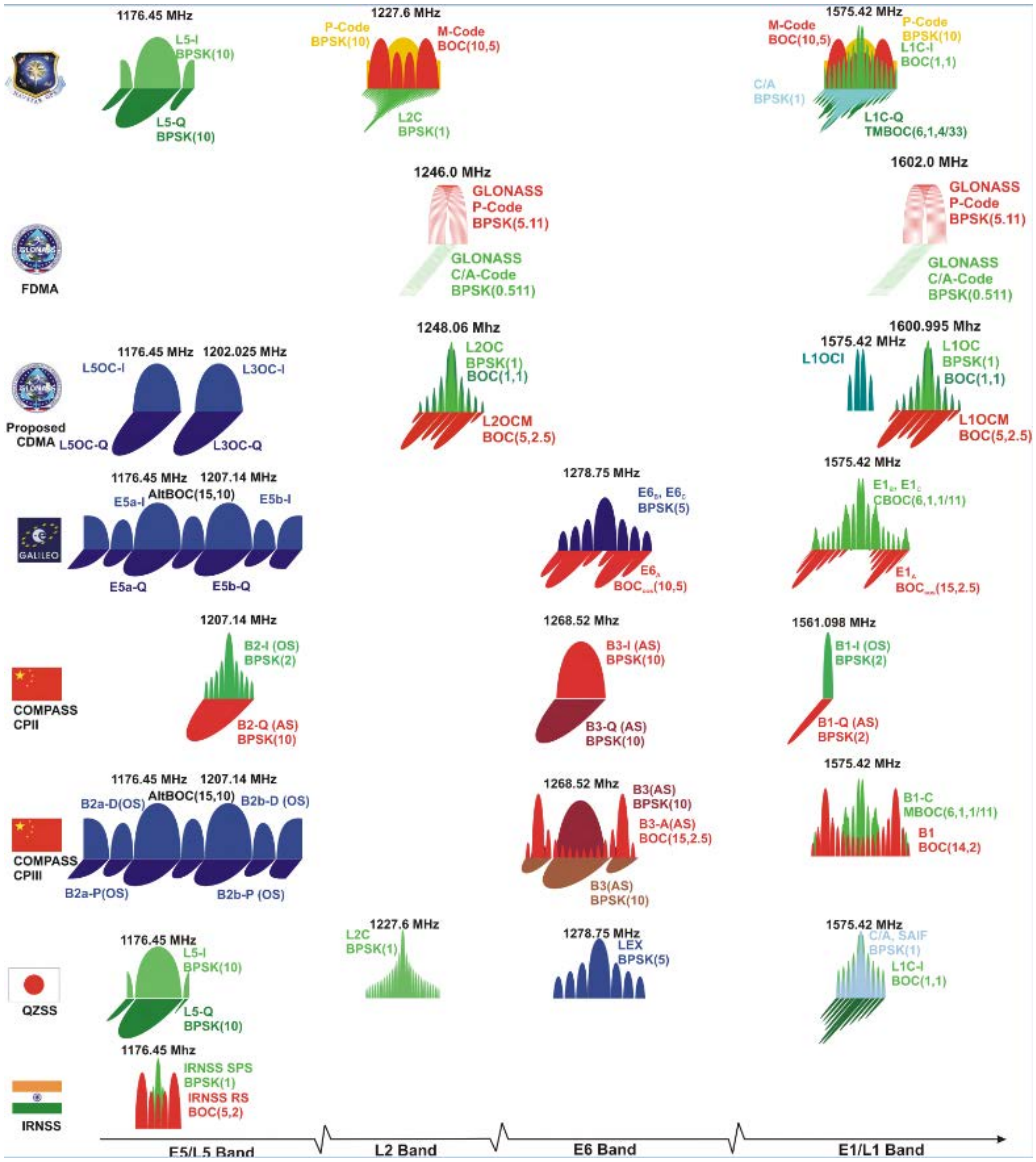

Figure 2.3: Overview of GNSS systems, signals, and frequency bands used. [Source: `http://www.navipedia.net/index.php/GNSS_signal`]

Since at the time this PhD Thesis was started the C/A code was the only available open code and the research group had vast experience using it, it was the one used along the entire PhD Thesis. However, all the theory and techniques applied can be easily extended to all the codes, taking into account their limitations. Consequently, since only the C/A code has been used, it is the only one that is described in this section.

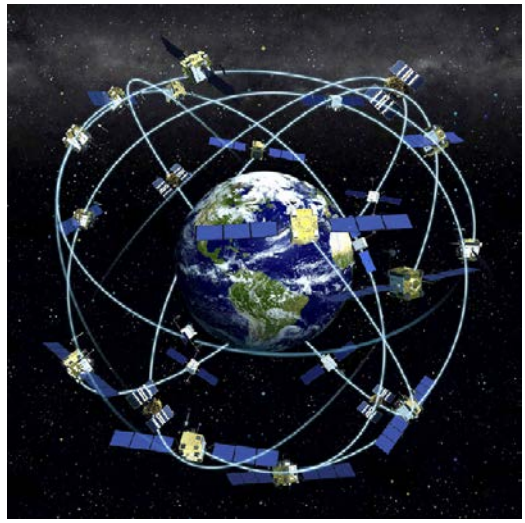

Figure 2.4: Artist view of the GPS constellation. [Source: `https://en.wikipedia.org/wiki/Space_and_Missile_Systems_Center`]

2.1.2 The GPS C/A Code

The GPS C/A code has a period of 1 ms with a length of 1023 chips. They are called chips because, differently from bits, they do not contain any information. This implies that the chip time (τ_{chip}) is equal to 977 ns, which corresponds to a chip rate of 1.023 MHz and a RF bandwidth of 2.046 MHz. They are formed by a smart combination of different PRN signals [44–46], in order to accomplish the four important properties that any GNSS signal must accomplish. Figure 2.5 shows a summary of the aforementioned GNSS system properties. In Fig. 2.5(a) the two first properties are specified, where the ACF function for the SV Number (SVN) 1 is shown. Therein, it is seen how the magnitude of the ACF is maximum for the zeroth delay. Furthermore, it is 75% of the time $\pm 1/1023$, 12.5% of the time 63/1023, and 12.5% of the time -65/1023. This means that any delay apart from the correct one is approximately 13 dB below the correct one for 25% of the time, and 30 dB below the correct one for 75% of the time. Figure 2.5(b) shows an example of the third property that must accomplish all GNSS systems, which is that the magnitude of the CF among different satellites must be approximately 0. As it can be seen, this property is accomplished in the same way than the second one thanks to the smart combination of different PRN sequences creating the so called Gold codes. Figure 2.5(c) shows the GPS signal's spectrum where the bandwidth can be distinguished. Figure 2.5(d) is an example of the fourth property of GNSS signals, which states that the correlation among different systems that share the spectral frequency band must be approximately 0. In this case, in order to provide a graphical example, the magnitude of the correlation between the GPS C/A code PRN 1 and one part of the Galileo E1B signal for the first SV is shown. Note that, those two signals share the same frequency band, but belong to different GNSS systems. Finally, recall that the out-of-band codes are filtered with the receiver's RF filter.

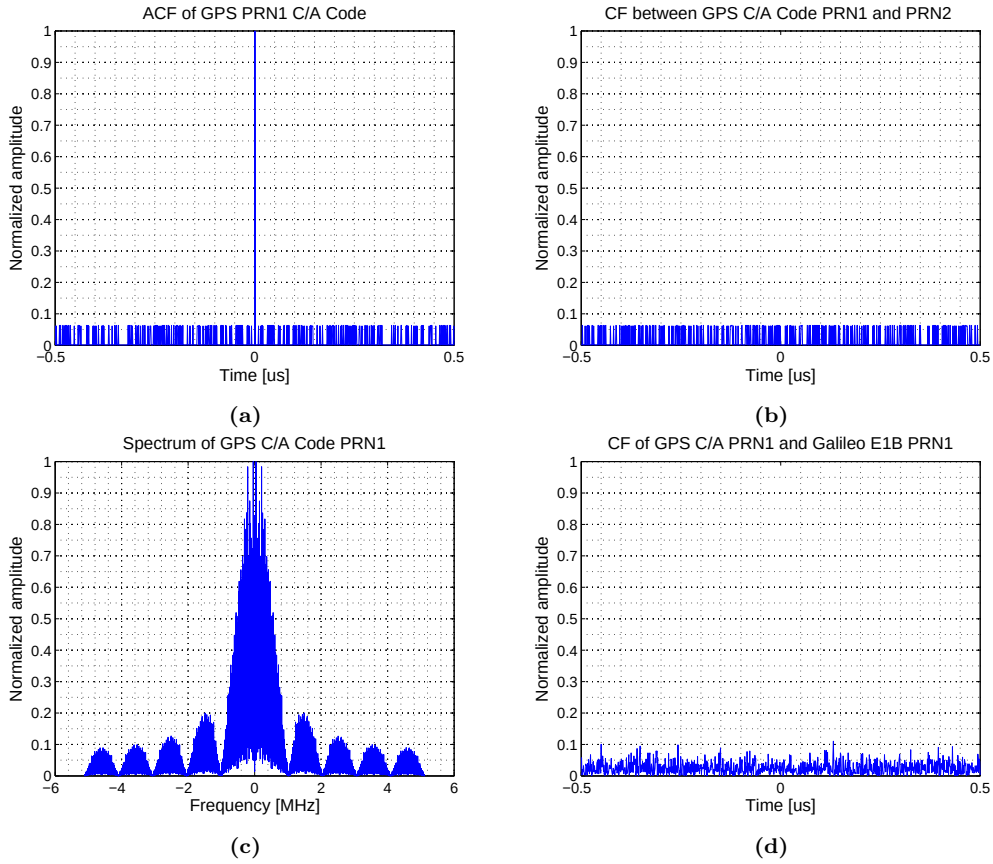

Figure 2.5: GPS signals C/A Code basic properties. (a) Autocorrelation function magnitude of PRN1, (b) Correlation function magnitude between PRN1 and PRN2, (c) PRN1 GPS signal's spectrum, (d) Correlation function magnitude of GPS C/A Code PRN1 and Galileo E1B Code PRN1.

2.1.3 The GPS Signal Structure

There are at least two more codes contained in the GPS signal apart from the C/A code, which are the P(Y) and the M codes. They have a bandwidth 10 times larger than the C/A code, which results in a chipping rate ten times faster. The duration of the P(Y) code is one week, so in order to get locked to it faster, an initial lock to the C/A code is required. The M code is transmitted in the quadrature component of the GPS signal, together with the C/A code, whereas the P(Y) code is transmitted in the in-phase component only. In order to avoid interference among the C/A and M codes, the M code signal is spread along the entire band using a BOC modulation [46].

Before it was mentioned that interference among satellites was avoided either through frequency filtering/rejection or code rejection, and now another technique has been introduced such as adding an extra modulation. One example of this is the BOC, which adds another modulation to the chips in order to spread the power differently in the entire

spectral band. Several variants of the BOC modulation are used in the Galileo system in order to make the system compatible with the GPS one [46].

Summarizing, the basic GPS signal structure at L1-Band is:

$$s_{L1}(t) = \left(\sqrt{2P_{C/A}}C_{C/A}(t) + \sqrt{2P_M}C_M(t)\right) D(t)\cos\left(2\pi f_{L1}t\right) + \sqrt{2P_P}C_P(t)D(t)\sin\left(2\pi f_{L1}t\right), \tag{2.1}$$

where P_X stands for the transmitted power for the X code, $C_X(t)$ for the code itself, $D(t)$ for the navigation data, and f_{L1} for the L1-band carrier frequency. In the case of the GPS system, the navigation data is transmitted also using a bi-phase modulation at 50 bps, which means that each C/A code is transmitted 20 times consecutively in order to generate a navigation bit.

One aspect of GNSS signals that has not been yet commented and it is worth mentioning is that they are buried below the noise level, due to the spreading of the power along the spectrum. In their detection, as the matched filter operation is applied, the power is again concentrated and they rise above the noise level if their SNR is large enough. If not, they can be coherently integrated up to 20 ms, which is the duration of the navigation bit, in order to rise them above the noise level. After that, if coherent integration is aimed to be performed, the possible change of sign in the navigation bit must be compensated for.

2.2 Origins of GNSS-R

It is possible to refer to 1988 as the beginning of the multistatic techniques using GPS signals for scatterometry applications, when they were proposed as a new tool for Earth Observation [47]. In 1993, Manuel Martin-Neira proposed the use of GNSS signals reflected over the ocean for mesoscale satellite altimetry, also known as PARIS [48]. However, it was not until 1994 when the first experimental evidence of a GPS receiver getting locked to the GPS reflected signals over the ocean was reported [49]. This publication reported an event that occurred in 1991, when the GPS receiver of a French military aircraft got locked to the reflected signals over the sea, giving erroneous altitude information. This fact showed the possibility of using GNSS-R as a multistatic technique for remote sensing purposes. Since then, several applications have appeared motivated by the opportunity that this technique might offer to the scientific community.

After Manuel Martín-Neira's proposal, Katzberg and Garrison proposed the use of the GNSS reflected signals to provide a better ionospheric correction to conventional radar altimeters [50]. Later, they presented the first GNSS-R reflectometer, the Delay Mapping Receiver (DMR), which is a modification of a conventional GPS receiver which recorded the whole waveform instead of only the peak or power value. They also used the DMR for altimetry applications over the ocean [51] using conventional methods instead of the interferometric one proposed in [48]. The same instrument was proposed to be used in open ocean to derive sea-state and associate it to sea surface wind-speed. In 2000, based on Kirchhoff Approximation (KA) and Geometric Optics (GO), Zavorotny and Voronovich (Z-V) derived a physical model to explain how GNSS signals were scattered from an ocean surface [52], which opened the door to the retrieval of different geophysical parameters from the same observable: the DDM. Several models have been proposed later trying to improve the performance of the Z-V one. However, the first one is still in

use as it explains the entire sea surface scattering process in a simple computational way. From then on, several applications derived by different authors have appeared targeting water surfaces and altimetric applications [46, 53–63].

Despite it may seem that all GNSS-R applications have been concentrated on sea observations (altimetry and scatterometry), the research for land applications starts as early as 2000, where the GPS SNR change and the BRCS for different polarization states, were compared to the SM content [64, 65]. This technique is based on a scatterometric approach. Several developments to improve this technique have been performed up to date and are presented in Chapter 4.

Apart from that, in the late 90s Kavak and Anderson developed a different technique known today as the IPT, which is based on exploiting the multipath created by the coherent addition of the direct and reflected GNSS signals [66–68]. While Kavak concentrated his studies over land observations, Anderson concentrated his studies on coastal sea observations. Since 2007, this topic was recovered and two different techniques were developed, the IPT at UPC using linearly polarized antennas pointing to the horizon, and the SNR-analysis at CU using Right Hand Circular Polarization (RHCP) antennas pointing at zenith. The developments along time regarding the use of this techniques are presented in Chapter 3.

2.3 GNSS-R Signal Model

The direct GNSS signal reaching the receiver can be expressed as [52]:

$$U_d\left(\vec{R}_r(t), t\right) = \alpha \cdot a(t - R_d(t)/c)\frac{e^{-jkR_d(t)}}{4\pi R_d(t)}e^{+j2\pi(f_c+f_{D\,d}(t))t}, \tag{2.2}$$

where α stands for the signal's transmitted amplitude and the transmitting antenna voltage gain, $\vec{R}_r(t)$ stands for the receiver's position, t for the time, U for the complex voltage measured, d for the direct signal, a for the signal modulation, c for the speed of the light, $R_d(t)$ for the direct path channel ($R_d(t) = |\vec{R}_t(t) - \vec{R}_r(t)|$), $\vec{R}_t(t)$ for the GNSS satellite's position, $k = 2\pi/\lambda$ for the wavenumber, λ for the wavelength, f_c for the central frequency, and $f_{D\,d}$ for the Doppler frequency. The Doppler frequency for the direct signal, which is caused by the relative motion of the transmitter and the receiver, is expressed as:

$$f_{D\,d}(t) = \left(\vec{V}_t(t) - \vec{V}_r(t)\right)\frac{\hat{R}_d(t)}{\lambda}. \tag{2.3}$$

According to the scattering theory, the received reflected signal can be decomposed in two different parts: the coherent component, and the incoherent component [69]. The coherent component can be expressed as [52, 70]:

$$U_{r\,coh}\left(\vec{R}_r, t\right) = \alpha \cdot a\left(t - \frac{|\vec{R}_t| + |\vec{R}_r|}{c}\right) r_{pq}\frac{e^{-jk\left(|\vec{R}_t|+|\vec{R}_r|\right)}}{4\pi\left(|\vec{R}_t| + |\vec{R}_r|\right)}e^{+j2\pi(f_c+f_{D\,r}(t))t}, \tag{2.4}$$

where r_{pq} stands for the rough surface Fresnel reflection coefficient for incident p polarization and reflected q polarization [71], and $f_{D\,r}(t)$ for the reflected Doppler frequency.

Note, that for the sake of simplicity, from now on the time dependence of several vectors has been avoided, but they follow the same ones that Eqn. (2.2). The Doppler frequency for the reflected signal differs from the direct one, and it is given in a general way by [52]:

$$f_{Dr}(\vec{\rho},t) = \left(\vec{V}_t(t)\cdot\hat{m}(\vec{\rho},t) - \vec{V}_r(t)\cdot\hat{n}(\vec{\rho},t)\right)\frac{1}{\lambda} + \frac{\vec{q}(\vec{\rho},t)\cdot\vec{v}(\vec{\rho},t)}{2\pi}, \tag{2.5}$$

where $\vec{\rho}$ stands for the scatterer position, $\hat{m}(\vec{\rho},t)$ is a unitary vector that points from the transmitting satellite to the scattering surface, $\hat{n}(\vec{\rho},t)$ is a unitary vector that points from the scattering surface to the receiver, $\vec{v}(\vec{\rho},t)$ is the surface speed, and $\vec{q}(\vec{\rho},t)$ is the scattering vector which is expressed as:

$$\vec{q}(\vec{\rho},t) = \frac{2\pi}{\lambda}\left(\hat{n}(\vec{\rho},t) - \hat{m}(\vec{\rho},t)\right). \tag{2.6}$$

Note that the reflected signal Doppler frequency has two components: one due to the satellite and receiver motion, and another one due to the surface motion. In order to have pure coherent scattering, the surface must be still and smooth, and therefore the Doppler shift is given by the relative motion of the transmitter and receiver, which is the first term of Eqn. (2.5). Furthermore, for the coherent scattering, all the radiation comes from the same small area, and $\vec{\rho}$ is assumed to be 0, as only one scatterer is considered at which the coordinate system is centered.

In order to express the incoherent component of the scattered signal, the KA under the GO assumption is applied to the reflected field [52], which leads to the following:

$$U_{rinc}(R_r,t) = \alpha\cdot\int_S \sqrt{G_r(\vec{\rho})}a\left(t - \frac{|R(\vec{\rho},t)| + |R_0(\vec{\rho},t)|}{c}\right)g(\vec{\rho},t)d\vec{\rho}, \tag{2.7}$$

where $\sqrt{G_r(\vec{\rho})}$ stands for the voltage antenna gain associated to each scatterer, $R_0(\vec{\rho},t)$ represents the distance from the transmitter to the each scattering point ($R_0(\vec{\rho},t) = |\vec{R}_s(\rho,t) - \vec{R}_t(t)|$), $\vec{R}_s(\rho,t)$ stands for a vector representing each scattering point position as a function of time, $R(\vec{\rho},t)$ is the distance from each scattering point to the receiver's position ($R(\vec{\rho},t) = |\vec{R}_r(t) - \vec{R}_s(\rho,t)|$), and $g(\vec{\rho},t)$ is a function that models the surface scattering function and it is given by:

$$g(\vec{\rho},t) = -r_{pq}(\vec{\rho})\frac{e^{j2\pi f_c t}}{j4\pi R R_0}e^{-j\frac{2\pi}{\lambda}(R_0+R)}\frac{q^2}{q_z}, \tag{2.8}$$

where q is the modulus of the scattering vector ($\vec{q}$), which can be divided in two components ($\vec{q} = (\vec{q}_\perp, q_z)$), with $\vec{q}_\perp$ standing for the (x,y) components and q_z for the vertical component.

2.4 GNSS-R Geometry

Figure 2.6 shows the GNSS-R scattering geometry model where two different curves have been added: the iso-delay (in red), and the iso-Doppler (in black). The iso-delay curves are defined by those scattering points where the signal's path traveled or their relative delay with respect to the specular one is equal, and they can be expressed by:

$$\delta\tau(\vec{\rho}) = \frac{R_0(\vec{\rho}) + R(\vec{\rho})}{c} - \frac{|\vec{R}_t| + |\vec{R}_r|}{c}, \tag{2.9}$$

where $(|\vec{R}_t| + |\vec{R}_r|)/c$ is the delay of the specular point, which, by definition, it is the minimum delay found. For a flat Earth, those curves are ellipses centered at the specular point, and their semi-major (a) and semi-minor (b) axes are given by [50]:

$$a = \frac{\sqrt{2\delta\tau(\vec{\rho})ch\sin(\theta_{el})}}{\sin^2(\theta_{el})}, \tag{2.10a}$$

$$b = \frac{\sqrt{2\delta\tau(\vec{\rho})ch\sin(\theta_{el})}}{\sin(\theta_{el})}, \tag{2.10b}$$

where h is height of the GNSS-R receiver, and θ_{el} its elevation. Those equations are a simplification of the real radius [69] assuming that the height of the GNSS satellite is much larger than the one of the GNSS-R receiver, which holds even for the case of a Low Earth Orbit (LEO) platform.

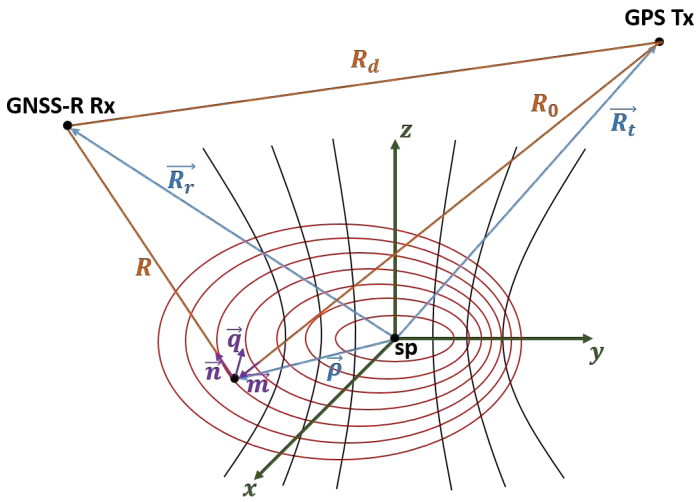

Figure 2.6: GNSS-R scattering geometry for a flat Earth. It is centered at the specular scattering point. The coordinate system used is shown in green. From there, the GNSS satellite position ($\vec{R}_t$), and the GNSS-R receiver position ($\vec{R}_r$) are defined and shown in blue. Each scattering point is determined by the vector ($\vec{\rho}$). The distances between the GNSS satellite and the GNSS-R receiver (R_d), between the GNSS satellite and the scattering point (R_0), and between the scattering point and the GNSS-R receiver (R) are shown in orange. The local scattering vectors ($\vec{m}$, $\vec{n}$, and $\vec{q}$) are shown in purple.

The iso-Doppler lines are, in fact, curves of a higher order than an hyperbola. However, under flat Earth approximation they are described by the hyperbola curves [52]. Their mathematical expression is:

$$\delta f_D(\vec{\rho}) = \left(\vec{V}_t(t)\cdot\hat{m}(\vec{\rho},t) - \vec{V}_r(t)\cdot\hat{n}(\vec{\rho},t)\right)\frac{1}{\lambda} - \left(\vec{V}_t(t)\cdot(-\hat{R}_t) - \vec{V}_r(t)\cdot\hat{R}_r\right)\frac{1}{\lambda} \tag{2.11}$$

where $\hat{R}_t$ and $\hat{R}_r$ are the unitary vectors $\vec{m}$ and $\vec{n}$ for the specular point position ($\vec{\rho} = 0$).

Those expressions are extremely important, and as it will be seen in Chapters 4 and 8, they determine the ground resolution of the GNSS-R derived products.

2.5 GNSS-R Main Techniques and Observables

There are two main techniques used by the GNSS-R community which are known as conventional GNSS-R (cGNSS-R) and interferometric GNSS-R (iGNSS-R) [58]. They are schematized in Fig. 2.7 where (a) and (b) are related to the cGNSS-R and (c) to the iGNSS-R.

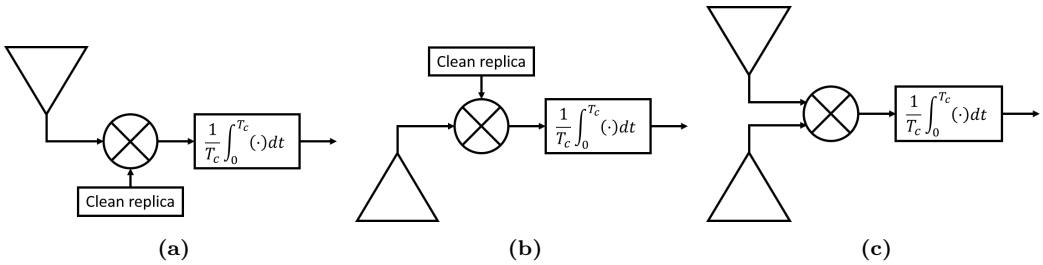

Figure 2.7: Two main GNSS-R techniques: (a) cGNSS-R for the direct signal as in a conventional navigation receiver, (b) cGNSS-R for the reflected signal, (c) iGNSS-R.

The cGNSS-R is based on correlating the received signal with a clean replica of the satellite code, as depicted in Figs. 2.7(a)–(b). The T_c parameter stands for the coherent integration time used. This is the same operation that applies a conventional GNSS receiver to decode the navigation bits, interpret the ephemeris and almanac messages, and to turn on its positioning/navigation engine. In the GNSS field, a receiver is only interested in the maximum value of the matched filter response, which is where the navigation data information is located. However, for remote sensing purposes, sometimes it is not enough with the maximum value, and the matched filter becomes a bank of filters for different delay-Doppler values. This is expressed in Eqns. (2.12)–(2.13) for the direct and reflected signals respectively. For remote sensing, strictly speaking, this should only be applied to the reflected signal, but in numerous techniques it is also applied to the direct signal for calibration purposes.

$$Y_d(\vec{R}_r, \delta\tau, \delta f_D) = \int U_d\left(\vec{R}_r, \delta\tau\right) \cdot a(t+\delta\tau) e^{-j2\pi(f_c+\delta f_D)t} dt, \tag{2.12}$$

$$Y_r(\vec{R}_r, \delta\tau, \delta f_D) = \int U_r\left(\vec{R}_r, \delta\tau\right) \cdot a(t+\delta\tau) e^{-j2\pi(f_c+\delta f_D)t} dt. \tag{2.13}$$

Surprisingly, the first application proposed for the GNSS-R techniques did not use the cGNSS-R, it used the iGNSS-R [48]. As it can be deduced from Eqns. (2.12)–(2.13) and Figs. 2.7(a)–(b), cGNSS-R requires the knowledge of the transmitting satellite code. In the case of the GPS signal, the only code that was available at that time was the C/A code which has a bandwidth of 2 MHz, and therefore a code length of 300 meters. This provided a very bad resolution and accuracy for mesoscale altimetry applications [48]. So, in 1993 Manuel Martín-Neira proposed correlating the direct signal acquired from an antenna looking to the GNSS satellite with the reflected GNSS signal, as it can be interpreted from Fig. 2.7(c) and expressed in Eqn. (2.14) [48]. Since the satellite code is present in both the direct and the reflected signals, there is no need to know the code, and by cross-correlating them the quasi-matched filter approach is obtained. This allows

to use the full signal bandwidth and the codes that are not publicly available, such as the P(Y), and currently the M code, as well.

$$Y_{dr}(\vec{R}_r, \delta\tau, \delta f_D) = \int U_r\left(\vec{R}_r, \delta\tau\right) \cdot U_d{}^*\left(\vec{R}_r, t+\delta\tau\right) e^{j2\pi\delta f'_D t} dt. \tag{2.14}$$

From a theoretical point of view, the iGNSS-R technique should provide a 10 times improvement in altimetric resolution with respect to the cGNSS-R due to a bandwidth 10 times larger. However, differently from the cGNSS-R where the clean replica is an ideal signal, one should note that the direct signal obtained contains also noise. Later studies [72, 73] have demonstrated that the performance of the iGNSS-R technique is degraded in front of the cGNSS-R from a 10 times improvement to approximately 2.7 times improvement. This occurs due to the use of a noisy direct signal instead of a clean one and also due to the fact that GNSS signals are buried below the noise level and by definition their SNR is low. Note that the degradation factor depends on the SNR of the direct signal, as if it was ideal the improvement would be 10. Furthermore, note that in order to apply the iGNSS-R the direct signal must be delayed, because if PRN codes are note aligned their correlation is close to 0. Also, unless signals are aligned, due to the delay between the direct and the reflected signals, a navigation bit might change and the coherent integration operation would not work correctly. This is specially important for spaceborne applications, where the delay between direct and reflected signals is larger. Currently, new larger bandwidth open codes may provide this 10 times factor improvement without the need of applying interferometric techniques.

Equations (2.12)–(2.14) have shown the complex signals after the coherent correlators. However, coherent integration is often not enough in GNSS-R due to the presence of another noise source (*speckle* [74, 75]). In order to mitigate that other noise source incoherent integration is applied which can be expressed as:

$$< \left|Y_X(\vec{R}_r, \delta\tau, \delta f_D)\right|^2 >= \frac{1}{N}\sum_{i=1}^{N} \left|Y_{Xi}(\vec{R}_r, \delta\tau, \delta f_D)\right|^2, \tag{2.15}$$

where X stands for either direct (d), reflected (r), or interferometric (dr), N for the number of coherent complex delay-Doppler correlations used, and the subindex i for the i-th complex coherent delay-Doppler correlation. In Appendix C another approach to incoherent integration is shown.

The complex DDM is defined in Eqns. (2.13)–(2.14), and it is the correlation of the received signal with either a clean replica of the satellite code or the direct signal for different Doppler values. It is normally used in its power version, which is expressed by Eqn. (2.15). The complex waveform is a cut of the DDM for a given Doppler frequency, which means that $\delta f_D = f_D$. This cut is normally performed along the DDM maximum as it is the one that has the best achievable SNR. It is also used in its power form, which is again a Doppler cut of the power DDM. The last main observable used is the peak value of the DDM either in its complex form or in its power form, since it gives information about the amplitude/power of the received signal respectively, specially in the cGNSS-R approach. If the reflection is coherent, the peak value also provides information about the signal's phase.

From now on, this work concentrates on the cGNSS-R, as it is the main purpose

of the PhD Thesis, and for the iGNSS-R the author encourages the readers to follow [48, 60, 72, 73, 76] and Appendix C for some extra theoretical developments.

2.6 Overview of Past, Current, and Forthcoming GNSS-R Space Missions

In 2002, the first GNSS-R reflected from space was detected [77]. In 2003, the UK-DMC satellite was launched, containing the first spaceborne GNSS-R payload. Data from this satellite demonstrated the feasibility of the GNSS-R technique specially for global wind mapping over the ocean following the Z-V model [52]. After that, the next GNSS-R spaceborne mission was carried out also by the UK with the UK TDS-1 in 2014. Note that there is a ten year gap among them. The data provided by UK TDS-1 is quite new at the time of writing this PhD Thesis dissertation, and there are several research groups that are analyzing it. Some applications of these data will be seen in this dissertation. The next GNSS-R mission is the ^{3}Cat-2 mission which was launched on August, 2016, and consists of a six-unit cubesat with the PYCARO payload on-board. Subsequently, the next one is the CYGNSS mission, which instead of being one satellite it is based on a constellation of 8 micro-satellites. The CYGNSS mission is led by the National Aeronautics and Space Administration (NASA), and it is programmed to be launched on November, 2016. Also, the European Space Agency (ESA) proposed the PARIS-In Orbit Demonstrator (PARIS-IOD) mission in 2008. However, after its phase A, all the theoretical studies have been directed to the GEROS-ISS mission, which will include most of the PARIS concept as well as other proposals. Finally, NASA is considering a potential CYGNSS continuation mission, which will change some parameters of the first CYGNSS mission in order to be opened to other applications beyond the original ones.

2.6.1 UK-DMC

The UK-DMC satellite was launched in 2003 as a part of a constellation of satellites for Earth Observation purposes. All those satellites contain GPS receivers for time keeping and navigation purposes. However, the UK-DMC had a difference, a GNSS-R payload. Figure 2.8 shows the down-looking GNSS-R antenna of the UK-DMC mission, which is based on an array of three circular patch antennas. The satellite had also two up-looking antennas based on single patch antennas. All antennas were connected to different and independent RF front-ends. Even though it had real-time processing capabilities, the GNSS-R payload was basically a sampler, and it sampled the RF signals from both the up-looking and down-looking channels. The sampled data was stored on a solid state data recorder and then moved to a larger storage device which was connected to the down-link channel. The UK-DMC satellite was decommissioned in 2011. Table 2.1 shows a summary of the UK-DMC GNSS-R payload characteristics. Finally, Fig. 2.9 shows an example of two DDM obtained over the ocean. Note that its shape is very different from the signal's Woodward Ambiguity Function (WAF), as the signal power is spread along the delay and Doppler domains. This is the result of the incoherent scattering mechanism that will be seen in detail in Chapter 4.

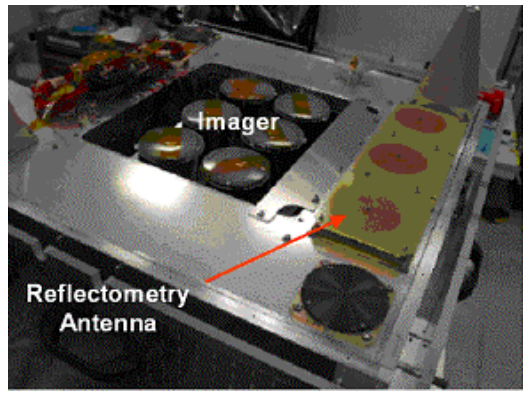

Figure 2.8: Down-looking GNSS-R antenna of the UK-DMC mission [78].

Table 2.1: UK-DMC satellite and GNSS-R payload parameters [78].

Sensor Parameter	**Magnitude**
Orbit Height	680 km
Orbit type	Sun-Synchronous
Sampling frequency	5.71 MHz, 2 bit (1-effective)
Frequency Band	L1
Up-looking antenna polarization	RHCP
Down-looking antenna polarization	LHCP
Down-looking Antenna Gain	11.81 dBiC
Delay-Resolution	0.18 C/A chips
Doppler-Resolution	100 Hz (Software)
Raw Data length	20 s continuous sampling

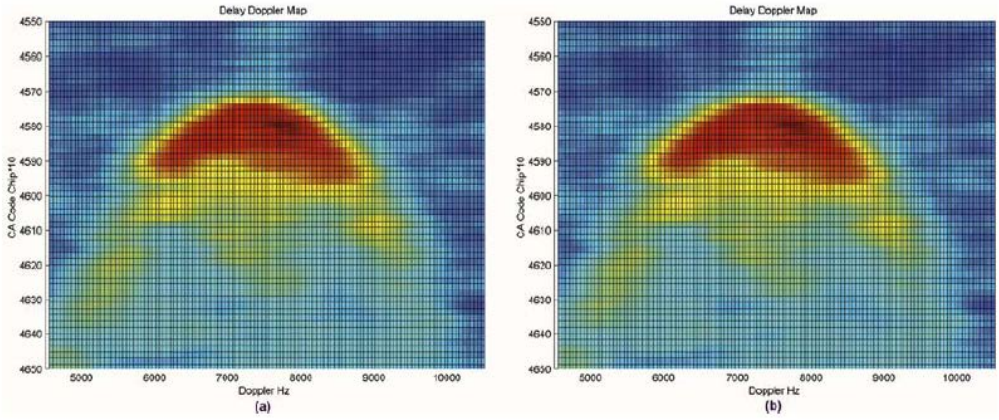

Figure 2.9: DDMs obtained from the UK-DMC dataset [57].

2.6.2 UK TDS-1

The GNSS-R experiment onboard the UK TDS-1 mission is the natural continuation of the pioneering GNSS-R experiment on the UK-DMC mission. This mission is led by the same organization than the UK-DMC, it learns from the mistakes made there, and challenges for new applications, since the first one was a pure technological demonstrator. The new applications include the validation of the ocean scattering models and the wind-mapping capabilities, soil moisture retrieval, and sea ice monitoring [79]. In this case, the main purpose of the payload is to do the processing in real-time on-board the satellite, saving a lot of time to the post-processing stage. Alternatively, it is able to store raw data like the UK-DMC payload. This mission is also a technological demonstrator since the GNSS-R payload is the same one that will be used on the CYGNSS mission. The UK TDS-1 satellite is shown in Fig. 2.10(a), where now the down-looking antenna is a 2x2 patch array, and the payload is shown in Fig. 2.10(b). Table 2.2 shows a summary of the main satellite and GNSS-R payload parameters.

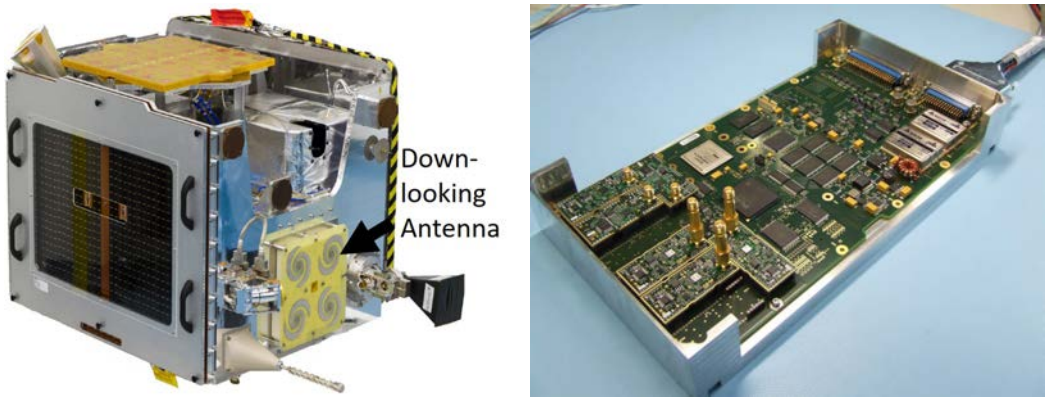

(a) **(b)**

Figure 2.10: UK TDS-1: (a) satellite, (b) payload [79].

It is worth to mention that performing real-time DDMs with the configuration mentioned in Tab. 2.2 reduces the data-rate generated between 100 and 1000 times. Differently from the UK-DMC GNSS-R payload, this allows continuous monitoring. Furthermore, it must be mentioned that in the case of UK TDS-1, the data have been made publicly available through the Measurement of Earth Reflected Radio-navigation Signals By Satellite (MERRByS) portal (`http://www.merrbys.co.uk/`). This has allowed many researchers to start developing new applications for the GNSS-R technique. Chapter 10 provides more details on the mission and products obtained.

2.6.3 ^{3}Cat-2

The ^{3}Cat-2 is a mission conceived, designed, and engineered by the Remote Sensing Laboratory (RSLab) and NanoSat Laboratory in the frame of several Spanish projects, with the support of the ICREA Academia, and the European GNSS-R Environmental Monitoring (EGEM) project which supports the launch costs [80–82]. It is based on a

Table 2.2: UK TDS-1 satellite and GNSS-R payload parameters [79].

Sensor Parameter	**Magnitude**
Orbit Height	635 km
Period	97.3 min
Inclination	98.391°
Frequency Band	L1/L2
Sampling frequency	16 MHz, 2 bits
Up-looking antenna polarization	RHCP
Down-looking antenna polarization	LHCP
Up-looking Antenna Gain	4 dBiC
Down-looking Antenna Gain	13 dBiC
Delay-Resolution	244 ns
Doppler-Resolution	500 Hz
Coherent integration time	1 ms
Incoherent integration time	1 s
Raw Data length	2.3 min

6-unit CubeSat structure (2 x 3 elementary blocks of 10 x 10 x 10 cm^3). The ^{3}Cat-2 aims to be a GNSS-R technological demonstrator to perform multi-constellation, dual-band (L1, L2), and dual-polarization GNSS-R scatterometry and altimetry measurements. The main goals of the ^{3}Cat-2 mission are: to evaluate the sensitivity of GNSS-R for sea state determination as a function of the wind speed or sea state conditions, to test new algorithms for sea ice and soil moisture retrieval, to perform a comparison between both the cGNSS-R and iGNSS-R for altimetric applications, and to evaluate the performance of the different GNSS systems for the retrieval of geophysical parameters. The satellite payload will be the PYCARO [29], a payload that has been entirely developed by UPC, deeply tested under different environments at the UPC NanoSat Lab [83], and in BEXUS 17 and 19 field experiments [84–87]. The expected payload data volume is up to $\sim$ 10 MB per day, which means that data will be pre-processed on-board to reduce their volume. The up-looking antenna is a dual-polarization single patch antenna, whereas the down-looking one is a dual-band (L1, L2) dual-polarization 3x2 patch antenna array. Table 2.3 shows a summary of the mission parameters and the payload properties.

2.6.4 CYGNSS

The CYGNSS mission is going to be the first exclusively dedicated GNSS-R mission for Earth Observation which will be launched in November, 2016. It consists of 8 small satellites that will receive both direct and reflected GPS signals. The mission will study several parameters, but its main goal is to retrieve wind maps using GNSS-R technology with satellites passing over the same region every 12 minutes. This is breaking out the revisit time currently found in spaceborne scatterometers. The products derived from the CYGNSS mission will be joined to the United States of America (USA) hurricane monitoring systems in order to predict better their behavior. Figure 2.11 shows an example of the wind maps that will be generated from the CYGNSS data, where a particular example of monitoring a hurricane can be easily identified due to the high winds. Therein,

Table 2.3: Intended $^3Cat-2$ mission parameters [80–82, 84–87].

Sensor Parameter	**Magnitude**
Orbit Height	510 km
Orbit Type	Sun-Synchronous
Revisit time	12 days
Frequency Bands	L1 and L2
Sampling frequency	5 MHz, 8 bits I/Q
Up-looking antenna polarization	LHCP and RHCP
Down-looking antenna polarization	LHCP and RHCP
Down-looking Antenna Gain	$\sim$ 13 dBiC at L1 and $\sim$ 11.6 dBiC at L2
Delay-Resolution	NA ns
Doppler-Resolution	NA Hz
Coherent integration time	NA ms
Incoherent integration time	NA s
Raw Data length	-

it is noticeable the effect of dealing with a non-imaging multistatic technique, where the developed products are a series of ground-tracks that require interpolation in order to convert them to an image. Table 2.4 shows a summary of the proposed CYGNSS mission parameters. The reflected antenna has 1 dBi more gain than the UK TDS-1 and consists of a 2x3 patch antenna array. Recall that most of the GNSS-R payload parameters are the same as in the UK TDS-1 mission because they use the same receiver. Note that the orbit's inclination is 35°, which will have some limitations in the mapping capabilities because only the tropical part of the Earth will be covered. This can be seen in Fig. 2.13, but it has no effects on the hurricane monitoring applications because it is where they appear.

2.6.5 PARIS-IOD and GEROS-ISS

Differently from previous GNSS-R missions which exploited the cGNSS-R technique, the PARIS-IOD mission was proposed following the PARIS concept, and consequently exploiting the iGNSS-R technique. Due to the degradation of the SNR of the iGNSS-R vs the cGNSS-R technique, one important requirement was the increase of the antenna size, as directivity should be increased, which led to a steerable dual-frequency multi-beam antenna array. ESA sponsored the phase A studies for the PARIS-IOD mission. Figure 2.14 shows an artist view of the PARIS-IOD proposed satellite.

After that, ESA sponsored the phase A study of the GEROS-ISS proposal [90, 91], which included the PARIS-IOD studies among other GNSS-Radio Occultations (GNSS-RO) applications. GNSS-RO are techniques based on sensing the transmitted GNSS signal when there is no Line Of Sight (LOS) between receiver and transmitter, but the RF signal reaches the receiver because the ionosphere and the atmosphere curve the RF signal path. At the time of writing this PhD Thesis dissertation, the phase A of the GEROS-ISS has just finished and ESA has given an internal go-ahead for phase B activities. However, part of the system parameters are yet to be determined. Conversely, what it is known is

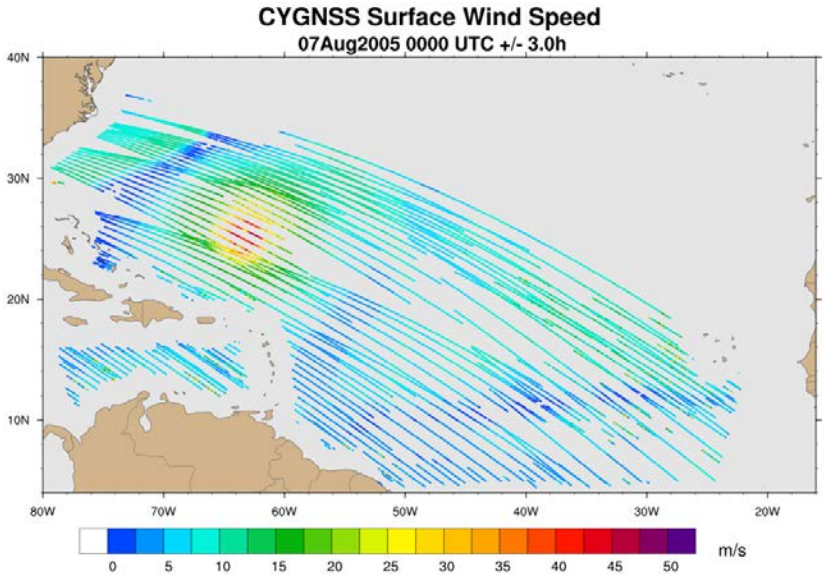

Figure 2.11: Example of CYGNSS product. [Source: `http://earthobservatory.nasa.gov/blogs/fromthefield/category/cygnss/`]

Table 2.4: Intended CYGNSS mission parameters [88, 89].

Sensor Parameter	**Magnitude**
Orbit Height	510 km
Orbit Type	Circular
Number of satellites	8
Inclination	35°
Revisit time	4 hours (mean)
Frequency Band	L1/L2
Sampling frequency	16 MHz, 2 bits
Up-looking antenna polarization	RHCP
Down-looking antenna polarization	LHCP
Up-looking Antenna Gain	4 dBiC
Down-looking Antenna Gain	14 dBiC
Delay-Resolution	244 ns
Doppler-Resolution	500 Hz
Coherent integration time	1 ms
Incoherent integration time	1 s
Raw Data length	2.3 min (1 GB)
DDM Size	128x52 (Del-Dop), 8 bits

that its orbit will be the same than the ISS (375–435 km, 51.6° inclination, and 92 min period), and that the instrument will be placed on the Columbus upper limb balcony.

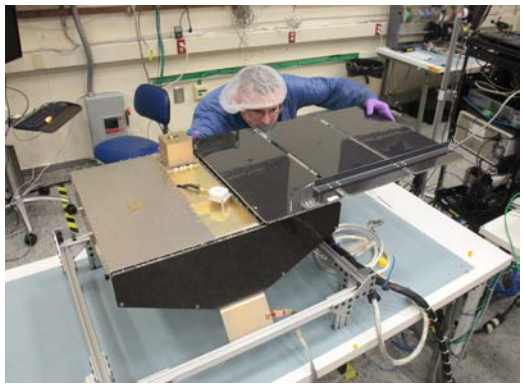

(a)

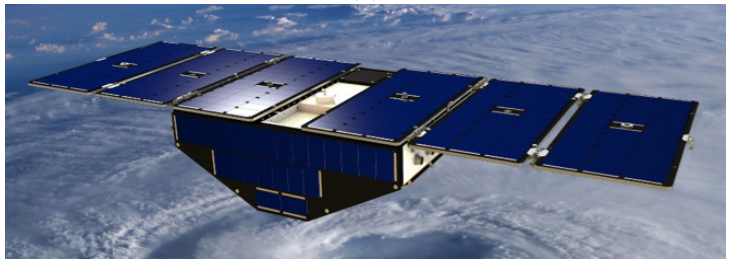

(b)

Figure 2.12: CYGNSS micro satellites overview: (a) Engineering model of CYGNSS satellite being constructed at the Southwest Research Institute. [Source: `http://earthobservatory.nasa.gov/blogs/fromthefield/category/cygnss/`], (b) Artistic view of the CYGNSS satellite on space [88].

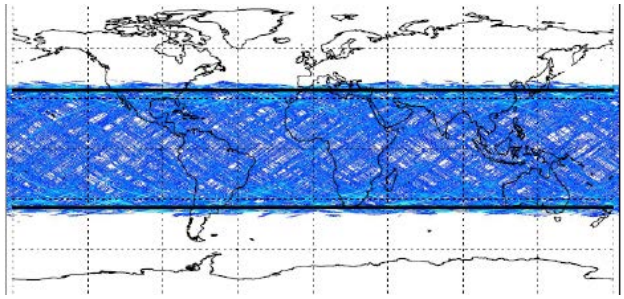

Figure 2.13: CYGNSS coverage map [88].

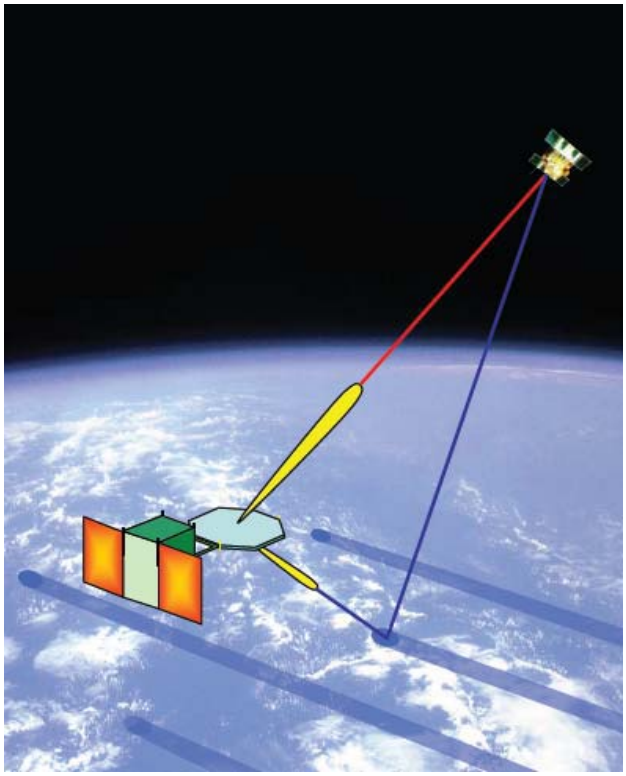

Figure 2.14: PARIS artist view [72].

3

Chapter 3

The Interference Pattern Technique

This chapter aims at giving an overview of one of the techniques used in this PhD Thesis dissertation for land and coastal sea monitoring. It starts with a theoretical background describing the used mathematical model used. A section explaining all previous developments achieved at UPC is added, which served as a base for the developments performed during this PhD Thesis. A similar technique known as the SNR-analysis is also shown emphasizing its differences with the conventional IPT. Finally, the developments and improvements performed along this PhD Thesis are summarized.

3.1 Reflection of a M-layer Interface and Fresnel Reflection Coefficients

The simplest reflection mechanism between two different media is shown in Fig. 3.1, when a plane EM wave traveling on a homogeneous medium impinges on another medium with different properties than the previous one with a flat interface between them. Figure 3.1 shows the reflection scheme where the separation between mediums is shown with a thick black line whereas its normal is shown with a thinner dashed line. The incidence (inc), reflected ($refl$), and transmitted ($trans$) angles, are always referred to the surface's normal. The media are generally characterized by their dielectric constant (ε_r), and their magnetic permeability (μ_r). As seen in Fig. 3.1, in the reflection process there is a part of the incident power transmitted to the other medium, and another one reflected. According to the specular reflection law, the reflected angle is the same than the incidence angle, and the transmitted angle satisfies Snell's law, which is shown in Eqn. (3.1), where $k_1 = \sqrt{\varepsilon_{r1}}$ and $k_2 = \sqrt{\varepsilon_{r2}}$ are the refraction index of media 1 and 2 respectively assuming a non-magnetic medium. Also, recall that EM radiation is polarized, so the incident electric and magnetic fields can be on the incidence plane, which is defined by the propagation vector or by the Poynting vector [92], they can be orthogonal to it, or they can be a linear a combination of both. Consequently, the incident electric field can be decomposed in two components, one component parallel to the incidence plane, and one component orthogonal/perpendicular to the incidence plane. The Fresnel reflection coefficient and the transmission coefficient for the parallel polarization are shown in Eqns. (3.2)–(3.3), respectively. The Fresnel reflection coefficient and the transmission coefficient for the perpendicular polarization are shown in Eqns. (3.4)–(3.5), respectively.

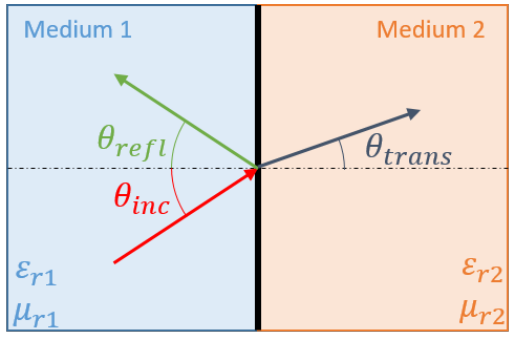

Figure 3.1: Two-layer interface simplest reflection mechanism.

$$k_1 \sin(\theta_{inc}) = k_2 \sin(\theta_{trans}), \tag{3.1}$$

$$r_{\parallel} = \frac{Z_2 \cos(\theta_{trans}) - Z_1 \cos(\theta_{inc})}{Z_2 \cos(\theta_{trans}) + Z_1 \cos(\theta_{inc})}, \tag{3.2}$$

$$t_{\parallel} = \frac{2Z_2 \cos(\theta_{inc})}{Z_2 \cos(\theta_{trans}) + Z_1 \cos(\theta_{inc})}, \tag{3.3}$$

$$r_{\perp} = \frac{Z_2 \cos(\theta_{inc}) - Z_1 \cos(\theta_{trans})}{Z_2 \cos(\theta_{inc}) + Z_1 \cos(\theta_{trans})}, \tag{3.4}$$

$$t_{\perp} = \frac{2Z_2\cos(\theta_{inc})}{Z_2\cos(\theta_{inc}) + Z_1\cos(\theta_{trans})}, \tag{3.5}$$

where Z_1 and Z_2 stand for the intrinsic impedance of media 1 and 2 respectively ($Z_i = \sqrt{\mu_i/\varepsilon_i}$), θ_{inc} for the incidence angle, and θ_{trans} for the transmitted angle.

However, polarization is expressed normally in its vertical and horizontal components, which corresponds to the parallel and perpendicular components, respectively. Also, the Fresnel reflection coefficients are normally given only as a function of the incidence angle, as the transmitted angle is related to the incidence one by Snell's law. So, after some mathematical manipulations (see Appendix B), Eqns. (3.2) and (3.4), become:

$$r_{\perp} = r_{HHi,i+1} = \frac{\sqrt{\varepsilon_{r_i} - \varepsilon_{r_i}\sin(\theta_{inc})^2} - \sqrt{\varepsilon_{r_{i+1}} - \varepsilon_{r_i}\sin(\theta_{inc})^2}}{\sqrt{\varepsilon_{r_i} - \varepsilon_{r_i}\sin(\theta_{inc})^2} + \sqrt{\varepsilon_{r_{i+1}} - \varepsilon_{r_i}\sin(\theta_{inc})^2}}, \tag{3.6}$$

$$r_{\parallel} = r_{VVi,i+1} = \frac{\varepsilon_{r_i}\sqrt{\varepsilon_{r_{i+1}} - \varepsilon_{r_i}\sin(\theta_{inc})^2} - \varepsilon_{r_{i+1}}\sqrt{\varepsilon_{r_i} - \varepsilon_{r_i}\sin(\theta_{inc})^2}}{\varepsilon_{r_i}\sqrt{\varepsilon_{r_{i+1}} - \varepsilon_{r_i}\sin(\theta_{inc})^2} + \varepsilon_{r_{i+1}}\sqrt{\varepsilon_{r_i} - \varepsilon_{r_i}\sin(\theta_{inc})^2}}, \tag{3.7}$$

where: r_{HH}, r_{VV} are the reflection coefficients for horizontal and vertical polarization respectively, and $\varepsilon_{r_{i,i+1}}$ are the dielectric constants of layer i and layer $i+1$ (in this case $i = 1$ and $i + 1 = 2$).

For circular polarization, such as RHCP, the one transmitted by GPS satellites, or Left Hand Circular Polarization (LHCP), the one in which the largest reflection takes place, the Fresnel reflection coefficients are a linear combination of the linear polarization reflection coefficients as follows [93]:

$$r_{RR} = r_{LL} = \frac{1}{2}\left(r_{VV} + r_{HH}\right), \tag{3.8}$$

$$r_{RL} = r_{LR} = \frac{1}{2}\left(r_{VV} - r_{HH}\right), \tag{3.9}$$

where RR stands for transmitted RHCP and received RHCP, LL for transmitted LHCP and received LHCP, RL for transmitted RHCP and received LHCP, and LR for transmitted LHCP and received RHCP.

The Fresnel reflection coefficients are generally complex values, and their effect is normally better seen by their reflectivity parameter, which is defined as the modulus square of the Fresnel reflection coefficient ($|r_{XX}|^2$). The reflectivity is the parameter that can be related to the power collected by an antenna, as the reflection coefficients are the coefficients that multiply the incident electric fields in order to obtain the reflected fields. Figure 3.2 shows the reflectivity values for the four different polarization states as a function of the soil moisture. There are several aspects to comment in this figure. The first one is the difference between the horizontal and vertical components. The horizontal component is monotonically increasing as a function of the incidence angle. The vertical is decreasing until it reaches a minimum amplitude point, known as the Brewster angle (Eqn. (3.10)), and then it starts to increase again. Note that the position of the Brewster angle depends on the soil moisture content, or the dielectric constant, as it can be deduced from Eqn. (3.10). As seen in Fig. 3.2(c), there is nearly no radiation for transmitted

RHCP and received RHCP unless the incidence angle is very slant. Conversely, most of the reflected radiation is LHCP as seen from Fig. 3.2(d), unless the incidence angle is very slant. Furthermore, the larger the dielectric constant, the larger the reflectivity for a given incidence angle for all polarization states except for the slant incidence angle zone for r_{VV} and r_{RR}. Wang's dielectric constant model has been used to relate soil moisture with dielectric constant in Fig. 3.2 [94], and their relationship is shown in Tab. 3.1.

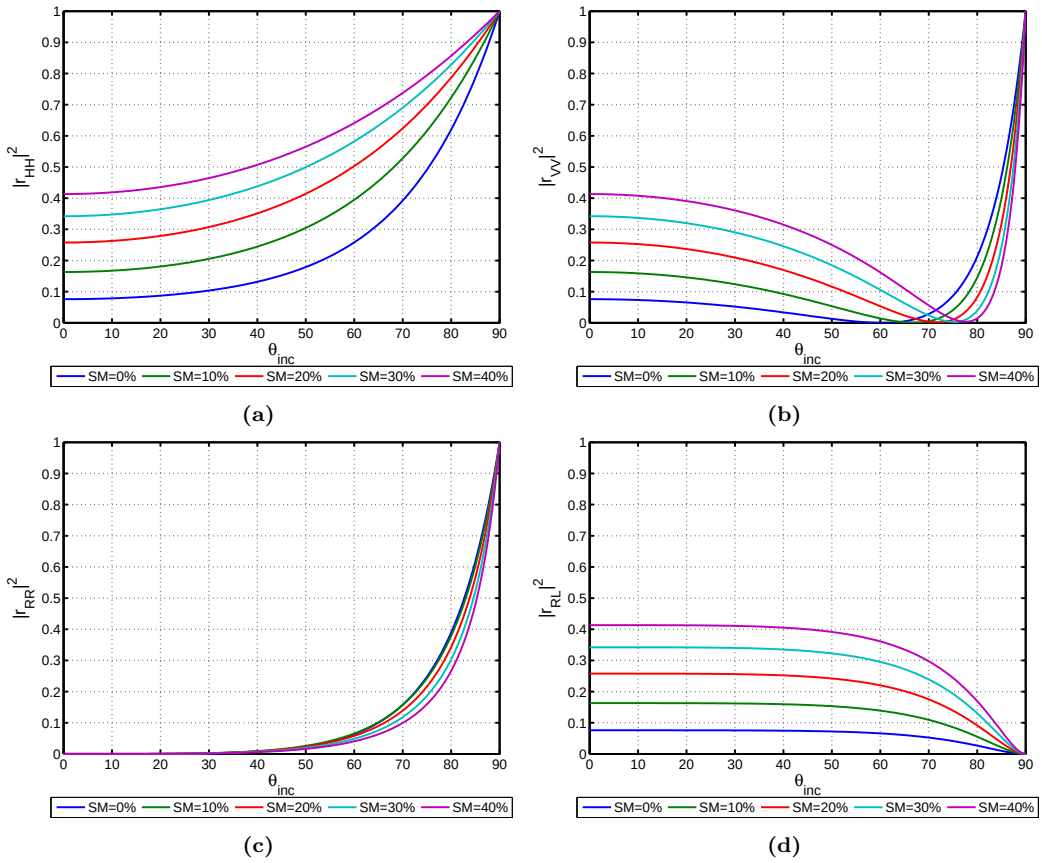

Figure 3.2: Reflectivity for the four different polarization states: (a) HH, (b) VV, (c) RR or LL, (d) RL or LR.

$$0 = \varepsilon_{ri+1}\sqrt{\varepsilon_{ri} - \varepsilon_{ri}\sin(\theta_B)^2} - \varepsilon_{ri}\sqrt{\varepsilon_{ri+1} - \varepsilon_{ri}\sin(\theta_B)^2} \rightarrow \theta_B = \arctan\left(\frac{k_2}{k_1}\right). \quad (3.10)$$

As previously mentioned, the reflection coefficient is a complex number which can be expressed by its modulus and its phase. For scatterometric applications, normally the modulus square or the reflectivity is used because scatterometers use power measurements. However, for one of the applications developed in this PhD Thesis it is necessary to look at their phase, at it has key implications. Figure 3.3 shows the reflection coefficient phase

Table 3.1: Soil Moisture and dielectric constant equivalence [94].

Soil Moisture	ε_r
0%	3.10 + j0.03
10%	5.47 + j0.70
20%	9.10 + j1.78
30%	13.99 + j3.26
40%	20.14 + j5.16

for the four aforementioned polarization states. Note that Fig. 3.3(a),(b),(d) follow the same phase pattern than the horizontal polarization coefficient. This occurs because the r_{HH} amplitude is larger than the r_{VV} amplitude, and when computing the phase it is the dominant term. Note that for those cases the phase is nearly constant. However, for vertical polarization the phase behavior is different. There is 180° difference between the horizontal and vertical polarization states except for slant incidence angles, where the phase gradually changes to be the same one for both polarization states. This explains why the transmitted polarization is RHCP and the reflected mainly LHCP, except for slant incidence angles where the main transmitted and received polarization is the same (see Fig. 3.2). Furthermore, the 90° phase shift for the vertical polarization corresponds to the Brewster angle position.

The reflection model proposed here is the simplest and oldest one (2-layer), and it has been extended to a M-layer reflection model in an iterative way following Eqn. (3.11) [95]:

$$r = \frac{r_{i,i+1} - r_{i+1,i+2}e^{-S}e^{j2\psi}}{1 - r_{i,i+1}r_{i+1,i+2}e^{-S}e^{j2\psi}}, \tag{3.11}$$

where:

$$\psi = \frac{2\pi\sqrt{\varepsilon_{ri+1}}}{\lambda}t_{i+1}\cos\left(\theta_{trans}\right) = \frac{2\pi}{\lambda}t_{i+1}\sqrt{\varepsilon_{ri+1} - \varepsilon_{ri}\sin^2\left(\theta_{inc}\right)}, \tag{3.12}$$

$$S = 8\left(\frac{\pi\sigma_l}{\lambda}\sqrt{\varepsilon_{ri+1} - \varepsilon_{ri}\sin^2\left(\theta_{inc}\right)}\right)^2, \tag{3.13}$$

t_{i+1} stands for the $i+1$ thickness layer, σ_l for the standard deviation of the roughness of the interface between layers, and S is the interface roughness correction factor.

In order to analyze the difference between the simple two-layer model and the M-layer model, a reflection coefficient simulator was developed. Figure 3.4 shows the simulator developed in Matlab. On the right hand side, the input parameters are found for up to 20 equally spaced layers. For each layer the soil moisture value must be specified. The soil composition, the thickness of the layers, the number of layers, and the surface roughness are specified in the first input parameters column. On the left hand side there are two graphs. The upper one shows the real part of the reflection coefficient and its reflectivity value for the horizontal and vertical polarization. The lower one shows the phase of the reflection coefficient for both polarization states.

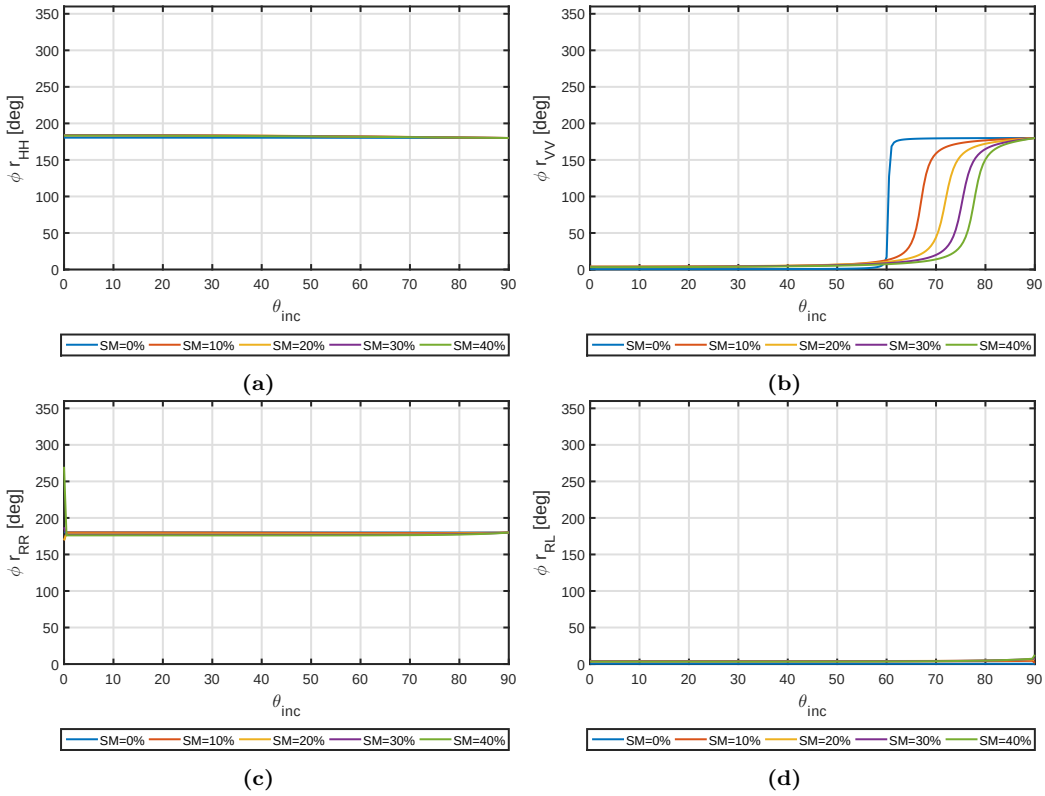

Figure 3.3: Phase of the reflection coefficients four different polarization states: (a) HH, (b) VV, (c) RR or LL, (d) RL or LR.

3.2 IPT Theoretical Overview

The IPT is defined by the pattern created due to coherent addition of the direct and reflected GNSS signals. In other words, the multi-path effect on the direct signal due to a reflection on its surroundings. Figure 3.5 shows the geometrical configuration of this technique. Therein, it is possible to identify the GPS satellite, the direct signal (black), the reflected signals (red), the reflection axes and the antenna reference frame (blue), the rough reflecting surface (black), and the antenna (black), either pointing to the horizon or pointing to the zenith. The antenna must be still, which means that the IPT is a static ground-based technique.

In a real case scenario, it is possible to assume to have an infinite number of scatterers. Since the GPS satellite is very far away, it is also possible to use the paraxial approximation within the far field approximation [96]. Consequently, the wavefront that reaches the receiver and the one that impinges on the ground are parallel. Furthermore, due to far-field approximation, the rays impinging the ground can be considered as a plane wave. Then, the contribution of each scatterer using its local scattering reference frame is taken into account at the antenna level. From the geometric configuration shown in Fig. 3.5 it is important to consider that h stands for the antenna height, θ_{inc} for the incidence angle

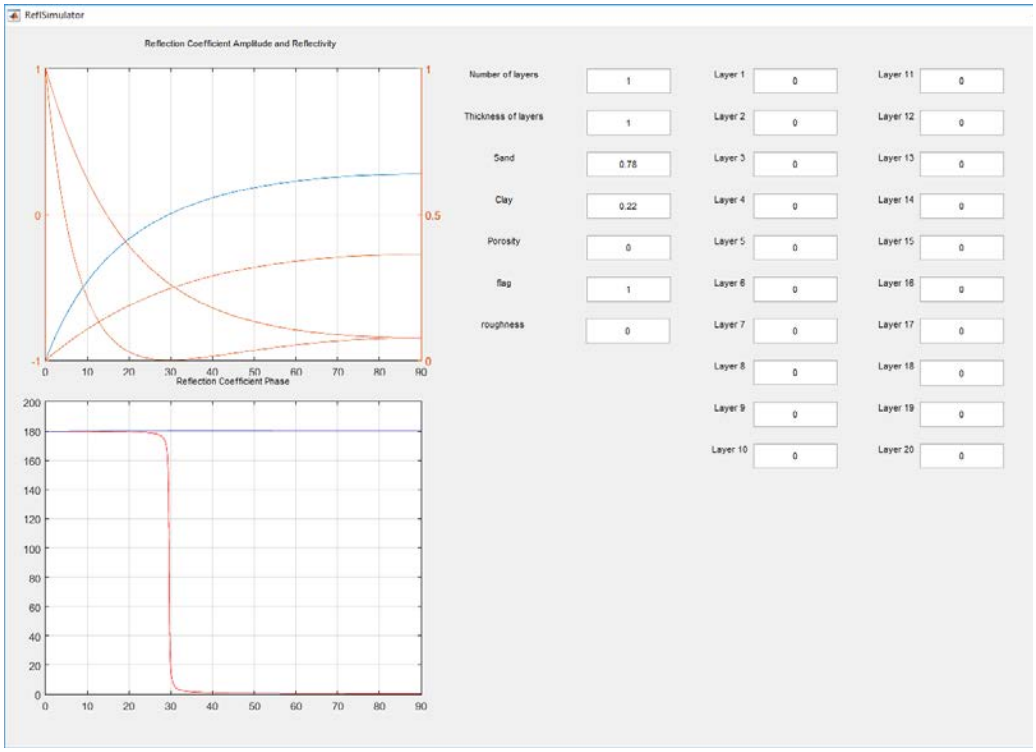

Figure 3.4: Reflection coefficient simulator for the M-layer model.

of the direct signal or $90 - \theta_{elev}$, where θ_{elev} is elevation angle of the GNSS satellite, θ_{inci} stands for the local scattering incidence angle of the ith scatterer, θ_{elevi} for the local scattering elevation angle of the ith scatterer, and σ_{rms} for the surface roughness parameter that characterizes the reflecting surface. Using the notation introduced in Chap. 2, the IPT can be expressed as:

$$U_{IPT} = U_d + U_{rcoh} + U_{rincoh} \tag{3.14}$$

Each of the direct and reflected waves (both coherent and incoherent components) should be weighted by the voltage antenna pattern in order to mathematically express what a system like that would measure. Another way to understand/visualize the IPT is shown in Fig. 3.6, where the vectors for the direct, reflected (both coherent and incoherent), and the resultant U_{IPT} are shown in different colors. Since the GPS satellite moves, those vectors or phasors are rotating. In the case of the direct signal, the rotation speed of the vector is only due to the GPS satellite movement and the Earth's rotation (recall that the antenna is still). In the case of the coherent reflected signal, the rotation speed of the vector is due to the satellite movement, the Earth's rotation, and when comparing it to the direct signal it also depends on the antenna height. In the case of the reflected incoherent component, the phase is by definition random, but there is a rotation speed defined due to the correlation among samples. If samples are uncorrelated, then there is no rotation speed and the phase just changes randomly. This results in an interference

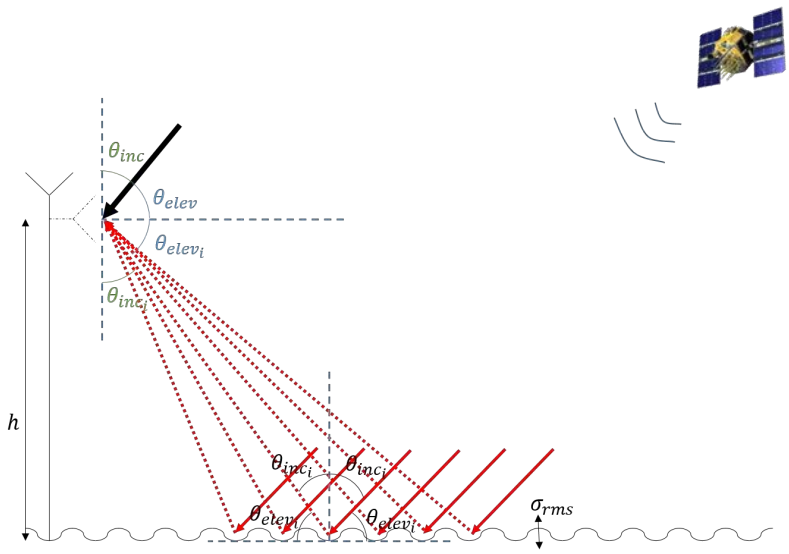

Figure 3.5: Geometrical configuration of the Interference Pattern Technique.

pattern vector rotating due to the movement of the GNSS satellite, and a fading effect that varies the interference pattern amplitude due to the multi-path contamination. This fading has two characteristics: one is that the coherent reflected signal will create a slow-time regular/semi-periodical fading, increasing its speed by increasing the antenna height, and the second one is a fast-time random fading due to the non-coherent component or *speckle*. Surface roughness and surface correlation time and length will determine the fading characteristics.

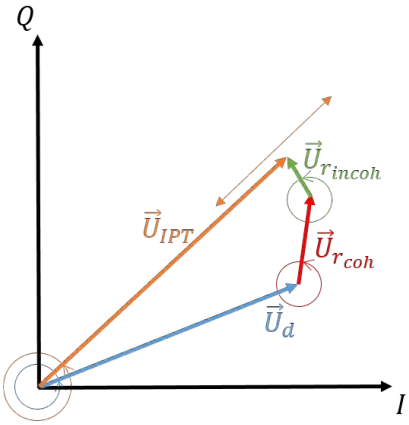

Figure 3.6: Vectorial notation of the Interference Pattern Technique.

From now on the case where an antenna is looking to the horizon is considered, which is the one used in the experiments performed along this PhD Thesis, and the zenith

looking antenna case, which is also known as the SNR-analysis, is left for Sec. 3.4.

3.2.1 Coherent IPT Model

The IPT model previously introduced in Eqn. (3.14) can be also expressed as [97]:

$$P_R \propto |U_{IPT}|^2 = |U_d + U_{rcoh} + U_{rincoh}|^2 = |U_{d_0}|^2 \cdot \left| F_n(\theta_{elev}, \phi_{elev}) + \right. \\ \left. + \sum_{m=1}^{M} F_n(\theta_m, \phi_m) A_m e^{j\Phi_m} e^{j\frac{4\pi h_m}{\lambda}\sin(\theta_m)} \right|^2, \tag{3.15}$$

where, P_R is the received power pattern, U_d the incident electric field, U_{rcoh} and U_{rincoh} the coherent and incoherent components of the reflected field over many scatterers, U_{d_0} the incident electric field amplitude, F_n the antenna radiation pattern, θ_{elev} and ϕ_{elev} the elevation and azimuth of the GNSS satellite respectively, λ the wavelength (i.e. 19 cm for GPS L1-Band), m the scatterer's index, M the total number of scatterers, θ_m and ϕ_m are the local elevation and azimuth angles of the mth scatterer, A_m is the m^{th} scatterer equivalent reflection coefficient amplitude, and Φ_m the m^{th} scatterer phase. So, the term $F_n(\theta_{elev}, \phi_{elev})$ is related to the direct signal whereas the term $\sum_{m=1}^{M} F_n(\theta_m, \phi_m) A_m e^{j\Phi_m} e^{j\frac{4\pi h_m}{\lambda}\sin(\theta_m)}$ is related to the reflected signal. In the reflected signal, the term $e^{j\frac{4\pi h_m}{\lambda}\sin(\theta_m)}$ is due to the extra path traveled by the signal reflected over the mth scatterer with respect to the direct signal, whereas $F_n(\theta_m, \phi_m)$ is related to the antenna pattern, and $A_m e^{j\Phi_m}$ is related to the surface conditions. In terrains such as snow, lakes, or bare-soil, the reflection can be considered specular [21, 40, 98], which simplifies the whole reflected term to $|r_{pq}(\theta, \phi)|e^{j\phi_{r_{pq}}}$, where r_{pq} is the Fresnel reflection coefficient and $\phi_{r_{pq}}$ is its phase at the specular reflection point. If the scattering surface is the sea, the result of the reflected signal term depends strongly on the incidence angle and the sea surface conditions, which define if the reflection is dominated by the specular component (calm sea) or by the diffuse one (rough sea).

In order to define Eqn. (3.15) the following assumptions have been made:

1. The height of the antenna is sufficiently small so $R_d \approx |\vec{R}_t| + |\vec{R}_r|$ for any reflection point (Fig. 2.6).
2. The height of the antenna is sufficiently small so the codes for the direct and reflected signals add up in phase. In other words, the delay between the reflected and direct signal is smaller than 150 meters for the GPS C/A code.
3. The receiver and the surface are not moving, so the Doppler shift on the direct and reflected signals is the same (Eqns. (2.3) and (2.5)).
4. $|\vec{R}_t| + |\vec{R}_r| - R_d \approx 2h_m \sin(\theta_m)$. This has a consequence on the signal's phase, but in terms of the signal's amplitude it is negligible, because this distance is some meters whereas $|\vec{R}_t| + |\vec{R}_r|$ and R_d are thousands of kilometers.
5. The antenna is pointing to the horizon with a rotationally symmetric pattern.
6. The addition of the coherent and incoherent reflected fields can be expressed as a sum of the contributions from all the scatterers. When the coherent scattering

mechanism dominates, the situation is equivalent to having just one scatterer. When the incoherent scattering dominates the modulus of the red vector in Fig. 3.6 is 0, and only a random field is present [69].

When the oscillation is random, or the incoherent scattering dominates, there is no useful information on the IPT, since the only observable available is the amplitude of the direct signal with a fast-fading presence. However, when the coherent scattering dominates, the reflected field can be expressed in terms of the direct field and the Fresnel reflection coefficient, as could be deduced from Eqn. (2.4). Consequently, taking into account the aforementioned assumptions, the coherent IPT is given by (see Appendix B.3):

$$P_R \propto |F_n(\theta_{elev})|^2 \cdot |U_{d_0}|^2 \cdot \left|1 + |r_{pq}(\theta_{elev}, \varepsilon_r)| e^{j(\Delta\phi(\theta_{elev}) + \phi_{r_{pq}}(\theta_{elev}, \varepsilon_r))}\right|^2, \tag{3.16}$$

where $\Delta\phi(\theta_{elev}) = e^{j\frac{4\pi h}{\lambda}\sin(\theta_{elev})}$. Note that since the antenna is pointing to the horizon and its radiation pattern is rotationally symmetric, the radiation pattern term can be taken as a common factor out of the coherent interaction between direct and reflected signals. Also note that there are some terms that depend only on the geometry, such as $\Delta\phi(\theta_{elev})$, and others that depend on the geometry and the terrain geophysical properties (ε_r).

In the next sections the effect of the following different aspects on the coherent IPT model is analyzed:

- Dielectric Constant.
- Polarization.
- Antenna Height.
- Topography.
- Surface Roughness.

3.2.2 Effect of Dielectric Constant on the IPT

As it was seen on Sec. 3.1, the larger the soil moisture content, the larger the dielectric constant, and the larger the reflectivity. This is shown in Fig. 3.7 for horizontal polarization and in Fig. 3.8 for vertical polarization. In Fig. 3.7 it is possible to see two interference patterns simulated for an antenna height of 2 m and two different soil moisture content values using the information provided in Tab. 3.1. Therein, it is possible to see that the larger the reflectivity, the larger the amplitude of the oscillation fringes on the IPT. As it can be seen, they follow the shape of the reflectivity curve which is plotted on the same figure in green. On the other hand, Fig. 3.8 shows the IPT for the same conditions that Fig. 3.7, but for vertical polarization. Herein, the envelope of the IPT, or the amplitude of the oscillation fringes also follows the vertical polarization reflectivity shape. Recall that the vertical polarization reflection coefficient did not behave as the horizontal one due to the Brewster angle presence. On the vertical polarization IPT, the presence of the Brewster angle is seen as a minimum amplitude point on the oscillation fringes of the IPT. This point is also called a "notch". Note that its position varies as a function of the soil moisture content, which means that it is dielectric constant dependent,

which was previously shown in Sec. 3.1.

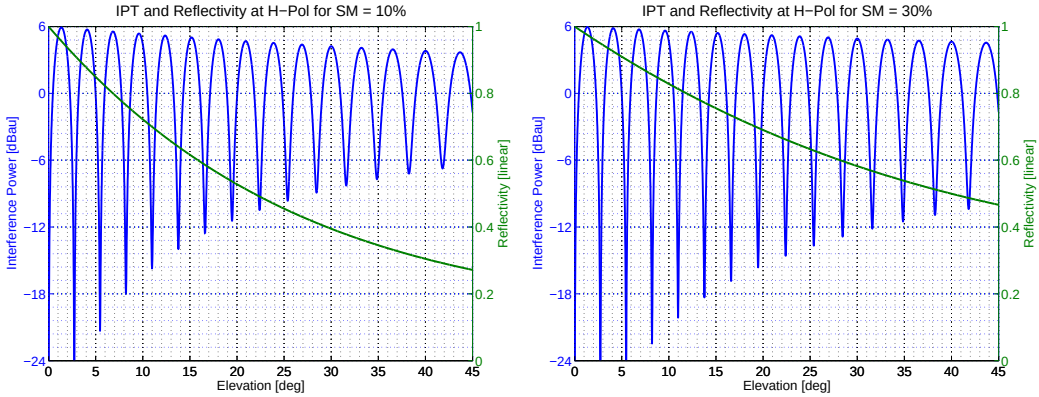

Figure 3.7: Dielectric constant effect on the H-Pol Interference Pattern: (a) SM = 10%, (b) SM = 30%.

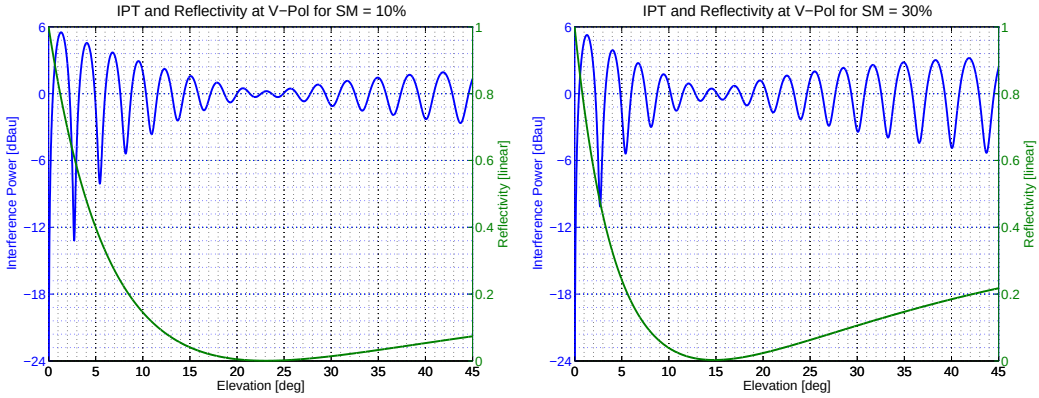

Figure 3.8: Dielectric constant effect on the V-Pol Interference Pattern: (a) SM = 10%, (b) SM = 30%.

3.2.3 Effect of Polarization on the IPT

The vertical polarization interference pattern shows the Brewster angle effect, which does not occur at horizontal polarization. This is one of the differences in both interference patterns that depends on polarization. However, it is not the only one. Figure 3.9 shows the polarization effects on the H- and V-Pol interference patterns. Therein, the Brewster angle is clearly identified. Furthermore, note that before the Brewster angle, both H- and V-Pol interference patterns are in phase, which means that maxima amplitude points on the H-Pol IPT are coincident with maxima amplitude points on the V-Pol IPT.

Conversely, after the Brewster angle position, maxima amplitude points on the H-Pol IPT are coincident with minima amplitude points on the V-Pol IPT, and vice versa. This is related to the reflection coefficient phase curves presented in Sec. 3.1 (Fig. 3.3(a)–(b)). For the low elevation angles, the phase of both reflection coefficients is the same, whereas for elevation angles larger than the Brewster angle, their phase is opposite and it is reflected on the interference patterns. This is the reason why the term $\phi_{rpq}(\theta_{elev}, \varepsilon_r)$ on Eqn. (3.16) was added to the previous theoretical model available from [21]. Also, in Fig. 3.9 the phase of the V-Pol reflection coefficient has been added, and one may note that the minimum amplitude point or Brewster angle position occurs for the 90° phase shift.

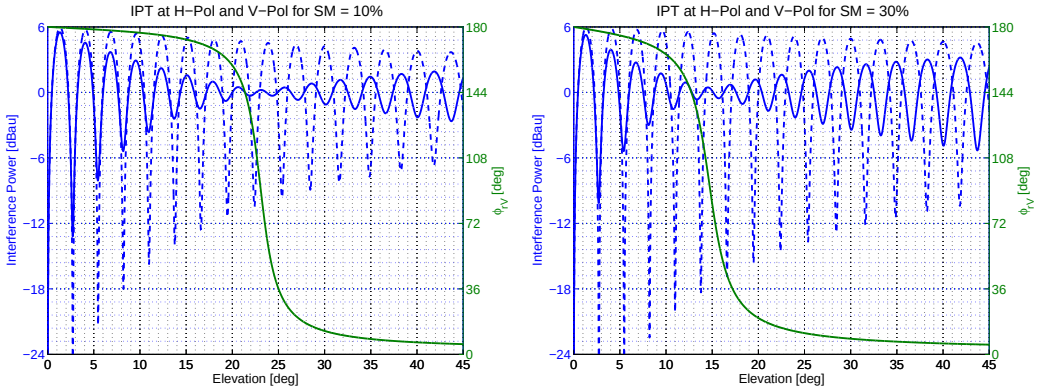

(a) **(b)**

Figure 3.9: Polarization effect on the H-Pol (blue dashed) and V-Pol (blue solid) Interference Pattern: (a) SM = 10%, (b) SM = 30%. The phase of the V-Pol reflection coefficient is shown in green.

3.2.4 Effect of Antenna Height on the IPT

In the IPT equation the only term that varies when varying the antenna height is the rotating phasor $\Delta\phi$ which is the one that determines the oscillation frequency that is produced due to the satellite movement. Figures 3.10–3.11 show the effect of changing the antenna height on the interference pattern. Basically, the lower the height, the lower the speed of the oscillation fringes and vice versa. The envelope of the oscillation fringes does not change due to the height and it follows the one determined by the reflection coefficients. It is also independent from polarization, a priori. Note that, the h parameter corresponds to the addition of the physical height of the antenna and the penetration depth of the EM wave, and not only the antenna physical height. For surfaces in which the penetration depth is different for H- and V-Pol, the h parameter should be separated in its two parameters ($h_{phys} + h_{depth}$). In those cases, the oscillation frequency will not be exactly the same for both polarization states. If the penetration depth is assumed to be the same, as it was done in Figs. 3.10–3.11, then the oscillation frequency will be the same.

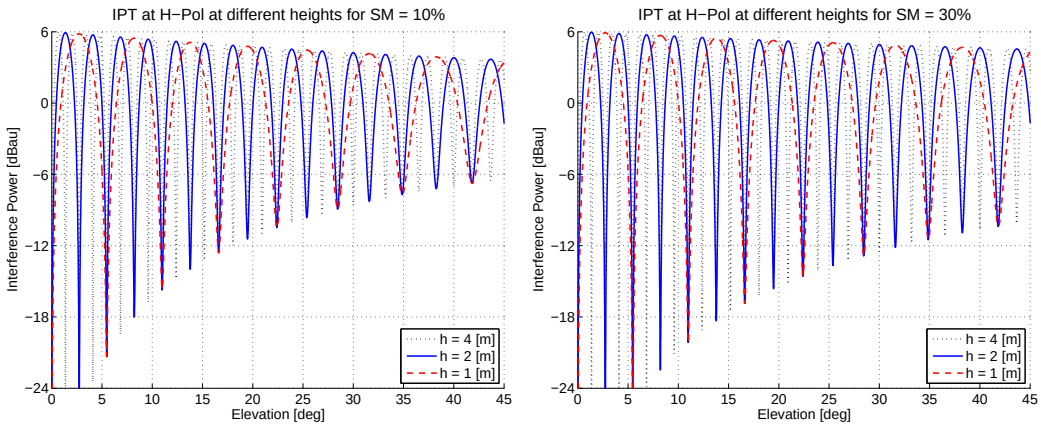

Figure 3.10: Height effect on the H-Pol Interference Pattern: (a) SM = 10%, (b) SM = 30%.

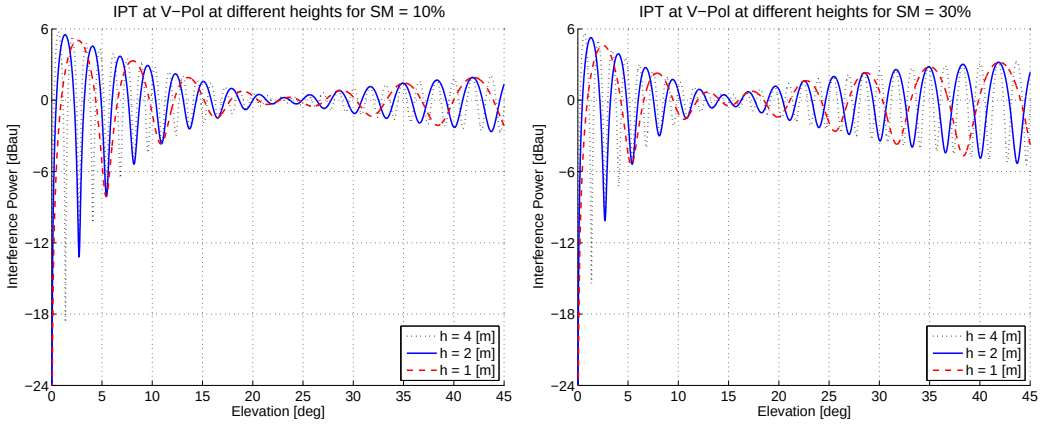

Figure 3.11: Height effect on the V-Pol Interference Pattern: (a) SM = 10%, (b) SM = 30%.

3.2.5 Effect of Topography on the IPT

If the height is not constant, this will create two effects on the interference pattern. The first one is a change in the geometry of observation, and the assumption that $\theta_{inc} = 90 - \theta_{elev}$ does not hold anymore. Specular reflection conditions must be applied to find the new θ_{inc} that matches each θ_{elev}. Apart from that, the oscillation frequency will change according to the distance of the antenna phase center to the floor. The larger the distance the faster the oscillation frequency and vice versa. This change in the oscillation frequency is shown in Figs. 3.12–3.13 for horizontal and vertical polarization, respectively, and for two different soil moisture values. Topography in Figs. 3.12–3.13 is represented

as the distance from the antenna to the floor. Remember that an elevation angle close to 0° corresponds to the furthest point, and close to 90° to the closest. Note that, the larger the distance between the antenna and the soil, the quicker the oscillation frequency of the interference pattern.

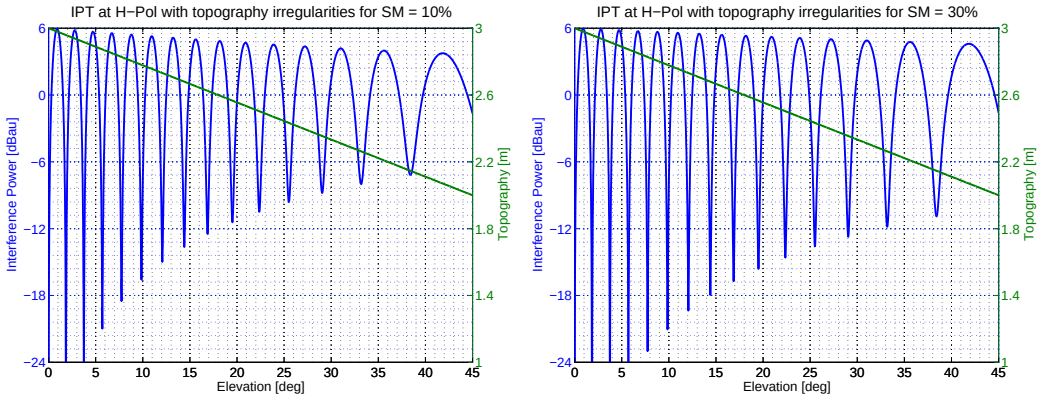

Figure 3.12: Topography effect on the H-Pol Interference Pattern: (a) SM = 10%, (b) SM = 30%.

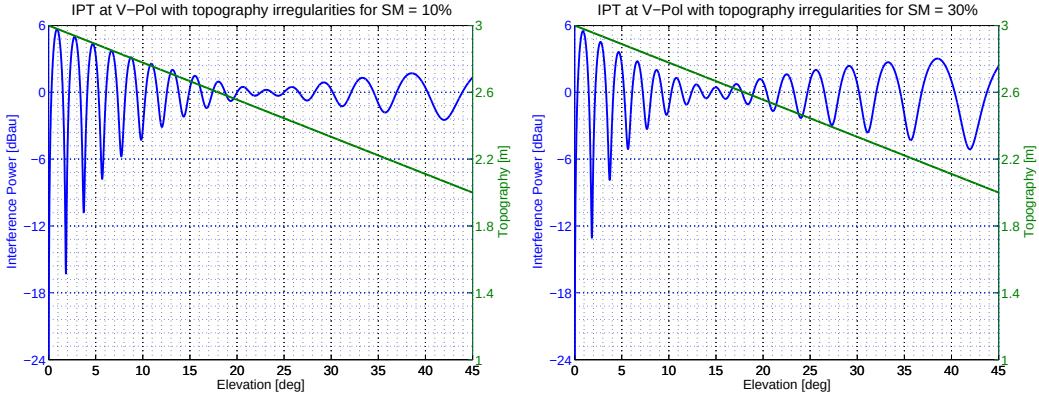

Figure 3.13: Topography effect on the V-Pol Interference Pattern: (a) SM = 10%, (b) SM = 30%.

3.2.6 Effect of Surface Roughness on the IPT

A surface without topography, an antenna height of 2 meters, and some roughness in the scattering interface are assumed in order to analyze the effect of a rough surface on the interference patterns. The physical optics reflection model has been taken into account multiplying the reflection coefficients by the so called Rayleigh attenuation parameter

($e^{-2k^2\sigma^2\cos^2(\theta_{inc})}$) [71]. This parameter is similar to the S parameter defined in Eqn. (3.13), and should be added to the IPT coherent equation (Eqn. (3.16)). However, the $\cos^2(\theta_{inc})$ function tends to 0 for the elevation angle range used in the IPT. This means that for grazing angles, the surface roughness does not have nearly any effect, whereas when the incidence angle decreases or the elevation angle increases the coherent reflected component decreases. Even though this effect was minimal in the field experiments, it has been described in Figs. 3.14–3.15: when the elevation angle increases, the amplitude of the interference pattern decreases quicker for H-Pol than without roughness, and increases less after the Brewster angle position for V-Pol. This might have some effects in the detection of the Brewster angle position as the amplitude of the V-Pol interference pattern reduces significantly. The model used here to simulate the surface roughness effect is the one that corresponds to the solution of the reflected signal using the Physical Optics (PO) approximation, but experimental evidence has shown that, at L-band, the attenuation is lower than the one predicted by the PO model [99]. This is justified by the two-scale scattering model, and it results that L-band is sensitive to the relatively large scale roughness [100].

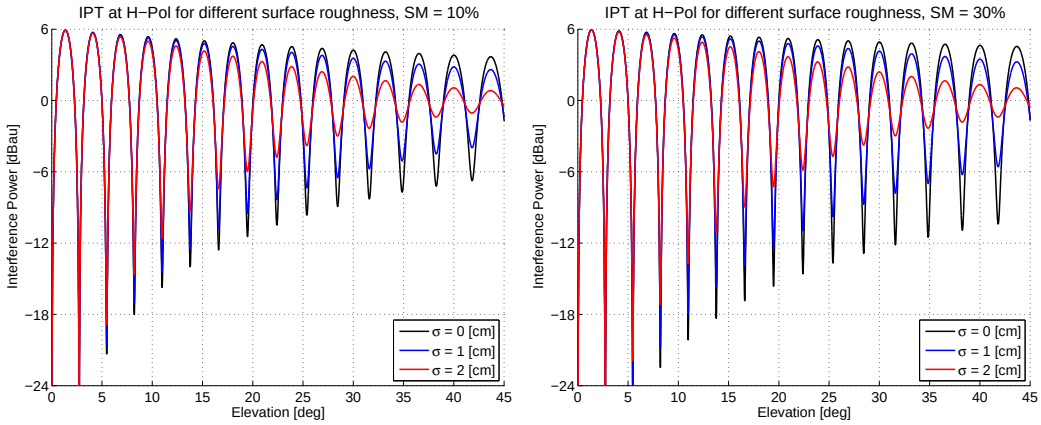

Figure 3.14: Surface roughness effect on the H-Pol Interference Pattern: (a) SM = 10%, (b) SM = 30%.

Another effect that has not been commented is that, with increasing roughness, apart from decreasing the coherent reflected component, the incoherent scattered component will increase in comparison to the coherent one. This will add some noise to the experimentally measured interference patterns, and they will be different from the clean ones shown here, which are based on the pure coherent model. It must also be mentioned that for the experiments performed during this PhD thesis land could be considered smooth (without roughness) (see Chapter 6), whereas the coastal sea experiment provided evidence of the roughness effects (Chapter 7). Furthermore, the presence of roughness has been measured and used to extract more information about the surface under observation.

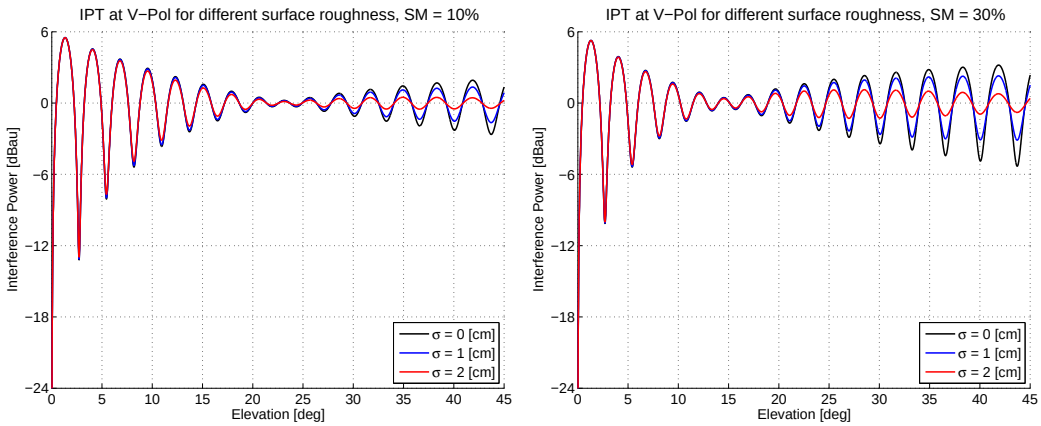

(a) **(b)**

Figure 3.15: Surface roughness effect on the V-Pol Interference Pattern: (a) SM = 10%, (b) SM = 30%.

3.3 The IPT Background

The beginning of the GNSS-R IPT goes back to 1996 when Kenneth D. Anderson asked to patent a methodology to remotely determine sea surface roughness and wind speed over a water surface [67]. It was based on sensing the amplitude of the interference pattern. The lower the amplitude of the oscillations, the larger the surface roughness, and consequently the larger the wind-speed. Therein, the interference pattern is compared to an older technique known as Lloyd's Mirror [101], which dates from 1834. However, only a theoretical overview of the technique is given since no experimental evidence appears demonstrating its performance. Furthermore, no information about the antenna pointing direction or the polarization used was provided.

A little bit later, during 1996-1998, A. Kavak et al. [66, 102] proposed the first IPT model using GNSS signals, justifying the specular reflection approximation and demonstrating it experimentally. Kavak used for the first time, a horizontally pointing looking antenna instead of a zenith looking antenna, but RHCP polarized, just like the transmitted GNSS signals. Also amplitude information on the interference pattern was used to determine the surface dielectric constant. Kavak performed his experiments over three different surfaces: grass ($\varepsilon_r = 3.7$), asphalt ($\varepsilon_r = 1.5$), and water ($\varepsilon_r \sim 81$). In his results it was shown, as expected, that the oscillations from a water surface were larger than for grass, and at the same time, those two larger than for asphalt (as it could be previously seen on Figs. 3.7–3.8). However, surface roughness and polarization effects were a little bit unclear, as a RHCP antenna rejects the reflected LHCP since it is its cross-polar polarization. Whether the reflection polarization is mostly RHCP or LHCP depends on the Brewster angle position, which at the same time depends on the dielectric constant. This means that data interpretation is not so straightforward for circular polarization.

In 2000, again Keneth D. Anderson proposed the use of the IPT to measure sea surface level and tides. In this case, instead of measuring the amplitude of the interference

pattern, the main interest was to measure the relative height between the surface and the antenna. This can be translated to a mean surface level estimation referred to the antenna reference frame, which can be translated to any reference frame by compensating the offset due to the antenna height. The methodology to measure accurately the height was basically correlate the measured interference pattern with simulated ones for different heights (h) (Figs. 3.10–3.11). Again circularly polarized antennas were used, and the results obtained compared to the ones from buoys. The variation of the estimated mean sea surface level can be seen as measuring sea tides, developing what is known as the first GPS tide gauge.

The IPT was not used anymore until 2007/2008 when two different independent research groups started to use this technique again for the retrieval of different geophysical parameters. The UPC research group decided to use the conventional IPT approach with a linear-polarized horizon/horizontal-looking antenna. The CU research group decided to take profit of the data provided by the geodetic GPS networks, which are based on zenith-looking antennas since many applications of those networks are related to improve the positioning accuracy and to GNSS atmospheric remote sensing applications. The latter geometrical configuration was renamed as the SNR-analysis because it relied on processing the SNR (or C/N0) pattern collected by these geodetic receivers. This section continues with an overview of the IPT developments at UPC.

3.3.1 IPT developments at UPC

The use of the IPT at UPC started with the research developed by N. Rodriguez-Alvarez in her PhD Thesis [28]. Differently from previous attempts, it was decided to use linear polarization antennas, and in particular vertical polarization. The first application developed was the measurement of the soil moisture content by sensing the minimum amplitude point or "notch" of the vertical polarization interference pattern. Figure 3.16 shows the V-Pol interference pattern for three different satellites (10, 15, and 26), and two different days (August 22, 2008 and September 25, 2008). Therein, it is possible to see that in the first row, which corresponds to August 22, the Brewster angle position is located between 22°–26°. The difference between satellites can be due to inhomogeneities in the soil moisture content, as each satellite reflects on a different soil part. The second row shows the V-Pol interference patterns for the same satellites on September 25. Therein, the Brewster angle is located between 18°–20°, indicating an increase in the dielectric constant due to an increase in the soil moisture content. Note that, due to surface irregularities, the experimental interference patterns have some noise, but the coherent model works pretty well to explain those data. Furthermore, surface irregularities may sometimes difficult the detection of the notch, as may happen with satellite 26 on August 22 and satellites 15 and 26 on September 25.

After estimating the soil moisture content by the Brewster angle detection and inversion, the oscillation frequency of the IPT was measured in order to obtain the topography of the surface under observation [103]. Each oscillation of the IPT was measured and the equivalent height computed. As GNSS satellites move, their signals are reflected in several surface points, and a map can be generated joining the height estimations for each oscillation and each satellite.

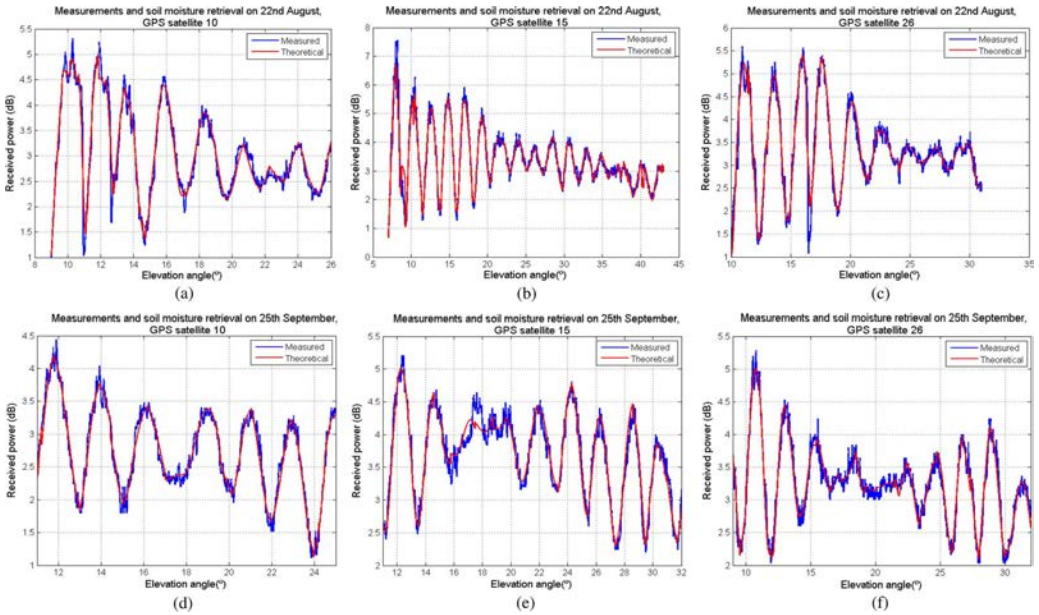

Figure 3.16: V-Pol interference patterns for three different satellites. First row corresponds to August 22nd 2008, and second row to September 25th 2008 [21].

Later, the IPT at V-Pol was tested over vegetated areas to infer some vegetation parameters apart from the soil moisture values [104, 105]. Figure 3.17 shows simulations of the IPTs at V-pol for different vegetation heights. In this case a 3-layer reflection model was used being the upper-layer the air, the mid-layer the vegetation, and the lower-layer the soil. In those situations, due to the reflection scenario, more than one notch appears, and their angular position can be related to the vegetation layer thickness/height. Figure 3.18 shows the reflectivity computed for different vegetation heights. Therein, it is straightforward to identify different notches, which will be detected in the IPT envelope too. Figure 3.19 shows the results for two different field campaigns where the vegetation height was estimated from the notch positions in the V-Pol interference pattern. In those field campaigns the vegetation observed was wheat. Figure 3.20 shows the results of the vegetation height estimation algorithm for a maize field, where the vegetation reached up to 3 m.

After developing three different land applications (soil moisture, topography, and vegetation height) [98], the research on the V-Pol IPT applications moved to its application over water surfaces following Anderson's oscillation frequency measurements. Figure 3.21 shows the experimental set-up with the SMIGOL instrument for that field experiment. Results showed centimeter precision in the measurement of the water level by averaging the results provided by each oscillation on the IPT [40]. Note that a reservoir is a very reflecting (water) flat surface, which is ideal for this kind of algorithms.

Finally, the research moved to the application of the V-Pol IPT to a surface covered by snow, in order to determine the snow level or snow depth, which is a parameter of interest in the avalanche risk prediction. In this case, a similar algorithm was developed

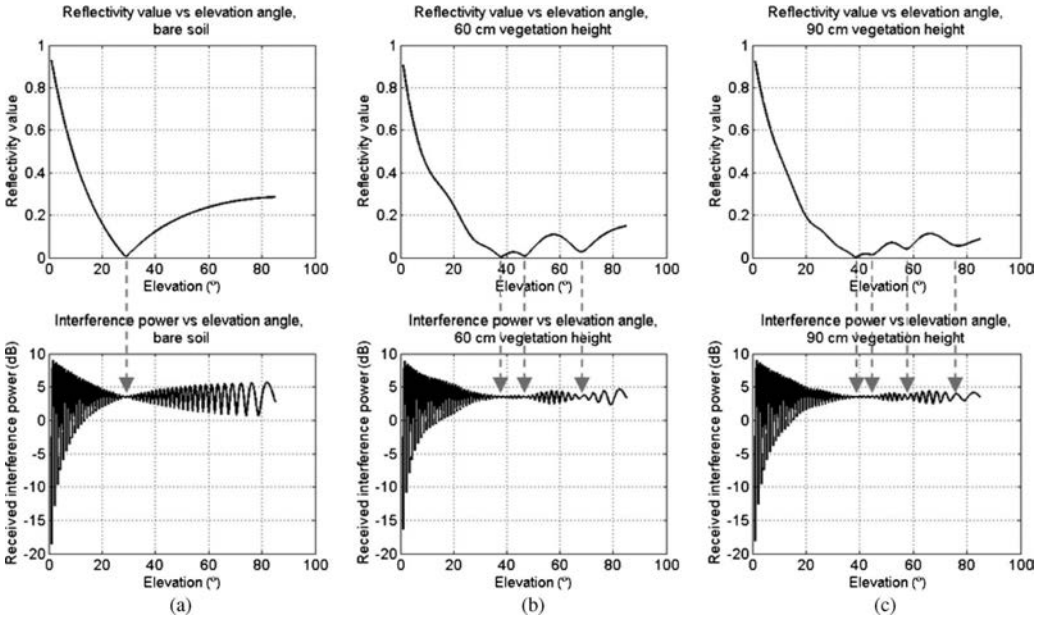

Figure 3.17: V-Pol interference patterns simulations for different vegetation heights [105].

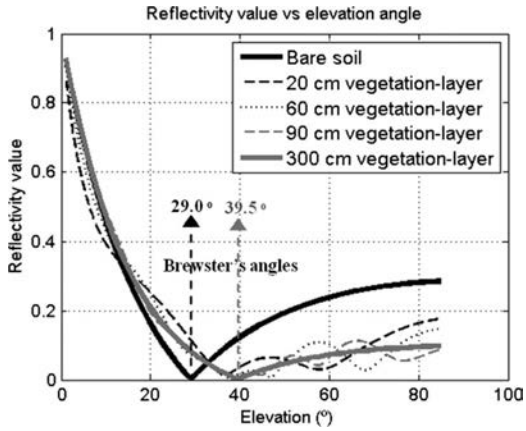

Figure 3.18: Reflectivity values at V-Pol for different vegetation heights [105].

dividing the reflection scenario in 3 different layers: air for the upper-layer, snow for the mid-layer, and soil for the lower-layer. As it occurred with the vegetation monitoring, more than one notch appears. In the vegetation sensing their number and positions were related to the vegetation height, and in the snow sensing they are related to the snow layer thickness, as it is shown in Fig. 3.22. Figures 3.23–3.24 show a summary of the snow sensing field campaign conducted on the Catalan Pyrenees.

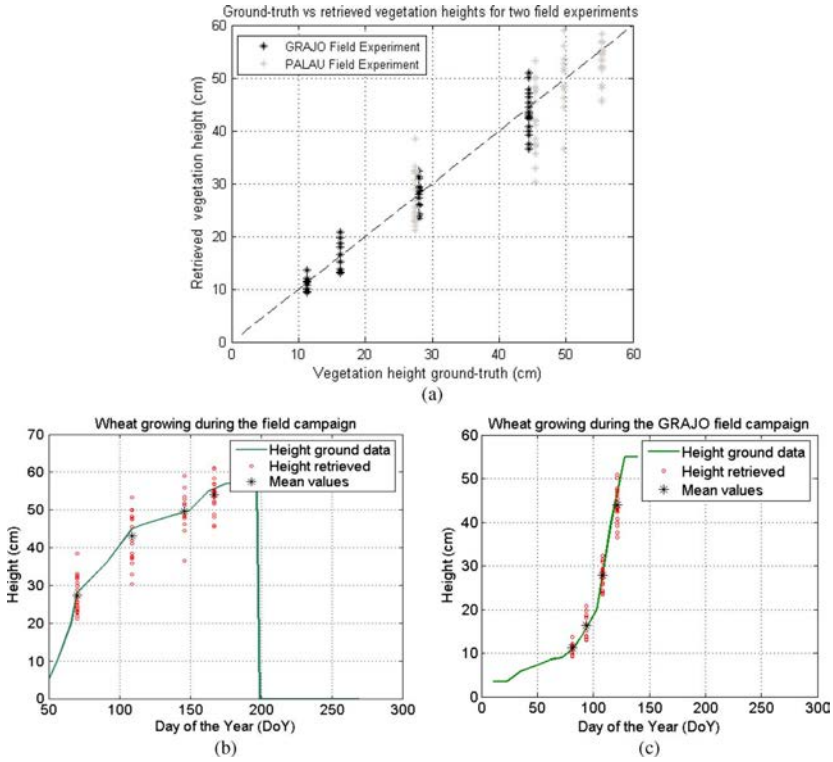

Figure 3.19: Vegetation height retrieved for two different field campaigns [105].

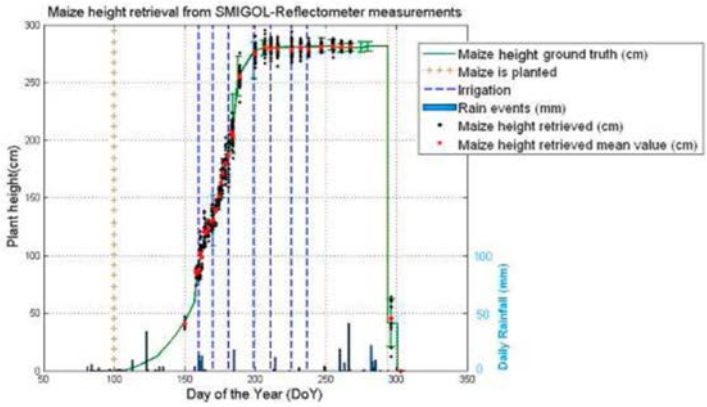

Figure 3.20: Vegetation height retrieved for growing season observing maize [98].

3.4 The SNR-analysis

The SNR-analysis is the technique followed by the CU research group. It is based on analyzing the multipath or interference pattern created on an antenna looking to the

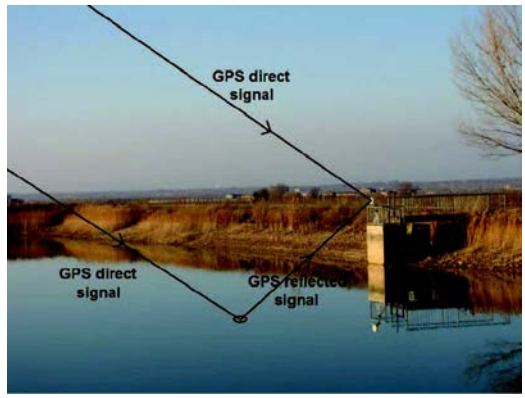

Figure 3.21: Experimental set-up of the water level measurement over reservoirs [40].

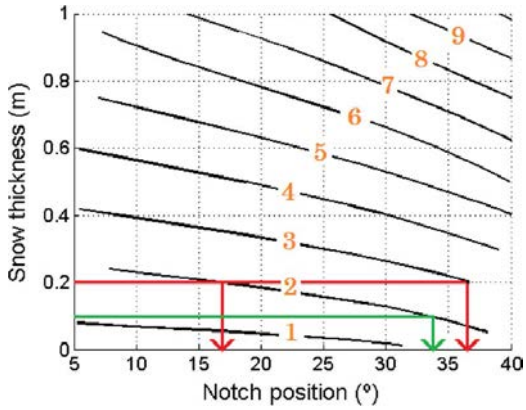

Figure 3.22: Notch positions as a function of snow thickness [106].

zenith. There are two main differences with respect to the IPT: the first one is that the antenna is looking to the zenith instead of to the horizon, and the second one is that it uses right hand circular polarized antennas instead of linear ones. Note that the multipath reflected polarization depends on the Brewster angle position. Sometimes the dominating polarization will be the RHCP, and sometimes it will be the LHCP. For instance, for sea scenarios it will always be LHCP as the Brewster angle occurs for θ_{elev} below 5°. So, there are some drawbacks found, such as not being sensitive to the Brewster angle (Fig. 3.2(c)–(d)), which is a good proxy for the dielectric constant determination. However, it has some advantages such as using commercial Off The Shelf (COTS) hardware without the need of designing and developing a dedicated hardware, such as the SMIGOL instrument. Furthermore, it can also use the data provided by the Plate Boundary Observatory (PBO) (Fig. 3.25) stations, which consists of more than 1.100 geodetic GPS stations. Despite not having the optimum geometric approach, the SNR-analysis can exploit a vast experimental opportunistic dataset. This is a great advantage as no economical investment is required to use this technique. Another network even bigger than the PBO is the Continuously Operating Reference Station (CORS)

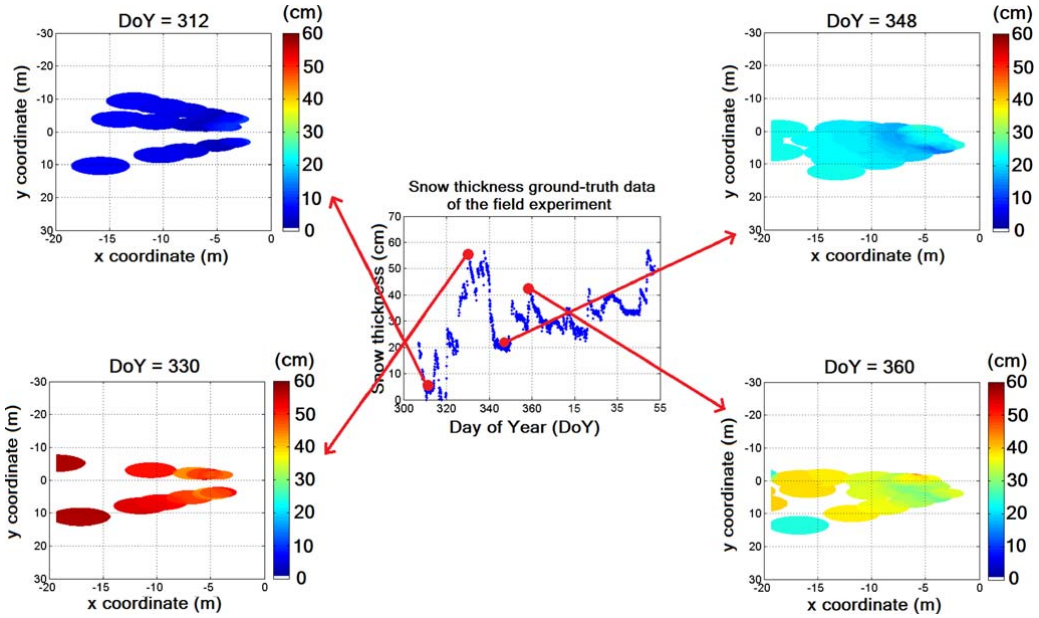

Figure 3.23: Snow growth summary [106].

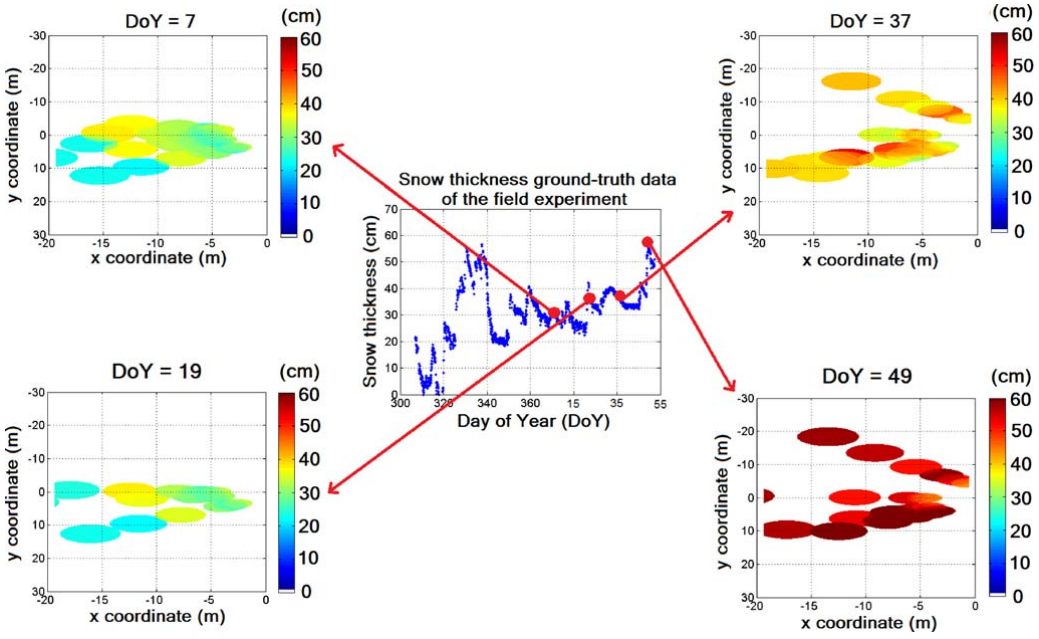

Figure 3.24: Snow monitoring summary [106].

network, owned and operated by the NOAA (Fig. 3.26).

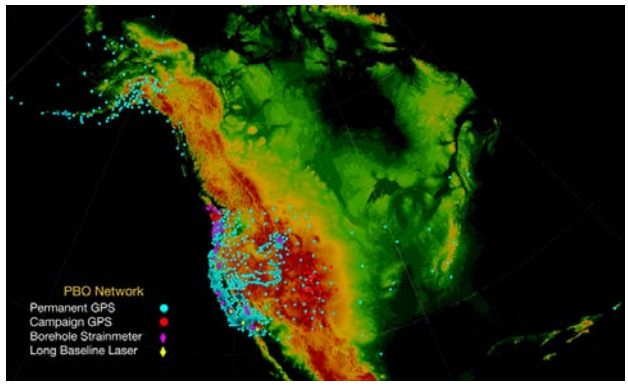

Figure 3.25: PBO network. Source: `http://pbo.unavco.org/`.

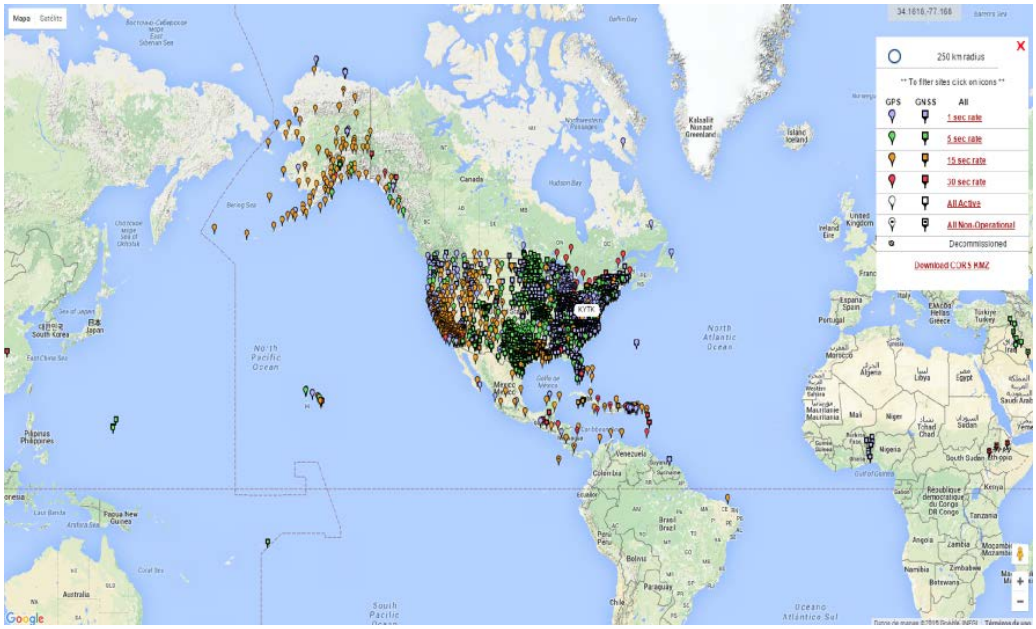

Figure 3.26: CORS network. [Source: `http://www.ngs.noaa.gov/CORS_Map/`]

3.4.1 Physical Model

Despite it has been used since 2007, their main applications were based on monitoring the multi-path oscillation frequency, whose full explanation was developed in Kavak's works [66, 102]. However, when analyzing other parameter measurements that include the dielectric constant effect, a physical model was lacking. In 2010, V.U. Zavorotny developed it in order to attempt the retrieval of soil moisture from those geodetic GPS stations [93]. This section summarizes the model developed, which is based on assuming only coherent scattering, such as the conventional coherent IPT. Figure 3.27 shows how an experimental SNR pattern of a zenith-pointing antenna looks like. As the satellite

rises, the antenna gain for the direct path increases while it decreases for the reflected path. This makes the oscillations vanish once their respective antenna gain is different enough. Below it, the detrended SNR pattern is shown where only the oscillations are seen.

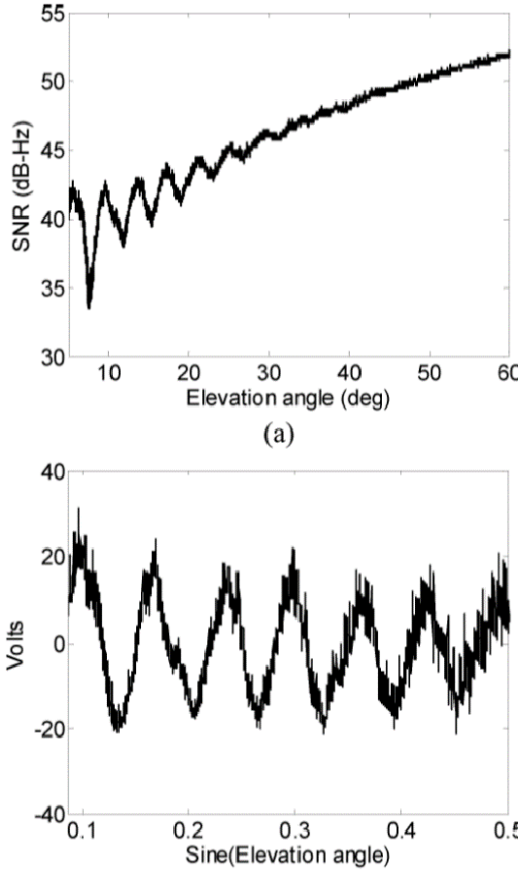

Figure 3.27: Example of experimental SNR-analysis data [93].

The physical model considers a direct signal purely RHCP, as the ellipticity of GNSS satellites antenna is lower than 1.2 dB [44] and a reflected signal made from two different components, one part RHCP (copolar), and one part LHCP (cross-polar) [52]. As already stated in Eqn. (3.15), the electric field resulting from the interference is [93]:

$$u_{SNR} = u_{0dir} + u_{0ref}, \tag{3.17}$$

and the power or SNR observed is:

$$P_{SNR} = |u_{SNR}|^2 = |u_{0dir} + u_{0ref}|^2, \tag{3.18}$$

where u_{0dir} stands for the direct field and u_{0ref} for the reflected field. Then, the P_{SNR} becomes:

$$P_{SNR} = |u_{0dir}|^2 + |u_{1ref}|^2 + 2|u^*_{0dir}u_{1ref}| \cos\left(\Phi(\theta) + \Psi(\theta)\right), \tag{3.19}$$

where $u_{0ref} = u_{1ref}e^{j\Phi(\theta)}$, $\Phi(\theta) = 2kh\sin(\theta)$ and stands for the distance difference between direct and reflected field, $A(\theta) = 2u^*_{0dir}u_{1ref} = 2|u^*_{0dir}u_{1ref}|e^{j\Psi(\theta)}$, and $\Psi(\theta) = \arctan(\mathrm{Im}\{A\}/\mathrm{Re}\{A\})$.

Once the electric field model is defined let's now introduce the antenna pattern effect. The direct field becomes:

$$u_{0dir} = u_0 F_R(\theta), \tag{3.20}$$

where u_0 is the electric field amplitude, $F_R(\theta)$ is a complex number that stands for the voltage antenna pattern, and R for the polarization. Consequently, the antenna gain ($G_R(\theta)$) is given by $|F_R(\theta)|^2$. Therefore, the reflected field becomes:

$$u_{1ref} = u_{1ref,R} + u_{1ref,L} = u_0\Big[r_{RR}F_R(-\theta) + r_{RL}F_L(-\theta)\Big], \tag{3.21}$$

$A(\theta)$ becomes:

$$A(\theta) = 2|u_0|^2\Big|F^*_R(\theta)\Big[r_{RR}F_R(-\theta) + r_{RL}F_L(-\theta)\Big]\Big|e^{j\Psi(\theta)}, \tag{3.22}$$

and $\Psi(\theta)$ becomes:

$$\Psi(\theta) = atan\left(\frac{\mathrm{Im}\{F^*_R(\theta)[r_{RR}F_R(-\theta) + r_{RL}F_L(-\theta)]\}}{\mathrm{Re}\{F^*_R(\theta)[r_{RR}F_R(-\theta) + r_{RL}F_L(-\theta)]\}}\right). \tag{3.23}$$

Note that the IPT could also be expressed using this physical model, but the author finds much clearer the way it is developed and presented in the final expression found in Sec. 3.2.1. In the end, there are two terms on the P_{SNR} that are offsets, and the oscillation pattern is determined by $A(\theta)$, $\Psi(\theta)$, and $\Phi(\theta)$. Those are the terms with geophysical information that are later analyzed for remote sensing purposes.

3.4.2 Applications

Using this SNR model, several applications have been developed, most of them similar to the conventional IPT ones, but looking to other observables. In the literature, four main applications have been found, which are similar to the IPT ones and parallel in time:

- Soil moisture.
- Vegetation.
- Snow.
- Sea.

As shown in Fig. 3.27, in order to apply signal processing techniques to estimate remote sensing parameters the SNR pattern must be previously detrended. This detrending process gets rid of the terms $|u_{0dir}|^2$ and $|u_{1ref}|^2$ in Eqn. (3.19), which are offsets that depend on θ due to the antenna gain θ dependence. Once this is done, a detrended SNR pattern is obtained with the experimental $A(\theta)$, the $\Psi(\theta)$, and the $\Phi(\theta)$ values. The estimation of those parameters from the experimental SNR pattern determines the feasibility and the performance of the technique for remote sensing purposes. The following subsections comment briefly the principles and evolution of each of the remote sensing applications aforementioned.

3.4.2.1 Soil Moisture

The first publications reporting the relation between soil moisture and SNR-multipath observables appeared in 2008 [107,108]. Therein, it was observed that there was a relation between the estimated reflected signal amplitude and the soil moisture content. The multipath model proposed in there is:

$$P_{SNR} = |A_d|^2 + |A_m|^2 + 2A_dA_m \cos\left(\Phi(\theta) + \Psi(\theta)\right) \tag{3.24}$$

where A_d is the amplitude of the direct signal, and A_m the amplitude of the reflected signal. Note that Eqn. (3.24) matches with the last term in Eqn. (3.19). In [107, 108] it is assumed that $A_d \gg A_m$, so for the multipath free region, A_d is computed taking into account the antenna pattern. Then, A_m is estimated by means of spectral analysis of the detrended multipath pattern. The A_m estimated values were compared against in-situ soil moisture measurements, and some correlation between the variation of soil moisture and the variation of A_m was found. Also the $\Psi(\theta)$ parameter was compared against in-situ soil moisture values in [108]. Therein, it is seen that there is no sensitivity for very low soil moisture values, whereas they seem to be linearly correlated for soil moisture values larger than 10%. Estimating $\Psi(\theta)$ is somehow a way to estimate the penetration depth, which it is well-known that varies with the soil moisture content [109]. Both observables correlated better with soil moisture measured at 0–5 cm depth than with soil moisture measured at 5–10 cm depth. However, in those works there is neither a retrieval algorithm for relative soil moisture changes nor an absolute soil moisture measurement. Furthermore there is an issue to be solved: A_m is assumed to be constant, whereas variations on the surface characteristics might change its value. Recall that it is a θ dependent parameter as was justified by the physical model described.

In 2010 two more works appeared. One of those is the physical model developed by V.U. Zavorotny which was summarized in previous subsection and in [93]. In [110] the multipath amplitude (A_dA_m) and phase (Ψ) are assumed to be constant (not θ dependent), and estimated for each satellite. This may provide a mean value soil moisture estimation. The height parameter (h) and consequently the Φ parameter is estimated using the Lomb-Scargle Periodogram (LSP). Comparisons between in-situ soil moisture measurements, estimated h, and estimated Ψ where performed, reassuring the correlation for Ψ and showing that there is also some correlation with estimated h. No information about the correlation with multipath amplitude (A_dA_m) is given. Again, differently from the IPT no soil moisture retrieval algorithm is provided.

The first attempt to develop a soil moisture retrieval algorithm for baresoil conditions from the SNR-analysis data appears in 2014 [111]. It is based on the physical model previously presented in [93]. As a first step, different SNR-patterns are simulated and computed for different soil moisture conditions. This implies to take into account both the reflected RHCP and LHCP components. Then, from the experimental data two different observables are defined: A_{mpi}, and ϕ_{mpi}, which correspond to A_dA_m and Ψ respectively. Again h was estimated using the LSP. Separately, an effective reflector height (H_{eff}) was calculated for the simulated data. Also, the simulated data was obtained from a simulator similar to the simulator developed on this PhD Thesis in Sec. 3.1. The ϕ_{mpi} or the Ψ parameter had a linear relationship with soil moisture, and a variation of 20° in the ϕ_{mpi} corresponded to a variation of 0.31 m^3/m^3 in volumetric soil moisture content. This

result seems logical as the ϕ_{mpi} is an indirect measurement of the dominant polarization as shown in Eqn. (3.23). The A_{mpi} differently from what was stated in [107, 110] does not seem to have any relation with the soil moisture content. This can be explained because the $A_{mpi} = 2A_dA_m$, and $A_d \gg A_m$, so an amplitude change on the A_{mpi} is more likely due to A_d, which does not depend on the soil moisture content. Finally, it was seen that also the H_{eff} or h did not have a strong relation with soil moisture despite the penetration depth depends on the soil moisture content. As a conclusion, a linear model measuring the Ψ parameter was proposed to estimate the soil moisture content.

3.4.2.2 Vegetation

The first publication that analyzed the effect of vegetation on the SNR pattern appeared in 2010 [112]. Therein, the main observable used is the amplitude of the multipath pattern or (A_{mpi}). Despite it is shown not to have a large correlation with soil moisture, it seems that the larger the vegetation height, the lower the amplitude of the multipath pattern observed. In that paper a parameter known as the $MP1_{rms}$ is used, which is the *rms* value of the PR pattern, once the mean PR has been compensated. It is also stated that the $MP1_{rms}$ parameter is not sensitive to the soil moisture content. What this means basically is that when there is no vegetation, there is a strong influence in the PR measurement from the multipath contamination. However, vegetation acts as an attenuator at L-band, which means that it attenuates the reflected signal, minimizing the multipath, and providing a less contaminated PR measurement with lower *rms* value. Even though this technique is not exactly the SNR-analysis, it is related to it, because the SNR pattern and the PR pattern are highly correlated.

The next step in vegetation remote sensing using the SNR-analysis came with the derivation of the Normalized Microwave Reflection Index (NMRI) in 2014 [113,114], which is a new index to take into account on the SNR-analysis that may provide extra information about vegetation. The PR multipath error (M_1) depends on:

$$M_1 = \frac{\alpha D \cos(\psi_1)}{1 + \alpha \cos(\psi_1)}, \tag{3.25}$$

where $\alpha = A_m/A_d$ is a damping factor, $D = 2h\sin(\theta)$ the excess path due to multipath, $\psi_1 = kD$, and subscript 1 for the L1-band. A_m is sensitive to vegetation height and vegetation water content. The larger the vegetation height or the vegetation water content for the same height, the lower A_m and the lower α. Then, the $MP1$ presented previously is:

$$MP1 = PR_1 - \frac{{f^2}_1 + {f^2}_2}{{f^2}_1 - {f^2}_2}\lambda_1\phi_1 + \frac{2{f^2}_2}{{f^2}_1 - {f^2}_2}\lambda_2\phi_2 = M_1 + C + X, \tag{3.26}$$

where M_1 is defined in Eqn. (3.25), C is a constant bias that can be calibrated, and X is not considered as it is 1 or 2 orders of magnitude below M_1 [113]. The NMRI is defined as:

$$NMRI = \frac{-\left(MP1_{rms} - max\{MP1_{rms}\}\right)}{max\{MP1_{rms}\}} \tag{3.27}$$

which is a normalization of the $MP1_{rms}$ previously presented in [112] and it is related to the vegetation height and or vegetation water content. Then, [114] validates this developed index showing a large correlation with the NDVI, but specially with the vegetation

water content. The normalization effect might reduce the dependence on the vegetation height.

Recently, new retrieval models attempting the measurement together of the vegetation parameters and soil moisture have been proposed [115, 116]. Therein, it is shown that under the presence of vegetation, the h parameter that determines the multi-path oscillation frequency is reduced. Furthermore, the ϕ_{mpi} parameter is not anymore constant, and suffers a "shift" similar to what occurs with the conventional IPT at the Brewster angle position. It concludes that due to the attenuation produced on the multi-path amplitude the best metric is the A_{mpi} normalized for the vegetation remote sensing, and the ϕ_{mpi} for the soil moisture retrieval. Also the vegetation height could be estimated if there is a reference of the true h when there was not presence of vegetation.

3.4.2.3 Snow

The measurement of snow parameters, specifically depth, using the SNR-analysis dates from 2009 [117]. Figure 3.28 shows a comparison of two SNR patterns for no snow presence (red), and for a surface with a layer of 35 cm of snow over it. It can be quickly seen that the oscillation period of the SNR pattern is smaller when there is snow presence, since the distance between the antenna and the surface decreases. The snow depth (SD) can be measured by estimating the h parameter of the SNR-analysis model using for instance the LSP [118], and then referring it to the one measured when there was no snow. So:

$$SD = \hat{h}_{nosnow} - \hat{h}_{snow} \tag{3.28}$$

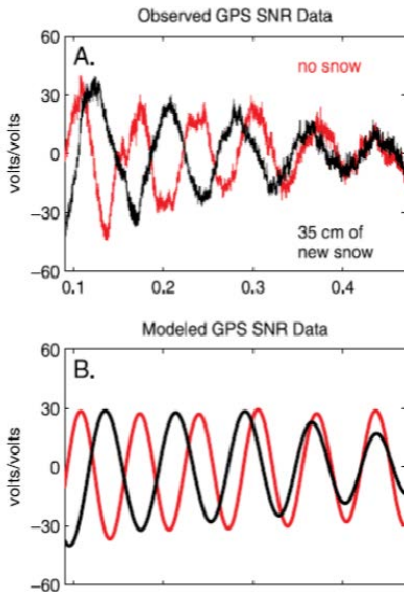

Figure 3.28: Comparison of the SNR patterns measured and simulated over a surface and over the same surface covered with a layer of 35 cm of snow [117].

Note that this retrieval algorithm is quite different from the conventional IPT one, which was based on measuring the number of notches and their position. Also, the conventional IPT derived a measurement of snow depth for each oscillation, whereas in here the whole pattern is averaged in the LSP computation to obtain the mean value. It is remarkable that snow presence is not always homogeneous and there may be some differences between in-situ measurements and the GPS derived one. However, Fig. 3.29 shows the same trend between the snow depth derived using this simple algorithm and the one derived from ultra-sound probes, demonstrating the good performance of the proposed technique.

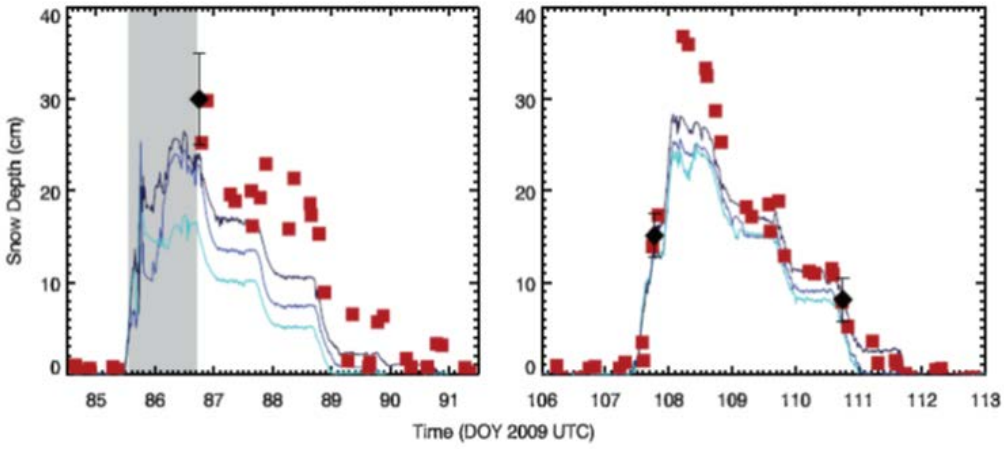

Figure 3.29: Comparison between snow depth derived from the SNR pattern and the one measured with ultra-sound probes [117].

Later, in 2012, another experiment to measure snow depth was conducted [119], which demonstrated the same behavior that was found in [117]. However, in this experiment it was taken into account the effect that dry snow and wet snow produced on the oscillation frequency. If the snow is wet, the error on the frequency estimation is reduced which gets the measurement closer to the real value. In Fig. 3.29 it is observed that the initial algorithm had a bias which tended to overestimate the snow depth parameter.

In 2013 another publication appeared [120] showing again the performance of the technique and its limitations, but no scientific development appears in there. In 2014, a reformulation of the SNR physical model proposed by V.U. Zavorotny [93] was published, but from a signal processing point of view and with the objective of snow remote sensing instead of baresoil observations [121]. One parameter that was added to that model is the presence of the incoherent component on the multi-path, which is important for the SNR-analysis geometric configuration, as the coherent reflected component is highly attenuated by the antenna pattern. The addition of the incoherent component is performed using a stochastic model. One thing missing that might create undesired fluctuations is the time and space correlation of the incoherent component, as differently from thermal noise, it comes from the *speckle* noise, and as the satellite moves very slowly, the incoherent component samples must be correlated. However, for the snow case the incoherent component was very small because it did not affect the performance of the technique as

was shown in [122]. In other words, for such grazing angles, the coherent model is enough to mathematically and physically model the multi-path over land and snow, as has been seen in previous sections.

3.4.2.4 Sea

The last product developed from the SNR analysis data is the measurement of the sea level by measuring again the oscillation frequency of the SNR pattern. In this topic, to the author's knowledge, three different research groups have performed some contributions. The first one is a research group from Chalmers University of Technology, Gothenburg, Sweden. The second one is from CU, Boulder, USA. The third one is a research group from the Centre Nationale d'Études Spatiales, Toulouse, France.

The one from Sweden started their research on the measurement of the sea level and using the GPS system as a GPS tide gauge [123]. Their technique was based on PR difference, an approach a little bit different from the SNR-analysis and more close to the $MP1$ parameter used to sense vegetation. However, in the signal patterns shown in [123], there was already evidence of the multi-path presence and that the SNR-analysis could be applied. So, together with the CU research group, they analyzed the performance of the SNR-analysis in comparison with the previous PR measurement technique [124]. The previous technique required two different GPS receivers, one for the direct signal and one for the reflected signal. The one based on the SNR-analysis only required one down-looking antenna and one receiver. Figure 3.30 sketches the traditional approach to the GPS tide gauge, based on two GPS receivers and PR measurements together with the new approach based on the SNR-analysis using only one down-looking antenna and one GPS receiver. Both techniques obtained a similar accuracy [124]. The measurement method of the SNR-analysis is based on estimating the h parameter, like the snow depth or the vegetation height algorithms, and relating it to a known reference level. An example of the data products obtained from this algorithm is shown in Fig. 3.31, where the blue dots are the GPS estimates and the black dashed line refers to the NOAA buoys ground-truth information.

In fact, later it was discovered that there was some inaccuracy in the model [125]. Up to then, the surface had always been considered still, or their variations, such as due to snow presence or vegetation growth, very small in terms of time. However, for the tides case, they are periodic over the day, and the change in the surface height is not so small. In that case, it is not enough to take into account for the modeling the path difference between the direct and reflected signals, also its derivative, which adds a kind of Doppler on the LSP retrieved. The derivative models the surface height speed change. In this case, the path difference is given by:

$$d = 2H\sin(\theta), \tag{3.29}$$

$$\dot{d} = \frac{\partial d}{\partial t} = 2H\cos(\theta)\frac{\partial \theta}{\partial t} + 2\frac{\partial H}{\partial t}\sin(\theta), \tag{3.30}$$

$$\ddot{d} = \frac{\partial d}{\partial \sin(\theta)} = \frac{\partial d}{\partial t}\Big/\frac{\partial \sin(\theta)}{\partial t} = 2H + 2\frac{\partial H}{\partial t}\frac{\tan(\theta)}{\frac{\partial \theta}{\partial t}}. \tag{3.31}$$

The first term is the periodicity that was already known, and the second term corrects

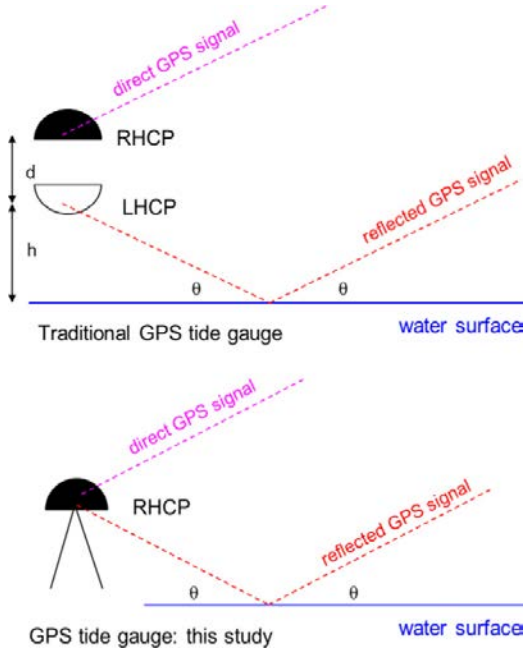

Figure 3.30: Traditional GPS tide gauge and the improved one based on the SNR-analysis [124].

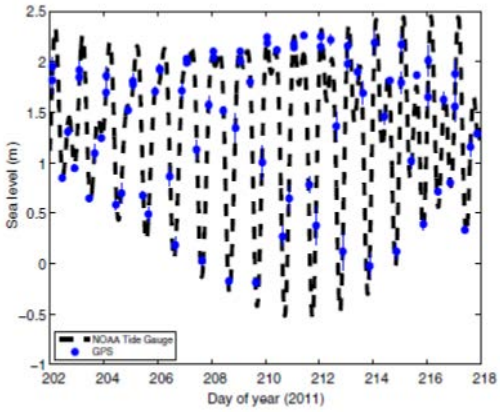

Figure 3.31: Sea level estimated using the SNR-analysis and compared against NOAA buoys [124].

for the bias added due to the movement of the reflecting surface, leading to improve the accuracy of the technique. In other words, one value stands for its position and the other for its movement speed. It results that for the SNR-analysis over some regions of the Earth, such as the Atlantic Ocean, the h parameter is not constant over time and it must be taken into account. After that, this variable term has been always added [126]. Then, the technique was even extended to other GNSS signals [127] and systems GLONASS

[128]. In [127] a detailed comparison between the SNR-analysis and the PR method for two different GPS signals is shown and their accuracy assessed. Finally, [129] presents a methodology to simultaneously estimate the static and dynamic parameters shown in Eqn. (3.31), in spite of the iterative method proposed in [125].

3.5 Comparison Between the IPT and the SNR-Analysis

In this chapter an overview of both the conventional IPT and the SNR-analysis have been discussed. Even though both can be summarized using Zavorotny's physical model [93], in here it has been shown a simplified model for the IPT [Eqn. (3.16)]. It is possible to see that the amplitude of the oscillations for the SNR-analysis depends on the antenna pattern, the surface under observation, and both the amplitude of the direct and reflected signals. Conversely, the amplitude of the oscillations for the IPT only depends on the antenna pattern (indirectly) and the reflected signal. So, there is no influence on its amplitude from the direct signal, and consequently amplitude measurements can be more accurately used. Then, the oscillation frequency is practically the same, and all derived techniques based on measuring the oscillation frequency can be applied to both models. Regarding the extra phase term ($\Psi(\theta)$), it is easier to explain it for the IPT than for the SNR-analysis. For the IPT it only depends on the reflection coefficient phase and the penetration depth on the surface. For the SNR-analysis it also depends on the direct signal phase and the voltage antenna pattern.

Having said so, the IPT has some clear advantages as compared to the SNR-analysis. First of all, the model is much better defined due to using linear polarization, and consequently, experimental data is easier to understand. Furthermore, due to using linear polarization the Brewster angle can be sensed, which is a good proxy for the determination of soil moisture, and it is why it was the first observable proposed in the retrieval algorithms. Also, due to pointing to the horizon, the antenna pattern is maximal for the grazing angles geometry, which emphasizes the multi-path effect and enhances the SNR in that elevation angle range. In the SNR-analysis it is possible to see how the amplitude of the oscillations decreases while the satellite rises.

Regarding some applications such as the estimation of the vegetation height or the snow height, both techniques have followed a different approach. The SNR-analysis follows a simple method based on estimating the oscillation frequency of the multipath generated. The IPT has focused its algorithms on measuring the number and position of the different notches that appear on the interference pattern since its envelope follows the reflection coefficient envelope. However, while the same approach used on the SNR-analysis can be applied on the interference pattern, as it will be seen on this PhD Thesis dissertation later, the IPT algorithm would be much more complicated to apply it to the SNR-analyisis data due to two main reasons. First, the amplitude envelope of the SNR-analysis is not directly the reflection coefficient. Second, for the SNR-analysis, as the satellite rises the amplitude envelope of the detrended SNR pattern is reduced, and no notches will be seen.

There are also some advantages of using the SNR-analysis in front of the IPT. First, it is that the SNR-analysis uses COTS devices. Second, there are several GNSS networks, such as the PBO and the CORS with opportunistic data available at no cost at all. Also,

those stations are already there for improving the GNSS positioning and for atmospheric GNSS remote sensing. So there is no need to create new infrastructure, there is no maintenance cost, and it is only necessary to develop a new remote sensing product from the same data record. On the other hand, the IPT requires the design of a high quality linear polarization antenna which are not normally commercially available, since GPS signals are not linearly polarized. Furthermore, there is not yet any network deployed with the IPT geometrical configuration, so an investment is required to use this technique. Consequently, even though data from the IPT is more robust, developing new hardware is a lengthy and costly process, and this is why many researcher/s have focused more on the SNR-analysis, and only the UPC group, and Monash University in a collaboration with the UPC group, have focused more on the IPT.

3.6 Summary of the IPT Developments Performed in this PhD Thesis

One part of this PhD Thesis is the natural continuation of N. Rodirguez-Alvarez PhD Thesis [28]. Therein, all the applications summarized in Sec. 3.3 were developed. However, there was one field that remained unexplored: the use of horizontal polarization. Due to the Brewster angle presence, all research was centered on the use of vertical polarization. However, horizontal polarization has two interesting aspects. First, the reflectivity is larger, which means that the oscillation fringes can be more accurately measured. In the H-Pol IPT, the oscillation fringes are only due to the reflected signals and antenna pattern (they do not depend directly on the direct signal), and it is expected that its amplitude provides more accurate soil moisture measurements. Also, the fact that before the Brewster angle the H- and V-Pol interference patterns are in phase, and after it, they are in counter-phase, adds an extra observable, which means that the reflection coefficient phase can be measured accurately as a function of the incidence angle, and then soil moisture inferred from that observable. In [34] the addition of the H-Pol to the IPT is analyzed in detail and its results compared to the V-Pol only ones. In [35] the phase difference tracking algorithm due to the combination of H- and V-Pol interference patterns is analyzed. When the surface is somehow rougher, the Brewster angle is not well detected by amplitude measurements, a fact that was been previously shown. Phase difference measurements provide an alternative much less sensitive to roughness than the amplitude measurements, and the Brewster angle is detected at the 90° phase shift position. The research performed using the dual-polarization IPT is detailed in Chapter 6.

Another point that remained unexplored was the use of the IPT over a dynamic surface such as the sea or coastal sea for mean sea level measurements, although it was tested over a lake. After some attempts, a 3-month field campaign was conducted and a similar approach to the SNR-analysis was followed to obtain the final product. However, different spectral estimators apart from the LSP were tested in order to improve the accuracy of the spectral estimation on the SNR-analysis. Furthermore, due to the observation geometry, there was one aspect not seen previously on the SNR pattern over the sea. When the surface becomes rougher, which is the natural state of the sea surface, the coherent model stops working as good as it works for land, vegetation, and snow surfaces. There is even an angle that depends on the sea state where coherency is lost. This parameter is used

to infer the equivalent Significant Wave Height (SWH). These results appear in [97]. The research performed regarding the use of the IPT over the sea surface is detailed in Chapter 7.

3.7 Conclusions

This chapter has presented the theoretical background of the IPT-based techniques. It starts with the simplest reflection model to expand it to a M-layer reflection model where a horizontally stratified soil moisture profile can be added. Therein, the Fresnel reflection coefficients are shown with the reflectivity behavior, and the phase behavior. This justifies why GNSS reflected signals are normally LHCP despite one small incidence angle region which is variable and depends on the Brewster angle position. The Brewster angle concept is also detailed, and how it can be used on the reflection coefficient to infer the surface's dielectric constant.

Later, the coherent IPT model is detailed and justified. Therein several factors are analyzed. A variation on the dielectric constant results in a variation of the interference pattern amplitude. Linear polarization interference patterns are different between them in two aspects: the Brewster angle presence for V-Pol and not for H-Pol, and the regions where both interference patterns are in-phase or in counter-phase. The distance between the antenna and the reflecting surfaces drives the oscillation frequency. The presence of topography is equivalent to a Frequency Modulation (FM), where the frequency varies as a function of time. Surface roughness attenuates the interference pattern amplitude as a function of the incidence angle. The smaller the incidence angle, the larger the attenuation induced.

After that, the applications developed prior to this PhD Thesis are presented. One of them is the retrieval of soil moisture based on the Brewster angle detection. Another one is the topography measurement based on the frequency estimation of each interference pattern oscillation. Vegetation height is estimated based on the presence of several notches on the interference pattern. A similar algorithm is used to measure the snow depth/thickness. Finally, the V-Pol IPT was tested over a reservoir to measure its water level very accurately.

A technique similar to the IPT is also described, which is known as the SNR-analysis. The theoretical background is similar to the IPT, and the physical model can be generalized for both techniques. After some approximations on the general physical model, it leads to the simple model of the IPT used before. However, the fact of having several GNSS geodetic networks and the availability of large datasets in the SNR-analysis geometrical configuration is an opportunity that cannot be disregarded. So, several applications have been developed using this kind of data based on the estimation of some multi-path parameters such as the A_{mpi}, ϕ_{mpi}, H_{eff}, and $MP1_{rms}$. The measurement of soil moisture has been correlated against the A_{mpi}, ϕ_{mpi}, and H_{eff}. The retrieval of vegetation height has been estimated based on the measurement of two different parameters: H_{eff}, and $MP1_{rms}$. Snow depth is determined based on estimating H_{eff}. Sea surface level is also measured based on estimating H_{eff}. Furthermore, the model was extended in order to account for the tides, which make the surface level not to be still during the entire measurement period.

Then, both the IPT and the SNR-analysis are compared. Note that all techniques applied on the SNR-analysis can be applied to the linear polarization IPT, but not the other way round. There are some other techniques that can only be applied to the IPT. However, the fact that the IPT requires a customized hardware limits its use in comparison with the SNR-analysis, since the already deployed GNSS networks are available at no cost. Finally, Appendix B.4 shows some limitations that both techniques suffer due to mainly the codes used.

4

Chapter 4
GNSS Scatterometry

This chapter provides an overview of the other technique exploited during this PhD Thesis dissertation for land, sea, and sea ice monitoring. It starts with a theoretical background describing precisely the mathematical models used. It discusses the difference between coherent reflection and incoherent scattering, and it shows some simulations about how coherent and incoherent scattered signals are. A section explaining how to estimate both components from the reflected signal measured is presented, using both real-value and complex-value data. Also, the general definitions of the SNRs found in GNSS-R are provided. Finally, a section explaining all the previous developments to this PhD Thesis is added to clarify the Thesis starting point. There are some specific aspects of this technique that are a particular case of each field campaign and they are developed in the corresponding chapter.

4.1 Introduction

The IPT is a static technique that allows to measure the soil moisture of a terrain and its surroundings. The fact that the antenna is looking to the horizon clustering the 360° Field of View (FOV) into 90°, which covers just 1/4 the total area. Furthermore, the total area covered depends also on the antenna height, as the larger the height the larger the area covered. Therefore, this kind of technique and instrumentation is good for deploying a network and continuously monitor a certain area. However, conventional remote sensing platforms such as airplanes, satellites, or the forthcoming Unnamed Aerial Vehicle (UAV)s are not static platforms, and therefore their characteristics do not allow to apply the IPT as it is. This kind of platforms require techniques that do not depend on having an instrument still and large exposure times. Also, the coverage of large scale terrains is only possible with moving platforms, since the coverage of a large terrain sample using the IPT would require the installation of a network of several P-SMIGOL instruments, which is not cost-effective. So, trying to increase the soil moisture spatial coverage, it was decided to move the research to techniques different from the IPT.

The only GNSS-R technique that allow us to achieve the proposed goal is GNSS scatterometry, which is based on measuring the reflected signal power without the need of interacting coherently with the direct one. As introduced in Chaps. 2 and 3, the reflected signal has two different components: a coherent and an incoherent one. Differently from the IPT, where the coherent component clearly dominates in land and in some sea scenarios (despite those ones very large waves), in GNSS scatterometry, whether one component is larger than the other depends mainly on the surface spectrum and the incidence angle. In the IPT the coherent component dominates due to the large incidence angles used. When the coherent component dominates, the signal model is quite simple and the coherent reflectivity can be easily estimated, from which the geophysical parameters can be inferred. When the incoherent component dominates, the signal model is a little bit more complex and in this chapter the KA-GO solution will be used to provide a mathematical expression that allows to represent it. In a situation when both components are close to each other, numerical simulations are necessary to compute the contribution of each component. The main difference between both components is that the coherent component has a constant phase whereas the incoherent component has a random phase uniformly distributed, a fact that was already mentioned in Chapter 3.

A land surface is generally considered as a flat surface with some topography, where normally the coherent component tends to dominate over the incoherent one, as the effective surface roughness is relatively small at L-Band. For a surface such as the sea, the dominating component is determined by its state and the EM wave incidence angle. According to the Rayleigh criterion for rough surfaces, for close to nadir incidence angles the incoherent component will tend to dominate whereas the coherent component will dominate for larger incidence angles [69]. If the SWH parameter or the large scale roughness are relatively large, the incoherent component will dominate in all situations independently from the incidence angle. Surfaces such as ice, and specially sea ice, tend to behave as land, since they are still surfaces without internal dynamic movements, and the reflection tends to be coherent unless the terrain is highly irregular.

The measurement of each scattering component determines the retrieval algorithm to be used for the geophysical parameter inversion, and the accuracy of the technique. For

land geophysical parameter inversion, e.g. soil moisture, we will be extremely interested in the coherent component, and both the thermal and incoherent components will be seen as noise sources that disturb the measurements. For sea surface geophysical parameter inversion, e.g. SWH or wind-speed, the useful signal will be the incoherent one because the coherent component is practically negligible [130], and therefore, only thermal noise will be considered as a noise source. As can be seen, different situations might be faced, and they have to be treated carefully in order not to misinterpret GNSS-R data.

4.2 Coherent and Incoherent Scattered Power

The received reflected field under the KA can be expressed as [52]:

$$U_r\left(\vec{R}_r, t\right) = \iint \sqrt{EIRP_T}\, a\left(t - \frac{R_0 + R}{c}\right) g\left(\vec{r}, t\right) d\vec{r} \tag{4.1}$$

where $EIRP_T$ stands for the transmitted equivalent radiated isotropic power.

As described in Chapter 2, in the cGNSS-R approach the reflected signal is gathered by the down-looking antenna and correlated against a clean replica of the satellite code. A coherent integration time of T_c ms is applied in the signal processing stage in order to generate the complex voltage waveform (Y_c). This is mathematically expressed as:

$$Y_c(t_0, \tau) = \frac{1}{T_c} \int_0^{T_c} \sqrt{G_R} U_r\left(t_0 + t' + \tau\right) a\left(t_0 + t'\right) e^{j2\pi f_c t'} dt' \tag{4.2}$$

where G_R stands for the receiving antenna gain, and f_c is a frequency compensation term. In this expression is where both coherent and incoherent components can be measured. If the scattering is purely coherent, the reflected field becomes a replica of the transmitted/direct one taking into account the surface reflectivity and the small surface roughness. So, if the scattering is purely coherent the complex coherent voltage waveform can be expressed as:

$$Y_{coh}(t_0, \tau) = \frac{1}{T_c} \sqrt{EIRP_T} \sqrt{G_R} r_{pq}(\theta) e^{-2k^2\sigma_{rms}^2 \cos^2(\theta)} \frac{R_{a,a}\left(\tau - \frac{R_t + R_r}{c}\right) S\left[f_t(t_0)\right]}{4\pi\left(R_t + R_r\right)} e^{j2\pi f_x t_0} \tag{4.3}$$

where $e^{-2k^2\sigma_{rms}^2 \cos^2(\theta)}$ is the PO approximation for modeling the decrease in amplitude of the Fresnel reflection coefficients [71], $R_{a,a}$ is the satellite's PRN code ACF which is detailed in Chapter 2, S models the frequency response of the codes, and f_x models a frequency misalignment between the system's beating frequency and signal's real frequency. f_x models a rotating phasor that occurs when the Doppler frequency is not perfectly compensated.

While the coherent voltage waveform expression is quite simple, the incoherent voltage one is the result of solving numerically Eqn. (4.2) for all surface points and removing the contribution of the coherent component. The received signal average power can be obtained by squaring the complex voltage waveform and computing the statistical average.

Therefore:

$$\begin{aligned}\mathrm{E}\{|Y_c(t_0,\tau)|^2\} =&\mathrm{E}\Big\{\frac{1}{T_c^2}\int_0^{T_c}\sqrt{G_R}U_r\left(t_0+t'+\tau\right)a\left(t_0+t'\right)e^{j2\pi f_c t'}dt'\\ &\int_0^{T_c}\sqrt{G_R}U_r^*\left(t_0+t''+\tau\right)a\left(t_0+t''\right)e^{-j2\pi f_c t''}dt''\Big\}.\end{aligned} \tag{4.4}$$

Rearranging those terms and solving for the temporal integral it is obtained that [52]:

$$\begin{aligned}\mathrm{E}\{|Y_c(t_0,\tau)|^2\} =&\frac{1}{16\pi^2}\int\int\mathrm{E}\{\Phi(\vec{r}',\vec{r}'')\}\left(\frac{\sqrt{G_R}R_{a,a}Sr_{pq}q^2}{R_0Rq_z}\right)'\left(\frac{\sqrt{G_R}R_{a,a}S^*r_{pq}^*q^2}{R_0Rq_z}\right)''\\ &e^{jk\left(R_0'+R'-R_0''-R''\right)}d\vec{r}'d\vec{r}'',\end{aligned} \tag{4.5}$$

where the key point of that integral is the function $\mathrm{E}\{\Phi(\vec{r}',\vec{r}'')\}$ which is the one that has to be treated statistically. If the coherent component is dominating the power waveform can be expressed in terms of the coherent bistatic radar equation which yields [70]:

$$\begin{aligned}\mathrm{E}\{|Y_{coh}(t_0,\tau)|^2\} =&EIRP_TG_R|r_{pq}(\theta)|^2e^{-4k^2\sigma_{rms}^2\cos^2(\theta)}\lambda^2\frac{\left|R_{a,a}\left(\tau-\frac{R_t+R_r}{c}\right)\right|^2|S\left[f_t(t_0)\right]|^2}{\left[4\pi\left(R_t+R_r\right)\right]^2}\\ =&\mathrm{P}_{\mathrm{coh}}(\tau).\end{aligned} \tag{4.6}$$

If the incoherent component is the dominating one and the coherent component can be neglected, Eqn. (4.5) can be expressed using the diffusive bistatic radar equation which yields [52]:

$$\mathrm{E}\{|Y_{incoh}(t_0,\tau)|^2\} = \int\frac{EIRP_TG_R\lambda^2\left|R_{a,a}\left(\tau-\frac{R_t+R_r}{c}\right)\right|^2|S\left[f_t(t_0)\right]|^2}{4\pi R_0^2R^2}\sigma_0(\vec{\rho})d\rho = \mathrm{P}_{\mathrm{incoh}}(\tau), \tag{4.7}$$

where $\sigma_0(\vec{\rho})$ represents the bistatic radar cross-section, and assuming KA-GO it is given by:

$$\sigma_0(\vec{\rho}) = \frac{\pi|r_{pq}(\theta)|^2q^4}{q_z^4}P\left(-\frac{\vec{q}_\perp}{q_z}\right), \tag{4.8}$$

and the term $P\left(-\frac{\vec{q}_\perp}{q_z}\right)$ stands for the *pdf* of the surfaces' slopes. However, other EM scattering models can be used to determine the σ_0 expression and substitute it on the diffusive bistatic radar equation.

Note that the main difference between the two scattering mechanisms is the distribution of the power along the delay domain. Also, in the case of coherent scattering the reflected signal phase history is kept, which is not kept for the incoherent scattering.

The coherent component signal is a replica of the transmitted one multiplied by the Fresnel reflection coefficient, by an attenuation factor that accounts for the small surface roughness, and by the WAF [131] that appears due to the coherent integration process. The incoherent component signal represents the result of a coherent wave being scattered on a diffusive rough surface. In this interaction, the power of the coherent impinging

wave is spread along the different delay annulus and the different Doppler hyperbolas, resulting in a similar leading edge than for the coherent component but an elongated trailing edge of the waveform, and the phase coherency is lost. This elongated trailing edge represents the power spread along the delay domain. In other words, the coherent scattering term is proportional to the WAF multiplied by the reflectivity whereas the incoherent scattering term is proportional to the convolution of the WAF with the average bistatic radar cross-section (σ_0) [56, 132, 133]. This convolution operation is another way to explain the spreading of the power along the delay domain. Figure 4.1 expresses the coherent and incoherent scattering concepts relating them to the waveform shape. In Fig. 4.1(a) the coherent scattering concept is shown where, for a flat surface, all the delay ellipses reflect specularly, and only the one corresponding to the First Fresnel zone reaches the receiver antenna. As the wavelength is much shorter than the pulse width, the reflected waveform results in a replica of the satellite ACF multiplied by the small rough surface reflectivity. In Fig. 4.1(b) the situation is different, because the surface is rough and each delay ellipse radiates the impinging EM wave in a Lambertian manner. This Lambertian radiation diagram makes the receiver's antenna observe radiation from several delay ellipses, elongating the trailing edge of the waveform, and generating the incoherent waveform shape.

4.3 Reflected Field Statistics

As seen in Chapter 3, the reflected field can be expressed as the summation of the contribution from the different scatterers in the FOV, which can be mathematically modeled as [69]:

$$U_{ref} = \sum_{n=1}^{N} A_n e^{j\phi_n}, \tag{4.9}$$

where n stands for the scatterer index, N for the total number of scatterers, A_n for the nth scatterer amplitude, and ϕ_n for the nth scatterer phase. When the coherent scattering mechanism dominates the reflected field is a replica of the incident field multiplied by the reflection coefficient (modulus and phase). Therefore, as was seen in Chapter 3:

$$U_{ref} = U_{inc}|r_{pq}|e^{j\phi_{pq}}, \tag{4.10}$$

where U_{inc} stands for the incident reflected field. In this case, the reflected field has no statistics, it is a deterministic value. However, when the incoherent scattering dominates, the ϕ_n parameter is considered a random variable uniformly distributed between 0 and 2π, which is also known as the Born model [74]. A_n normally follows a Gaussian distribution making U_{ref} follow a zero mean complex Gaussian distribution. A situation in the middle, where there is presence of a coherent component and an incoherent one, would result in a combination of both models. In other words, a Hoyt vector, which has a non-zero mean value associated to the coherent component and a random component.

If the power of the reflected field is computed, the contribution of each scattering component is directly obtained as [69]:

$$P_R \propto \mathrm{E}\{|U_{ref}|^2\} = \mathrm{E}\{U_{ref}\}^2 + Var\{U_{ref}\}, \tag{4.11}$$

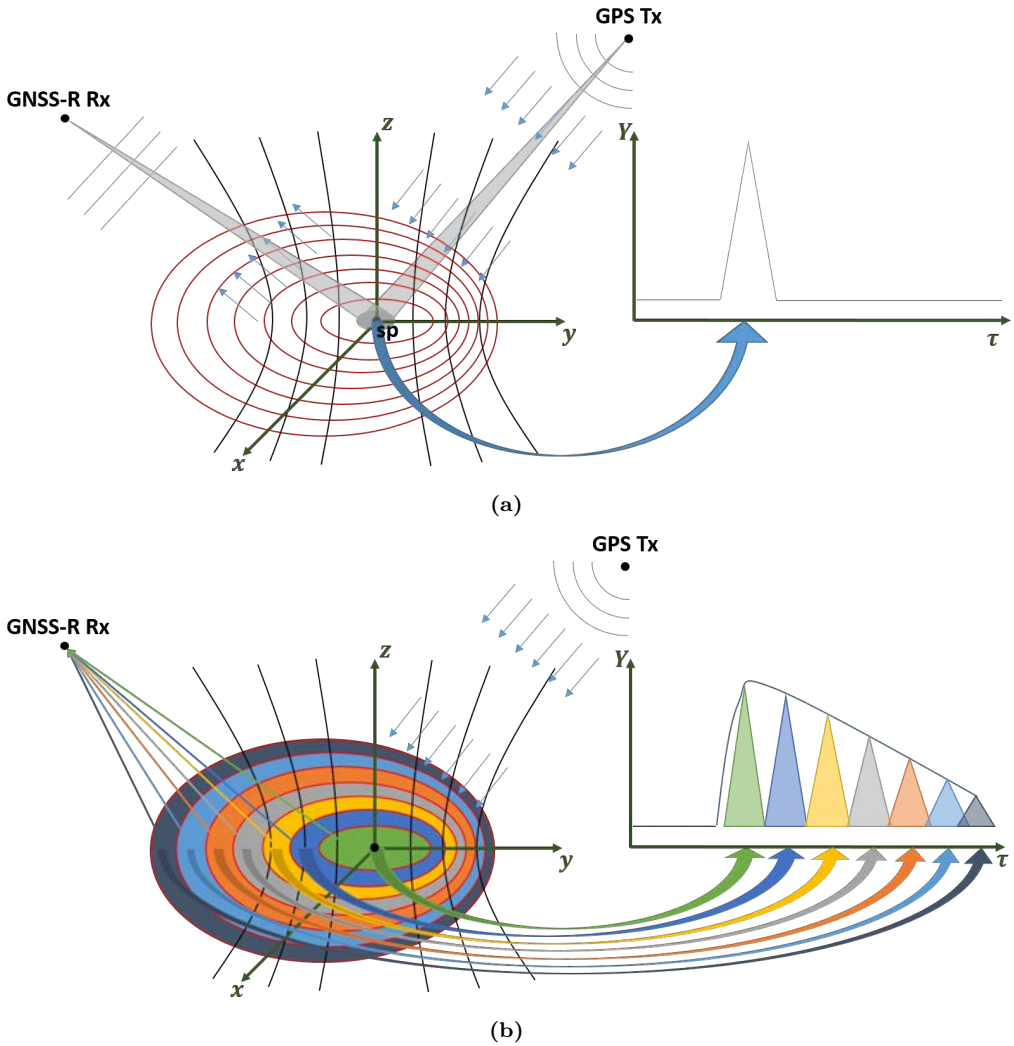

Figure 4.1: Graphical representation of coherent and incoherent waveform shapes: (a) coherent waveform, (b) incoherent waveform

where the term $\mathrm{E}\{U_{ref}\}^2$ is proportional to the coherent reflected component ($\mathrm{P}_{\mathrm{coh}}$), and the term $Var\{U_{ref}\}$ is proportional to the incoherent scattered component ($\mathrm{P}_{\mathrm{incoh}}$). In other words, the mean value squared of the Hoyt vector or the received electric field is related to the coherent component power, whereas the variance of the Hoyt vector or the received electric field is related to the incoherent component power. In [69] the parameter B, which stands for the coherent to incoherent component ratio, is defined as:

$$B = \frac{\mathrm{E}\{U_{ref}\}^2}{Var\{U_{ref}\}} = \frac{\mu^2}{s_1 + s_2} = \frac{\mathrm{P}_{\mathrm{coh}}}{\mathrm{P}_{\mathrm{incoh}}}, \tag{4.12}$$

where μ represents the mean value of the Hoyt vector, and s_1 and s_2 represent the variance

of its real and imaginary parts, which are normally assumed to be equal and independent among them. Therefore, the resulting variance is the addition of the variances of the real and imaginary parts.

At this point, a graphical representation of the described concepts is shown for two different situations, one when the signal is perfectly tracked in amplitude (E-P-L correlators) and phase ($f_x = 0$), and one when there is an excess Doppler not correctly compensated ($f_x \neq 0$). The first case is represented by Fig. 4.2. Figure 4.2(a)–(b) shows the complex reflected field statistics and its amplitude statistics in a situation when the incoherent component is dominating the coherent component ($B = 0.01$). Therein, the 2-D Gaussian distribution is observed and it is seen that the mean value of the real and imaginary parts are approximately 0. Also, the amplitude distribution resembles perfectly the Rayleigh distribution, which is the result of the square root of the addition of two Gaussian random variables. Figure 4.2(c)–(d) shows the same information than (a)–(b) but in a situation when the coherent component is equal to the incoherent one ($B = 1$). In those figures it is shown that the mean value of the real part is 1, and now the amplitude distribution resembles more a Rice distribution than a Rayleigh one. Figure 4.2(e)–(f) shows again the complex and amplitude distribution of the electric field in a situation where the coherent component dominates the incoherent one ($B = 100$). Therein, it is seen that the mean value of the Hoyt's vector real part is ten times larger than its variability (2-D). In this case, the coherent power is 100 times larger than the incoherent one. In the amplitude distribution, the result is a Rice distribution with a very large coherent component that even resembles a Gaussian distribution.

Figure 4.3 shows the same information than Fig. 4.2, but for a reflected field that is not perfectly tracked ($f_x \neq 0$). This would be the normal situation because the reflected signal power/amplitude is very small, and another noise source that has not yet been taken into account should be considered which is the thermal noise. While the amplitude distributions are exactly the same than for a reflected field perfectly tracked, the complex I/Q diagrams are different. Particularly, when the coherent component dominates the incoherent one ($B = 100$), a ring shape is seen in the I/Q diagram, which is the effect of having a coherent rotating phasor. In those situations if the mean value of the reflected field is computed, it would be zero, but a coherent component is present and can be detected. The next section will show that it is possible to estimate both components in both situations, when only amplitude data is available, and when I/Q data is available. Note that in this section, the navigation data has not been included, which plays a role in the estimation of the coherent and incoherent components and in the shape of the I/Q complex diagrams. It has been decided to express only the scattering effect in this section and leave the navigation data effect for other section and for the experimental demonstration.

Finally, as aforementioned, the thermal noise should not be neglected, and it must be considered in the reflected signal statistics. Both coherent and incoherent components depend on each other. The larger the coherent component is, the smaller the incoherent one is, and vice versa. The incoherent component is sometimes known as a multiplicative or self-noise also called *speckle* [74]. The *speckle* noise is a noise that is only present when signal is present. If the signal is purely incoherent, the signal term only contains *speckle*. The larger the coherent component is, the smaller the *speckle* noise term is in comparison to the total signal power. Differently from *speckle*, the thermal noise term is

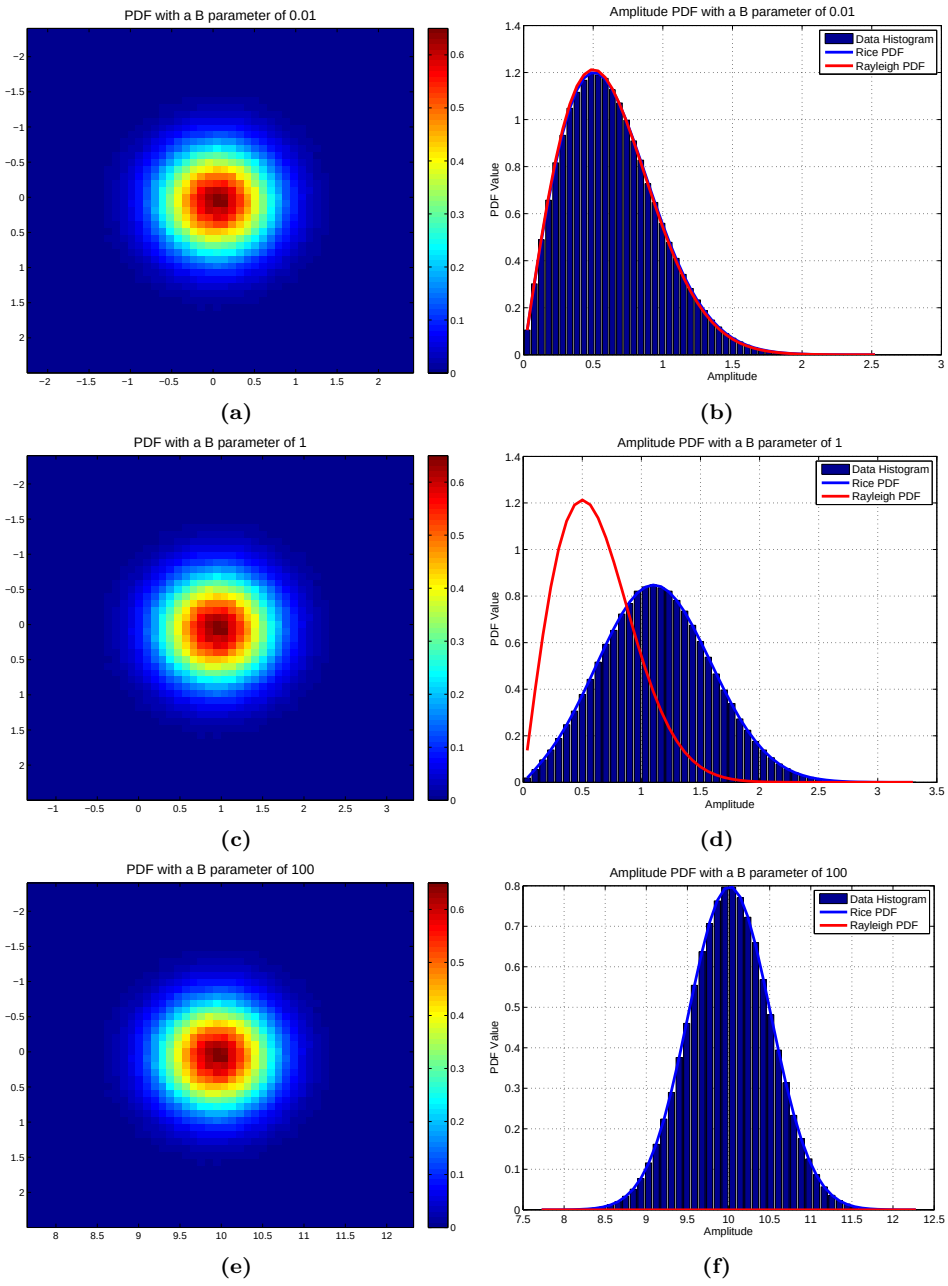

Figure 4.2: Complex (a),(c),(e) and amplitude (b),(d),(f) statistics of the reflected field for different B parameters: (a)-(b) B = 0.01, (c)-(d) B = 1, (e)-(f) B = 100

an additive noise and it is always present, independently from the presence of useful signal. Furthermore, its value does not depend on the useful signal value, neither the coherent nor the incoherent components. Therefore, the thermal noise is an additive noise, which only

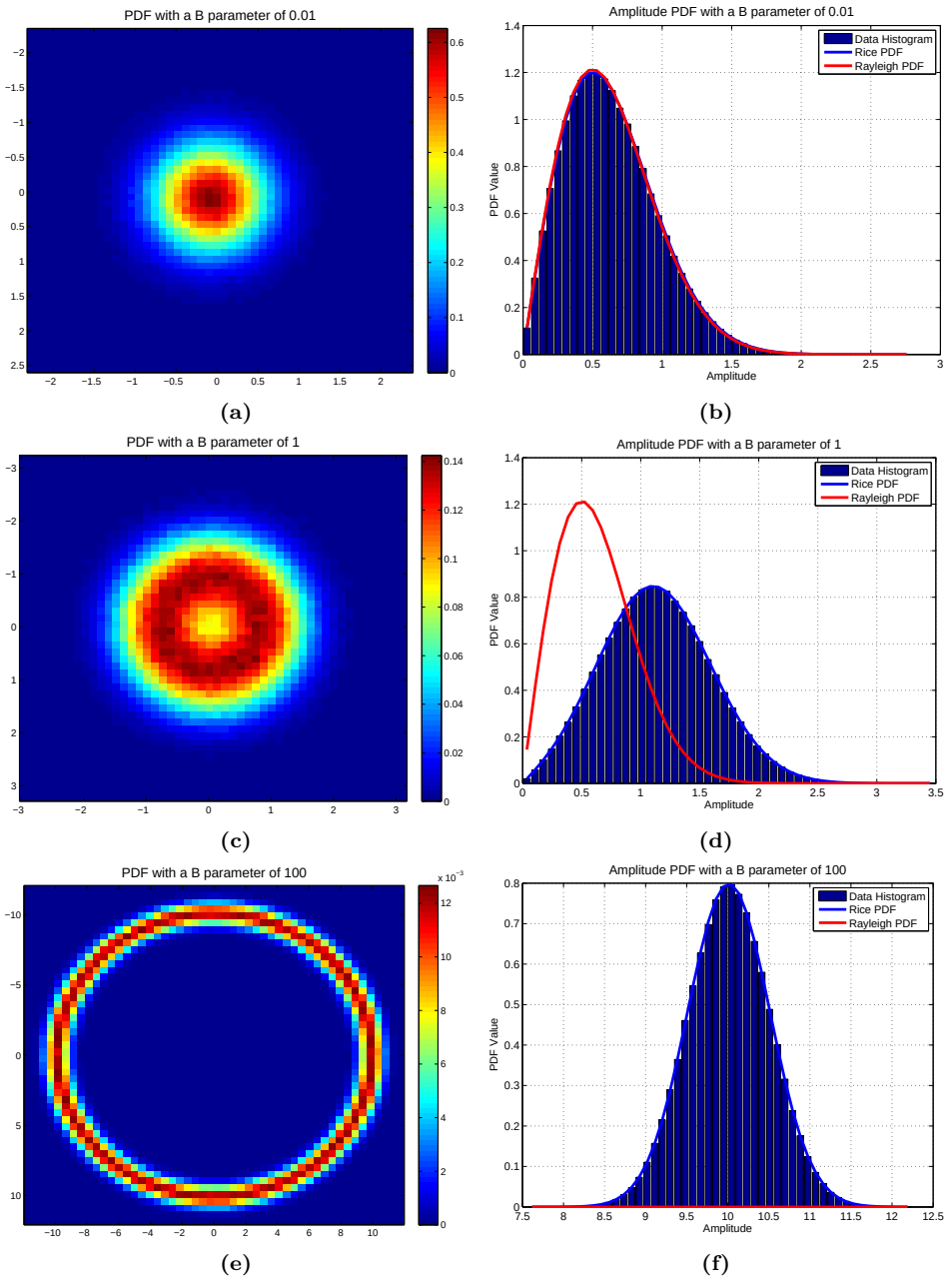

Figure 4.3: Complex (a),(c),(e) and amplitude (b),(d),(f) statistics of the reflected field for different B parameters and a Doppler not perfectly compensated: (a)-(b) B = 0.01, (c)-(d) B = 1, (e)-(f) B = 100

depends on the surface under observation (its temperature and its emissivity), and on the system's parameters (equivalent noise temperature or equivalent Noise Figure (NF)).

However, the thermal noise can be modeled as the *speckle* noise, as a complex zero-mean random Gaussian variable, and therefore its variance corresponds to the thermal noise power. Furthermore, both thermal and *speckle* noises are assumed to be independent among them because they come from a different nature.

Summarizing, the *speckle* noise is related to the surface scattering properties (imaging noise) whereas the thermal noise depends on the surface physical temperature and emissitivity. As shown in Chapter 2 and in Appendix C, the thermal noise power is given by Eqn. (E.5). In the observation of a LOS signal or a perfectly specular reflected signal, when computing their variability only the thermal noise power is computed, since there is no presence of incoherent component or *speckle* noise. However, in the observation of a non-perfectly specular reflected signal, when computing its variability, the addition of both the incoherent power and the thermal noise power is computed. In other words, the B parameter defined ideally in Eqn. (4.12) as the ratio between the coherent and incoherent power (mean value squared divided by its variance), it will be indeed the ratio between the coherent power and the addition of the incoherent power and the thermal noise power unless appropriate corrections are applied. So, in order to obtain the ratio between the coherent and incoherent components, the thermal noise contribution to the signal variability must be estimated. The algorithms to do it are described in the next section. In all those algorithms the thermal noise power is estimated using the data before the waveform's leading edge (Fig. 4.1). The B parameter will determine the algorithm to use in the geophysical parameters retrieval, as the geophysical model functions for the coherent and incoherent components are very different, which can be deduced from the different waveform shape shown in Fig. 4.1.

4.4 Estimation of the Coherent, Incoherent, and Thermal Noise Components

The estimation of the thermal noise, the coherent component, and the incoherent components can be performed after the waveform is computed. They can be obtained using both, amplitude data (real-value), or complex-data. This section starts with the real-value data, because the amplitude statistics are the same independently from a Doppler misalignment, as has been shown in Figs. 4.2–4.3.

4.4.1 Real-value Data

The reflected field follows a Hoyt distribution, which for the amplitude statistics only becomes a Rice distribution. The *pdf* of the Rice distribution can be expressed as [134]:

$$f_R(x) = \frac{2(K+1)x}{\Omega} exp\left(-K - \frac{(K+1)x^2}{\Omega}\right) I_0\left(2\sqrt{\frac{K(K+1)}{\Omega}}x\right) \tag{4.13}$$

where K and Ω are the shape and scale parameters respectively, and I_0 is the zeroth order Bessel function of the first kind. K is defined as the ratio between the coherent and "incoherent" components, in other words, the ratio between the coherent component power and the addition of the incoherent component power and the thermal noise power.

Ω is the addition of the signal (coherent and incoherent) and noise powers, which is equivalent to $\mathrm{E}\{R^2\}$, where R is the Rice random variable.

In [134] a simple methodology is proposed to estimate K, based on the measurement of the second and fourth order moments of the Rice random variable. The γ parameter of the Rice distribution is:

$$\gamma = \frac{Var\{R^2\}}{\mathrm{E}\{R^2\}^2} = \frac{\mathrm{E}\{R^4\}}{\mathrm{E}\{R^2\}^2} - 1 = \frac{2K+1}{(K+1)^2}, \tag{4.14}$$

and therefore:

$$K = \frac{\sqrt{1-\gamma}}{1-\sqrt{1-\gamma}}. \tag{4.15}$$

So, the ratio between the coherent and the addition of the incoherent or *speckle* and thermal noise components can be estimated by computing the second and fourth order moments of the Rice random variable or Hoyt vector. Furthermore, the second order moment is equivalent to the Ω, which means that $\mathrm{E}\{R^2\} = \Omega$.

Summarizing, there are now two equations (K and Ω) and 3 parameters to determine, which are the coherent component, the incoherent component, and the thermal noise. Even though it seems an undetermined system, the thermal noise component can be estimated prior to the trailing edge of the waveform, where there is no signal term, and therefore there it not a coherent or incoherent component. Even though it has not been directly mentioned until now, the coherent component only appears around the waveform's peak, a fact that can be deduced from Fig. 4.1 and from the coherent reflection model presented, since it corresponds only to the specular reflection point. Out of the ACF function, no coherent component will be found and only incoherent component or thermal noise will be present. So, once the thermal noise is estimated it is necessary to go back to the K and Ω equations in order to estimate the coherent component, and the incoherent component. At this point, the coherent to incoherent component ratio (B parameter) can be precisely computed, having taken into account and removed the contribution of the thermal noise to that computation. As can be seen, it is not as simple as shown in Eqn. (4.12) when the B parameter was computed as the mean value squared divided by its variance, which only holds in the absence of thermal noise.

The use of this methodology allows to estimate which is the contribution of each scattering component, and therefore select the appropriate retrieval algorithm for the geophysical parameter inversion. For instance, if there is no presence of a coherent component, and both the incoherent component and the thermal noise can be modeled as complex Gaussian random variables, their fourth order moment will be twice their second order moment squared. This results in a $\gamma = 1$ and a $K = 0$, which is the correct value of K in the absence of coherent component. Another example, which in this case is ideal, would be when there is no incoherent component and no thermal noise. That would result in a $\gamma = 0$, and $K = \infty$, which is the correct value of the ratio between coherent and incoherent components in the absence of incoherent component. This last example is ideal because thermal noise will always be present.

This methodology to estimate the real B parameter, and therefore choose the appropriate retrieval algorithm seems quite simple and efficient. It was initially suggested in [135] and later generalized in [136, 137], as the Rice distribution can be seen as a particular case of the Nakagami distribution. While it works well for high values of K, where

the coherent component is perfectly detectable and the Rice distribution even resembles the Gaussian distribution, it performs very poorly for low values of K ($K \leq 1$), as was already stated in [134, 136, 138]. The use of this methodology when the K parameter is very small leads often to solutions with complex K values because the γ estimator provides sometimes values larger than 1, due to the limited number of samples used. Those solutions are not realistic and show the limitations of the presented methodology.

Note that the navigation data has not been considered in this method, since while working with amplitude data, the phase information is lost, and therefore, it does not affect the overall performance. It is also worth to mention that this method was derived for multi-path environments when normally the thermal SNR is large and the main concern is the multi-path and not the thermal noise. Disappointingly, this is not the GNSS-R case, when the thermal SNR is normally very low and therefore the dominant term among the three terms that are being estimated is the thermal noise. In such situations the use of the I/Q samples is necessary, and another methodology can be used to estimate the three components and to select the appropriate retrieval algorithm.

4.4.2 Complex-value Data

In this section the algorithm proposed for an open-loop system is presented. The one for closed-loop systems is described in Chapter 5. After the correlation against the satellite code the full waveform is obtained. Before the leading edge, only thermal noise is found. The statistics of the waveform's peak have already been shown in the previous sections. The trailing edge of the waveform is either formed by the incoherent component and the thermal noise, or only by the thermal noise in case of specular reflection. Taking all that into account, the waveform's peak in the complex domain can be also expressed as the following phasor:

$$Y(t,\tau)|_{peak} = exp\left(j2\pi f_x t\right) exp\left(j\phi_D(t)\right) \sum_{n=1}^{N} A_n exp\left(\phi_n\right), \tag{4.16}$$

where f_x stands for the Doppler misalignment, $\phi_D(t)$ for the navigation data modulation, and the last term models the reflection as was done in Eqn. (4.9), and shows whether the coherent or incoherent component dominates. Due to the Binary Phase Shift Keying (BPSK) modulation in the GPS C/A code (recall Chapter 2), $\phi_D(t)$ only takes values of 0 and π which may change every 20 ms.

So, when I/Q data is available it is proposed to follow the process detailed in [138] in order to estimate the coherent and incoherent components, which was specifically designed for I/Q data and low SNR environments, which is exactly the GNSS-R case. Differently from the real-value case, here the first step needed is to remove the navigation data from the waveform's peak. Otherwise, assuming equal number of zeros and ones for the navigation data, the mean values of the reflected signal would be 0. The removal of the navigation data can be performed using the direct signal which is always acquired in any GNSS-R application without facing the low SNR and randomness issues of the reflected signal. For ground-based and airborne field campaigns, the navigation bits for the direct and reflected signals will coincide in time, so they can be straightforwardly estimated in the direct signal channel/data and compensated in the reflected one. Conversely, for

space-borne field campaigns they must be delayed due to the delay between direct and reflected signals. Therefore, once the navigation bits have been compensated, either multiplying $Y(t,\tau)$ by $e^{(j\phi_D(t))}$ or by its conjugate due to the BPSK modulation, the resulting signal is:

$$Y(t,\tau)|_{peak} = exp\left(j2\pi f_x t\right) \sum_{n=1}^{N} A_n exp\left(-\phi_n\right), \tag{4.17}$$

where if the reflection is coherent the rotating phasor shown in Fig. 4.3(c) will be seen. If it is not coherent the Gaussian randomness shown in Fig. Fig. 4.3(a) will be seen.

The excess Doppler frequency can be estimated computing the signal's spectral density and finding its maximum as follows:

$$X_{Y,SDF}(\omega) = \frac{1}{N} \left| \sum_{n=1}^{N} Y(t_n, \tau_{peak}) e^{-j\omega t_n} \right|^2. \tag{4.18}$$

Once the excess Doppler frequency (f_x) has been estimated from the resulting spectral density maximum, it is straightforward to compute the mean and variance values of the resultant signal to compute the K and the Ω parameters and follow previous section to compute B. An alternative methodology is computing the Ω parameter using the maximum likelihood estimator as [138]:

$$\Omega_{MLE} = \frac{1}{N} \sum_{n=1}^{N} |Y(t_n, \tau_{peak})|^2, \tag{4.19}$$

which can be done using the I/Q samples or its Discrete Fourier Transform (DFT) version using Parseval's theorem. Then, the mean squared value is estimated as:

$$\hat{\mu}^2 = X_{Y,SDF}\left(\omega_{max}\right) \tag{4.20}$$

ω_{max} is the frequency value that compensates the excess Doppler and maximizes the estimated spectral density. Then, the K estimated parameter is:

$$\hat{K} = \frac{\hat{\mu}^2}{\Omega_{MLE} - \hat{\mu}^2}. \tag{4.21}$$

After, K and Ω_{MLE} have been estimated, the thermal noise is estimated before the waveform's leading-edge, and then the B parameter is computed as it was done in the previous section.

4.5 SNR Definitions

As it has been already seen there are two different noise sources which itself provide different SNR definitions. To clarify this point is better to look at Fig. 4.4, where (a) represents better the GNSS/cGNSS-R signal processing stage and (b) the iGNSS-R signal processing stage, and the different SNRs at each stage are defined.

The fundamental operation in a GNSS/cGNSS-R signal acquisition system is the cross-correlation of the digitized received signal with either a digitized version of the direct signal (iGNSS-R) or a clean replica of the satellite code (cGNSS-R) in order to obtain the so-called waveform. This computation can last up to 20 ms, which is the duration of a navigation bit. Longer coherent integration times can be always applied after compensating for the navigation bit sign change. After coherent integration, non-coherent integration is performed, which consists of summing the waveforms obtained in power units to improve the visibility or detectability of the satellite presence. Non-coherent integration requires a squaring operation which changes the statistics of the obtained samples, and therefore, leads to a redefinition of the resulting SNR. Figure 4.4(a) shows a typical block diagram of a coherent or I/Q detector. Therein, it is possible to introduce four different definitions of the SNR, but they are, in fact, two. The first one is the $\mathrm{SNR_{c,in}}$, which is the SNR before correlation with the clean replica of the satellite code, or pre-correlation SNR. It is always negative (in dB units) since GNSS signals are below the noise level, unless a very high directivity antenna is used to acquire them. The second one is the $\mathrm{SNR_{c,out}}$, which is the SNR after correlation either with the direct signal or with the clean replica of the satellite code. It is related to the $\mathrm{SNR_{c,in}}$ by the signal's bandwidth times the coherent integration time. Basically, the thermal noise bandwidth is reduced in the coherent integration process, letting the signal rise above the new thermal noise level. The third one is the $\mathrm{SNR_{nc,in}}$, which is the SNR resulting from a non-coherent detection scheme where no phase information is available. The $\mathrm{SNR_{nc,in}}$ is related to the $\mathrm{SNR_{c,out}}$ by the squaring-loss parameter [139]. The last one is the $\mathrm{SNR_{nc,out}}$, which is the SNR after the non-coherent integration/averaging.

One way to determine the SNR is by applying the detectability criterion [140, 141], which is based on a comparison of the signal mean value with its variability (noise power):

$$d = \frac{\mathrm{E}\{f_{S+N}\} - \mathrm{E}\{f_N\}}{\sqrt{\mathrm{E}\{{f_N}^2\} - \mathrm{E}\{f_N\}^2}}, \tag{4.22}$$

where f_{S+N} is a function with a subscript which stands for the signal (S) plus noise (N) components, and f_N is a function with a subscript which indicates that it only stands for the noise components. The numerator is a measurement of the signal's mean value removing the noise contribution to it, and the denominator is a measurement of the thermal noise standard deviation.

The already defined detectability criterion is an amplitude/voltage signal-to-noise ratio if the function f_{S+N} is defined in Volts [V] units, and it is a power signal-to-noise ratio if the same function is defined in Volts squared [$\mathrm{V^2}$] units [141]. For instance, if it is applied to a constant signal of value A disturbed by complex zero-mean Additive White Gaussian Noise (AWGN), in its amplitude form it is equivalent to:

$$d = \frac{\mathrm{E}\{f_{S+N}\} - \mathrm{E}\{f_N\}}{\sqrt{\mathrm{E}\{{f_N}^2\} - \mathrm{E}\{f_N\}^2}} = \frac{A - 0}{\sigma_n}, \tag{4.23}$$

which is the signal's mean value divided by the noise standard deviation. Differently, in its power (squared) form is equivalent to:

$$d = \frac{\mathrm{E}\{f_{S+N}\} - \mathrm{E}\{f_N\}}{\sqrt{\mathrm{E}\{{f_N}^2\} - \mathrm{E}\{f_N\}^2}} = \frac{A^2 + \sigma_n^2 - \sigma_n^2}{\sqrt{2\sigma_n^4 - \sigma_n^4}} = \frac{A^2}{\sigma_n^2}, \tag{4.24}$$

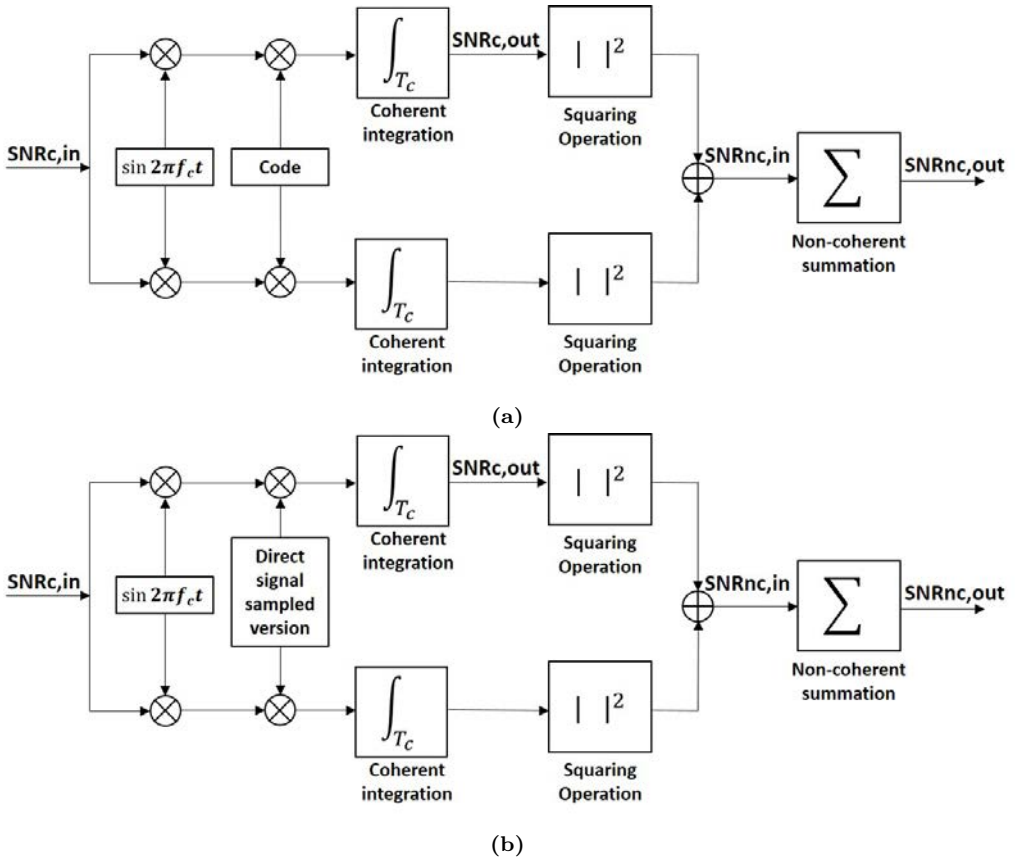

Figure 4.4: (a) Typical GNSS/cGNSS-R receiver block diagram, (b) Simplified iGNSS-R receiver block diagram.

which coincides with the traditional definition of the SNR under the presence of Gaussian noise.

However, since in the GNSS-R case the useful signal component has also a variability (*speckle*), the aforementioned detectability criterion is not enough to evaluate the overall signal SNR at its peak [142,143]. Therefore, another definition must be used which takes into account this effect which is:

$$d' = \frac{\mathrm{E}\{f_{S+N}\} - \mathrm{E}\{f_N\}}{\sqrt{\mathrm{E}\{f_{S+N}{}^2\} - \mathrm{E}\{f_{S+N}\}^2}}, \tag{4.25}$$

where, as it can be seen, in the denominator the variability is computed under the signal presence, and therefore it takes into account both the contribution of the *speckle* and thermal noise sources.

If those criteria are applied to the both cGNSS-R and iGNSS-R schemes in order to determine the $\mathrm{SNR}_{\mathrm{nc,out}}$ after a non-coherent integration of T seconds, where $T \gg T_c$,

the following expressions are obtained:

$$d_{nc} = \sqrt{\frac{1}{\overline{\overline{T}}_n}} \frac{\mathrm{P_{coh}}(\tau) + \mathrm{P_{incoh}}(\tau)}{\mathrm{P_{T_c}}(\tau)} = \sqrt{\frac{1}{\overline{\overline{T}}_n}} d_c = \sqrt{\frac{1}{\overline{\overline{T}}_n}} \mathrm{SNR_{TH,c}}, \tag{4.26}$$

$$d'_{nc} = \frac{\mathrm{P_{coh}}(\tau) + \mathrm{P_{incoh}}(\tau)}{\sqrt{2\bar{t}_s \mathrm{P_{coh}}(\tau)\mathrm{P_{incoh}}(\tau) + 2\bar{t}_n \mathrm{P_{coh}}(\tau)\mathrm{P_{T_c}}(\tau) + 2\bar{t}_s\bar{t}_n \mathrm{P_{incoh}}(\tau)\mathrm{P_{T_c}}(\tau) + \overline{T}_n \mathrm{P}^2_{\mathrm{T_c}}(\tau) + \overline{T}_s \mathrm{P}^2_{\mathrm{incoh}}(\tau)}}, \tag{4.27}$$

$$d_{ni} = \sqrt{\frac{1}{\overline{\overline{T}}_n}} \frac{\mathrm{P_{coh}}(\tau) + \mathrm{P_{incoh}}(\tau) + \mathrm{P_{T_c}}(\tau)\frac{SNR_r}{SNR_d}}{\left(1 + \frac{1}{SNR_d}\right)\mathrm{P_{T_c}}(\tau)} = \frac{d_{nc}}{1 + \frac{1}{SNR_d}} + \sqrt{\frac{1}{\overline{\overline{T}}_n}} \frac{SNR_r}{SNR_d + 1}, \tag{4.28}$$

$$d'_{ni} = \frac{\mathrm{P_{coh}}(\tau) + \mathrm{P_{incoh}}(\tau) + \mathrm{P_{T_c}}(\tau)\frac{SNR_r}{SNR_d}}{\sqrt{2\bar{t}_s \mathrm{P_{coh}}(\tau)\mathrm{P_{incoh}}(\tau) + 2\bar{t}_n \mathrm{P_{coh}}(\tau)\mathrm{P_{T_i}}(\tau) + 2\bar{t}_s\bar{t}_n \mathrm{P_{incoh}}(\tau)\mathrm{P_{T_i}}(\tau) + \overline{T}_n \mathrm{P}^2_{\mathrm{T_i}}(\tau) + \overline{T}_s \mathrm{P}^2_{\mathrm{incoh}}(\tau)}}, \tag{4.29}$$

where the normalized correlation times $\bar{t}_s$, $\bar{t}_n$, $\overline{T}_s$, and $\overline{T}_n$ are defined as:

$$\bar{t}_s = \frac{1}{T}\int_{-T}^{T} \Lambda\left(\frac{\xi}{T}\right) \gamma_{s,s}(\xi,\tau) d\xi, \tag{4.30a}$$

$$\bar{t}_n = \frac{1}{T}\int_{-T}^{T} \Lambda\left(\frac{\xi}{T}\right) \gamma_{n_{T_c},n_{T_c}}(\xi,\tau) d\xi = \frac{T_c}{T}, \tag{4.30b}$$

$$\overline{T}_s = \frac{1}{T}\int_{-T}^{T} \Lambda\left(\frac{\xi}{T}\right) |\gamma_{s,s}(\xi,\tau)|^2 d\xi, \tag{4.30c}$$

$$\overline{T}_n = \frac{1}{T}\int_{-T}^{T} \Lambda\left(\frac{\xi}{T}\right) |\gamma_{n_{T_c},n_{T_c}}(\xi,\tau)|^2 d\xi = \frac{2}{3}\frac{T_c}{T}, \tag{4.30d}$$

where $\gamma_{s,s}(\xi,\tau)$ is the *speckle* noise correlation function, $\gamma_{n_{T_c},n_{T_c}}(\xi,\tau)$ is the thermal noise correlation function, $\mathrm{P_{coh}}(\tau)$ is the coherent component power, $\mathrm{P_{incoh}}(\tau)$ is the incoherent component power, $\mathrm{P_{T_c}}(\tau)$ is the thermal noise power for the cGNSS-R case, $\mathrm{P_{T_i}}(\tau)$ is the thermal noise power for the iGNSS-R case, and it is related to the $\mathrm{P_{T_c}}(\tau)$ as [72]:

$$\mathrm{P_{T_i}}(\tau) = \mathrm{P_{T_c}}(\tau) \cdot \left(1 + \frac{SNR_r(\tau) + 1}{SNR_d(\tau)}\right), \tag{4.31}$$

where SNR_d and SNR_r are the pre-correlation SNR or $\mathrm{SNR_{c,in}}$ in Fig. 4.4 for the direct (d) and reflected (r) signals respectively.

Apart from the overall SNR defined at the correlation peak which allows to determine the scatterometric performance of this technique, it might be of better use to define other SNRs such as the thermal SNR at the peak (from now on $\mathrm{SNR_{TH}}$), which is mentioned in the d_{nc} computation, or the *speckle* SNR (from now on $\mathrm{SNR_{SP}}$).

The $\mathrm{SNR_{TH}}$ for the cGNSS-R case is defined as the ratio between the signal power and the thermal noise power:

$$\mathrm{SNR_{TH,c}}(\tau) = \frac{\mathrm{P_{coh}}(\tau) + \mathrm{P_{incoh}}(\tau)}{\mathrm{P_{T_c}}(\tau)}, \tag{4.32}$$

and for the iGNSS-R case as (also derived in [72]):

$$\mathrm{SNR}_{\mathrm{TH,i}}(\tau) = \frac{\mathrm{P}_{\mathrm{coh}}(\tau) + \mathrm{P}_{\mathrm{incoh}}(\tau)}{\mathrm{P}_{\mathrm{T}_i}(\tau)} = \frac{\mathrm{SNR}_{\mathrm{TH,c}}(\tau)}{1 + \frac{SNR_r(\tau)+1}{SNR_d(\tau)}}, \tag{4.33}$$

where only the thermal noise power considered changes.

The $\mathrm{SNR}_{\mathrm{SP}}(\tau)$ is the same for the cGNSS-R and iGNSS-R case, since it is defined as the ratio between the total useful signal power and the incoherent signal power, as:

$$\mathrm{SNR}_{\mathrm{SP}}(\tau) = \frac{\mathrm{P}_{\mathrm{coh}}(\tau) + \mathrm{P}_{\mathrm{incoh}}(\tau)}{\mathrm{P}_{\mathrm{incoh}}(\tau)} = B + 1. \tag{4.34}$$

Note that for $\mathrm{SNR}_{\mathrm{SP}}(\tau)$, if the coherent component dominates, it tends to B since $B \gg 1$, where B is the ratio between the coherent and incoherent component powers, and if the incoherent component dominates the it tends to 1 because $B \to 0$. Also note that any backward scattering remote sensing system like SARs always find a $\mathrm{SNR}_{\mathrm{SP}} = 1$ due to the back-scattering geometry and the absence of a coherent component in the scattered signal. These last SNR expressions can be used to simplify the overall SNR expressions

Finally, it is possible to define the coherent SNR or the ratio between the signal's coherent component and the thermal noise for the cGNSS-R case, which is the computed by the LARGO instrument described in Chapter 5 and the one used in Chapter 8 to compare reflectivity and brightness temperature measurements. Therefore, the coherent SNR is:

$$\mathrm{SNR}_{\mathrm{TH,coh}} = \frac{\mathrm{P}_{\mathrm{coh}}}{\mathrm{P}_{\mathrm{n}}}. \tag{4.35}$$

All mathematical developments that appear in this section are detailed in Appendix C, and are not included here to improve the chapter's readability.

4.6 Previous Works Related to GNSS scatterometry for Land Observations

As mentioned in Chapter 2, GNSS-R started with the goal of measuring mesoscale altimetry in 1993. Since then, several applications have appeared. Scatterometry applications can be divided in three different groups. The first group is related to analyze the waveform's leading-edge and which is related to the altimetry retrievals. The second group, which is the one used on this PhD Thesis, observes the waveform's peak value and uses the reflectivity or SNR measurement at that point for the retrieval of geophysical parameters. This group is generally related to the coherent scattering model and they have been used mainly for land and sea ice monitoring. The third group is the one that focuses on the trailing-edge of the waveform and it is related to the incoherent scattering model, because on the trailing-edge there is only presence of thermal noise and incoherent component or *speckle*. This group is mainly focused on sea surface observations, e.g. wind mapping [52, 144], as it is where the incoherent scattering model normally works best [51, 52]. Chapters 8 and 9 are based on the analysis of the second group that is the one that is going to be introduced here. Chapter 10 deals with the difference between second and third groups, and the theoretical background is introduced in there.

The analysis of the peak value of the DDM/waveform started in 2000, when its value was related to the water content of the reflecting surface [64, 65]. This approach was mainly theoretical, and the experimental waveform's shape shown in [65] suggested the existence of a coherent component in the scattering process over land. Later, in 2004, with the analysis of the SMEX02 experiment the existence of a dominating coherent component was confirmed, and the reflected signals proved to be sensitive to the soil moisture content [145]. Figure 4.5 shows some GPS reflected thermal SNR transects where the transitions between different field types can be easily detected. In the same publication the reflected power was compared qualitatively against the brightness temperature provided by an L-Band microwave radiometer without extracting any clear conclusion. Also some correlation between the thermal SNR and the in-situ soil moisture measured using soil moisture probes located at 1 cm was found for two different fields with two different types of vegetation (soybean and corn). It can be deduced from the figures shown, e.g. Fig. 4.6, that the reflected power was not sensitive to the vegetation type of the field, even though corn and soybean have different growing schemes and different VWC.

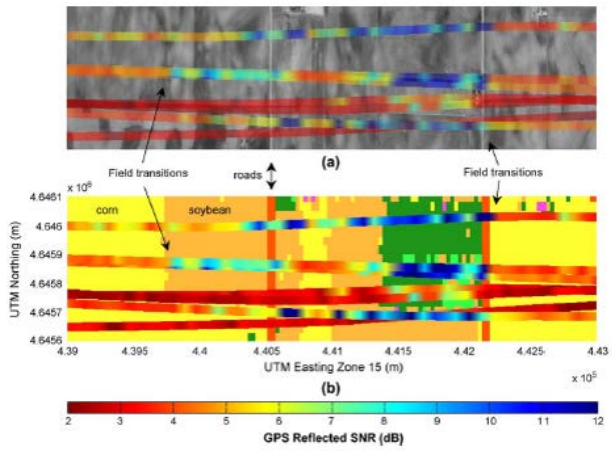

Figure 4.5: GPS reflected SNR from the SMEX02 field campaigns [145].

In 2006, another publication appeared analyzing the same dataset, but providing more developments on the GNSS-R data analysis [146]. Therein, a more advanced signal processing algorithm is proposed including two different calibration algorithms. The first calibration algorithm proposed was to use a well-known water body on the field campaign to calibrate the reflected signal power and provide calibrated reflectivity values with respect to the water ones. The second calibration algorithm proposed was related to estimate the multi-path free direct signal power and use it to obtain a calibrated reflectivity with respect to the direct signal power. Once the reflectivity was calibrated, the dielectric constant of the terrain was estimated. From the estimated dielectric constant the soil moisture content of the terrain was inferred and compared against the one provided by in-situ measurements, as shown in Fig. 4.7. It can be inferred that the GPS method provided a noisier measurement and tended to underestimate both dielectric constant and therefore soil moisture content. However, relative errors were found to be very large [146].

In 2012 Egido et al. kept on the scatterometry research on soil moisture using a similar

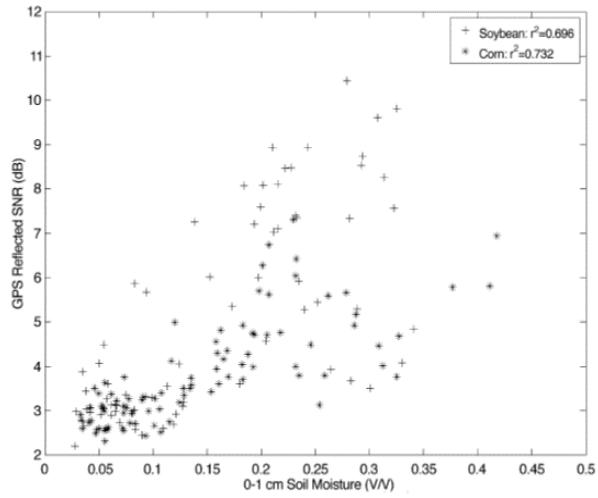

Figure 4.6: Comparison between GPS reflected SNR and SM for two different fields with two different vegetation types (soybean and corn) [145].

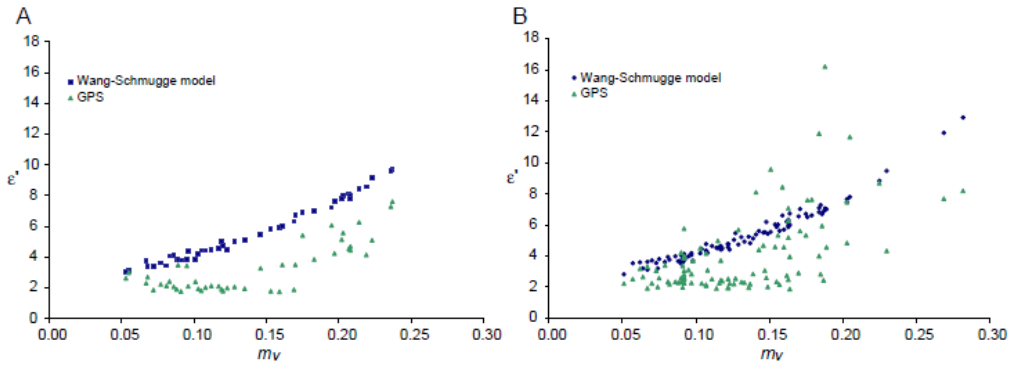

Figure 4.7: Comparison between dielectric constant estimated from the GPS reflected signals and from the in-situ soil moisture probes for two different fields: A → soybean, B → corn [146].

approach to the one proposed by Katzberg in 2006, calibrating the reflected signals against the direct one [147]. Furthermore, they decided to use, for the first time, reflected signals at both polarization states, LHCP and RHCP, which were calibrated against the RHCP direct signal component. In that publication a ground-based static field campaign is introduced (LeiMON) and the estimated $|r_{RL}|^2$, $|r_{RR}|^2$, and $|r_{RR}|^2/|r_{RL}|^2$ are compared against the in-situ soil moisture as shown in Fig. 4.8. Not a large correlation between the reflectivity parameters and the in-situ soil moisture is found. However, the polarization ratio shows a correlation of 0.84 with respect to the soil moisture, indicating that it could be used to mitigate the detrimental effects of surface roughness.

Also, in the same publication the reflectivity was compared against the in-situ mea-

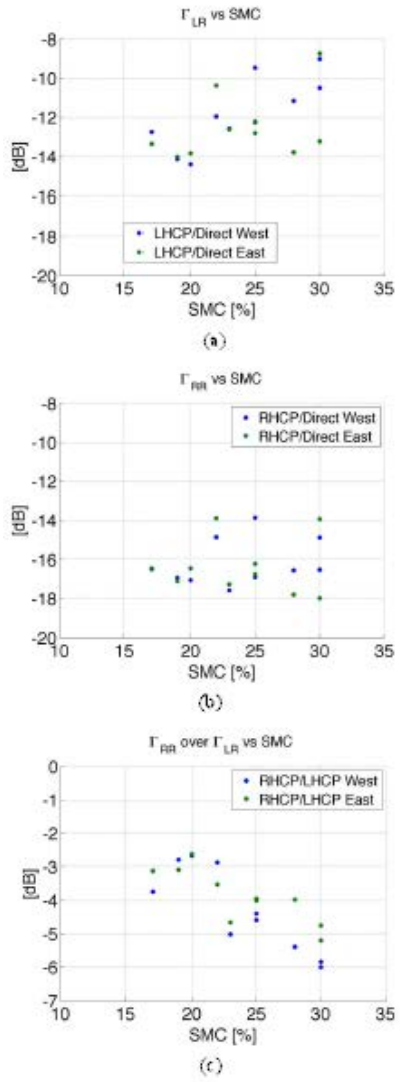

Figure 4.8: Comparison between estimated reflectivity and in-situ soil moisture for: (a) $|r_{RL}|^2$, (b) $|r_{RR}|^2$, and (c) $|r_{RR}|^2/|r_{RL}|^2$ [147]. The blue and green colors represent two different fields with different vegetation conditions and types.

sured plant water content of each of the two fields under analysis, which is shown in Fig. 4.9. A larger correlation with both parameters is found (on the order of 0.8 for the $|r_{RL}|^2$), suggesting, as expected, that the vegetation acts as an attenuator for the L-Band GNSS signals. This attenuation depends on the plant water content, which is predicted by general microwave scattering models.

Finally, in 2014, also Egido et al. presented the results of an airborne field campaign (GRASS) using the same reflectivity parameters [148]. Four different reflectivity maps

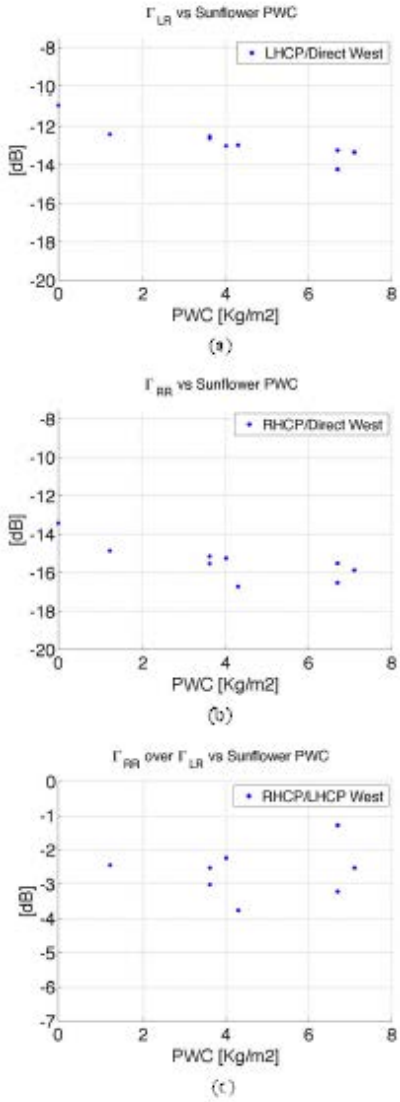

Figure 4.9: Comparison between estimated reflectivity and in-situ plant water content for: (a) $|r_{RL}|^2$, (b) $|r_{RR}|^2$, and (c) $|r_{RR}|^2/|r_{RL}|^2$ [147]. The blue and green colors represent two different fields.

are shown in Fig. 4.10, where (a) and (c) represent the $|r_{RL}|^2$, and (b) and (d) the $|r_{RR}|^2$. A sensitivity analysis to soil moisture and vegetation biomass was also performed for those two components, obtaining the results shown in Fig. 4.11, where it indicates that the ratio of the estimated reflectivities ($|r_{RR}|^2/|r_{RL}|^2$) is sensitive to soil moisture, and the $|r_{RL}|^2$ component is sensitive to vegetation biomass. This is in agreement with the ground-based results previously presented for both the soil moisture and the vegetation

biomass parameters [147].

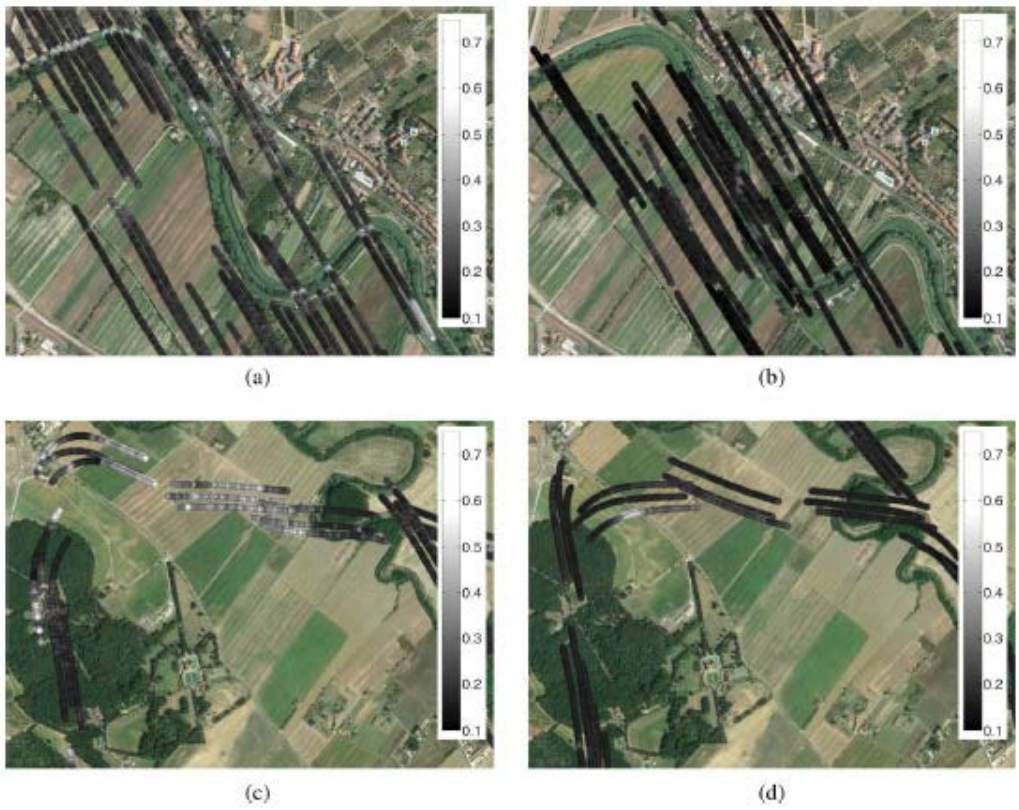

Figure 4.10: Reflectivity maps for two different test sites: (a) $|r_{RL}|^2$, (b) $|r_{RR}|^2$, (c) $|r_{RL}|^2$, and (d) $|r_{RR}|^2$ [148].

4.7 Summary and Conclusions

This Chapter has described the basics of the GNSS scatterometric technique. Differently from the IPT, in the scatterometric technique and due to the nature of the reflection mechanism, both coherent and incoherent scattered components are present in the reflected signal. The section related to the signal model describes those components, the model used for them, and associates them to the waveform nature and shape. Therein, it is described how the coherent component is a replica of the transmitted point spread function or WAF multiplied by the rough surface Fresnel reflection coefficient, whereas the incoherent component shows a distribution of the reflected power along the delay domain. This is mentioned later in this PhD Thesis dissertation, and it is described as the convolution between the transmitted signal point spread function or WAF and the bistatic radar cross section σ_0. Subsequently, the reflected field statistics are described, highlighting the main differences among them. To do so, three different scenarios are

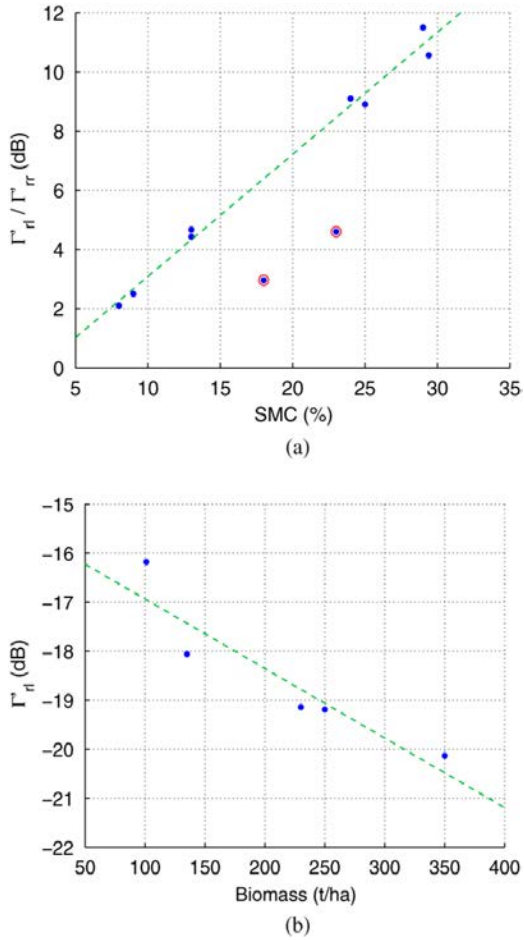

Figure 4.11: Reflectivity sensitivity analysis to soil moisture and vegetation biomass: (a) SM, and (b) Vegetation biomass [148].

shown, one when the incoherent component clearly dominates the coherent component, one when they have the same value, and another one when the coherent component clearly dominates the incoherent one. Those situations are shown for both, the amplitude data (real-value) and the amplitude-phase data (complex-value), in the case of having and excess Doppler frequency compensated or not. The effect of thermal noise is also described, which is similar to the incoherent component term (*speckle*). Different estimators are proposed to deal with both, real-value and complex-value data, in order to estimate the coherent component, the incoherent component, and the thermal noise. This last step is extremely important since the estimation of those components determines the algorithm to be used in the geophysical parameter inversion. After that, the overall signal SNR, which allows to compute the accuracy of the technique is presented, together with other SNR definitions that will help in the geophysical parameter inversion presented in Chaps. 8–10. Finally, representative previous works performed prior to this PhD Thesis dissertation are described, which basically include the ones by Masters and Katzberg et

al. during the SMEX02 field campaign, and the ones performed by Egido et al. during his PhD Thesis [149].

5

Chapter 5

Hardware developed for the field experiments

This chapter gives an overview of the instruments developed during this PhD Thesis. In particular, the SMIGOL instrument, which is one of the instruments previously designed at the research group, has been improved, converting it into a dual-polarization instrument. A new cost-effective GNSS-R scatterometer called LARGO has been developed and manufactured. Apart from that, this PhD Thesis has also contributed to the PAU payload analysis and testing, leading to an autonomous PAU instrument. Finally, an instrument based on GNSS remote sensing for vegetation has also been developed which has been named after McGiver. Other hardware instruments involved in the development of the whole PhD Thesis dissertation such as the DUO instrument will be detailed in later chapters.

5.1 Introduction

Different GNSS-R instruments have been developed since the DMR proposed by Garrison and Katzberg in 1997. The DMR was the first receiver intended for GNSS-R remote sensing. It was able to process the GPS signal in real-time with enough quality to let a software receiving system reconstruct the signal and compute the so-called waveforms. The waveform was the first GNSS-R observable considered to determine the ionospheric correction via the reflected channel [50]. The next generation receivers were based on sampling the signal with high enough sampling frequency and number of bits, which is a technique that has been followed until now, when it is possible to reach sampling frequencies up to 80 MHz to reconstruct the new wider-band GNSS signals. For instance, some of the instruments developed using this technological approach are:

- DODEREC: designed and developed by UPC for the Institut d'Estudis Espacials de Catalunya (IEEC) [27].
- GPS Open Loop Differential Real-Time Receiver (GOLD-RTR): designed and developed by IEEC [61].
- SAM: designed and developed by Starlab [149].
- PIR: designed and developed by IEEC [150].
- PAU first version: designed by UPC and manufactured by AD Telecom.
- PIR Aircraft (PIRA): designed and developed by IEEC [151].

Generally, most of the instruments in the literature were based on the sampling and storing approach, and all of them were custom-made for the desired application. So, bandwidth and sampling frequency were fixed parameters on the instrument.

The first commercial instrument available not intended for a unique application is the SiGe receiver, which can be found in `https://www.sparkfun.com/products/retired/10981`. It allowed to perform GNSS remote sensing to those not interested in hardware development with a relatively low-cost instrument. This receiver was revolutionary because it was the first Software Defined Radio (SDR) receiver intended for a general GNSS raw data signal processing, and consequently it could also be used to process the GNSS reflected signals too. After that, SDRs have revolutionized the GNSS-R hardware design, as they solve the back-end receiving part completely. New SDR instruments such as the Universal Software Radio Peripheral (USRP) [152] allow to change the sampling frequency, the filter bandwidth, and with some code tuning even the number of bits used in the sampling process.

The main drawback of the technology described above is the large amount data generated that has to be pre-processed. For instance, for a 16 MHz sampling frequency with 8-bit resolution, the system generates a data-rate of 16 Mbytes/s, which is roughly 1 Gbyte/min. In other words, 60 GB/h/channel, which increases the total amount of data with increasing the number of channels, and the storage time. These sampled data is then correlated either against a clean replica of the satellite code (cGNSS-R) or against a sampled version of the direct signal (iGNSS-R) in order to generate the waveform. This pre-processing stage is largely time consuming, because the optimum Doppler frequency has to be computed during that operation. Once the pre-processing stage is finished, the GNSS-R field is only interested in a few lags from the entire correlation function (those

ones around the peak value) reducing the data needed, and even sometimes it is only interested on the peak value. While the fact of having the signal sampled and stored allows the application of any kind of signal processing algorithm, this typical pre-processing stage can last for 12 hours per satellite per minute in a normal computer.

Therefore, in order to reduce the pre-processing time and looking forward to make GNSS-R applications cost- and time-effective, some initial real-time processing techniques were conceived for the next generation of GNSS-R receivers. They were based on the fact that GPS receivers already perform this preliminary processing stage at a hardware level in real-time. So, a similar scheme to the GPS signal acquisition one with the early, prompt, and late (E-P-L) correlators was implemented in the GriPAU instrument, but with with a larger number of correlators to compute correlations over more delay and Doppler bins (32 x 24, respectively) [18]. Figure 5.1 shows a comparison between the two different kind of approaches presented for the GNSS-R hardware receivers. Therein, it is possible to identify in both a common part, which is the superheterodyne receiving scheme, and an added block on the real-time approach which contains the real-time processing scheme. The superheterodyne receiver down-converts the received signal to Intermediate Frequency (IF) or Base-Band (BB) in two steps (although in the figure only one is shown), and has the samples prepared for the storage device. If signals are at IF they are sampled using real data sampling schemes, whereas if they are in BB an I/Q sampling scheme is used. The real-time data processing block will be presented in section 5.4, as there are different solutions to implement it, and the PAU uses one of them. The real-time processing approach has been followed by the recent spaceborne GNSS-R missions, evolving from the UK-DMC mission payload, which used the off-line software processing approach, to the recent UK TDS-1 mission, which performs real-time DDM computation using up to 4 different satellites. This approach is preferred for satellite data as it highly reduces the amount of data to be downloaded later through the down-link channel.

Furthermore, there are applications that need less information, and simpler hardware schemes can be used. One of them is the IPT, which only needs power measurements of the received signal, which can be directly obtained using the National Marine Electronics Association (NMEA) messages from conventional GPS receivers. This requirement even simplifies more the hardware scheme, and it reduces even more the amount of data generated, as the back-end receiver performs the real-time correlations and the signal power estimation. This reduces to hundreds of bytes per second the data-rate generated. Other techniques such as the GNSS scatterometry, which is based on measuring the signal peak power, require an intermediate solution between the simple IPT hardware and the complex hardware described above that either sample the signal or compute the entire DDMs. In the scatterometric approach two different noise sources are involved, the thermal noise and the *speckle* noise, as previously seen on Chapter 4. Information about both noise sources can be retrieved using high-performance GPS receivers, which deliver the promptly I/Q correlators outputs which can be processed to estimate the surface reflectivity. This intermediate solution leads to the development of the LARGO instrument used in this PhD Thesis dissertation.

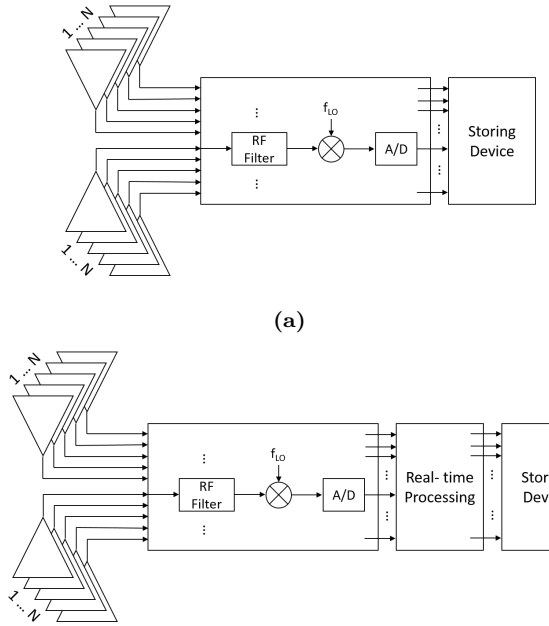

Figure 5.1: (a) Simple GNSS-R receiver scheme, (b) Real-time GNSS-R processing scheme.

5.2 Dual-Polarization SMIGOL

The Dual-Polarization SMIGOL is the natural evolution of the SMIGOL instrument previously available at the research group and developed in N. Rodriguez-Alvarez PhD Thesis [28]. The SMIGOL instrument was based on the use of a linear Vertical (V)-Pol antenna pointing to the horizon, and a RF amplifier to amplify the signal to reach the sensitivity level of the back-end GPS receiver. Data from the GPS receiver was captured by a micro-controller and stored on a microSD card for the data processing on an external computer. Figure 5.2 shows the block diagram of the V-Pol SMIGOL instrument emphasizing the blocks mentioned before, and a RF filter in order to mitigate any kind of out-of-band Radio Frequency Interference (RFI). No more amplification was used in order to avoid saturating the GPS receiver used as a back-end. It is worth to mention that the SMIGOL instrument is an autonomous instrument, which is why it has a power supply system consisting of solar panels, lithium batteries, and a battery charger that commutes smartly between the two main power sources.

So, working with the inherited SMIGOL instrument the main goal was to add an extra polarization to the whole block diagram in order to be able to measure both Horizontal (H)- and V-Pol at the same time, and prove the theoretical concepts shown on Chapter 3. In order to add the extra polarization there are two different possible solutions. The first one is to add an extra antenna and compensate for the baseline between the two antennas. The second one is to modify the linear V-Pol antenna and convert it into a dual-polarized

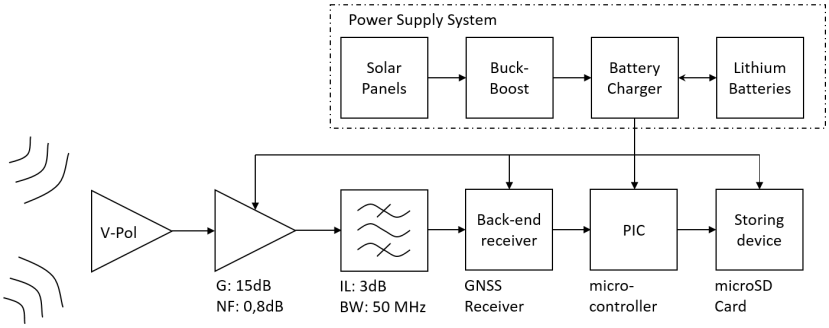

Figure 5.2: V-Pol SMIGOL block diagram.

one. The latter was chosen for simplicity in the data processing. Consequently, an extra receiving chain was added to measure the H-Pol interference pattern. This doubled the information to be stored and required more intelligence and resources from the micro-controller. Then, the micro-controller did not need to store only the data, but it had to tag it according to the receiving chain, and to locally time-tag it, which required some interpretation of received bytes. Apart from that, the addition of an extra receiving chain required more energy and the power supply system had to be redesigned to fit the new system power requirements. Taking into account all the required modifications, the dual-polarization SMIGOL block diagram is summarized in Fig. 5.3. In Fig. 5.3, it is possible to identify the main changes performed to the single polarization SMIGOL, such as a change in the micro-controller, a change in the power supply system, and the replica the receiving chain for H-Pol. This process is detailed in the following subsections.

5.2.1 Antenna

The main goal with this modification is to design a dual-polarized antenna without degrading the performance of the previous linear V-Pol antenna. To do so the main scheme was preserved, which was based on a patch antenna fed symmetrically at two different points to keep the symmetry of the antenna pattern. The electric field distribution of a patch antenna has exactly the same value but opposite phase at any point on the feeding plane whose distance is equal to the center, as shown in Fig. 5.4. Consequently, the feeding points are combined using a 180° hybrid to add them up in phase. Then, the signal goes into the receiving chain.

In order to convert it into a linear dual-polarization antenna two extra feeding points were added on the orthogonal plane without modifying the antenna properties, as in that plane, the electric field amplitude for the orthogonal polarization is minimum. The previous 180° hybrid was redesigned into a circuit board with two different hybrids, one for each polarization. Figure 5.5 shows the basic structure of the hybrids, and how the 180° phase shift is created. The first 90° phase shift is performed by using different transmission line lengths, and the second 90° phase shift to obtain the total 180° phase shift is performed using a well-known structure to design 90° hybrids with microstrip technology [154].

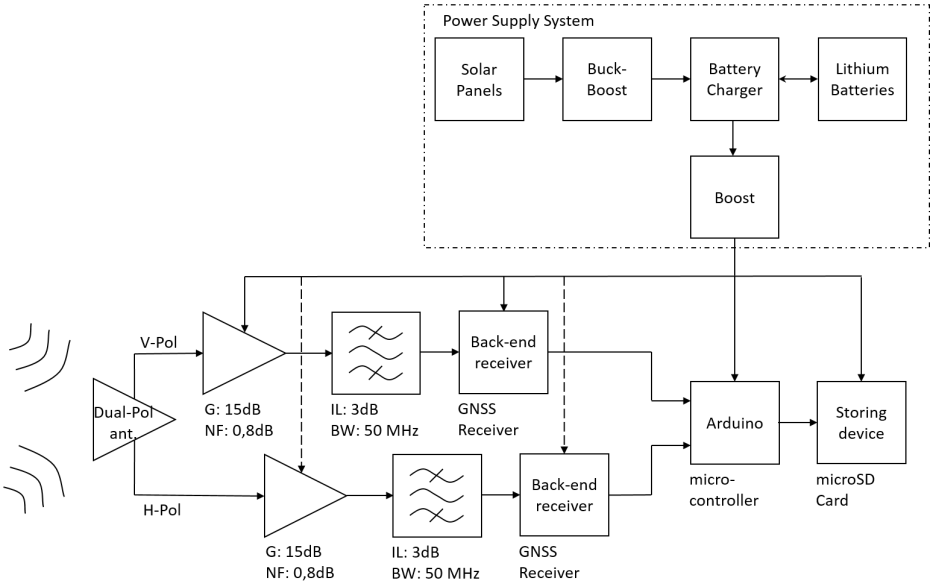

Figure 5.3: Dual-Pol SMIGOL block diagram.

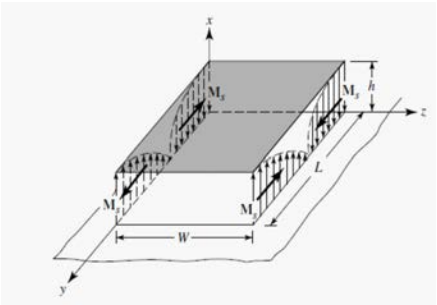

Figure 5.4: Electric field representation of a patch antenna [153].

Figure 5.6 shows an overview of the entire antenna design. Figure 5.6(a) shows the antenna patch on the software used to design it. The patch antenna has a square shape with its edges measuring 48.6 mm, which is a little bit less than $\lambda_0/(2\sqrt{\varepsilon_r})$, being $\lambda_0 = 19.04$ cm approximately, and $\varepsilon_r = 3.55$, which corresponds to the dielectric material ROGERS4003C. The feeding points were separated 6 mm from the center of the antenna which corresponds to 50 Ω impedance. Figure 5.6(b) shows the hybrid's design. Figure 5.6(c) shows the manufactured antenna front view, where it is possible to see the dielectric material used, the radiating element, and that the antenna has a two layer structure, which enlarges the separation between the radiating element and the ground-plane, in order to enlarge the antenna bandwidth. Figure 5.6(d) shows the antenna from the back where the hybrids board is seen together with the antenna ground-plane. This figure is linked to Fig. 5.5 where the hybrid parts can be identified. In Fig. 5.6(d) it is seen

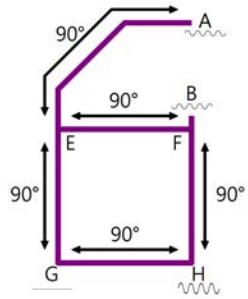

Figure 5.5: Microwave 180° hybrid scheme used behind the antennas to combine both feeding points.

that one of the hybrid outputs is matched with two 100 Ω resistors in parallel. Although a destructive addition of electric fields occurs on that port (G), it was matched to avoid undesired reflections due to imperfections in the hybrid's design.

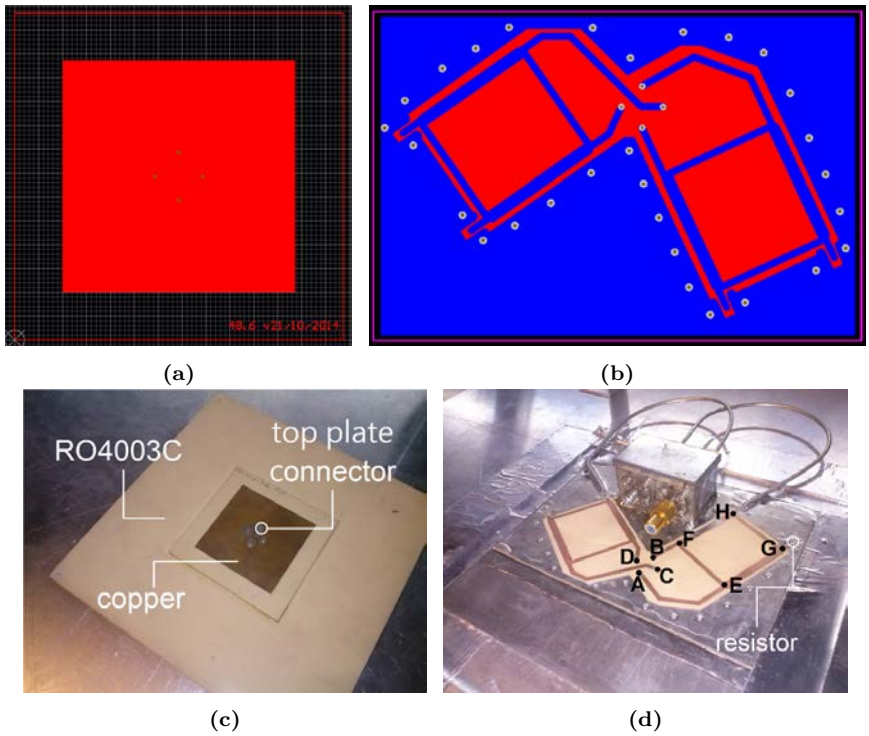

Figure 5.6: Overview of the linear dual-polarized antenna: (a) Antenna designed using Altium Designer, (b) Microstrip hybrids designed using Altium Designed, (c) Manufactured antenna front view, (d) Manufactured antenna back-view.

Once the antenna was manufactured and the measured parameters met the specifications (Return Loss (RL) ≤ -20 dB for the entire bandwidth, and Bandwidth ≥ 2 MHz,

see Fig. 5.7 for more details), the radiation pattern was measured at the UPC anechoic chamber [155] to check its symmetry and the preservation of the co-polar and cross-polar polarization behavior. Figure 5.8 shows a summary of the radiation patterns measured for H-Pol and V-Pol. Those figures represent the azimuth angle with the polar angular axis (ϕ) and the incidence angle (θ) with the radial axis (r, which ranges from 0 to 1 equally spaced, where $0 \rightarrow 0°$ and $1 \rightarrow 180°$). The smaller the radius the lower the θ. Along the antenna beamwidth ($r = 1/4$, $\Delta\theta = 90°$) both co-polar radiation patterns are symmetric. This assertion holds true considering up to a beamwidth of 120° (r= 1/3). For H-Pol the beamwidth is ±40° in the vertical axis and ±45° in the horizontal one. For V-Pol the beamwidth is ±40° in both axis. The cross-polar radiation patterns for both polarization states behave differently. While the H-Pol assures a V-Pol rejection larger than 20 dB, the V-Pol assures a H-Pol rejection larger than 25 dB, which is necessary because the H-Pol reflection coefficient is always larger than the V-Pol one.

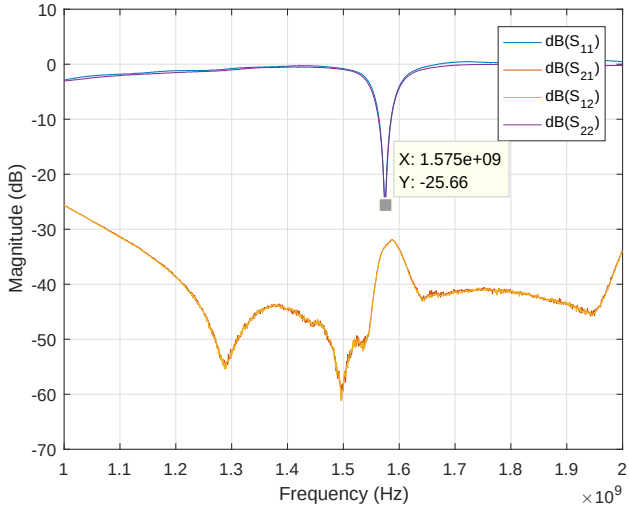

Figure 5.7: Linear dual-polarization antenna S-parameters where the H-Pol is connected to Port 1 and V-Pol to Port 2.

5.2.2 Receiving Chain

Each of the antenna polarization outputs was connected to an individual receiving chain that amplified and filtered the signal. Finally, the filtered signals were connected to the back-end GPS receiver for each chain. In this case a low-cost GPS receiver was chosen as a back-end receiver because the IPT only needs to monitor the signal power to measure the whole interference pattern [156]. The GPS back-end receiver amplifies more the signal to optimize it for its dynamic range. It also filters the signal using a Surface Acoustic Wave (SAW) filter before digitization, and a digital filter after digitization. Then, it initiates the signal processing algorithms inside it such as the signal pre-processing (correlation with a clean replica of the satellite code) and the navigation engine. The chosen GPS receiver used the NMEA protocol for communications. Only two packets from

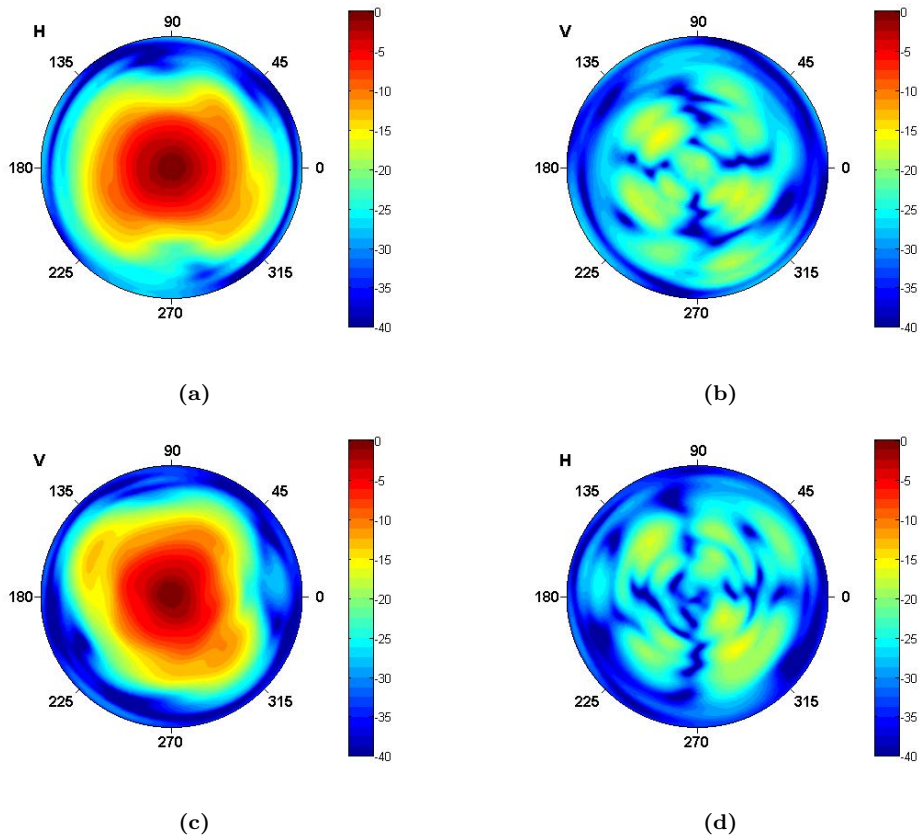

Figure 5.8: Linear dual-polarization antenna radiation patterns: (a) H-Pol Co-polar, (b) H-Pol Cross-polar, (c) V-Pol Co-polar, (d) V-Pol Cross-polar.

it were used, the Recommended Minimum sentence C (RMC) and the GPS Satellites in View (GSV). The useful information from the RMC package are: the measured position to geo-locate the instrument, and the timing information to time-reference the information. The useful information from the GSV package are: the satellite identification number, the azimuth to locate the satellite on the azimuth plane, the elevation which is one of the important parameters to interpret the interference patterns and it is also used to geo-locate the reflection points, and the C/N0 which is a measure of the signal power with respect to the thermal noise power considering 1 Hz tracking loop bandwidth, in other words, an equivalent coherent integration time of 1 s. Further information on the NMEA protocol can be found in Appendix D.

5.2.3 Microcontroller

The addition of an extra channel has two main consequences. The first one is that the data rate is doubled. The second one is that an extra I/O output must be attended. Also,

the GPS receiver used in the previous SMIGOL version was changed, which changed the communication protocol and led to a higher data-rate. This required a change on the micro-controller, and the PIC micro-controller was replaced by an Arduino Mega micro-controller. The Arduino Mega has 4 I/O ports to deal with serial data, which is more than enough for the desired application, as only two were needed. Also, it operates at a higher frequency and it has more memory, which helps to deal with the new data-rate that arises from the changes on the receiving chains. Furthermore, there is a large community using the Arduino software, which also reduces the developing time by reducing the problem-solution intervals.

The software used and implemented on the Arduino Mega micro-controller has three different parts:

1. Variable declaration and functions definition: In this stage the global variables to be used are initially declared. Those variables include the ones to turn on/off the peripherals, the communication variables (SPI port and buffers to read data from GPS receivers), and timing variables. The timing variables are used to locally time-tag each of the GPS messages received and to control the time that the system is turned on. Note that it is an autonomous receiver which is why it is very important not to run out of batteries in cloudy days. After that, the functions used are declared and defined. There are functions used to configure appropriately the GPS receivers, to process the GPS messages, to check the validity of the GPS messages, to control timing, and to generate new ".TXT" files on the SD card and write on them. Fig. 5.9 shows an overview of this first stage of the Arduino code.
2. Setup: This stage is executed when the Arduino is turned on, and it is executed only once. It turns on the GPS receivers, it turns on the SD card and starts a new file where data is stored, it configures the GPS receivers to work with the appropriate parameters (communication, types of packets, and performance), it monitors GPS receivers until they are in tracking mode, and it checks battery status. Summarizing, it prepares the instrument for its normal functioning. Figure 5.10 shows an overview of the Setup phase.
3. Main Loop: After the Setup, the instrument enters in its nominal working mode, which consists of an infinite loop that alternates two different phases, the measuring one and the sleep mode. Once the instrument is started and configured, during the first 6 hours it polls each of the GPS receivers ports to check if there is new information. If there is a new byte from any of the GPS receivers, it is sent to its processing function. Once the two ports are served the batteries' status is checked, and in case they are not performing well the instrument is sent to sleep mode. If they are performing well, it keeps on polling the GPS receivers and checking the batteries' status. Every second, which is the receiver's equivalent integration time, the data packages sent from the GPS receivers are stored on the SD Card. Once the 6-hour period has been completed correctly, the instrument enters in sleep mode to let the batteries recharge. In the sleep mode the GPS receivers are sent to sleep to avoid them consuming power. After that, the system waits for 6 hours to restart again the main loop. Prior to restart the normal working performance, the GPS receivers are awaken and a new file is generated to avoid corrupting the previous file due to unpredictable instrument malfunctions. Note that for an instrument powered directly with electricity, the sleeping mode can be discarded, but it is advisable to

generate a new file every 6 hours to avoid data corruption and its consequent loss. Figure 5.11 shows a summary of the main loop.

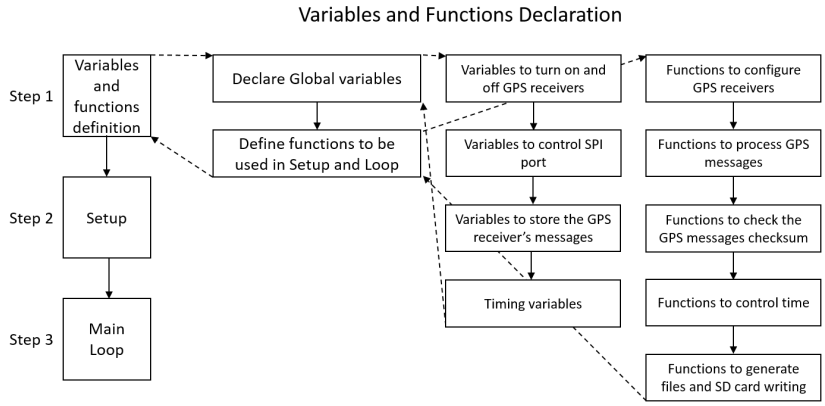

Figure 5.9: Dual-Polarization SMIGOL Variables and functions declaration Description.

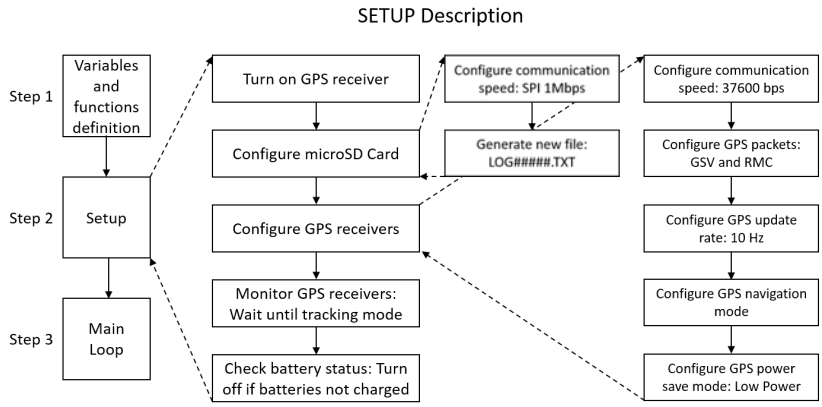

Figure 5.10: Dual-Polarization SMIGOL Setup description.

Finally 5.12 shows the design of the main board where all the Dual-Polarization SMIGOL peripherals are placed. This board is mounted on top of the Arduino Mega, which is why a part of it has exactly the Arduino Mega board shape. Note that there is an extension for the SD card shield used, and some LEDs are used to check the instrument's performance during the manufacturing process.

5.2.4 Power Supply System

Due to the changes in the receiving chain, the power supply system must be redesigned in order to hold the characteristics of the new instrument. By comparing Figs. 5.2-5.3 it can be immediately appreciated that at least one block was added to this system while the others seemed to be kept equal. However, the only circuit that was kept was

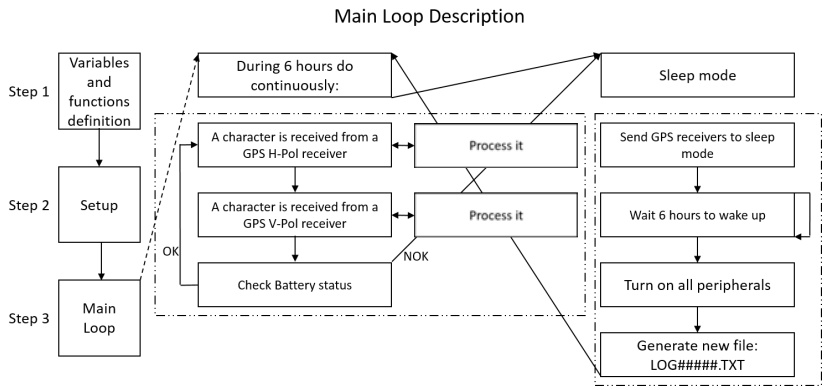

Figure 5.11: Dual-Polarization SMIGOL Main Loop Description.

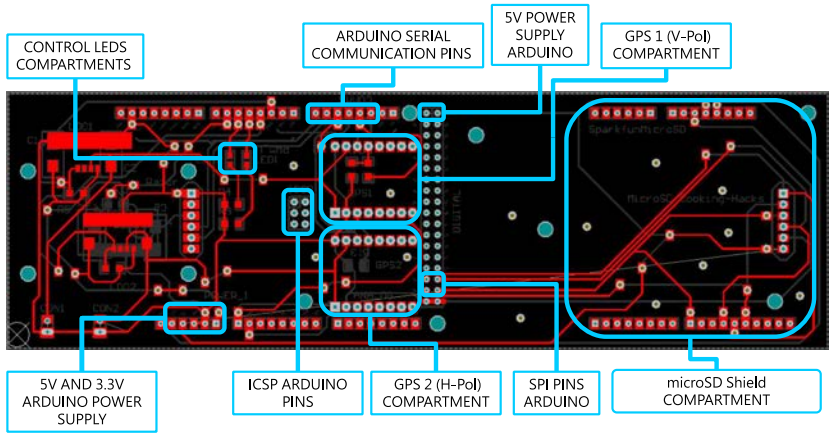

Figure 5.12: Dual-Polarization SMIGOL General board mounted on top of the Arduino.

the battery charger as lithium batteries were used for the system. Taking into account the power consumption of the Arduino Mega, the GPS receivers, the RF amplifiers, and the losses on some voltage regulators, the instrument was consuming 200 mA at normal performance and 40 mA in the sleep mode both powered at 9 V. This leads to a power consumption of 1.8 W at normal performance and 0.36 W in sleeping mode. In order to be able to recharge the batteries as well as power the instrument, 10 W solar panels were used, which could provide at most 19 V and 550 mA. A commercial buck-boost system was used after the solar panels to stabilize the voltage provided by them, which depends on the solar conditions and the load charge. It was also used to set the output voltage at an appropriate fixed value, since the input voltage to the battery charger must be 14 V. A capacitor was added to the buck-boost system to reduce the instantaneous amount of current demanded by the buck-boost coil, and to avoid an excessive instantaneous load on the solar panels that would degrade severely their performance. The output of the buck-boost power supply was connected to the battery charger, where the batteries were connected too. A 3-cell 6600 mAh lithium battery was selected for the system which

allows to power the instrument for two-days without sun light. This requirement remained the same than for the V-Pol SMIGOL instrument, but the batteries' capacity had to be increased due to an increase on the instrument's power consumption. The output of the battery charger was 6 V and it had to be stepped up as the Arduino Mega requires a minimum of 7 V. A commercial boost converter was used to step up the voltage of the battery charger.

Finally, the Dual-Polarization SMIGOL instrument is shown in Fig. 5.13. In that figure, the solar panels are clearly seen, and the antenna described in section 5.2.1 is located below the radome with the UPC RSLab Logo.

Figure 5.13: Dual-Polarization SMIGOL instrument at a Field campaign at Yanco, Australia.

5.3 LARGO

The LARGO instrument is a dual-channel receiver that tries to overcome the coverage limitations of the IPT using a scatterometric approach instead of an interferometric one. It can be used in both mobile and static platforms. LARGO was developed by UPC for the Monash University to perform the GELOz field campaigns which intended to estimate soil moisture from an airborne platform using GNSS-R technology. Except for DMR and GriPAU, previous GNSS-R receivers using scatterometric approaches only sampled and stored the raw data, and the post-processing was performed off-line on a computer [145–148]. Trying to minimize the duration of the pre-processing stage, and looking forward to operational applications, the LARGO instrument works totally on a closed-loop mode, and the correlations are computed internally in the instrument storing only the estimated peak SNR for both the up-looking and down-looking channels. In other

words, it requires to use the signal acquisition scheme of a GPS receiver, with its three main subsystems: the Frequency Locked Loop (FLL), the Delay Locked Loop (DLL), and the Phase Locked Loop (PLL). The instrument also includes an Inertial Measurement Unit (IMU) in order to monitor the platform movements and consequently compensate them on the antenna patterns. Having learned some lessons from the dual-polarization SMIGOL design, the core of the instrument was maintained, and some necessary changes were made on the design since the scatterometric approach requires more complexity than the IPT technique.

Two versions of the LARGO instrument have been manufactured: an initial one which consisted of the dual-channel receiver, and an improved one that included a calibration matrix. The main LARGO block diagrams of both versions are shown in Fig. 5.14(a)–(b), respectively. The first version is a dual-channel receiver like the dual-polarization SMIGOL, but in this case the antennas are different. Also the back-end receiver is different as a higher performance GPS receiver is used that delivers the I/Q information too. The second version adds the calibration matrix which allows to connect each back-end receiver to each of the antennas independently. This helps to calibrate the receiver and furthermore, it speeds up the initialization process. Also, differently from the dual-polarization SMIGOL both LARGO versions add an IMU in order to track the platform movements which are used in the post-processing stage. Consequently, the LARGO micro-controller needs to attend one extra serial port communication apart from estimating the coherent reflectivity at the instrument, which requires extra intelligence in the system's firmware.

5.3.1 Antennas

The LARGO instrument was designed for both airborne and ground-based conditions, so the antennas must be carefully designed. Taking into account those considerations, three different kind of antennas have been used. The first version used commercial Antcom antennas, since it was designed to fly on a commercial airplane, and they must accomplish airborne navigation regulations. The antennas used were measured at the UPC anechoic chamber [155] with the same ground-plane used later on the field experiments. Figure 5.15 shows a summary of the radiation patterns for both direct (RHCP) and reflected (LHCP) antennas. In Fig. 5.15(b) it is seen that the direct channel antenna does not have a good cross-polarization behavior although it is not a necessary requirement because the direct signal can be assumed to be a purely RHCP transmitted signal [44]. For that polarization state, the beamwidth is $\pm 60^\circ$ in the horizontal direction and $\pm 50^\circ$ in the vertical one. The minimum cross-polar in the beamwidth is -5 dB. However, the reflected channel antenna (LHCP) has a better behavior, as desired, even though it could be improved. In this case the beamwidth is $\pm 60^\circ$ in both the vertical and horizontal axes. The minimum cross-polar in the beamwidth is -10 dB. Those antennas were the ones chosen for the GELOz field campaigns.

The same antennas were tested for ground-based applications. They were mounted on the ground-based platform (rover) one looking to the zenith and the other one looking to nadir, as was done for the airborne campaigns. Their wide beam and their not-so-good polarization behavior showed some multi-path coming from the metallic structure of the platform. This fact did not occur on the airborne campaign as the reflected antenna

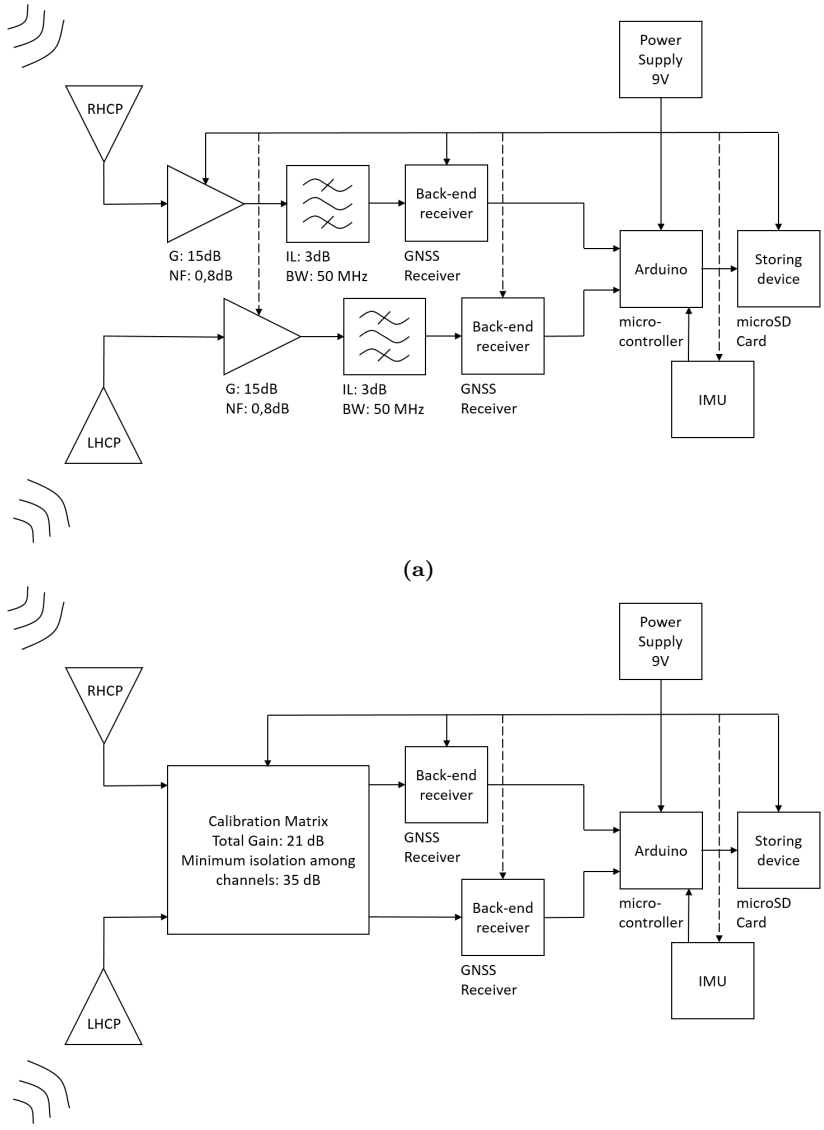

Figure 5.14: (a) LARGOv1 block diagram, (b) LARGOv2 block diagram which includes the calibration matrix.

was located below the aircraft with a clean LOS to the reflecting surface. To mitigate the multi-path in the ground-based applications the antennas should be changed. The first change should be the geometrical configuration, and instead of looking to nadir and zenith, the antennas should be inclined. The second change should be a narrowing on the antenna beamwidth, which implies enlarging the antenna size. This was achieved by designing and manufacturing a hexagonal 7-patch antenna array uniformly fed which

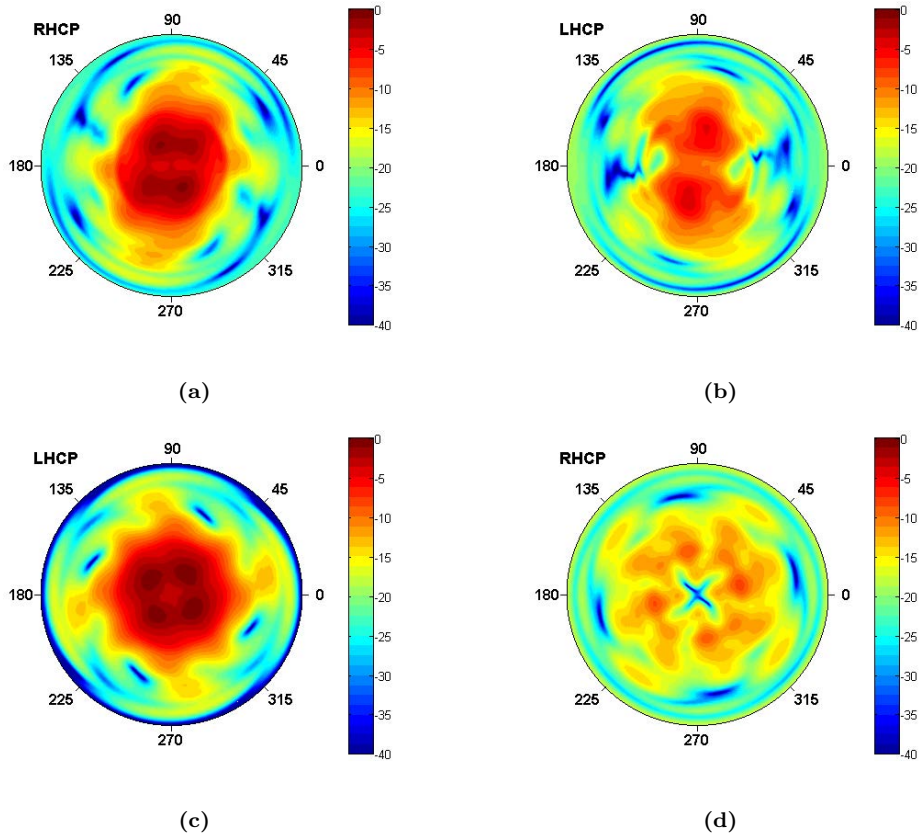

Figure 5.15: Antcom antenna radiation patterns: (a) RHCP Co-polar (direct), (b) RHCP Cross-polar (direct), (c) LHCP Co-polar (reflected), (d) LHCP Cross-polar (reflected).

was used later for the Grains Research & Development Corporation (GRDC) project. Figure 5.16 shows a summary of the antenna array used for that project where the beam narrowing is clearly identified. Also, the sidelobes due to the array factor are clearly identified at the co-polar radiation patterns. The elements used to manufacture the array were commercial Sangshin patch antennas at the desired polarization (either RHCP or LHCP). The beamwidth for both the up-looking and down-looking antennas was $\pm 20°$ in both axis. The cross-polar was at least -10 dB for both antennas too.

Finally, an airborne field campaign was performed in *Salamanca*, Spain, using a paramotor as a platform. This kind of platform is highly suitable for experimental field campaigns as there is no requirement for aviation qualified antennas, and higher performance antennas can be designed for this purpose. In this case the dual-polarization SMIGOL antennas were replicated adding an extra 90° hybrid where the two linear polarization were connected. The appropriate polarization was picked for each channel and the other output of the hybrid was connected to a matched load. The resulting antenna patterns of those custom-made antennas for both channels are shown in Fig. 5.17. In Fig. 5.17 it is possible to see that the pattern is highly symmetric as for the dual-

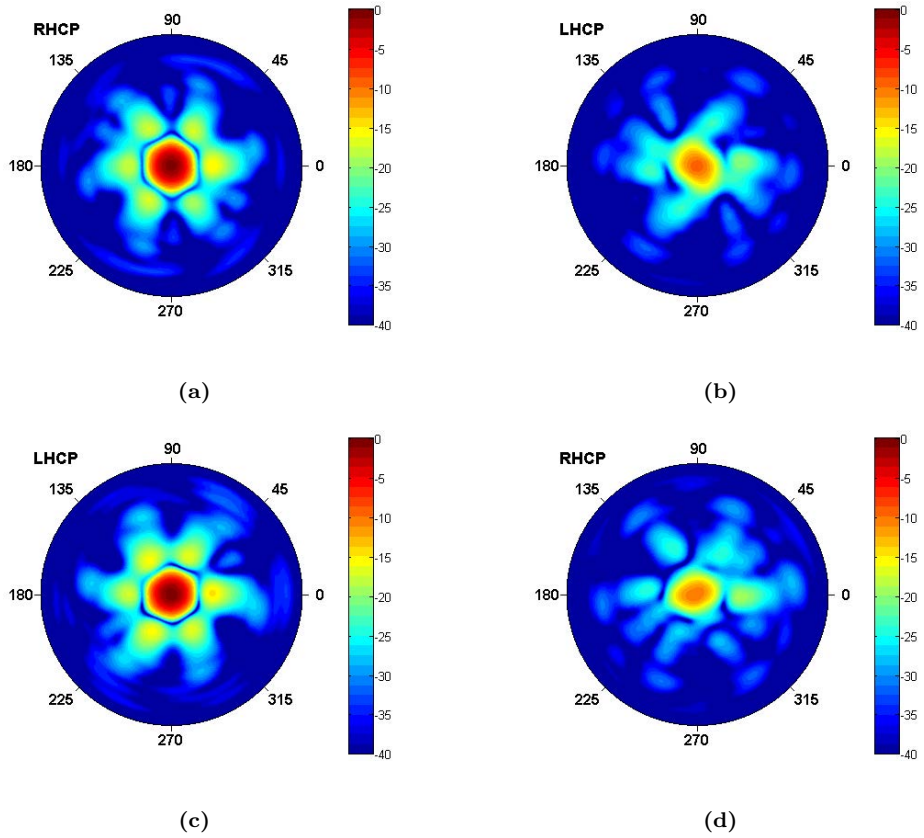

Figure 5.16: GRDC antenna radiation patterns: (a) RHCP Co-polar (direct), (b) RHCP Cross-polar (direct), (c) LHCP Co-polar (reflected), (d) LHCP Cross-polar (reflected).

polarization SMIGOL antennas, and that the cross-polar behavior (Fig. 5.17(b),(d)) is much better than when using COTS antennas (below -35 at the boresight direction, below -20 dB in ±22.5°, and below -15 dB in ±45°).

5.3.2 Calibration Matrix

As aforementioned, in the second version of the LARGO instrument the antennas were connected to a custom-made calibration matrix that allows to connect any antenna input to any of the back-end receivers. The calibration matrix structure is shown in Fig. 5.18. The filters used were SAW filters with a 3 dB bandwidth of 47 MHz in order to reject any out of band interference. The amplifiers used were Low Noise Amplifier (LNA)s with a minimum Gain of 15 dB and a NF of 1.1 dB. Then, the signals are split using a chip-based power splitter. Two high isolation (up to 63 dB nominal) absorptive switches were used to commute between channels, and were the ones that provided the overall isolation properties of the calibration matrix. Finally, the signal was again amplified

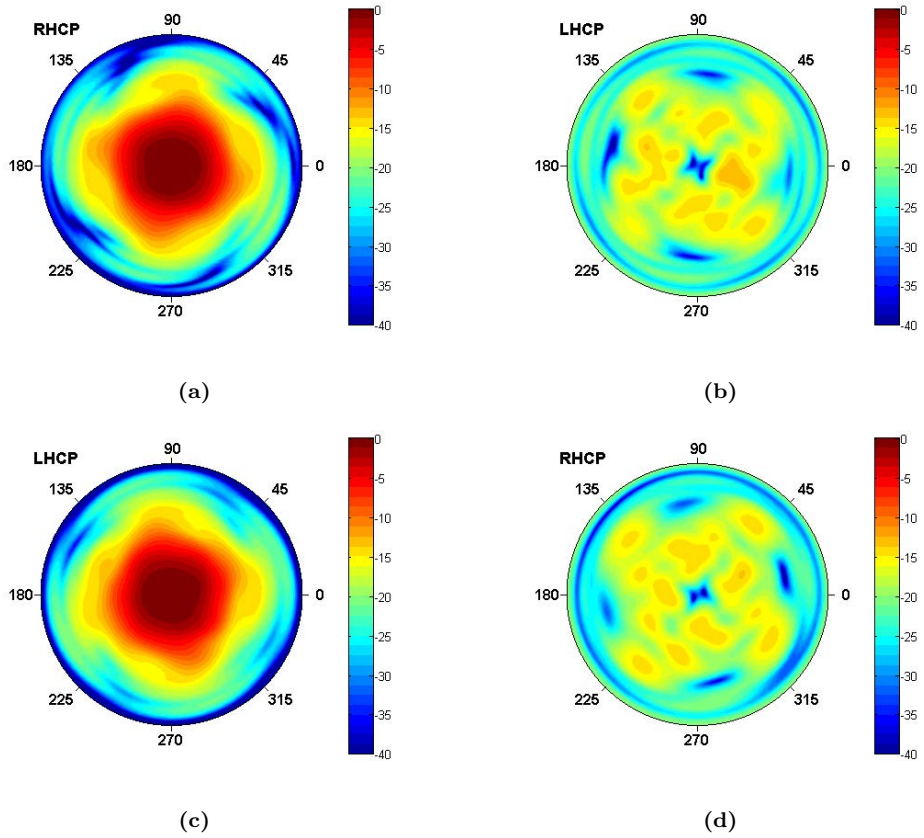

Figure 5.17: Salamanca antenna radiation patterns: (a) RHCP Co-polar (direct), (b) RHCP Cross-polar (direct), (c) LHCP Co-polar (reflected), (d) LHCP Cross-polar (reflected).

using the same LNA amplifiers before reaching the back-end receiver. The performance of the calibration matrix was measured using a vector network analyzer, and its results are shown in Fig. 5.19. Furthermore, detailed tables showing the complete S-Parameters modulus at the desired frequency are also included. On the diagonal of the S-parameters tables it is possible to identify the matching of each of the ports. The positive values of the matrices show to which port (back-end) the signal acquired by each antenna is transmitted to. Note that last amplifier used on the calibration matrix is not shown in the tables as it was added later. However, its performance did not change. Apart from interconnecting channels and allowing to train the reflected/down-looking channel with the direct/up-looking channel, the calibration matrix also allowed to compensate for unbalances between channels.

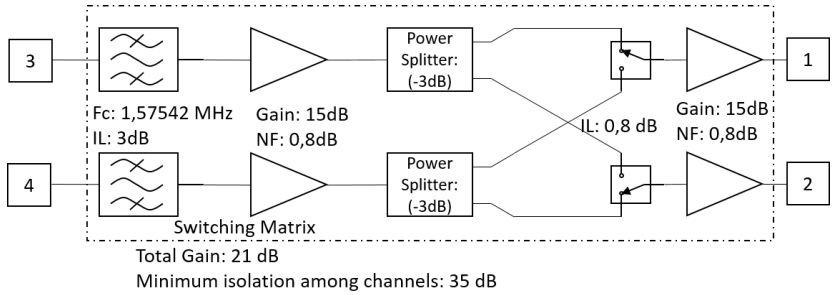

Figure 5.18: Calibration matrix block diagram of the LARGOv2 instrument.

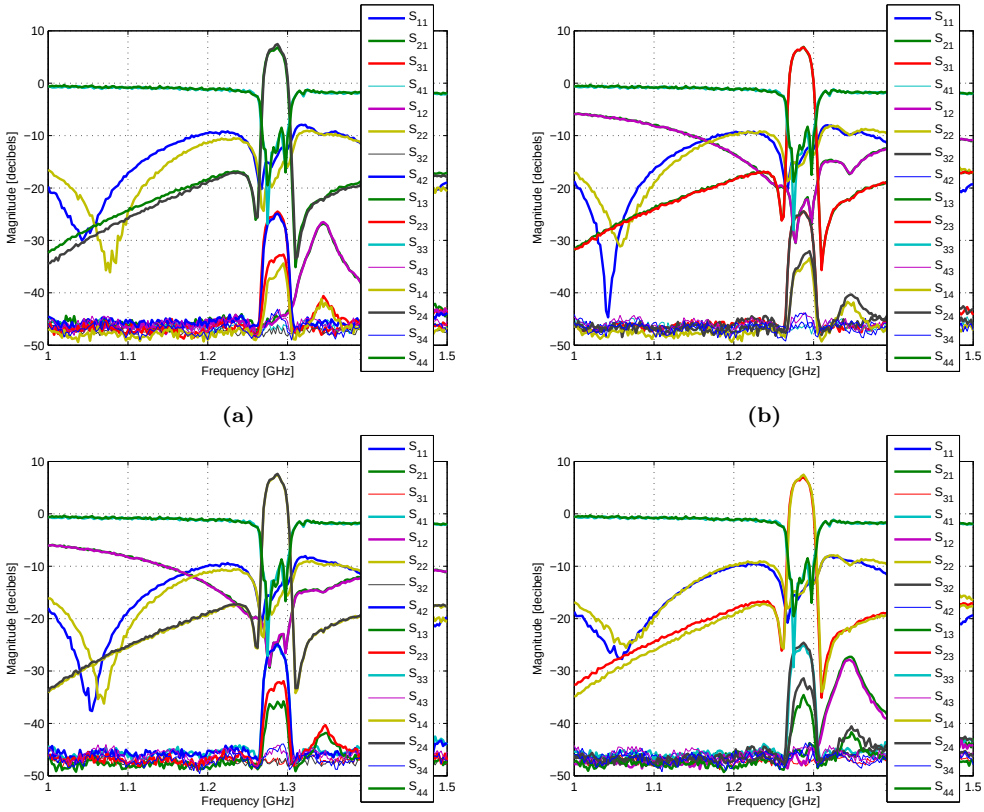

Figure 5.19: Calibration matrix S-Parameters: (a) 3→1, 4→2 (b) 4→1, 4→2 (c) 3→1, 3→2 (d) 3→2, 4→1.

5.3.3 Microcontroller

The firmware programmed to the LARGO is similar to the dual-polarization SMIGOL with some extra features needed due to its increased complexity. The first step which is

Table 5.1: Modulus of the S-parameters at 1.575 GHz state 1: 3→1, 4→2, (S_{ij}, i=row, j=column) [dB].

$\mathbf{S}_{ij}$	1	2	3	4
1	-13.76	-45.02	6.86	-35.97
2	-44.66	-18.01	-33.09	7.48
3	-24.49	-46.28	-11.26	-43.12
4	-46.08	-24.89	-43.73	-12.75

Table 5.2: Modulus of the S-parameters at 1.575 GHz state 2: 4→1, 4→2, (S_{ij}, i=row, j=column) [dB].

$\mathbf{S}_{ij}$	1	2	3	4
1	-14.65	-24.51	-35.86	7.51
2	-24.73	-17.43	-32.18	7.63
3	-46.58	-48.06	-11.04	-45.41
4	-25.30	-24.89	-44.15	-13.28

Table 5.3: Modulus of the S-parameters at 1.575 GHz state 3: 3→1, 3→2, (S_{ij}, i=row, j=column) [dB].

$\mathbf{S}_{ij}$	1	2	3	4
1	-13.77	-23.35	6.95	-34.58
2	-23.18	-15.21	6.84	-32.83
3	-24.42	-24.45	-11.66	-44.17
4	-46.40	-45.86	-43.82	-12.02

Table 5.4: Modulus of the S-parameters at 1.575 GHz state 4: 3→2, 4→1, (S_{ij}, i=row, j=column) [dB].

$\mathbf{S}_{ij}$	1	2	3	4
1	-14.46	-47.12	-34.58	7.48
2	-46.34	-14.88	6.97	-31.39
3	-47.34	-24.58	-11.46	-44.66
4	-25.20	-46.01	-44.75	-12.53

the variable declaration and the function definitions is exactly the same, and the files to log the data are identically generated. During the second stage, which is the set-up, the same operations are performed, but in this case the back-end GPS receivers are programmed to deliver another packet from the NMEA protocol. The extra packet needed is the altitude of the platform, so the Global Positioning System System Fixed Data (GGA) packet is also requested. More information on this packet can be found in Appendix D. Also the output I/Q data from the promptly correlators were requested every ms (for each satellite), which means that the GPS receivers were using 1 ms of coherent integration time. During the set-up the IMU was initialized.

The LARGOv2 instrument which includes the calibration matrix initially connects

the two back-end receivers to the direct channel and waits until both GPS receivers enter in tracking mode. Then, a sweep for all the possible stages of the calibration matrix was performed, remaining at each stage 1 minute with the platform holding still. Finally, the calibration matrix was programmed at the stage 1 for the measuring/main loop.

During the main loop, the three subsystems connected to the micro-controller (two GPS receivers and the IMU) were polled. Every time a new byte was received it was sent to process. The NMEA packets are processed in the same way than in the dual-polarization SMIGOL, they were tagged by the channel and by an internal timestamp. The IMU data (yaw, pitch, roll) was also time-tagged in order to combine it with the GPS receivers data. When the I/Q data from the prompt correlators was received the coherent component SNR (from now on SNR_{cc}) was computed, which was possible because the system was working under a perfect closed-loop mode (excess Doppler was estimated and compensated, see Chap. 4). After compensating for the navigation bit, which is done automatically by the receiver, the SNR_{cc} can be estimated as:

$$\mathrm{SNR}_{cc} = \frac{\left(\frac{1}{N}\sum_{n=1}^{N} I_n + jQ_n\right)^2}{\mathrm{P}_n}, \tag{5.1}$$

where the numerator is the mean square value of the I/Q samples and the denominator is the thermal noise power. The thermal noise power is computed at a lag were the is no signal presence (out of the triangle region of the ACF function). These data is also provided by the GPS receiver to compute the equivalent C/N0 from the received samples in order to use a different algorithm from the default one programmed in the receiver. Instead of computing directly the received power, the SNR is computed. This is performed because each GPS receiver use its own Automatic Gain Control (AGC), which is not accessible. The data samples from each GPS receiver are provided in arbitrary units and scaled according to its AGC levels. Therefore, the only way to make comparisons between both receivers data, and to compute a calibrated coherent reflectivity, is to use a normalized observable such as SNR. The computed SNR_{cc} for each satellite is also stored and time-tagged. One thousand samples are used to estimate each satellite SNR_{cc}, which is equivalent to a data-rate of one measurement per second per satellite in view. This operation is performed continuously in real-time on the Arduino Mega. This instrument is not conceived to be fully autonomous, which is why it depends on a 9 V power supply source and no effort was dedicated to design any particular power supply system.

Finally, an overview of the LARGO instrument can be seen in Fig. 5.20. On the left, the second version of the LARGO is pictured while the calibration matrix was being repaired. In the middle, the latter and reduced size version of the LARGO instrument is depicted which was flown on a UAV platform. On the right, the initial version of the LARGO instrument used on the GELOz field campaign is shown with its ruggedized enclosure.

5.4 PAU

The PAU instrument is a combination of a TPR and a GNSS-R receiver designed to measure the brightness temperature of the sea surface to infer SSS and correct the bias

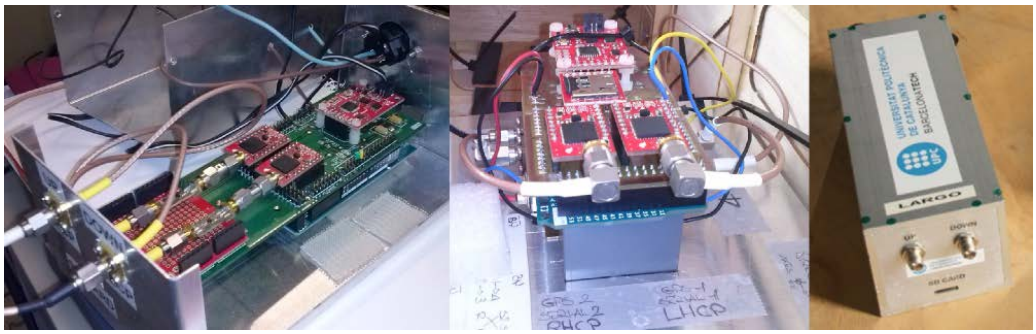

Figure 5.20: LARGO instrument with its different versions.

introduced by surface roughness using GNSS-R observables [22, 23]. The concept implemented by the PAU instrument was previously tested and implemented by the GriPAU instrument for ground-based scenarios [18, 157]. The main difference between the PAU and the GriPAU is that whereas the PAU instrument uses the same receiver front-end and frequency band to measure brightness temperature and GNSS reflected signals, the GriPAU uses the 1.4 GHz frequency band to measure brightness temperature, and the L1 GNSS frequency band to measure the GNSS reflected signals. So, the GriPAU is a combination of two instruments intended to prove the concept of correcting brightness temperature using GNSS-R observables, while the PAU instrument has the two instruments joined together working at the same frequency band in order to apply the proved concept. This PhD Thesis dissertation only used and helped to develop the GNSS-R part of the PAU instrument, which is why it is the only one detailed. The main contributions are related to the antenna analysis, simulation, and measurement and to test the final assembly of the instrument in its initial version, and the open-loop near real-time hardware processing version.

5.4.1 The MicroSAT-1 Mission

The PAU instrument was conceived to fly first in the SeoSAT satellite and later on the INTA MicroSAT-1 satellite. The latter satellite was part of the MicroSAT Spanish space program which has some standardized parameters, which are the following:

- *Total mass*: between 100–150 kg.
- *Orbit*: between 600–700 km.
- *Solar panels*: 200 W maximum output power.
- *Bateries*: 18 Ah, 28 V SAFT LiIon.
- *Voltages*: unregulated 22–28 V, and regulated ±12 V, ±5 V, +3.3 V, +1.5 V.
- *Down-link*: 10 W RF in X-Band link with dedicated antenna (40–80 Mbps) or 5 W RF S-Band link with two INTA antennas (2–8 Mbps).
- *OBDH*: ERC-32 Processor or FPGA (ESA Leon-2).

Apart from the common specifications of the MicroSAT program, the MicroSAT-1

mission, which was the first mission of the program, had some more specific parameters summarized in the following bullets:

- Evaluation of the platform in a LEO (Low Earth Orbit) SSO (Sun Synchronous Orbit):
  - Inclination: 98.2°.
  - Right Ascension of Ascending Node (RAAN): 156°.
  - Local Time of Ascending Node (LTAN): 22:30.
  - Semi-major axis: 7081–7089 km.
  - Argument of perigee (ω): 66°.
- Lifetime: 8 years.

Apart from the PAU instrument as a technological demonstrator, other technical devices were also under test in the MicroSAT-1 mission, such as the CAN (Commands & Reconfiguration) bus, the Space-Wire data bus, and the behavior of some COTS devices in space (a GPS receiver entirely made with COTS components). Apart from those technical devices, the main payloads of the MicroSAT-1 mission were:

- *CINCLUS*: two wide swath cameras with 5 narrow MS bands to provide in-land water quality control.
- *MS-WAC*: two cameras with 5 MS bands and 320 km wide swath for remote sensing of the Spanish territory.
- *PAU*: experimental radiometer + GPS reflectomer to study SSS.
- *Laser Link*: with the OGS until 150 Mbps.
- *Optical sensors*: new sensors μFSS and μES.

Disappointingly, after reaching phase D and with all the flight hardware already developed and manufactured, the project and mission were postponed *sine die*, which closed the door to prove the proposed GNSS-R concept from a spaceborne platform. However, as part of the phase D the PAU instrument was fully developed up to an operational performance. It was entirely manufactured by the Spanish company AD Telecom SL (`http://www.adtelecom.es/`) in a collaborative project with UPC, which was in charge of determining the instruments' specifications, supervising the entire manufacturing process, testing the different hardware versions delivered, and validating its operational functioning. Once the mission was postponed, some more improvements were performed on the PAU instrument by the same company in order to improve its performance. The flight model of the PAU is now seeking for a flight of opportunity.

5.4.2 Antenna

The design of the antenna was performed in two different phases. There were four main specifications for the initial design which were: maximize the directivity to reduce the footprint size in the radiometry case, maximize the antenna efficiency to maximize the radiometric sensitivity, a maximum size of 37.5 cm x 37.5 cm taking into account the ground-plane due to an area limitation on the satellite, and LHCP polarization since the reflected signals are mainly LHCP polarized. The first antenna model proposed is shown

in Fig. 5.21 which consists of a 2 x 2 antenna array on the center and four more patches located on the outer part to increase the antenna directivity. Directivity is proportional to the effective occupied by the antenna, so the larger the area, the larger the directivity. Those antennas were designed using ROGERS4003C, and provided an antenna efficiency of 0.71, which is not acceptable for the radiometric applications because its sensitivity is highly degraded.

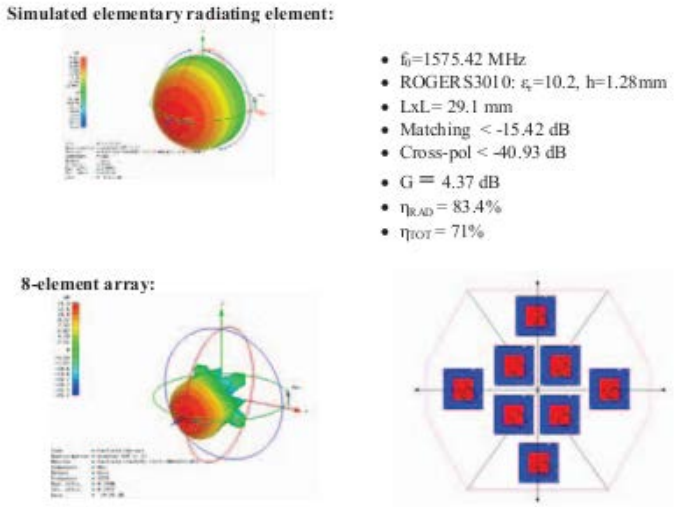

Figure 5.21: Simulation of the first PAU antenna iteration.

As a consequence, a critical design review was performed for the PAU engineering model antenna and a new model was developed, using air as the dielectric material. The size of the antenna patches became larger, and only a 2 x 2 antenna array could fit on the space provided. A draft of the antenna design is shown in Fig. 5.22(a). The patches were fed at linear polarizations (H- and V-Pol), and then combined using low-loss microwave stripline 90° hybrids and the combining network shown in Fig. 5.22(b) to create the LHCP polarization. Furthermore, note that the antenna patches are rotated one against the other, so all the feeding points are found looking to the antenna center. This was performed to improve the cross-polar rejection and the pattern symmetry. This rotation adds a phase shift to the antenna electric fields that must be taken into account in the combining network. Once the design was validated, AD Telecom manufactured the antenna, its pattern was measured at the UPC anechoic chamber, and a summary it is shown in Fig. 5.23. Therein, it is seen that the antenna is purely LHCP polarized with a cross-polar rejection larger than 20 dB in the entire hemisphere, and between 30–40 dB in the antenna beamwidth. This fact is clearly seen on the ϕ cuts of the co-polar pattern shown on the same figure. The directivity of the designed antenna was 14 dB, a little bit larger than the antennas from the UK-DMC and UK TDS-1 space missions.

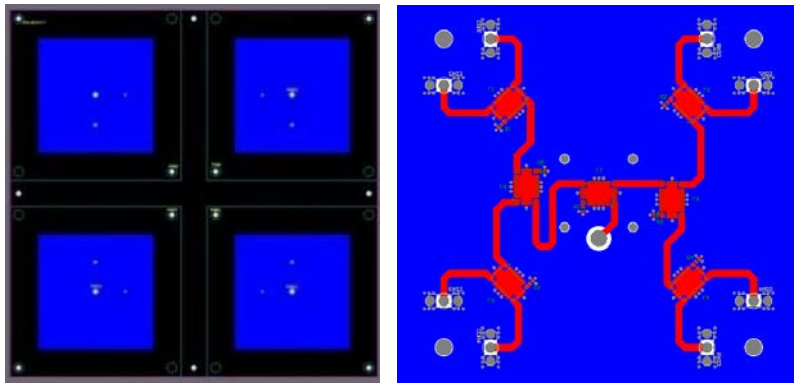

(a) **(b)**

Figure 5.22: (a) New model for the PAU antenna array, (b) Combining network.

5.4.3 GNSS-R Payload

The payload's design had 4 different blocks. The first one is the radio, and it contained all RF circuitry duplicated. The second one was the Digital Processing Unit (DPU), which was made using totally space qualified components. The third one was a replica of the DPU using COTS components, in order to test the behavior of those components under space conditions. Finally, the last block was the power supply unit.

The payload's block diagram and the engineering model front view are shown in Fig. 5.24(a)–(b) respectively. The radio receiver acquires the direct signal with a single patch antenna and the reflected one with the antenna array described in previous section. It combines them using a 20 dB coupler to try to equalize the power received from both channels. In other words, the direct signal is attenuated in order to have an amplitude/power comparable to the reflected one. It also performs a superheterodyne detection bringing the signal to IF and sending it to one of the DPUs. At the DPU the signal is digitized and then two different working modes were used. The first one just stored the digitized signal, which lasted for one second. The signal was initially sampled at 16.386 MHz with 8 bits, but then it was internally down-sampled at one fourth of the sampling frequency (4.096 MHz), with two bits for the I channel and two bits for the Q channel. This led to raw binary data files of 2 MB/s to be post-processed on a computer using the software processing approach presented on this chapter's introduction. The second one, which was an evolution of the first one. The latter performed near real-time DDM computations using programmable coherent and incoherent integration times with a Doppler step of 500 Hz in an open-loop mode. In other words, no tracking of the signal was performed and correlations ranging from -15 kHz up to 15 kHz in Doppler and all the delay lags were computed for all satellites. The correlations computed were circular correlations using the FFT properties. A Virtex-4 Field Programmable Gate Array (FPGA) was used to perform them. The instrument required 3.2 s to perform the correlations, so its working mode was 1 s of data acquisition and 3.2 s of data processing. Consequently, continuous measurements such as the ones performed by the UK TDS-1 payload could not be done. However, this occurred because the PAU instrument was designed previously

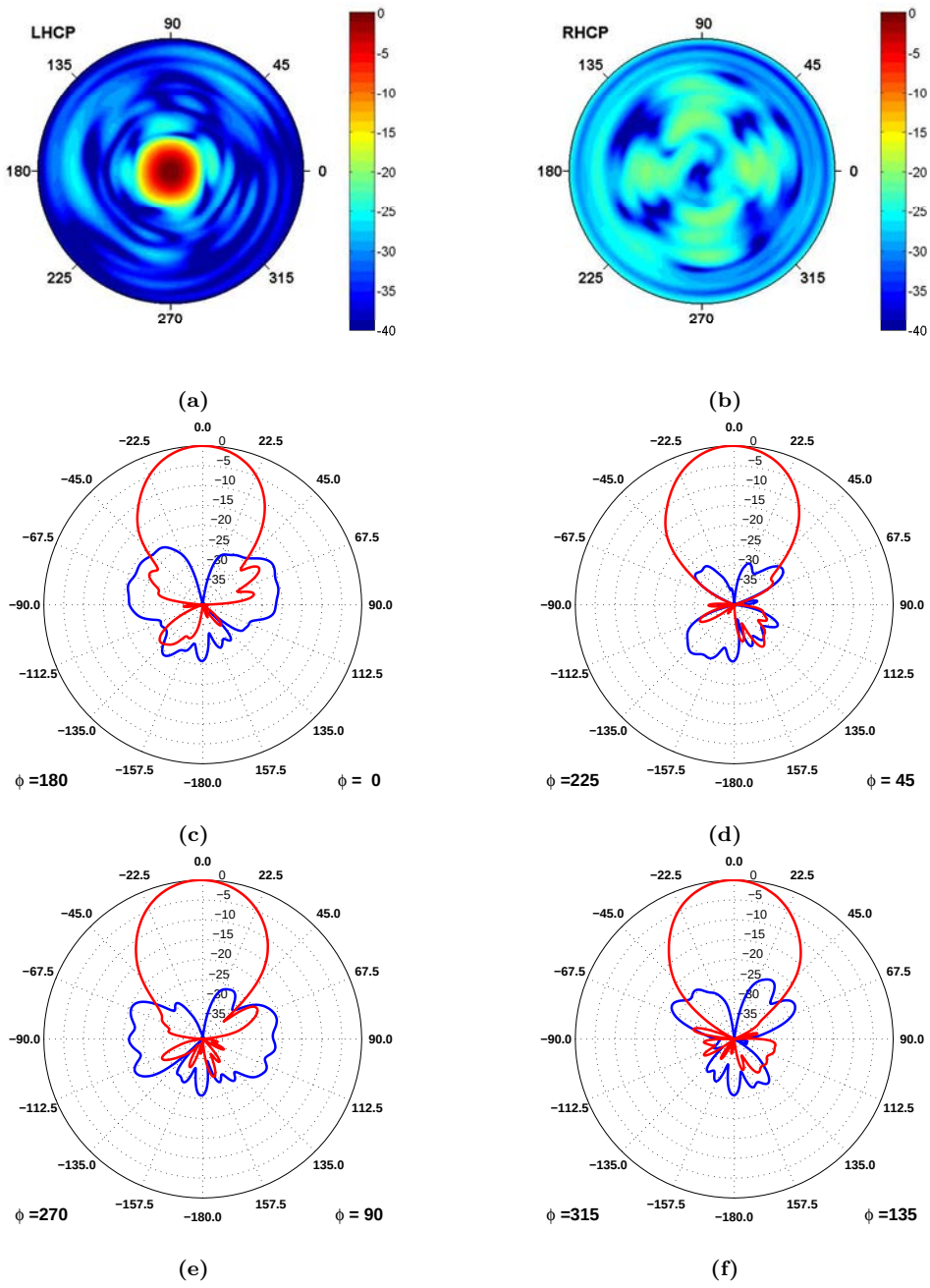

Figure 5.23: (a) Co-polar LHCP antenna pattern, (b) Cross-polar LHCP antenna pattern, (c)–(f) 0°, 45°, 90°, and 135°, ϕ cuts on the co-polar antenna pattern respectively.

than the UK TDS-1 GNSS-R payload, and therefore using older and slower technology.

The computed DDMs had an image format (RGB) which was based on 10 rows and 4096 columns corresponding to the delay lags. This resulted in an image of 120 kB for each 5 kHz of Doppler sweep. Therefore, six of those images were required to obtain a full DDM for the entire Doppler range previously defined. However, since not all the data was useful, the image that had the largest pixel value (maximum) and its two adjacent images were joined and stored on the RAM to download, which resulted in an image file of approximately 360 KB. The power supply unit was designed to satisfy the electrical specifications of the MicroSAT-1 satellite. Figure 5.25 shows all the PAU flight model blocks and how they are assembled using a back-panel.

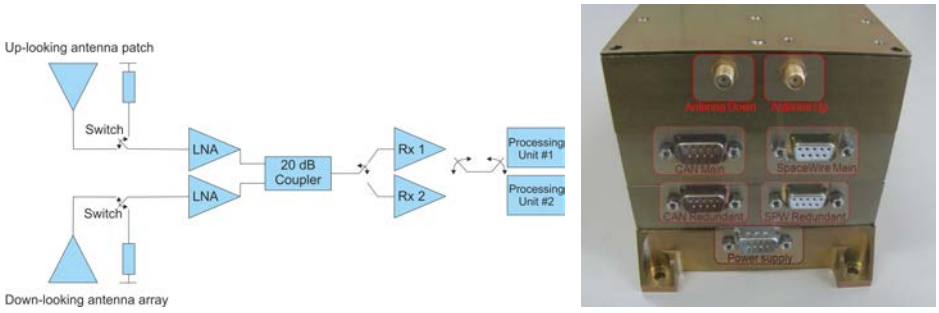

(a) **(b)**

Figure 5.24: (a) PAU payload schematic (b) PAU EM model front view.

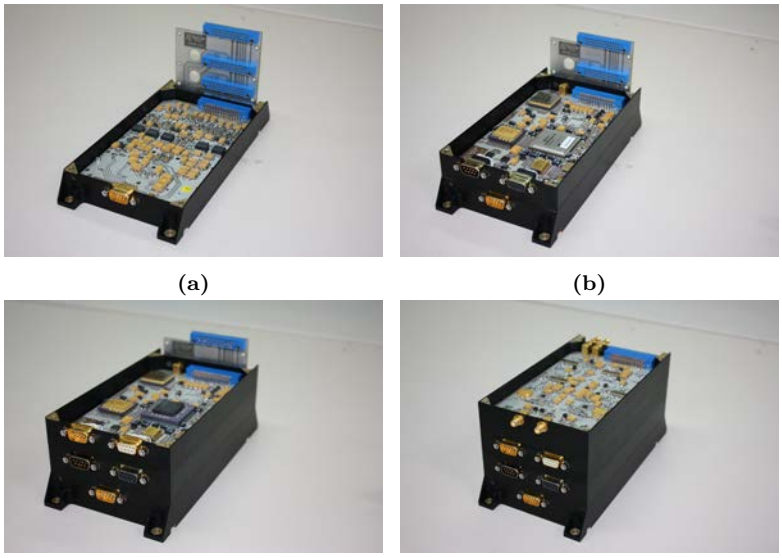

(a) **(b)**

(c) **(d)**

Figure 5.25: PAU payload parts and assembling: (a) Power Unit, (b) DPU COTS, (c) DPU Spaceborne (d) RF.

5.4.4 Payload's Evolution

After the decision of postponing the launch of the MicroSAT-1 satellite was made, it was proposed to improve PAU engineering model instrument processing algorithm in order to reduce the time spent during the data processing stage. The main improvement consisted of the addition of an external high-performance GPS receiver directly connected to a power splitter on the direct signal antenna. In this way, the GPS receiver monitors the satellites in view and its Doppler frequency for the direct signal. Hence, instead of making correlations against all satellites, the PAU engineering model now has an external controller that sends the FPGA the satellites in view. Code correlations only against those satellites are now performed. Apart from that, it also provides the Doppler frequency measured for the direct signal, so now the Doppler frequency is centered at the direct signal one, and therefore DDMs measured are also centered at the direct's signal Doppler with again a window of 5 kHz. The central Doppler frequency and the two adjacent DDMs are still computed, leading to images with the same exact format. Currently, the number of satellites to correlate has been reduced by a factor of 3 approximately and the Doppler window has been reduced a factor of two. With this modification the instrument should speed up the processing part being 6 times faster, which is much closer to a real-time processing instrument. So, the PAU evolved from an open-loop tracking mode to a partially closed-loop tracking mode. An extra modification planned for the future is to center also the delay correlation window in order to obtain the DDMs only where the useful signal is present, which means that it will not be necessary to compute code correlations for all delay lags. However, a tracking window must be kept to follow the signal's movement along the Delay-Doppler plane.

5.5 McGiver

The last instrument developed in this PhD Thesis is called McGiver and it is very similar to the dual-polarization SMIGOL. This instrument was conceived to be located under a forest to measure the GNSS signals that pass through the vegetation layer. The main purpose of the instrument is to apply a GNSS-T technique similar to the one proposed in [158], but using only a single GPS receiver placed at one location. With those specifications it is straightforward to think that a single polarization SMIGOL instrument using a zenith-looking RHCP antenna, which is the polarization of the GNSS transmitted signals could be used. However, a forest structure leads to different scattering and attenuation processes. On one hand, penetrating through vegetation leads to attenuation of the signal which occurs due to the leafs' VWC, and to less extent due to branches. On the other hand, the signal gets scattered on the trees' trunks leading to a multiple scattering process that can change the polarization of the signal. In order to measure the amount of signal power that has been lost due to polarization change and not due to the attenuation mechanism a LHCP channel is also used. So, the McGiver instrument is a dual-channel instrument like the dual-polarization SMIGOL instrument with an antenna that can acquire the two circular polarization states, which turns to be the one of the LARGO antennas used. The back-end of the instrument are in this case the same GPS receivers used on the dual-polarization SMIGOL as only signal power measurements are needed. There is no need to look at the I/Q components of the signals, as any process

changing them will be a very slow process, since the receiver is still, and the GNSS satellites move very slowly. Consequently, any signal statistics is seen directly on the power measurements of the back-end GPS receivers. Furthermore, the McGiver instrument must be powered directly using electricity since it is under a forest with limited sunlight, a fact simplifies the power system of the instrument. Therefore, it can acquire data continuously without the need to stop to recharge batteries. Summarizing, the McGiver instrument is a combination of the LARGO instrument (antenna and power supply system) and the SMIGOL instrument (receiving chain and part of the firmware).

Figure 5.26 shows the antenna S-parameters where the matching frequency is highlighted. Figures 5.27 and 5.28 show the co-polar ϕ cuts of the antenna used on the McGiver instrument for the two polarization states and their corresponding cross-polar pattern. The antenna design is the same one that was explained in section 5.2.1 fed with linear polarization and converted to circular polarization using the 90° hybrid described in section 5.3.1, which broadens the antenna bandwidth.

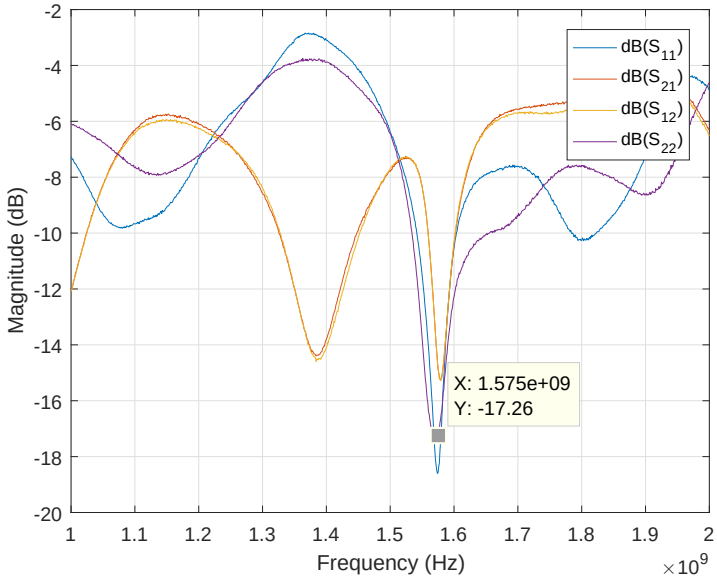

Figure 5.26: Antenna S-parameters where the RHCP component is connected to port 1 and the LHCP component to port 2.

Finally, Fig. 5.29 shows how the McGiver instrument final assembly looks like and its location in the field campaign where it was deployed. The two outputs of the antenna are connected to each of the receiver's channels which can be seen on the same figure. The instrument has four legs ending in a sharp cone in order to accommodate the instruments' ground plane perfectly on a horizontal position with the help of a level.

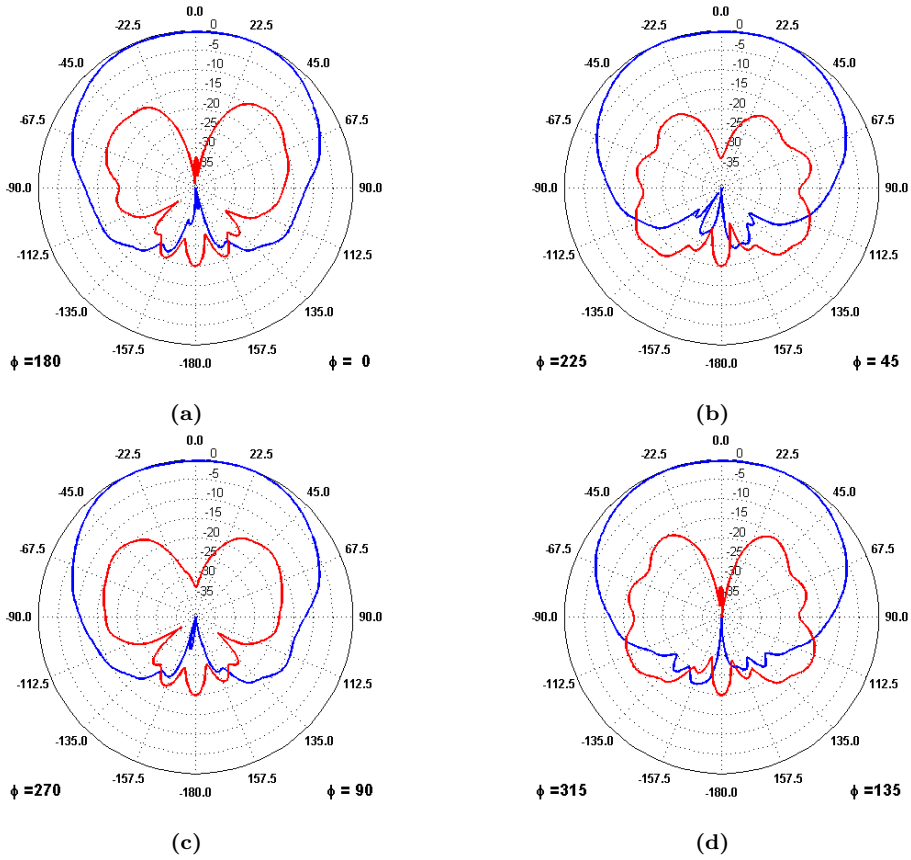

Figure 5.27: Co-polar (RHCP, blue) and Cross-polar (LHCP, red) McGiver RHCP antenna pattern: (a) - (d) 0°, 45°, 90°, and 135°, ϕ cuts respectively.

5.6 Summary

This chapter has tried to provide a clear and concise description of the hardware instruments developed and used in this PhD Thesis. The first instrument developed is the dual-polarization SMIGOL instrument which was used in one part of the ground-based GELOz field campaigns. It is an evolution of the single polarization SMIGOL instrument developed by Nereida Rodriguez Alvarez during her entire PhD Thesis. The addition of an extra polarization required some changes at the antenna, at the receiving chain, and specially at the micro-controller, since it had to be changed. Furthermore, the power supply system had to be redesigned for the new instrument's specifications. The second instrument developed is the LARGO with its two versions. The initial version was used for the airborne part of the GELOz experiments, whereas the version that included the calibration matrix was used in the *Salamanca* field experiment, and in the GRDC project. As it has been shown, LARGO is a dual-channel receiver whose structure has been kept as similar as possible to the dual-polarization SMIGOL, changing the antennas, the back-end receivers (higher performance receivers were needed), and the system's firmware.

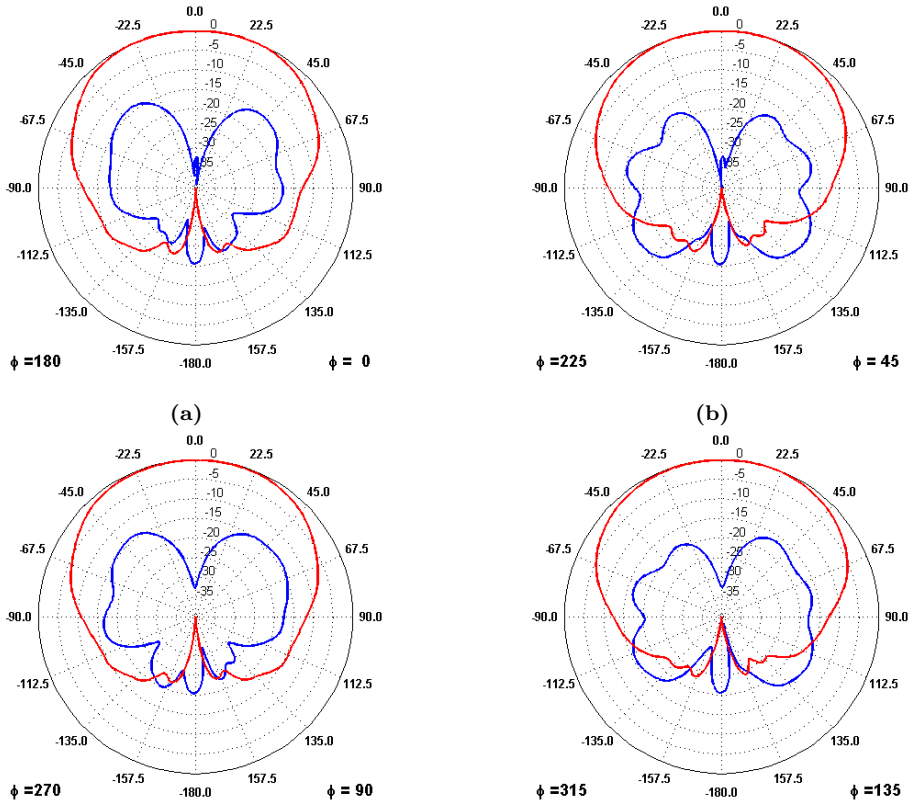

Figure 5.28: Co-polar (LHCP, red) and Cross-polar (RHCP, blue) McGiver LHCP antenna pattern: (a) - (d) 0°, 45°, 90°, and 135°, ϕ cuts respectively.

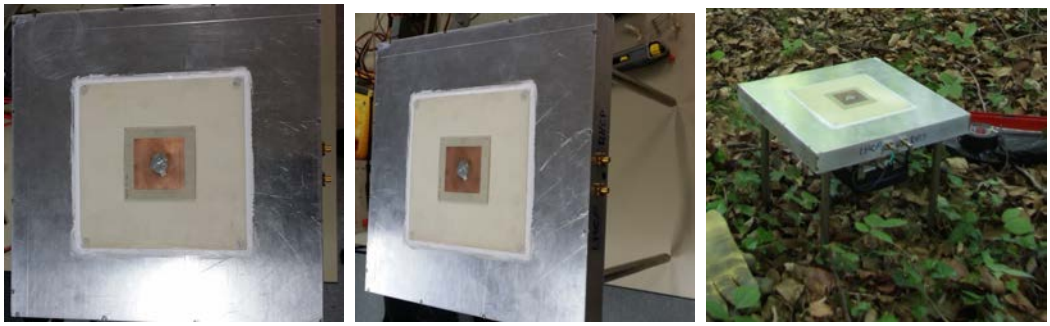

(a) **(b)** **(c)**

Figure 5.29: McGiver instrument final appearance.

However, since the instrument was powered using batteries for the field campaigns, there was no need for a specific autonomous power supply system. The third instrument in-

volved in this PhD Thesis is the PAU payload. The author's personal contribution to that instrument has been more dedicated to the new antenna analysis, simulation, and measurement. The author contributed to test the final assembly of the instrument in its initial version, and the open-loop near real-time hardware processing version. Therefore, for this instrument no direct hardware manufacturing was involved. The fourth instrument involved in this PhD Thesis is the McGiver, which is designed specifically to measure direct signals instead of the reflected ones. McGiver is a combination of the LARGO and the dual-polarization SMIGOL, using the simplest designs from both of them in each case.

In this chapter the antenna radiation patterns from all the antennas used are detailed and described. They should be taken into account in the data analysis of the experimental field campaigns that are shown in the subsequent chapters. There is another instrument that has been manufactured and designed called DUO, which will be described in its own chapter since its GNSS-R part is identical to the McGiver instrument, and it only changes in the antenna used. However, some other features were added to the DUO which are worth describing.

6

Chapter 6
Ground-based GNSS-R experiments over land

This chapter summarizes the ground-based GNSS-R experiments performed over land surfaces with the goal of retrieving the soil moisture content of the surface under observation. It starts presenting the dual-polarization SMIGOL experiments conducted in Australia. This part contains the application of the theory described in Chapter 3. It continues with a static ground-based scatterometry experiment conducted in *Tarragona* using the DUO instrument, which is described in here too. Subsequently, a static ground-based experiment conducted in *Viladecans* is described. Due to the presence of RFI and the characteristics of the experiment no soil moisture time series could be retrieved. Then, a dynamic ground-based experiment conducted during the GELOz field campaigns is presented. The platform used produced multi-path which complicated the retrieval of geophysical parameters. Having learned the lessons from those two latter field campaigns, the GRDC project started which the goal of measuring near real-time soil moisture with a LARGO mounted on a tractor.

6.1 Dual-polarization IPT in GELOz Experiments

The dual-polarization SMIGOL instrument was mounted on the test site (Yanco, New South Wales, Australia, 34°59'21.2"S 146°17'26.5"E) on July 16, 2013. Figure 6.1 shows the final installation, where the instrument is mounted on the top of the wooden mast. Non-metallic tensors were used to protect the structure from the wind. A wooden fence was also installed to protect the structure from the animals on the field. Non-metallic materials were used in the entire structure to avoid undesired reflections. Near the test site there was a soil moisture station from the OzNet soil moisture network [159] with a SDI-12 soil moisture probe which measured the soil moisture content of the first 5 cm. Another experiment for soil moisture retrieval was being conducted simultaneously which used a new technology called the Cosmic Ray Probe (CRP) [160]. A comparison among all the available data is presented at the end of this section.

Figure 6.1: Yanco test site with the dual-polarization SMIGOL instrument installed.

This field campaign allowed to develop two different algorithms to retrieve soil moisture from the observed interference patterns. The first one is based on observing the amplitude of the H-Pol interference patterns. As seen in Chapter 3, the H-Pol reflection coefficient is larger than the V-Pol one, resulting in larger amplitude oscillations on the H-Pol interference patterns. This fact increases the sensitivity to soil moisture changes as compared to the V-Pol amplitude fringes. The second algorithm was derived to improve the accuracy on the estimation of the Brewster angle position, because sometimes the minimum amplitude point covers a wide range of angles. To do so, the phase difference between both interference patterns was measured. The 90° phase shift point can be associated to the Brewster angle position.

6.1.1 Soil Moisture Estimation from the H-Pol Interference Pattern

From Chapter 3 the coherent IPT can be expressed as:

$$P_R \propto |F_n(\theta_{elev})|^2 \cdot |U_{d_0}|^2 \cdot \left|1 + |r_{pq}(\theta_{elev}, \varepsilon_r)| e^{j(\Delta\phi(\theta_{elev}) + \phi_{r_{pq}}(\theta_{elev}, \varepsilon_r))}\right|^2. \tag{6.1}$$

As shown in Chapter 3 from Eqn. (3.16), there are points in the interference pattern of minimum and maximum amplitude. Minimum amplitude points occur when the phase term is an odd multiple of π or $(2n+1)\pi = \Delta\phi(\theta_{elev}) + \phi_{r_{pq}}(\theta_{elev}, \varepsilon_r)$. Maximum amplitude points occur when the phase term is an even multiple of π or $2n\pi = \Delta\phi(\theta_{elev}) + \phi_{r_{pq}}(\theta_{elev}, \varepsilon_r)$. So, the maximum ($P_{Rq_{max}}$) and minimum ($P_{Rq_{min}}$) power values are obtained according to Eqns. (6.2)–(6.3), respectively.

$$P_{Rq_{max}}(\theta_{elev}, \varepsilon_r) = |F_n(\theta_{elev})|^2 \cdot |U_{d_0}|^2 \cdot \left|1 + |r_{pq}(\theta_{elev}, \varepsilon_r)|\right|^2, \tag{6.2}$$

$$P_{Rq_{min}}(\theta_{elev}, \varepsilon_r) = |F_n(\theta_{elev})|^2 \cdot |U_{d_0}|^2 \cdot \left|1 - |r_{pq}(\theta_{elev}, \varepsilon_r)|\right|^2. \tag{6.3}$$

Provided that the instrument's height is larger than three meters, the angular separation between consecutive maxima and minima is smaller than one degree. Taking into account that one degree angular variation in the absolute value of the reflection coefficient is negligible, and that the observed surface is practically the same, the overall reflection coefficient at q polarization as a function of the elevation angle (θ_{elev}) can be estimated from the interference pattern using Eqn. (6.4):

$$|\hat{r}_q(\theta_{elev}, \varepsilon_r)| \approx \frac{\sqrt{\frac{P_{Rq_{max}}(\theta_{elev}, \varepsilon_r)}{P_{Rq_{min}}(\theta_{elev}, \varepsilon_r)}} - 1}{\sqrt{\frac{P_{Rq_{max}}(\theta_{elev}, \varepsilon_r)}{P_{Rq_{min}}(\theta_{elev}, \varepsilon_r)}} + 1}. \tag{6.4}$$

Equation (6.4) is an estimator of the reflection coefficient modulus, and therefore, it ranges from 0 to 1. Furthermore, there is a strong link between Eqn. (6.4) and the Voltage Standard Wave Ratio (VSWR) definition [154], since $|\Gamma| = (\text{VSWR} - 1) / (\text{VSWR} + 1)$. The VSWR in a microwave transmission line is the ratio between the maximum and the minimum voltage (V_{max}/V_{min}). If the transmission line is perfectly matched (ended with a matched load), there is no reflected wave and the VSWR value is 1, since V_{max}=V_{min}, which is something that occurs at the θ_B position. However, if is not perfectly matched, there is a reflected wave and the VSWR value is larger than one. A link between the IPT and the VSWR concept can be directly obtained if the VWSR is defined as in Eqn. (6.5). In the IPT, the observable is the power fluctuations of the incoming wave (direct signal) due to a mismatch of the reflecting medium (reflected wave). This occurs because the transmitting medium (air) is not perfectly matched (the soil layer is not a matched load for the air). However, there is a difference between the VSWR and the IPT. While the VSWR is a constant value for the whole transmission line, for the IPT it is not constant as the reflectivity depends on the incidence angle and the soil dielectric properties. As the GNSS satellites move, both parameters change, and therefore, the reflectivity is estimated as a function of the incidence angle. Hence, it is necessary that the instrument is at a certain height in order to see the maxima and minima points under the same soil and angular conditions. From the reflectivity estimation it is straightforward to simulate

different reflection coefficients for different ε_r and θ_{elev} and make an inversion using a least-square algorithm.

$$VSWR = \sqrt{10^{P_{Rq_{max}}(\theta_{elev},\varepsilon_r)/P_{Rq_{min}}(\theta_{elev},\varepsilon_r)}} \tag{6.5}$$

6.1.1.1 System Limitations and SM Uncertainty Margins

Due to natural effects such as surface roughness, or induced effects such as quantization in the receiver's back-end (C/N0 values are normally rounded to their nearest integer), there is an uncertainty in the estimation of the SM value. First of all, quantization errors and noise lead to an uncertainty in the reflection coefficient amplitude estimation. As seen in Chapter 5, the dual-polarization SMIGOL instrument measures the satellites' C/N0. Since the noise level is nearly constant, the measurement of the C/N0 fluctuations is equivalent to the measurement of the fluctuations of the received signal power. Secondly, the C/N0 was quantized in the GPS receivers back-end used in steps of 1 dB. In this quantization operation there is an intrinsic uncertainty of ± 0.5 dB (uniformly distributed), which leads to an uncertainty in the estimated reflection coefficient. If the reflection coefficient estimator is given by Eqn. (6.4), and considering the definition shown in Eqn. (6.6), the uncertainty in the reflection coefficient estimation ($\Delta|\hat{r}_q(\theta,\varepsilon_r)|$) is given by Eqn. (6.8).

$$u(\theta,\varepsilon_r) = 10^b, \tag{6.6}$$

where:

$$b = \frac{P_{Rq_{max}}(\theta,\varepsilon_r)[dBau] - P_{Rq_{min}}(\theta,\varepsilon_r)[dBau]}{10}, \tag{6.7}$$

$$\Delta|\hat{r}_q(\theta,\varepsilon_r)| = \frac{ln10}{10}\frac{\sqrt{u}}{(\sqrt{u}+1)^2}. \tag{6.8}$$

The uncertainty in the reflection coefficient estimation at H-Pol is translated into an uncertainty in the ε_r estimation. At H-Pol, the dielectric constant uncertainty ($\Delta|\hat{\varepsilon}_{r_h}(\theta,\varepsilon_r)|$) is given by Eqn. (6.9). Then, using for instance Wang's model [94] to relate the SM content and the dielectric constant, the uncertainty in the SM retrieval (ΔSM) is given by Eqn. (6.10).

$$\Delta|\hat{\varepsilon}_{r_h}(\theta,\varepsilon_r)| = 4\cdot\frac{1+|\hat{r}_q(\theta,\varepsilon_r)|}{(1-|\hat{r}_q(\theta,\varepsilon_r)|)^3}\cdot\Delta|\hat{r}_q(\theta,\varepsilon_r)|. \tag{6.9}$$

$$\Delta SM = \frac{1}{\sqrt{(17.36)^2 - 4\cdot 63.12\cdot(1-|\hat{\varepsilon_r}_h(\theta,SM)|)}}\cdot\Delta|\hat{\varepsilon_r}_h(\theta,SM)|. \tag{6.10}$$

Table 6.1 shows a summary of the uncertainty budget propagation at H-Pol due to quantization. It covers the three steps; from the uncertainty in the estimation of the reflection coefficient up to the SM uncertainty. Note that the larger the SM content, the larger the reflection coefficient, and the larger the amplitude of the interference pattern. Consequently, the lower the quantization uncertainty effect is on the reflection coefficient estimation. Unlike the reflection coefficient estimation uncertainty, the uncertainty on ε_r increases with increasing SM values. Despite the uncertainty on the reflection coefficient decreases with increasing SM, the fact that the larger the SM, the larger the ε_r value

compensates the decreasing factor of the uncertainty in the reflection coefficient estimation. The same behavior observed in the ε_r occurs in the uncertainty of the SM. The larger the uncertainty in the ε_r, the larger the uncertainty in the SM estimation.

Table 6.1: Uncertainty budget summary table due to quantization errors assuming $\pm 0.5dB$ at H-Pol.

Soil Moisture	$\Delta\lvert\hat{r}_q(\theta,\varepsilon_r)\rvert$	$\Delta\lvert\hat{\varepsilon}_{r_h}(\theta,\varepsilon_r)\rvert$	ΔSM
0%	0.0190	0.2755	1.5%
10%	0.0160	0.4878	1.7%
20%	0.0122	1.0772	2.4%
30%	0.0010	1.8189	3.0%
40%	0.0087	2.5582	3.5%

For V-Pol, the uncertainty on the reflection coefficient due to quantization is also given by Eqn. (6.8). As the interference pattern amplitude at V-Pol is lower than at H-Pol, the uncertainty obtained will be larger. However, a final expression for the dielectric constant inversion at V-Pol cannot be derived due to the amplitude ambiguity of the reflection coefficient. This expression changes as a function of the Brewster angle position, which is not known a priori. As seen in Tab. 6.1 the uncertainty in the soil moisture retrieval is below 4%, which is the usual requirement for a soil moisture probe.

Another aspect in the error estimation is the goodness of the fit between the dielectric constant model used and the real one. If the imaginary part is larger than the one predicted by the model at the Brewster angle position, the reflection coefficient will have a minimum amplitude point, but not as close to 0. This is seen on the V-Pol interference pattern as a "notch" with a larger amplitude. This fact also affects the H-Pol interference pattern just by a smaller amplitude uncertainty.

As seen in [21] the "notch" amplitude value as a SM content estimator with 1 dB quantization can provide SM uncertainties larger than 20% [21]. This indicates that H-Pol reflection coefficient estimations using amplitude observations seem to be more accurate than the V-Pol ones.

6.1.1.2 Theoretical Simulations and Retrieval Algorithm

Interference patterns with and without quantization errors have been simulated to assess the least-square algorithm performance. First, the IPTs simulated for H- and V-Pol are shown in Figs. 6.2(a)–(b) respectively. It is worth highlighting that the amplitude of the IPT envelope at H-Pol is larger than at V-Pol due to the difference in the reflection coefficient amplitude. Also the presence of the Brewster angle is seen in Fig. 6.2(b) with its position varying as a function of the SM.

By applying the algorithm described by Eqn. (6.4), an estimation of the reflection coefficient at each polarization is obtained (Fig. 6.3). Note that the retrieval has started at $\theta_{elev} = 5°$, as for lower elevation angles the dependence of the reflection coefficients on SM is not large enough to get a valuable retrieval. Moreover, an elevation mask in the dual-polarization SMIGOL back-end receivers avoids measuring the interference patterns at lower elevation angles. Note that the estimated reflection coefficient oscillates due to

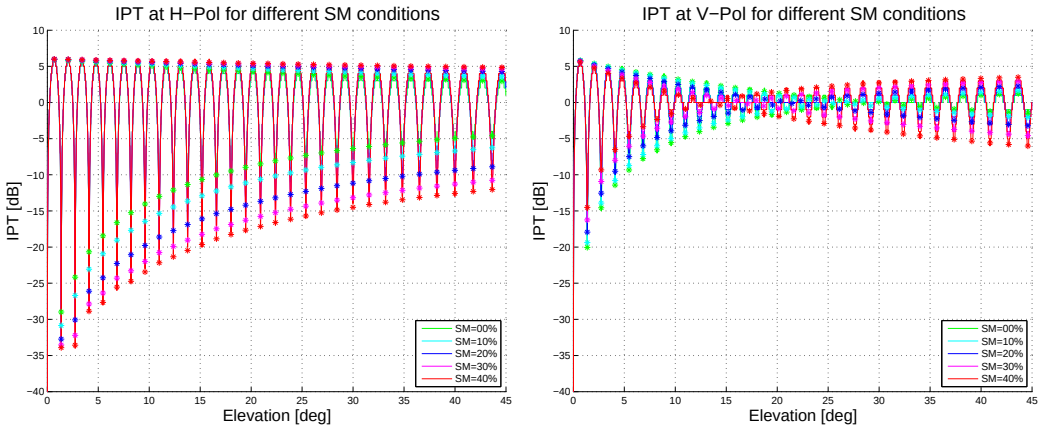

(a) **(b)**

Figure 6.2: Interference patterns simulated at (a) H-Pol, (b) V-Pol for different SM values.

the 1 dB quantization of the receivers. In Fig. 6.3(b) the position of θ_B is presented, as well as the amplitude ambiguity. Differently, at H-Pol (Fig. 6.3(a)), the entire range of elevation angles can be used for the retrieval.

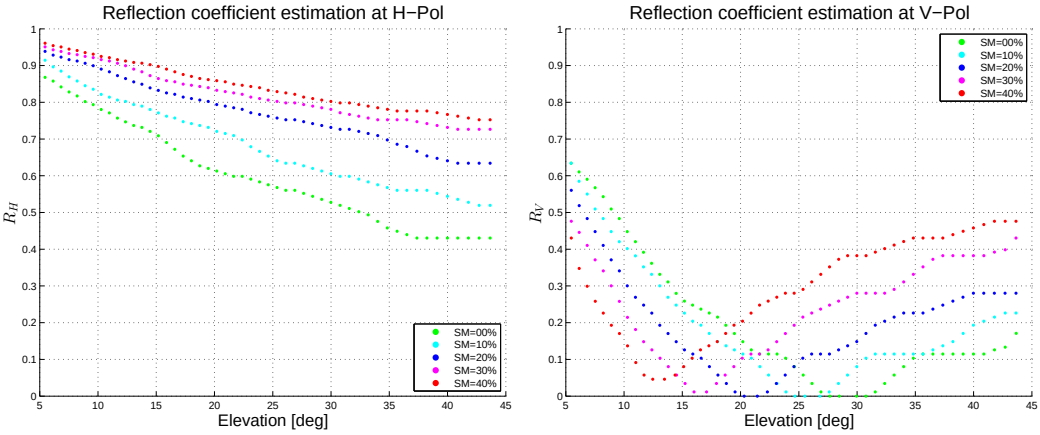

(a) **(b)**

Figure 6.3: Reflection coefficients retrieved from the simulated interference patterns: (a) H-Pol, (b) V-Pol, for different SM values. Its accuracy is analyzed in Table 6.3. The oscillation seen on the estimated reflection coefficient curves is due to the 1 dB quantization of the receivers.

From the estimated reflection coefficients, the SM at H-Pol can been inferred (Fig. 6.4), showing the evolution of the estimated SM as a function of the elevation angle. Table 6.2 shows the estimated SM value using the Brewster angle position information. As expected, V-Pol gives very precise information on the SM content. To characterize the H-Pol information, a scatter plot representing the true SM values against the estimated

ones is presented in Fig. 6.5, where a small bias in the mean values of the estimated SM using H-Pol is observed.

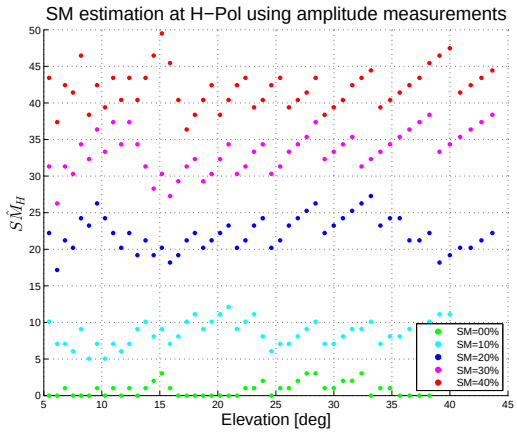

Figure 6.4: SM estimation at H-Pol for different SM values using the amplitude of the IPT simulated taking into account quantization effects.

Table 6.2: Comparison between true SM and SM retrieval using the Brewster angle position.

True SM [%]	**Estimated SM** [%]	**Error** [%]
0	5.08	5.08
10	9.88	0.12
20	18.61	1.39
30	28.47	1.53
40	39.60	0.40

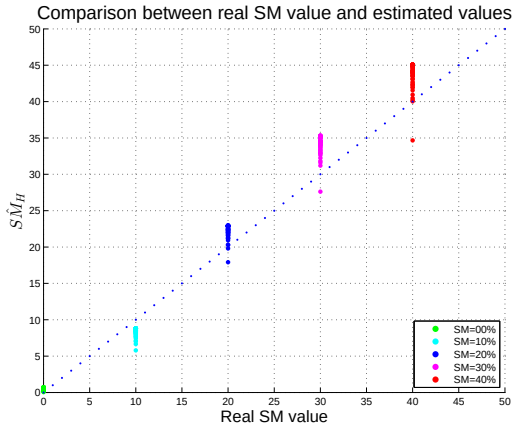

Figure 6.5: Scatter plot of the true SM values (x-axis) against the estimated SM values (y-axis). The 1:1 line added to facilitate the comparison.

So, the first algorithm proposed consists of the estimation of the reflection coefficient as a function of the incidence angle from each interference pattern. Using simulated reflectivities, a least-square algorithm can be applied to obtain point soil moisture information. Figure 6.6 shows a summary of how the algorithm works.

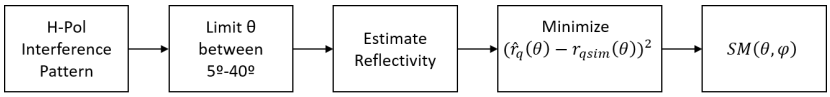

Figure 6.6: H-Pol IPT soil moisture retrieval algorithm.

However, there are two aspects here that must be corrected. One is the small bias seen on the H-Pol interference pattern retrieval, and the other one is the effect of surface roughness. As previously seen in Chapter 3, surface roughness attenuates the coherent reflectivity, which makes the oscillation amplitude of the interference patterns smaller. This would result in a lower estimation of the reflection coefficient. However, as stated in [21], the Brewster angle position is nearly insensitive to the surface roughness. So, the second algorithm proposed is to apply the first algorithm to the H-Pol interference pattern and compensate the mean value of the H-Pol retrieved soil moisture by the one estimated using the Brewster angle position. Figure 6.7, shows how the two (H- and V-Pol) interference patterns can be combined in order to compensate for the bias and surface roughness. Figure 6.8 is the result of applying the proposed correction to Fig. 6.5. In this case, since no roughness has been considered in the simulated interference pattern, the bias that has been corrected is the one induced due to the quantization of the C/N0 values.

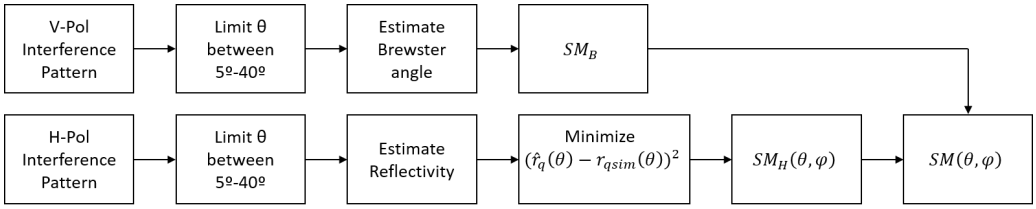

Figure 6.7: Combined H- and V-Pol IPT soil moisture retrieval algorithm.

In order to summarize the simulation analysis section and show the improvement of the combination algorithm, the theoretical mean and the standard deviation values of the simulated retrievals, in ideal case and with quantization, have been computed and presented in Table 6.3. Therein, it is seen that when the soil moisture content is very small ($\leq 5\%$) the algorithm overestimates it, because the Brewster angle position provides an optimistic soil moisture value (bias of 5%). This occurs because the minimum amplitude point becomes an angular region due to the quantization, as seen in Fig. 6.3(b). However, for larger soil moisture values the proposed combined algorithm the bias of the retrieval.

6.1.1.3 Experimental Data Analysis

Figure 6.9 shows two experimental interference patterns: (a) from satellite PRN 1 on July 16, 2013, and (b) from satellite PRN 23 on July 27, 2013. It is seen that the amplitude of

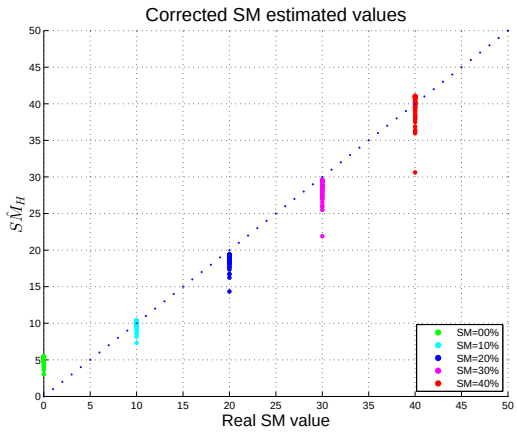

Figure 6.8: Corrected soil moisture estimates using H- and V-Pol interference patterns.

Table 6.3: Statistics of the simulated retrievals at V-Pol and H-Pol.

SM [%]	**H-Pol**				**H-Pol and V-Pol Combined**			
-	**ideal**		**quantized**		**ideal**		**quantized**	
-	mean [%]	std [%]	mean [%]	std [%]	mean [%]	std [%]	mean [%]	std [%]
0	0.89	0.32	1.01	1.02	5.08	0.32	5.08	1.02
10	8.79	0.51	8.77	1.58	9.89	0.51	9.89	1.58
20	21.9	0.57	22.09	2.22	18.62	0.57	18.62	2.22
30	33.58	0.87	33.49	2.77	28.46	0.87	28.46	2.77
40	42.67	1.09	42.08	2.69	39.6	1.09	39.6	2.69

the H-Pol IPT is larger than that from the V-Pol due to the larger reflection coefficient value. Note that both H- and V-Pol interference patterns are not aligned. This is due to the effect of the two phase terms in the IPT, and it is related to the retrieval algorithm proposed in the next section. One phase term is related to the different path length of the direct and reflected signals, which is the same for both polarizations. The other term comes from the reflection coefficient phase at each polarization, which is different, and so it is the resulting phase of both interference patterns. The sensitivity to different surface points as the satellite moves is also seen in the envelope of the interference pattern, since its amplitude changes due to different elevation angles and SM conditions.

The absolute value of the reflection coefficient as a function of the elevation angle is estimated for both polarization states using the previously described algorithms. From the reflection coefficient estimation, the SM values are inferred for each satellite as a function of the elevation angle. Figure 6.10 shows the estimated soil moisture from the interference patterns pictured in Fig. 6.9, where the θ_B SM estimation is marked in red and the blue marks are related to the H-Pol retrievals.

Several interference patterns retrieved between July 16, 2013, and July 31, 2013, were analyzed and processed. The data between the SM value retrieved using the Brewster angle information and the mean value of the different point SM estimates using H-Pol for

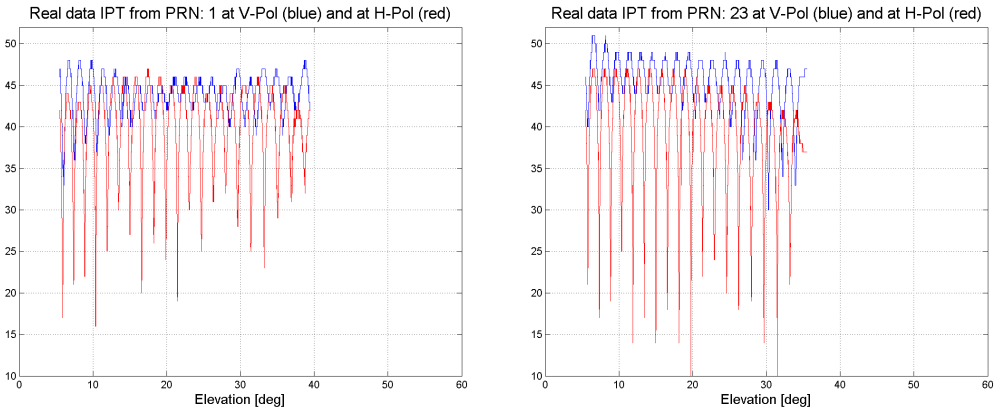

(a) **(b)**

Figure 6.9: Real interference patterns retrieved, V-Pol (blue) and H-Pol (red): (a) PRN 1 of July 16, 2013, (b) PRN 23 of July 27, 2013.

each satellite in view is compared in Fig. 6.11. A good linear fit (R^2=0.895 and RMSE= 2.2%) between both independent methods for estimating SM is found. This indicates that surface roughness attenuation for the field experiment was negligible, and there is no need to use the algorithm described in Fig. 6.7.

6.1.1.4 Comparison Against Ground-truth Data

The results obtained for the range of days between July 16, and July 31, 2013, were compared with in-situ SM instruments and rainfall events in that period. Figure 6.12 shows a summary of the entire ground-truth information retrieved during the field experiment (Fig. 6.13). The bars represent the rain events (in [mm/day]) from the closest information stations available: in blue the Yanco Agricultural Institute (YI) and in red the Narrandera Airport (NA) (see Fig. 6.13). Rainfall information at those points is either collected with the traditional "Manual Rain Gauge", which is a manual measurement of the total amount of rain, or with the "Tipping Bucket Rain Gauge", which is an automatic measurement of the total amount of rain. The SM measurements shown in Fig. 6.12 have been obtained with two different instruments: the CRP and a SDI-12 SM probe [161]. The CRP probe counts the number of neutrons emitted spontaneously by the soil to measure an area-average SM. The penetration depth of the CRP probe ranges between 10–25 cm, being lower for high SM values, and vice versa. The data shown from the CRP is a 12-hour average of the 30 min time series data measured. The YB7 SM measurement station contains a SDI-12 SM probe, which provides point measurements of the top 5-cm volumetric soil moisture content. The dual-polarization SMIGOL instrument falls in the coverage area of the CRP sensor (200 m diameter) whereas the SDI-12 probe available is 700 meters away from the instrument's location.

The soil moisture data from the dual-polarization SMIGOL instrument presented in Fig. 6.13 are the average of at least 5 interference patterns obtained per day. The esti-

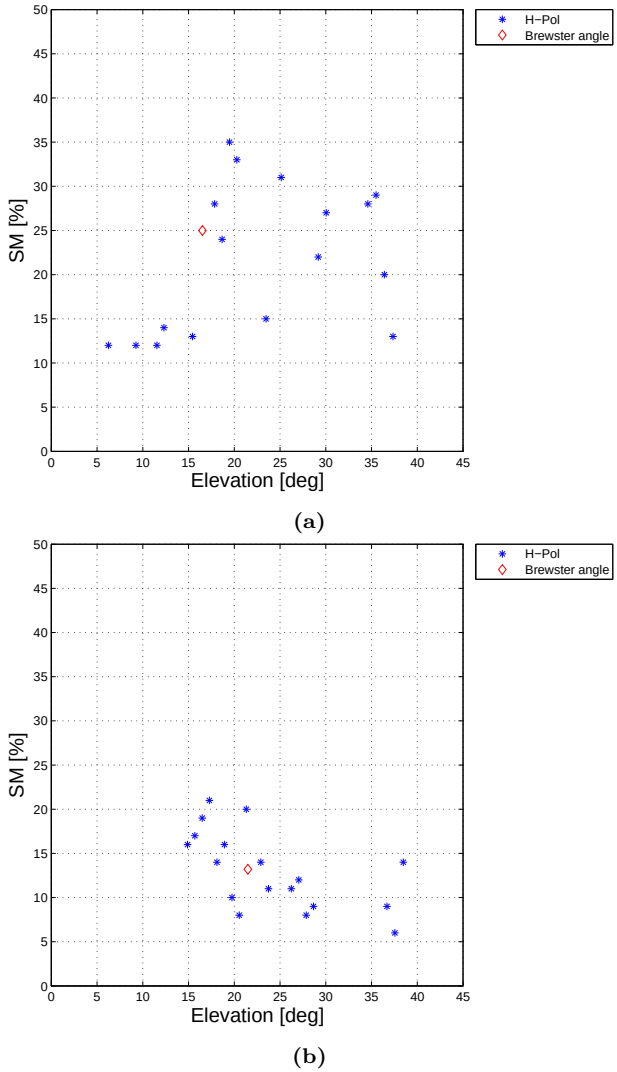

Figure 6.10: SM retrieved (a) from PRN1 on July 16, 2013, and (b) from PRN 23 July 27, 2013. Red diamonds correspond to the Brewster angle SM estimation. Blue asterisks correspond to the H-Pol amplitude estimations of SM.

mated soil moisture values using either the mean value of the H-Pol information or the Brewster angle information are in between the data retrieved from both SM sensors. This agrees with the principles of the technique, being the penetration depth of the GNSS-R instrument between 7–15 cm depending on the SM conditions. Since the penetration depth of the dual-polarization SMIGOL is larger than the SDI-12 and lower than the CRP sensor, it is expected to obtain SM values in between both sensors. It is also seen that after a rain event, SM increases and then it starts a decreasing trend which is seen by all the instruments installed. Note that, as Fig. 6.11 showed, it was not necessary to

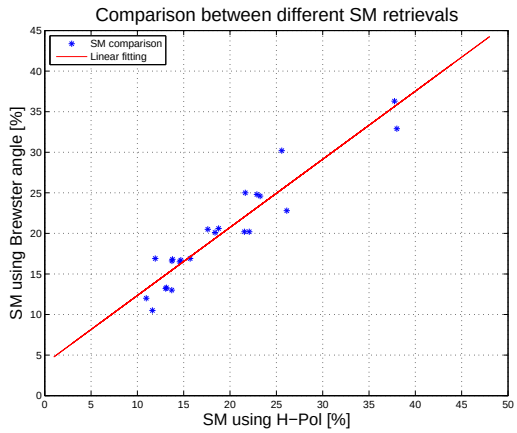

Figure 6.11: Comparison between retrieved SM using the mean value of the H-Pol samples (x-axis) and the SM retrieved using the Brewster angle information (y-axis); R^2=0.895 and a RMSE=2.2%.

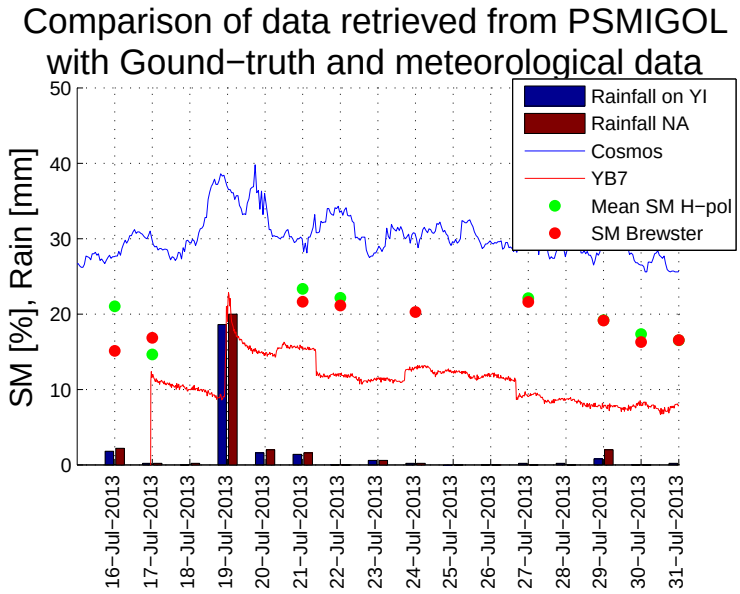

Figure 6.12: Summary of the results obtained from the field campaign. Bars represent the rainfall events in mm/day. The blue bar shows the information of rain events from the Yanco Agricultural Institute (YI). The red bar shows the information from the Narrandera Airport (NA). The blue line shows the information from the Cosmos SM sensor (CRP, Cosmos). The red line shows the information of the YB7 SM probe. Green dots correspond to the mean SM value obtained from the H-Pol measurements. Red dots correspond to the mean SM value obtained from Brewster angle information.

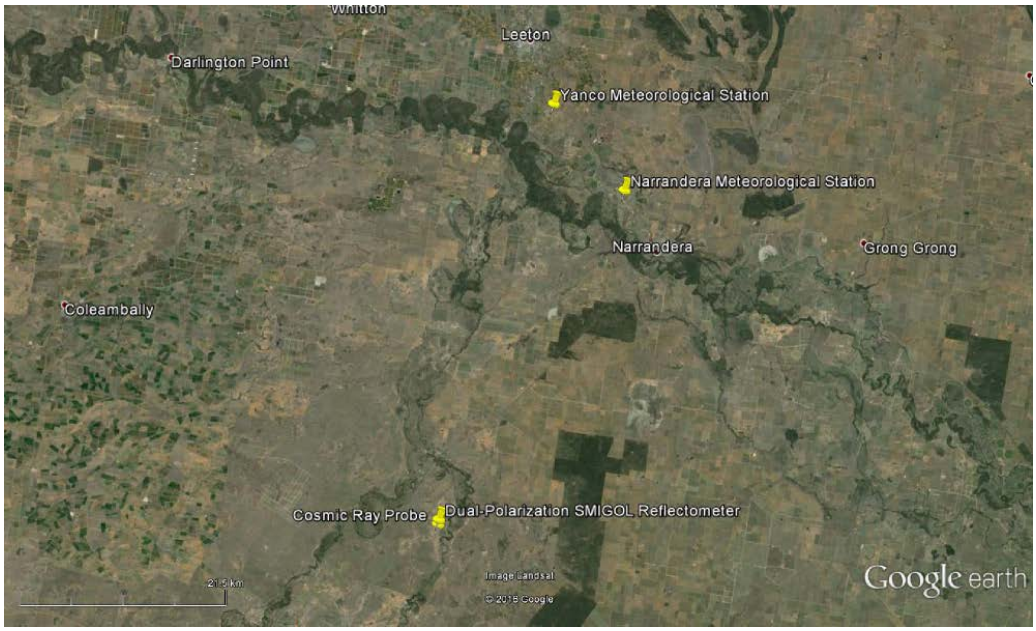

Figure 6.13: Description of the dual-polarization SMIGOL field test site locating the ground-truth sensors.

use the combination algorithm, and correct the H-Pol estimations using V-Pol Brewster angle retrievals. Therefore, the two IPT soil moisture retrievals shown in Fig. 6.12 are independent.

6.1.2 Soil Moisture Estimation from the Phase Difference between H-Pol and V-Pol Interference Patterns

Eqn. (3.16) shows that the interference pattern has two different phase terms, one corresponding to the extra path covered by the reflected ray, and the other one corresponding to the reflection coefficient phase. In Chapter 3 it was shown that the phase of the H-Pol reflection coefficient is always negative and 180°. However, the phase of the V-Pol reflection coefficient changes as a function of the incidence angle and SM conditions. Figure 6.14 shows the reflection coefficient squared (reflectivity) and the reflection coefficient phase as a function of soil moisture using a 3-layer reflection model. Figure 6.15 shows two simulated interference patterns for two different soil moisture values for an antenna height of 3.6 m, which is very close to the actual one installed in the Yanco region. Comparing the blue dashed lines (H-Pol) with the green lines (V-Pol), it is seen that, for low elevation angles ($\theta_{elev} < \theta_B$), the H- and V-Pol interference patterns are in phase, whereas for larger elevation angles ($\theta_{elev} > \theta_B$) they are in counter phase. This is better seen just by comparing the position of the maxima and the minima points, because they are first coincident ($\theta_{elev} < \theta_B$), whereas for $\theta_{elev} > \theta_B$ local maxima at H-Pol are coincident with local minima at V-Pol, and vice versa. This trend is observed in both figures changing the θ_{elev} range when they are in phase or in counter phase due to the change in the θ_B

position, which is directly related to a SM change.

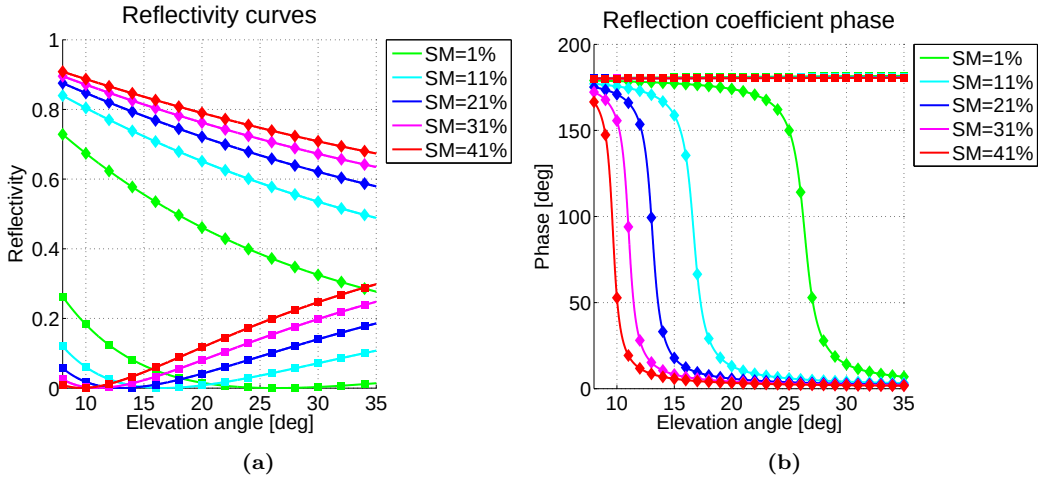

Figure 6.14: (a) Reflectivity at H-Pol (blue dashed) and V-Pol (green) as a function of soil moisture, (b) H- and V-Pol reflection coefficient phase.

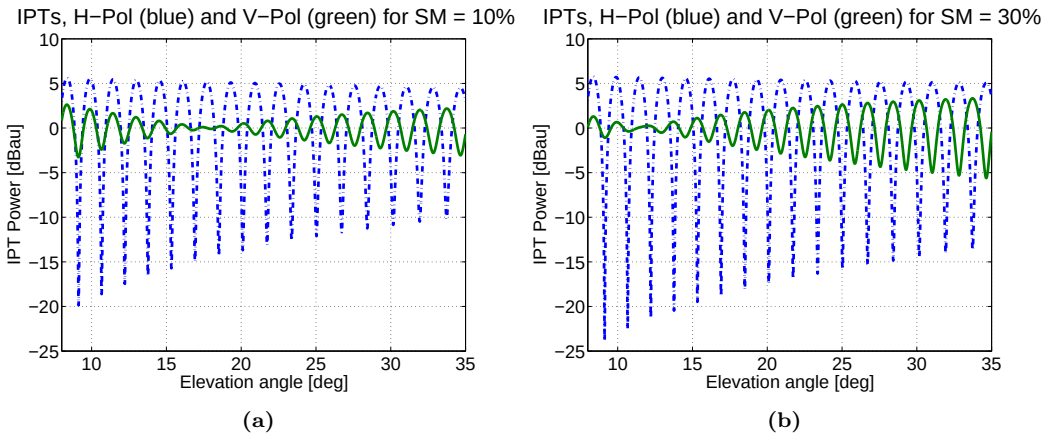

Figure 6.15: (a)–(b) H- and V-Pol simulated interference patterns for a soil moisture content of 10% and 30% respectively for a 3.6 m antenna height.

6.1.2.1 Methodology and Retrieval Algorithm

To measure the phase difference between the H- and V-Pol interference patterns, the whole phase evolution of each interference pattern must be retrieved separately. To do so, the first step is to retrieve the position of maxima and minima points. The phase difference between consecutive relative maxima and minima is 180°. The first relative maximum or minimum for each interference pattern is taken as a reference and from there, the entire phase of the interference pattern is inferred. Considering that the phase

evolution between consecutive maxima and minima follows a quasi-linear phase variation, the entire interference pattern phase is retrieved with 2π phase jumps. After that, the phase must be unwrapped to obtain the phase evolution. After phase unwrapping, the phase difference between H- and V-Pol is directly the difference between the phase of the reflection coefficients at each elevation angle. Figure 6.16 shows the phase difference between the H- and V-Pol interference patterns from Fig. 6.15 as a function of θ_{elev}. A ripple in the phase retrieved curve occurs for $\theta_{elev} > \theta_B$ due to the uncertainty in the determination of the maxima and minima positions. However, the key point is the identification of the 90° phase difference, which corresponds to position of θ_B. This algorithm is summarized in Fig. 6.17. A sensitivity analysis has been performed based on a series of simulations varying the surface roughness and SM conditions. The precision of the technique at the 90° phase shift is 2.5%, which is comparable to calibrated conventional SM probes.

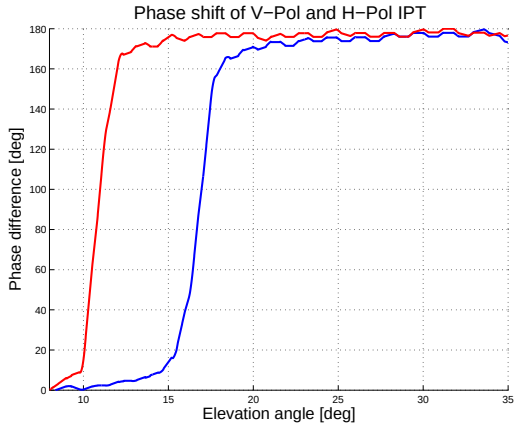

Figure 6.16: Phase difference of the interference patterns simulated at H- and V-Pol for two different SM values: 10% (blue), 30% (red).

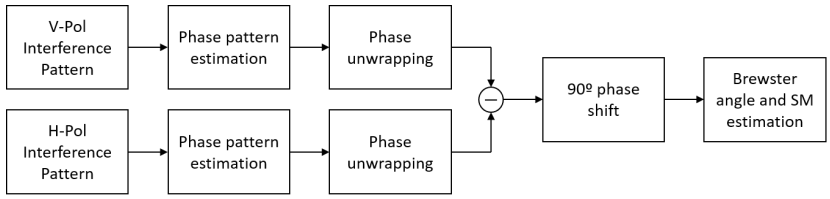

Figure 6.17: Phase difference retrieval algorithm summary.

6.1.2.2 Analysis of Experimental Data

Data from the GELOz field experiment described in the previous section has been used to test the proposed algorithm. Two different datasets are shown in Fig. 6.18. As seen in Fig. 6.18(a), sometimes the identification of the θ_B by looking to the notch is not so straightforward when the frequency of the oscillations is not high enough, or what is the

same, when there is a height limitation; since the lower the height, the lower the frequency of the oscillations. Conversely, the 90° phase difference position is clearly identified and it corresponds to the θ_B value (23°). The same effect occurs in Fig. 6.18(b), but now the amplitude of the oscillations at V-Pol are nearly the same for θ_{elev} in the range of 10°–17°. Using the phase difference observable, the θ_B position can be precisely detected (18°). Note that SM is not necessarily constant in the whole field and the phase difference curves do not have to follow exactly the sharp shape shown in Fig. 6.16. The 90° phase shift is a precise proxy of θ_B.

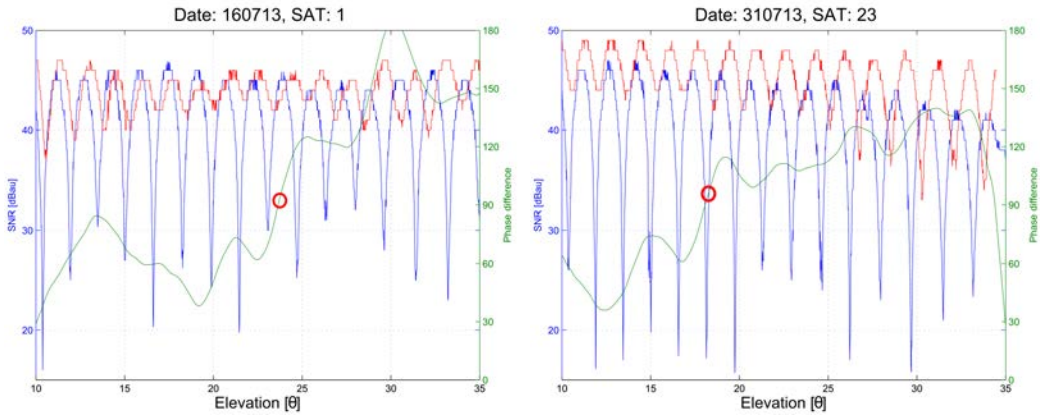

Figure 6.18: IPT at V-Pol (red), H-Pol (blue) and phase difference (green) between them. (a) PRN 1 on July 16, 2013 (b) PRN 23 on July 31, 2013.

Finally, Fig. 6.19 compares the data series of the mean SM values retrieved using the phase retrieval algorithm with the Brewster angle position algorithm, with external ground-truth SM data, and with the rainfall events during the period under analysis from the two closest meteorological stations. During that period there was only one significant rain event on July 19, 2013. As it can be observed, the SM retrieved from the phase algorithm is more constant than the one retrieved with θ_B, following better the soil moisture variations measured by the ground-truth instrumentation. The SM retrieved is generally in between the SDI-12 SM probe and the CRP. This occurs again due to the different penetration depth and ground resolution of all instruments.

6.2 Soil Moisture Estimation from Ground-based Static Scatterometry Using Linear Polarization

After testing the dual-polarization IPT it was decided to move the soil moisture retrieval research to scatterometric techniques, which could overcome the problem of having a limited spatial coverage. However, prior to attempting a dynamic application it was decided to test the scatterometric technique under controlled static conditions. The first experiment under those conditions was performed in *Tarragona*, using linear polarization.

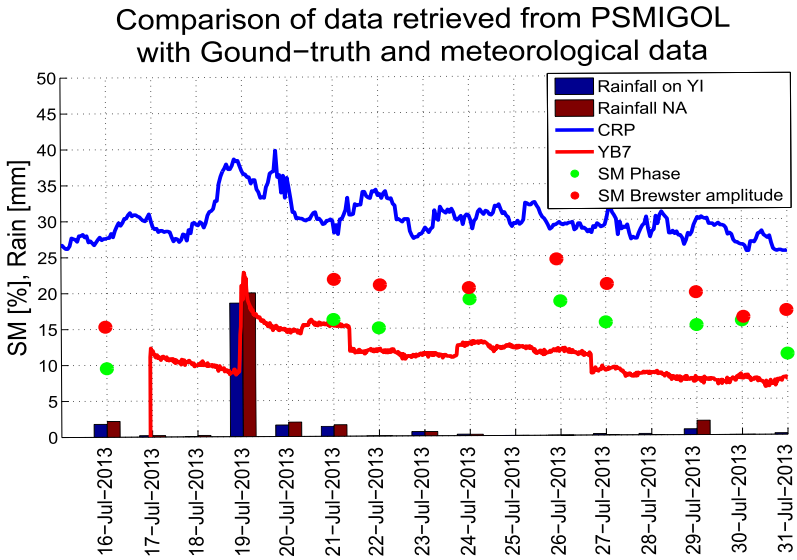

Figure 6.19: Summary figure comparing with ground-truth retrievals. The blue and red bars represent rainfalls. The blue line represents the data from the CRP. The red line shows the data from the SDI-12 SM probe. The green dots represent the mean SM retrieved from phase measurements. The red dots represent the mean SM retrieved from Brewster angle position.

6.2.1 The Tarragona Field Campaign

A field campaign was conducted at *La Pobla de Mafumet, Tarragona*, Spain, from August 2012 until February 2015 (see Fig. 6.20). The field was covered by hazelnut trees, and a particular location that had one part free of vegetation was used to install the DUO instrument, which is described in next section. Hazels are a deciduous type of tree, and therefore, winter was the best season to test the algorithms in order to minimize the effect of trees. The DUO instrument was mounted on a 6 m metallic tower, and a parabolic reflector with 1.5 m diameter dish was used as the antenna. This high directivity antenna should mitigate any type of multi-path coming from the trees. Figure 6.21 shows the DUO installation with the metallic tower, the big parabolic reflector and a step-motor (model BIG-RAS [162]) to move the parabolic reflector towards the direct and reflected signals, which is sketched in Fig. 6.22. In Fig. 6.21 there is also a white box coming out of the metallic tower and it corresponds to the first dual-polarization SMIGOL instrument tested.

The *Tarragona* field campaign was performed in two steps. In the first one a Matlab program installed on a computer prepared for harsh environments was used to move the step-motor and gather the signal power of the satellite under observation at two different polarization states (H- and V-Pol). The feeder of the parabolic reflector was made using the same antenna design of the dual-polarization SMIGOL. This system had three main issues:

Figure 6.20: Tarragona field campaign location.

Figure 6.21: DUO instrument installation.

1. Matlab is not prepared to work with I/O data which resulted in a 90% loss of data and a lot of system errors under the Windows environment.

(a) **(b)**

Figure 6.22: (a) DUO looking to the direct signal (b) DUO looking to the reflected signal.

2. The motor controller provided by the manufacturer was used to move the step-motor, but, surprisingly, it was not working properly and some steps were lost. Hence, after a while, the antenna was not pointing to the appropriate direction and satellites were out of the antenna beamwidth due to its high directivity. This resulted in a lot of discarded data.
3. There were three different thefts during the entire campaign including the copper of the power lines which compromised even more the experiment.

During 2014, a critical design review of the entire instrumentation was performed in order to overcome those problems. In order to solve for the first issue a McGiver-like instrument was used as the back-end receiver and data acquisition system. Simple GPS receivers were used as back-end because, due to the static conditions, the reflected power would seem locally coherent, and the measured SNR corresponds to the SNR_{cc}. An extra Arduino was added to control and give the commands to the step-motor controller. So, a PC running Matlab was replaced by a McGiver-like instrument and an Arduino with a GPS connected to it. To solve for the second issue, the step-motor controller was redesigned from its basis and its entire description can be found in [163]. In the final assembly, the mechanical relays were changed by custom-made electronic relays, which used CMOS technology, because after 3 weeks of continuous operation, the mechanical relays tended to get stuck. The third issue was solved by making more difficult the access to the instrumentation. That was achieved by fitting the entire instrumentation in a IP-68 plastic box, as shown in Fig. 6.23. In Fig. 6.23 all external connectors, the electronic relays, part of the custom-made motor controller, and the power supply system can be easily identified. This box was placed behind the parabolic reflector. Also a wireless transmitter was added to the system in order to avoid opening the instrument every-time data had to be collected. Furthermore, data were also stored in an internal SD-card for back-up purposes. The final assembly of the instrumentation can be seen in Fig. 6.24, and it is the one detailed in the next section.

6.2.2 The DUO Instrument

The core of the instrument is found in the Arduino added to control the step-motor, as the back-end used was a McGiver-like instrument using the simple back-end GPS receivers

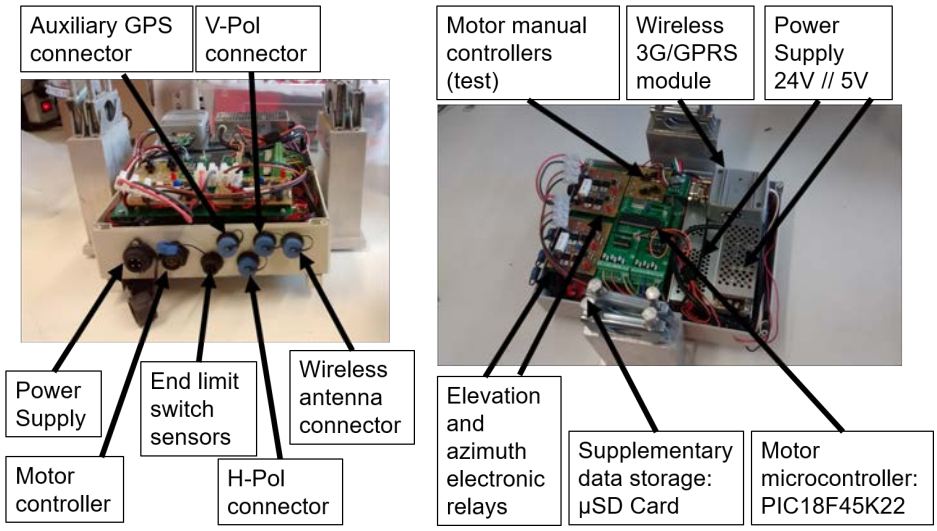

Figure 6.23: Compact version of the DUO instrument. (a) DUO external connectors (b) DUO internal hardware.

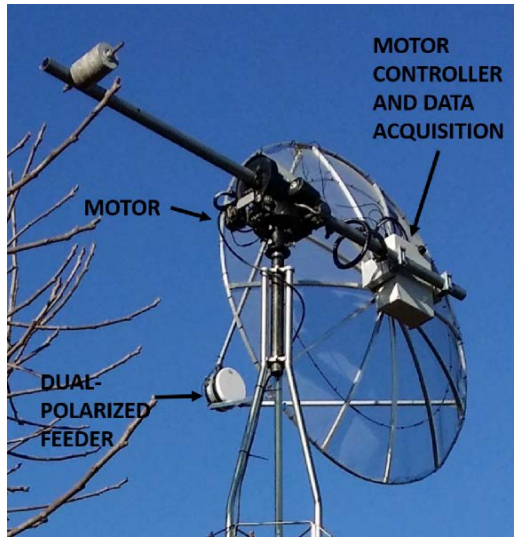

Figure 6.24: DUO final assembly.

of the dual-polarization SMIGOL instrument. Only, one extra feature was added to this McGiver-like instrument which was monitoring the output the motor controller, which was indicating when the instrument was either in calibration mode, or moving, or pointing towards the direct signal, or pointing towards the reflected signal, apart from the satellite ID being monitored at each time. The operational mode of the system was quite simple.

The first step was to calibrate the position of the parabolic reflector in order to start pointing to the North. Then, the satellite with the highest C/N0 and with an elevation range between 30°–85° was selected. The lowest limit was selected to avoid multi-path from ground/trees due to looking at too slant angles. The largest one to avoid multi-path from the tower when looking to the reflected signals. Subsequently, the antenna pointed directly to the selected satellite and measured the C/N0 for 1 minute. Then, it moved to the specular reflection point and monitored the same parameter for 5 minutes, re-positioning the pointing direction in case the azimuth or elevation parameters of the satellite had changed. Once the reflected signal was measured the direct signal was monitored again, and a loop of 1 min–5 mins started until the satellite was out of the elevation range selected. At this point the system calibrated the motor position again and started the same loop looking to the satellite with the highest C/N0 in the elevation range conditions selected. Figure 6.25 shows a summary of the DUO operational mode. The McGiver-type receiver was acting all the time as a passive receiver gathering the data from all the system peripherals (V- and H-Pol, and motor controller), storing them on an auxiliary SD card, and transmitting them via the wireless transmission module.

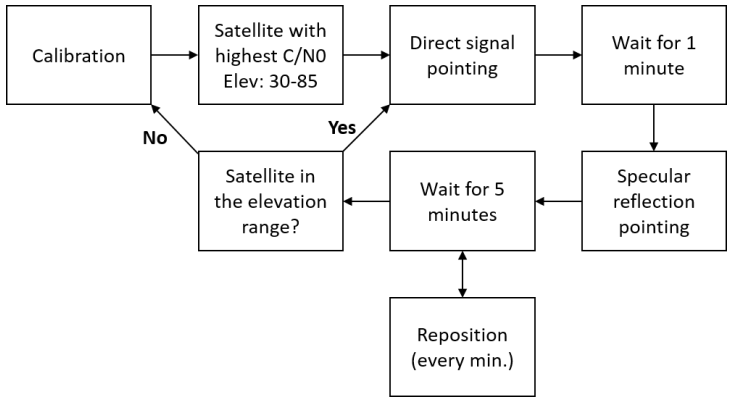

Figure 6.25: DUO operational mode.

It is worth to mention that to have this system fully operational required an uncountable number of hours of test prior to the final installation. A full-test of the instrumentation was performed during more than 3-months at the UPC D3 building roof. It was there when the failure of the mechanical relays was found after 3 weeks of continuous operation. Therefore, they were replaced by the custom-made electronic relays and the instrument worked continuously during 1 month and a half. Consequently, after having passed successfully all tests it was installed on the field. Disappointingly, 16 hours after the instrument was installed there was a mechanical failure on the motor elevation rotor, which could not be repaired successfully. However, those 16 hours of data were processed obtaining successful soil moisture retrievals.

6.2.3 Data Analysis and Direct Signal Leakage Cancellation

Figures 6.26(a)–(c) show all the data gathered during the field campaign prior to the mechanical failure. Therein, the H-Pol is represented in blue whereas the V-Pol is repre-

sented in red. The peaks on the signals correspond to the antenna pointing to the direct signal, whereas the valleys correspond to the antenna looking to the reflected signal. In green the elevation angle of the satellite under observation is shown which summarizes the operation mode of the DUO. Those data correspond to the end of December 29, 2014, and the beginning of December 30, 2014.

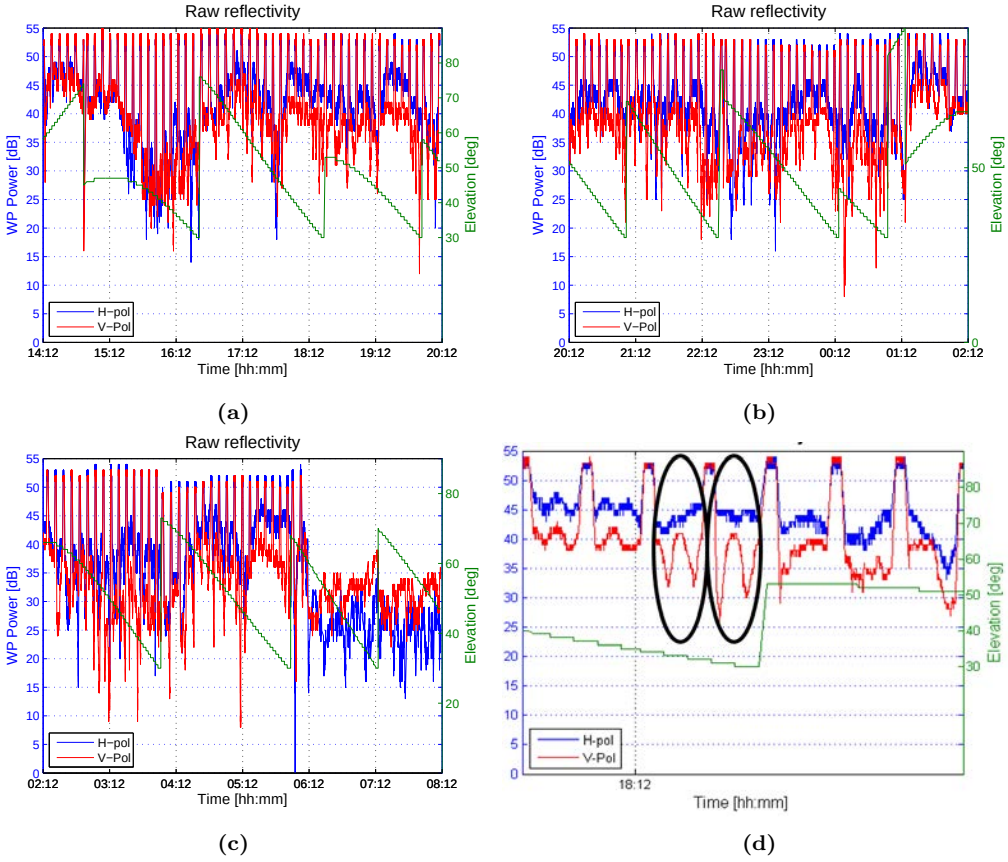

Figure 6.26: DUO raw data, H-Pol (blue), V-Pol (red): (a) First 6 hours, (b) Second 6 hours, (c) 4 hours until mechanical failure, (d) zoom of (a).

In Fig. 6.26(d) a zoomed version of Fig. 6.26(a) is presented, emphasizing some type of multi-path. However, it is not multi-path and it corresponds to a leakage of the direct signal picked directly from feeder antenna. It was possible to determine that it was the direct signal because the periodicity corresponds to a height of 5.6 meters, which is approximately the vertical distance between the feeder and the ground surface when looking to the reflected signals. However, this leakage can be estimated and mitigated by processing the maximum and the minimum of an oscillation. Therefore:

$$P_{R_{max}} \propto |E_0|^2 (1+\beta)^2 , P_{R_{min}} \propto |E_0|^2 (1-\beta)^2 , P_{refl} = \frac{P_{R_{max}}}{(1+\beta)^2} = \frac{P_{R_{min}}}{(1-\beta)^2}, \quad (6.11)$$

and the reflected signal power (P_{refl}) free of direct signal contamination is obtained.

Note that this effect is more remarkable at V- than at H-Pol, because V-Pol has a lower reflection coefficient, and therefore, less reflected power, which is more prone to be contaminated by the same amount of direct signal power leaked.

6.2.4 Retrieved Soil Moisture Maps

Data shown in previous section was processed in order to obtain the terrain's reflectivity at each polarization. The reflectivity was obtained by dividing direct and reflected measured SNRs. Once the reflectivity was estimated it was compared against simulated ones, considering 1 cm *rms* roughness of the soil, for different soil moisture conditions. The estimated soil moisture maps are shown in Fig. 6.27. The ground resolution corresponds to the First Fresnel zone projected on ground. Therein, it is observed that Fig. 6.27(a) and (c) contain overlapped areas, and in the absence of any irrigation or rain event, they estimate the same values for the same region. On the wetter area of those figures the soil moisture probe shown in Fig. 6.27(d) was installed, and estimated a moisture content of 0.15 m^3m^{-3} for that period of time, while the DUO estimated a soil moisture content of 0.13 m^3m^{-3}. The soil moisture patches observed are due to the drop-by-drop irrigation system seen on the field, which creates soil moisture differences in the entire field.

6.3 Soil Moisture Estimation from Ground-based Static Scatterometry Using Circular Polarization

The next step was the retrieval of soil moisture using circular polarization which would be the preferable polarization state for a dynamic scenario. Furthermore, a ground-based experiment in similar conditions to the one performed in *Tarragona*, but using circular polarization antennas, would provide a full-characterization of the reflected signals over land at any polarization state. With those two goals in mind a field experiment in *Viladecans* was designed in collaboration with the UPC civil engineering department.

6.3.1 The Viladecans Field Campaign

The *Viladecans* field experiment was conducted very close to the Barcelona airport, at the *Agrópolis* facilities of UPC. The main goal of the field experiment was to relate the formation of soil cracks to soil moisture. In order to avoid touching the soil, GNSS-R scatterometry was proposed as the remote sensing technique. Microwave radiometry was considered, but due to the airport proximity it was discarded due to the presence of RFI. The GNSS-R part of the experiment consisted of measuring the reflectivity of a 3 m x 3 m x 0.5 m soil sample that was lifted 1 m from the mean ground level. Figure 6.28 shows a summary of the entire experiment where in black it appears the container that was filled with the soil sample. The two inclined antennas on the top part are the hexagonal shape arrays used to gather direct (RHCP) and reflected (LHCP) signals. They were mounted on a fixed structure always looking South, since in the Northern hemisphere it is where more satellites can be found. Figure 6.28(b) shows the geometrical configuration of the experiment. The antennas were placed at the appropriate height that ensured

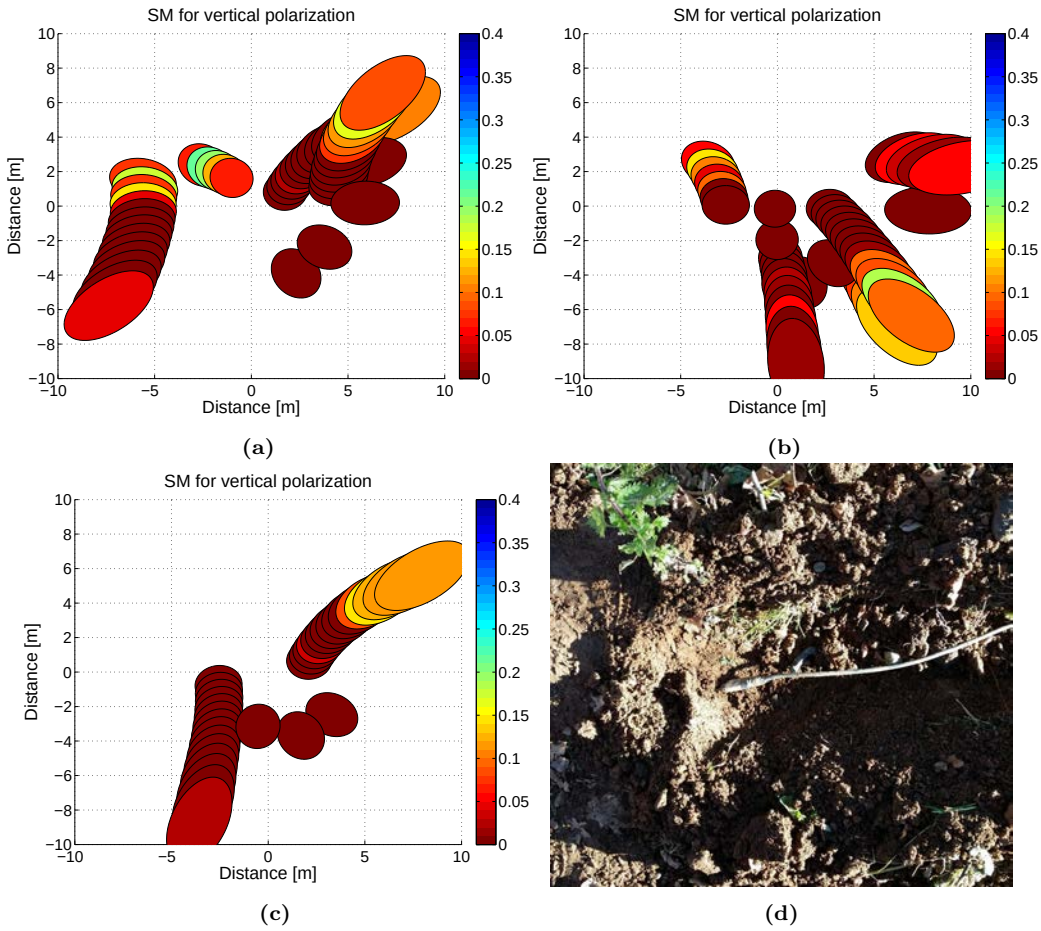

Figure 6.27: Soil moisture maps: (a)–(c) First, second, and third 6 hours period, (d) Soil moisture probe EC-5 from Decagon Devices [164].

that the black container was inside the antenna beamwidth. Also, the inclination of the antennas was computed to mitigate any multi-path coming from the structure. This led to an inclination of 30° with respect to the horizontal plane. The black container was mounted on a set of scales that were measuring the soil sample weight continuously, from which the weight loss due to water evaporation could be measured. Different soil moisture probes at different depths as well as other sensors to measure porosity, temperature, and soil suction were placed inside the container.

The back-end receiver was identical to the one used in the *Tarragona* field campaign (McGiver-type), but in this case one channel was measuring the direct signals and the other one the reflected signals. The instrument was connected to the electrical network, so there was no need for solar panels. Also no wireless communication was installed since the instrument was much more accessible than in the *Tarragona* field experiment. Data was stored in different files, each of them containing 12 hours of measurements, which

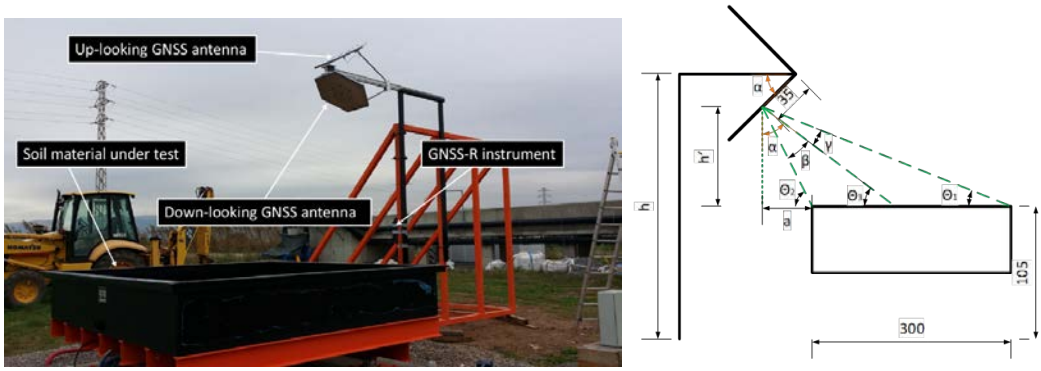

(a) **(b)**

Figure 6.28: *Viladecans* field experiment overview: (a) field and instrumentation, (b) geometrical configuration.

were later processed on a computer.

6.3.2 Data Analysis and Problems Faced

The campaign was divided in different steps from December 2014 until May 2015. The first step was an initial calibration of the test site. To do so, the black container was covered by an aluminum mosquito net as depicted in Fig. 6.29. Direct and reflected signals were gathered for two weeks, and it was when the first problems came out. First, the satellite passes were recorded for one day, to check the amount of reflected signals on the surface under observation. Figure 6.30 shows the sky projection of the satellites together with the black container projection (red closed curve). A lot of reflection points were located on the container region. A specific software tool was developed to process the data from this field campaign which is shown in Fig. 6.31. The software showed direct (green) and reflected (orange) signals as a function of time, elevation, and azimuth in three different plots. It also had the possibility to filter the data in order to see only those points whose first Fresnel zone was entirely on the soil sample region. In Fig. 6.31 it is seen that both direct and reflected signals have very similar power due to the reflection over a metallic surface. Furthermore, they followed the shape of the antenna pattern.

However, for some satellites a coherent fading event was observed, as it can be seen in Fig. 6.32. A critical analysis was performed because the fading looked like a multi-path contamination, but nothing in the surrounding area could be producing it. Furthermore, the directivity of the antennas would be mitigating that effect. The antennas were measured again in the anechoic chamber to check that there was no problem in the radiation patterns that could be causing that fading. Moreover, this fading was only occurring for certain satellites. Eventually, it was associated to irregularities in the metallic network that would be mitigated during the experimental work, and the solution was to filter out that data and use only data without fading for calibration purposes, like the one depicted in Fig. 6.31. Another problem related to RFI was observed during the field campaign which is described at the end of this section.

Figure 6.29: Viladecans field experiment: Initial calibration.

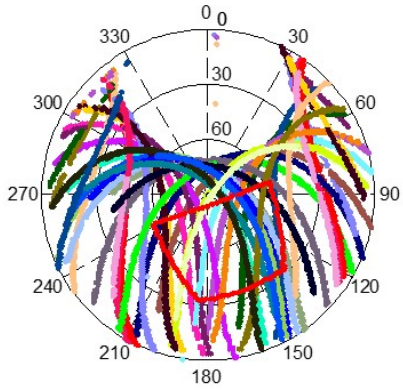

Figure 6.30: Satellite Sky map for one day of the field campaign.

The second step of this field experiment was to pour the soil sample on the black container and start processing real data measurements. The soil sample was poured very wet, but due to water evaporation it was becoming drier and drier, until the first soil cracks started. As it was becoming drier, the soil cracks started to separate, until their aperture was close to 5 cm and its depth larger than 30 cm (Fig. 6.33). Data retrieved during that period was processed, and a sample of it is shown in Fig. 6.34, when the soil was still moist and very few soil cracks were present. It is possible to see that, taking into account the calibration data, reflectivity was around -5 dB which corresponds to a SM content of 0.3 m^3m^{-3} assuming a perfectly flat surface, which matched with data from the soil moisture probes on the experiments. However, not all the retrieved data was valid, and some unexplained fading events were observed, avoiding the development and validation of an automatic retrieval algorithm for the entire dataset. Subsequent activities were addressed to determine the origin of those problems.

A detailed study to determine the cause of some fading events was performed con-

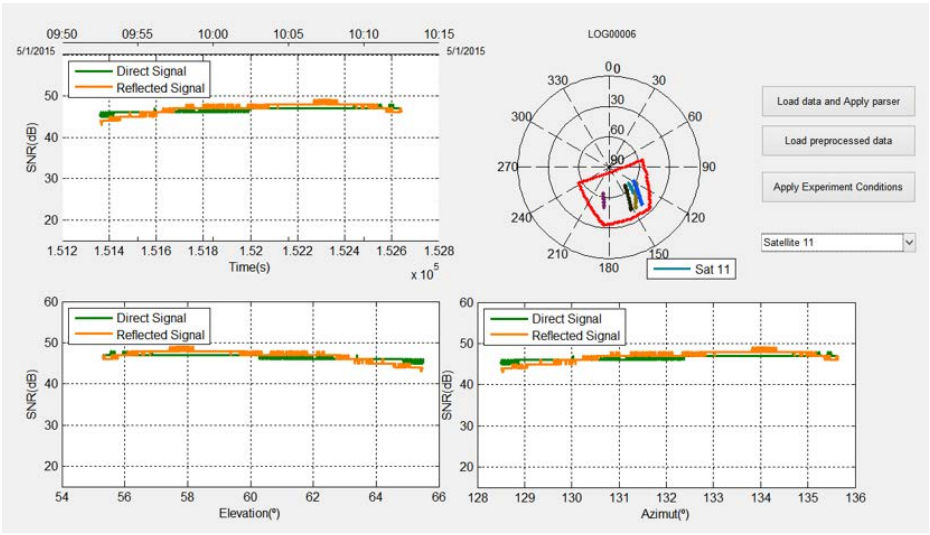

Figure 6.31: Software to process the Viladecans field experiment during the calibration stage.

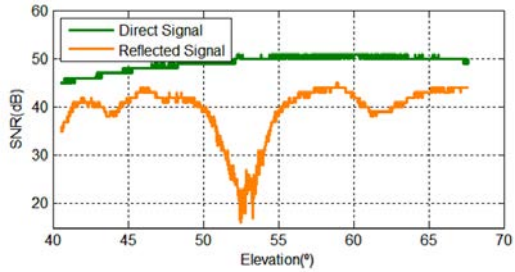

Figure 6.32: Coherent fading observed when satellites were at 52° elevation angle.

Figure 6.33: Soil sample in April 2015.

sidering six different aspects: multi-path, Fresnel zones, near-field radiation, hardware, diffraction effects, and soil cracks. A review of those points is subsequently presented, and further information can be found in [165].

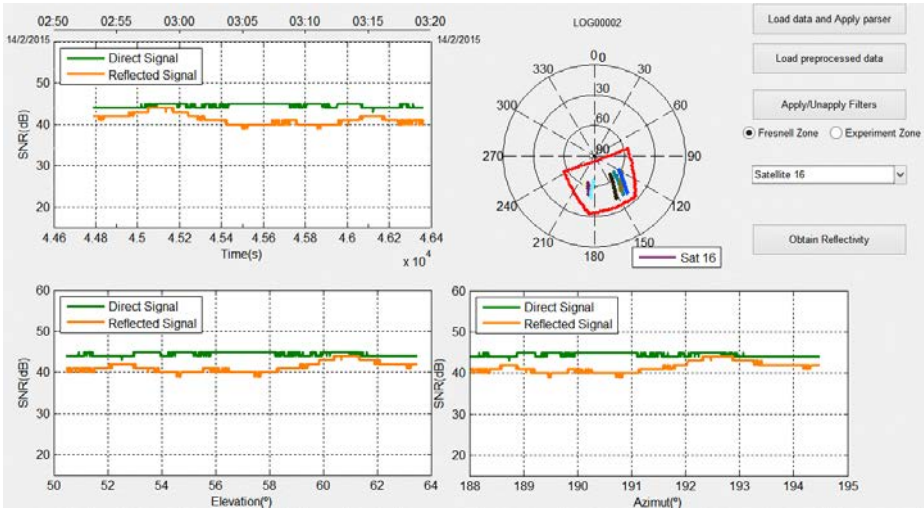

Figure 6.34: Real data example on February 14th 2015.

1. The multi-path contribution was discarded because there was no periodicity, and the angle where the fading appeared belonged to the antenna beamwidth, and any contribution from outside it would be mitigated by the antenna pattern itself.
2. Simulations considering more Fresnel zones than the first one were performed, just in case the larger order zones would not cancel out leaving only radiation contributing from the first one. Simulations indicate that outer zones were canceling among them.
3. As the antenna could be considered large due to the high directivity, it was possible that far field approximations used would not work. A smaller antenna which accomplished the far field approximation conditions was also tested during one day, facing also other slow and fast fading issues, which could not determine if this was exactly the issue. However, this would not solve the problem because using smaller antennas results in some leakage from the direct signal.
4. The hardware was entirely tested at the laboratory without any problem found, so that reason could be discarded.
5. The size of the field experiment was large enough as compared to the wavelength and the First Fresnel zone, so diffraction effects under those conditions should be minimal. However, in order to experimentally check if that was the problem, the reflected signals for a surface not elevated from the terrain level should be measured. Disappointingly, this was not possible in that campaign. A solution which consisted of moving the antenna was proposed, but it could damage some experiment's conditions and therefore it was not followed.
6. Due to its depth and size ($\lambda/4$) they could affect the scattering properties of the terrain and be seen as an effective surface roughness. However, this would not explain the fading seen at exactly 52° and not at other incidence angles, and in particular its unexplained azimuth dependence.

After discarding the multi-path, the near/far-field contributions, and the hardware, the other problems required a change in the geometrical configuration which was impossible due to the field campaign conditions. Further research was conducted to find and solve the problems faced in that field campaign without success.

Finally, during the entire campaign, there was a RFI problem that was attenuating the direct signal more than 20 dB, invalidating the data for some days between 0 AM and 7 AM. This RFI was observed during several days without any explanation. Later research conducted showed that there were transmissions at a frequency band where it is forbidden to transmit. Figure 6.35 summarizes the RFI issues for both the direct and reflected channels. In red it is seen when some kind of RFI was affecting each of the channels.

6.4 Soil Moisture Estimation from Ground-based Dynamic Scatterometry Using Circular Polarization

Even though the *Viladecans* field experiment has been described previously, the chronological order of the field experiments using circular polarization was different. First the dynamic ground-based GELOz field experiment was performed. After observing several multi-path contributions from the platform, it was decided to perform an static field experiment which was the one performed in *Viladecans*. Therein, the geometry of observation and the antennas were changed, inclining the antennas 30° with respect to the horizontal plane and enlarging their directivity to mitigate the multi-path. After that field experiment, the GRDC project started which was a dynamic field experiment using the geometry of observation from the *Viladecans* field experiment, but avoiding a soil sample elevated from the terrain level.

6.4.1 GELOz

This was the first field experiment conducted using circular polarization. The first version of the LARGO instrument was mounted on a buggy as shown in Fig. 6.36. The initial data gathered showed some multi-path contamination of the reflected signals. However, as it was a collaboration project the data processing and analysis of the data retrieved from the buggy was conducted by a research team at the Monash University. Therefore, here there are no more developments shown than a reflectivity map obtained in one of the field trials (Fig. 6.37)

6.4.2 GRDC

This is the result of the combination between the GELOz ground-based dynamic field experiment and the *Viladecans* static field experiment, trying to overcome the problems faced in both field campaigns. The final goal of this project was to estimate soil moisture in real time, because the algorithms that could be used are not high-resource consuming and can be executed on a simple computer in real-time. For this project a LARGO instrument which included the calibration matrix was manufactured. Specific antennas were

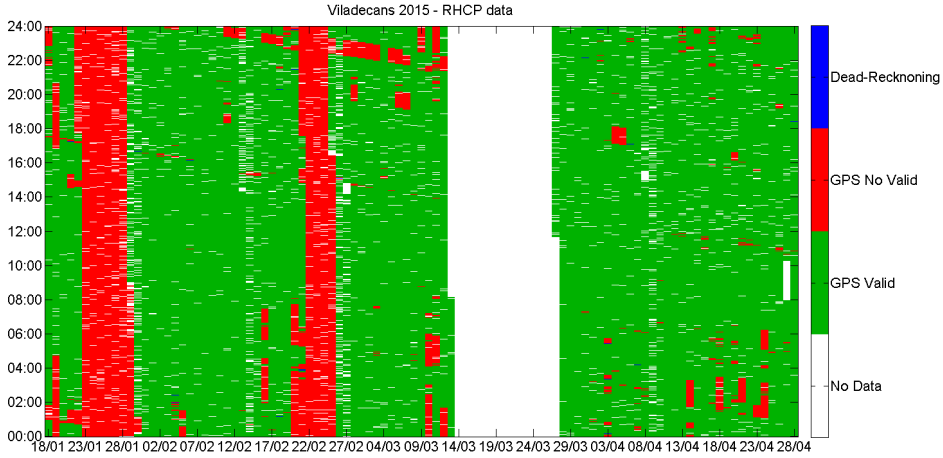

(a)

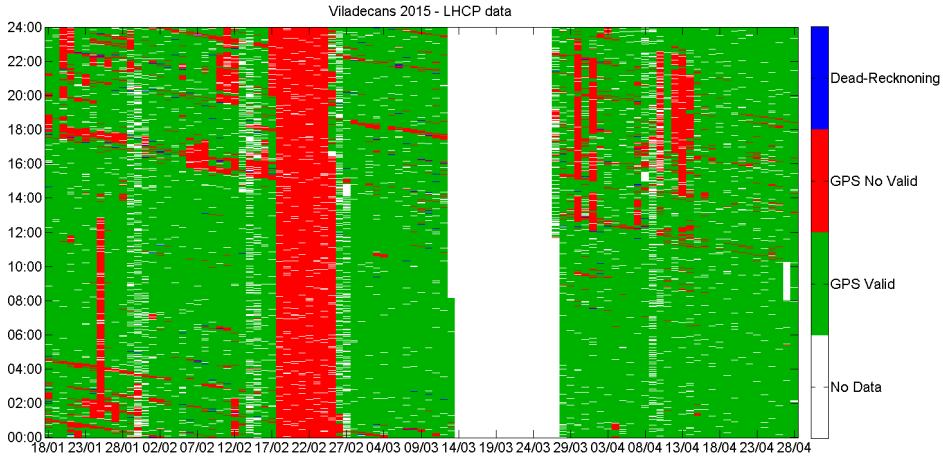

(b)

Figure 6.35: (a) Direct signal (RHCP) RFI, (b) Reflected signal (LHCP) RFI.

also designed which are shown in Chapter 5 section 5.3.1. Figure 6.38 shows the geometrical configuration adopted for that field campaign. Initial calibration of the instrument was performed at UPC premises observing that the reflectivity measured against a perfectly metallic reflector was 0 dB, while it was -7 dB when the reflection surface was a ceramic soil. The experimental back-to-front ratio of the antenna was larger than 35 dB within the beamwidth. The cross-polar measurements of the antenna pattern at the anechoic chamber coincided with the ones experimentally measured pointing the reflected antenna to the direct signals. A summary of the preliminary calibration is shown in Fig. 6.39 together with the aspect of the real-time software developed for this particular

Figure 6.36: LARGO mounted on the buggy.

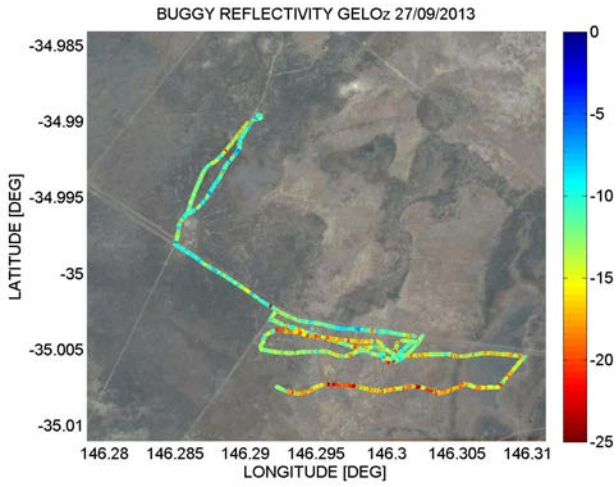

Figure 6.37: Reflectivity Map from one of the buggy experiments.

field campaign.

For this specific field campaign the data processing must be performed more carefully. Initially the satellites in view must be filtered by the antenna pattern, and only use those present on the antenna beamwidth. Due to the geometrical configuration and its large reflectivity, normally only one satellite fell into the beamwidth. To filter the data, the platform direction of movement must be known, and in the LARGO instrument this information comes from the RMC NMEA data packet obtained from the up-looking high performance GPS back-end receiver. After data filtering, the reflectivity can be estimated. A secondary correction of the antenna pattern described in Chapter 8 is also applied to take into account the different antenna gain seen by the direct and reflected sig-

(a) (b)

Figure 6.38: LARGO mounted on the tractor for the GRDC project. (a) FOV, (b) geometrical configuration of the system.

nals, respectively. This correction is on the order of 1 dB which should not affect severely the performance of the retrieval algorithm. Again, the proposed retrieval algorithm is based on a least-square algorithm between simulated and experimentally measured data. Figure 6.40 shows one of the reflectivity maps resulting from the three field campaigns performed. No performance of the retrieval algorithm is shown as the data is being processed by the Monash University team at the time of writing this PhD Thesis dissertation. Due to the same reason, no more reflectivity maps are shown.

6.5 Summary and Conclusions

This Chapter has presented all the ground-based field experiments over land conducted in this PhD Thesis. Some of them were successful, but some of them showed some issues that should be taken into account in the future. Firstly, the experiments performed using the dual-polarization SMIGOL in Australia are shown, aiming at proving the theoretical developments shown in Chapter 3. One conclusion from the dual-polarization SMIGOL field experiment is that IPT H-Pol amplitude measurements are useful for soil moisture retrievals achieving results similar to the Brewster angle ones. However, surface roughness can be an issue to take into account and an algorithm combining V- and H-Pol soil moisture estimations is derived in this Chapter. An algorithm based on detecting the 90° phase difference between H- and V-Pol interference patterns to improve the Brewster angle position determination is presented, in order improve the accuracy of soil moisture estimations. All the algorithms and experiments presented here are new contributions from this PhD Thesis dissertation. Retrieved soil moisture data have been compared against in-situ soil moisture data obtained from different sources with highly positive results, a fact that validates the part of theoretical developments presented in this PhD Thesis dissertation.

Subsequently, all ground-based scatterometric experiments conducted have been described and presented. The first scatterometric experiment presented is the one performed

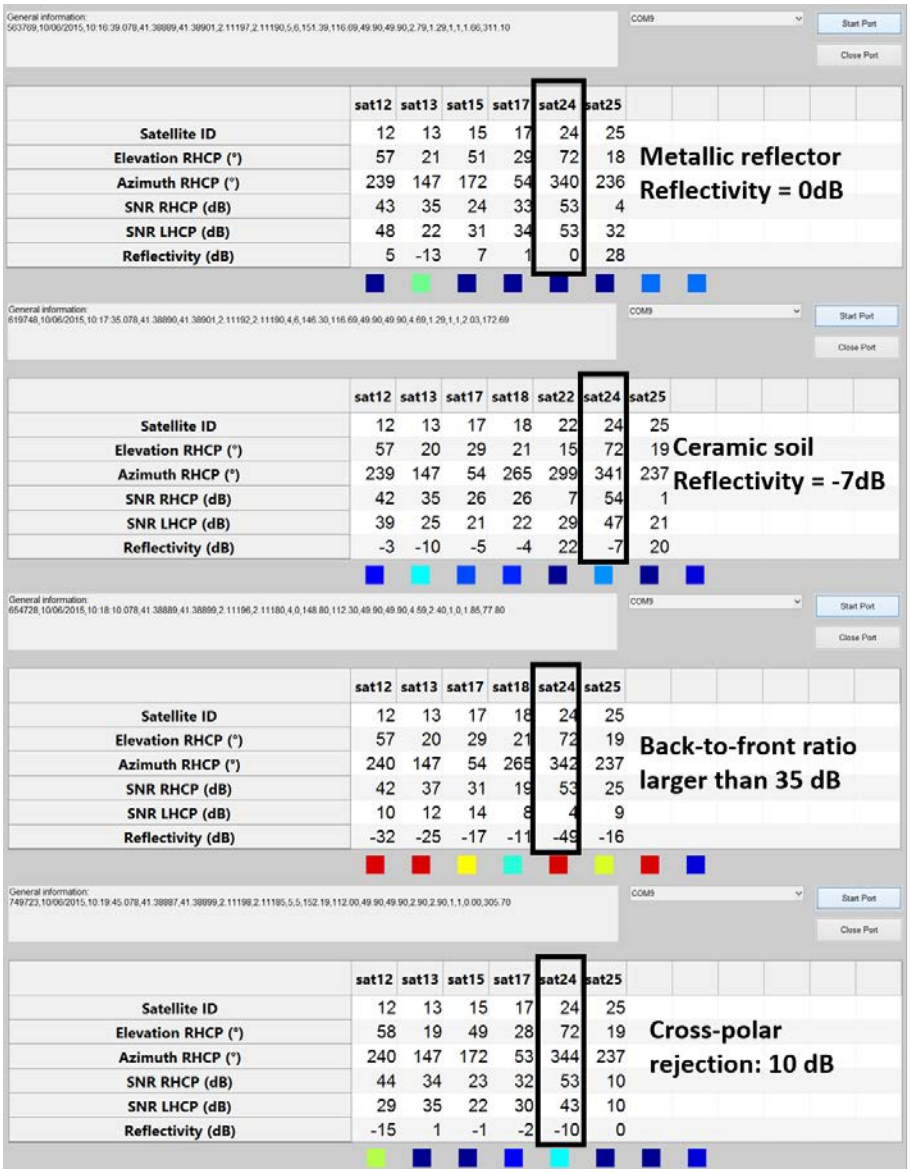

Figure 6.39: LARGO preliminary experimental tests and real-time software.

in *Tarragona*. It was based on a dual-linear polarization antenna, and the acquisition of direct and reflected signals at both H- and V-Pol. From those data the surface reflectivity is estimated at both polarizations, and a least-square algorithm comparing them to simulated reflectivity at each polarization is used to retrieve the soil moisture values. Retrieved soil moisture values are compared against in-situ ones, which are measured with a soil moisture probe collocated on the field, obtaining similar results. Disappointingly, the elevation motor of the DUO suffered a mechanical failure, preventing the analysis of

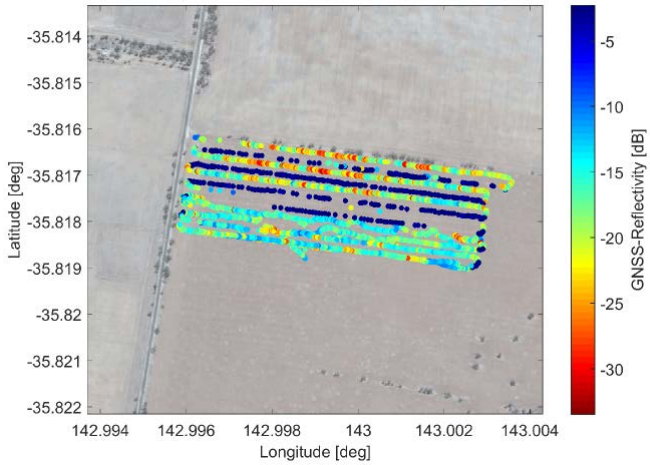

Figure 6.40: Preliminary reflectivity map from the GRDC experiments on July 11, 2015.

longer time series.

The second scatterometric experiment presented is the one performed in *Viladecans*. Even though it seemed an ideal experiment that combined with the *Tarragona* one would help to characterize ground-based reflections for soil moisture retrieval at any polarization, there were several issues involved in that experiment that prevented its success. Some soil moisture estimated values were in agreement with soil moisture measured in-situ. However, long data series could not be used due to several unexpected problems. Some of their possible sources were discarded, but there are still some points that need to be further explored such as the effect of soil cracks on the scattered signals, diffraction effects, and near/far field regimes. Last but not least, there was an important issue related to the presence of RFI at L1-band, where it is strictly forbidden to emit any kind of EM radiation. This corrupted a lot of data and it is a point under further research at the time of writing this PhD Thesis dissertation. RFI can degrade some measurements and even corrupt them, which is something that was not previously considered in cGNSS-R, since the spreading codes should provide an extra rejection of it.

Finally, two ground-based dynamic experiments are presented. One was the GELOz experiment, which was developed to determine the performance of cGNSS-R for soil moisture estimations using circular polarization instead of linear. Multi-path contamination from the platform used (buggy) was detected indicating that a different antenna configuration should be used, and triggered the field campaign performed in *Viladecans*. Finally, the GRDC experiment is presented with the goal of measuring soil moisture in real-time. For that field experiment a new specific version of the LARGO instrument was designed and manufactured, together with two high-directivity antennas (direct and reflected signals) and a software to initially process the data in real-time. A retrieval algorithm software was also developed as a part of the project, which post-processed the gathered raw data taking into account the effect of vegetation. Data are still under analysis by the University of Monash research team at the time of writing this manuscript.

7

Chapter 7
Ground-based GNSS-R experiments over the coastal areas

This chapter summarizes the ground-based GNSS-R experiment performed over the coastal areas. The field experiments shown used IPT geometrical configuration to measure the sea surface level, and demonstrate the concept previously proposed on a more dynamic surface. After data processing also the SWH for a certain dynamic range of values (0.1–0.7 m) could be retrieved.

7.1 Introduction

The conventional IPT using V-Pol was extensively tested for soil moisture and vegetation parameters retrievals in the past [21,105]. The same technique was used later to estimate the snow height/thickness [106], and finally it was tested on a reservoir for mean water level estimations [40]. However, those surfaces are practically constant or their change rate is very slow. Therefore, unless surface roughness is excessively large, the coherent model for modeling the reflection process works nicely. Conversely, coastal sea is a much more dynamic scenario that is continuously changing due to the presence of waves.

In 2013, the use of the SNR-analysis/multi-path technique was proposed as a GPS tide gauge [125]. Later, different models to retrieve the mean sea surface level have been developed including a pseudo-dynamic model that considers the variations of the sea surface level in the same SNR pattern due to tide variations [123–127,129,166]. In those references also the combination of different GNSS systems was tested [127]. Although the correlation between the estimated sea surface level using the GPS tide gauge and conventional tide gauges was quite good, the Root Mean Square Error (RMSE) of the retrieval was quite large (in all cases ≥ 0.5 m).

In the SNR-analysis the antenna is looking to the zenith, and the reflected signal is highly rejected by the antenna pattern, resulting in a very low number of oscillations observed unless the GPS receiver is at a certain height. A very low number of oscillations results in a bad frequency estimation and a large error. If the receiver is at a certain height, the oscillation frequency is larger, and therefore, more oscillations are seen. Since the geometrical configuration of the SNR-analysis (antenna pointing to the zenith) is a drawback to the performance of the developed algorithms, it was decided to test the conventional IPT geometrical configuration (antenna pointing to the horizon) over coastal sea, which was one of the future research lines described in [28]. The test site chosen was the *Pont del Petroli, Badalona*, Spain (Fig. 7.2). It was chosen because it had available in-situ ground-truth data using a K-Band radar, and there was a group at UPC that managed the facilities and could perform the maintenance of the SMIGOL instrument installed there. This field campaign led to results with much less RMSE than using the SNR-analysis geometrical configuration, and to the determination of the SWH parameter, which could not be measured previously in a different geometrical configuration.

7.2 Theoretical Analysis

The conventional IPT described in Chapter 3 is based on the coherency of the reflected signal to describe the oscillations of the SNR-pattern due to multi-path. Furthermore, in a horizon-looking configuration and with a properly designed antenna, both direct and reflected signal are observed with the same antenna gain. However, when the signal is reflected over sea or coastal sea, the dynamics of the surface and its natural roughness due to waves requires to redefine the conventional coherent model into a more generic one. This was done in also in Chapter 3, leading to the following equation:

$$P_R \propto |U_{IPT}|^2 = |U_d + U_{r\,coh} + U_{r\,incoh}|^2 = \\ = |U_{d_0}|^2 \cdot \left| F_n(\theta_{elev}, \phi_{elev}) + \sum_{m=1}^{M} F_n(\theta_m, \phi_m) A_m e^{j\Phi_m} e^{j\frac{4\pi h_m}{\lambda}\sin(\theta_m)} \right|^2, \tag{7.1}$$

where the terms of previous equation were detailed in Chapter 3 (Eqn. (3.15)).

7.2.1 Specular and Diffuse Scattering

The scattering process has been analyzed by several authors, developing different models depending on the surface conditions (i.e. [69]). In general, the reflected signal has a specular component and a diffuse one. The specular component dominates when the surface is "smooth" enough. When the specular component dominates, the reflection process can be modeled as the incident wave multiplied by the Fresnel reflection coefficient amplitude and phase, and considering an attenuation factor that depends on the surface's roughness. The diffuse or incoherent component dominates when the surface is "rough" enough. In this case, the scattering coefficient and its phase is different for each scatterer. The total reflected power is the power of the sum of the electric fields coming from each scatterer, resulting in a random amplitude, which is lower than when the coherent component dominates, and a random phase.

A widely used criterion to differenciate between smooth and rough surfaces is the "Rayleigh criterion" [69]. A surface is considered smooth if:

$$\sigma_h < \frac{\lambda}{8\sin(\theta_{elev})}, \tag{7.2}$$

which means that the phase difference between all the scatterers is lower than $\pi/2$. More restrictive criteria have been proposed by replacing the factor 8 in Eqn. (7.2) by 16 or 32 (Fraunhofer criterion) [69], which means that the maximum phase difference between all the scatterers is $\pi/4$ or $\pi/8$, respectively. In Eqn. (7.2) it is seen that, for the same surface's roughness conditions, whether the surface is smooth or rough depends on the electromagnetic wavelength and the incidence angle. The larger the incidence angle or the lower the elevation angle, the smoother the surface appears to be and vice versa. Hence, the lower the elevation angle, the higher the contribution of the coherent component will be as compared to the incoherent one.

Other models have been developed trying to improve the accuracy of the "Rayleigh criterion" depending on the observation surface characteristics. Assuming that the sea surface height can be modeled spatially as a 2-D random Gaussian stochastic process [167], Beckmann and Spizzichino computed the mean scattering coefficient [69] under the assumption of the Kirchhoff approximation as:

$$< \rho\rho^* > = < \rho >< \rho^* > + Var\{\rho\}, \tag{7.3}$$

where ρ stands for the reflection coefficient in a perfectly conductive surface without shadowing, or multiple scattering. Equation (7.3) is the second order moment of the

reflection coefficient (power) and separates the coherent component ($< \rho >< \rho^* >$) from the incoherent component ($Var\{\rho\}$). In Eqn. (7.3) the coherent component is described by Eqn. (7.4),

$$< \rho >= \rho_0 e^{-g/2}, \tag{7.4}$$

where ρ_0 is the specular reflection coefficient of a perfectly conductive smooth surface without shadowing in all the scattering directions, which vanishes away from the specular reflection direction, and the g factor:

$$g = \left(\frac{4\pi\sigma_h \sin(\theta_{elev})}{\lambda} \right)^2, \tag{7.5}$$

represents how rough is the surface with respect to the wavelength. For $g << 1$ the surface is considered smooth, and for $g >> 1$ the surface is considered rough. In Eqn. (7.3) the incoherent component is given by Eqn. (7.6) [69]:

$$Var\{\rho\} = \frac{\pi T^2 F^2 e^{-g}}{A} \sum_{m=1}^{\infty} \frac{g^m}{m!m} \cdot exp\left(-\frac{{u_{xy}}^2 T^2}{4m} \right), \tag{7.6}$$

where T is the correlation length of the surface, A is the scattering area, F is given by Eqn. (7.7):

$$F = \frac{1 + \cos\theta_i \cos\theta_s - \sin\theta_i \sin\theta_s \cos\phi_s}{\cos\theta_i \cdot (\cos\theta_i + \cos\theta_s)}, \tag{7.7}$$

being θ_i the incidence angle, θ_s the scattering angle, ϕ_s the azimuth scattering angle, and ${u_{xy}}^2$ is given by Eqn. (7.8):

$${u_{xy}}^2 = k^2 \left(\sin^2\theta_i - 2\sin\theta_i \sin\theta_s \cos\phi_s + \sin^2\theta_s \right), \tag{7.8}$$

being k the wavenumber ($2\pi/\lambda$).

Equation (7.4) indicates that the coherent component vanishes away from the specular reflection and it decreases exponentially with the root mean square roughness (σ_h^2). The incoherent component depends on the scattering area, which means that it depends on the receiver's height.

In [168], the above formulation was compared to empirical multi-path data over the sea at 1.575 GHz. In the cases of calm sea ($g << 1$) and rough sea ($g >> 1$) those equations can be simplified. Under calm sea conditions the coherent component dominates because the incoherent component is highly attenuated as g^m in the summation (Eqn. (7.6)) tends rapidly to 0. Under rough sea conditions the incoherent component dominates as the exponential function in Eqn. 7.4 highly attenuates the coherent term.

Nevertheless, when $g \approx 1$ the dominant component must be computed. To do so, the total reflection coefficient coefficient can be normalized by its variance:

$$\frac{< \rho\rho^* >}{Var\{\rho\}} = 1 + \frac{< \rho >< \rho^* >}{Var\{\rho\}}, \tag{7.9}$$

which results in:

$$\frac{< \rho\rho^* >}{Var\{\rho\}} = 1 + \frac{{\rho_0}^2}{\frac{\pi T^2 F^2}{A} \sum_{m=1}^{\infty} \frac{g^m}{m!m} \cdot exp\left(-\frac{{u_{xy}}^2 T^2}{4m} \right)}. \tag{7.10}$$

The second term in Eqn. (7.10) is the relationship between the coherent and incoherent components. When it is larger than 1 the coherent component dominates in front of the incoherent component, and vice versa. Remember that, away from the specular reflection direction the incoherent component always dominates as ρ_0 vanishes. However, for the specular reflection direction, the relationship between coherent and incoherent components varies depending on the elevation angle, and the roughness conditions.

7.2.2 Sea Surface Characteristics

The sea surface is fully described by its directional height spectrum $S(k, \phi)$, which can be derived from its time series measurements [169]. However, a simplified description involving fewer parameters can also be used. These parameters are:

1. the fundamental wavelength, which is the spatial distance between two consecutive wave crests,
2. the fundamental wave period, which is the time between two consecutive wave crests,
3. the SWH or $H_{\frac{1}{3}}$, which is the average height of the one-third highest waves, and it can be related to the surface roughness parameter as $H_{\frac{1}{3}} \approx 4\sigma_h$, being the σ_h the sea surface height standard deviation [167, 170], and
4. the steepness, which is the ratio between the wave height and the wavelength.

Simulations using the "Rayleigh Criterion" and Eqn. (7.10) for different surface correlation lengths and SWH have been performed in order to understand the behavior of both the "Rayleigh criterion" and the Beckmann and Spichizzino model [69]. Figure 7.1 represents the cut-off elevation angle up to where the coherent component dominates against the incoherent one. The blue and red dashed lines show these angles computed using the "Rayleigh criterion" (Eqn. (7.2)) for 8 and 16 coefficients in the denominator, respectively. The solid lines show the same cut-off angles for different surface correlation lengths, from 0 m up to 2 m in steps of 0.4 m. The lower the correlation length, the larger the dynamic range of elevation angles where the coherent component dominates. When the SWH is larger than 0.5 m the dynamic range becomes almost independent on the correlation length. In the same figure, the solution provided by Beckmann and Spizzichino [69] is in between the "Rayleigh criterion" for the two lowest restrictions (8 and 16).

Figure 7.1 depicts the largest elevation angle up to which the interference pattern will be observed. At the same time, it gives information on the smallest elevation angle where the interference pattern is masked by the incoherent scattering power. The computation of this cut-off angle in the experimental interference patterns will be used later to infer the SWH.

7.3 Field Experiment Description and Instrumentation

A three-month field campaign with the SMIGOL instrument [21, 40, 98, 105] at the *Pont del Petroli, Badalona*, Spain was conducted between the end of November, 2012, and

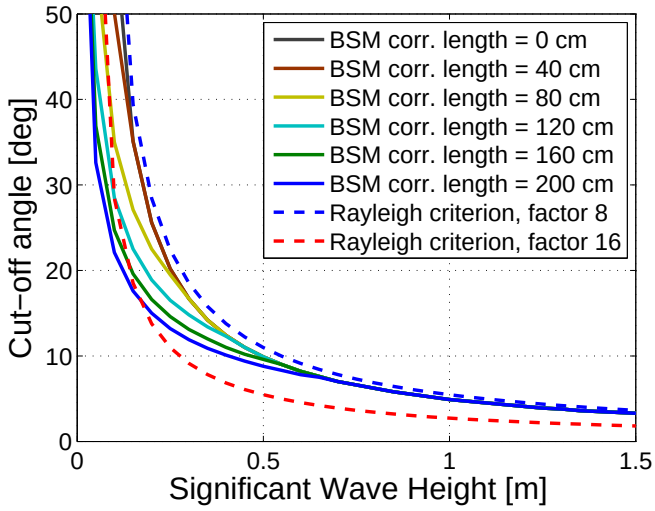

Figure 7.1: Comparison between Beckmann and Spizzichino model (BSM) and the Rayleigh criterion. This figure shows the cut-off angle up to when the coherent dominates in front of the incoherent one for both scattering models.

February, 2013, (see Fig. 7.2(a) for accurate location). The *Pont del Petroli* is a 250 meters long pier. The SMIGOL instrument was installed near the tip of the pier, the closest possible to other instruments permanently installed, such as the radar VEGAPULS62 [171], which monitors continuously the SWH, the wave period, the mean sea level, and the wind-speed. Figure 7.2(a) shows the *Pont del Petroli* top view indicating the location of the SMIGOL reflectometer and the radar VEGAPULS62 on it. The red arrow indicates the SMIGOL instrument antenna pointing direction. Figure 7.2(b) shows the instrument installed at the pier with the black arrow representing the direct GNSS signals and the red arrow the GNSS reflected signals.

The SMIGOL reflectometer used in this field experiment is similar to the one used in previous conventional IPT field experiments, because there was one unit available at the research group [21, 40, 98, 105]. It consisted of a V-Pol antenna with an azimuth and elevation symmetric pattern, and 90° antenna beamwidth in both horizontal and vertical planes. After the antenna, there was a LNA, and the back-end receiver. For this field campaign, the operation mode was acquiring GNSS signals for 12 hours, and then 12 hours in idle mode. The power supply was taken from the electrical installation in the pier. The main difference between this SMIGOL version and previous ones used by Nereida Rodriguez-Alvarez in her PhD Thesis is the ruggedized external structure to protect it from harsh environmental conditions and water splashes.

The *Pont del Petroli* is a construction devoted to scientific and oceanic research. It has a number of instruments installed permanently to provide continuous meteorological and oceanographic data. For the purpose of this experiment, only oceanographic data is necessary, specifically the SWH and the Mean Sea Surface Level (MSSL). These data are measured using the radar VEGAPLUS62 [171]. Figure 7.3(a) shows a picture of

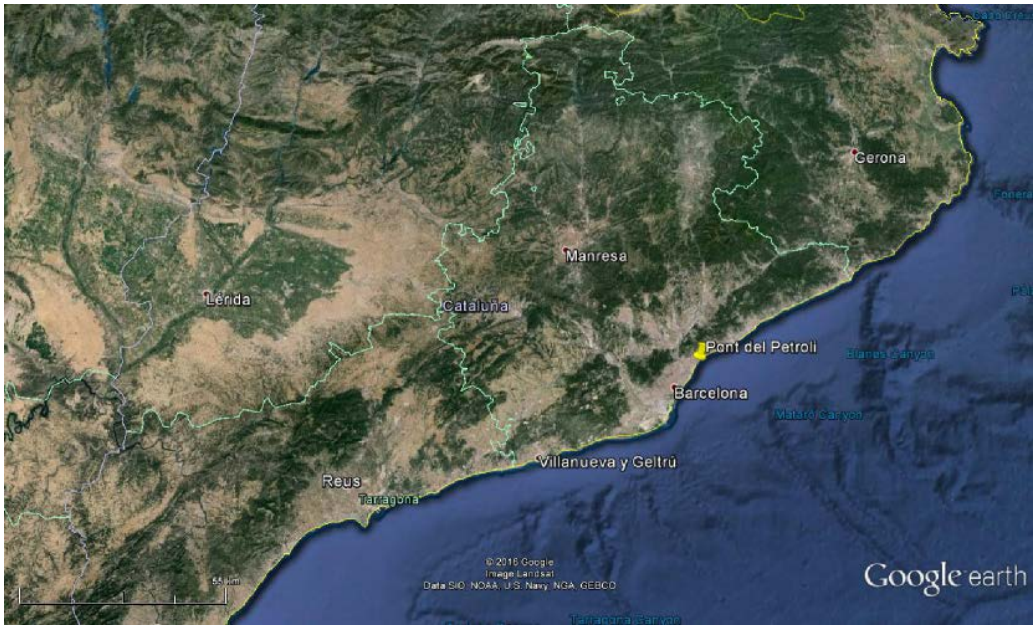

(a)

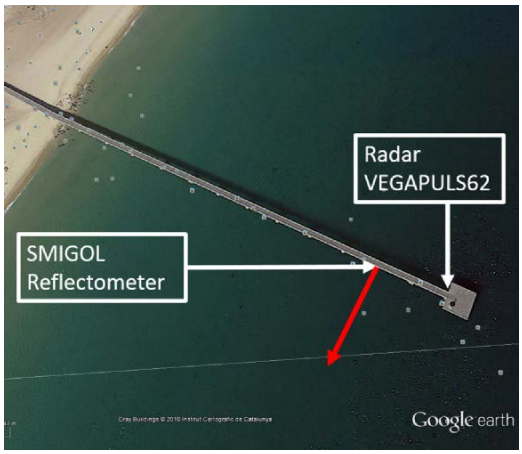

(b)

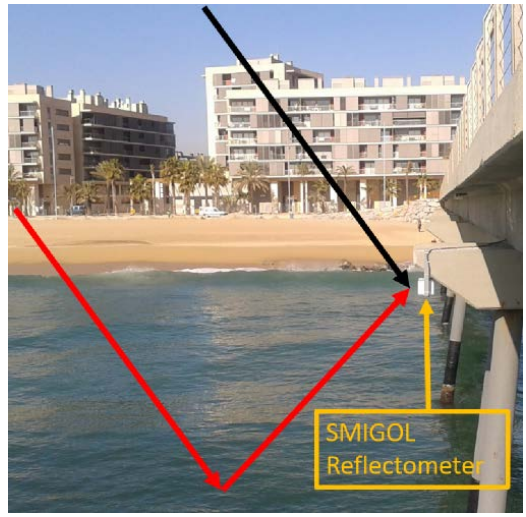

(c)

Figure 7.2: Summary of the *Pont del petroli* field campaign: (a) location, (b) top view, (c) SMIGOL instrument installed.

it, whereas Fig. 7.3(b) shows where the radar is installed and to where the radiation is emitted (nadir-looking). The VEGAPULS62 is a high-precision (±2 mm) low-power pulsed K-Band (26 GHz) radar with a maximum range of 35 m. It measures continuous time-series of the mean sea surface height. From this time-series, the sea wave spectrum is derived (but not stored), from which the main sea descriptors are retrieved.

(a) (b)

Figure 7.3: Ground-truth instrumentation for measuring oceanographic data: (a) Radar VegaPULS62 picture, (b) Radar VegaPULS62 installed at the *Pont del Petroli*

7.4 Significant Wave Height Retrieval

Figures 7.4, 7.5, 7.6 show three interference pattern examples from the field campaign. Figure 7.4 shows the interference pattern for GPS satellite 23 on December 4, 2012, when the SWH was 20 cm. Figure 7.4(a) shows the raw data retrieved whereas Fig. 7.4(b) shows a low-pass filtered version of it to reduce noise. In the low-pass filtered data it is seen that the coherent component is larger than the incoherent component for GNSS satellite elevation angles $\leq\sim 30°$. At this point the phase information is lost because it becomes random, and consequently no more oscillations are seen for larger elevation angles. Also note that, in Fig. 7.4, the envelope of the interference pattern is increasing. This occurs because the Fresnel reflection coefficient is monotonically increasing after the Brewster angle position ($\sim 5°$ elevation angle for sea water), and is not compensated by the surface roughness attenuation.

Figure 7.5 shows the interference pattern for GPS satellite 23 on December 6, 2012, when the SWH was 62 cm. Therein, the coherent component is larger than the incoherent one until an elevation angle of $\sim 11°$, when the incoherent becomes larger. In those conditions, for higher elevation angles, no more oscillations are detected. Also, note that the amplitude of the interference pattern oscillations is smaller in Fig. 7.5 than in Fig. 7.4, and this is related to the exponential attenuation factor (g function) on the coherent component in Eqn. (7.4).

Figure 7.6 shows the interference pattern for GPS satellite 23 on December 7, 2012, when the SWH was 38 cm, a situation in between December 4 and 6, 2012. The elevation angle of the GNSS satellite until the coherent component is larger than the incoherent one is $\sim 17°$. This angle also in between the previous results, as it occurs with the SWH conditions. Also, the envelope of the interference pattern is in between them, a fact that also matches with the theoretical aspects shown in section 7.2.

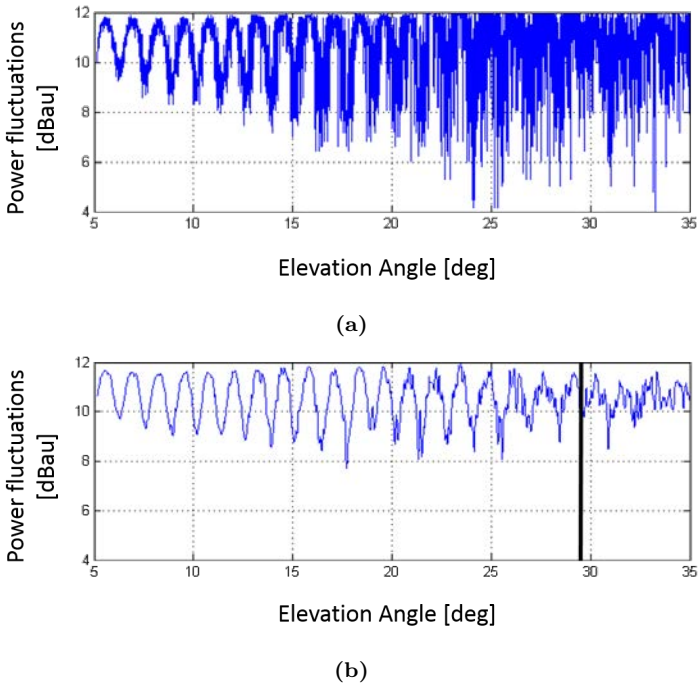

Figure 7.4: Interference pattern retrieved measured in dBau (dB arbitrary units) for GPS PRN 23 on December 4, 2012, and SWH = 20 cm: (a) raw data, (b) low-pass filtered data.

Therefore, the elevation angle up to which the oscillations of the IPT are seen, can be related to the surface roughness conditions, which was proposed theoretically, and it is experimentally shown in Figs. 7.4, 7.5, and 7.6. This threshold angle will be called in this PhD Thesis from now on, the cut-off angle. Its estimation can be performed using overlapped spectrograms [172]. First, since the GNSS satellites can have ascending or descending orbits, the interference patterns are sorted in an ascending elevation angle order. Then, they are split in several consecutive overlapped windows of length 1000 samples, and with a 95% overlapping factor in order to have very fine time-delay resolution. In the interference patterns, time is directly related to the elevation angles. In this particular case, there will be at least 4 oscillation in each window. For each of these windows, the FFT is computed in order to create the entire spectrogram. Then, the fundamental frequency is searched and tracked until its power falls below a threshold (20 dB). This point is related to a time value that is directly converted to the corresponding elevation angle. Note that the IPT is periodic as a function of the $\sin(\theta_{elev})$, but for low elevation angles $\sin(\theta_{elev}) \approx \theta_{elev}$, and an accurate enough frequency measurement can be performed. This algorithm is described in Fig. 7.7.

Figure 7.8 shows the corresponding spectrograms associated to data in Figs. 7.4, 7.5, and 7.6 respectively. The fundamental frequency is marked in black. The spectrogram corresponding to Figure 7.5(b) shows how the fundamental frequency power vanishes due to the loss of coherency in the reflected signal, as opposed to that corresponding to Fig. 7.4(a), where the fundamental frequency power does not vanish until almost the end

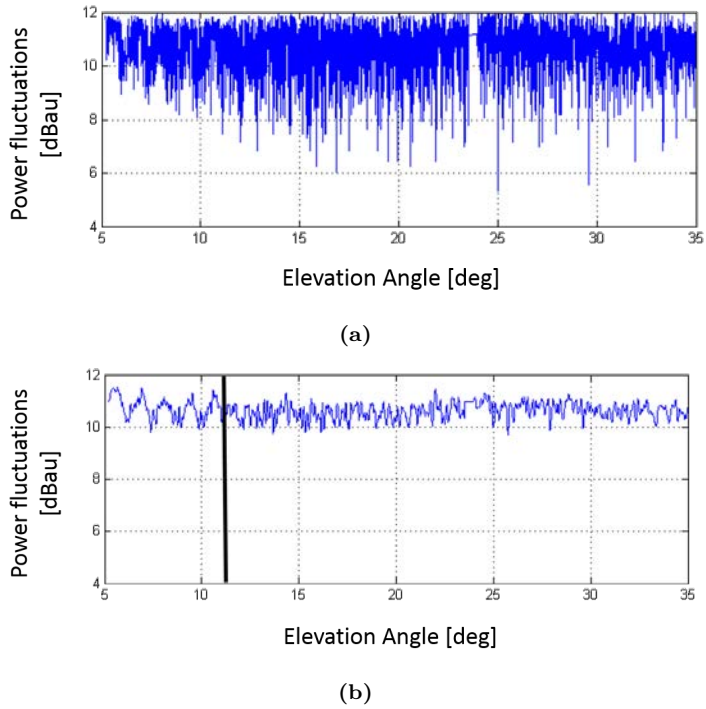

Figure 7.5: Interference pattern retrieved measured in dBau (dB arbitrary units) for GPS PRN 23 on December 6, 2012, and SWH = 62 cm: (a) raw data, (b) low-pass filtered data.

of the spectrogram.

The algorithm described in Fig. 7.7 was applied to all the interference patterns acquired during the entire three-month field campaign (more than 1000 interference patterns). The cut-off angle computed for each interference pattern was compared against the SWH parameter retrieved from the radar measurements. Figure 7.9 shows this comparison, the "Rayleigh Criterion" for 8 and 16 factors in the denominator (green and red respectively), and the best fit (Eqn. (7.11)), which leads to an empirical relation between the estimated cut-off angle and the SWH parameter. From Fig. 7.9 two main aspects should be remarked. First, due to antenna beamwidth (90°), the interference pattern shape can only be retrieved for elevation angles lower than 45°, and therefore SWH $\leq$ 10 cm cannot be measured. However, this is a very rare situation even for coastal seas. Second, the receivers have an elevation angle mask, so $\theta_{elev} \leq 5°$ cannot be seen. This makes this technique saturate for SWH larger than 70 cm, because in order to measure coherence a minimum of two oscillation cycles are needed. If the antenna height is lower than 3 meters, then the maximum value of SWH that can be estimated will decrease as not enough oscillation cycles will be seen in the coherent region [21]. In order to enlarge this dynamic range three different things can be done. First, to measure SWH $\leq$ 10 cm an antenna with a larger beamwidth is needed. Second, to measure SWH $\geq$ 70 cm the SMIGOL instrument should be installed at a higher platform to obtain a higher oscillation frequency, in order to observe more oscillations for the same angular region. The

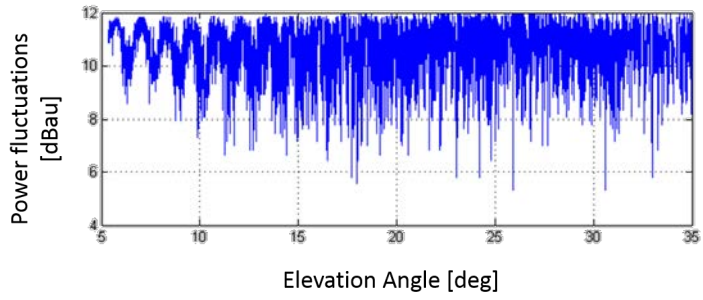

(a)

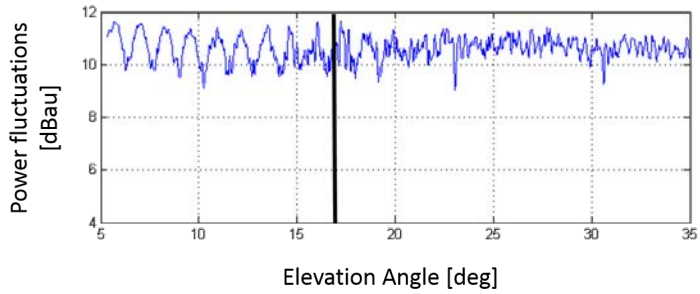

(b)

Figure 7.6: Interference pattern retrieved measured in dBau (dB arbitrary units) for GPS PRN 23 on December 7, 2012, and SWH = 38 cm: (a) raw data, (b) low-pass filtered data.

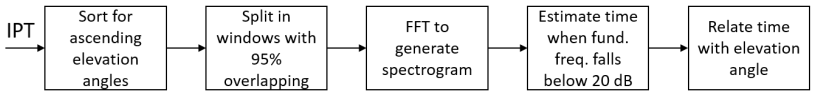

Figure 7.7: Cut-off elevation angle estimation.

maximum height at which the instrument can be installed is limited by the GPS C/A code [21], or see Appendix B. The last thing that could be modified is the elevation angle mask on the back-end receiver.

$$\theta_{cut-off}[deg] \approx 55.44 \cdot e^{-3.3 \cdot SWH} \tag{7.11}$$

$$\theta_{cut-off}[rad] \approx e^{-\pi \cdot SWH} \tag{7.12}$$

$$\widehat{SWH} = -\frac{1}{3.3} \cdot ln\left(\frac{\theta_{cut-off}[deg]}{55.44}\right) \tag{7.13}$$

$$\widehat{SWH} = -\frac{1}{\pi} \cdot ln\left(\theta_{cut-off}[rad]\right) \tag{7.14}$$

By inverting Eqn. (7.11), the SWH can be estimated (Eqn. (7.13)). Note that, Eqn. (7.13) can be approximated by (7.14) expressing the cut-off angle in radians. Figure 7.10 shows 15 days of the SWH evolution in blue and the estimated SWH from the

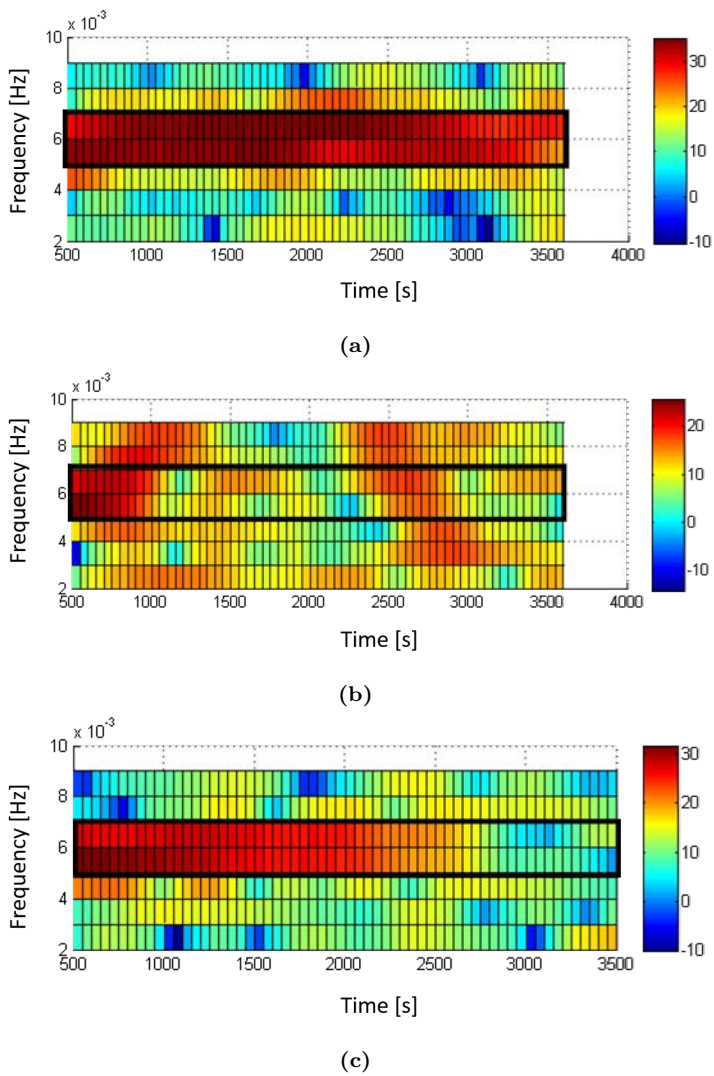

Figure 7.8: Spectrograms of satellite 23 on (a) December 4, 2012, (b) December 6, 2012, and (c) December 7, 2012, corresponding to data from Figs. 7.4, 7.5, and 7.6.

interference patterns (red). The trend of the SWH evolution is followed by the estimated SWH quite precisely except around January 3rd 2013, when SWH is too high. In this region, not enough oscillations were seen in the interference pattern to compute the cut-off angle, and therefore the SWH could not be retrieved. The Pearson correlation coefficient (R) for the pictured data is 0.9. Figure 7.11 shows a scatter plot that compares the estimated SWH with the ground-truth SWH from the entire field campaign. In red the 1:1 line is added to qualitatively show the correlation between the estimated SWH and the ground-truth information. The Pearson correlation coefficient (R) is 0.86. Analyzing the data from the whole field campaign, an RMSE of 5.7 cm in the SWH estimation was

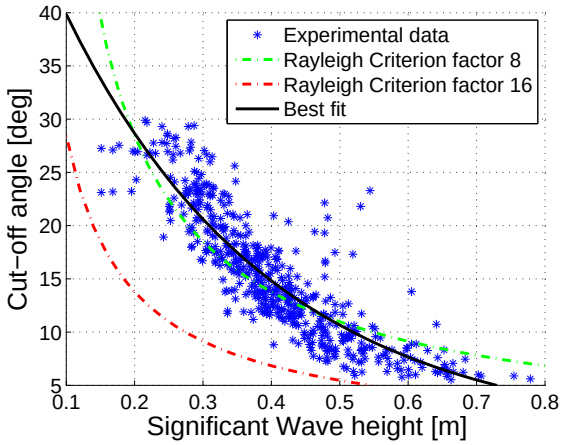

Figure 7.9: Comparison between the computed cut-off angle with ground-truth SWH. The best fit has a correlation coefficient of R^2=0.75 and a RMSE of 3°.

achieved for SWH values lower than 0.7 m.

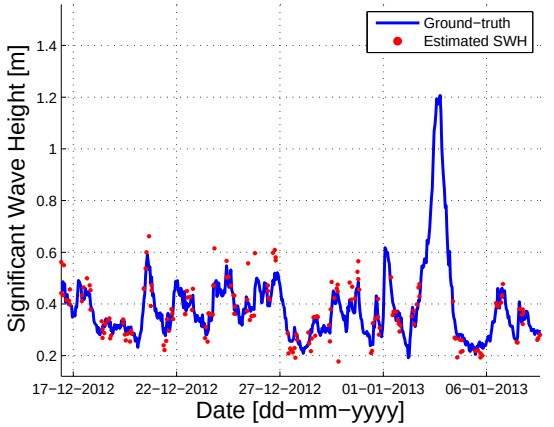

Figure 7.10: Comparison between IPT GNSS-R estimated SWH and ground-truth data from December 17, 2012, until January 6, 2013. Note that the method performs well up to SWH $<$ 0.7 m, with a Pearson correlation coefficient (R) of 0.9 in the specified period of time.

7.5 Mean Sea Surface Level or Tides Retrieval

In section 7.4 it was seen that only the coherent part of the interference patterns can be used to retrieve geophysical information. This is the part where the reflection coefficient can be modeled as $Re^{j\phi_R}$, and the interference pattern phase term $\left(exp\left\{j\frac{4\pi h\cos(\theta_{elev})}{\lambda}\right\}\right)$

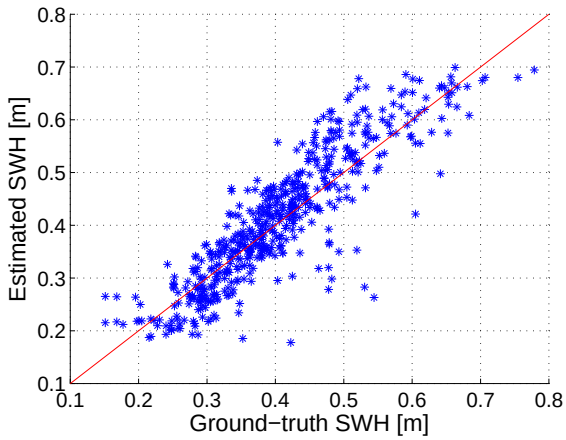

Figure 7.11: Comparison between estimated SWH and ground-truth with a Pearson correlation coefficient (R) of 0.86 for the three-month field campaign.

information is preserved. Equation (3.15) can be converted into Eqn. (7.15) considering the proposed approximation, which leads to a similar result previously shown in [93]:

$$P_R \propto |E_{0_i}|^2 \cdot \left(|F_n|^2 + |F_{-n} \cdot R|^2 + 2 \cdot F_n F_{-n} R \cos\left(\frac{4\pi}{\lambda} h \sin(\theta_{elev}) + \phi_R + \phi_{F_{-n}} - \phi_{F_n} \right) \right), \tag{7.15}$$

where F_n stands for $F_n(\theta, \phi)$, F_{-n} for $F_n(-\theta, \phi)$, R for $R(\theta, \phi)$, h the vertical distance between the antenna phase center and the reflecting surface, and θ_{elev} the elevation angle of the GNSS satellite. The fundamental phase term is identified as $\frac{4\pi}{\lambda} h \sin(\theta_{elev})$. The other terms are also phase terms that may vary slightly the fundamental phase term. However, their contribution can be considered negligible because they remain mainly constant along the antenna beamwidth. The phase terms associated to the antenna pattern may vary at most 0.2 rad in the entire interference pattern acquisition, whereas the value associated to the coherent reflection coefficient phase remains mainly constant. Consequently, the entire phase function will be driven by the cosine function, and it will be only sensitive to the height variations. Recall that when the incoherent scattering dominates, the reflection coefficient phase is random and this assumption no longer applies. To estimate the interference pattern fundamental oscillation frequency and infer h it is necessary to apply spectral analysis techniques.

Nevertheless, as mentioned in Chapter 3 the oscillation frequency is not constant in terms of θ_{elev}, but it is in terms of the $\sin(\theta_{elev})$. If θ_{elev} is very small, the $\sin(\theta_{elev})$ can be approximated by its argument, and therefore be constant, but for larger values of θ_{elev} this approximation is no longer valid. Therefore, a change of variable can be performed, and the interference pattern can be plotted as a function of the $\sin(\theta_{elev})$ instead of plotting it as a function of θ_{elev}. Then, the oscillation frequency becomes constant ($\frac{2h}{\lambda}$) if the mean sea surface level does not change during the interference pattern acquisition. This change of variable is very useful to find the oscillation frequency, but unfortunately the properties of the acquired data change. Before, the interference pattern was regularly sampled at 1

Hz. The change of variable converts the regular sampling pattern to an unevenly sampling pattern and conventional spectral analysis techniques such as FFT are no longer valid. Unevenly sampling patterns have been already analyzed in the astronomy field, where it is quite difficult to obtain regularly sampling patterns. Several techniques have been developed in order to analyze periodicity and frequency estimation in those conditions. The most used techniques are the general Fourier Periodogram (FP) [173], the LSP or Least-Squares Periodogram (LS) [118, 173–175], and the CAPON (CAP) [176]. All of them have been applied to the interference patterns obtained in this field experiment and their performance is evaluated independently.

7.5.1 Spectral Analysis Techniques Used

The classical Fourier transform-based periodogram [173] is given by:

$$P_F(w) = \frac{1}{N^2}\left|\sum_{n=1}^{N} y(t_n)e^{-jwt_n}\right|^2, \tag{7.16}$$

where w is the frequency factor, N the number of samples, n the sample number, and $t_n = \sin(\theta_{elev}(n))$ the sampling time. Note that the sample $(y(t_n))$ and the sample time (t_n) are intrinsically related in the equation, consequently this method is suitable for unevenly sampling patterns. Equation (7.16) comes from a least-squares data fitting problem and it is suitable for complex-value data. However, for the case of real-value data, which is the one used in this work, the LS or LSP are more suitable methods.

The LSP [175] is given by:

$$P_{LSP}(w) = \frac{1}{\widehat{YY}}\left(\frac{\widehat{YC_{\hat{\tau}}}^2}{\widehat{CC_{\hat{\tau}}}^2} + \frac{\widehat{YS_{\hat{\tau}}}^2}{\widehat{SS_{\hat{\tau}}}^2}\right) \tag{7.17}$$

where:

$$\widehat{YY} = \sum_{n=1}^{N} y(t_n)^2, \tag{7.18a}$$

$$\widehat{YC_{\hat{\tau}}} = \sum_{n=1}^{N} y(t_n)\cdot\cos w(t_n-\hat{\tau}), \tag{7.18b}$$

$$\widehat{CC_{\hat{\tau}}} = \sum_{n=1}^{N} \cos^2 w(t_n-\hat{\tau}), \tag{7.18c}$$

$$\widehat{YS_{\hat{\tau}}} = \sum_{n=1}^{N} y(t_n)\cdot\sin w(t_n-\hat{\tau}), \tag{7.18d}$$

$$\widehat{SS_{\hat{\tau}}} = \sum_{n=1}^{N} \sin^2 w(t_n-\hat{\tau}), \tag{7.18e}$$

$$\tan 2w\hat{\tau} = \frac{\sum_{n=1}^{N}\sin 2wt_n}{\sum_{n=1}^{N}\cos 2wt_n}. \tag{7.18f}$$

Again, every sample its related to its acquisition time so it is a suitable spectral estimator for both uniform and non-uniform sampling patterns.

The LS [173] is the least-squares FP for real-valued data and it is given by:

$$P_{LS}(w) = \frac{1}{N}\mathbf{r}^T(w)\mathbf{R}^{-1}(w)\mathbf{r}(w), \tag{7.19}$$

where:

$$\mathbf{R}(w) = \sum_{n=1}^{N} \begin{bmatrix}\cos(wt_n)\\ \sin(wt_n)\end{bmatrix} \begin{bmatrix}\cos(wt_n) & \sin(wt_n)\end{bmatrix}, \tag{7.20a}$$

$$\mathbf{r}(w) = \sum_{n=1}^{N} \begin{bmatrix}\cos(wt_n)\\ \sin(wt_n)\end{bmatrix} y(t_n). \tag{7.20b}$$

The periodograms described above sometimes have leakage or low resolution components due to correlation between different spectral components. The CAP method tries to overcome these problems by estimating the covariance matrix between samples. The CAP periodogram is given by [176];

$$P_{CAP}(w) = \frac{1}{\mathbf{a}^H(e^{jw\Delta})\hat{\mathbf{R}}^{-1}\mathbf{a}(e^{jw\Delta})}, \tag{7.21}$$

where:

$$\mathbf{a}(e^{jw\Delta}) = \begin{bmatrix}1 & e^{jw\Delta} & \cdots & e^{jw\Delta m}\end{bmatrix}^T, \tag{7.22}$$

$$\hat{\mathbf{R}} = \frac{1}{\tilde{N}\Delta}\sum_{p=0}^{\tilde{N}-1} \mathbf{a}(e^{jw_p\Delta})\mathbf{a}^H(e^{jw_p\Delta})P_{FP}(w_p), \tag{7.23}$$

which can also be related to the standard covariance matrix,

$$\Delta = \frac{1}{N-1}\sum_{k=0}^{N-2}\left(t_{k+1} - t_k\right), \tag{7.24}$$

which is the average sampling period, m the length of the CAP filters, and $\tilde{N} \geq N$ as it is related to the number of spectral components to be estimated, which is normally larger than the number of samples.

7.5.2 Experimental Results

All spectral estimators described above have been applied to the three-month field campaign, and their results compared against the ground-truth data from the radar installed at the *Pont del Petroli*. Figure 7.12 shows the spectra for the interference pattern presented on Fig. 7.4 using the different proposed spectral estimators. The FP, the LSP and the LS provide similar spectral estimations despite an amplitude or normalization term that can be compensated for. They coincide in the spectra estimated and in the height retrieval. However, the CAP estimator differs slightly in the spectra and the height retrieval

estimation. As seen in Fig. 7.12(d), the CAP estimator tries to reduce the contribution of the sidelobes in the spectra and to improve the accuracy of the fundamental oscillation frequency estimation. In the same way, Fig. 7.13 shows the four spectral estimation of the interference pattern presented in Fig. 7.6. Comparing Figs. 7.12 and 7.13 it is seen that one has larger power than the other one due to having more oscillations on the interference pattern, and having a larger amplitude of the oscillations, which are translated in less SWH. However, the cut-off angle algorithm worked better than the spectral amplitude for estimating the SWH and this is why it has not been analyzed before in this PhD Thesis dissertation.

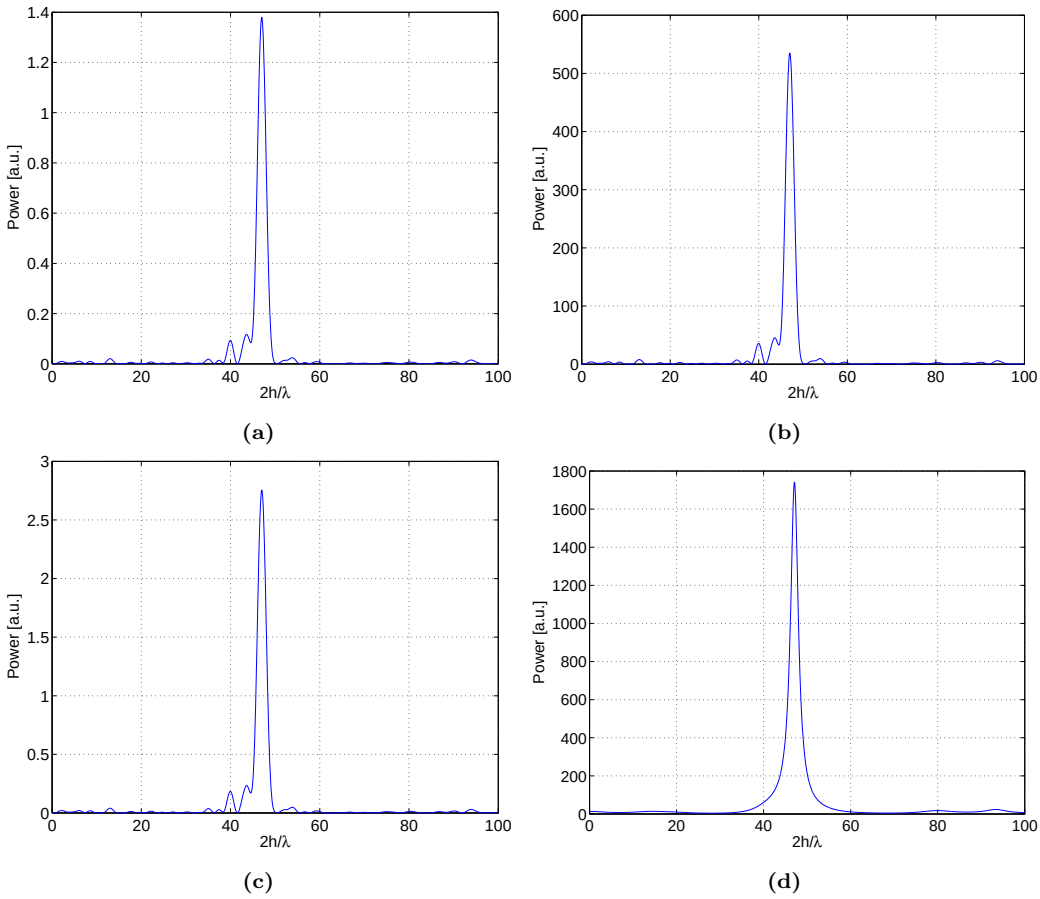

Figure 7.12: Spectra for the satellite 23 interference pattern on December 4, 2012: (a) FP, (b) LSP, (c) LS, (d) CAP.

Figure 7.14 shows the comparison between the estimated SMIGOL height and the ground-truth measured by the radar. Figure 7.14(a) compares the results obtained using the FP spectral estimator to retrieve the mean SMIGOL height with the gound-truth mean sea level. Figure 7.14(b) shows the results obtained using the LSP spectral estimator. Figure 7.14(c) shows the results obtained using the LS. Figure 7.14(d) shows the results obtained using the CAP spectral estimator. The FP, the LSP and the LS provide

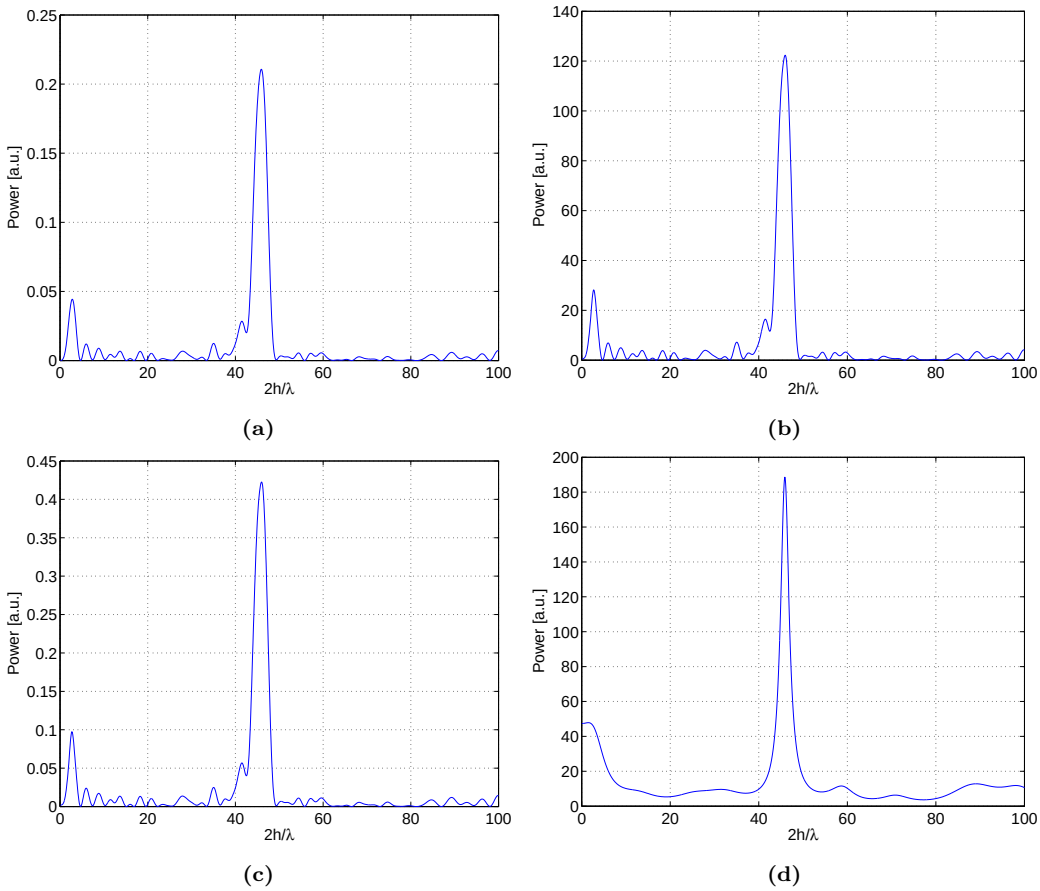

Figure 7.13: Spectra for the satellite 23 interference pattern on December 7, 2012: (a) FP, (b) LSP, (c) LS, (d) CAP.

similar results. Conversely, the CAP seems to provide a better estimation as there are less outliers, and the points are closer to the best linear fit curve. Table 7.1 shows the statistical parameters of the best linear fits in Fig. 7.14. In the "Best fit" field the linear fit equation is presented where SH stands for the SMIGOL Height, and MSL stands for the the Mean Surface Level. In the R^2, the Pearson product-moment correlation coefficient squared is indicated. The RMSE field indicates the fit standard error or root mean square error.

Table 7.1: Statistical parameters of the best linear fits in Fig. 7.14

Estimator	**Best fit**	$\mathbf{R^2}$	**RMSE [cm]**
FP	$SH = -0.9745 \cdot MSL + 4.345$	0.695	5.08
LSP	$SH = -0.9783 \cdot MSL + 4.345$	0.698	5.06
LS	$SH = -0.9783 \cdot MSL + 4.345$	0.698	5.06
CAP	$SH = -1.001 \cdot MSL + 4.333$	0.782	4.15

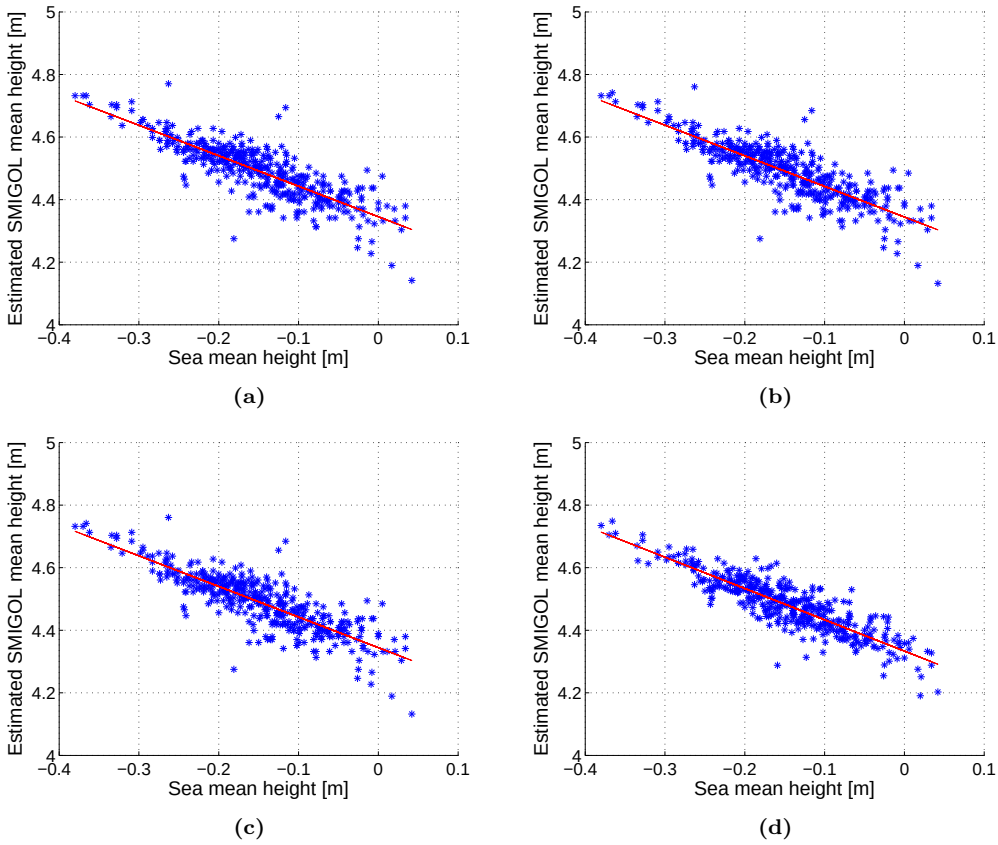

Figure 7.14: Mean sea surface level retrieval. Comparison between Instrument height estimation and mean sea level ground-truth information. In red the best linear fit. (a) FP, (b) LSP, (c) LS, (d) CAP.

There are two remarkable aspects in Fig. 7.14 and Tab. 7.1. First, the relationship between the SMIGOL height estimation and the sea surface mean level is negative. This occurs because an increase in the sea surface level means a decrease in the vertical distance between the SMIGOL antenna phase center and the reflection surface, and vice versa. Furthermore, this relationship must be -1, as 1 cm increase in sea surface height is equivalent to 1 cm decrease in the estimated SMIGOL height. The best linear fits shown in Tab. 7.1 indicate that this relationship is accomplished. The CAP method gives the best performance among them, since the slope of the best linear fit is -1.001 whereas the other estimators provide values between -0.975 and -0.978. Second, the FP, the LSP and the LS provide a similar RMSE ($\sim$5 cm) in the MSSL retrieval. Nevertheless, the CAP method provides approximately 4 cm RMSE, improving the results obtained with previous estimators.

To use this kind of system as a tide gauge instrument, even in the case of moderately rough sea, the following steps must be followed, which are also described in Fig. 7.15:

1. Determine the fundamental oscillation frequency from the interference patterns (∼15–30 mins of data).
2. Convert the fundamental oscillation frequency to the instrument equivalent height using Eqn. (7.25).
3. Define a Mean Sea Surface Reference Level (MSSRL).
4. Determine the actual MSSL with respect to the reference level using Eqn. (7.26).

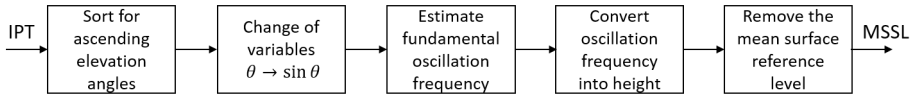

Figure 7.15: Mean sea surface level retrieval algorithm.

$$H_{eq} = \frac{f_{osc} \cdot \lambda}{2}, \tag{7.25}$$

$$\text{MSSL} = -(H_{eq} - \text{MSSRL}). \tag{7.26}$$

Equation (7.26) emphasizes the fact that an increase in the actual MSSL is related to a decrease in the observed H_{eq} and vice versa. To end this section, Fig. 7.16 shows a time series of the estimated MSSL values in red dots and the ground-truth information in a blue solid line in order to validate the proposed algorithm. The same time axis than for Fig. 7.11 has been used.

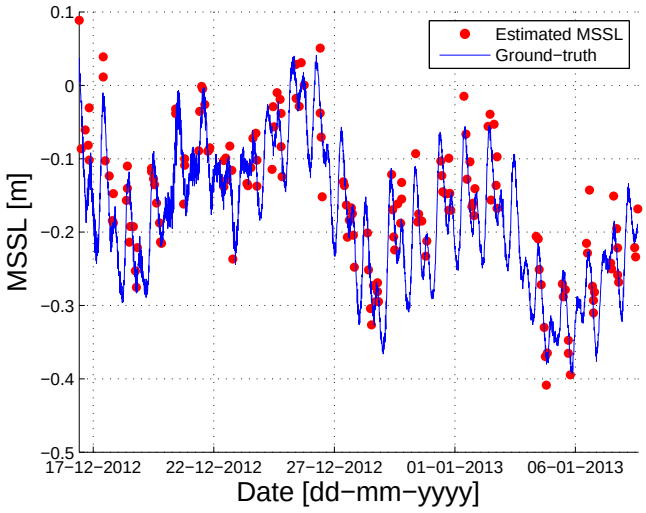

Figure 7.16: Comparison between estimated MSSL and ground-truth with a Pearson correlation coefficient (R) of 0.88.

Note that in this field campaign using the IPT, the precision of the retrieved mean sea surface level is ten times better than the one reached with the SNR-analysis approach [126].

7.6 Summary and Conclusions

This Chapter has presented the results of a three-month field campaign using the IPT to retrieve the SWH and MSSL from the interference patterns obtained with a horizon looking geometry. The RMSE on the SWH estimation of 5.7 cm and of 4.1 cm on the MSSL is demonstrated using the experimental data for SWH values up to 70 cm. Estimations of both parameters can be obtained every 30 minutes, approximately.

The point where the coherency in the reflection process is lost is used to estimate the SWH. At this point, the interference pattern is blurred and the incoherent reflection dominates in front of the coherent one, randomizing the reflected phase. Using spectrogram techniques, this point can be easily determined in time and related to the GNSS elevation angle or surface incidence angle. This angle is related to surface roughness. For the GPS L1-band, the observed surface roughness can be related to the fundamental sea waves. Consequently, surface roughness is related to the SWH. The proposed technique works for SWH values between 10 cm and 70 cm. An empirical equation to determine the SWH depending on the cut-off coherency angle is retrieved from the dataset. It is worth to mention that empirical data has demonstrated that the less restrictive "Rayleigh criterion" for rough surfaces (factor 8) is the theoretical model that works better to identify the cut-off coherency angle. Also, it is worth to add that this new technique proposed in this PhD Thesis dissertation can only be applied to the IPT geometry, since the SNR-analysis technique masks this angle due to the zenith-looking antenna.

The retrieval of the MSSL has also been performed from the coherent part of the interference pattern, where the fundamental oscillation frequency is present. This frequency is not constant because it depends on the sine of the GNSS satellite elevation angle. However, a change of variable can be used to make it constant. Consequently, data becomes unevenly spaced, and spectral techniques for that particular type of data are used to estimate the fundamental oscillation frequency. Among the different spectral techniques described suitable for unevenly spaced data, the CAPON method has shown the best performance over the FP periodogram, the LSP periodogram, and the LS periodogram, because it tries to overcome the problem of having correlated samples. The estimated oscillation frequency is finally related to the vertical distance between the SMIGOL antenna phase center and the average height of the reflection surface, which is related to the MSSL using a reference value. Using the CAPON method a RMSE of 4.1 cm in the measurement of the mean sea surface level is obtained.

8

Chapter 8

Airborne experiments over land using the LARGO instrument

This chapter summarizes the airborne GNSS-R experiments performed over land surface using the LARGO instrument. In particular, two different field campaigns with their results are shown. The first part is the analysis of the first three GELOz flights, where the coherent reflectivity measured by the LARGO instrument is compared against the brightness temperature measured by the PLMR radiometer. In the second part a experiment performed over a vineyard field is described. Therein, an algorithm combining different multispectral bands and the reflectivity estimated by LARGO is developed to estimate soil moisture. Furthermore, a topography correction algorithm was developed because the reflectivity was highly affected by the topography faced in that field campaign.

8.1 Airborne GELOz Experiments

This section compares the performance of L-Band microwave radiometry and GNSS-R, which are techniques that operate at very close frequency bands (1.4 GHz for microwave radiometry and 1.575 GHz for the L1/E1/B1 frequency band used in the GPS, Galileo, and Beidou systems respectively). Three different flights are used for that comparison, the three of them performed under different soil moisture conditions. For those unfamiliar with L-band microwave radiometry, a basic introduction is given in Appendix E. The first publication stating some correlation between GNSS-R and L-band microwave radiometry appeared in 2006 [177], but only qualitative relations have been shown until now. For the analysis made here, two different land-covers have been chosen: grass-land and crops. The correlation results between both techniques lead to a possible combination of the two techniques for spatial resolution enhancement of microwave radiometry data (brightness temperature, and consequently their estimated parameters such as soil moisture). This approach will not give as good spatial resolution as previous presented approaches, for instance [178–180], but it does not depend on weather as optical or multi-spectral data does. Furthermore, this approach would use two techniques very close in frequency, and consequently, sensitive exactly to the same geophysical parameters. Also, it is different to previous down-scaling approaches, which used different techniques working at different spectral bands.

8.1.1 Theoretical Relationship Between GNSS-R Reflectivity and L-Band Microwave Radiometry

For a flat surface, both the reflectivity and the emissivity depend on two parameters: the incidence angle (θ_i), and the soil dielectric constant (ε_r). There are several models to obtain the soil dielectric constant as a function of the soil moisture content [94, 181–183]. To illustrate the reflectivity and emissivity curves and explain the relationship among them, the Wang's model [94] has been used given its simplicity. To generate the dielectric constant as a function of soil moisture a soil composition of 50% clay, and 20% sand has been chosen.

Figure 3.2 showed the reflectivity curves for a flat surface with different soil moisture values and different polarization states, as a function of the incidence angle. On the top-left (a), the horizontal reflectivity value was shown, which is monotonically increasing with SM content. On the top-right (b), the reflectivity for vertical polarization was shown, which in this case was decreasing until the Brewster angle position, where there was minimum reflectivity, and then started increasing towards 1. Reflectivity for the transmitted RHCP polarization and reflected RHCP polarization was shown on the bottom-left (c), and it was much smaller than the other ones. However, at grazing angles it was quite large, and comparable to the vertical and horizontal ones. This occurred because, for an incidence angle above the Brewster angle, both components (H- and V-Pol) change their phase in the reflection process, and therefore, polarization is preserved. The point where the $|r_{RR}|^2$ started to be noticeable was related to the Brewster angle position [35]. Finally, the bottom-right of the figure (d), showed the reflectivity for a transmitted RHCP wave and a reflected LHCP wave. This is the general case in GNSS-R scatterometry, where the transmitted polarization by GNSS satellites is RHCP, and as it

can be seen from the figure, the main received power is LHCP. Furthermore, if roughness is negligible, there is one region between 0°–45° incidence angle where the reflectivity is insensitive to incidence angle variations.

Figure 8.1 shows the emissivity ($1 - |r_{XX}|^2$, see Appendix E) curves for linear polarization, the first stokes parameter normalized, and the Microwave Polarization Difference Index (PI). The top-left (a), shows the emissivity curves at horizontal polarization. If reflectivity for horizontal polarization was monotonically increasing, it has to be the contrary for the emissivity curves. Herein, the larger the soil moisture value, the lower the emissivity, and therefore, the lower the T_B observed. The top-right (b), shows the vertical polarization emissivity curves. Again, their behavior is opposite to the reflectivity one, observing a maximum in emissivity at the Brewster angle position. As happened before, the larger the soil moisture, the lower the emissivity. On the bottom-left (c), the first Stokes parameter divided by two is shown, which is a combination of the r_{RL} and r_{RR} curves. It is understood to represent a measurement of the total incident brightness temperature at circular polarization independently from the rotation sense. From now on this parameter will be indicated as $I/2$, and it is defined as:

$$I/2 = \frac{1}{2}\left(T_{BH} + T_{BV}\right). \tag{8.1}$$

This is done for very flat surface areas in order to mitigate the dependence of the emissivity and/or T_B on the incidence angle up to $\sim 40°$. Finally, on the bottom-right part (d), another concept is presented in the emissivity curves, also known as PI [184, 185]. It is defined as:

$$\mathrm{PI} = \frac{T_{BV} - T_{BH}}{\frac{1}{2}\left(T_{BV} + T_{BH}\right)} = 2\frac{e_V - e_H}{e_V + e_H} \tag{8.2}$$

The PI is interesting because it normalizes the T_B measurement, making it independent from the physical temperature. This independence from the physical temperature is very important, since it means that measurements are automatically calibrated, as they are relative. The two bottom graphs on Fig. 8.1 are highly related to the first two Stokes parameters [186–188]. However, there is a normalization factor in the PI that does not appear in the Stokes parameters.

One aspect mentioned before, but not discussed, is the effect of surface roughness on the emissivity and reflectivity curves. Surface roughness disperses radiation which attenuates coherent reflectivity and makes the reflectivity curves closer among them (in linear units as presented in Fig. 3.2). For the emissivity, its curves rise their level, resulting in a biased brightness temperature observation. Furthermore, the emissivity curves also become closer, which means that the retrieval is less accurate.

8.1.2 GELOz Field Campaigns and Instruments Used

The GELOz field campaigns are a series of three flights conducted between September and November, 2013. Those flights were performed under different soil moisture conditions, and the LARGO scatterometer [37] was flown together with the PLMR radiometer [189]. The first flight was conducted when the average SM was 0.15 $\mathrm{m^3 m^{-3}}$. In the second one, the terrain was very dry and the average soil moisture below 0.08 $\mathrm{m^3 m^{-3}}$. The third flight was performed after a rain event to see the contrast between the previous scenarios.

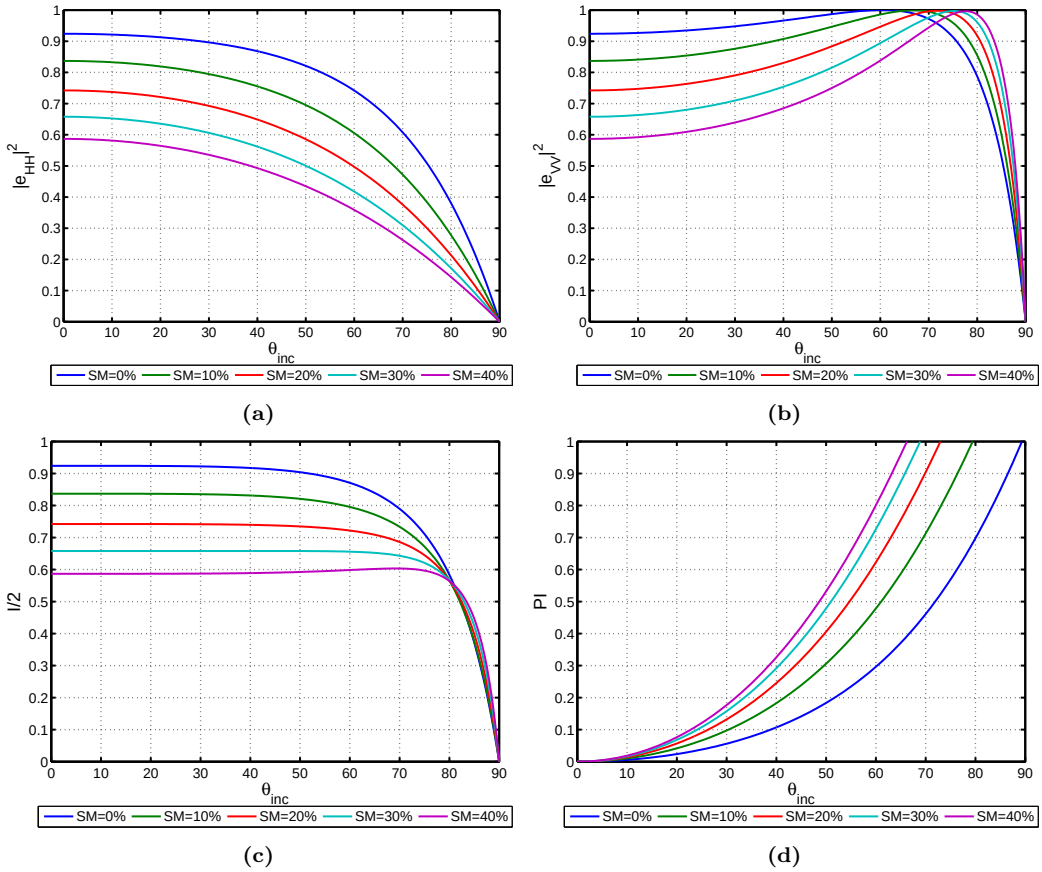

Figure 8.1: Emissivity curves for different polarization states as a function of incidence angle and soil moisture content using Wang's dielectric constant model. (a) horizontal polarization, (b) vertical polarization, (c) first Stokes parameter or normalized intensity divided by two ($I/2$), and (d) PI.

The three flights followed approximately the same path over the target area, departing from Tyabb, Victoria, Australia, and landing on a regional airport (Narrandera) close to the Yanco region, New South Wales, Australia. Figure 8.2 shows the route for one of the flights, as an example.

The LARGO instrument used for that field campaign was the initial version which did not include the calibration matrix. As explained in Chapter 5, one channel was connected to a zenith looking antenna and the other one to a nadir looking antenna. Recall that the LARGO instrument was only sensitive to the coherent component due to the way the direct and reflected SNRs are estimated (see Chapter 5, SNR_{cc}). However, the final ground resolution depends on the platform speed and height. The first two flights were made at 220 meters height at a speed of 220 km/h, whereas the third flight was made at a height of 150 meters at the same speed. Taking into account the size of the first Fresnel zone for those scenarios, it leads to a ground resolution of 67 m x 8 m for the first

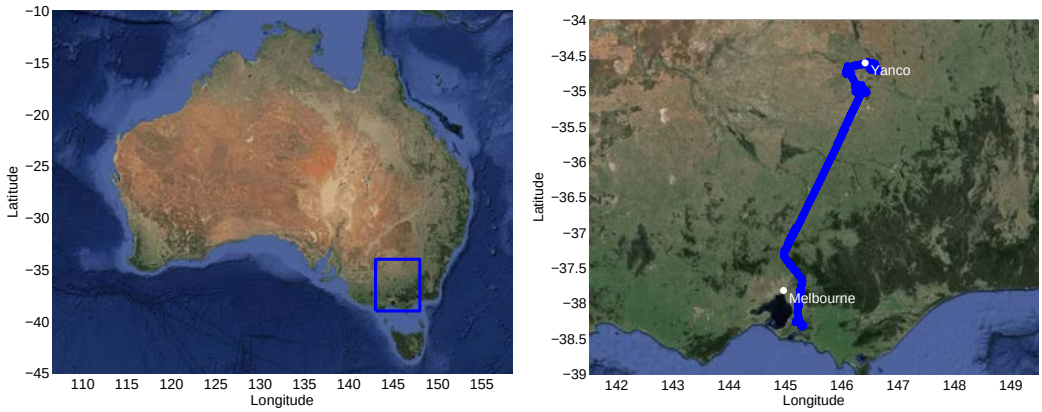

(a) **(b)**

Figure 8.2: Flight route followed for the three field campaigns in south-eastern Australia: (a) Australian map with the field campaign region indicated/highlighted in blue, (b) Zoom of the field campaign region with the whole flight route route in blue highlighting Melbourne's location and Yanco's location in black.

two flights and 66.7 m x 6.8 m for the third one, which is roughly the same for the three flights despite the height difference. Note that the incoherent integration time lowers the achievable instantaneous ground resolution severely, which would be on the order of 10 m x 10 m.

The PLMR is a microwave radiometer working at L-band (1400-1426 MHz) [189,190]. It measures the brightness temperature in the range of 0–350 K with an accuracy of 0.7 K for one second of integration time. It has an 8 x 8 patch antenna array with vertical and horizontal polarization feeds. PLMR also uses analog beamforming to generate six different beams at a time pointing to ±8°, ±21°, ±38° off nadir, each with a beamwidth of 15°. The ±38° beams correspond to beams 1 and 6, the ±21° correspond to beams 2 and 5, and the ±8° correspond to beams 3 and 4. Its size is 94 x 94 x 20 cm^3 and weights approximately 40 kg. Figure 8.3 shows the flight setup, including a picture of the radiometer mounted on the plane used to perform the field campaigns (c). Part of the LARGO setup is also shown.

The ground-resolution of PLMR is determined in this case by the antenna footprint projected onto the ground, the beam used (incidence angle), and the platform height. For the first two flights the ground-resolution is approximately 120 m x 58 m for the ±8° beams, 127 m x 62 m for the ±21°, and 153 m x 93 m for the ±38°. For the third flight the ground resolution is approximately 101 m x 40 m for the ±8° beams, 106 m x 42 m for the ±21°, and 110 m x 63 m for the ±38°. In this case the integration time does not degrade as severely the instantaneous ground-resolution. It will be seen later on that the reflectivity pixels are approximately 10% overlapped, whereas the radiometry pixels are at least 50% overlapped. This will have an impact on the data correlation.

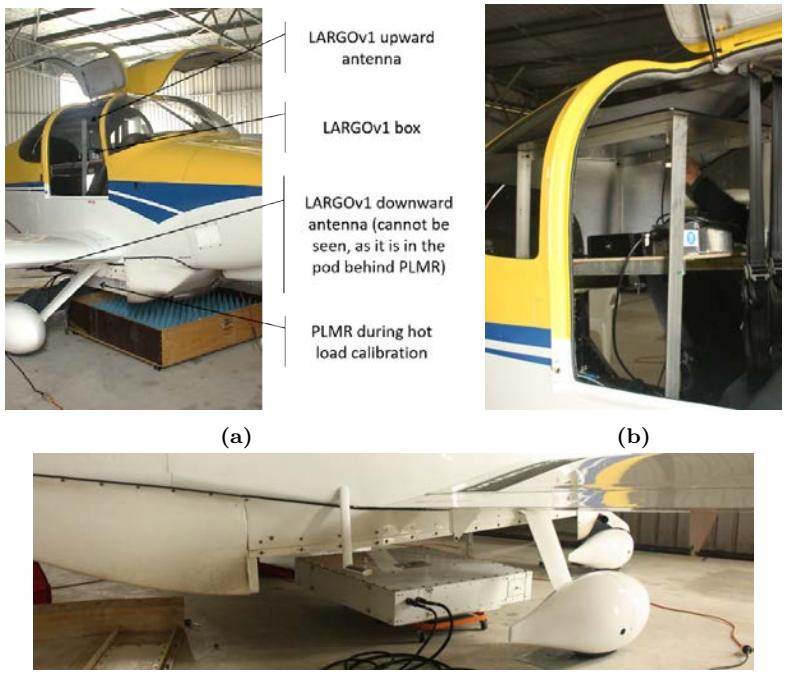

Figure 8.3: Flight setup with the LARGO and PLMR instruments: (a) General set-up, (b) LARGO instrument zoomed with up-looking antenna connection, (c) PLMR instrument.

8.1.3 Data Analysis

8.1.3.1 GNSS-R Dataset

The measured coherent thermal SNR for the waveform peaks for the direct/up-looking LARGO channel after the correlation with the satellite code is given by:

$$\mathrm{SNR}_U = \frac{EIRP_T G_{R_U}(\theta_{R_U}, \phi_{R_U}) \rho_{R_U}(\theta_{R_U}, \phi_{R_U}) \lambda^2}{(4\pi R_U)^2 k \left(T_{ant_U} + T_0 \left(F_U - 1\right)\right) B_U}, \tag{8.3}$$

where $EIRP_T$ stands for the Equivalent Isotropically Radiated Power transmitted by the GNSS satellites, G_{R_U} for the receiving antenna gain, θ_{R_U} and ϕ_{R_U} for the incoming signal direction in the antenna reference frame, ρ_{R_U} for the antenna polarization mismatch factor, R_U for the distance path traveled by the direct signal, T_{ant_U} for the up-looking antenna temperature, $T_0 = 290$ K, F_U for the receiving chain noise figure, and B_U for the system's bandwidth after the correlation with the satellite code.

The measured coherent thermal SNR for the reflected/down-looking channel after the correlation with the satellite code is:

$$\mathrm{SNR}_D = \frac{EIRP_T G_{R_D}(\theta_{R_D}, \phi_{R_D}) \rho_{R_D}(\theta_{R_D}, \phi_{R_D}) \lambda^2 |r_{RL}(\theta_i)|^2}{(4\pi R_D)^2 k \left(T_{ant_D} + T_0 \left(F_D - 1\right)\right) B_D}, \tag{8.4}$$

where G_{R_D} stands for the receiving antenna gain, θ_{R_D} and ϕ_{R_D} for the incoming signal direction in the antenna reference frame, ρ_{R_D} for the antenna polarization mismatch factor, $|r_{RL}(\theta_i)|^2$ for the coherent reflectivity, θ_i for the local incidence angle, R_D for the distance traveled by the signal in the downwelling and upwelling paths, T_{ant_D} for the down-looking antenna temperature, F_D for the receiving chain noise figure, and B_D for the system's bandwidth after the correlation with the satellite code. Consequently, the coherent reflectivity for transmitted RHCP and received LHCP can be estimated as:

$$|r_{RL}(\theta_i)|^2 = \frac{SNR_D}{SNR_U}\frac{G_{R_U}\rho_{R_U}}{G_{R_D}\rho_{R_D}}\frac{T_{ant_D} + T_0\,(F-1)}{T_{ant_U} + T_0\,(F-1)}, \tag{8.5}$$

considering that the system's equivalent bandwidth is the same for both channels, which it is because the two channels use 1 ms of coherent integration, the noise figure (F) is also the same for both channels, which is accomplished by proper instrument design, and that the distance R_U and R_D are nearly the same for ground-based and airborne conditions. After having compensated for the different antenna gains seen by both the direct and reflected signals, the terrain's coherent reflectivity can be estimated.

The geolocation of the specular reflection points is done by ray tracing and assuming the paraxial approximation of rays, which means that direct signal, and the one that impinges on the terrain are parallel. In other words, for a flat surface, the incidence angle (θ_i) is the complementary angle of the GNSS satellite elevation angle (θ_e). The LARGO back-end receivers provide the necessary information about the satellites' constellation. For an airborne receiver, the specular reflection point for each satellite, or center of the First Fresnel zone, is:

$$x = \frac{(H - H_0)\sin\phi_a}{\tan\,(90 - \theta_e)}, \tag{8.6a}$$

$$y = \frac{(H - H_0)\cos\phi_a}{\tan\,(90 - \theta_e)}, \tag{8.6b}$$

where both x and y coordinates are expressed in meters, and are referred to the platform position, H_0 is the geoidal separation to the WGS84, H the platform height with respect to the WGS84, θ_e the GNSS satellite elevation angle, and ϕ_a the GNSS satellite azimuth angle, which is defined clockwise starting from the geographic North. In order to geolocate the specular reflection points for each acquisition, it is necessary to change from latitude and longitude coordinates to Universal Transverse Mercator (UTM) coordinates, add the x and y computed to the platform's position, and then go back to latitude and longitude coordinates[1].

Once the preliminary data processing is finished, Figs. 8.4(a)–(c) are produced to show the reflectivity maps obtained for a particular sub-set of the entire field campaign. They include the pass over a lake (blue region), in order to have a water body as a reference, and the Yanco area, where several flight passes were performed. The main focus area (latitude: from $-35.05°$ to $-34.9°$) shows a reflectivity range of -12 dB to -16 dB [Fig. 8.4(a)] for

[1]This methodology is valid only for ground-based and low-height airborne conditions since the paraxial approximation and the flat Earth model apply in those conditions. In order to geolocate from a spaceborne point of view, it is necessary to obtain the satellite position from the almanac and ephemeris data, work with data in Earth-Centered, Earth-Fixed (ECEF) coordinates, and consider the elliptical shape of the Earth. An example of the specular point computation for spaceborne observations can be found in [46].

the first flight, for the second flight [Fig. 8.4(b)] reflectivity is between -14 dB and -18 dB, and for the third flight [Fig. 8.4(c)] it ranges from -8 dB to -12 dB. In all the flights, the reflectivity of the water body ranged from -5 dB to 0 dB. This coincides qualitatively with the experiment explanation seen in section 8.1.2 where the SM content for the first flight was around 0.15 m^3m^{-3}, it was very dry for the second flight (less than 0.08 m^3m^{-3}), and the third flight was performed after a rain event without intensive soil moisture ground-truth. This is also in agreement with Fig. 3.2 where a larger reflectivity is caused by higher levels of soil water content or even open water bodies. In particular, when observing small open inland water bodies, the reflectivity can be as large as -1 dB, behaving as expected very close to a mirror in the microwave L-band spectrum. Also, in the reflectivity maps it is possible to see at least two different tracks. These appear due to the different satellites in view that are monitored at the same time, which shows the multistatic properties of GNSS-R scatterometry [47]. These tracks are not the same in the three figures due to two main reasons: 1) the plane did not follow exactly the same flight path, 2) the satellites' positions were not the same in the three field campaigns (geometry changed).

8.1.3.2 PLMR Dataset

Figures 8.4(d)–(f) show the H-Pol brightness temperature maps for the three GELOz flights. In Fig. 8.4(d) (first flight) it is easy to identify the lake that was seen on the reflectivity data, and also some other water bodies. Looking to the Yanco area, the T_{BH} ranges from 250 K to 265 K, changing to 260–280 K for the second flight (Fig. 8.4(e)), and about 210 K for the third flight (Fig. 8.4(f)). This depicts the general surface conditions of the area, going from relatively wet to dry, and then significantly wetting up again. The same patterns are seen in the T_{BV} data (Figs. 8.4(g)–(i)).

If comparing H- and V-Pol radiometry data, it can be concluded that both behave as a function of the SM content. Both, T_{BH} and T_{BV} maps have a middle state in the first flight. Then, the highest T_Bs are seen for the second flight, where there was the lowest SM content. Finally, the lowest T_Bs are seen for the third flight, just after a rain event. As expected, and predicted by radiometric models, T_{BV}s are always larger than T_{BH}s.

8.1.3.3 GNSS-R and Microwave Radiometry Relationship

Qualitatively, the behavior of the reflectivity and brightness temperature data across both polarizations depending on the field conditions has been explained: when the soil moisture increases, reflectivity rises, and emissivity decreases, and consequently T_Bs, and vice versa. Again, qualitatively, there is a negative relationship between the reflectivity maps and the T_B maps. Note that in Figs. 8.4(a)–(c) the color scale has been inverted, to reflect this relationship, and to make sure that dry surface conditions are represented in red for both types of measurements.

In the previous qualitative analysis there are several parameters that must be taken into account in order to perform a quantitative analysis and study the correlation between GNSS-R and microwave radiometry. The main parameters to take into account that may differ in both situations are:

1. Incidence angle (θ_i): while for the PLMR data it is very clear and it is determined

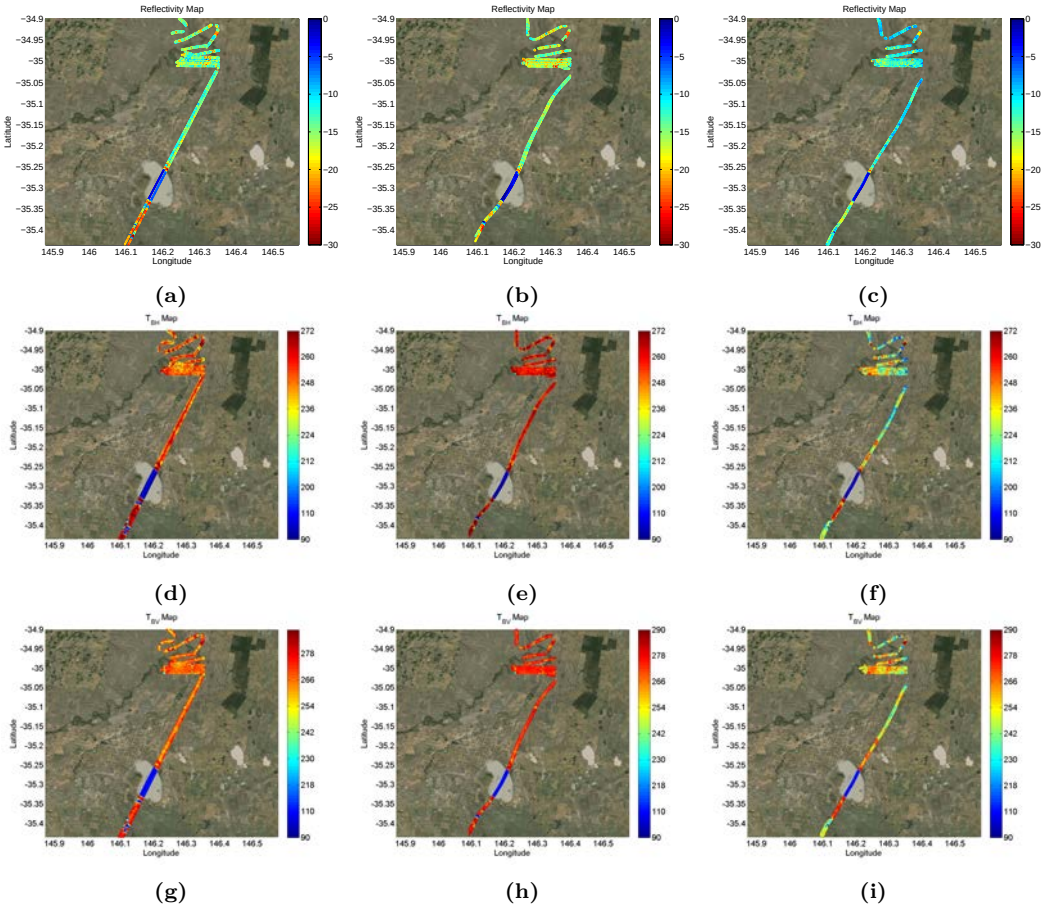

Figure 8.4: Summary of the reflectivity and T_B maps for the three GELOz field campaigns for a sub-set of the field campaign: (a)–(c) Reflectivity maps for the first, second, and third flight respectively, (d)–(f) T_{BH} maps for the first, second, and third flight respectively, (g)–(i) T_{BV} maps for the first, second, and third flight respectively.

by the beam pointing direction (taking into account the platform's attitude), in GNSS-R it depends on the satellite geometry, and as discussed above, it was different for the three field campaigns. This feature is seen by comparing Figs. 8.4(a)–(c) where the separation between satellite tracks is different.

2. Polarization: while GNSS satellites transmit in RHCP and GNSS-R data is mainly LHCP, microwave radiometry data has been measured at linear polarization. This yields a noticeable change, as for circular polarization there is almost no dependence with the incidence angle up to 45°, whereas for linear polarization there is, as seen in Figs. 3.2,8.1. This means that it is not possible to directly compare both measurements for a quantitative analysis.

3. Surface roughness: the effect of surface roughness is not the same for the two types of measurements, since GNSS-R relies on a forward scattering mechanism, which

is mainly based on the coherent reflection model, and microwave radiometry on the emissivity, which is an integral over half hemisphere of the co- and cross-polar bistatic scattering coefficients.

4. Land Cover: the surface cover may have an impact on the reflectivity and T_Bs measured, as it will not be the same to have bare soil, grass-land, or some crops which may have a taller vegetation and different water content.

In order to solve the first two points, T_{BH} and T_{BV} are combined to form the $I/2$ and the PI, as shown in Fig. 8.1. To study the third point (roughness), the reflectivity data has been binned into two different regions: incidence angles ranging from 30° to 50°, where the reflection is assumed to have a larger coherent part, and incidence angles ranging from 0° to 30°, where the reflection may be more influenced by the incoherent scattering. Incidence angles larger than 50° are discarded because they are out of the antenna beamwidth, and the main polarization is not guaranteed to be LHCP. This binning is also used in [191] to analyze the correlation between GNSS-R data and optical, near-infrared, and thermal indexes. To study the last point (land cover), a dedicated analysis for a grass-land region and a crops region is performed, because Figs. 8.4(a)–(i) show a big region of the entire field campaign where different land covers and surface types were found. Figures 8.5(a)–(i) show the reflectivity, T_{BH}, and T_{BV} for the three GELOz field campaigns over the grass-land focus area. Figures 8.6(a)–(i) show the reflectivity, T_{BH}, and T_{BV} for the three GELOz flights over the crops focus area. Again, qualitatively the same relationship than with the previous figure is obtained.

Observations acquired with a roll or a pitch larger than 10° were discarded, as well as data collected during the steep banking of the turns. Also if roll and pitch had changed more than 5° per second, the data was also discarded as it would be an indication of a quick plane maneuver and antenna pattern compensation algorithms would not work properly.

After describing qualitatively the datasets used, a quantitative correlation analysis is performed. Figures 8.5(a)–(i) show a summary of the grass-land dataset used for this analysis. A minimum distance algorithm is used to associate each reflectivity point to each PLMR beam, guaranteeing that the distance is less than 100 m according to the LARGO and PLMR ground-resolution for the three flights. If more than one PLMR T_B measurement fell within the same reflectivity point, they were averaged weighting them according to the inverse of their distance to the center of the reflectivity point. Once the data were matched, the $I/2$ parameter was computed and a correlation analysis between the reflectivity data and the $I/2$ performed. Figure 8.7 shows this comparison for the different reflectivity incidence angle groups with Figs. 8.7(a)–(c) corresponding to the largest incidence angle group and Figs. 8.7(d)–(f) to the lowest one. Both reflectivity incidence angle groups are compared to the data from the PLMR beams at their respective incidence angles from the boresight. In red the best fit with the following shape is shown:

$$I/2 = a(1 - 10^{\frac{R_{RL}[dB]}{10}}) \tag{8.7}$$

where:

$$I/2 = \frac{T_{BH} + T_{BV}}{2} = T_F \left(1 - \frac{R_H + R_V}{2}\right), \tag{8.8}$$

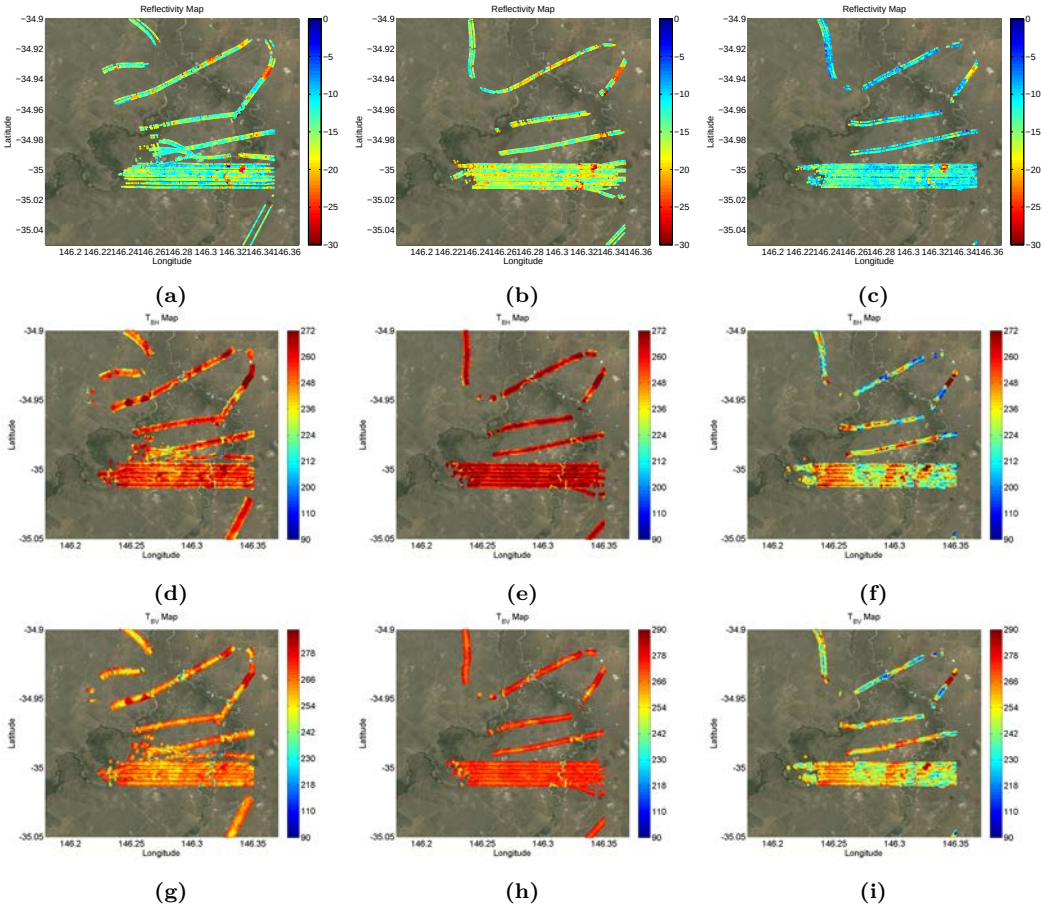

Figure 8.5: Summary of the reflectivity and T_B maps for the three GELOz field campaigns over the grass-land area: (a)–(c) Reflectivity maps for the first, second, and third flight respectively, (d)–(f) T_{BH} maps for the first, second, and third flight respectively, (g)–(i) T_{BV} maps for the first, second, and third flight respectively.

and:

$$R_{RL} \approx \frac{R_H + R_V}{2}, \tag{8.9}$$

for the reflectivity incidence angle range used.

Table 8.1 shows the correlation of the data presented in Fig. 8.7 as well as the parameters of the proposed fit. The correlation among reflectivity and $I/2$ for the PLMR beams $\pm 38°$ and $\pm 21°$ is 0.6, while it decreases for the PLMR $\pm 8°$ beams, probably due to surface roughness effects, since roughness affects more the forward scattering geometry at more nadir incidence angles. It is also remarkable that for the largest reflectivity incidence angle group the RMSE of the fit is lower than for the lowest one, which is also an indicator of the surface roughness effects. Finally, the a parameter of the fit in all cases ranged from 270 K to 278 K, and this parameter did not significantly change the

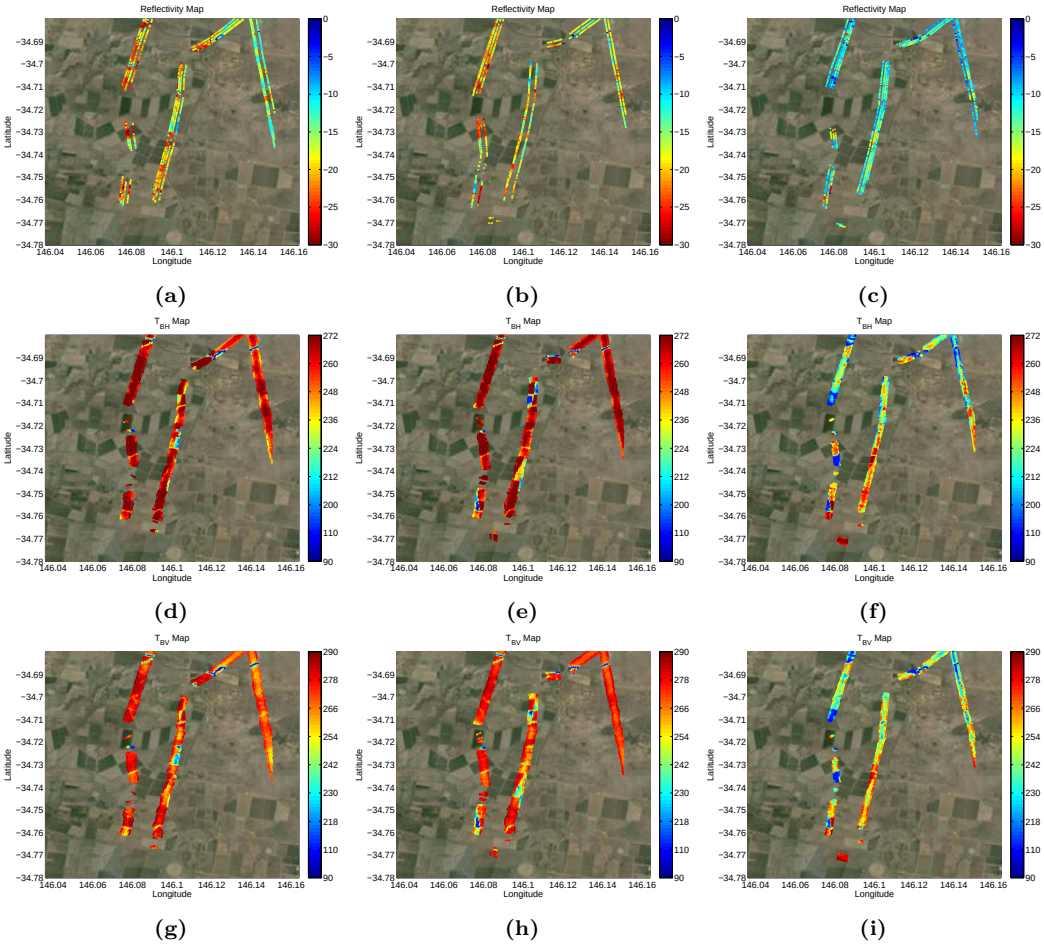

Figure 8.6: Summary of the reflectivity and T_B maps for the three GELOz field campaigns over the crops area: (a)–(c) Reflectivity maps for the first, second, and third flight respectively, (d)–(f) T_{BH} maps for the first, second, and third flight respectively, (g)–(i) T_{BV} maps for the first, second, and third flight respectively.

goodness of the fit.

Despite the proposed fit was not highly sensitive to the a parameter or the physical temperature of the terrain (T_F), the reflectivity values were compared to the PI, which is a self-calibrated parameter independent from the physical temperature. This comparison follows the same structure than the one with the $I/2$, and it is shown in Fig. 8.8. The best fit proposed in this case is a potential one:

$$T_B = a10^{bR_{RL}[dB]} \tag{8.10}$$

Table 8.2 shows the correlation between the reflectivity data and the PI computed from the PLMR T_Bs as well as the best fit parameters. Correlation increased to approximately 0.65 due to the self-calibrated nature of the data. Furthermore, the same behavior that

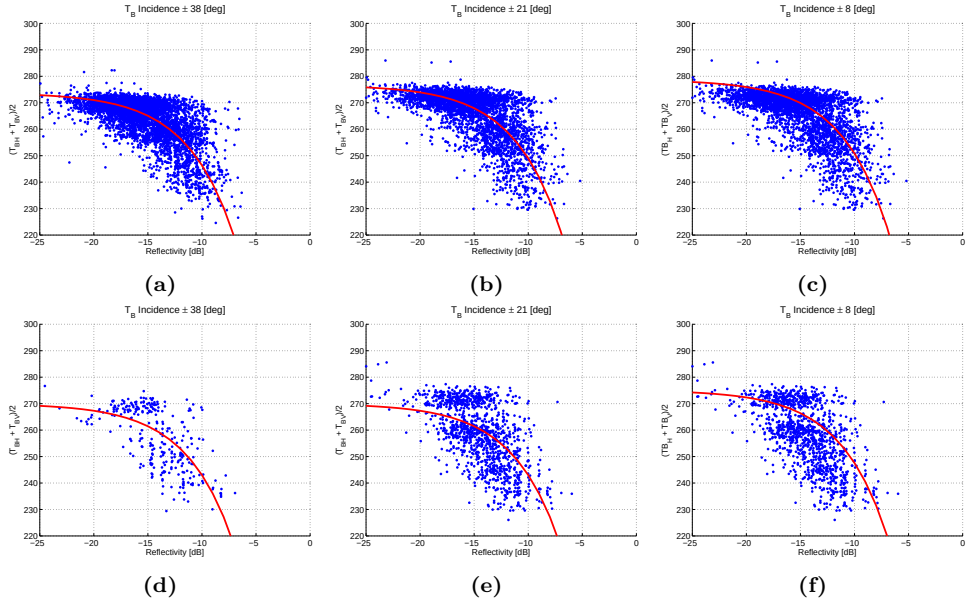

Figure 8.7: Comparison between LARGO reflectivities and the first Stokes parameter divided by two for the grass-land regions. In (a)–(c) the reflectivity data corresponds to incidence angles ranging from 30° to 50°. In (d)–(f) the reflectivity data corresponds to incidence angles lower than 30°. In (a),(d) PLMR data from the ±38° incidence angles beams is used. In (b),(e) PLMR data from the ±21° incidence angles beams is used. In (c),(f) PLMR data from the ±8° incidence angles beams is used. In red the best fit is presented.

Table 8.1: Correlation and RMSE between LARGO reflectivity and the first Stokes parameter divided by two for the grass-land regions as well as the fit parameters, $\left[I/2 = a\left(1 - 10^{\frac{R_{RL}[dB]}{10}}\right)\right]$.

Param.	**Inc. angle**	±38°	±21°	±8°
a [K]	30-50	273.7	276.7	278.7
R	30-50	0.6	0.61	0.51
RMSE [K]	30-50	6.6	7.1	8.9
a [K]	0-30	270	270	275
R	0-30	0.6	0.58	0.41
RMSE [K]	0-30	9.2	9.8	10.2

with the $I/2$ is seen, the RMSE of the fits proposed is lower for the largest incidence angle reflectivity group, also indicating that surface roughness affects them less. However, the PI parameter only seems useful for the large PLMR incidence angles, because when the incidence angle is close to nadir, both T_{BH} and T_{BV} are practically equal, and the PI tends to 0. The use of self-calibrated data allows the removal of any parameter affecting the relation between reflectivity and brightness temperature and mitigates the surface roughness effects. However, the dependence of brightness temperature on the incidence angle becomes important, making the PI only useful for the large incidence

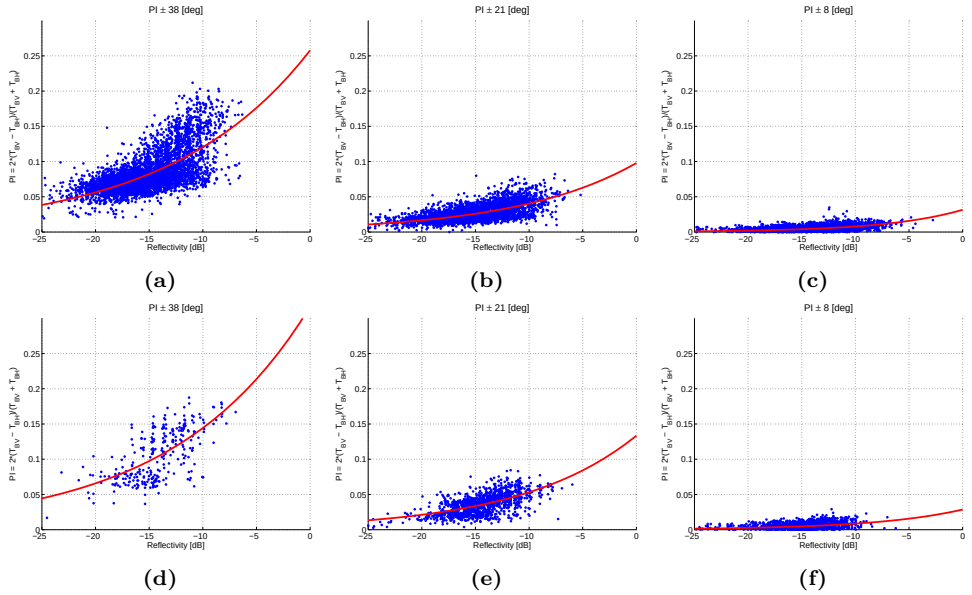

Figure 8.8: Comparison between LARGO reflectivities and the PI for the grass-land regions. In (a)–(c) the reflectivity data corresponds to incidence angles ranging from 30° to 50°. In (d)–(f) the reflectivity data corresponds to incidence angles lower than 30°. In (a),(d) PLMR data from the ±38° incidence angles beams is used. In (b),(e) PLMR data from the ±21° incidence angles beams is used. In (c),(f) PLMR data from the ±8° incidence angles beams is used. In red the best fit is presented.

angles regions. Conversely, the incidence angle dependence was mitigated using the first Stokes parameter.

Table 8.2: Correlation and RMSE between LARGO reflectivity and the PI for the grass-land regions as well as the fit parameters $\left[T_B = a10^{bR_{RL}[dB]}\right]$.

Param.	**Inc. angle**	±38°	±21°	±8°
a	30-50	0.26	0.1	0.03
b	30-50	0.03	0.04	0.06
R	30-50	0.68	0.66	0.52
RMSE	30-50	0.02	0.008	0.003
a	0-30	0.32	0.13	0.03
b	0-30	0.03	0.04	0.05
R	0-30	0.66	0.63	0.31
RMSE	0-30	0.03	0.01	0.04

The area under analysis is now changed from the grass-land region to the crops region. Figures 8.6(a)–(i) show a summary of the crops dataset used for this analysis. The dataset has been pre-processed in the same way as the grass-land dataset, in order to match reflectivity and T_Bs. The $I/2$ parameter was computed, and a correlation analysis between the reflectivity data and the $I/2$ performed. Figure 8.9 shows this comparison for

the two different reflectivity incidence angle groups. In red the best fit line is represented following the same linking model shown in Eqn. (8.7).

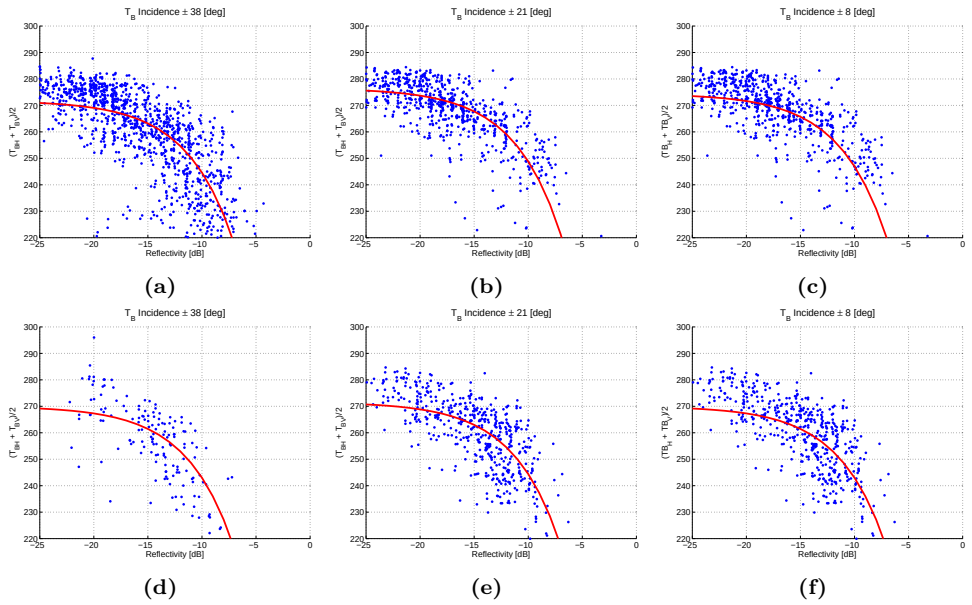

Figure 8.9: Comparison between LARGO reflectivities and the first Stokes parameter divided by two for the crops region. In (a)–(c) the reflectivity data corresponds to incidence angles ranging from 30° to 50°. In (d)–(f) the reflectivity data corresponds to incidence angles lower than 30°. In (a),(d) PLMR data from the ±38° incidence angles beams is used. In (b),(e) PLMR data from the ±21° incidence angles beams is used. In (c),(f) PLMR data from the ±8° incidence angles beams is used. In red the best fit is presented.

Table 8.3 summarizes the correlation analysis of the data presented in Fig. 8.9 as well as the parameters of the proposed fit. The correlation among reflectivity and $I/2$ for the three PLMR beams was between 0.74 and 0.8 for the reflectivity larger incidence angles, and between 0.64 and 0.69 for the lower incidence angles. For the crops area, the correlation increased in comparison to the grass-land area. This indicates that the crops area, due to the agricultural works, is a more regular region in terms of surface roughness as compared to the grass-land area. However, the RMSE also increased slightly. The increase in the RMSE can be justified by the presence of higher vegetation, which adds some noise to the received signals, and therefore more variability. Also, the same behavior than in the grass-land analysis is found, being the correlation smaller for the lower incidence angle group.

Again, the same analysis than for the grass-land region with the PI parameter has been performed for the crops region, and it is shown in Fig. 8.10. The same fit as the one presented in Eqn. (8.10) is shown in red. Table 8.4 shows the correlation between the reflectivity data and the PI computed from the PLMR T_Bs as well as the best fit parameters. For the crops region the correlation values were similar to the grass-land region, increasing for the ±38° beam and large incidence angle group. Again, no conclusion could be obtained for the ±8° beam, since it was always nearly 0 (by definition).

Table 8.3: Correlation and RMSE between LARGO reflectivity and the first Stokes parameter divided by two for the crops region as well as the fit parameters $\left[I/2 = a\left(1 - 10^{\frac{R_{RL}[dB]}{10}}\right)\right]$.

Param.	**Inc. angle**	$\pm 38^\circ$	$\pm 21^\circ$	$\pm 8^\circ$
a [K]	30-50	271.8	276.5	274.4
R	30-50	0.8	0.74	0.78
RMSE [K]	30-50	8.7	9.8	11.4
a [K]	0-30	270	271.5	270
R	0-30	0.69	0.66	0.64
RMSE [K]	0-30	11.3	11.4	15.4

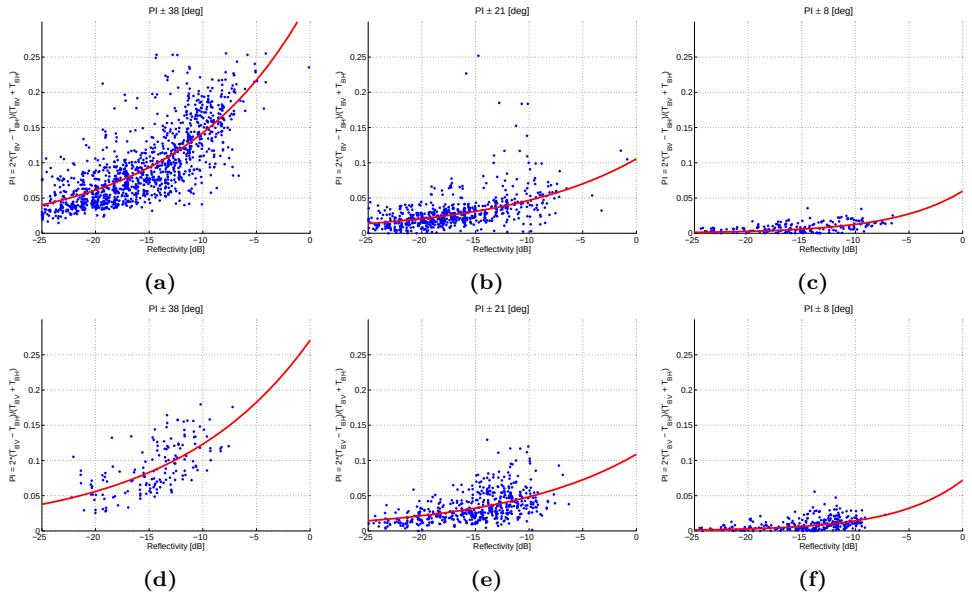

Figure 8.10: Comparison between LARGO reflectivities and the PI for the crops region. In (a)–(c) the reflectivity data corresponds to incidence angles ranging from 30° to 50°. In (d)–(f) the reflectivity data corresponds to incidence angles lower than 30°. In (a),(d) PLMR data from the $\pm 38^\circ$ incidence angles beams is used. In (b),(e) PLMR data from the $\pm 21^\circ$ incidence angles beams is used. In (c),(f) PLMR data from the $\pm 8^\circ$ incidence angles beams is used. In red the best fit is presented.

8.1.4 Discussion

There are several issues to take into account when analyzing the correlation between GNSS-R and microwave radiometry data, such as: incidence angle, surface roughness, land cover, polarization, and pixel size. Using the first Stokes parameter divided by two ($I/2$) it was possible to compensate for the polarization difference between PLMR T_Bs and the LARGO reflectivity. If the land surface is smooth, the $I/2$ curves are also flat, as the reflectivity, and the dependence on the incidence angle is also avoided. Using

Table 8.4: Correlation and RMSE between LARGO reflectivity and the PI for the crops region as well as the fit parameters $\left[T_B = a10^{bR_{RL}[dB]}\right]$.

Param.	**Inc. angle**	±38°	±21°	±8°
a	30-50	0.33	0.1	0.06
b	30-50	0.04	0.03	0.07
R	30-50	0.74	0.6	0.58
RMSE	30-50	0.035	0.022	0.007
a	0-30	0.27	0.11	0.07
b	0-30	0.03	0.04	0.07
R	0-30	0.66	0.51	0.45
RMSE	0-30	0.03	0.01	0.04

the PI it is possible to self-calibrate the data, whereas the dependence on the incidence angle is increased. Even though both areas analyzed were quite homogeneous, the two instruments were not looking at the same type of land surface cover due to differences in their pixel size. Moreover, the footprint size of the GNSS-R technique, and the sample interval is such that measurements taken every second are nearly independent, as there is only a 10% overlapping factor among pixels. However, this is not the case with microwave radiometry data, since the pixel size is such that they are partially overlapped (50%), and consequently correlated.

8.1.4.1 Sensitivity to Incidence Angle and Surface Roughness

It has been shown that independently from the land cover, the group of reflectivity values with incidence angles ranging from 30° to 50° has larger correlation with both the $I/2$ and the PI than those below 30°. This indicates that mainly surface roughness, and with less importance vegetation structure and its water content, might have to be dealt with when trying to retrieve geophysical parameters such as soil moisture. For very large incidence angles (larger than 50°), the coherent component is the dominant component in the scattering process [37, 93, 105, 110, 148], unless the surface is very rough, where the coherent component finally disappears [97, 149]. For incidence angles from 30°–50°, the coherent component dominates in most regions, except in some highly vegetated regions or with high topography. For low incidence angles (lower than 30°) the surface roughness makes the coherent component decrease, and the incoherent component larger. Despite the coherent component is still measurable, its decrease is shown in the loss of correlation between the microwave radiometry and the GNSS-R data. Spaceborne data from the UK TDS-1 mission also supports that over land there is a coherent component present [79, 192], as the DDMs retrieved over land look like more to the WAF than to the sea surface (non-coherent) scattering model [52, 58, 193]. This is relevant because while the forthcoming GNSS-R satellite missions will have close to nadir-looking observations [194–196] mainly due to the antenna directivity requirements, results from field campaigns indicate that for GNSS-R scatterometry it may be useful to observe more slant angles, where the coherent scattering component becomes larger. Also, a way to take into account and correct the surface roughness effect is the use of the polarization ratio, as depicted in Chapter 4 and proposed by [148].

8.1.4.2 Land Cover Effects

In this work two different regions have been analyzed: a grass-land area, and a crops area. The crops area is normally a more regular area, and all fields have similar vegetation height and structure. Conversely, the grass-land is a vegetated area with different vegetation heights and some patches of bare soil. Surprisingly, whereas a crops area is vegetated and the grass-land area can vary its conditions, but it is normally low vegetated, the correlation between GNSS-R data is larger for the crops area than for the grass-land area. This occurs because unless the crops area has plants with very high vegetation water content, the L-band microwave GNSS waves pass trough vegetation and impinge on the ground beneath them. In those cases, the land surface is normally flatter and more regular than for the grass-land area, where there are more irregularities, or at least this was the case of the field campaign test sites. So, the reflection over the crops area is more coherent than over the grass-land area, and this is seen in a larger correlation between reflectivity, $I/2$ and PI parameters for the crops area. Furthermore, it must be considered that the roughness affecting L-band is the large scale roughness, referring that also to the surface's slopes instead of only the surface heights RMSE.

8.1.4.3 Sensitivity to Pixel Size

The difference in the pixel size of the two instruments also plays a role in the data analysis performed. This effect is better seen in the two examples shown in Fig. 8.11. Therein, the reflectivity measurements from LARGO are plotted with small circles whereas the T_{BH} measurements from PLMR are written as colored text. Both measurements have been plotted over Google Earth interface. Figure 8.11(a) shows how a water spot is detected as a bright reflectivity, whereas the water body is not present in the Google Earth Map. The T_{BH} for the left beam ($\pm 38^{\circ}$) reduces, but it never reaches the water value ($\approx$ 100 K) because of the beam filling factor. The water spot sensed by the GNSS-R instrument is at most 150 m size (2.5 reflectivity pixels), whereas the microwave radiometer resolution for that beam is 153 m x 73 m at 220 m height. So, due to the beam filling factor, the T_{BH} observed is a mixture of the one coming from the water spot and the surrounding land, and due to that it never reached the $\approx$ 100 K. Note that in the same figure, the right T_{BH} PLMR beam also reduces, which occurs again due to the pixel size and the beam filling factor effect. It is also noticeable that PLMR data varies more smoothly whereas there is a sharp transition in the GNSS-R data. This shows some time correlation for the radiometer data which is not present on reflectivity data. This can also be understood as the difference in the pixel overlapping factor between the two techniques. Figure 8.11(b) shows a similar effect with a much smaller water area ($\sim$ 30 m x 30 m) detected over Google Earth, which is clearly seen in the GNSS-R data while the radiometer data only decreases 10 K. This effect is also related to the RMSE of the fits proposed, because the reflectivity data has stronger variations than the T_B data and adds some noise to the correlation curves, explaining the large RMSE observed.

Table 8.5 compares the different ground resolution (pixel size) for both instruments at different heights: 220 m and 1 km, which would correspond to normal flight heights during airborne campaigns, and 630 km for spaceborne conditions (UK TDS-1 mission parameters). The antenna beamwidth of the PLMR has been preserved for the data

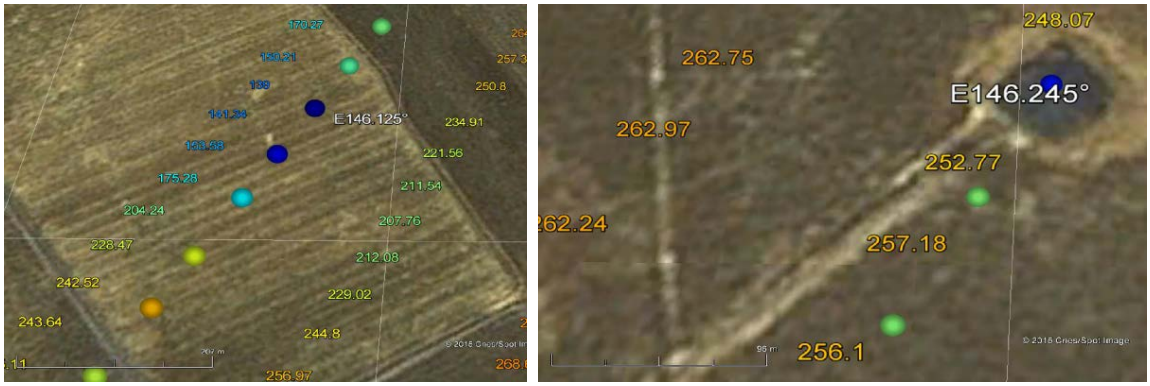

(a) **(b)**

Figure 8.11: Effect of the pixel size in the comparison among reflectivity and microwave radiometry data.

shown in that table in all conditions. For very low heights, such as 220 m, the ground-resolution of the reflectivity data is approximately half of the pixel size for the radiometry data in the along-track direction, and 1/10 in the across-track direction. For intermediate heights, such as 1 km, the ground resolution of the reflectivity data is between 1/4 and 1/5 the pixel size of the radiometry data in the along-track direction, and 1/20 in the across-track direction. For the spaceborne conditions the reflectivity data pixel size is much smaller than the radiometry data, specially for the across-track direction due to the integration time.

Also if a microwave radiometry spaceborne mission with different antenna parameters is considered, such as the SMOS mission (a ground spatial resolution of 40 km x 40 km roughly), the reflectivity data pixel size is also much smaller than the radiometry data, leading to the concept of spatial resolution enhancement, which would be of particular interest for spaceborne applications. Furthermore, differently from other synergy techniques [178–180, 191], in this case, both techniques work at very close frequency bands, which means that they are sensitive to the same geophysical parameters. This idea of down-scaling microwave radiometry data with GNSS-R data has been proposed recently by NASA, after the end of operations of SMAP radar [197].

8.2 Salamanca Field Experiment

The field experiment took place in an agricultural area near the *Guareña* River, tributary of the *Duero* River in the center of the Iberian Peninsula (5.36°W; 41.30°N). The main land use was vineyard (100 ha), but some areas of pasture, fallow, irrigated crops, and forest were also present (see Fig. 8.12). Two different flights were conducted: one on August 6, 2014, and another one on August 7, 2014. Both flights height was between 500–700 m, and they lasted from 8 AM to 10:30 AM. During the first flight, field measurements of soil moisture (0–6 cm depth) and surface temperature were taken at 119 ground points, which is depicted by Fig. 8.12. The probes were inserted vertically into the soil and the

Table 8.5: Comparison of the ground resolution for both sensors at different flight heights and speeds. The incidence angle is measured in degrees, the height in meters, the speed in m/s, and the resolutions in m x m

Sensor	θ_{inc} [°]	**Height** [m]	**Speed** [m/s]	**Inst. Res.** [m x m]	**Integ. Res.** [m x m]
LARGO	± 8	220	61.1	6.6 x 6.6	67.7 x 6.6
PLMR	± 8	220	61.1	58.2 x 58.7	119.3 x 58.7
LARGO	± 21	220	61.1	6.8 x 7.2	67.7 x 7.2
PLMR	± 21	220	61.1	61.7 x 66.1	122.8 x 66.1
LARGO	± 38	220	61.1	7.4 x 9.3	68.5 x 9.3
PLMR	± 38	220	61.1	73.1 x 92.8	134.2 x 92.8
LARGO	± 8	1000	61.1	14.0 x 14.1	75.1 x 14.1
PLMR	± 8	1000	61.1	264.4 x 267.0	325.5 x 267.0
LARGO	± 21	1000	61.1	14.4 x 15.4	75.5 x 15.4
PLMR	± 21	1000	61.1	280.4 x 300.4	341.5 x 300.4
LARGO	± 38	1000	61.1	15.7 x 19.9	76.8 x 19.9
PLMR	± 38	1000	61.1	332.2 x 421.6	393.3 x 421.6
LARGO	± 8	630000	$6{\cdot}10^3$	351.3 x 354.8	6351.3 x 354.8
PLMR	± 8	630000	$6{\cdot}10^3$	166554.5 x 168191.3	172554.5 x 168191.3
LARGO	± 21	630000	$6{\cdot}10^3$	361.8 x 387.6	6361.8 x 387.6
PLMR	± 21	630000	$6{\cdot}10^3$	176667.8 x 189236.8	182667.8 x 189236.8
LARGO	± 38	630000	$6{\cdot}10^3$	393.8 x 499.7	6393.8 x 499.7
PLMR	± 38	630000	$6{\cdot}10^3$	209303.7 x 265610.3	215303.8 x 265610.3

measurement integrates the soil water content of the first 6 cm of the top layer. Four measurements were acquired at each location within an area of 1 m^2 and geolocated in the field using a Differential GPS (D-GPS) [198] instrument. Surface soil temperature was also measured with an infrared thermometer TFA-ScantTemp 380 [191].

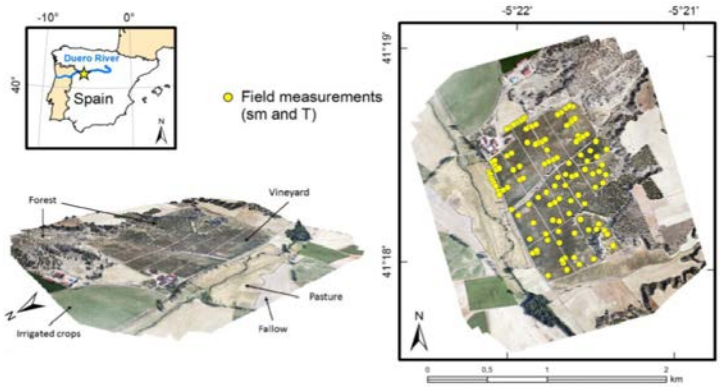

Figure 8.12: Description of the Salamanca field campaign test site [191].

One thing that has not been mentioned up to now is how the LARGO can differ whether it is locked to the direct or the reflected signal. The antenna has not an infinitely large ground-plane, and due to that, there can be some leakage of the direct signal from

the back of the down-looking antenna. If the reflected signal power is too small, the instrument will see this leakage larger than the reflected signal, and therefore, get locked to it. As it operates in a closed-loop mode, once the loop is locked, it is very difficult to get out of it, and this problem was only faced once in all the experiments shown in this dissertation, and it was on this field campaign. Figure 8.13 pictures the problem just by observing the height measurement of each high-performance GPS receiver back-end. Whereas for August 6, 2014, the LARGO instrument worked properly, while rising the height the direct channel measures an increase of the height and the reflected channel a decrease (Fig. 8.13(a)), for August 7, 2014, they follow the same height retrieval, which indicates that both were locked to the direct signal. Therefore, refectivity measurements for August 7, 2014, are not valid. The reason why when the platform is going up the direct signal should measure a rise in the height estimation and the reflected signal a decrease in it is depicted clearly in Fig. B.1. Furthermore, it is possible to see in Fig. 8.13(a) that on August 6, 2014, the platform did one part of the field campaign, it landed to refuel, and it continued with the second part of the flight. Note that the city of *Salamanca* is already 700 m above the sea surface level, and the GPS receivers always measure their height estimation with respect to a reference ellipsoid, typically the WGS84.

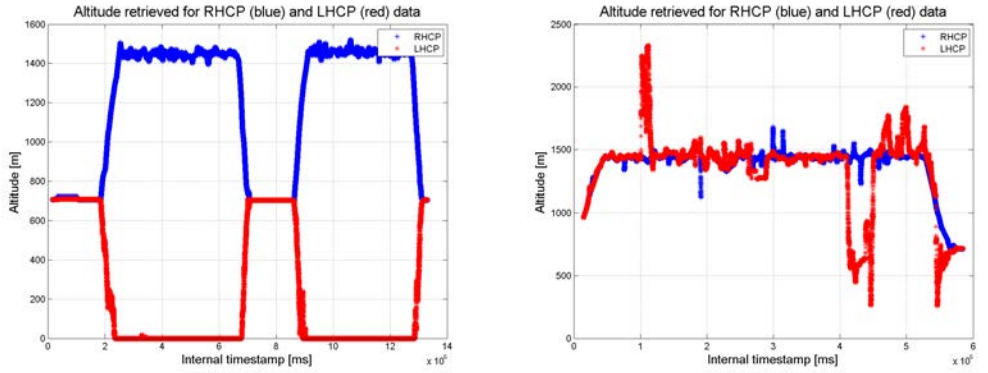

(a) **(b)**

Figure 8.13: Height measured by each LARGO channel. (a) August 6, 2014, (b) August 7, 2014.

The goal of this field campaign was to test a new approach to enhance the reflectivity provided by LARGO using thermal and multi-spectral maps. The flights were performed using a manned aerial platform, a paramotor, as can be seen in Fig. 8.14. Therein, it is observed that there were different payloads: LARGO to measure coherent reflectivity, a Flir thermal camera to measure surface temperature, an optical Canon EOS 5D camera, and a multi-spectral camera. The flight on August 7, 2014, was conducted because the multi-spectral camera did not perform as expected on the August 6, 2014, flight. Disappointingly, the issues with the multi-spectral camera were not solved, and the LARGO data for that day was not valid too. However, a LANDSAT pass on August 12, 2014, helped to achieve the goal of that field campaign. In this part only the reflectivity estimation will be explained, as due to the the type of platform used and the severe topography conditions of the field, extra corrections were developed. However, a summary of the

results achieved in this collaborative work is also presented here. Finally, it is worth mentioning here that the campaign results suggested that the combined use of optical, near-infrared, and thermal data with the GNSS-R signal improves the sensitivity to soil moisture obtained with each of the sensors separately.

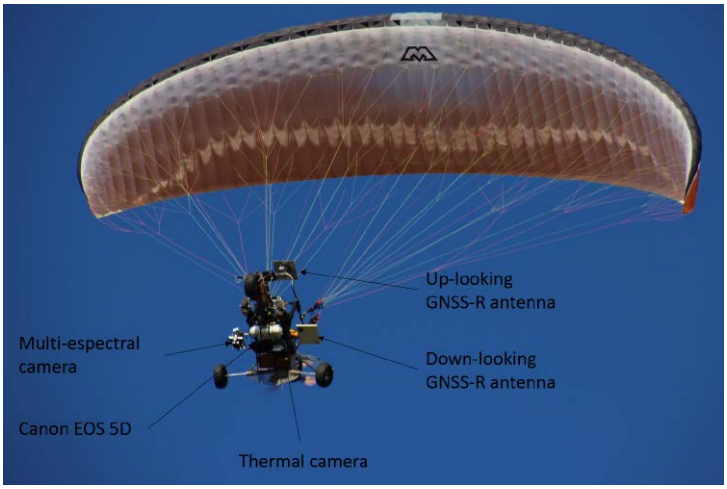

Figure 8.14: Platform and payloads used for the field campaigns.

8.2.1 Reflectivity Estimation

An airplane platform is a very steady platform when it is flying horizontally, with roll and pitch values very small during those periods. However, while turning, the roll of the plane is very high to do the maneuvering quick enough. In the GELOz field campaigns those data were discarded. Differently, a paramotor is a manned platform whose speed is much lower than an airplane, but its local movements are much larger. Due to being hold by a wing, the platform faces a continuous oscillatory movement. So, the reflectivity for this field campaign is equal to the GELOz field campaigns, but adding an antenna pattern compensation mechanism which is required to compensate for this pendulum movement. Basically, it is required to find the new spherical coordinates from where the radiation is coming in the antennas reference frames. The antenna pattern compensation applied is a little bit tedious and it is mathematically detailed in Appendix F. It is based on a coordinate transformation. Two different coordinate systems must be taken into account, a fixed one and an inertial one, and the inertial system is moved with respect to the fixed one the rotations the IMU measures. Then, it is necessary to compute the new antennas reference frames in the Global Cartesian System (GCS) coordinates and finally retrieve its spherical coordinates. Once the spherical coordinates on the antennas reference frames have been computed, the antenna pattern compensation coefficients, which are $(APC_{up}(\theta_{up}, \varphi_{up}))$ and $(APC_{down}(\theta_{down}, \varphi_{down}))$, can be retrieved from the antenna radiation patterns measured at the UPC anechoic chamber [155], and the antenna radiation pattern compensated reflectivity becomes:

$$\Gamma = SNR_L - SNR_R - k_{calib} + APC_{up}(\theta_{up}, \varphi_{up}) - APC_{down}(\theta_{down}, \varphi_{down}), \quad (8.11)$$

where k_{calib} is a compensation term estimated during the calibration phase if there is a calibration matrix installed in the LARGO instrument, which was the case of this field campaign.

Apart from the antenna pattern compensation, it was found that the correlation between the reflectivity estimated by LARGO and the Digital Surface Model (DSM) of the field campaign was on the order of 0.6, which indicated that topography is affecting largely the measured reflectivity. This fact was already stated in [199]. The initial geolocation was made via ray-tracing as described by Eqn. (8.6b). This correlation is qualitatively pictured in Fig. 8.15.

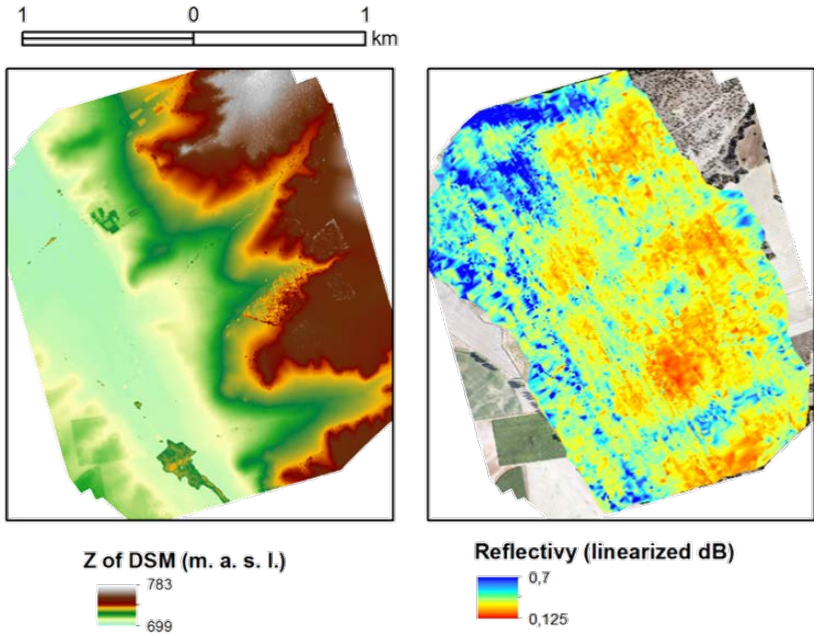

Figure 8.15: Qualitative correlation between DSM and LARGO reflectivity.

In order to reduce this effect, a geolocation algorithm based on specular reflection conditions is applied. For each platform position, the surface under observation is discretized and the surface normal is computed for each point, which is named as $\hat{n}$. Also for each surface point the vector from the surface point to the platform is computed ($\hat{R}_{pr}$). The last vector taken into account is the vector from each surface point to the satellite, known as ($\hat{R}_{ps}$). Once this three vectors are known, three different conditions are applied:

$$\left(\hat{R}_{pr} \times \hat{R}_{ps}\right) \cdot \hat{n} = 0, \tag{8.12}$$

which ensures that the three vectors are on the same plane, and this plane is the incidence plane,

$$\left(\hat{R}_{pr} - \hat{R}_{ps}\right) \cdot \hat{n} = 0, \tag{8.13}$$

which checks that the local incidence angle and the local reflection angle are the same,

and

$$\hat{R}_{pr} \cdot \hat{R}_{ps} < 1, \tag{8.14}$$

which assures that both incidence and reflection angles are not physically the same, and that the geometry follows a forward scattering configuration instead of a backward one.

The effect of this topographic correction is depicted in Fig. 8.16, where in (a) it is seen that for a flat surface both approaches coincide, and for a rough surface (b) the specular reflection methodology is more accurate.

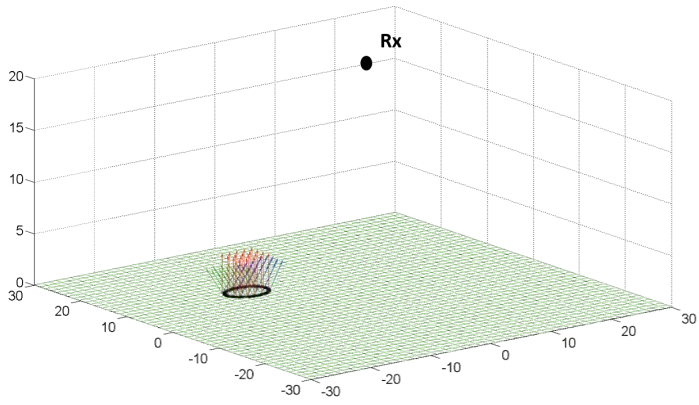

(a)

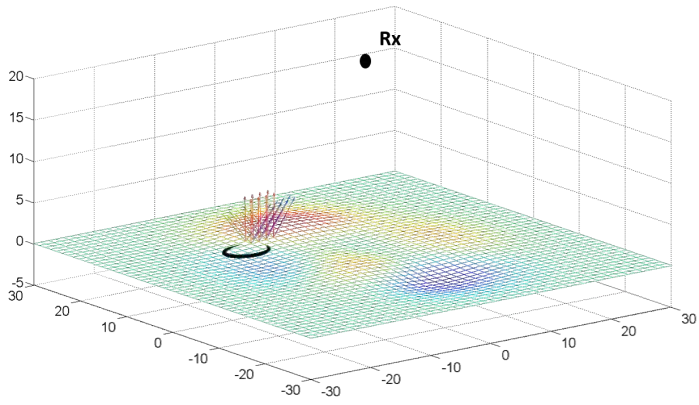

(b)

Figure 8.16: Comparison between the ray-tracing geolocation using the first Fresnel Zone area and the specular reflection methodology proposed: (a) flat surface, (b) rough surface.

The central point of the new geolocated reflectivity is the average of the reflection points that accomplish the specular reflection conditions. This methodology also allows to determine if there can be more than one specular reflection areas, which in that case data must be discarded as it is not known if the addition of the radiation coming from

each area was constructive or destructive. A drawback of this methodology is that it must be computed for each platform position, which makes the geolocation a lengthy and tedious process and it is not recommended unless the field site requires it, which happened with the *Salamanca* field campaign. This methodology lowered the correlation between the DSM and the newly geolocated reflectivity to 0.05. The entire topography based geolocation algorithm is detailed in Appendix G. Note that in [199] it was already mentioned that topography is an issue to deal with and it affects severely the reflectivity values.

8.2.2 Summary of Correlation Results with Thermal and Multi-Spectral Data

A preliminary analysis of the data from the field campaign was presented in [200]. Therein, it was first mentioned that topography should be corrected for the retrieval of geophysical parameters. Also it was shown that the field test site had such a high topography that even soil moisture was also negatively correlated with the topography, both the Digital Elevation Model (DEM) and the DSM. In other words, the larger the elevation the lower the soil moisture content of the terrain. Even though they were correlated, the reflectivity should be corrected because some particular field test site parts suffered from slopes up to a 30% inclination.

After knowing that the data from the multi-spectral camera on-board the paramotor was useless, it was decided to use a LANDSAT overpass over that region corresponding to August 12, 2014. Using the data from LANDSAT, two different works were developed. In [201] a first approach to the correlation between soil moisture and all available data is presented. Different combinations of optical, Near InfraRed (NIR), Short-Wave InfraRed (SWIR), and Thermal InfraRed (TIR) indexes were tested, each of them indicating different parameters of the surface under observation. Ones were linked to the surface temperature, others to vegetation health, others to its opacity, etc. The largest correlations were found for the Green-Red Vegetation Index (GRVI)-based and Normalized Difference Water Index (NDWI)-based indexes. The comparisons with soil moisture were made at a point level with the in-situ ground-truth.

Finally, [191] analyzed much deeply the work presented in [201]. It proposed a linking model based on a linear combination of three parameters such as the Land Surface Temperature (LST), the LARGO reflectivity, and one of the derived indexes. In [191] it was proved that the combination of those parameters improved the estimation of the soil moisture content as compared to using themselves alone, reaching correlations up to 0.7 between the measured soil moisture and the estimated one. Half of the ground-truth points were used as testing for deriving the coefficients of the linking model, and the other half were used to validate the model proposed. This pioneering works have opened the door to pixel disaggregation algorithms using a similar to the one used with microwave radiometry and multi-spectral data [178–180].

8.3 Conclusions and Future Lines

This Chapter has first presented a comparison between airborne GNSS-R data and L-band microwave radiometry data, making use of three datasets from three different airborne field campaigns conducted over an experimental field site in South-Eastern Australia. In the field campaigns, a GNSS-R scatterometer (LARGO v1) and the PLMR L-band microwave radiometer flew together. In order to be able to compare the two datasets, linear polarization microwave radiometry data were converted to the first Stokes parameter divided by two. The PI was also computed from the brightness temperature measurements. Correlation results between both datasets for the three flights indicate that for large incidence angles ($> 30°$) the coherent microwave radiometry model behaves quite well, since the surface seems to be smoother, which is in accordance with the "Rayleigh criterion". Also, this indicates that the main dominating scattering mechanism for those incidence angles is the coherent one. For the crops region the correlation is between 0.74–0.8. For the grass-land region it is between 0.51–0.61. For lower incidence angles in the reflectivity data ($< 30°$), the correlation between reflectivity and $I/2$ is smaller, ranging from 0.64–0.69 for the crops region and 0.41–0.6 for the grass-land region. In those cases, the surface appears rougher due to the scattering geometry, and the incoherent component starts to be noticeable in the reflectivity data. Furthermore, if the surface appears rougher, the received reflected power is smaller, and reflectivity measurements are more affected by noise, which is translated in larger RMSEs for the proposed fits. The best correlation results were obtained when the coherent model works better (i.e. higher incidence angles), and occurred for reflectivity incidence angles ranging from $30°$ to $50°$ and the $\pm 38°$ beams for the crops region.

The differences between L-band microwave datasets and the GNSS-R datasets is discussed in detail. It is mainly focused in three aspects: incidence angle and surface roughness, land cover, and pixel size. Regarding the pixel size, it is seen that due to the scattering properties of GNSS-R, measurements are nearly uncorrelated among them, and the spatial resolution is smaller than the radiometer data. This shows that GNSS-R data is able to detect features not seen in the T_Bs measured, which means that both datasets can be used together to improve the spatial resolution of the brightness temperature data. Furthermore, correlation among both techniques indicate that they are sensitive to the same geophysical parameters.

In the second part of the Chapter the field campaign performed in *Salamanca*, Spain is described. In this case a paramotor was used as a platform, and the field test site had a highly developed topography. The behavior of the platform required the use of an antenna gain pattern compensation algorithm, which was necessary to correct for the induced oscillatory effect. The correlation between GNSS-R reflectivity and both the surface DSM and DEM led to the development of a new geolocation algorithm based on specular reflection conditions. Once those corrections were applied, data from that field campaign was compared against different indexes derived from the different spectral bands of the closest (in time) LANDSAT image available. A linear linking model was developed using data from the LARGO estimated reflectivity, the LST, and one of the LANDSAT derived indexes [191]. This linking model showed that the linear combination of those surface parameters improved the performance of the soil moisture retrieval that using them alone [191]. This is in agreement with the previous disaggregation algorithms

used to down-scale L-band microwave radiometry. The large correlation between L-band microwave radiometry and GNSS-R reflectivity might explain why the same approach (linear linking model) works correctly for both cases.

Looking to the retrieval of soil moisture from a spaceborne point of view, the results from the field campaigns analyzed show that L-band microwave radiometry data could be down-scaled using spaceborne GNSS-R data as they are largely correlated. Note that GNSS-R data is largely insensitive to any atmospheric issues or clouds, leading to improved spatial resolution L-band microwave radiometry derived products, which would be independent from weather conditions. Later, further disaggregation models based on other sensors can be applied to improve even more the spatial resolution of the derived products.

9

Chapter 9

Airborne experiments with open-loop receivers over land and sea

This chapter summarizes two field campaigns performed with receivers that use an open-loop approach to obtain the GNSS-R data instead of the closed-loop approach used by the LARGO receiver. The first field campaign is performed along the Catalan coast, uses the PAU receiver described in 5, and it includes the observation of a small part of land and mainly sea and coastal sea surface. The second field campaign is part of the work performed at NOAA, it uses the SiGe receiver developed at CU, and it was mainly developed over land in spite of a small transect over sea.

9.1 Introduction

This Chapter describes two different field campaigns performed using two different open-loop receivers over land and sea surfaces. The first field campaign described is one performed along the Catalan coast in 2012, using the PAU receiver described in Chapter 5. This field campaign was an opportunity flight used to test the performance of the first version of the PAU receiver which was basically a sampler. With this field campaign the statistics of the reflected signal described in Chapter 4, over land and sea surfaces, are demonstrated using experimental data. Due to the hardware implementation of the PAU receiver, the direct signal was also available, resulting in some basic altimetry results. The second field campaign described is one departing from Florida and landing in Oklahoma, and basically obtaining reflected signals over land. In this case, the direct and reflected signals are sampled by two different, but synchronized front-ends using the SiGe receiver [20]. Then, they are processed by a SW receiver developed at CU in order to obtain the waveforms. In this case, the statistics of the reflected signal over land are detailed using experimental data.

9.2 Analysis of the *Sabadell* Field Campaign

9.2.1 Field Experiment Description

The Sabadell field campaign was conducted on September 13, 2012 along the Catalan coast. Figure 9.1 shows a sketch of the approximate flight path followed for the entire field campaign that included departing from *Sabadell*, reaching *Mataró*, flying along the Catalan coast at least 15 km separated from the coast to assure only sea surface reflections, reach the town of *Cadaqués*, and then go back. The main idea of the Field campaign was to test the altimetric performance of the PYCARO receiver [29, 202], and the PAU instrument was added as an extra payload to test its behavior. Figure 9.2 shows the aircraft used and both direct and reflected antenna positioning on the plane. Specific structures were built to make the antennas parallel to the aircraft reference level and to avoid antenna pattern corrections.

Figure 9.3 shows a summarized block diagram of the instrumentation used with all the connections between them described. First, the signal from both direct an reflected signals is amplified after being acquired by their respective antenna. Then the signals are split using 3 dB Wilkinson power dividers. Each instrument receives on one channel the direct signal and on the other one the reflected signal. Both instruments are controlled by different laptops so once the signals are split the experiments can be considered totally independent. The power supply for all the instrumentation is taken from the airplane battery/alternator system. Using a sinusoidal wave generator connected to the airplane's power system the laptops and the PAU instrument are powered. The PYCARO and the amplifiers are powered by a 5 V power supply system that is connected to the signal wave generator. Due to power restrictions of the plane, the laptop connected to PAU instrument had to be disconnected as the primary experiment was the PYCARO one. The laptop connected to the PAU instrument configured the instrument in order to sample direct and reflected signals during 1 s (maximum memory of the PAU insturment) every 20 s,

Figure 9.1: Flight path followed along the entire field campaign.

Figure 9.2: Flight set-up for the entire field campaign where the position of the up-looking and down-looking antennas is highlighted. The hardware part was located inside the airplane.

and then transfer the sampled data to the laptop's hard drive. Due to the continuous transmission, the laptop's battery lasted only for 1 hour. However, there was enough time to reach the town of *Cadaqués*, allowing to acquire data from half of the experiment and reflected signals from both land and sea surfaces.

The GNSS satellite geometry for the entire field campaign is shown in Fig. 9.4, where it can be seen that the available satellites were the SV: 2, 12, 14, 21, 25, 29, 30, 31. It can also be seen that the ones within the antenna beamwidth ($\pm 50°$) were satellite 25,

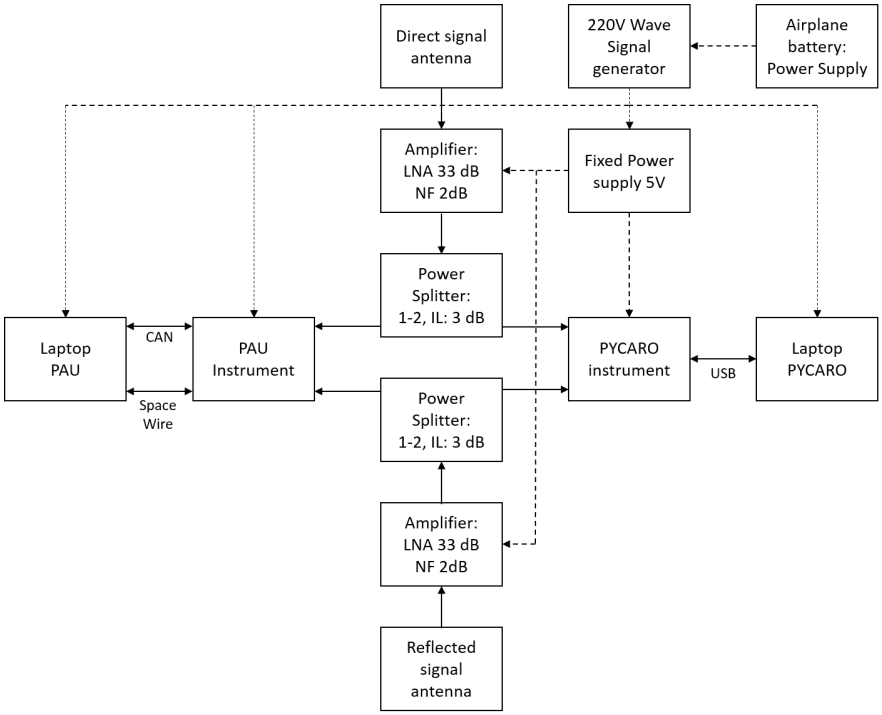

Figure 9.3: Block diagram of the instrumentation used.

29, 31, and 12 only for the beginning of the flight. Figure 9.5 shows the elevation angle of the aforementioned satellites as a function of time. The flight height was between 1–3 km, and the flight speed was between 50–80 m/s. The wind speed conditions for the sea surface were between 12–17 m/s.

The data sampled by the PAU instrument was processed off-line with a specifically designed SW receiver, since the hardware implementation of the DDM computation was not yet available at the time of conducting the field campaign. The SW receiver was based on generating the DDMs using 1 ms of coherent integration time and up to 1 s of incoherent averaging without using partially overlapped waveforms. The delay spacing was 244 ns (0.25 C/A chips) and the Doppler spacing 500 Hz. Those parameters were used to get an initial estimation of the delay and Doppler bins of the peak position. After that, the data were reprocessed again, but instead of computing the full DDMs only the waveform for the estimated Doppler was generated. By using the waveform peak information, the excess Doppler from the 500 Hz was partially estimated and also the retracking (τ) of the waveforms was computed. After that, a new set of retracked waveforms was generated storing them (matrix form) and also storing in smaller pieces of data their peak value (vector form). Figure 9.6 summarizes the SW receiver processing algorithm developed highlighting the two outputs. Once that was done, the statistics of the reflected field for both land and sea are shown.

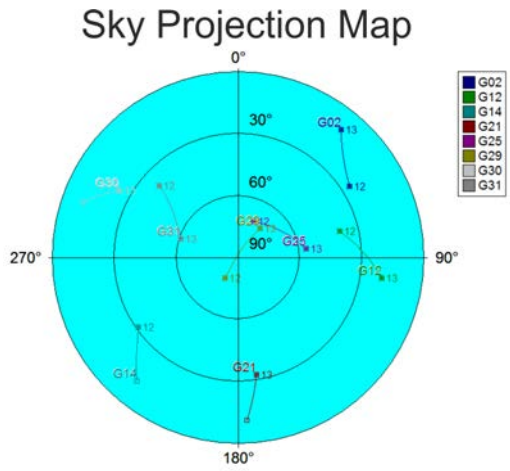

Figure 9.4: GNSS Satellite sky map for the *Sabadell* field campaign where the location of the satellites (elevation and azimuth) for the entire field campaign is shown. It summarizes the constellation geometry.

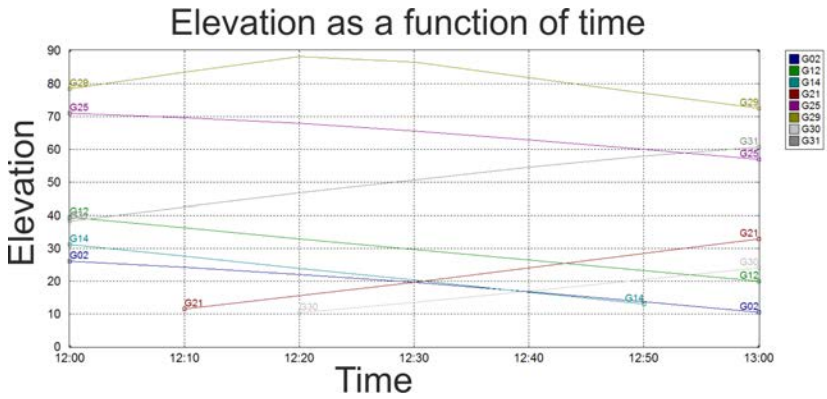

Figure 9.5: GNSS Satellite elevation angle [deg] as a function of time.

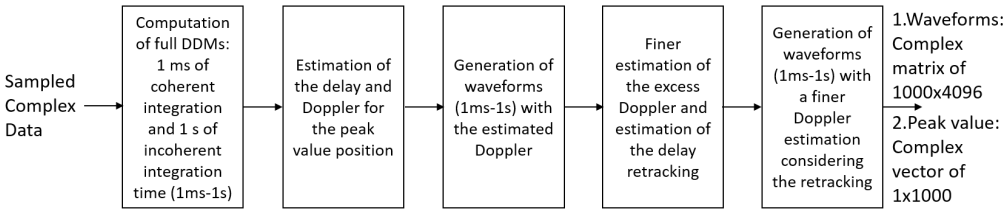

Figure 9.6: SW receiver processing algorithm for the PAU instrument.

9.2.2 Reflected Field Statistics Over Land for the *Sabadell* Data

In this subsection two different examples are shown. The first one corresponds to the reflected data over the airport, which is a flat area, and therefore with a coherent reflected component in the reflected signal. Figure 9.7 shows the 1ms-1s DDMs for all satellites in view reflected on that area. Particularly, it is interesting to look at Fig 9.7(f)–(g) where the WAF can be distinguished due to high thermal SNR. Figure 9.8 shows the I/Q diagrams for the peak value for those data. The ring shape is only clearly appreciated in Figs. 9.8(f)–(g) since the thermal SNR is high enough not to affect the signal statistics, and they resemble better the ideal theoretical developments mentioned in Chapter 4. As it can be inferred from the previous presented data, thermal SNR is important to observe the reflected field statistics and quantify the *speckle* noise. Figure 9.9 shows the pdf of the waveform peak amplitude (blue) as compared to a Rayleigh (red) and a Rice (black) fit. It is seen in Fig. 9.9(a)–(c),(f)–(g),(i) that the Rice fit resembles more to the experimental data pdf than the Rayleigh fit, indicating the presence of a coherent component due to the flat surface scattering mechanism. Conversely, Fig. 9.9(e),(h) have a very bad SNR (Fig. 9.7) which is why they resemble more to the Rayleigh distribution.

Differently, the second example is for rough land covered by a forest. It is seen there that the coherent component disappears, leading to a complex 2-D Gaussian random variables in the I/Q diagrams and to Rayleigh pdfs for the peak amplitude values. Figures 9.10–9.12 shows the same data than Figs. 9.7–9.9 but for the forest area. Herein, it is possible to identify that thermal SNR (relation between the DDM peak value and its noise level) is lower due to the scattering mechanism over the rough land covered by a forest (rough surface and lower reflectivity). The I/Q diagrams represent now the 2-D complex Gaussian random variable, highlighting the incoherent scattering as the main scattering mechanism (Fig. 9.11). Finally, the amplitude distribution of the waveform peak now resembles more the Rayleigh pdf, which in the end is a particular case of the Rice pdf when the coherent component is negligible (Fig. 9.12).

9.2.3 Reflected Field Statistics Over Sea for the *Sabadell* Data

Figures 9.13–9.15 show the DDMs for the sea surface scattering case in order to compare them to Figs. 9.7–9.12. Recall that the wind-speed conditions over the sea were between 12–18 m/s. First, it is possible to see that the dispersion of the I/Q diagrams shown in Fig. 9.14 is much larger than in Figs. 9.8 and 9.11, which occurs due to the larger reflectivity of the sea/water surface as compared to the land surface reflectivity. Also, it is seen in Fig. 9.14 that the pdf of the waveform peak amplitude resembles the Rayleigh distribution, highlighting the incoherent nature of the scattering process over the sea. Even though the scattering is mainly incoherent, Fig. 9.13(f),(g),(i) show the sidelobes of the signal WAF.

9.2.4 Comparison Between the Partially Coherent Land Scattering and Incoherent Sea Scattering

In order to better compare the effect of the coherent and incoherent nature of the scattering process Figs. 9.16–9.19 show the waveforms retrieved for the same satellite stacked.

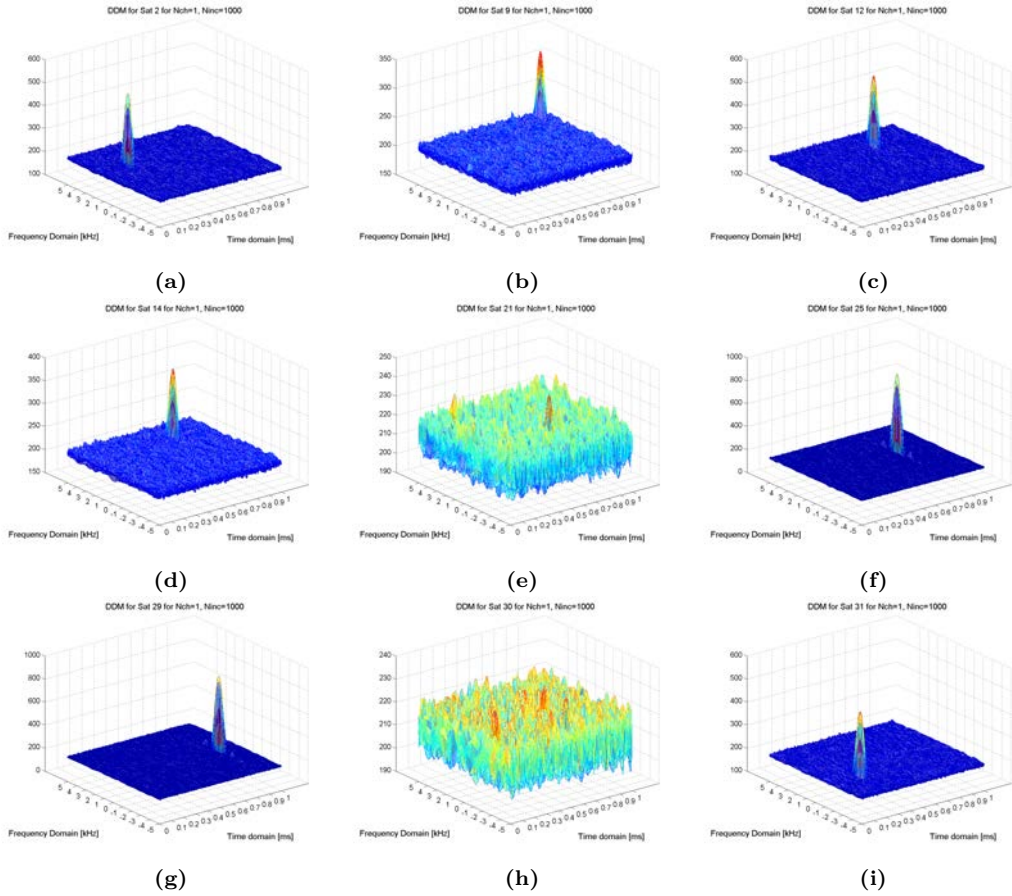

Figure 9.7: DDMs retrieved at 12h 00m 52s for all satellites in view using 1ms-1s. The scattering surface was flat land. (a) Sat 2, (b) Sat 9, (c) Sat 12, (d) Sat 14, (e) Sat 21, (f) Sat 25, (g) Sat 29, (h) Sat 30, (i) Sat 31.

Figures 9.16 and 9.18 show the waveforms stacked for 1 ms of coherent integration time and no incoherent averaging. Figures 9.17 and 9.19 show the same waveforms stacked using 1 ms of coherent integration time and 10 ms of incoherent integration time. Therefore, Figs. 9.16 and 9.18 contain 1000 waveforms, whereas Figs. 9.17 and 9.19 contain only 100 waveforms. The best comparison between the two scattering cases is obtained by looking to Figs. 9.16–9.19(f),(g), which are the ones with the highest thermal SNR due to higher elevation and therefore higher antenna gain. For the land case, a constant waveform amplitude is observed in the 1ms-1ms waveforms with some fading effects due to the thermal noise presence. One characteristic of this fading is that it does not totally cancel the signal presence. Therefore, the fading can be attributed to an additive noise such as the thermal. Apart from that, it can be attributed to the thermal noise because it is uncorrelated, while for that speed and height the speckle noise should be correlated as occurs with the sea case. For the sea case, the amplitude of the 1ms-1ms is larger due to larger reflection coefficient. Comparing them to the land case, there is a total cancel-

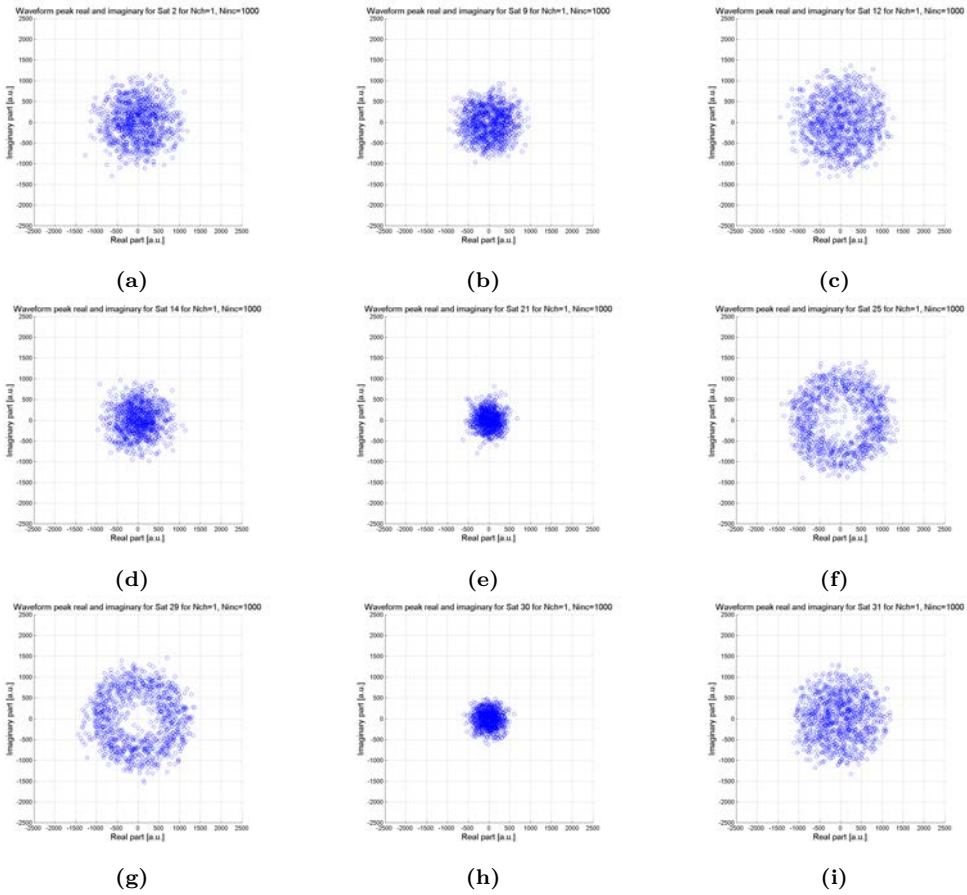

Figure 9.8: I/Q diagrams of the DDM peak for the data retrieved at 12h 00m 52s for all satellites in view. The scattering surface was flat land. (a) Sat 2, (b) Sat 9, (c) Sat 12, (d) Sat 14, (e) Sat 21, (f) Sat 25, (g) Sat 29, (h) Sat 30, (i) Sat 31.

lation of the signal amplitude due to the presence of *speckle* noise, which is also known as Rayleigh fading. Therefore, the fading can be attributed to a multiplicative noise. The 1ms-1ms waveforms are seen as bursts of signal coming and disappearing. However, this does not occur between consecutive waveforms and it is possible to appreciate this effect with the naked eye. This induces another concept which is that the *speckle* noise is, in this case, correlated, because the fading is not totally random and has a determined correlation time.

9.2.5 Altimetric Analysis of the Waveforms

The sampled data contains information from both the direct and reflected signals due to the coupler in the RF hardware design chain of the PAU receiver. However, the direct signal is highly attenuated because the coupling is 20 dB unbalanced, since for spaceborne

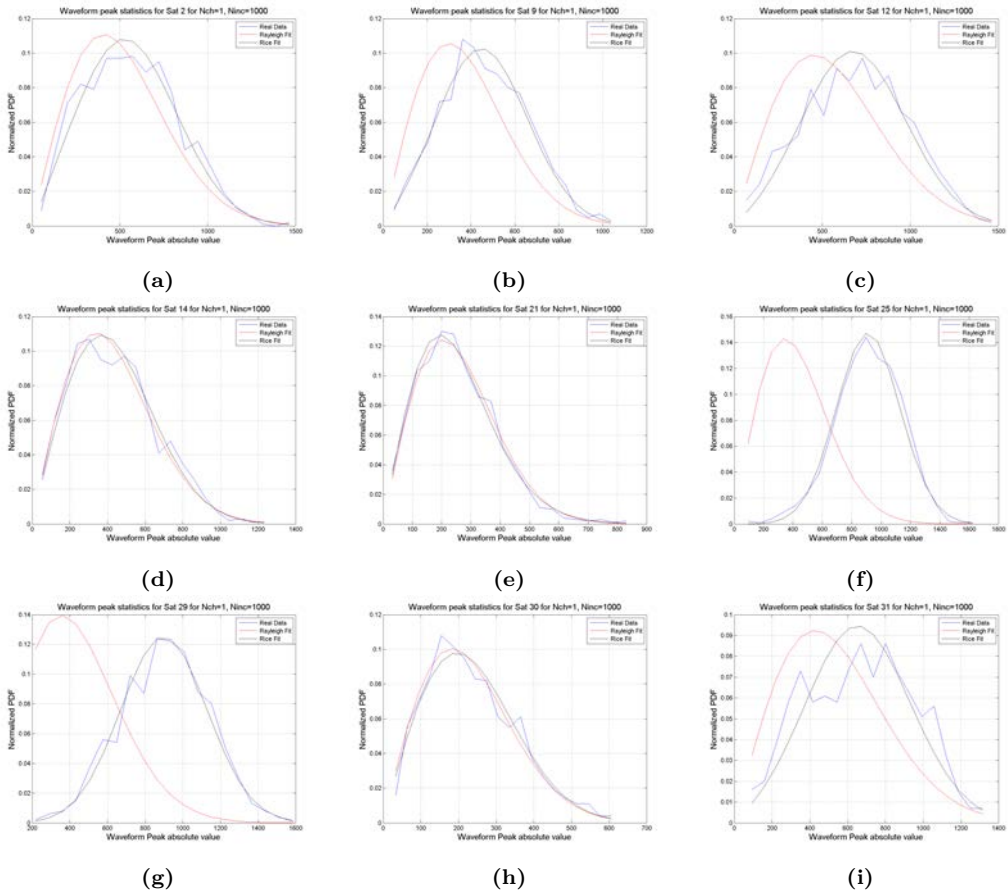

Figure 9.9: PDF of the absolute value of the DDM peak for the data retrieved at 12h 00m 52s for all satellites in view. The scattering surface was flat land. (a) Sat 2, (b) Sat 9, (c) Sat 12, (d) Sat 14, (e) Sat 21, (f) Sat 25, (g) Sat 29, (h) Sat 30, (i) Sat 31.

applications it is expected to received less signal power than for airborne applications. The presence of both signals may lead to the retrieval of sea surface altimetry by measuring the peak to peak delay between the direct and reflected signals. In [25] the altimetric performance of the PAU receiver for this field campaign was analyzed. Figure 9.20 shows the waveforms retrieved for the entire field campaign using 1 ms coherent integration time and 1 s incoherent integration time stacked one after the other. The separation between 1ms–1s waveforms is 20 s as was programmed by the PAU laptop. It is observed that the direct signal is much smaller than the reflected one due to the 20 dB coupling unbalance. A better view of this is depicted in Fig. 9.21 where 1ms–1s waveforms for satellites 29 and 31 are shown highlighting both the direct and reflected signals. It is noticeable that the curvature of the reflected waveforms trailing edge evidences the incoherent scattering mechanism and its sensitivity to surface roughness.

The time difference between direct and reflected signals can be related to the elevation

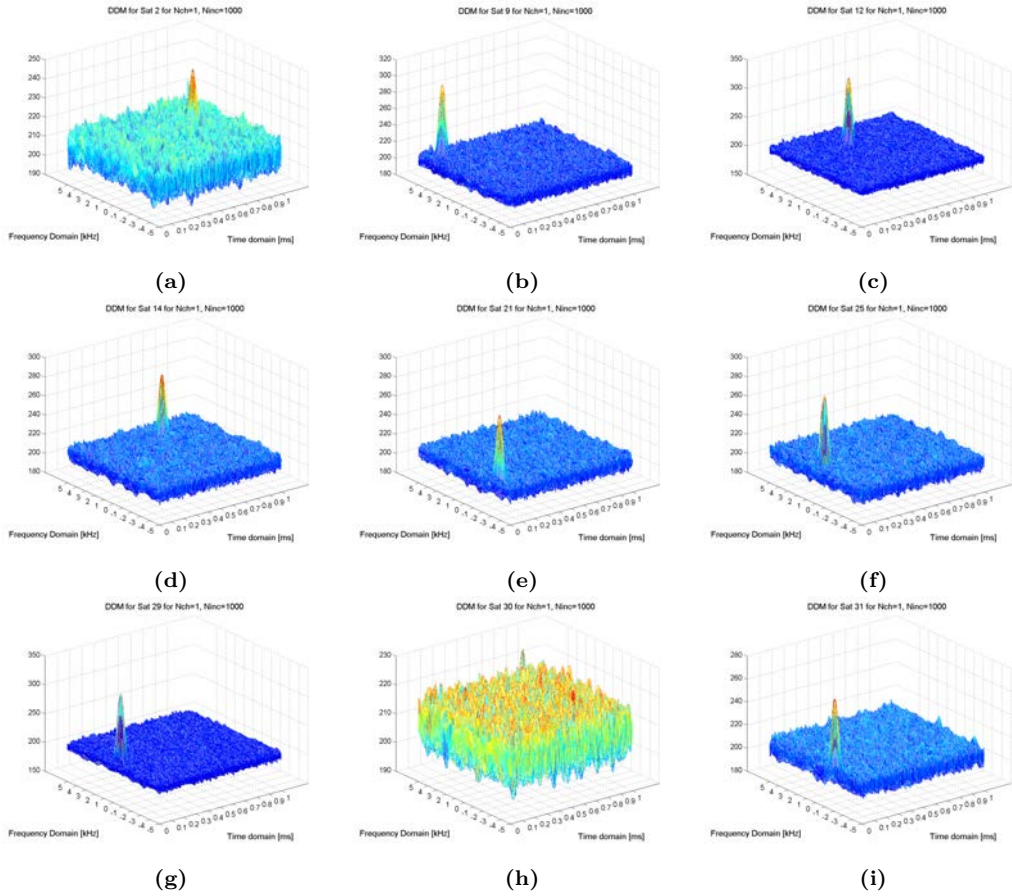

Figure 9.10: DDMs retrieved at 12h 06m 52s for all satellites in view using 1ms-1s. The scattering surface was rough land covered by a forest. (a) Sat 2, (b) Sat 9, (c) Sat 12, (d) Sat 14, (e) Sat 21, (f) Sat 25, (g) Sat 29, (h) Sat 30, (i) Sat 31.

of the platform/aircraft with respect to the surface where the signals are reflected as shown in Fig. B.1. Therefore, the delay between direct and reflected signals can be mathematically related to the platform height as:

$$\tau_{ref} - \tau_{dir} = 2hc \sin \theta_{elev} \tag{9.1}$$

where τ_{ref} represents the lag where the peak of the reflected waveform is, τ_{dir} represents the lag where the peak of the direct waveform is, h the platform height, c the speed of the light, and θ_{elev} the satellite elevation angle. Figure 9.22 shows the altimetric results for the three different satellites that fall within the antenna beamwidth, and compares them to the ones from a high precision GPS receiver inside the airplane. Even though the maximum derivative point should have been used for the estimation of the specular reflected signal lag (τ_{ref}) [62], due to the low power of the reflected signal the peak value has been used. This results in a bias between the true height and the one estimated using the GNSS-R altimetry algorithm. Also the height provided by the receiver is given

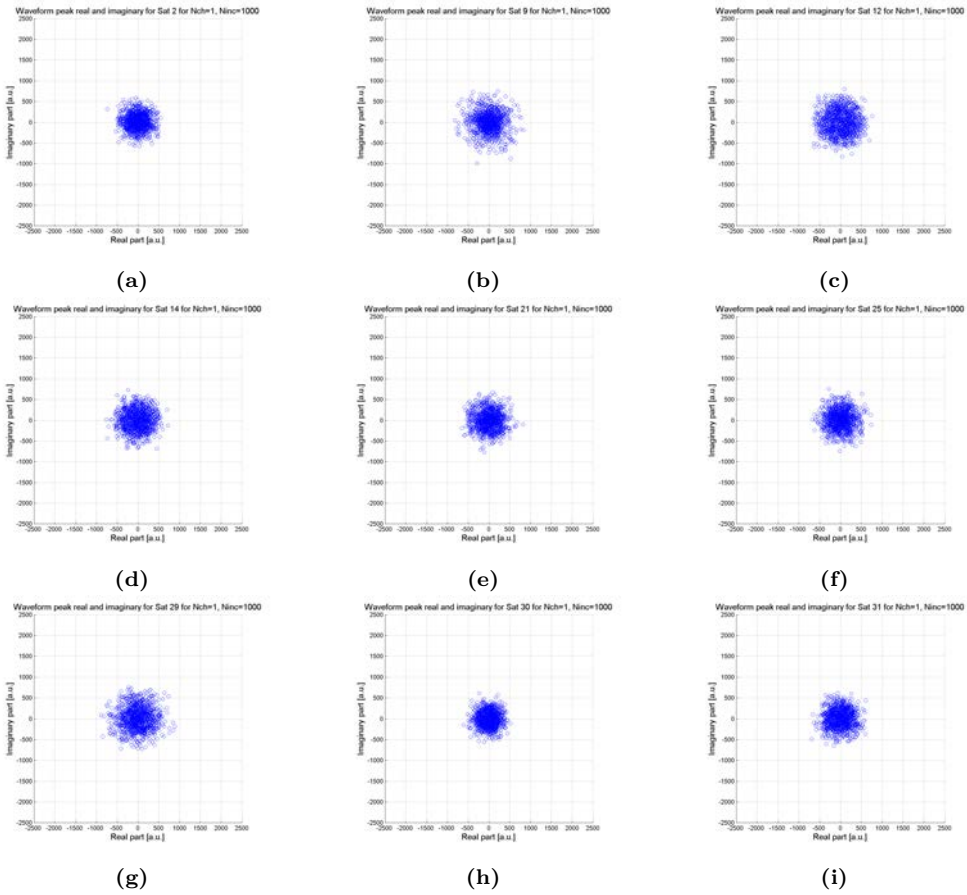

Figure 9.11: I/Q diagrams of the DDM peak for the data retrieved at 12h 06m 52s for all satellites in view. The scattering surface was rough land covered by a forest. (a) Sat 2, (b) Sat 9, (c) Sat 12, (d) Sat 14, (e) Sat 21, (f) Sat 25, (g) Sat 29, (h) Sat 30, (i) Sat 31.

with respect to the World Geodetic System 84 (WGS84), while the GNSS-R altimetry algorithm corresponds to the real distance with respect to the reflecting surface, which is the cause for differences between both datasets compared. Those are the main reasons for the bias observed between the high precision GPS receiver altimetry data and the GNSS-R data. However, they show a similar trend highlighting also some altimetric capabilities of the PAU instrument.

9.2.6 Summary

The Sabadell field campaign using the PAU instrument has experimentally demonstrated several issues of the reflected signals that were theoretically detailed in Chapter 4. First, the scattering from land can be coherent or incoherent depending on the surface roughness. When the coherent component dominates, a Hoyt vector for the reflected field is seen.

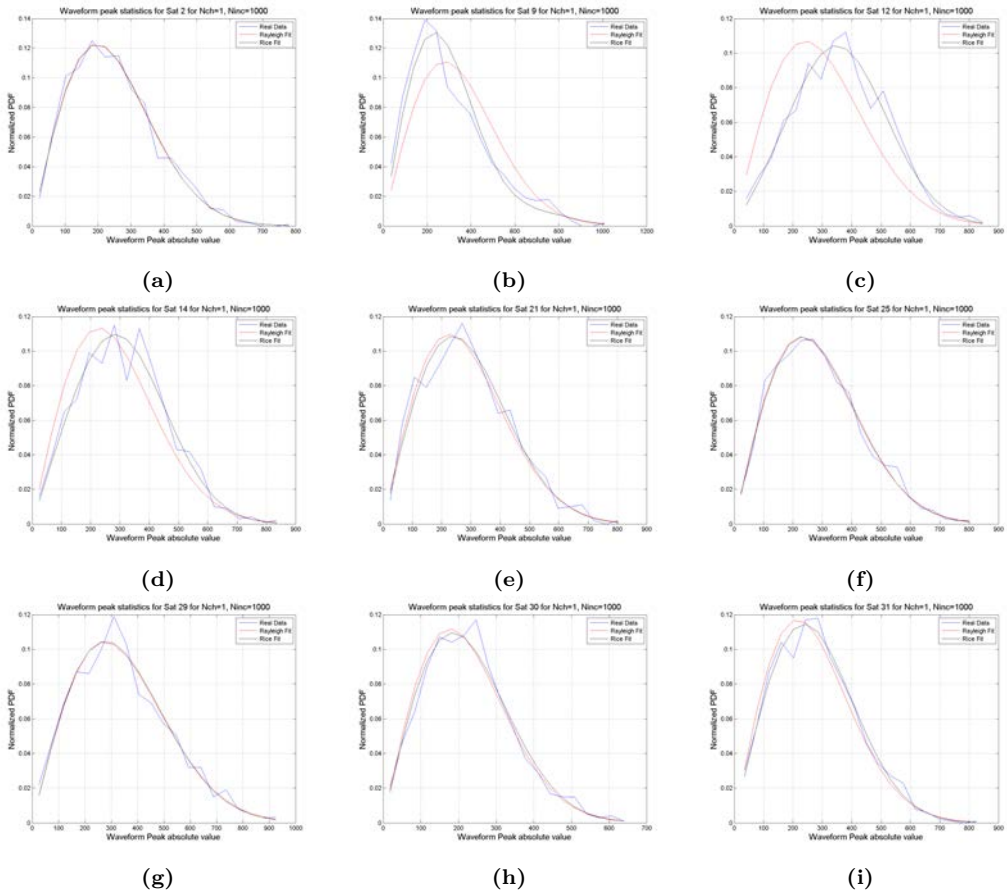

Figure 9.12: PDF of the absolute value of the DDM peak for the data retrieved at 12h 06m 52s for all satellites in view. The scattering surface was rough land covered by a forest. (a) Sat 2, (b) Sat 9, (c) Sat 12, (d) Sat 14, (e) Sat 21, (f) Sat 25, (g) Sat 29, (h) Sat 30, (i) Sat 31.

When the incoherent component dominates, a 2-D complex Gaussian random variable is seen. Depending on the amount of coherent scattering with respect to the incoherent one, the amplitude distribution of the reflected field resembles more a Rice distribution or a Rayleigh one. The amplitude of the sea surface reflected signals is larger than the one from land surfaces due to larger reflectivity. It is also seen the effect of the *speckle* noise on the reflected signals, specially on Figs. 9.16–9.19. Finally, the hardware design of the PAU instrument denotes some altimetric capabilities. The GNSS-R altimetric product obtained from the PAU instrument is compared against the GPS measured height showing the same trend.

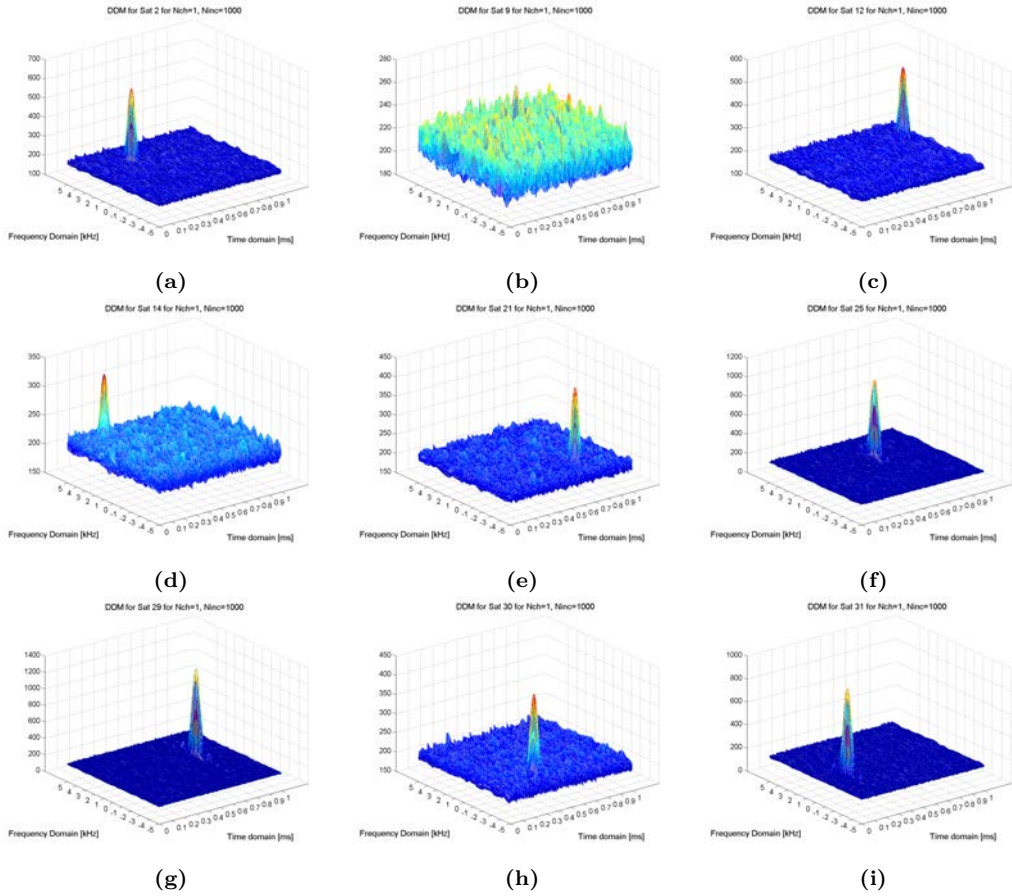

Figure 9.13: DDMs retrieved at 12h 40m 52s for all satellites in view using 1ms-1s. The scattering surface was relatively rough sea. (a) Sat 2, (b) Sat 9, (c) Sat 12, (d) Sat 14, (e) Sat 21, (f) Sat 25, (g) Sat 29, (h) Sat 30, (i) Sat 31.

9.3 Analysis of the Oct 19, 2009 NOAA flight

9.3.1 Field Experiment Description

The second field experiment described in this Chapter is a flight conducted on Oct 19, 2009. In that flight two synchronized SiGe receivers were the GNSS-R payload flown. One RHCP antenna looking to the zenith and one LHCP antenna looking to nadir were connected to each front-end. The system amplified and down-converted both signals to an IF of 4.1304 MHz prior to sampling. The sampling frequency of the system was 16.3676 MHz with 8 bits for each channel. Two files of 152 GB each were generated, corresponding to the direct and reflected channels. Those files were processed using the GNSS SW receiver and the GNSS Bistatic SW receiver, both developed at CU. The GNSS SW receiver was used only on the up-looking data (direct signal) and it was used to search for the GPS signals present on the sampled data, apply the Early-Promptly-Late (E-P-L)

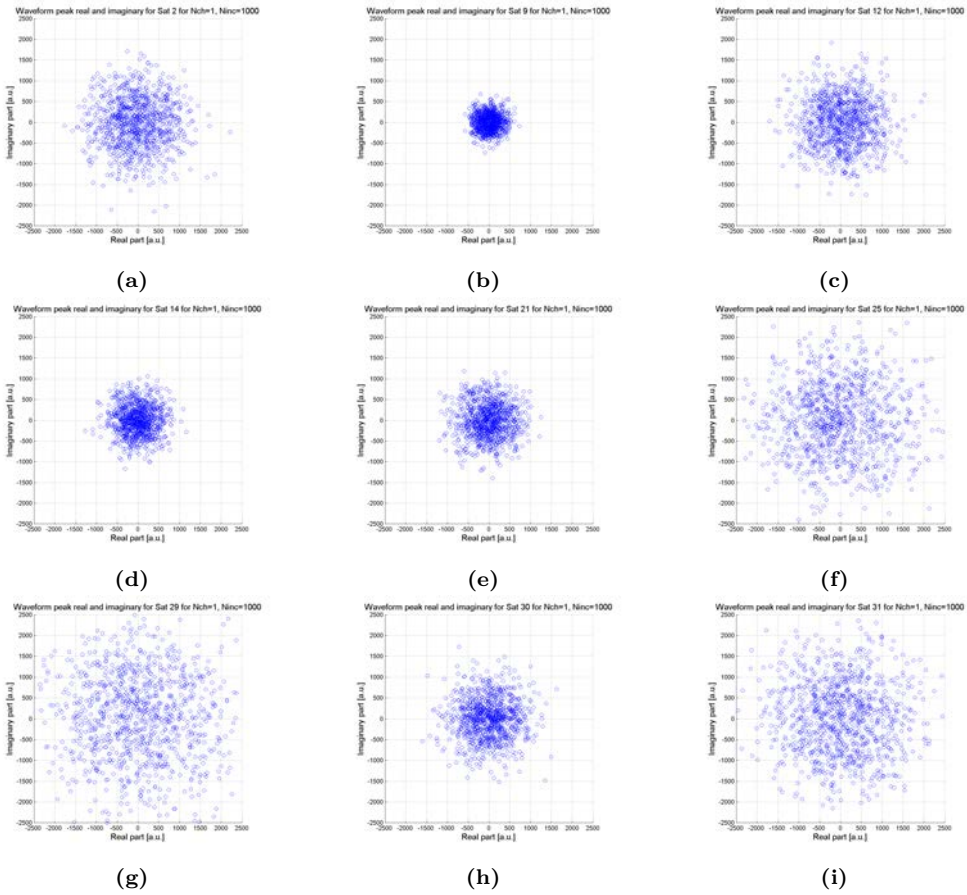

Figure 9.14: I/Q diagrams of the DDM peak for the data retrieved at 12h 40m 52s for all satellites in view. The scattering surface was relatively rough sea. (a) Sat 2, (b) Sat 9, (c) Sat 12, (d) Sat 14, (e) Sat 21, (f) Sat 25, (g) Sat 29, (h) Sat 30, (i) Sat 31.

correlation scheme to estimate the delay/pseudo-range to each satellite, and initiate the software navigation engine. This software was able to generate the standardized NMEA output that a conventional GPS receiver generates. From that output, a summary of the flight conditions was obtained and it is shown in Fig. 9.23. Figure 9.23(a) shows a summary of the flight path followed departing from Tampa, Florida, USA, passing above a coastal sea region, and then going back to land up to the Southern part of the state of Oklahoma. The platform position in Fig. 9.23(a) is marked in red finding some gaps along the trajectory. Those gaps occur because the number of satellites available was below four as can be seen in Fig. 9.23(d), and four is the minimum number of satellites required to obtained a position on Earth. Important cities such as Dallas and New Orleans are highlighted in white in order to better geo-reference the reader. As it can be interpreted by linking Fig. 9.23(a),(b), the sea surface scattered signals were obtained for an altitude of 2000–4000 m whereas the land scattered signals were obtained for an altitude of 13.5 km. The flight speed when the system was acquiring the sea surface

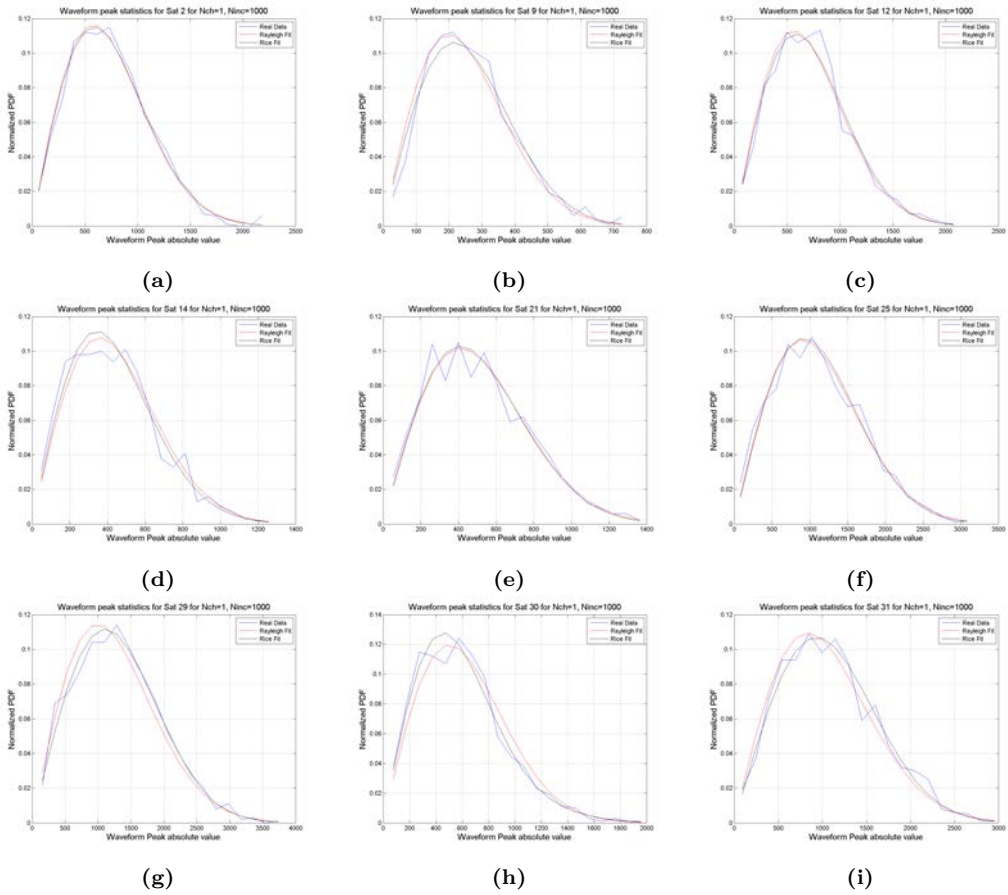

Figure 9.15: PDF of the absolute value of the DDM peak for the data retrieved at 12h 40m 52s for all satellites in view. The scattering surface was relatively rough sea. (a) Sat 2, (b) Sat 9, (c) Sat 12, (d) Sat 14, (e) Sat 21, (f) Sat 25, (g) Sat 29, (h) Sat 30, (i) Sat 31.

reflected signals was between 500 km/h and 700 km/h, whereas it was a little bit larger than 800 km/h when the system was acquiring the land surface reflected signals. The aircraft speed as a function of time is depicted in Fig. 9.23(c). Figure 9.24 shows the elevation (a) and azimuth (b) angles of the GPS satellites in view along the entire flight.

9.3.2 The GNSS Bistatic SW Receiver

Differently from the GNSS SW receiver, the GNSS Bistatic SW receiver used the two data streams (direct and reflected) in order to initiate the data processing algorithm. Each satellite was processed independently, so the same processing algorithm was applied to all satellites. The direct channel was first used to estimate its Doppler and lag due to higher thermal SNR for the selected SV. Subsequently, the reflected signal was converted to baseband and the Doppler was compensated using the one estimated from the direct

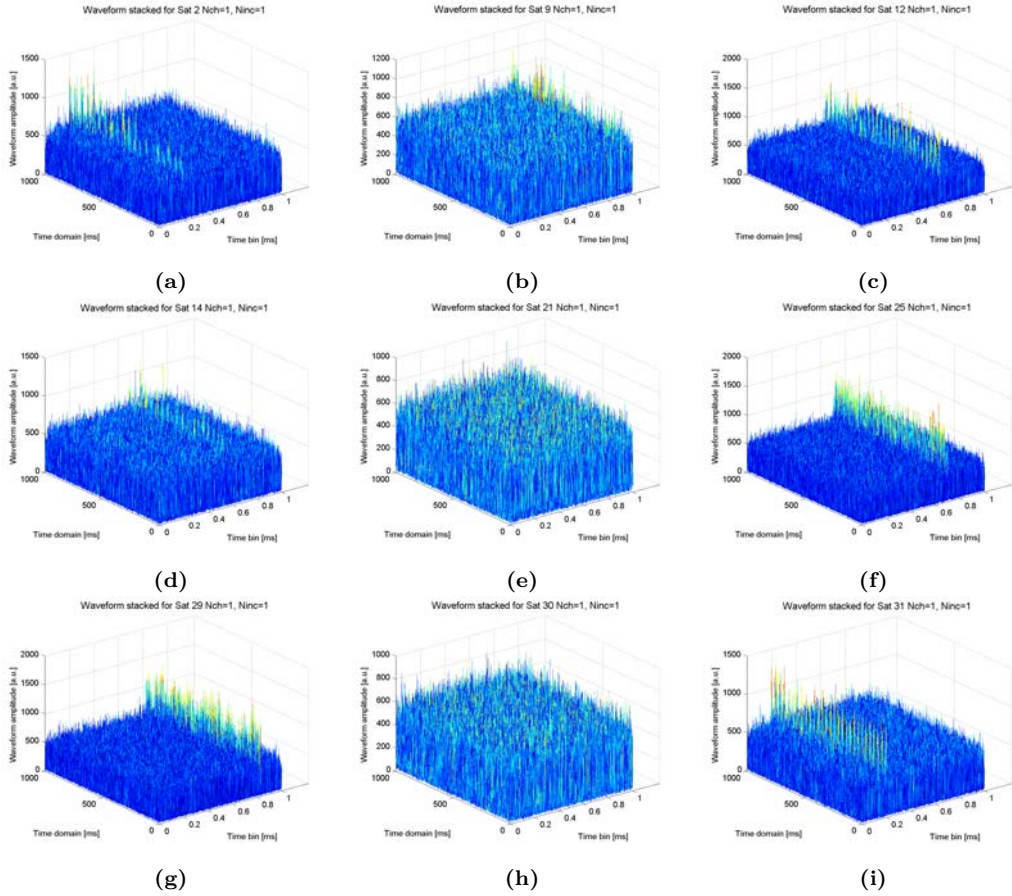

Figure 9.16: 1ms-1ms waveforms retrieved at 12h 00m 52s stacked as a function of time for the flat land scattering case.

channel. This could result in an excess Doppler for the reflected signal, but it was lower than the 1 kHz Doppler bandwidth of the system due to using 1 ms of coherent integration time. Then, a bank of correlators for different delay lags was defined, which started at -1.1 μs before the prompt lag of the direct signal and it ended at 101.1 μs lag with respect to the prompt lag of the direct signal. This is equivalent to approximately 30.000 m of delay range between the direct and reflected signals. If the maximum height is 13.500 m, then the round-trip for a satellite with an elevation angle of 90° would be 27.000 m, and it would be lower for lower elevation angles. Therefore, all possible lags where the reflected signal may fall were covered with the selected ending value of the bank of correlators. If the peak value for the reflected signal was detected, the correlation window was reduced and centered at the lag where the peak value of the reflected signal was found. The new tracking correlation window ranged from -5.1 μs to 10.1 μs, which implied reducing a factor of six the processing time. If the peak value was not detected, the entire tracking range was kept. After that, the GNSS SW receiver was launched for the direct channel data in order to estimate the platform position, time-tag the reflected data, and geolocate

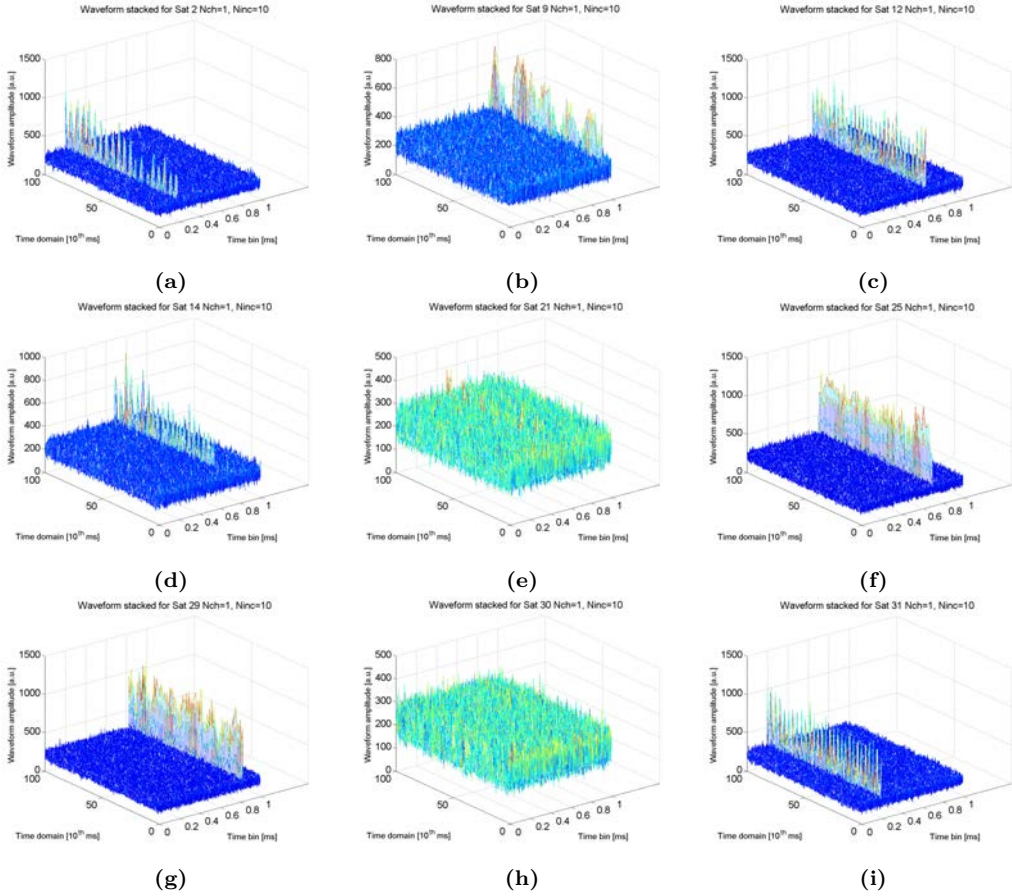

Figure 9.17: 1ms-10ms waveforms retrieved at 12h 00m 52s stacked as a function of time for the flat land scattering case.

it. Figure 9.25 shows a block diagram that summarizes the steps followed in the bistatic SW receiver.

9.3.3 Data Processing

Once the GNSS bistatic SW receiver was used on the sampled data to obtain the 1 ms waveforms for the direct and reflected signals, different steps were followed in the data analysis process. First, the direct waveforms were analyzed to check their validity and the correct performance of the tracking algorithm in the GNSS bistatic software receiver. Second, their peak was used to estimate the navigation data for each SV in view. The validity of the navigation message was analyzed by showing the I/Q diagrams generated by the samples. It was not necessary to interpret the data, just realize if it showed a BPSK modulation or not. Third, the thermal SNR of the direct data was estimated by estimating the K parameter of the Rice random variable formed by the direct signal and

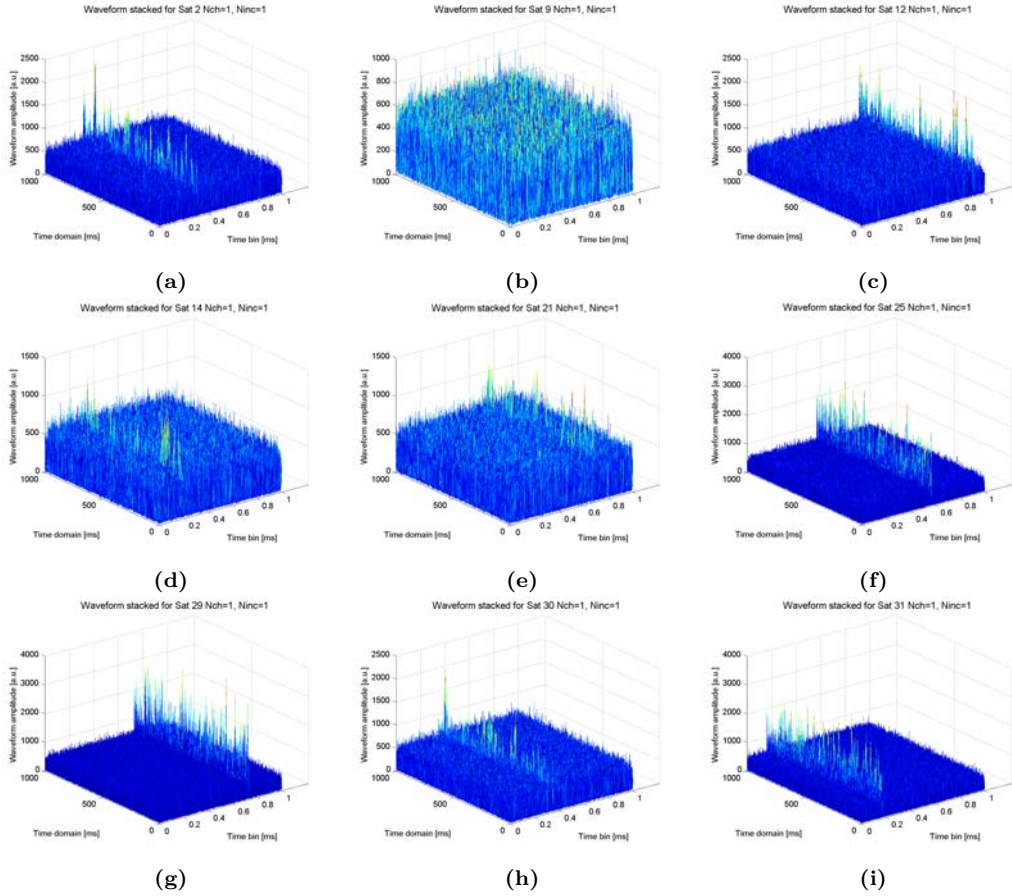

Figure 9.18: 1ms-1ms waveforms retrieved at 12h 40m 52s stacked as a function of time for the sea scattering case.

the thermal noise. The two methods proposed in Chapter 4 using real-value data and complex-value data were used, even though the complex-value data method was preferred since it works well independently from the SNR value. In this case, the thermal SNR could be estimated directly from the K parameter, because there is no *speckle* noise in the LOS transmissions. Fourth, the navigation data was used to compensate for the navigation bit change on the reflected signal just by multiplying each sample by the navigation bit sign, as suggested in Chapter 4. Fifth, the K parameter was also estimated for the reflected signal data using both real-value and complex-value data. In this case, the *speckle* noise was taken into account, and the K parameter and the reflected thermal SNR were highly different as it will be later seen. All K parameters for direct and reflected signals were estimated using 100 peak-value samples, which is equivalent to 100 ms. The following sections show the difference between the signals scattered over the ocean and over land in a similar way that was done with previous field experiment.

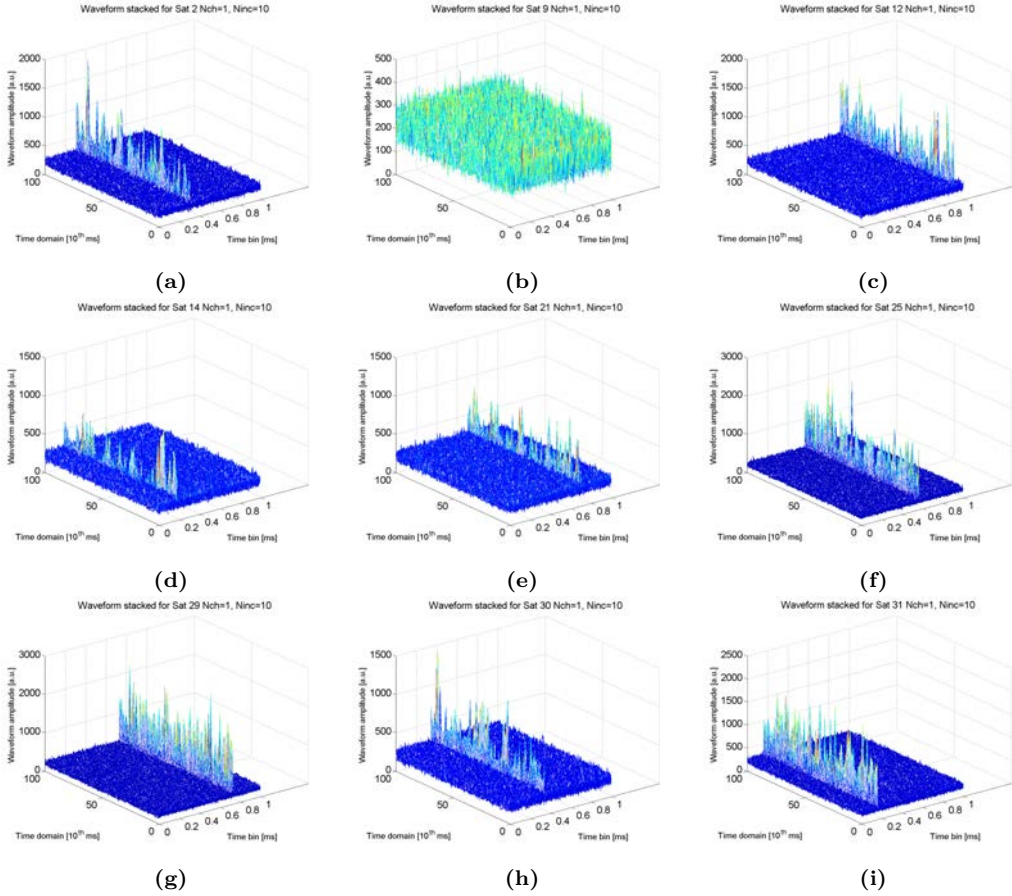

Figure 9.19: 1ms-10ms waveforms retrieved at 12h 40m 52s stacked as a function of time for the sea scattering case.

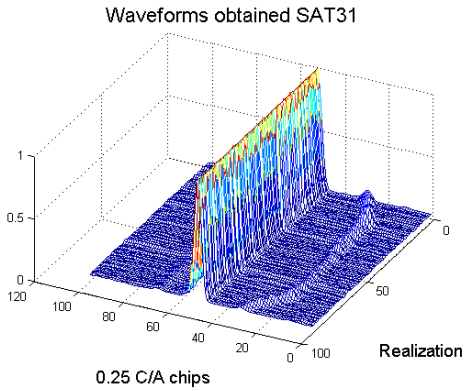

Figure 9.20: 1ms-1s waveforms stacked for the entire field campaign.

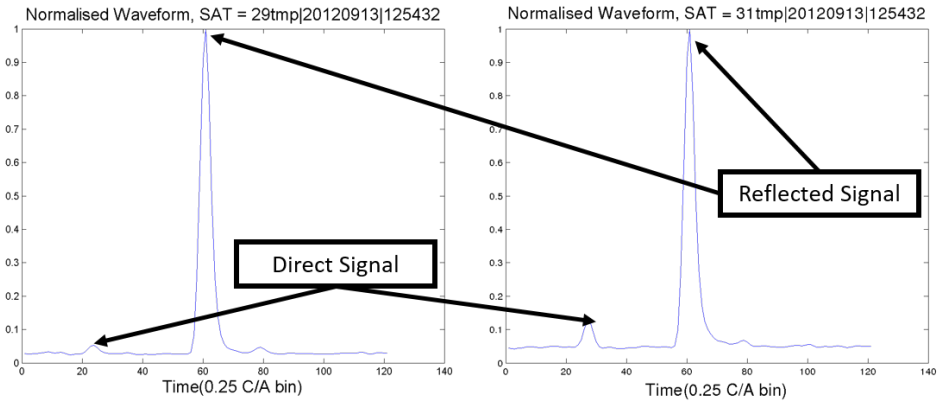

Figure 9.21: Example of two independent waveforms from satellites 29 and 31 highlighting the presence of direct and reflected signals.

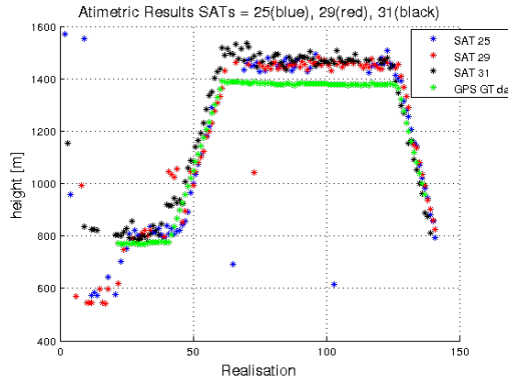

Figure 9.22: Summary of the altimetric results for satellites 25, 29, and 31, which are the ones on the antenna beamwidth.

9.3.4 Sea Surface Reflected Data

The sea surface data gathered corresponds to data from 15:07–15:08. Figure 9.26 shows the 1ms-1s waveforms retrieved for SV 13, 19, 23, 25, which were the ones that fell within the antenna beamwidth. As can be seen the peak value is quite constant with very few variations, and the trailing edge curvatures show the sensitivity to surface roughness. However, for satellite 19, Fig. 9.26(b), its is seen that the peak rises at the end. This is related to a coherent scattering mechanism that occurs in that area, as the scattering area is close to the coast and that region might be probably protected from wind, resulting in a flatter surface. As it can be also observed in Fig. 9.27, where geolocated maps of the K_{IQ} and the reflectivity parameters are shown, for satellite 19, there is a rise of the coherent component in front of the incoherent at the end, which makes the coherent component rise.

Figure 9.28 show the direct and reflected thermal SNRs, the K_{IQ}, and the reflectivity

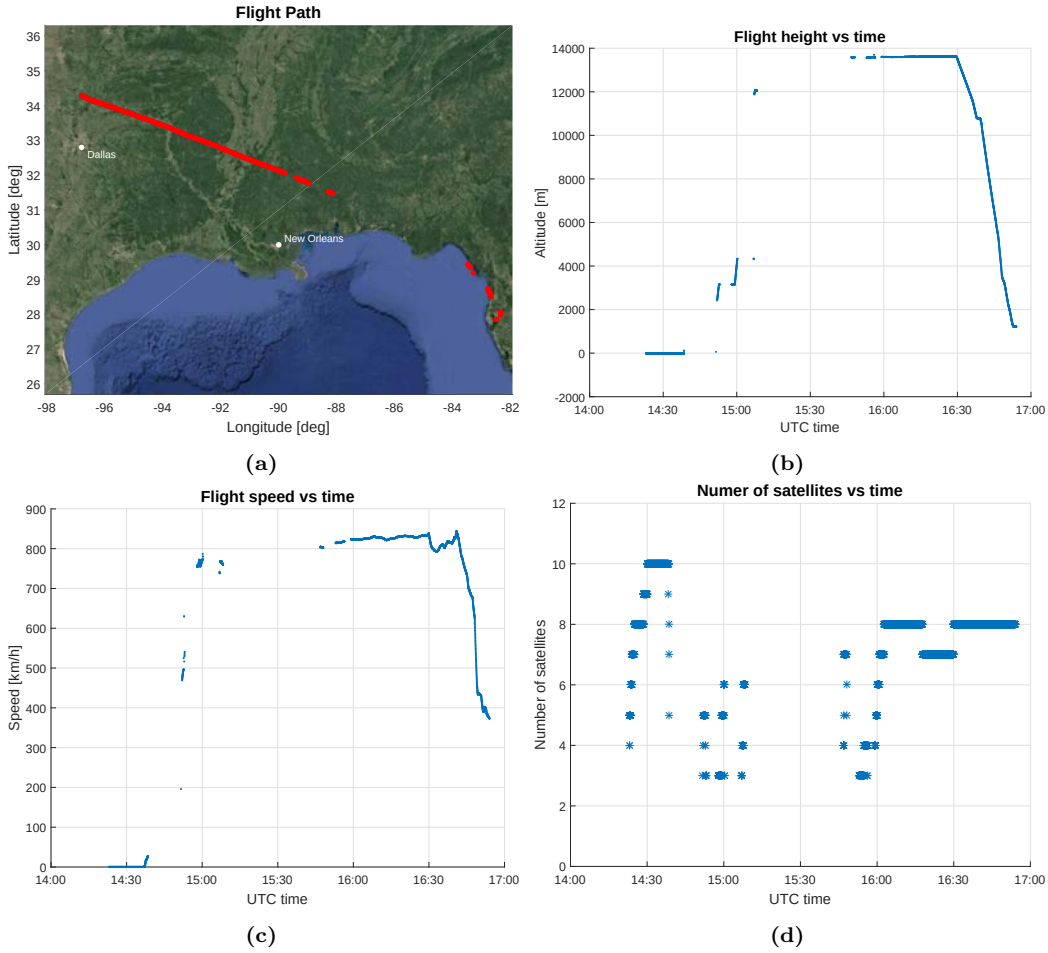

Figure 9.23: Summary of Oct 19, 2009 flight parameters: (a) Flight route, (b) Altitude, (c) Speed, and (d) Number of satellites seen.

as a function of time. Herein, the rise of the coherent component in front of the incoherent one is clearly seen for satellite 19, where the coherent component has sometimes twice the power the incoherent component has. Furthermore, it is seen that the reflectivity for the sea surface reflected signal is close to -10 dB, whereas it is much smaller for the regions outside the antenna beamwidth. This fact was also observed in Fig. 9.27(b). It is also seen that even though the coherent component rises in front of the incoherent one, both thermal SNR for the reflected signals, and therefore the reflectivity, do not change severely.

The difference between out of beamwidth signals scattered over land and sea can be determined by comparing the waveforms for satellites 3 and 28, which are depicted in Fig. 9.29. While the land scattered signal looks like a burst of power that is lost and starts appearing from time to time (satellite 3), the sea surface scattered waveforms for satellite 28 follow the incoherent scattering waveform shape with an elongated trailing

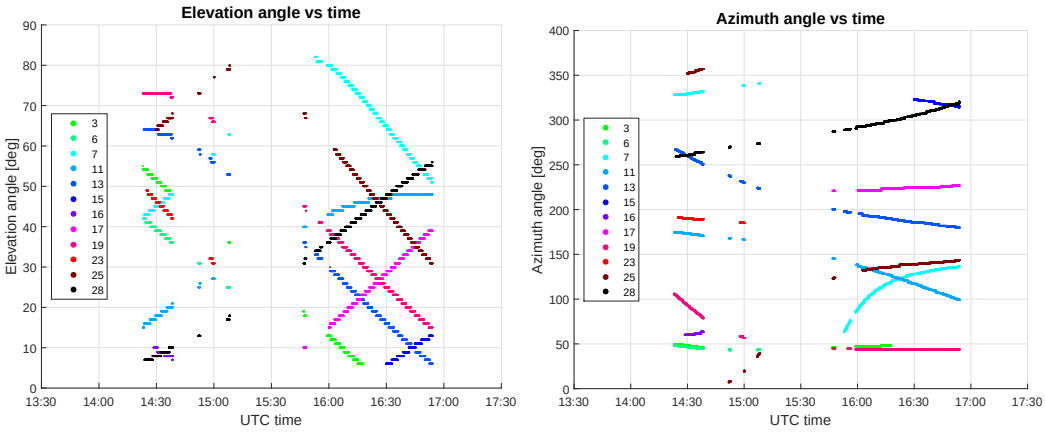

(a) (b)

Figure 9.24: GPS constellation for Oct 19, 2009 flight: (a) Elevation angle, (b) Azimuth angle.

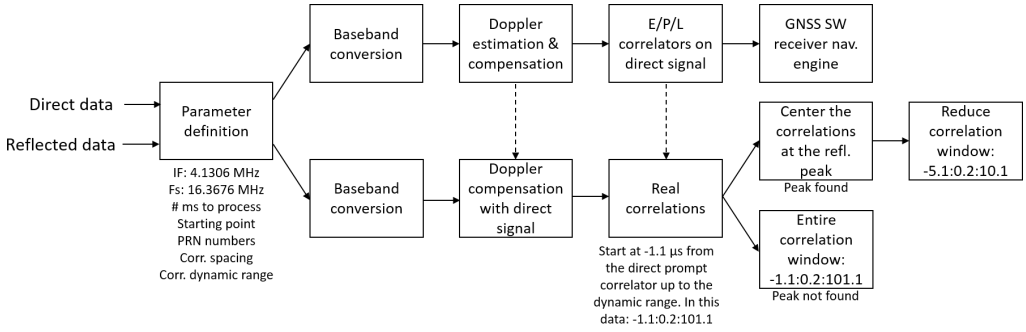

Figure 9.25: SW bistatic receiver block diagram.

edge. However, a lower thermal SNR is observed for the out-of-beamwidth satellites in comparison to the satellites that fell within the antenna beamwidth due to lower antenna gain. Note that the peak value for satellite 28, even though it has a lower SNR, it has a peak value mainly constant, which indicates that the sea surface scattering process is a stationary random process which does not occur with the land scattering process. The fact that the scattering process for the land surface is not stationary will be highlighted in the next section.

9.3.5 Land Surface Reflected Data

The land reflected data in this section corresponds to data gathered from 16:08–16:18. Five different datasets of 120.000 ms are used: 16:08–16:10, 16:10–16:12, 16:12–16:14, 16:14–16:16, and 16:16–16:18. Figure 9.30 shows consecutive 1ms-1s waveforms for the land scattering case and four different satellites. The data shown in that figure corre-

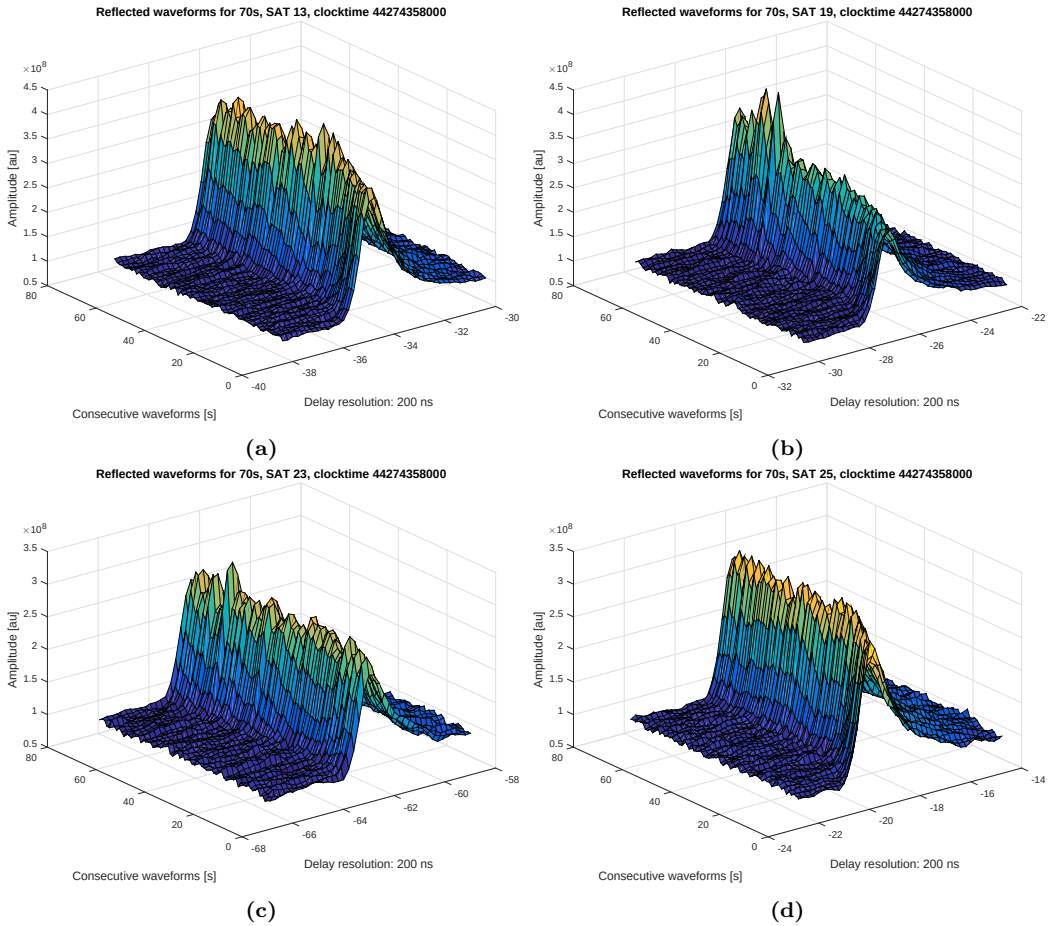

Figure 9.26: 1ms-1s waveforms scattered over the sea for satellites (a) 13, (b) 19, (c) 23, (d) 25, which were the ones that fell within the antenna beamwidth.

sponds to the first dataset (16:08–16:10). Differently from the sea surface scattering case, the peak amplitude is varying severely between 1ms-1s waveforms. This is an indicator of the sensitivity to the surface dielectric constant, which may be varying due to varying the land cover and/or soil moisture conditions, and to surface roughness. Also note that the trailing edge of the waveform is not as elongated as occurred with sea surface scattering case. This occurs because of two main reasons. First, because the effective roughness is smaller for the land surface as compared to the sea surface. Second, the land surface is much more irregular than sea surface (more parameters vary). Even though the scattering is mainly incoherent for the sea surface, it can be easily modeled due to its homogeneity. Conversely, since the land surface can change so drastically from one place to another, it is not so straightforward to model it. Note that some regions of partially coherent waveforms are seen for the land scattering case. Also, in Fig. 9.30 it is observed that satellite 28 faces a smaller thermal SNR than the other satellites, which is detected by observing a lighter blue color on the thermal noise level. However, the waveforms'

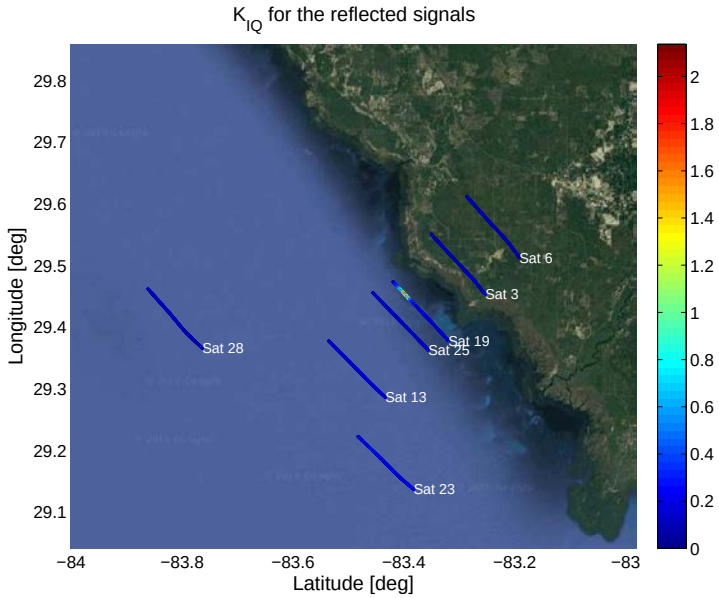

(a)

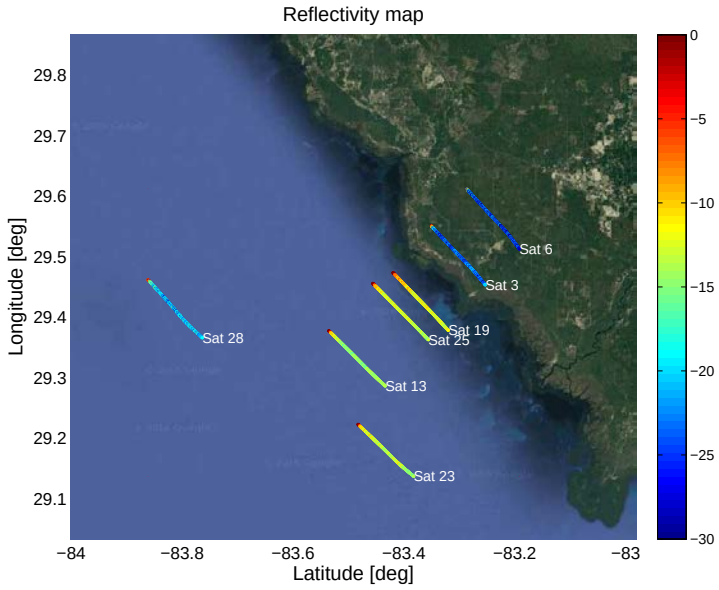

(b)

Figure 9.27: (a) K_{IQ}, and (b) Reflectivity maps for the reflected signals.

shape and statistics do not change.

Figures 9.31–9.32 show the K_{IQ} and reflectivity maps for the land scattered signals. Therein, it is seen that for the regions where the river is present it seems to be quiet and

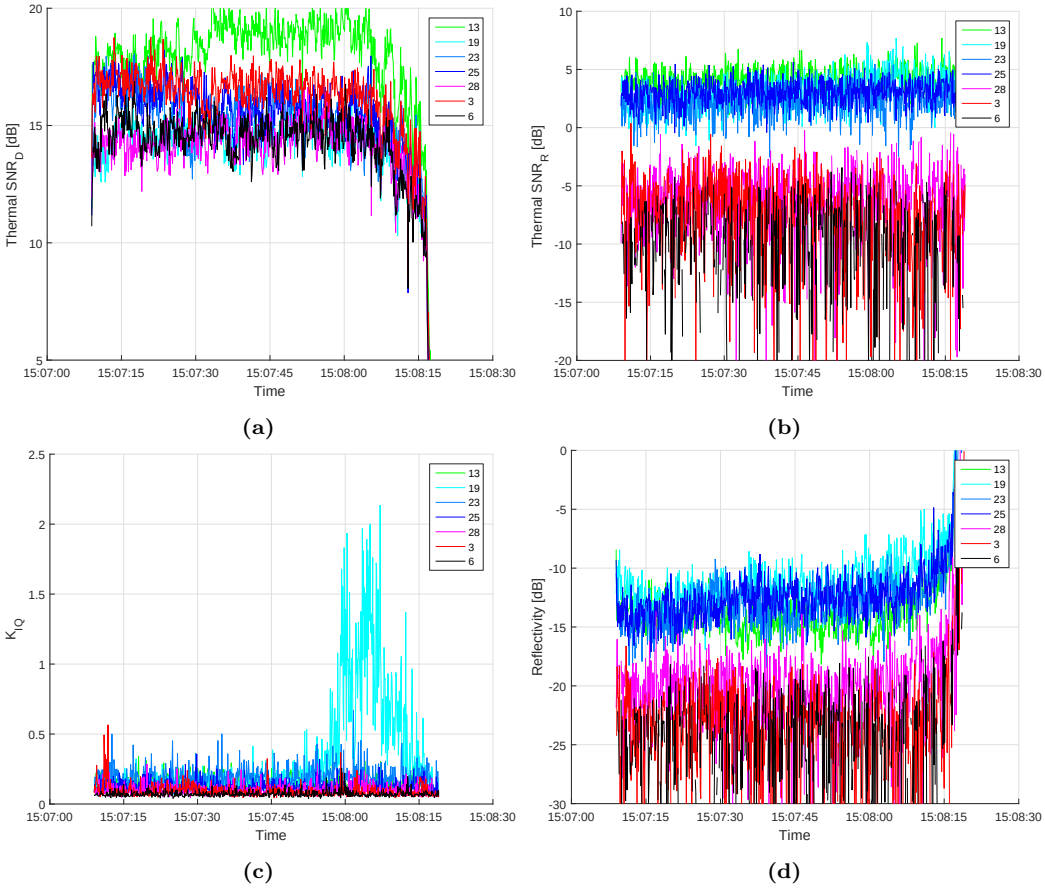

Figure 9.28: (a) Direct signal thermal SNR, (b) reflected signal thermal SNR, (c) K_{IQ}, and (d) reflectivity, for all satellites in view and the sea surface reflections dataset.

flat since the coherent component is larger in that area. It is also seen that for flat land areas the coherent component also dominates the incoherent one. In the other cases, the incoherent component seems to dominate or be equal to the coherent one. However, when observing the reflectivity parameter computed as the ratio between direct and reflected thermal SNRs, it is seen that for the water regions (rivers and lakes) it is larger due to larger surface reflectivity. It is also seen that it is between -10 dB and -20 dB for land-covers different from forests, which might be crops areas or grass-land areas. For forest areas reflectivity is below -20 dB.

Figure 9.33 show the time series of the direct and reflected thermal SNRs, (a)–(b) respectively, K_{IQ} or the ratio between the coherent and incoherent scattered components (c), and the reflectivity (d). In this figure it is again seen what has been already highlighted. Figure 9.33(a) shows that the direct signal SNR has similar levels than the one for the sea surface case. Figure 9.33(b) shows a much larger variability of the reflected thermal SNR than the one for the sea surface case, because for the land surface, apart from varying the surface roughness conditions, the dielectric constant may vary from

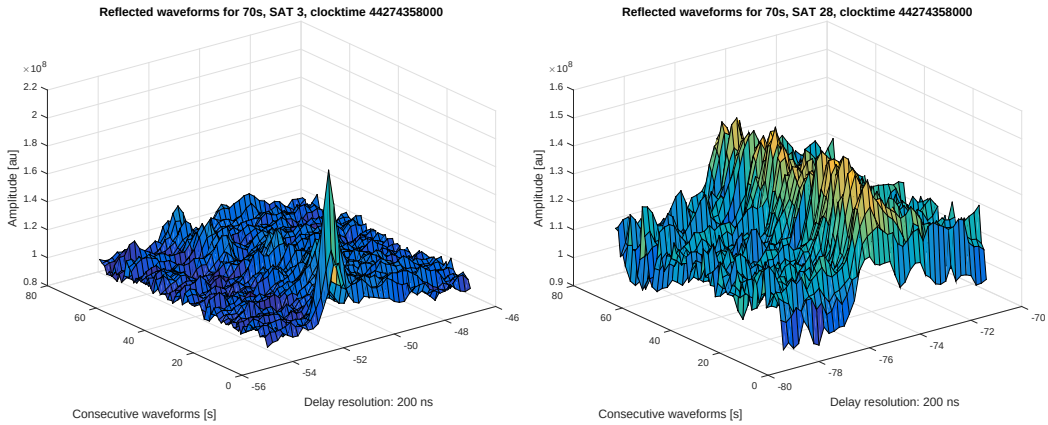

(a) **(b)**

Figure 9.29: 1ms-1s waveforms for out-of-beamwidth satellites: (a) satellite 3, (b) satellite 28.

pixel-to-pixel. Figure 9.33(c) shows that the presence of the coherent scattering mechanism in the land scattering case can be much larger than for the sea surface scattering case, being the coherent component up to 10 times larger than the incoherent one. Note that effect is seen for all satellites. Finally, Fig. 9.33(d) shows that the same behavior found in the thermal reflected SNR parameter is observed in the reflectivity parameter. Its variability is much larger than for the sea surface scattering case (Fig. 9.28(d)), as aforementioned, due to changes on the dielectric constant and land-cover apart from the changes of surface roughness conditions. Also, the trend observed is lower reflectivity values than for the sea surface scattering case, unless there is some presence of coherent scattering.

9.3.6 Summary

This second part of the chapter presents the data analysis of a field campaign performed by NOAA in October 19, 2009. This part is more concentrated on comparing the different behavior of the land and sea surface scattering mechanisms. While the sea surface seems to follow the incoherent scattering mechanism which is only driven by surface roughness or the mean square slope parameter, the land scattering mechanism is much more complex and depends on more variables. It has been shown that the sea surface scattering mechanism can be considered a random stationary process, whereas the land scattering one, due to its dependence on more parameters it is not stationary. In this part also the algorithms to estimate the coherent and incoherent scattering components presented in Chapter 4 are tested. No ground-truth data was available in that field campaign which is why no retrieval of geophysical parameters was tried.

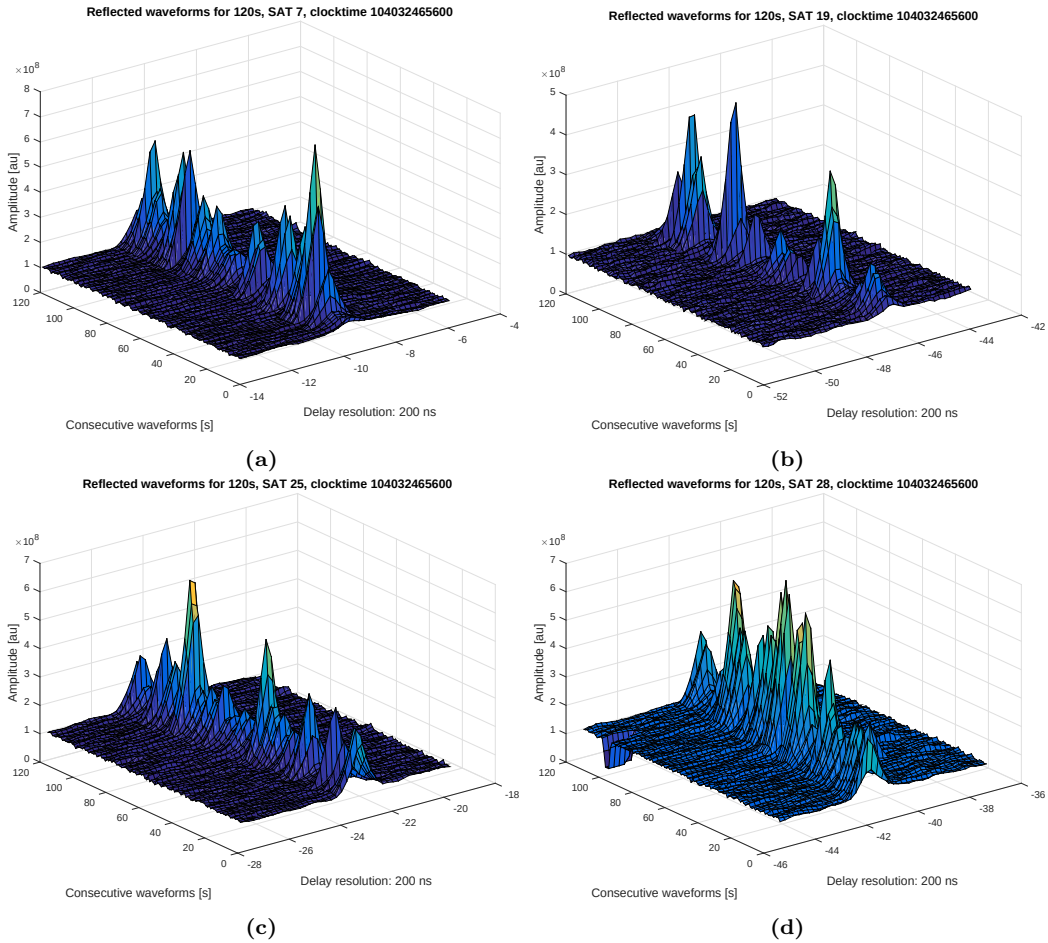

Figure 9.30: 1ms-1s waveforms for the land scattering case and two different satellites: (a) satellite 7, (b) satellite 19, (c) satellite 25, (d) satellite 28.

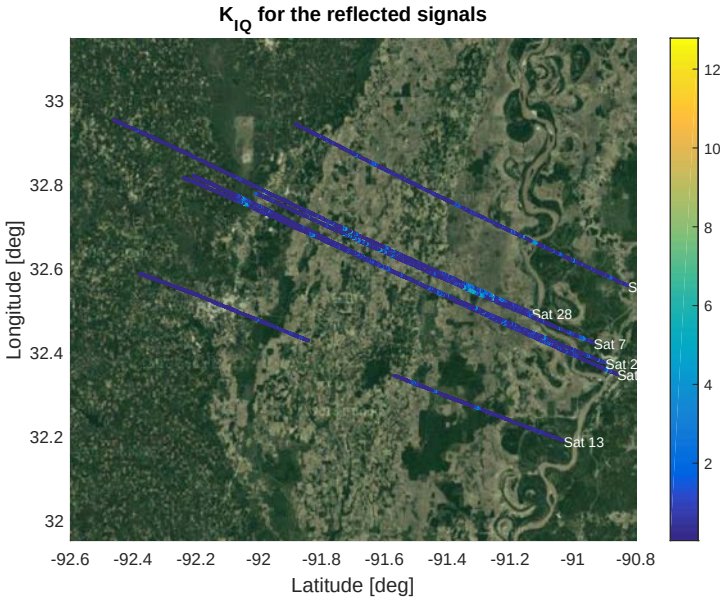

Figure 9.31: K_{IQ} map for the reflected signals over land.

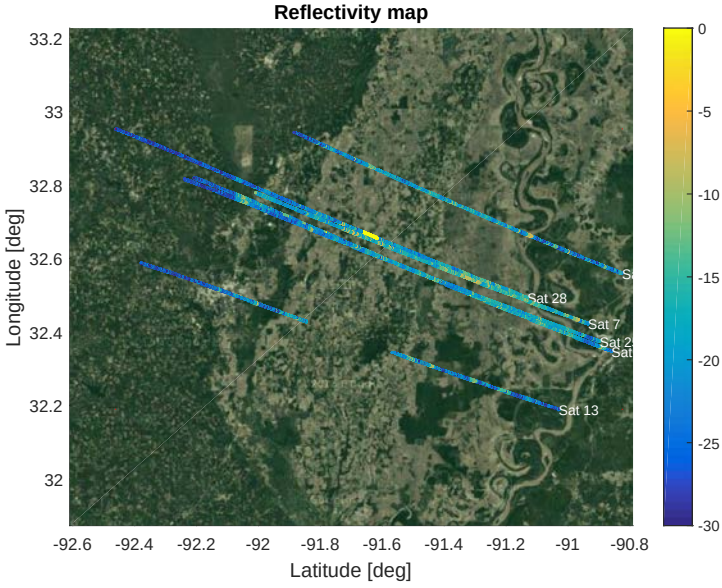

Figure 9.32: Reflectivity map for the reflected signals over land.

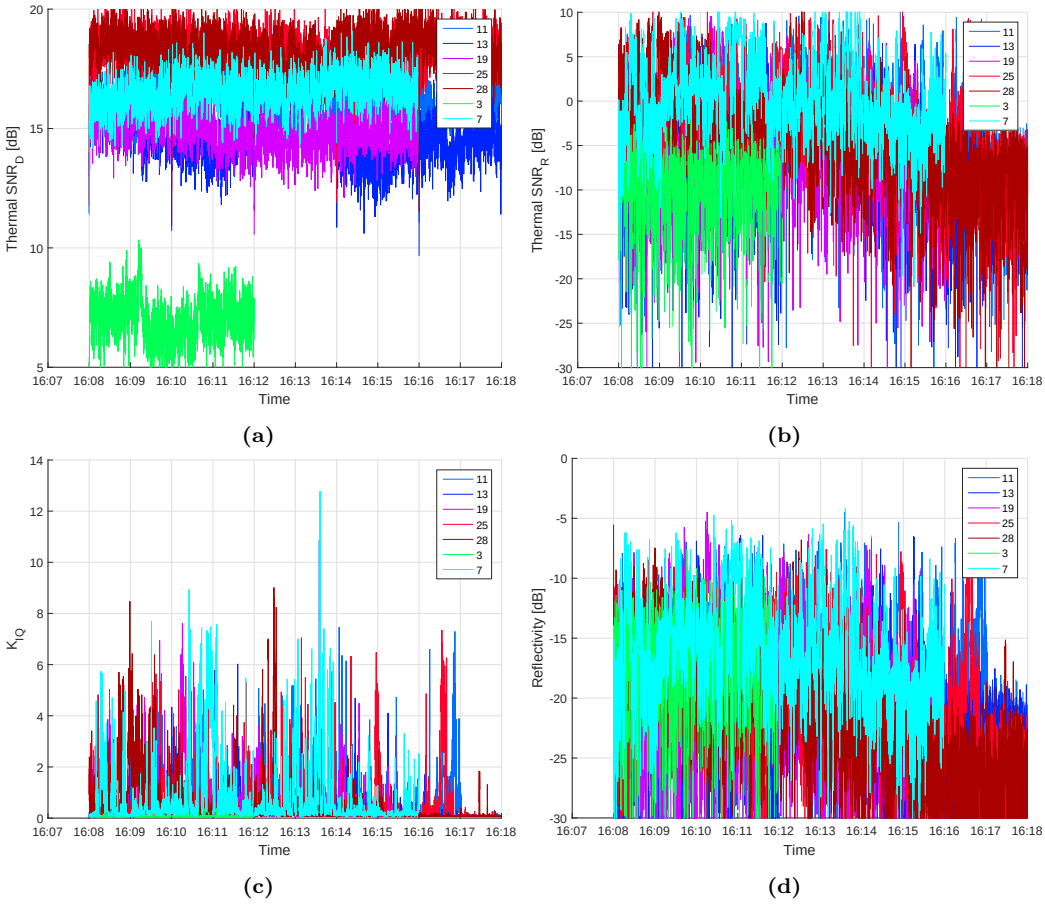

Figure 9.33: (a) Direct signal thermal SNR, (b) reflected signal thermal SNR, (c) K_{IQ}, and (d) reflectivity, for all satellites in view and the land surface reflections dataset.

10

Chapter 10

Sea Ice Detection Using UK TDS-1 Data

This chapter is a summary of one part of the work that the author performed during his research stay at the NOAA under the supervision of PhD Valery Zavorotny. The basics of this chapter is the understanding of a purely coherent surface scattering model and a purely incoherent scattering model. From the difference on the GNSS-R waveform's shape the presence or not of sea ice is detected, and daily sea ice maps are generated. Those maps have been compared with two independent ground-truth obtaining significant results that propose GNSS-R as a good technique for sea ice detection.

10.1 Introduction

Active and passive remote sensing techniques have been used to monitor sea ice. Passive techniques based on microwave radiometry have been used to determine the Sea Ice Concentration (SIC) parameter, which is the percentage of ice on a pixel [203]. For instance, 0% indicates open water, 50% indicates that half of the pixel is covered by ice, and 100% indicates that the entire pixel is solid ice [204]. Active techniques based on real aperture radar and synthetic aperture radar generally measure surface roughness, which leads to sea ice type classification, as the waveform shape is highly sensitive to surface roughness [205]. However, in order to achieve high altimetric resolution, the frequency bands used are normally Ku-band or K-band (12–18 GHz and 18–26 GHz respectively), which make the radar technique sensitive to small–($\sim$ cm) and large–($\sim$ m) scale roughness [69].

Sea ice monitoring using GNSS-R started in 2000, when initial results comparing the waveform peak power of the GNSS reflected signals over ice against RADARSAT backscattering echoes were presented [206]. In 2003, a theoretical model explaining the sea ice scattering mechanism was proposed [207], which was based on the one presented by Zavorotny and Voronovich in 2000 [52] but adding an extra convolution due to the sea ice depth, and it is described in next section. In 2006, it was shown that there is a strong presence of the coherent component in the GNSS-R bistatic scattering echoes [78], indicating a deficiency of the purely diffusive scattering model. This was confirmed later in 2010 with a detailed study using the UK-DMC GNSS-R dataset [208]. However, unambiguous relations between waveform peak power or shape and sea ice parameters have not been found. Airborne studies using GNSS-R data were also performed in 2010 for the determination of sea ice parameters [209]. In [209] the effect of surface roughness was also analyzed and compared to lidar measurements.

In this chapter the use of GNSS reflected signals for sea ice detection with simple and straightforward algorithms that can be implemented on future spaceborne platforms is proposed and demonstrated. Data from the UK TDS-1 mission will be used for the demonstration. Section 10.2 shows the theoretical background that justifies the analysis performed in the entire work and it is related to the state of the art theory presented in Chapters 2 and 4. Section 10.3 describes the approach followed based on the experimental evidence from UK TDS-1 mission. Section 10.4 describes the ground-truth data used to validate the analysis performed. Section 10.5 evaluates the GNSS-R approach against the available ground-truth data. Finally, Section 10.6 discusses the results achieved, the error sources, the applicability of the technique proposed, and summarizes the main achievements of this Chapter.

10.2 Theoretical Background

Conventional satellite radar altimetry has been used for sea ice studies since the early 1980's [210, 211]. It relies on scattering of EM waves from the surface while the radar antenna is looking at nadir. In that situation, the power waveform or returned power as a function of the delay is composed of three different components [210, 212, 213]:

$$W(\tau) = S_r(t) * P_{FS}(t) * r(t), \tag{10.1}$$

where $S_r(t)$ is the shape of the transmitted pulse or point target response, $P_{FS}(t)$ is the flat surface response, which is the radar cross section as a function of the delay time (over the horizontal surface) weighted by the gain pattern, and $r(t)$ characterizes the surface roughness, and it is the mean density of point scatterers as a function of the delay time in the nadir direction. In other words, $S_r(t)$ is a Doppler cut of the so-called WAF [131] through its maximum. $P_{FS}(t)$ depends on the antenna pattern and the radar cross section, which at the same time depends on the probability density function of the surface's slopes. It determines the trailing-edge shape of the waveform while it affects also the leading-edge shape. Finally, $r(t)$ characterizes the surface roughness parameter, and it is the main contributor to the leading-edge shape although it does not affect so severely the trailing-edge shape.

If a transmitted signal with a pulse width of 300 m is considered, such as the one used by cGNSS-R for the public C/A-code, Eqn. (10.1) can be approximated by:

$$W(\tau) = S_r(t) * P_{FS}(t), \tag{10.2}$$

since the radar pulse width is much larger than the immediate *rms* elevations, or what is the same, the distribution of point scatterers at the nadir direction can be approximated by a delta function. Note that a nadir-looking geometry is a particular case of the forward-scattering mechanism found in GNSS-R, and consequently, part of the previous work performed for satellite radar altimetry can be used to understand the GNSS-R sea ice scattering mechanism.

The GNSS-R waveform model was previously shown in Eqn. (4.7), and it is a particular case of the waveform/DDM model proposed by Zavorotny and Voronovich in 2000 [52] to determine the shape of the rough ocean scattered signals. Note that this model is based on the Kirchoff-Approximation Geometric-Optics (KA-GO), like Eqn. (10.1), and only takes into account the non-coherent/incoherent component, assuming that the coherent component is negligible. Equation (4.7) can be expressed in a simplified form as in [56, 132, 133]:

$$W(\tau, f_D) \triangleq |\chi(\tau, f_D)|^2 * *|\sigma^0(\tau, f_D)|^2, \tag{10.3}$$

where f_D takes into account the power spreading in the Doppler domain, χ stands for the WAF, σ^0 for the normalized bistatic radar cross section which already includes the antenna pattern projection over the surface, the distance parameters, and the surface parameters such as the pdf of the surface slopes, and $**$ expresses a two-dimensional convolution in both domains, τ and f_D. Taking a cut over the Doppler domain, which results in the so-called waveform, makes Eqn. (10.2) and Eqn. (10.3) equivalent. In both altimetric and cGNSS-R models, only surface scattering is taken into account. However, in 2003, Wiehl et al. [207] proposed a model that took into account the sub-surface reflection that may occur on the ice sheets, converting Eqn. (10.3) into a triple convolution which can be expressed as:

$$W_v(\tau, f_D) = Z(\tau) * W(\tau, f_D), \tag{10.4}$$

where Z models the subsurface scattering or the power echo from each different ice layer, and W is the DDM model shown in Eqn. (10.3). An image of the W function and its effect can be obtained in [214].

Although different theoretical models were proposed, no experimental cGNSS-R waveforms obtained from space were available until 2005 with the launch of the UK-DMC

satellite [78], which contained a GNSS-R payload. It was observed that the waveforms reflected from the ocean surface and from sea ice were significantly different. While over the ocean there was a noticeable Delay-Doppler spreading of the signal power scattered leading to the "horseshoe" shape, the DDM over the sea ice resembled the WAF itself, without a Delay-Doppler spreading. Furthermore, for several regions the phase of the reflected signal at the DDM peak could be tracked, even identifying the navigation bits, which indicated the presence of a strong coherent component [78]. This demonstrated experimentally that the assumption of a negligible coherent component is mostly valid for the sea surface, but not for sea ice scattering mechanism. In Fig. 2 of [211], this fact was conceptually illustrated for near-normal incidence angle, and the near-normal incidence scattering cross section for the coherent and incoherent components was computed. It can be seen that the pdf of the slopes is much narrower for the sea ice than for the open sea, tending to a delta function centered at zero for new ice. In other words, the sea ice surface is mostly flat and mainly coherent scattering occurs. However, the transition to an almost flat surface cannot be done within Eqns. (4.7),(10.4). The use of the slope probability function in the form of a delta function in these equations would lead to an incorrect result. The coherent form of the DDM should be based on the original Kirchhoff approximation for the scattered field under the assumption that the surface roughness is very small (the Rayleigh parameter is significantly less than 1). The DDM model for the coherent component was introduced in [58]. Instead of a convolution, as shown in Eqn. (10.3), it is a product between the WAF and the surface reflectivity, times the factor that takes into account the loss of the spatial coherence due to the presence of some relatively weak surface roughness [69, 70]. The general mathematical expression for the coherent scattering has already been seen in previous Chapters.

10.3 GNSS-R Approach

10.3.1 The "K-shape" DDM Concept

Taking advantage from the recently launched UK TDS-1 mission whose data is freely accessible, several datasets passing through the Polar regions have been analyzed, and it was observed that the shape of the measured DDM was different depending on the surface on which the GNSS signal was reflected. Figure 10.1 shows two different extracts of the data retrieved from February 19, 2015 using the receiver specifications identification number RD000019, and the tracklist identification number TD000071. Figure 10.1(a)–(b) correspond to data from the Northern Hemisphere (Arctic), and their spatial distance is less than 60 km, since there is only 10 s difference among their acquisition. In Fig. 10.1(a) on the left, it is possible to see the DDM over a sea ice-covered surface. Particularly, the distribution of the power in the DDM resembles the shape of the letter "K" (rotated 90°). It is also possible to identify two different features. One of them is the vertical element of the "K" (horizontal line on the image), stretching along the Doppler frequency axis and depicting a partially coherent DDM component. It corresponds to the WAF multiplied by the reflectivity, times the second-order coherence function [70]. The rest of the DDM, which spans over the Delay-Doppler domain with the "horseshoe" shape, corresponds to the incoherent component. For that particular DDM, that region has power levels similar to the WAF Doppler sidelobes, which are at least 13 dB below its maximum, indicating

that the coherent component was the dominating scattering mechanism.

On the right-hand side of Fig. 10.1(a), the Doppler Integrated Waveform (DIW) in blue, a Doppler cut of the WAF in cyan, which is called IdealACF[2], and a Doppler cut of the DDM in green are shown. The DIW is the integral of the DDM over the Doppler domain. This is a way to see the power spreading due to surface roughness, but only in one dimension (the delay domain). Without doing that, the spreading of the power over the delay domain is barely noticeable, as it can be seen on the Doppler cut shown in the same figure in green. The leading edge is barely affected by surface roughness, due to the large pulse width of the GNSS signals and the low roughness conditions. Also, due to the integral over the Doppler domain, the thermal noise below the leading edge is averaged and reduced (blue), showing the incoherent scattered power that could barely be seen on the conventional waveform (green)[1]. This incoherent power is detected because the waveform power level after the purely coherent WAF (for delay values larger than the maximum) does not go down again to the thermal noise level found before the waveform's leading edge. It is the result of the incoherent scattered power coming from the different delay-Doppler bins.

On the contrary, Fig. 10.1(b) shows a totally different effect, highlighting only the "horseshoe" shape of the DDM without the WAF Doppler sidelobes presence. Also, even though the "horseshoe" shape of the DDM is an indicator of the surface roughness, the shape of the waveform's leading-edge is again barely affected, which occurs due to the small bandwidth or large pulse width of the C/A code. Conversely, the trailing edge of the DIW is very different. In Fig. 10.1(a) there are two different regions on the trailing edge, one where the slope is very large and follows the WAF shape (associated to the coherent component), and one where the slope is smoother and corresponds to the incoherent power. In Fig. 10.1(b) there is only one smooth region that can be identified which indicates the lack of coherent power, since there is no power drop after the WAF delay decay.

These features are seen in most of the data gathered from the UK TDS-1 that have been analyzed, depending on the scattering surface type, and indicate that two different scattering mechanisms affect the scattering over sea ice or open water. When the reflection is purely coherent there is no Delay-Doppler spreading, and the reflected waveform is the WAF multiplied by the power Fresnel reflection coefficient. If the reflection is purely incoherent, there is a large Delay-Doppler spreading. The spreading depends on the roughness and in particular on the pdf of the slopes [See Eqn. (4.7)]. It might be logical that when the reflection has a coherent part and a non-coherent part, the waveform is a linear combination of both models, as shown in Fig. 10.1(a) and also identified in [215]. The more coherent the reflection is, the more it will tend to the WAF shape. The more incoherent the reflection is, the more it will tend to the model in [52]. The combination of both models tends to the "K-shape" DDM model. Furthermore, the larger the coherent component, the smaller the incoherent one, and vice versa [69].

[1]The Doppler domain integration of the DDM is needed only occasionally for GNSS-R spaceborne data, because due to the geometry and the platform's relatively high speed, the power is spread largely on the Doppler domain. Note that the GPS satellite effective speed is much smaller than the platform's effective speed. For the airborne case, since the platform's speed is much lower, the Doppler spreading is not as large as the spaceborne case, and the waveform shows all the sensitivity to surface roughness on the trailing edge slope [52], without the need of a Doppler integral. Note that the slope of the DIW was proposed as an indicator of the ocean's *mss* [52].

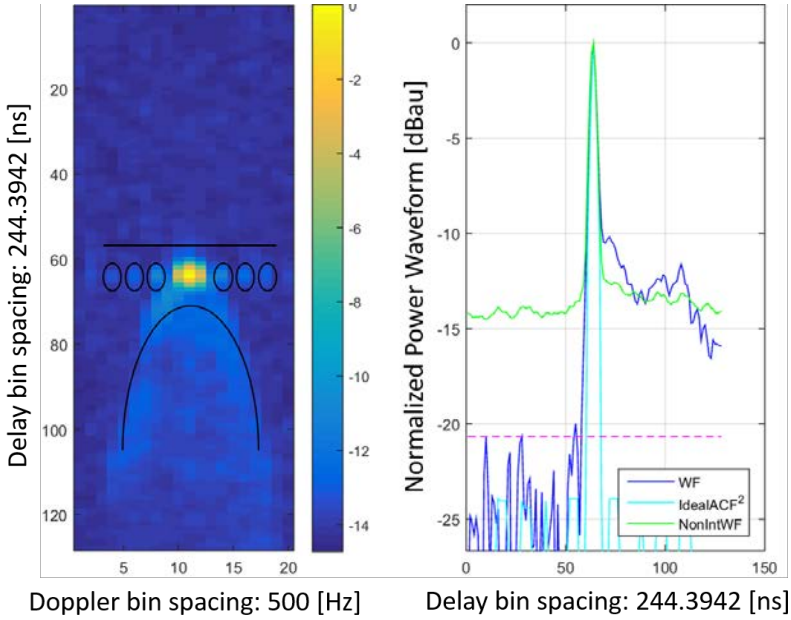

(a)

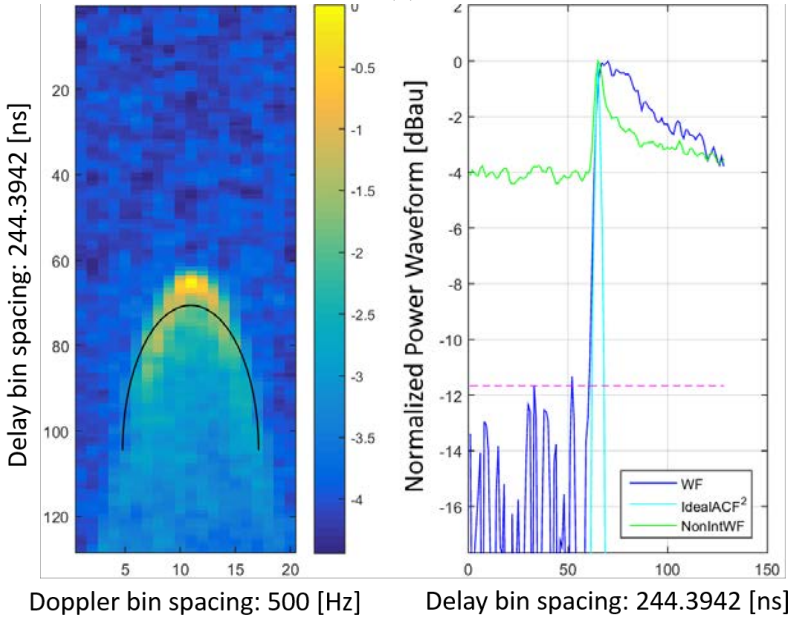

(b)

Figure 10.1: Two DDMs and the corresponding waveforms for (a) sea ice and (b) open water regions.

It has been shown both theoretically [52] and empirically [57, 78, 144, 216] that under open ocean conditions, even at weak winds, the sea surface can be nearly always considered rough, and the coherent component negligible [52]. On the other hand, there is no correct theoretical model that matches the waveforms obtained from the sea ice, since it is a combination of the purely coherent model and the purely diffusive model. The coherent component can be introduced into the non-coherent model in two different ways. The first one, as described in previous section, could be comprised of a bistatic radar equation [Eqn. (4.7)] as a DDM incoherent part plus a separate DDM term which describes a coherent (or partially coherent) component. The second one is to devise a single bistatic radar equation which would have, under the surface integral, a single combined bistatic radar cross section similar to that in [217]. The equivalent bistatic cross section will consist of a sum of two terms: one, similar to Eqn. (4.7) describing the incoherent diffuse scattering, and another one, describing the coherent reflection from the flat component of the surface. Formally, this can be done, and previously this approach was used to simulate the coherent and incoherent received scattered power under the bistatic geometry [217, 218]. However, it makes the combined bistatic radar cross section distance and antenna parameters dependent [218], putting this approach at odds with a traditional definition of the radar cross section which should only be a surface dependent parameter.

10.3.2 Definition of the GNSS-R Observables

There are several approaches that have been used previously to match simulated GNSS-R data with real data in order to retrieve the geophysical parameters. One of the most common ones is the waveform fitting [53, 63, 144], which consists of minimizing the cost function created using measured data and simulated data. This one has been widely used for the retrieval of wind-speed data over the ocean. Other heuristic approaches have been used in order to infer the surface roughness, such as the Volume under the normalized DDM (V_{DDM}), or the area under the normalized waveform (A_{WF}) [157]. Furthermore, different heuristic approaches have been compared against the wind speed over the ocean such as the DDM Average (DDMA), the DDM Variance (DDMV), the Allan DDM Variance (ADDMV), the Leading Edge Slope (LES), and the Trailing Edge Slope (TES) [219]. In [157] it was already stated the correlation between the (V_{DDM}), which can be seen as the DDMA for a large Delay-Doppler region, and the TES was 0.74.

The L1b product of UK TDS-1 data are DDMs time-referenced and geo-located with a coherent integration time of 1 ms and an incoherent one of 1 s. In other words, there is no access to the 1 ms complex DDMs generated in the operation to obtain the 1 s incoherently integrated DDM, and therefore there is no phase information available. The delay bin is approximately 244 ns, and the Doppler bin is 500 Hz (both shown in Fig. 10.1). Consequently, any operation that can be done using the 1 ms coherently integrated complex DDMs, such as the DDMV or the ADDMV, must be discarded. Data processing techniques such as the ones described in Chapter 4 for the complex data case must also be discarded. Furthermore, data from UK TDS-1 are not calibrated, since there is no information about the direct signal power impinging on the ground or about the signal power at satellite level. This prevents the use of parameters such as the SNR, as the transmitted power or Equivalent Isotropically Radiated Power (EIRP) depends on the satellite used and they may vary with time. Consequently, all L1b DDMs from UK TDS-1 have been

normalized to their maxima. So, for instance, the CYGNSS approach to the wind-speed retrieval which is based on the the measurement of the signal power received cannot be applied to UK TDS-1 data [220, 221].

The lack of a simple theoretical model for sea ice surface forward scattering geometry at L-band that determines both the coherent and incoherent scattered power prevents us from applying the cost function approach. Therefore, initially, the methodology proposed will focus on detecting the degree of coherence of the scattered signal to determine the sea ice presence from the waveform's shape. The following three heuristic approaches have been selected, which basically measure the peakedness of the WAF or its similarity to the coherent model:

Table 10.1: Estimators proposed to measure the degree of coherence of the reflected signal.

Estimator	Description
DDMA33	Average value of the normalized DDM around its peak using 3 Doppler bin cells x 3 Delay bin cells
DDMA35	Average value of the normalized DDM around its peak using 3 Doppler bin cells x 5 Delay bin cells
DDMA37	Average value of the normalized DDM around its peak using 3 Doppler bin cells x 5 Delay bin cells
TES1	Trailing-edge slope computed between the maximum of the normalized DIW and its value at approximately 750 ns after the peak power (3 delay bins)
TES2	Trailing-edge slope computed between the maximum of the normalized DIW and its value at approximately 1.5 µs after the peak power (6 delay bins)
TES3	Trailing-edge slope computed between the maximum of the normalized DIW and its value at approximately 2.25 µs after the peak power (9 delay bins)
MF	Maximum value of the correlation between the unitary energy DIW waveform and the unitary energy WAF Doppler cut for the same PRN code. It is an indirect measurement of how coherent the reflection (or scattering) process is.

Other estimators such as the LES were also tested. However, the results obtained were not satisfactory and therefore have not been included. One of the reasons is that at L-band, the waveform's leading edge is not as sensitive to surface roughness as it is at higher frequency bands, such as Ku-band, or K-band, which are the frequency bands of conventional radar altimeters, which also have much larger bandwidths. Furthermore, the higher the frequency used, the more sensitive it is to small scale roughness [100].

Similar observables for sea ice detection and classification have been used in conventional altimetry such as the SIGPK, which is the peak backscatter power in the returned echo, and the SIGTD, which is the average power computed between eight early and eight late delay bins of the DIW [222]. Note that the SIGTD is similar to the DDMA approach, and it is a measurement of the signal/waveform peakedness, or how coherent is the echo returned. Also note that the SIGPK cannot be used with UK TDS-1 data due to the lack of calibrated data. Other authors have also developed different algorithms for the waveform shape detection such as the Pulse Peakiness (PP) [223–225], which are similar to the DDMA algorithm and basically measure how different the waveform is from the incoherent model. Conversely, the approach proposed and used to detect sea ice in this Chapter is based on how similar the DIW is to the coherent model, and not detecting if

they are different from the incoherent one.

10.4 Ground-truth Description

In order to detect the presence of sea ice and compare it to the GNSS-R waveform shape, two different ground-truth SIC datasets have been used. The first one is the ARTIST Sea Ice (ASI) [203] algorithm using AMSR2 (Advanced Scanning Microwave Radiometer) data. The second one is the OSISAF [204] which is computed using data from the different channels of the SSMIS sensor. Subsequently, a short description of them is presented and the appropriate references are provided to the reader for more exhaustive information.

10.4.1 ASI Algorithm Using AMSR2 Data

The ASI algorithm was originally developed to use the high resolution provided by the 85 GHz channel of the SSM/I sensor. In this Chapter it is applied to the AMSR2 data, whose platform (GCOM-W1) was launched on May 18, 2012. The AMSR2 is a multi-frequency microwave radiometer with channels at 6.93, 7.3, 10.65, 18.7, 23.8, 36.5, and 89 GHz. The ASI algorithm is based on the polarization difference of the H and V channels ($P = T_{BV} - T_{BH}$). At 89 GHz the polarization difference for all types of ice is very small, either first-year, multi-year, or pure ice, whereas for open water it is much larger. The SIC is determined by a linear model, which decomposes the polarization difference in the contribution from open water, and the contribution of sea ice. Both of them are multiplied by a term that depends on the SIC. The lower the polarization difference, the larger the SIC and vice versa. Using this model a third degree polynomial is finally fitted to obtain the SIC as a function of the polarization difference. However, the 89 GHz frequency band is highly prone to atmospheric effects. Even though they have a poorer resolution, the lower-frequency channels of the AMSR2 data are used to assess the quality of the retrievals obtained from the 89 GHz channel, taking into account atmospheric effects and discarding data without sufficient quality. The SIC maps[2] used as a ground truth for the analysis developed along this work are obtained from [226]. For more information about the ASI algorithm, see [203].

10.4.2 OSI SAF Data

The OSISAF algorithm is based on the combination of the data provided by the different channels of the SSMIS (Special Sensor Microwave Imager/Sounder [227]) radiometer, in particular the 19 GHz, the 37 GHz, and the 91 GHz. The combination is generally performed using a Bayesian approach. Generally, the 91 GHz channel provides the high resolution product (12.5 km x 12.5 km), and the other channels are used to compensate atmospheric factors, as was done with the AMSR2 data. The retrieval algorithm is also based on the polarization difference between the V and H channels. However, in this algorithm the other channels are used in the model, besides for quality assessment,

[2]Those maps are given in the polar stereographic coordinates for both hemispheres (Northern and Southern) using a grid resolution of 6.25 km. This implies that the GNSS-R data is converted into those coordinates in order to make the appropriate comparisons.

resulting in a smoother transition between the open water and SIC larger than 80%. The SIC maps[3] used as a ground truth for the analysis developed along this work are obtained from [228]. The OSISAF dataset provides other information apart from the SIC maps, such as the sea ice edge, and the ice type. In order to develop those products, data from ASCAT scatterometer is also used. Apart from all those combination algorithms, the OSISAF dataset provides some quality flags that characterize the quality of the SIC retrievals. In this work a minimum confidence data level of 3 is required, as specified by [204]. Lower confidence levels mean that the retrieval is either unreliable, erroneous, or unprocessed.

10.5 Sea Ice Monitoring Using UK TDS-1 Data

Section 10.3 showed that the coherence level on the GNSS-R waveform is an indicator of the sea ice presence. In order to assess the performance of the proposed estimators, which basically measure the coherency level of the GNSS-R waveform, some intermediate steps have been performed to the UK TDS-1 L1b GNSS-R data product. First, all available UK TDS-1 data with a latitude larger than 50° for the Northern Hemisphere, and lower than -50° for the Southern Hemisphere have been used. The temporal range of that dataset includes the following dates: 1/09/2014, 30–31/10/2014, 8/10/2014, 15–17/10/2014, 23/10/2014, 26–28/01/2015, 3–5/02/2015, 11–13/02/2015, 19–21/02/2015, 27–28/02/2015, 1/03/2015, 07/03/2015, 15–17/03/2015, 23–25/03/2015, 31/03/2014, 1–2/04/2015, 8–10/04/2015, 16–18/04/2015, which were all the available data at the time of writing this PhD Thesis dissertation. Note that there is a gap in the GNSS-R data between November 23, 2014, and January 26, 2015, because there was a Christmas break, and orbital parameters were corrupted [229]. Apart from that, two days of data are available every eight days, because the payload was not operating continuously due to power restrictions on the satellite. For the aforementioned dataset, only those DDMs in the useful latitude range with a thermal SNR larger than 0 dB were used, since lower SNR indicates that the DDMs do not have good quality. In a previous analysis of UK TDS-1 data, this parameter was even more restrictive (3 dB minimum SNR required) [216]. However, as UK TDS-1 orbit and GPS constellation were not designed to monitor polar areas, it was decided to lower this constrain because otherwise the dataset becomes very limited.

Regarding the ground truth, the data have been split in Arctic and Antarctic regions, and the two different ground-truth datasets used, which leads to four different analyses. Also, a pixel has been considered as an ice pixel if the SIC value is larger than 15% [224, 225]. The pixel correspondence between the GNSS-R data and the ground truth has been performed by a minimum distance algorithm between the geolocated GNSS-R data and the ground-truth grid. A landmask was applied to avoid land contaminated pixels on the data analysis.

[3]Same as OSISAF maps, but using a grid resolution of 10 km.

10.5.1 Performance Evaluation of the Estimators Proposed

Taking into account the previous assumptions, the sea ice detection performance for the different proposed estimators has been evaluated through a Bayesian approach. The pdf of the estimator value for the ice pixels and for the open water pixels was computed, and the threshold to determine the presence of ice was chosen using a maximum likelihood criterion, assuming there was no a priori information about the pixels' content [230]. This means that the probability of having an ice pixel or an open water pixel, in the entire dataset, is assumed to be equal. Figures 10.2–10.5 show the pdf of the estimators proposed for the different combination of Hemisphere and ground-truth used. Figure 10.2 shows the result for Northern Hemisphere using the AMSR2 dataset as ground truth. Figure 10.3 shows the result for Southern Hemisphere using the AMSR2 dataset as ground truth. Figure 10.4 shows the result for Northern Hemisphere using the OSISAF dataset as ground truth. Figure 10.5 shows the result for Southern Hemisphere using the OSISAF dataset as ground truth. Figures 10.2–10.5(a)–(c) show the performance of the DDMA algorithm for the three different parameters selected, using three Doppler bins and three, five, and seven delay bins, respectively. As it can be seen, the three of them look similar, and as the delay bins used increase, the threshold decreases. What occurs with this algorithm is that the smaller the average computed is, the more similar to the WAF the reflected signal is. If the reflection is incoherent, then the reflected signal does not drop so quickly and the normalized DDMA increases. Figures 10.2–10.5(d)–(f) show the performance of the TES algorithm for the three different regimes selected. In this case, the sharper the slope, the more similar to the Doppler cut of the WAF the DIW is. Consequently, ice values appear on the right, whereas with the DDMA they appear on the left. Qualitatively, this estimator seems to perform better than the DDMA in each of its three different versions. Finally, the matched filter approach is shown in Figs. 10.2–10.5(g). It is possible to see that the pdf looks narrower and sharper than with previous estimators. Qualitatively, it seems to be the best estimator to distinguish between sea ice and open water.

Note that the pdfs obtained are similar among each other independently from the ground-truth selected, indicating a similar behavior. This shows that the algorithms proposed performed in the same way independently from the data origin. Table 10.2 summarizes the results obtained and evaluates quantitatively the performance of all the estimators proposed. In Tab. 10.2, four parameters are computed for each ground truth available (OSISAF and ASI AMSR2), and each region (Arctic and Antarctic): the probability of detection (Pd), the probability of false alarm (Pfa), the probability of error (Pe), and the threshold selected [230].

In general, it is possible to see that, independently from the algorithm used, for any region and any ground-truth dataset, the Pd is larger than 97%, reaching larger values for the OSISAF ground truth. For ASI dataset, the Pd is lower and the Pfa is larger, which indicates that the selected approach is more similar to the OSISAF ground-truth. Note that the estimators with the worst performance, which is evaluated using the probability of error, are the ones based on the DDMA. However, those are more consistent and independent from the ground truth and the region observed, as they all have a similar threshold. This occurs because the threshold is determined by the shape of the pdfs, and for those estimators they are closer, and the slopes around the threshold are larger. On the other hand, the threshold for the other estimators is not as consistent.

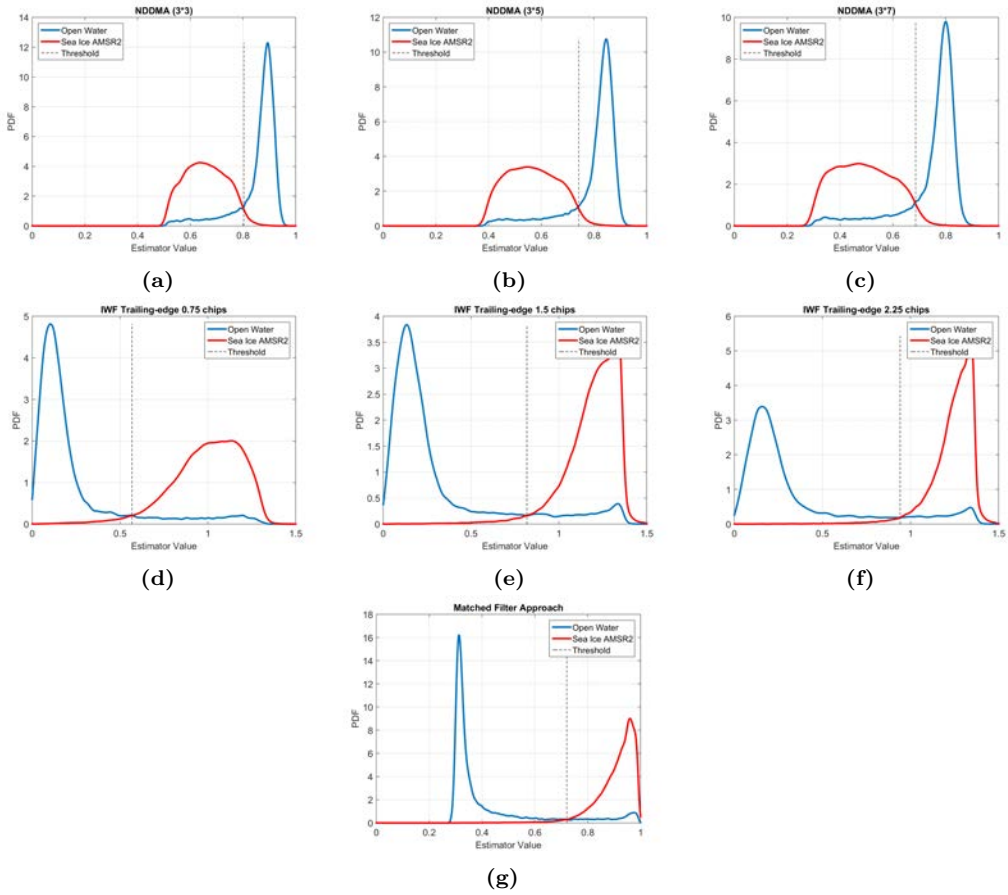

Figure 10.2: Estimators' performance for the Northern Hemisphere using the AMSR2 dataset. (a) Normalized DDMA 3x3, (b) Normalized DDMA 3x5, (c) Normalized DDMA 3x7, (d) TES 750 ns, (e) TES 1.5μs, (f) TES 2.25μs, (g) Matched Filter.

Looking to the pdfs presented in Figs. 10.2–10.5, they are more separated for the TES and Matched Filter (MF) estimators than for the DDMA one, and the slopes around the threshold are also smaller. This means that, the threshold selection is not so important for the TES and MF cases, and the Pd and Pfa values will not change much by changing the computed threshold. Also note that the performance of the TES estimators and the MF one is similar. However, the matched filter approach seems to be less sensitive to the threshold selection just by qualitatively exploring the pdfs. Furthermore, the MF estimator is the simplest one to be implemented as it only requires one FFT and one Inverse FFT (IFFT). For this reason, it is the preferred approach, as it can be easily implemented in a real-time processing software onboard the satellite, without the need of further algorithm intelligence such as peak re-tracking. Finally, it is also worth mentioning why the results obtained are more similar to the OSISAF dataset than to the ASI algorithm over the AMSR2 dataset, which occurs because the OSISAF uses a combination of different frequency bands which are closer to L-band, whereas the ASI

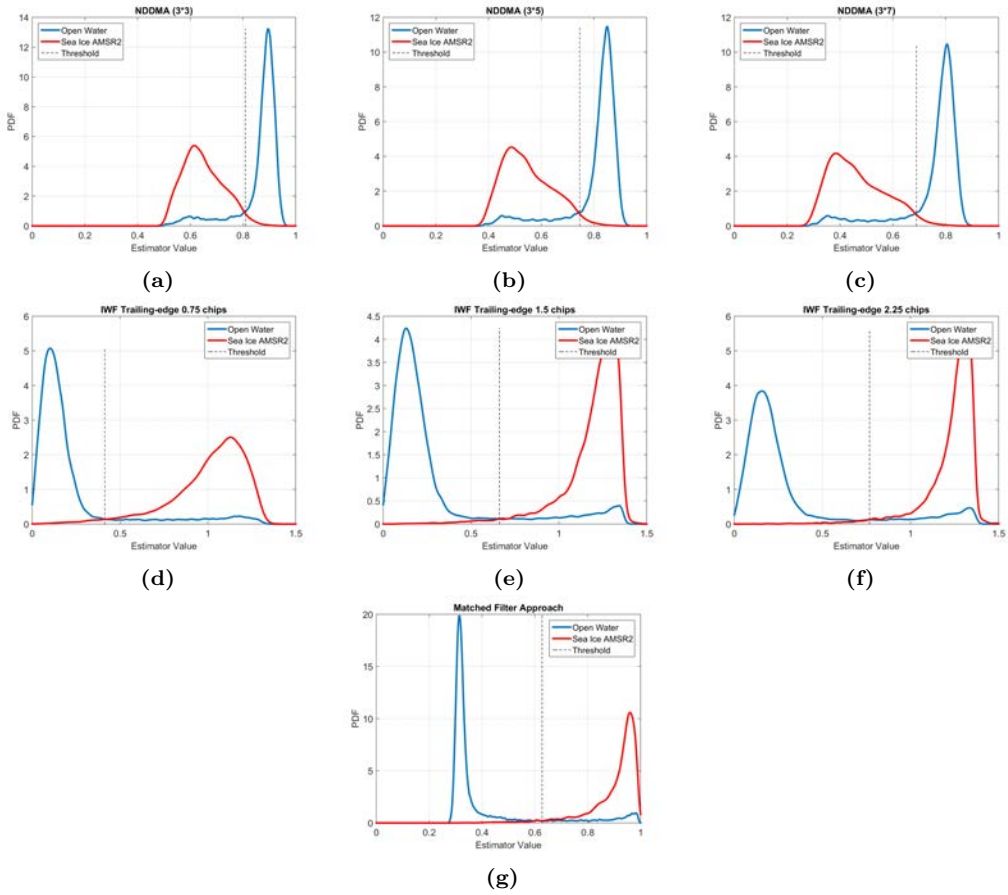

Figure 10.3: Estimators' performance for the Southern Hemisphere using the AMSR2 dataset. (a) Normalized DDMA 3x3, (b) Normalized DDMA 3x5, (c) Normalized DDMA 3x7, (d) TES 750 ns, (e) TES 1.5μs, (f) TES 2.25μs, (g) Matched Filter.

algorithm uses only the 90 GHz band, being sensitive at some points to different parameter scales. Also note that the OSISAF ground truth has the quality control flag, which has been used in the data processing, while in the AMSR2 ground truth there is not a quality control flag and all pixels are considered as reliable.

10.5.2 SIC Maps from Ground Truth and GNSS-R data

Figures 10.6–10.8 show three examples of sea ice detection maps created from the GNSS-R data using the matched filter approach together with the SIC maps from the two ground truths available for both the Arctic and Antarctic regions. Note that February 20, 2015 (Fig. 10.6), is the middle of the winter in the Northern Hemisphere, and the middle of the summer in the Southern Hemisphere, which is why the North Pole has more sea ice than the South Pole. In all maps, the presence of ice is shown by purple whereas the presence

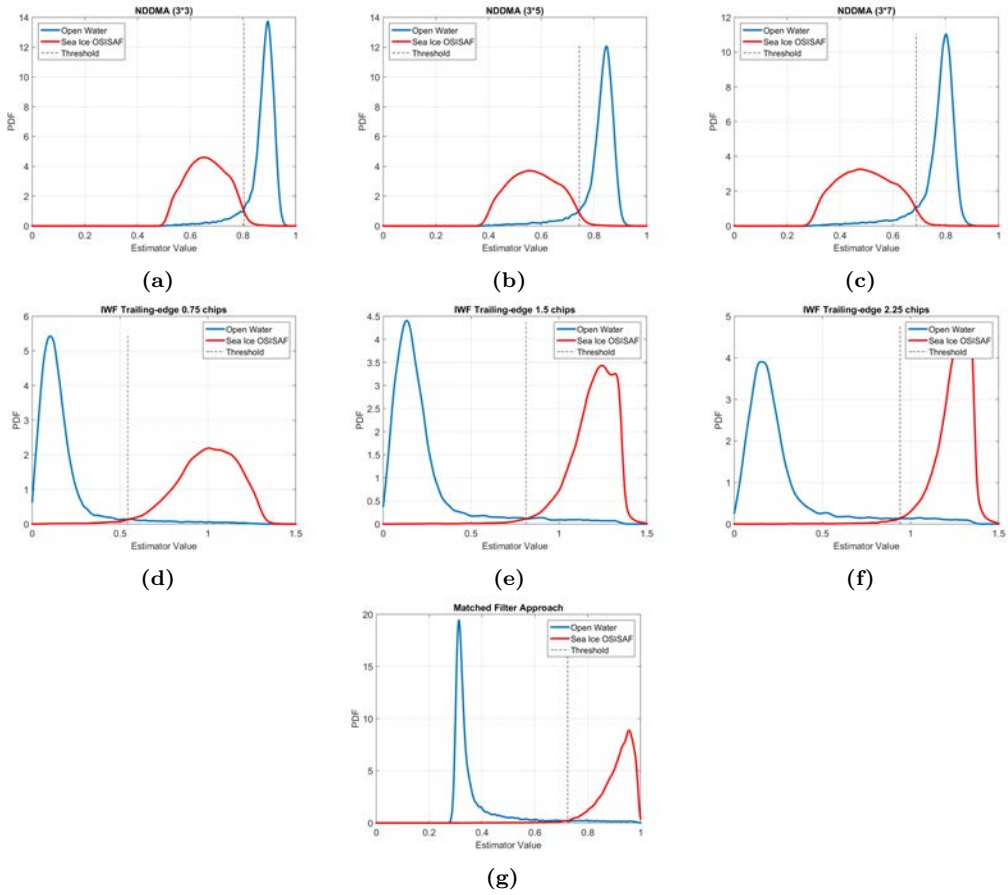

Figure 10.4: Estimators' performance for the Northern Hemisphere using the OSISAF dataset. (a) Normalized DDMA 3x3, (b) Normalized DDMA 3x5, (c) Normalized DDMA 3x7, (d) TES 750 ns, (e) TES 1.5μs, (f) TES 2.25μs, (g) Matched Filter.

of open water is shown by the light blue, which correspond to the colorbar on the right of the figures. The gaps are due to GNSS-R data with thermal SNR lower than 0 dB or land contaminated pixels. Also in the OSISAF maps, there might be gaps in the case of unreliable retrievals due to the quality flag. The SIC values from OSISAF and ASI AMSR2 are scaled from 0% to 100%, with the 0% the dark blue and the 100% the bright yellow, which correspond to the colorbar on the left of the figures. The coordinate system used to represent those maps is the polar stereographic coordinate system (see Appendix H for more information about this coordinate system). In all maps, it is seen how the transitions between open water and sea ice are monitored, and the change observed is very drastic, as expected from the pdfs shape. The sea ice edge seems to be accurately detected using the GNSS-R data (Fig. 10.9). As done in previous chapters, based on the specular reflection theory, the spatial resolution is $\sim$ 6 km x 0.4 km (400 m x 400 m for 1 ms of coherent integration time blurred to 6 km x 400 m due to the 1 s of incoherent integration time). This spatial resolution assumes coherent reflection for the sea ice regions, and it has been

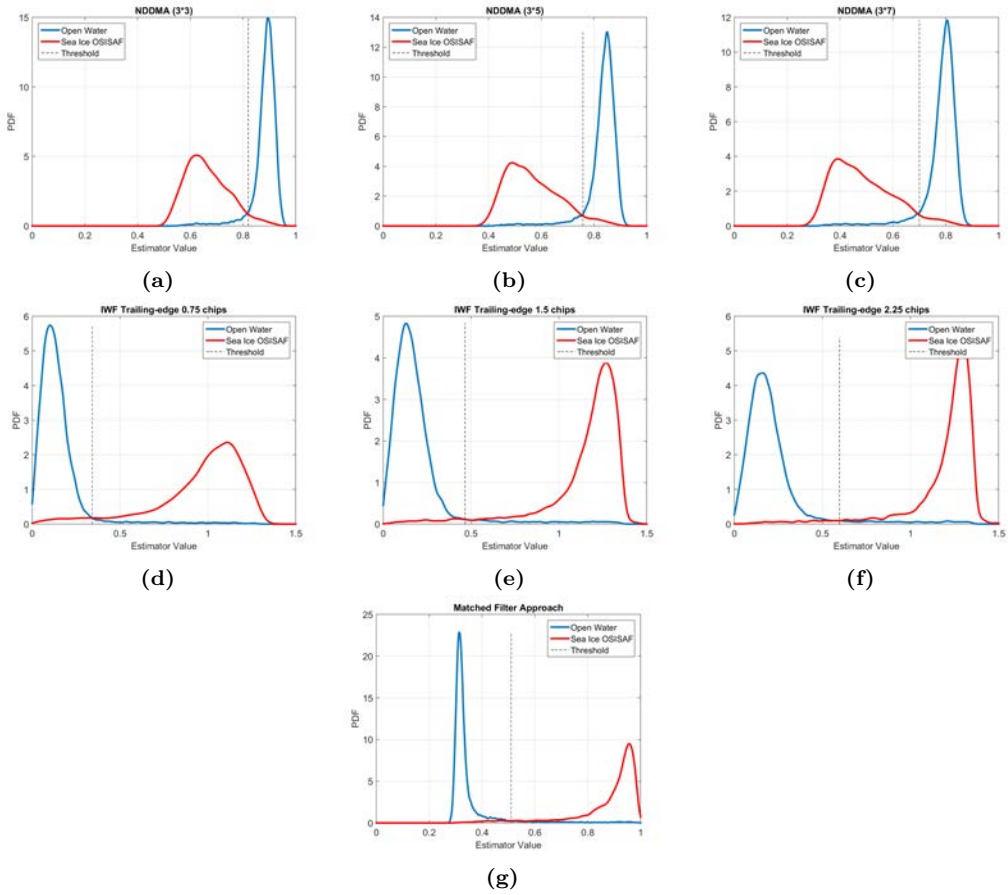

Figure 10.5: Estimators' performance for the Southern Hemisphere using the OSISAF dataset. (a) Normalized DDMA 3x3, (b) Normalized DDMA 3x5, (c) Normalized DDMA 3x7, (d) TES 750 ns, (e) TES 1.5μs, (f) TES 2.25μs, (g) Matched Filter.

computed using the UK TDS-1 satellite parameters. Note that for instance, it is half of the SSMIS pixel in the along-track track direction.

Furthermore, note that as was seen in Chapters 8–9 GNSS-R data look like different transects. This is again one of the properties of the multi-static GNSS-R techniques. Instead of being an image like a SAR or a microwave radiometer, it is a collection of transects with all the satellites in view. In order to generate a map with GNSS-R data, interpolation is required. Herein, the interpolation has not been applied because the mission specifications do not allow one to obtain sufficient points to generate a reliable map. However, a GNSS-R mission with the appropriate specifications to monitor the polar regions such as the one simulated in [58] would provide enough quality data to generate polar images.

Figure 10.7 which corresponds to November 15, 2014, shows that the Arctic regions are less frozen than in February, as the freezing period has just started, whereas the

Table 10.2: Performance evaluation of the estimators proposed for Arctic and Antarctic regions as a function of the two different ground truths used, the OSISAF, and the ASI AMSR2 datasets.

		Arctic				Antarctic			
	Estimators	**Pd**	**Pfa**	**Pe**	**Th.**	**Pd**	**Pfa**	**Pe**	**Th.**
OSISAF	**NDDMA (3*3)**	0.9822	0.0633	0.0401	0.802	0.9792	0.1254	0.0726	0.805
	NDDMA (3*5)	0.9794	0.0659	0.0428	0.739	0.9796	0.1261	0.0729	0.742
	NDDMA (3*7)	0.9749	0.0732	0.0487	0.682	0.9801	0.1323	0.0758	0.688
	TE (0.75 CA Chips)	0.9827	0.0351	0.0262	0.534	0.9810	0.1022	0.0605	0.495
	TE (1.5 CA Chips)	0.9853	0.0374	0.0260	0.795	0.9808	0.0997	0.0594	0.765
	TE (2.25 CA Chips)	0.9824	0.0383	0.0279	0.936	0.9830	0.1019	0.0594	0.825
	MF	0.9869	0.0379	0.0254	0.707	0.9803	0.0972	0.0583	0.668
ASI AMSR2	**NDDMA (3*3)**	0.9745	0.1347	0.0795	0.798	0.9756	0.1745	0.0990	0.808
	NDDMA (3*5)	0.9753	0.1384	0.0811	0.737	0.9758	0.1741	0.0988	0.744
	NDDMA (3*7)	0.9726	0.1464	0.0864	0.681	0.9755	0.1789	0.1013	0.688
	TE (0.75 CA Chips)	0.9678	0.0886	0.0601	0.577	0.9755	0.1529	0.0886	0.454
	TE (1.5 CA Chips)	0.9764	0.1018	0.0626	0.804	0.9733	0.1488	0.0877	0.737
	TE (2.25 CA Chips)	0.9744	0.1015	0.0635	0.942	0.9808	0.1579	0.0885	0.782
	MF	0.9764	0.0985	0.0609	0.725	0.9748	0.1506	0.0878	0.642

Antarctic regions have a great deal of sea ice as the melting process is just starting. Again, the transitions are monitored by the GNSS-R data. Note that in the Antarctic, there is an area close to the coast that melted before the outer ice layer, and it is detected by the GNSS-R data. Also, note that for those images, there is much less GNSS-R data available. This occurs because the UK TDS-1 2014 dataset comes from the beginning of the mission, whereas the 2015 one comes from a more consolidated period of the mission. Figure 10.8 shows when the ice in the Antarctic is starting to grow again due to the beginning of the freezing period in that area. Also note that as it is a more advanced period of the mission, more valid data is available showing a similar performance with more transects.

Finally, in order to show the performance of the algorithm at a higher resolution, Fig. 10.9 is added. Fig. 10.9(a)–(b) represent a zoomed area on the Arctic region, whereas Fig. 10.9(c)–(d) represent a zoomed area on the Antarctic region. It can also be seen how the spatial resolution of the SIC maps from the ASI algorithm is better than the one from the OSISAF, the images of which are more blurred. Recall that ASI uses one single frequency to estimate SIC, whereas the OSISAF algorithm uses a combination of frequencies resulting in smooth transitions or this blurring effect. Note that there are some missing points on the GNSS-R dataset in the OSISAF maps in comparison to the ASI maps and this occurs because the SIC value from the OSISAF map was flagged as unreliable. If the SIC ground-truth value is unreliable the GNSS-R data are not plotted. No quality flag was available from the ASI maps, so only the GNSS-R SNR data filtering is affecting those maps and all ground-truth pixels are considered reliable.

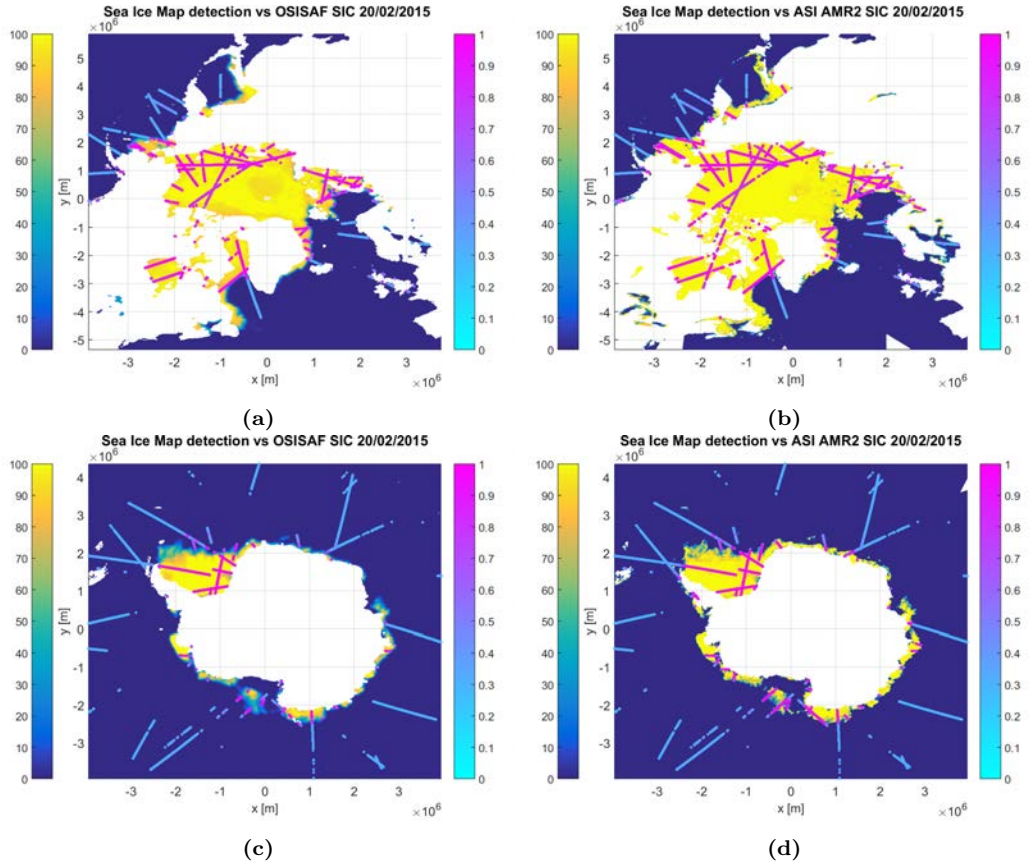

Figure 10.6: Sea Ice Concentration Maps of February 20, 2015 from OSISAF and ASI AMSR2 of the Northern and Southern Hemisphere overlayed with the matched filter GNSS-R approach, (a) Arctic OSISAF, (b) Arctic ASI AMSR2, (c) Antarctic OSISAF, (d) Antarctic ASI AMSR2. The gaps are due to GNSS-R data with thermal SNR lower than 0 dB or land contaminated pixels. In the OSISAF maps, there might be also gaps in the case of unreliable retrievals due to the quality flag.

10.6 Summary and Discussion

This Chapter has presented a methodology to monitor and detect sea ice presence over the Arctic and Antarctic regions using UK TDS-1 GNSS-R data. The detection is based on the analysis of the coherency of the measured DIW or DDM, as when the reflection occurs over a sea ice region, the scattering is mostly coherent, whereas when it occurs over open ocean, it follows the incoherent model. Three different estimators with different properties are used along the manuscript for the sea ice detection: the normalized DDMA, the TES, and the MF estimators. Among them, the MF estimator is preferred as it classifies with only one value between 0 and 1 if it is an ice pixel or an open ocean pixel. Furthermore, it is the one that requires less computational cost and it can be implemented easily on the onboard processing. In order to assess the validity of the algorithms proposed,

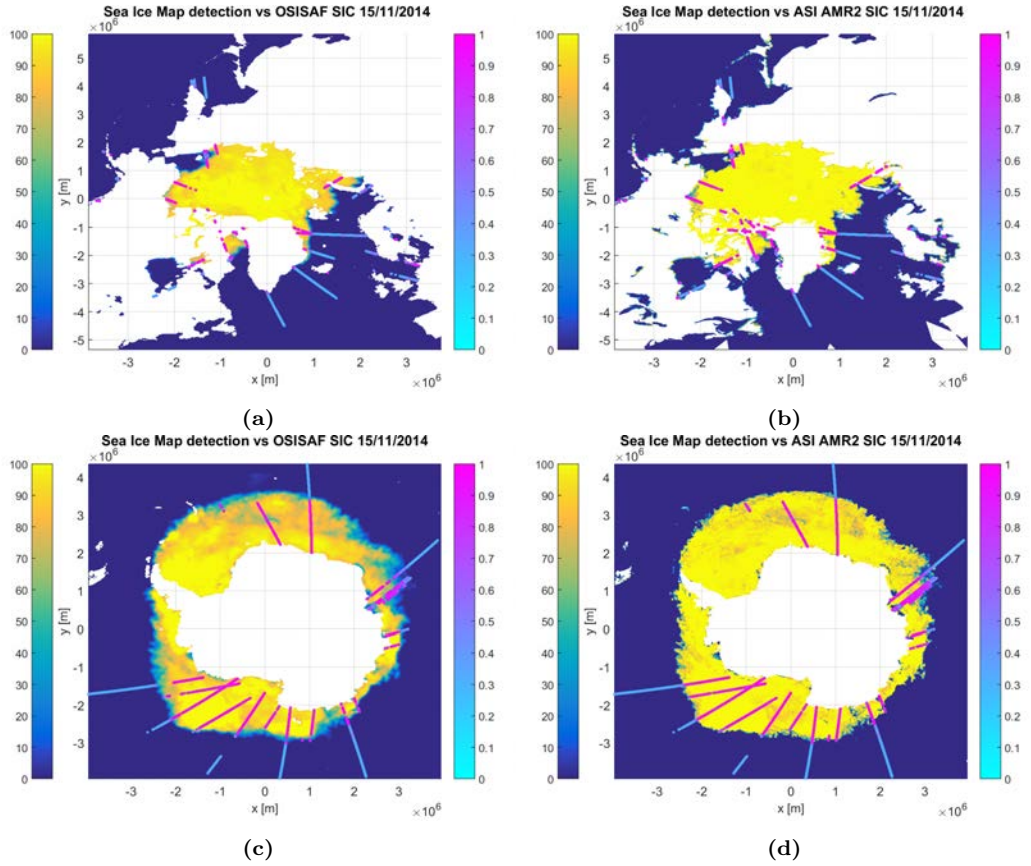

Figure 10.7: Sea Ice Concentration Maps of November 15, 2014 from OSISAF and ASI AMSR2 of the Northern and Southern Hemisphere overlayed with the matched filter GNSS-R approach, (a) Arctic OSISAF, (b) Arctic ASI AMSR2, (c) Antarctic OSISAF, (d) Antarctic ASI AMSR2. The gaps are due to GNSS-R data with thermal SNR lower than 0 dB or land contaminated pixels. In the OSISAF maps, there might be also gaps in the case of unreliable retrievals due to the quality flag.

two different ground-truth datasets have been used: the OSISAF dataset, and the ASI algorithm over AMSR2 data. The best results are obtained for both, the TES estimator in its three versions and the MF estimator, over the Arctic region and using the OSISAF dataset as ground truth, obtaining a Pd larger than 98% and a Pe of approximately 2.5%. The Pfa is between 3.5%–4%.

Apart from that, it has been attempted to go deeper and determine if the coherent GNSS-R waveform was sensitive to other parameters apart from the sea ice presence, and therefore if it could be used, for instance, for sea ice classification (first year, multi-year, or pure ice [231]). Following the ice scattering coherent model, one would expect to find the largest power received when there is thin ice, since the water is freezing and calm (a property of new ice formation [211]), and water has a very large dielectric constant. When the SIC increases, the equivalent dielectric constant is a mixture of the ice one and

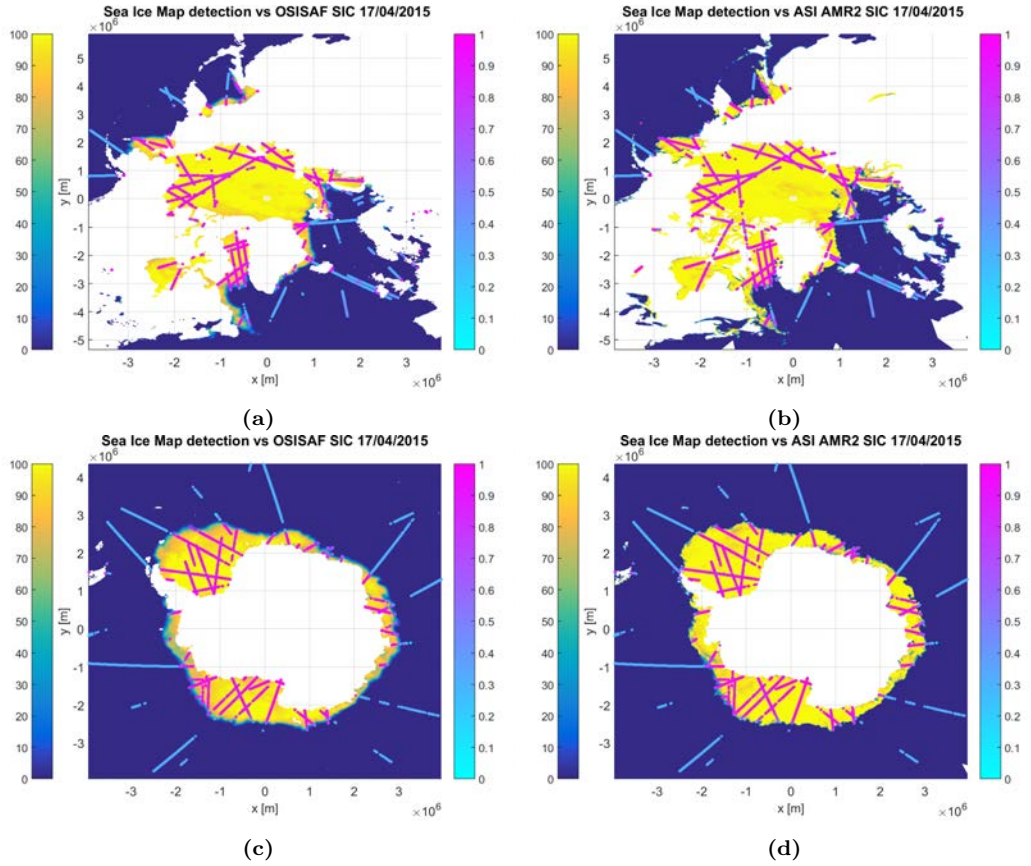

Figure 10.8: Sea Ice Concentration Maps of April 17, 2015 from OSISAF and ASI AMSR2 of the Northern and Southern Hemisphere overlayed with the matched filter GNSS-R approach, (a) Arctic OSISAF, (b) Arctic ASI AMSR2, (c) Antarctic OSISAF, (d) Antarctic ASI AMSR2. The gaps are due to GNSS-R data with thermal SNR lower than 0 dB or land contaminated pixels. In the OSISAF maps, there might be also gaps in the case of unreliable retrievals due to the quality flag.

water one, and since the dielectric constant of ice is much smaller than the water one, the equivalent dielectric constant decreases, and therefore so does the reflected power or the reflected SNR. This means in the limit, when the SIC is 100%, the coherent model would work, but with a lower power echo received. The same reasoning applies to first-year ice, the dielectric constant of which is larger than the one of multi-year ice, which in its turn has the dielectric constant larger than the one of the pure ice. Conversely, no correlation was found between the SNR received and the SIC. This might be interpreted as GNSS-R not being sensitive to the SIC. However, UK TDS-1 data were not calibrated, therefore, having a mixture of data from different satellites with an unknown transmitted power and different antenna gains prevents the extraction of any robust and reliable conclusion from the dataset used. This relation should be explored in the future with calibrated data and larger SNR values. Also, different roughness scales may apply to this analysis,

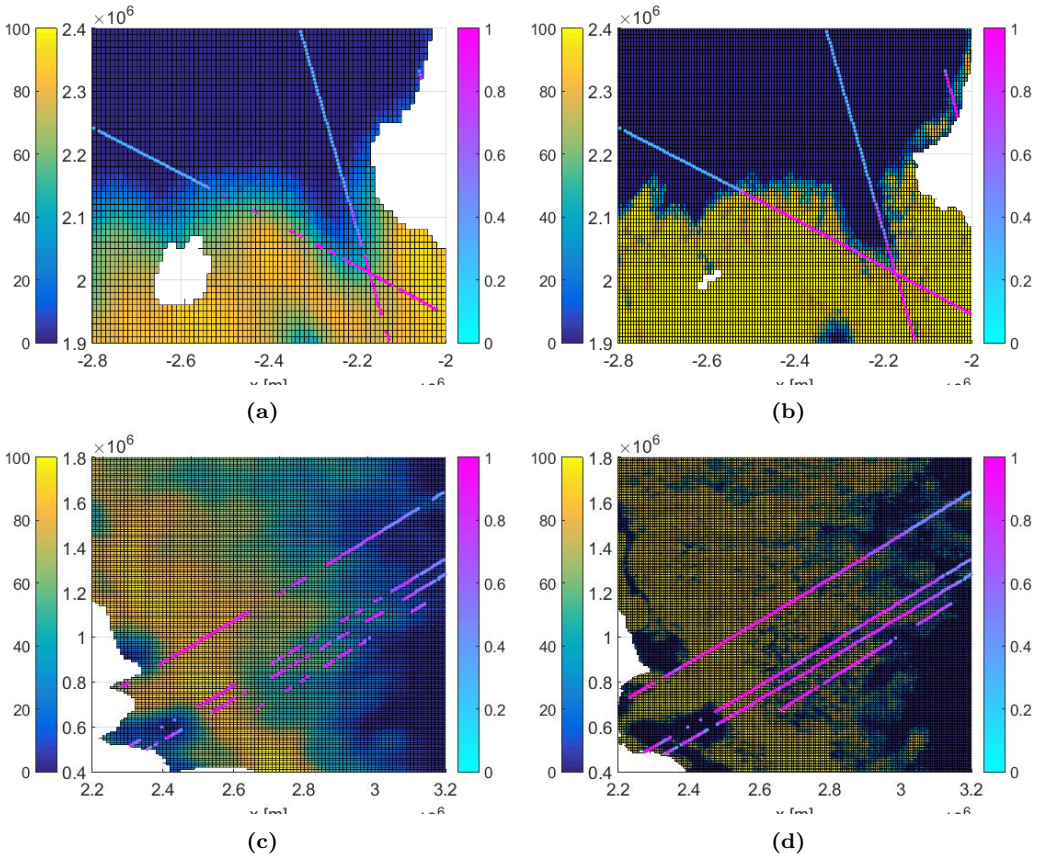

Figure 10.9: Zoom of Sea Ice Concentration Maps of February 20, 2015 for the Arctic data and from November 15, 2014 for the Antarctic data, for both OSISAF and ASI AMSR2 ground truth overlaying the matched filter GNSS-R approach, (a) Arctic OSISAF, (b) Arctic ASI AMSR2, (c) Antarctic OSISAF, (d) Antarctic ASI AMSR2. The gaps are due to GNSS-R data with thermal SNR lower than 0 dB or land contaminated pixels. In the OSISAF maps, there might be also gaps in the case of unreliable retrievals due to the quality flag.

making it more difficult to obtain a clear and unambiguous relation. CYGNSS mission will provide calibrated data, but its orbit, which was selected to monitor tropical cyclones, will preclude picking reflections from sea ice. In order to test this hypothesis, data from the forthcoming ESA GEROS-ISS mission will be needed. Furthermore, NASA may consider a potential continuation of the CYGNSS mission, and new scientific challenges such as the SIC monitoring could be one of its goals.

Due to the scattering properties of the L-band GNSS signals when the reflection is coherent, the ground resolution of the GNSS-R data corresponds to the First Fresnel Zone [145, 146], which is approximately 400 m x 400 m meters for a satellite at 650 km altitude. Taking into account the satellite's speed (6 km/s) and 1 s of non-coherent integration, this leads to a final ground resolution of approximately 6 km x 0.4 km. This resolution is similar to the one achieved by microwave radiometers working at 90 GHz, in

the along-track direction, and much better in the across-track direction. Furthermore, the spatial resolution of coherently scattered GNSS signals is much better than microwave radiometers working at the same frequency band, such as SMOS, Aquarius, and/or SMAP. This is a major point regarding this technique, since technology at L-band is much cheaper than at 90 GHz. Furthermore, L-band is much less sensitive to atmospheric effects than the 90 GHz frequency band [232], requiring fewer corrections. However, when the reflection is produced rough water, the spatial resolution is largely degraded, as the reflection is mostly incoherent, and it becomes 40 km x 40 km for the first iso-range ellipse and it varies depending on the DDM cell [233].

One disadvantage of the GNSS-R approach that is worth mentioning is that, currently, due to the dearth of available satellite data, the product derived contains much less information than the one derived from the conventional radiometric data. Consequently, at the time of writing this dissertation, the sea ice product derived from the GNSS-R is not competitive enough in comparison to the radiometric one. However, the planned launch of new GNSS-R satellite constellations and the rise of available GNSS satellites would help to cover this gap, and therefore generate a product with the same spatial resolution and the same coverage than the higher frequency passive techniques, at a fraction of their cost.

One aspect that has not yet been discussed is the Pfa obtained by all the estimators, and the reasons why a false alarm may be produced. The sea ice presence is determined by the coherence of the received signal, which means that the reflected surface must be flat. In several of the datasets used, it has been noticed that close to the sea ice edges the GNSS-R data were detecting ice presence, whereas the ground-truth had not yet detected ice. The ground-truth data used are SIC maps obtained averaging several images of several radiometer orbits passes, and each pixel data is not time referenced. However, the GNSS-R data are time referenced. Several continuous data observations showed that when ice was detected close to the ice edges by the GNSS-R technique, but not with the radiometric data, the following day it was detected as an ice pixel by the radiometric data. This indicates that either the OSISAF data and the AMSR2 data were obtained sometimes hours before the GNSS-R data, or that in the freezing process (new ice formation) the sea might become calmer before freezing, and the proposed GNSS-R technique detects ice also when sea becomes calmer (coherent reflection). This occurs because coherent reflection has been directly associated to a flat surface and to sea ice, whereas the sea has been assumed to be always rough. A flat sea will therefore result in a false alarm or an incorrect detection. This last observation was analyzed using the TDS-1 data plotted over Google Earth together with MASIE-NH data from the Northern hemisphere plotted over GE too (MASIE-NH data obtained from: `https://nsidc.org/data/masie/`).

The results presented in this chapter are encouraging for future GNSS-R missions, since the presented GNSS-R technique is more cost-effective, has the same ground resolution as compared to microwave radiometers at 90 GHz, and it is less prone to atmospheric influence. Currently available GNSS-R data show much less coverage than passive microwave sea ice data, but future missions will help to evaluate how competitive this technique can be against the traditional ones. Unfortunately, the CYGNSS mission that will be launched in 2016 will not be able to test these algorithms due to its orbit inclination (35°), but other forthcoming GNSS-R missions such as GEROS-ISS, or a potential CYGNSS follow-on mission will be able to.

11

Chapter 11

Vegetation Canopy Monitoring Using a GNSS-T Technique

This chapter describes the campaign performed at *La Fageda d'en Jordà, Girona*, Spain. The field experiment was conducted to measure some vegetation canopy parameters using a single GPS receiver placed under the vegetation. The attenuation induced by the vegetation layer on the GPS signal received power is related to some of its parameters.

11.1 Introduction

Since one part of this PhD Thesis dissertation is the continuation of the research lines proposed in [28], a particular field campaign was conducted aiming at simplifying the GNSS-T algorithm developed in [158] and presented in the next subsection.

11.1.1 The Walnut Field Experiment

In [158] two GPS receivers were collocated in open-sky conditions (a) and under a walnut forest (b), as depicted in Fig. 11.1, respectively. They were collocated in those conditions the closest possible to each other, in order to see the GPS satellites in the same sky position at the same time. The attenuation induced by the vegetation layer was inferred from the ratio between the open sky signal power and the signal power under the vegetation layer [158]. Therefore:

$$\frac{P_{veg}}{P_{sky}} = \frac{|E_{veg}|^2}{|E_{sky}|^2} = \gamma, \tag{11.1}$$

where P_{veg} stands for the signal power under the vegetation layer, P_{sky} for the signal power in open sky conditions, E_{veg} for the electric field amplitude under the vegetation layer, E_{sky} for the electric field amplitude in open sky conditions, and γ for the attenuation parameter.

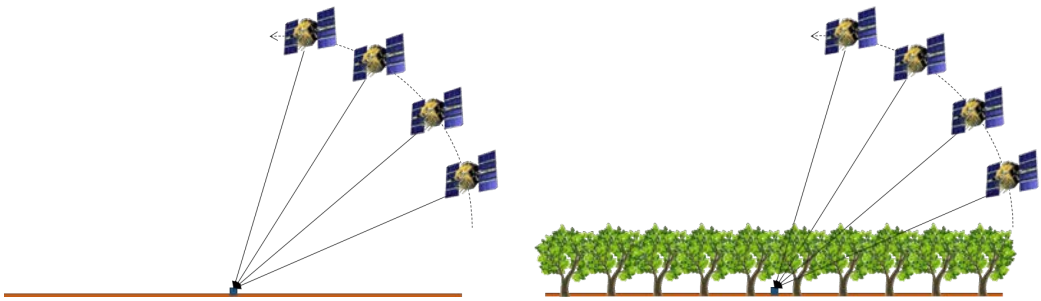

Figure 11.1: Initial GNSS-T vegetation experiment configuration.

Following the $\tau-\omega$ vegetation model used in L-band microwave radiometry, e.g. in the SMOS retrieval algorithm [234–236], and assuming a negligible single scattering albedo parameter, the γ parameter is expressed by:

$$\gamma = exp\left(-\frac{\tau}{\cos\left(90-\theta_{elev}\right)}\right), \tag{11.2}$$

where τ stands for the vegetation opacity, and θ_{elev} for the GPS satellite elevation angle. Also in [158, 234, 236, 237] the vegetation opacity is given as a function of the vegetation water content (VWC) parameter, and a specific canopy parameter (b) which depends on the particular type of vegetation. In such case:

$$\tau = b \cdot VWC, \tag{11.3}$$

where the b parameter takes values of 0.125 for a wheat field, 0.2 for a soybean field [234], and larger values for a corn field (0.4–0.6) [235].

In [158] the estimated values of τ from the GPS measurements were compared to the VWC from the leaves measured from the walnut trees. Figure 11.2 provides and overview of the field experiment conditions. The VWC or Leave Water Content (LWC) was estimated by weighting some leaves samples in moist and dry conditions. Figure 11.3 shows the vegetation opacity estimated as a function of the incidence angle. Using the estimated opacity and the LWC measured, the b parameter was estimated for the walnut trees. The b parameter also changed with the incidence angle as it could be seen in [235]. It was also significantly larger than for the conventional vegetation models used (around 0.8 while vegetation models use a value around 0.15), but as predicted in [234, 235, 237] it is highly dependent on the vegetation canopy type. Finally, Fig. 11.4 shows a comparison between the estimated LWC and the measured one for the entire field campaign using the estimated b parameter.

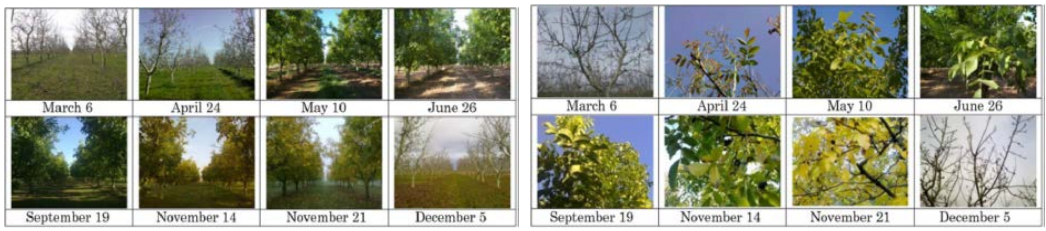

(a) **(b)**

Figure 11.2: Walnut trees (a) and leaves (b) field experiment conditions [158].

11.1.2 Other Experiments

Even though not much more data from GPS receivers located under forest has been analyzed for the retrieval of geophysical parameters, and has been made publicly available, there are other sources which are worth to mention. In [238] there are two examples of GPS receivers in open sky conditions (unobstructed) and below vegetation canopy (obstructed) for two different vegetation types: one for corn, and the other one for a deciduous forest. Figure 11.5 shows those examples obtained from [238]. For the corn field, an elevation angle dependency is observed such as the one explained in the previous section, which is driven by the vegetation opacity and the satellite elevation angle. For the forest case, and differently from the corn and from the theory explained in the previous section, two effects are observed: a bias, and an elevation angle dependence, but not as high as the bias.

In [239] it is shown that the amount of leaves on a deciduous forest degrades severely the accuracy of the GPS solution calculated from GPS receivers located under the vegetation canopy. The larger the percentage of sky obstruction due to the presence of leaves, the larger the error (σ) in the position estimation leading to a degradation of 2 mm per percentage of sky cover. Generally, the larger the percentage of sky cover, the larger the attenuation due to leaves, the lower the SNR of the GPS signals, and therefore the poorer

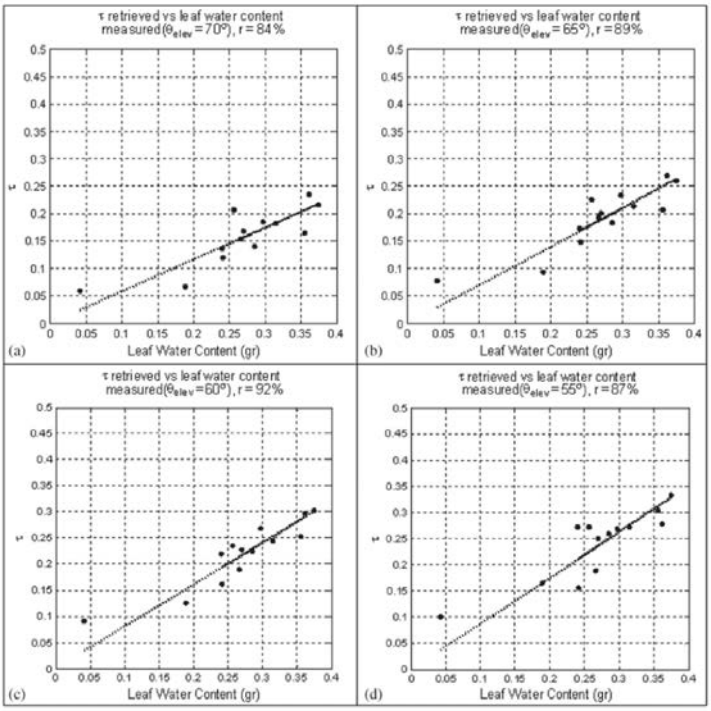

Figure 11.3: Vegetation opacity estimated as a function of the incidence angle [158].

the GPS performance. In [240] similar conclusions than in [239] were found through other field experiments. In [241] the effect of stems and canopy on the GPS SNR data is analyzed, concluding that the major degrading factors are the satellite elevation angle and the wood resistance quantity (directly related to the wood water content). In [242] the effect of moisture in wood materials on the GPS SNR data is also estimated.

Generalizing, despite several investigations have been conducted, they have practically all been related to the evaluation of the GPS accuracy degradation, instead of using that degradation to retrieve some vegetation canopy parameters. Also, apart from that, a forest is a complex structure with different layers: the upper layer (crown) contains leaves, branches and the trunk, a second layer where only the trunk appears, a third layer for some forests where the understory is found, and a final layer with the litter and the soil. These also complicates a little bit more the analysis of the effect of the vegetation canopy on the measured GPS SNR.

The goals of the field experiment described in this Chapter are the retrieval of vegetation parameters using a single GPS receiver instead of two, and the analysis of both RHCP and LHCP received power as a function of the vegetation canopy status. The relationship between GPS SNR data and different vegetation parameters obtained from satellite data and from in-situ data is also studied.

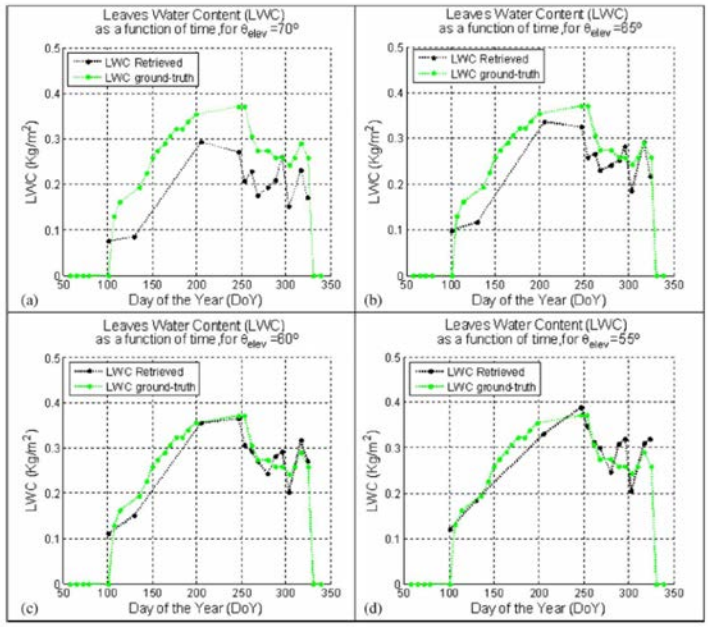

Figure 11.4: Estimated and measured LWC for the entire field campaign [158].

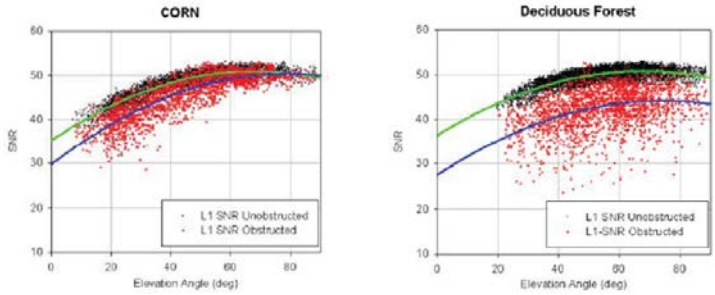

Figure 11.5: Comparison between GPS receivers located in open sky conditions and below two different vegetation canopies: corn, and a deciduous forest [238].

11.2 Field Experiment Description

A field experiment using the McGiver instrument described in Chapter 5 started in August 3, 2015 at *La Fageda d'en Jordà, Girona*, Spain, and it is scheduled to end in October, 2016. *La Fageda d'en Jordà* is a highly populated beech forest (deciduous tree), located close to the city of *Olot* (42° 10′ 56″N, 2° 29′ 20″E). Figure 11.6 shows precisely where it is located highlighting larger cities such as *Girona* and *Barcelona*. The main interest is to gather data from two different periods: the first one is when leaves fall during the autumn season (defoliation), and the second one is when leaves grow again during the spring season. With those data the effect of the presence of leaves on the crown can be analyzed. Apart from that, the effect of branches and trunks can be analyzed

by comparing the received signal power when the leaves have fallen with the open sky conditions estimated in a preliminary calibration stage.

Figure 11.6: Location of *La Fageda d'en Jordà*.

11.2.1 Preliminary Calibration

After the McGiver instrument was manufactured and the antennas were measured at the UPC anechoic chamber [155], a preliminary test was conducted at UPC premises (roof of D3 building). The instrument measured continuously the received signal power in both receiving channels (RHCP and LHCP) for 6 days. Figure 11.7 shows the average measured C/N0 for different blocks of azimuth and elevation angles after compensating the antenna pattern effect. In this case, the elevation/incidence angle (polar radial axis) has been binned in blocks of 5°, whereas the azimuth angle (polar angular axis) in blocks of 10°. The larger the radius, the lower the elevation angle or the larger the incidence one. As it can be observed, due to the compensation of the different antenna gains observed in the different directions, the mean received C/N0 is mainly constant, a fact that should be accomplished according to the GPS system design properties. There are also some white spots and a white region on the top of each figure. The former occurs because for that particular day the GPS constellation did not fill that area. It can be observed that there are very few white spots not covered. The latter occurs because for the Northern hemisphere there are no GPS satellites in the North direction.

Figure 11.8 shows the analogous figure to Fig. 11.7 for the LHCP channel also compensating for the LHCP antenna radiation gain pattern. In this case the same white spaces than in Fig. 11.7 are observed due to the same reasons. According to the radiation pattern diagrams for the McGiver instrument shown in Chapter 5, only a small part of the LHCP radiation pattern accomplishes a 20 dB cross-polar rejection, which is the minimum required to analyze and use that polarization state. This is reflected in Fig. 11.8, where even after compensating by the radiation pattern, the received power is not con-

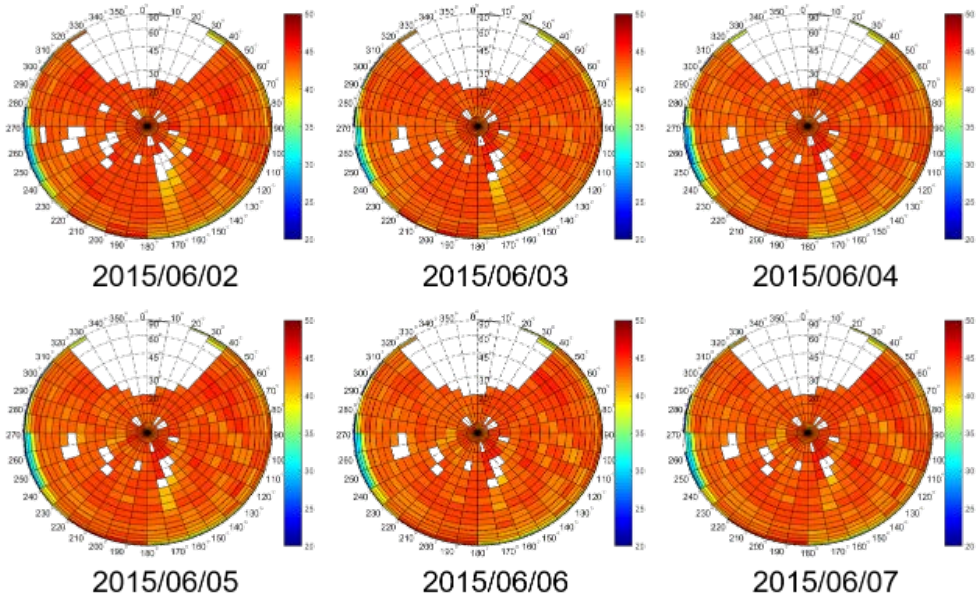

Figure 11.7: RHCP received C/N0 from June 2, 2015 until June 7, 2015 during the preliminary test after compensating the antenna pattern effect. Data have been binned in blocks of 5° in the elevation angle parameter and in blocks of 10° in the azimuth angle parameter.

stant as it should be according to the GPS system design specifications. This reduces the use of the LHCP channel to elevation angles between 0°–30°, where the requirements are satisfied.

Finally, Fig. 11.9 shows the average C/N0 for different satellite elevation angles at the two channels. To compute them, all azimuth blocks with available data have been used (maximum of 36 blocks) and the white spots have been treated as missing data. The constant behavior for the six days can be quickly appreciated for any satellite elevation angle for the two channels. Figure 11.9 shows, as previously claimed, that for the RHCP channel there is nearly no differences with the satellite elevation angle after the antenna pattern compensation. Conversely, as previously commented, the use of the LHCP channel is limited by the elevation angle due to the LHCP antenna cross-polar pattern behavior (±22.5°), even though the gain pattern was compensated.

11.2.2 Test Site Description and Evolution

After the success of the validation/calibration stage, the McGiver instrument was finally installed at the test site on August 3, 2015. Figure 11.10 shows the instrument installed. The leveler was used to install appropriately the instrument and align it with the horizontal plane. The azimuth reference used for measuring the pattern at the anechoic chamber was pointed towards the North direction with the help of an electronic compass.

Different pictures of the vegetation state were taken during the falling and growing

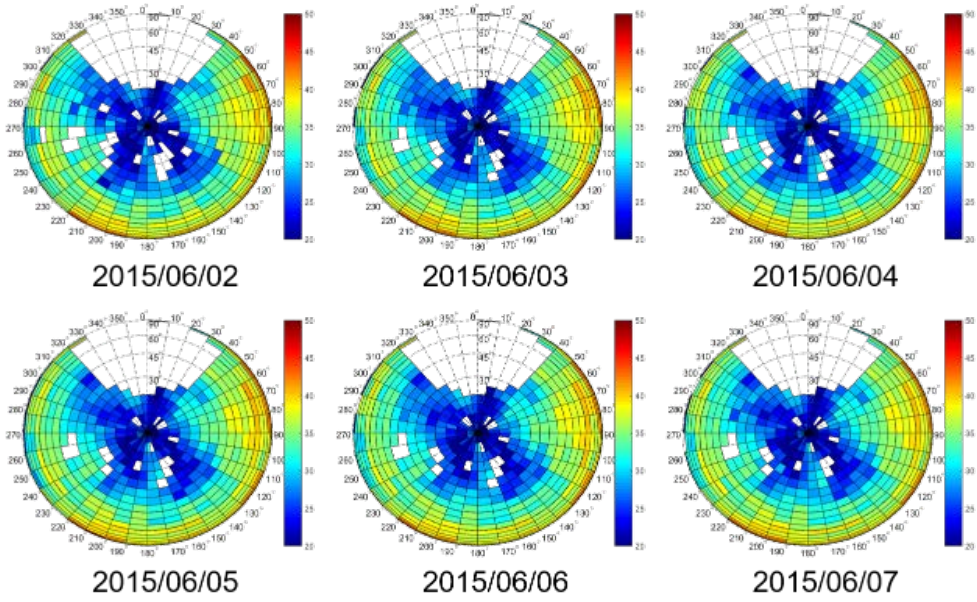

Figure 11.8: LHCP received C/N0 from June 2, 2015 until June 7, 2015 during the preliminary test after compensating the antenna pattern effect. Data have been binned in blocks of 5° in the elevation angle parameter and in blocks of 10° in the azimuth angle parameter.

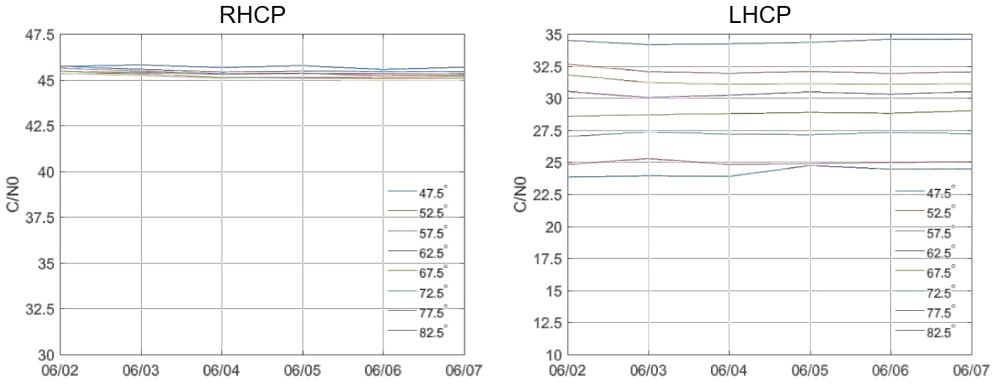

Figure 11.9: Average C/N0 for different satellite elevation angles.

seasons with a camera located at the instrument's position looking to the zenith. They are shown in Figs. 11.11–11.12, respectively. Both defoliation and growing processes are clearly identified. As it can be seen, even though there is a chestnut tree on the pictures, the main predominant vegetation on the test site were beeches, with nearly no understory during the entire field campaign (Fig. 11.10), and some litter which did not affect at all the measurements made.

Figure 11.10: McGiver installed at *La Fageda d'en Jordà*.

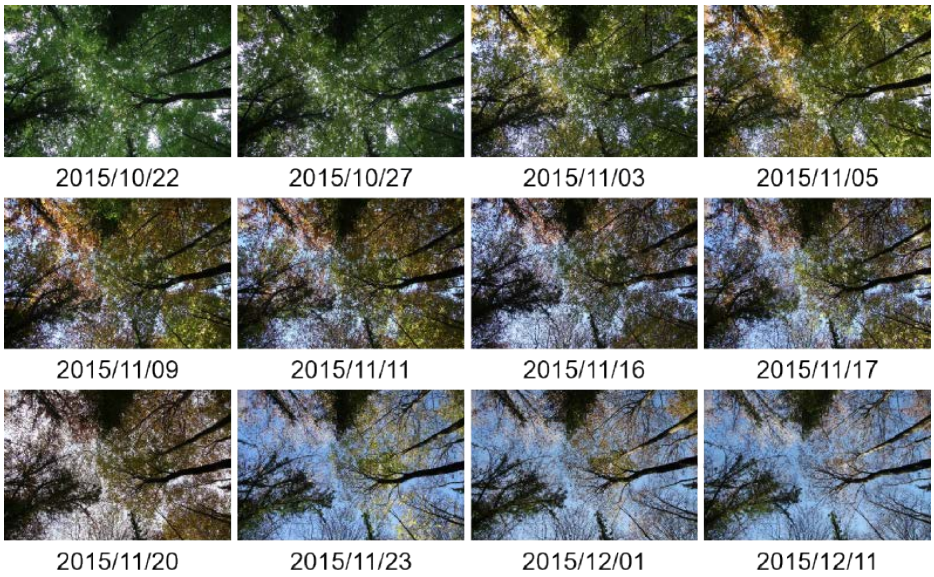

Figure 11.11: Vegetation observed from a camera located at the instrument's position looking to the zenith during the falling season.

11.2.3 Ground-truth Available

Different sources have been taken into account for the data analysis. Figures 11.11–11.12 were taken using a Canon EOS 50-D, with the exposure perfectly compensated. The camera was oriented towards the North, like the antenna, it used a focal length of 17 mm,

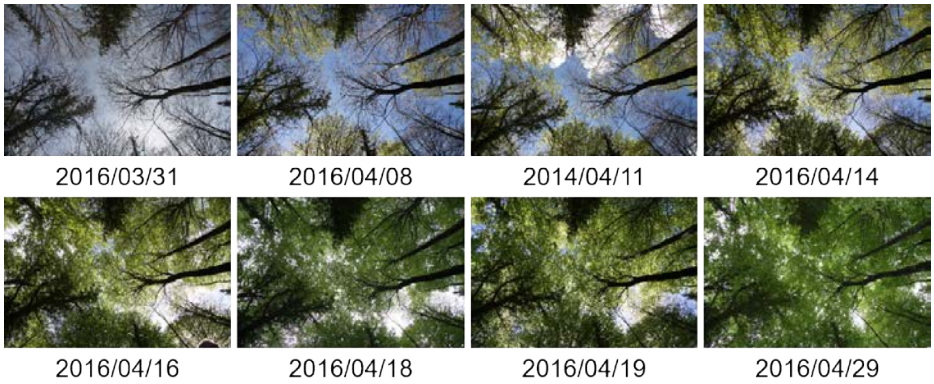

Figure 11.12: Vegetation observed from a camera located at the instrument's position looking to the zenith during the growing season.

and it was aligned with the horizontal plane too. The camera sensor is an APS-C type whose size is 22.3 mm x 14.9 mm. The FOV of the camera is 66.5° in one direction and 47.3° in the other one, which is far from the hemispherical photography properties. In the next section, different parameters such as the greenness or the percentage of sky cover will be computed from those pictures, and compared against the received signal power.

Apart from the pictures taken from the camera, LAI and NDVI maps downloaded from [243] have been used to obtain the vegetation parameters from a product derived using other frequency bands apart from the optical one. These maps were derived using data from the MODIS spaceborne sensor. The LAI maps have 0.1° resolution (10 km x 10 km at the ecuator) and a refresh rate of 8 days. The NDVI maps have the same angular and spatial resolution, but a refresh rate of 16 days. Figure 11.13 shows an overview of the entire range of NDVI maps used as ground-truth. As observed, a zoom at the Iberian peninsula has been made even though only information from the closest pixel to the instrument's location was used. The scale of the NDVI maps range from -0.1 to 0.9. The scale of the LAI maps range from 0 to 7 m^2/m^2.

Finally, rain data from a meteorological station located in *Olot* was used to analyze also the effect of rain on the measurements made [244].

11.3 SNR Data Analysis

On one hand, Figs. 11.14,11.16 show different examples of the received C/N0 in polar coordinates for the two channels RHCP and LHCP, respectively, during the defoliation period. It is clearly seen for the RHCP that the smaller the number of leaves on the trees, the redder the polar diagram due to less attenuation. Apart from that, one may think that leaves can be also a cause of depolarization. Therefore, the LHCP received power should reduce after the leaves have fallen. Conversely, it increases too (Fig. 11.16), indicating that the leaves' effect is attenuation instead of depolarization. The color of Fig. 11.16 changes from blue/green to green/yellow.

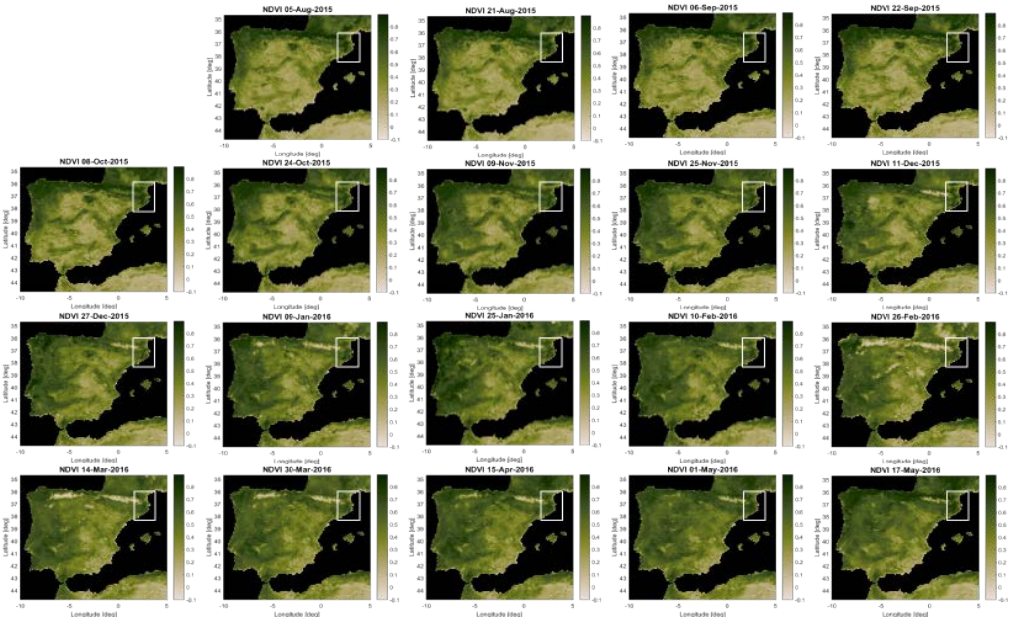

Figure 11.13: Zoom at the Iberian Peninsula of the NDVI maps obtained for the entire field campaign duration. The closest pixel to the instrument's location was the one used as ground-truth.

On the other hand, Figs. 11.15,11.17 show different examples of the received C/N0 when the leaves are growing. The red color in Fig. 11.15 is going down smoothly as leaves start to grow. The same occurs to Fig. 11.17 where the yellow/green color of the LHCP received power goes down to the blue/green received power, highlighting again the attenuation effect of leaves instead of the depolarization one.

Due to the vertical tree structure of the forest and the thick trunks of trees, which partially block the signal if they are extremely moist, an azimuthal asymmetry on the received power distribution is produced in comparison to Figs. 11.7–11.8. Despite this asymmetry, which is clearly observed in Figs. 11.14–11.17, the received C/N0 has been averaged azimuthally as in Fig. 11.9, in order to study its evolution with the elevation/incidence angle. The resulting C/N0 curves are now compared against different parameters such as:

- rain events obtained from the regional meteorological station,
- blueness, greenness, redness, and sky cover percentage computed from the pictures in Figs. 11.11–11.12,
- NDVI computed from MODIS, and
- LAI computed from MODIS.

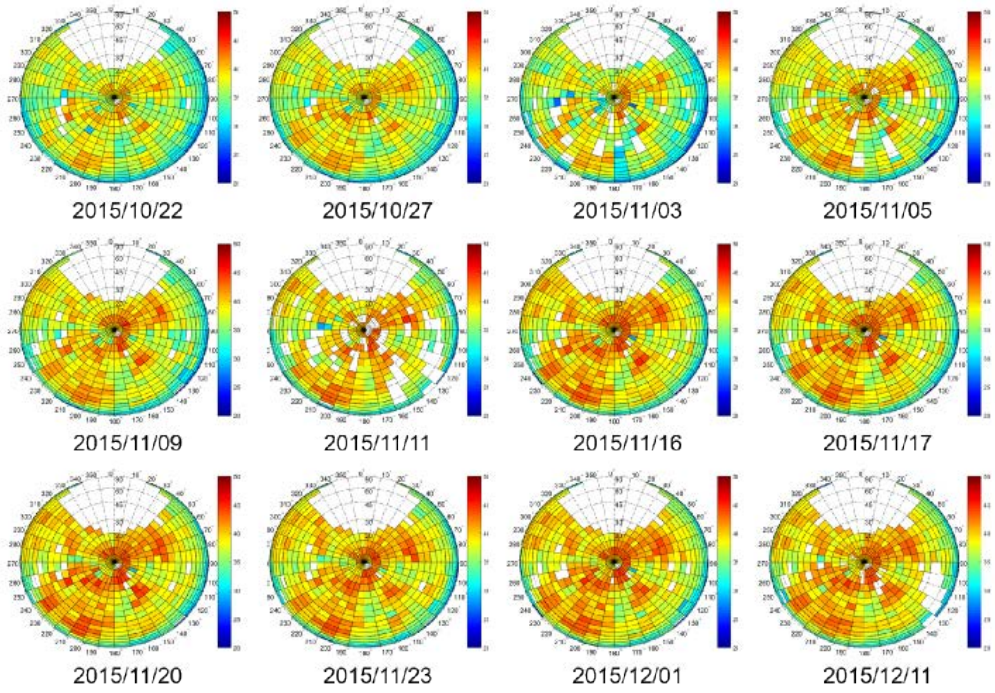

Figure 11.14: RHCP received C/N0 during the falling season for different dates when vegetation pictures were taken.

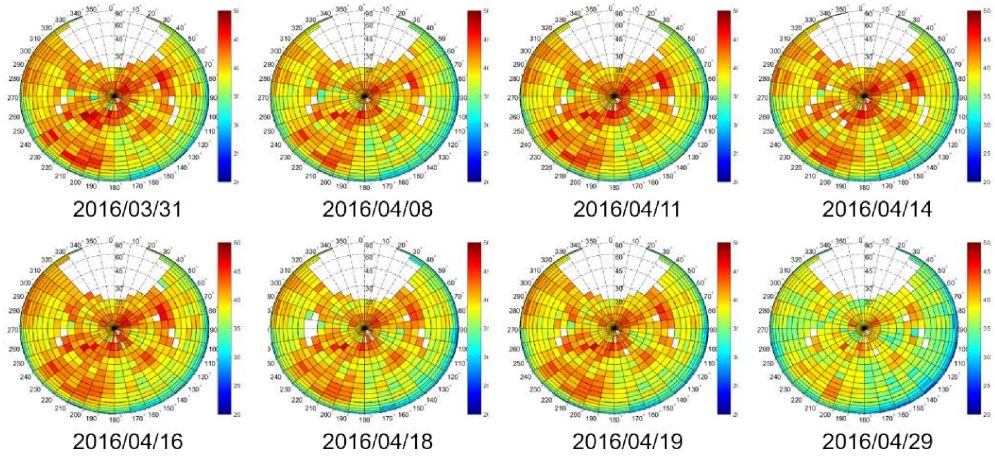

Figure 11.15: RHCP received C/N0 during the growing season for different dates when vegetation pictures were taken.

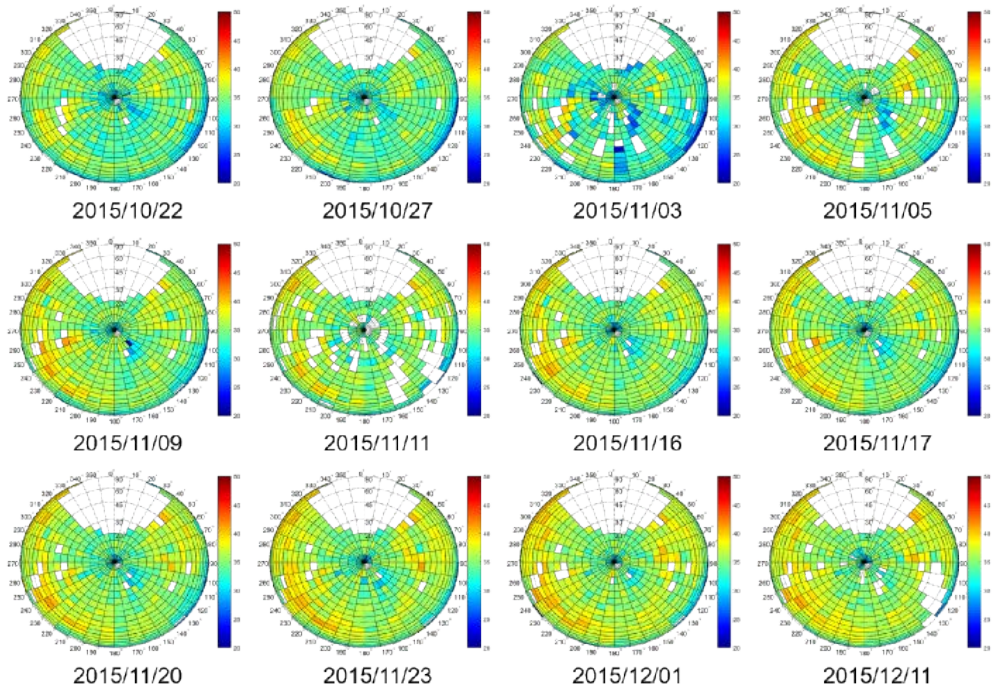

Figure 11.16: LHCP received C/N0 during the falling season for different dates when vegetation pictures were taken.

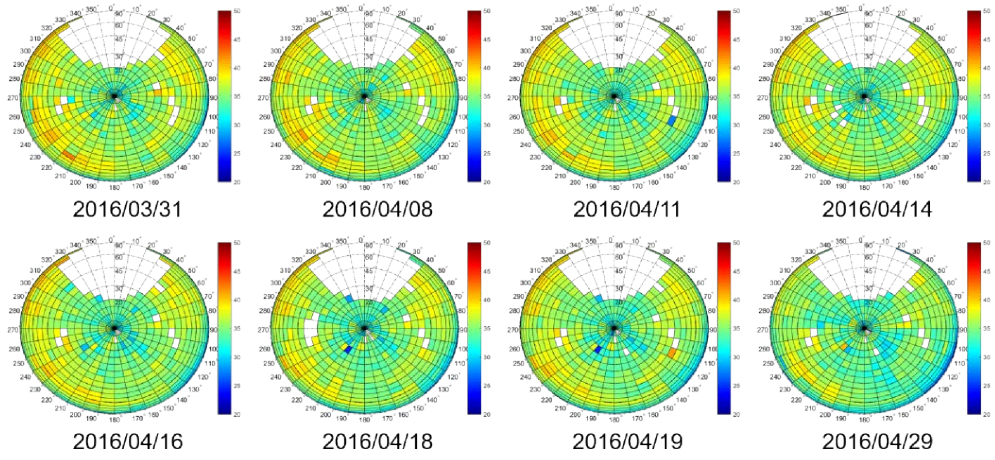

Figure 11.17: LHCP received C/N0 during the growing season for different dates when vegetation pictures were taken.

11.3.1 Rain Effect

Figure 11.18 shows the azimuthally averaged RHCP and LHCP C/N0 curves for different satellite elevation angles as a function of time together with the rain events present during

the field campaign. It can be clearly appreciated that the rain events appear as a fading on the C/N0 curves specially for the RHCP channel. This means that rain attenuates the signal transmitted by the satellites due to two main factors. The first one is the presence of water drops in the atmosphere that reduces a little bit its transmissivity, and the ones that stay on the leaves' surface, which also increase the attenuation induced by the leaves. The second one is the fact that after the rain event, trees absorb the water that falls to the soil, sending it to the leaves and therefore increasing their water content. Note that during the period without leaves (December 2015–April 2016), the fading events due to rain are much smaller than in the period with leaves because it is mainly the atmosphere transmissivity that is reduced and attenuates the signal.

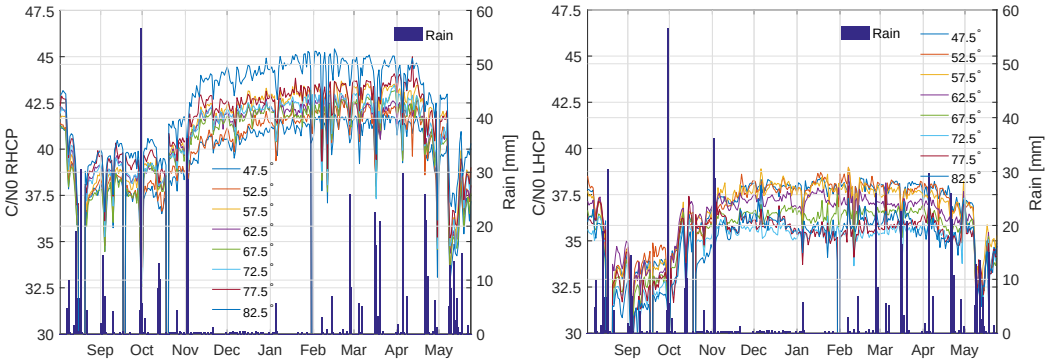

Figure 11.18: Effect of rain to the azimuthally averaged C/N0 curves: (a) RHCP, (b) LHCP.

11.3.2 Greenness

From Figs. 11.11–11.12 the greenness, blueness, and redness of the pictures can be measured using its RGB histogram as:

$$GR, RD, BL = \frac{\rho_{G,R,B}}{\rho_G + \rho_R + \rho_B}, \tag{11.4}$$

where GR, RD, BL stand for greenness, redness, and blueness, respectively; subindices G, R, B for green, red, and blue, respectively; and ρ_X for the amount of X color. Figure 11.19 shows the evolution of the greenness estimated from the pictures together with the azimuthally averaged RHCP C/N0 curves. It is expected that, the larger the greenness parameter, the larger the amount of leaves, and therefore, the larger the attenuation induced by them. During the defoliation process (October–December 2015), the R^2 parameter between the greenness and the different C/N0 curves is 0.76–0.87, it does not depend on the incidence angle, and the mean slope of the linear fit is -31 dB/au. For the growth of the leaves period (March–April 2016), the R^2 parameter goes down to 0.46–0.66, again it does not depend on the incidence angle, but the mean slope in this case is reduced to -17 dB/au. The different slope in the two periods seems to indicate that even though the greenness is related to the amount of leaves in the figures, it is not as related to their water content, which should be measured differently.

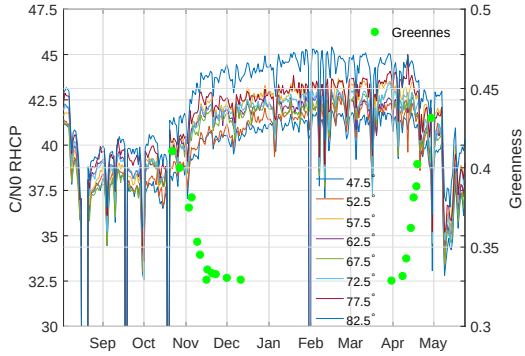

Figure 11.19: Evolution of greenness and C/N0 curves as a function of time.

11.3.3 Redness

Figure 11.20 shows the RHCP C/N0 curves together with the redness parameter. The R^2 parameter for both falling and growing season is below 0.05 for any elevation angle, and it does not depend on the season.

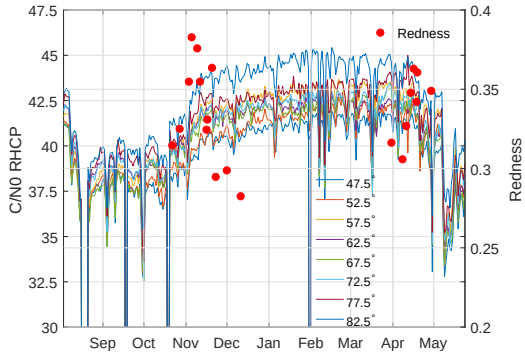

Figure 11.20: Evolution of redness and C/N0 curves as a function of time.

11.3.4 Blueness

Figure 11.21 shows the RHCP C/N0 curves together with the blueness parameter. As it occurred with the greenness parameter, the C/N0 curves and the blueness are correlated, but not as correlated as with the greenness. During the defoliation process, the R^2 parameter is between 0.46–0.58 with a slope of 14 dB/au. During the growing process the R^2 is between 0.25–0.43, with a slope of 10 dB/au. Again, the slope is different depending on the season and there is no incidence angle dependence. In this case, the correlation between curves appear because the amount of blue is related to the amount of sky observed, and therefore, the larger the amount of sky observed, the lower the amount of leaves. However, the amount of blue color seems to be a poorer vegetation indicator than the amount of green color, a fact that seems reasonable.

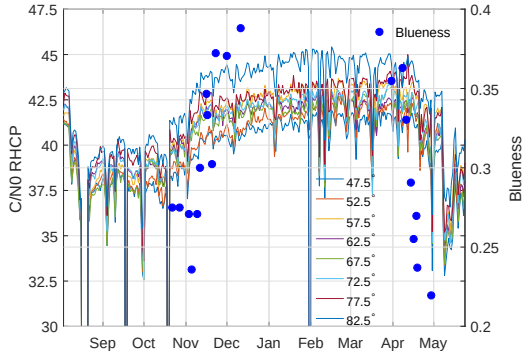

Figure 11.21: Evolution of blueness and C/N0 curves as a function of time.

11.3.5 Sky Cover

Figure 11.22 shows the RHCP C/N0 curves together with the percentage of sky covered computed in two different ways. On the left, the RGB images from Figs. 11.11–11.12 were converted to gray-scale (intensity, 0–255), and a threshold of 155 was selected to differ between vegetation and sky. This threshold was chosen in $[245, 246]$ to automatize the sky cover measurement from RGB pictures. Below 155 it was classified as vegetation, and equal or above 155 it was classified as open sky. On the right hand side of Fig. 11.22, the blue channel of the RGB image was selected as the observable for sky classification, and the same threshold applied. The larger the sky cover percentage, the larger the vegetation presence (leaves) and the larger the attenuation.

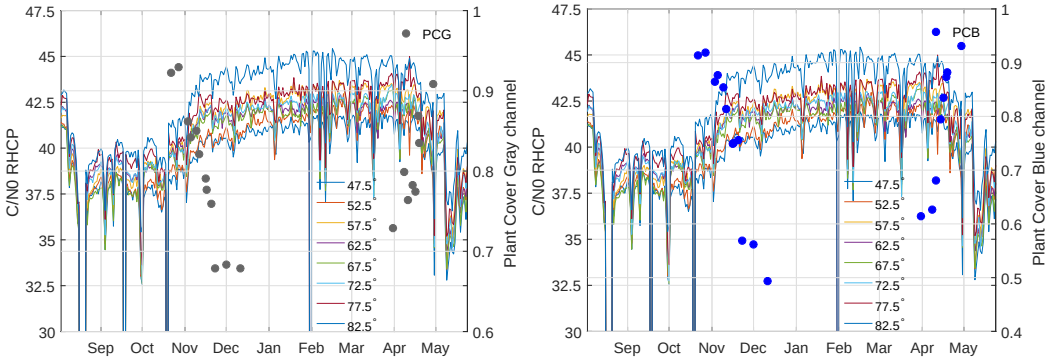

(a) gray-scale **(b)** blue channel

Figure 11.22: Evolution of the percentage of sky covered and C/N0 curves as a function of time: (a) using a gray-scale image, (b) using the blue channel of the RGB image.

Regarding the percentage of sky cover computed from the gray-scale image, the R^2 parameter between the different C/N0 curves and the percentage of sky cover is 0.6–0.7 for the falling season, whereas it is between 0.67–0.82 for the growing season. The slopes in this case are -9 dB/au and -12 dB/au, respectively, and again with no elevation angle dependence. If falling and growing seasons are combined, since the slopes are quite

similar, the R^2 parameter becomes 0.4–0.6, and the mean slope is -10 dB/au for all incidence angles. However, when using the blue channel to estimate the percentage of sky cover, the R^2 parameter is between 0.47–0.57 for the falling season, and 0.3–0.5 for the growing season. Again both are independent from the elevation angle. The slopes are around -5 dB/au in both cases. For the blue channel intensity, if falling and growing seasons are combined the R^2 reduces to 0.3–0.4 with a slope of -4.5 dB/au.

11.3.6 NDVI

Figure 11.23 shows the evolution of the NDVI parameter and the RHCP curves for different elevation angles. As mentioned before, the NDVI was retrieved from the closest pixel to the instruments' position in the global NDVI maps. There is a very high correlation between the received signal power or C/N0 and the NDVI. Figure 11.24 compares the NDVI values against the mean C/N0 value for different satellite elevation angles. For all satellite elevation angles the R^2 parameter is between 0.87–0.94, and the slope of the fit around -19 dB/au. Table 11.1 shows the fit parameters of Fig. 11.23. This relationship shows a clear sensitivity of the technique to the vegetation canopy status.

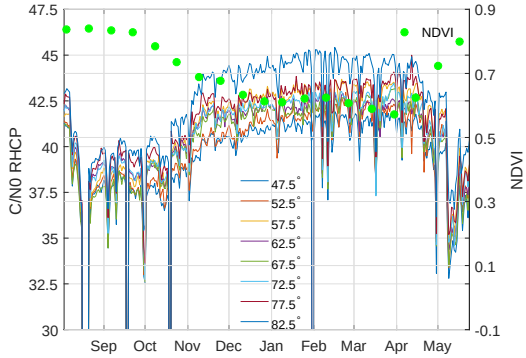

Figure 11.23: Evolution of NDVI and C/N0 curves as a function of time.

Table 11.1: NDVI fitting parameters.

Elevation angle	R^2	Slope [dB/au]	RMSE [dB]
82.5°	0.897	-22.6	0.67
77.5°	0.874	-18.8	0.65
72.5°	0.886	-18.8	0.62
67.5°	0.944	-20.7	0.48
62.5°	0.864	-17.9	0.65
57.5°	0.908	-21.1	0.61
52.5°	0.918	-17.6	0.49
47.5°	0.890	-16.9	0.55

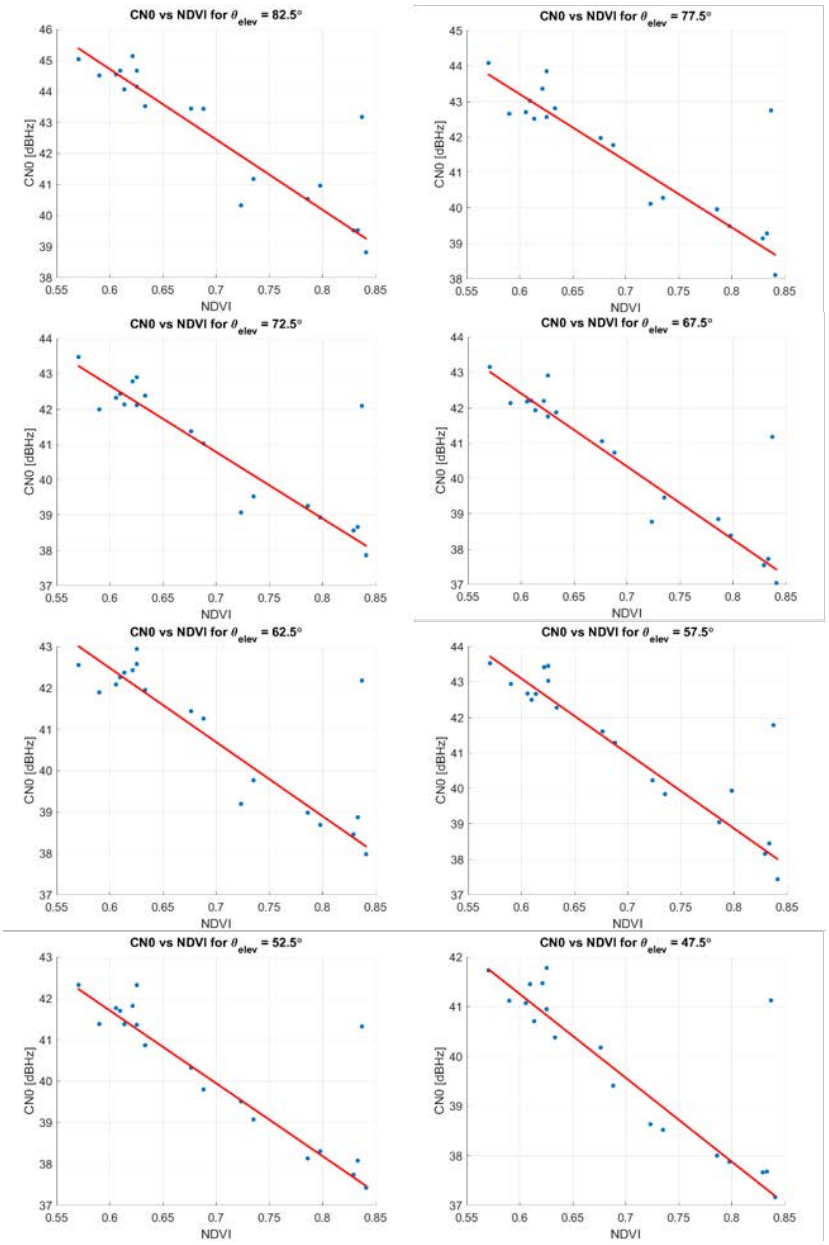

Figure 11.24: Comparison between NDVI and received signal power for different satellite elevation angles.

11.3.7 LAI

Figure 11.25 shows the evolution of the LAI parameter and the RHCP C/N0 curves for different elevation angles. The LAI parameter was retrieved in the same way than the

NDVI parameter, but using twice the number of maps due to their availability. There is some correlation between the received signal power and the LAI parameter, but it is not as high as with the NDVI. Figure 11.26 shows the same comparison than Fig. 11.24 but for the LAI parameter. This indicates that part of the attenuation observed on the GPS received signals comes from the leaves, but there is another part that comes from the branches and the trunks. The R^2 parameter is between 0.5–0.65 and the slope of the fit is around -1 dB/au in all cases as shown in Tab. 11.2.

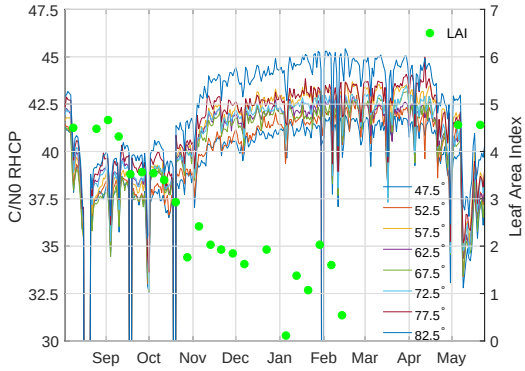

Figure 11.25: Evolution of LAI and C/N0 curves as a function of time.

Table 11.2: LAI fitting parameters.

Elevation angle	R^2	Slope [dB/au]	RMSE [dB]
82.5°	0.62	-1.44	1.20
77.5°	0.51	-0.94	1.28
72.5°	0.51	-0.89	1.47
67.5°	0.55	-1.12	1.27
62.5°	0.51	-0.90	1.21
57.5°	0.50	-1.15	1.46
52.5°	0.52	-0.87	1.28
47.5°	0.51	-0.87	1.20

11.4 Opacity Estimation

The previous section has shown the relationship between the received signal power and several parameters such as rain, greenness, redness, blueness, sky cover, NDVI, and LAI. For the NDVI and LAI cases, numerical relationships have been established. However, whether these data can be used for the vegetation opacity estimation is a question not yet answered. Following the τ - ω model [235], assuming homogeneity in the vegetation status, and a negligible effect from the understory, it can be deduced that the expected received SNR follows:

$$\mathrm{C/N0}\left(\theta_{elev}\right) = \mathrm{C/N0}\left(90°\right) exp\left(-\frac{\tau}{\cos\left(90° - \theta_{elev}\right)}\right). \tag{11.5}$$

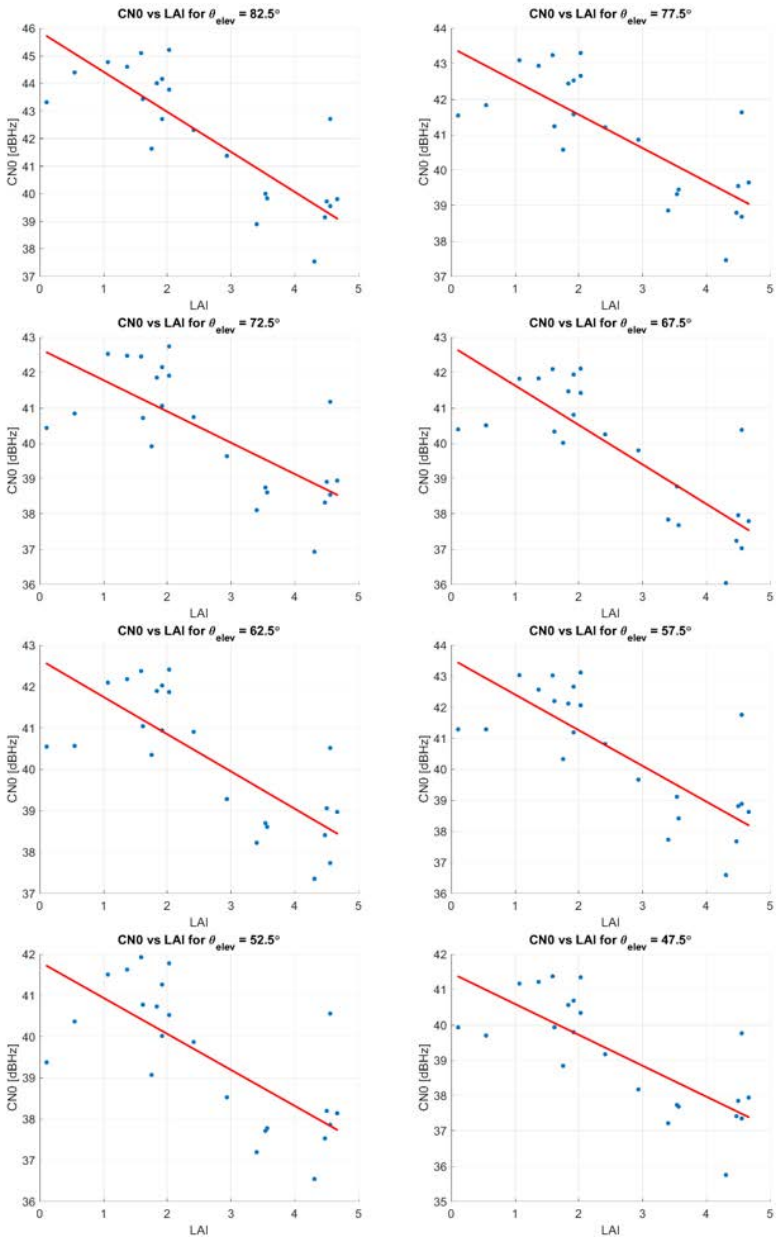

Figure 11.26: Comparison between LAI and received signal power for different satellite elevation angles.

Therefore, using two points like $\theta_{elev} = 90°$ and $\theta_{elev} = 30°$, the τ parameter could be theoretically estimated if the vegetation status and distribution was homogeneous. Basically, the attenuation induced by vegetation for $\theta_{elev} = 30°$ should be twice the one for $\theta_{elev} = 90°$. This methodology to estimate the opacity was tested, but the results

obtained were not fully satisfactory. There might be different causes that explain those results, such as:

- 30° incidence angle is out of the antenna beamwidth (±45°).
- Multipath from the different tree trunks which were thicker than the wavelength.

In order to change the approach and try to obtain more valuable results, instead of using only two points, the entire range of elevation angles available that fall into the antenna beamwidth can be used. Then, using a best fit approach the opacity can be estimated. In order to simplify the best fit approach, since the C/N0 data are normally provided in dB/Hz units, a transformation can be applied to Eqn. (11.5) leading to:

$$10\log_{10}\left[\mathrm{C/N0}\left(\theta_{elev}\right)\right] = 10\log_{10}\left[\mathrm{C/N0}\left(90^{\circ}\right) exp\left(\frac{\tau}{\cos\left(90^{\circ}-\theta_{elev}\right)}\right)\right], \tag{11.6}$$

which simplifies into:

$$\mathrm{C/N0}\left(\theta_{elev}\right)\left[\mathrm{dB/Hz}\right] = \mathrm{C/N0}\left(90^{\circ}\right)\left[\mathrm{dB/Hz}\right] - \frac{\tau}{\cos\left(90^{\circ}-\theta_{elev}\right)} 10\log_{10}\left(e\right), \tag{11.7}$$

which is a simple linear fit. With this theoretical curve and assuming that τ is constant for all elevation angles, which is assumed by the $\tau-\omega$ model, a minimum square estimation can be applied to Eqn. (11.7) with the different C/N0 measurements for elevation angles between 47.5°–82.5°, leading to an overdetermined system.

Figure 11.27 shows the vegetation opacity estimated using the proposed approach where its temporal evolution can be compared against the NDVI parameter. It can be shown that both follow the same trend, highlighting the sensitivity of the GNSS-T signals to the vegetation water content.

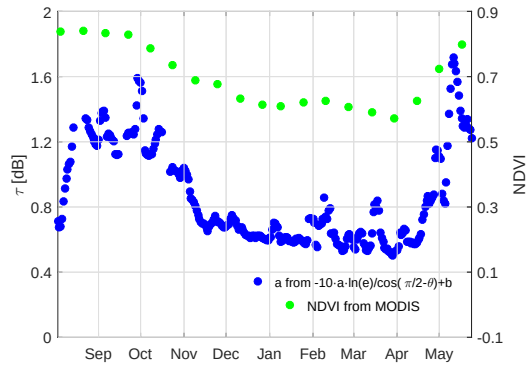

Figure 11.27: Comparison between NDVI and vegetation opacity estimated as a function of time.

Other approaches such as the one given in [247] can be used, where empirical relations between NDVI and vegetation opacity at L-band are given. Due to the high correlation between RHCP C/N0 curves and the NDVI, the NDVI can be estimated from the RHCP received power. Then, the estimated NDVI could be used to estimate the vegetation opacity. Using those relationships, the τ parameter could be also derived from the C/N0 measurements in the absence of rain.

Finally, in order to estimate the daily opacity and analyze the azimuthal dependence, a technique similar to the one presented in [158]. However, instead of using an extra GPS outside the vegetation layer, it is suggested to use the calibration data, which has shown a high temporal stability. In this case, the technique reduces again to the use of one GPS receiver below the vegetation layer.

11.5 Summary and Conclusions

This Chapter has described a field experiment conducted at *La Fageda d'en Jordà* forest intended to measure vegetation canopy properties. First, previous works related to this experiment are presented highlighting the available data before this experiment was conducted. The main goal of the proposed experiment is to determine vegetation canopy parameters using a single GPS receiver, and therefore improving what was presented in [158]. The test site and the ground-truth instrumentation available are also described. The power of the RHCP received signals during the falling and growing seasons is analyzed in detail and compared to other parameters such as rain, greenness, redness, blueness, sky cover, NDVI, and LAI. Rain generates fading events in the received signal power, which correlates against all indexes despite the redness. Both NDVI and LAI seem to be the parameters that correlate better with the received signal power, especially the NDVI with a R^2 parameter of at least 0.85 for all RHCP curves, and showing no incidence angle dependence. Finally, assuming homogeneity on the vegetation layer, a methodology to estimate the vegetation opacity at L-Band using multi-angular observations is presented. For the beech forest the result is around 1.2–1.3 dB when leaves are present and 0.6 dB when they are not. This last point indicates that roughly half of the attenuation comes from the leaves, and the other half from the branches and trunks.

12

Chapter 12
Conclusions

12.1 Main Conclusions

This PhD Thesis has been devoted to the analysis of two different GNSS-R techniques and therefore to assess their potential for the geophysical parameter retrieval. The first technique analyzed was the IPT. This technique was previously introduced in [28] using vertical polarization. This thesis has extended the conventional IPT technique to the use of only horizontal polarization for soil moisture retrieval, including an analysis of the expected system errors. Furthermore, the combination of both linear polarization interference patterns has been tested developing a new retrieval algorithm. The conventional IPT has also been tested in a new scenario that was not previously tested in [28], which is a coastal sea. In that case two retrieval algorithms of two different geophysical parameters were developed: one to estimate SWH, and the other one to estimate the MSSL. The former was based on measuring up to which angle the coherent reflection dominated the incoherent reflection. The latter was based on measuring the variations in the oscillation frequency of the coherent region of the IPT using different spectral estimators.

The second technique tested was GNSS-scatterometry. For this technique several field experiments under several conditions were conducted in order to fully characterize the technique. For the ground-based applications using still instrumentation two field experiments were performed, one using linear polarization (H- and V-Pol), and one using RHCP for the direct signals and LHCP for the reflected signals. The former, even though there were several hardware problems, it led to a soil moisture retrieval algorithm based on a least-square minimization of the measured reflectivity. The latter suffered from several issues, including non-explainable RFI issues, which are still under analysis, and prevented from developing a soil moisture retrieval algorithm. For the ground-based applications using moving instrumentation (rover and tractor) two field experiments were also conducted. For this case the data is being analyzed by a research group from Monash University. For the airborne applications four field experiments were analyzed. The first two field experiments used the LARGO instrument. The former was a series of three flights flying together a L-band microwave radiometer and the LARGO reflectometer. A correlation analysis between the data gathered by the two instruments was performed deriving theoretical and empirical relations among the datasets in order to improve the spatial resolution of the brightness temperature data. The latter was a flight using a paramotor as a platform where the LARGO instrument was flown together with an optical camera, a multi-spectral sensor, and a thermal camera. The data from the second analysis was used to assess a potential synergy among different sensors and techniques for soil moisture retrieval. The other two field experiments analyzed used instruments working in an open-loop approach, an approach different from the LARGO one. The first one was a flight departing from *Sabadell*, reaching *Mataró*, flying along the Catalan coast, and going back, and used the first version of the PAU instrument. That flight was used to experimentally observe the statistics of the reflected field over land in two different situations (flat and rough surface), and over sea, were mainly rough surface scattering mechanism was observed. It was also used to perform a preliminary analysis of the PAU instrument and its altimetric capabilities. The second one was a flight conducted on the USA were mainly the land scattering case was analyzed, since practically the entire flight was performed over land. That flight was used to estimate the amount of coherent and incoherent scattering components, and to assess how that information could be used for the development of geophysical parameter retrieval algorithms. The last

data analyzed using the GNSS-scatterometry approach was based on using data from the recently launched UK TDS-1 satellite. That data were used to observe the shape of the DDMs when the signal was scattered over different surface types. In those data, the coherent scattering mechanism was associated to the presence of sea-ice, whereas the incoherent scattering mechanism to the situation when only open-water is present. Taking into account that, different sea-ice detection algorithms with different estimators were proposed, analyzing their detection performance based on a Bayesian approach.

Summarizing, this PhD Thesis can be divided in two different parts. One part is the continuation of the work derived in [28], testing the IPT in different scenarios when it had not been tested, and developing new retrieval algorithms based on different observables. The other part is the extension to the analysis of the GNSS-scatterometry technique, because the IPT can only be used for ground-based applications with a limited coverage. For the GNSS-scatterometry technique different field experiments covering several combination of platform-polarization scenarios were performed. For the fixed platforms (ground-based) all polarization states were tested despite the transmitted RHCP and reflected RHCP. For the moving platforms (ground-based, airborne, and spaceborne), only the transmitted RHCP and reflected LHCP polarization state was tested.

Taking into account the brief summary just presented, the main conclusions of the different studies developed in this PhD Thesis are summarized in the following points:

For the IPT technique:

- Under a relatively flat land surface surface scenario, the dominating scattering mechanism is the coherent one. In such situation, two different retrieval algorithms have been developed. One is based on measuring the reflection coefficient at horizontal polarization and use a least-square approach to estimate soil moisture. The theoretical precision of this technique was computed, which was approximately 2.5% disregarding the effect of surface roughness. The phase difference between horizontal and vertical interference patterns was also analyzed and used to estimate soil moisture. Before the Brewster angle position both are in phase, whereas after the Brewster angle position they are in counter-phase. The 90° phase shift point is related to the Brewster angle position which is used to estimate the soil water content. The theoretical precision of this methodology is approximately 2%, but it seemed to be insensitive to surface roughness, which attenuates the signal without changing its phase.
- The sea surface scattering properties under the IPT geometry is a little bit different from the land surface. For very large incidence angles, or very low elevation angles the coherent scattering dominates, whereas for lower incidence angles or higher elevations angles the incoherent scattering dominates. The angle were both scattering components are equal is determined by the sea state, and it was used to estimate it. Spectrogram analysis on the interference patterns was used to estimate that cut-off incidence/elevation angle, and therefore infer the sea state with an accuracy of 6 cm in the 10–70 cm dynamic range. The former due to the antenna pattern. The latter because a minimum number of oscillations is required. From the oscillation frequency of the interference pattern the MSSL level was retrieved. Four spectral estimators were tested, obtaining an accuracy of 5 cm for the FP, the LSP, and the LS, and of 4 cm using the CAP periodogram.

For the GNSS-scatterometry technique:

- For ground-based fixed instruments linear polarization can be used for the retrieval of soil moisture over land with the same accuracy than calibrated probes. The power at linear polarization for direct and reflected signals must be computed in order to obtain calibrated reflectivity measurements. Any interference from the direct signal on the reflected signal can be mitigated using a large enough observation time. A least-square approach is proposed for the inversion of geophysical parameters. In such conditions, if the surface is smooth enough, the coherent component dominates the scattering mechanism.
- For ground-based fixed instruments the use of circular polarization to retrieve soil moisture over land could not be assessed due to RFI presence on the field campaign performed. The fact that the soil under analysis was elevated from the terrain was another issue that prevented the geophysical parameter inversion. However, if the least-square algorithm proposed for linear polarization was working correctly, it is deduced that it should work equally for circular polarization. Also, in such situations, the coherent component dominates the scattering mechanism.
- For ground-based moving instruments it is seen that the platform can generate some interference (multi-path) that can be mitigated modifying the observation geometry and increasing the antenna directivity. Soil moisture inversion results are currently being analyzed by another research group, but preliminary results indicate an accuracy of 4% in comparison with calibrated probes.
- For airborne observations and when the coherent component dominates, the estimated coherent reflectivity and the L-band brightness temperature derived parameters (first Stokes parameter and PI) have a high correlation. This concept might be of interest in the future in order to enhance the spatial resolution of microwave radiometry products like the ones from SMAP, after the end of operations of the active system. When the coherent component does not dominate or it is too small (high effective roughness), the noise in the coherent component estimation might kill the high correlation among both techniques.
- For airborne observations, it has also been shown that over land, when the coherent component dominates (smooth surface), the reflected field statistics follow a Hoyt vector, or a ring shape in case the Doppler is not perfectly compensated. Conversely, over land, when the incoherent component dominates, the reflected field statistics follow a complex Gaussian distribution. For sea the surface, unless it is very calmed, the incoherent scattering mechanism is the one that dominates, leading also also to a complex Gaussian distribution of the reflected field statistics.
- For airborne observations, if the waveform peak is analyzed, their statistics change severely depending on the surface under observation. For the sea surface, after incoherently averaging for 1 s, the reflected peak amplitude remains mainly constant, changing only if the surface roughness changes, since the reflectivity remains constant. Therefore, the sea surface can be considered a stationary surface. For the land surface, dielectric constant and consequently reflectivity can change along the integration time, as well as roughness, and therefore the peak amplitude has a large variability. Therefore, the land surface is far from a stationary surface. This indicates that, even though the main scattering mechanism for the sea surface is

the incoherent one, the inverse problem for the retrieval of geophysical parameters is somehow simpler for the sea surface than for the land case.

- For spaceborne observations, it is seen that for the sea surface the main dominating scattering mechanism is the incoherent one. However, when the signal is reflected over lakes or sea ice, the coherent scattering mechanism dominates, since the reflected waveform shape changes severely. This was found on the experimental data gathered by the GNSS-R payload on-board the recently launched UK TDS-1 satellite. The similarity of the waveform to the coherent reflection model can be used effectively to detect the presence of sea ice, which was demonstrated in an in-depth analysis performed using different estimators.

12.2 Future Research Lines

After having established the main conclusions of this work, several research lines can be drawn as a continuation of the research developed during this PhD Thesis. They can be split by the technique, as it was done with the conclusions.

For the IPT technique:

- The measurement of SM could also be performed by looking at the interference pattern oscillation frequency. The larger the SM, the lower the penetration depth, and the lower the effective antenna height estimated. This idea should be tested using either the H-Pol or V-Pol interference patterns. Furthermore, the difference of the effective antenna height at each polarization should also be related to the SM content, since depending on the polarization, the penetration depth will change.
- The measurement of the MSSL should be tested in more dynamic scenarios with larger tides than the Mediterranean sea in order to see how the system will behave. It has been tested using the SNR-analysis, but the author believes that the benefit of the linear polarization IPT is on the horizon-looking geometry, which would improve the accuracy of the SNR-analysis data. Furthermore newer spectral estimators such as the Real-value Iterative Adaptive Approach (RIAA) should be tested in order to check if the performance of any technique would improve [173]. Increasing the dynamic range to observations of $\theta_{elev} < 5^\circ$ is another important point in order to measure larger SWH values.
- The dual-polarization IPT should be tested in scenarios such as snow, where the dielectric constant is relatively small, and it depends on the snow wetness (snow water content). The phase difference retrieval algorithm would help to accurately estimate the snow water content and be able to obtain two different snow parameters: thickness and water content. With those measurements snow could be better characterized. One of its applications would be a more accurate estimation of the avalanche risk, which depends on both snow parameters.

For the GNSS-scatterometry technique more doors and research lines are opened, and some of them are highlighted in the following points.

- First, the ground-based scatterometry experiment with still instrumentation using circular polarization should be repeated in a RFI-clean environment with a soil

sample not elevated from the terrain level. This would help to complement the linear polarization study, and to obtain a full characterization of the reflected signals under ground-based conditions. This would also facilitate the development of soil moisture retrieval algorithms in controlled environments. Those algorithms should be tested in other environments afterwards such as airborne or spaceborne.

- Second, the data from the ground-based scatterometry experiments with moving instrumentation should be analyzed, since it was developed in a RFI-clean environment. This could be the key to overcome the problems faced in the experiment with still instrumentation.
- Third, after showing the high correlation between GNSS-R reflectivity and L-band microwave radiometry, a new study towards a soil moisture retrieval algorithm from those data should be developed. The correlation results are already proven, which means that a similar algorithm to the L-band Microwave Emission of the Biosphere (L-MEB) used with microwave radiometry data could be developed [248].
- Fourth, the use of the orthogonal scattered polarizations as it was also done in [149] should be considered because it would help to simplify the scattering problem and specially the roughness effect on the scattered signals. Also the separation of the coherent and incoherent scattered components as was done in Chapter 9 should be considered in order to develop the soil moisture retrieval algorithms. The author believes that an accurate soil moisture retrieval algorithm will benefit from the addition of the two scattering components in the geophysical model function, and it has been shown that they can be estimated in a straightforward manner. Data from the recent ^{3}Cat-2 experiment will help to develop those algorithms.
- Fifth, the sensitivity of the GNSS-R peak value or thermal SNR to the sea ice concentration parameter should be better evaluated from the UK TDS-1 data. Even though only a few months of data are public, at the time of defending this PhD Thesis there will be more than two years of data. Those data should be accurately filtered and only those satellites whose reflections fall within the antenna beamwidth should be taken into account. Then, the thermal SNR of those points where the coherent scattering model behaves as expected should be compared against the SIC products already described in this PhD Thesis dissertation. L-band microwave radiometry data from SMOS would benefit from this research and specially the new sea ice thickness retrieval algorithms that are being developed.
- Sixth, considering these last three points it seems straightforward to notice that the synergy of spaceborne GNSS-R data and spaceborne L-band microwave radiometry should be evaluated. The correlation in airborne scenarios has already been shown in this work. Also the fact that in the future more GNSS-R data will be available from the CYGNSS mission, and more L-band radiometry data will be available with the SMAP mission, is the right trigger to study the proposed synergy. This analysis can be already started using data from UK TDS-1 and SMOS.

Even though more research lines can be drawn apart from the ones aforementioned, those are the ones that would directly contribute or complement the research conducted and described in this PhD Thesis dissertation.

A

Appendix A

Summary of GNSS Signals and Systems

This Appendix shows a summary of the main signal parameters for the four different GNSS systems. It begins with the two operational systems, which are the American GPS system and the Russian GLONASS system, to end with the forthcoming Galileo and BeiDou systems. Information about frequency bands, signals, bandwidth, and modulation used in each in-phase and quadrature components is expressed. This may help the reader to compare all GNSS systems and signals, and to complement the basic information provided in Chapter 2. So, those interested in going beyond the basic information provided in Chapter 2, which is the strictly necessary to understand all developments in this PhD Thesis, are encouraged to look carefully at this Appendix. Last but not least, the author would like to acknowledge the help of Daniel Pascual to understand, concentrate, and classify all the information about all GNSS systems in all their corresponding Interface Control Document (ICD)s.

Table A.1: GPS main parameters summary.

GNSS	GPS																
BAND	L1[2]							L2[2,3]						L5[4]			
CARRIER FREQ. (Fc) [MHz]	1575.42							1227.6						1176.45			
Wavelength (λ) [cm]	19.0							24.4						25.5			
TX BW (RF) [MHz][18]	IIA/IIR/IIR-M/IIF: 20.46 III: 30.69							IIA/IIR/IIR-M/IIF: 20.46 III: 30.69						24.00			
ITU BW (RF) [MHz][17]	24							24						24			
I/Q[6]	I	Q		I	Q		I	I		Q		I		I		Q	
SERVICES[7,19]	P(Y)	C/A		L1C			M	P(Y)		L2C		M		L5C (SoL)			
COMPONENT	DATA	DATA		L1D (DATA)	L1P (PILOT)		N/A	DATA		DATA (L2CM)	PILOT (L2CL)	N/A		DATA (L5I)	PILOT (L5Q)		
MODULATION	BPSK-R10	BPSK-R1		TMBOC(6,1,1/11) [8]		BOCs(10,5)		BPSK-R10		BPSK-R5 (time mux.)		BOCs(10,5)		BPSK-R10	BPSK-R10		
				BOCs(1,1)	BOCs(6,1) (time mux)												
CODE FREQ. (fc) [MHz]	10.23	1.023		1.023		5.115		10.23		5.115		5.115		10.23			
SUB-CARRIER FREQ. (fs) [MHz]	-	-		1.023	6.138	10.23		-		-		10.23		-			
PRIMARY CODE FAMILY	short cycided + m-Sequence	Gold		Weil		N/A		short cycided + m-Sequence		m-Sequence		N/A		short cycided + m-Sequence			
PRIMARY CODE LENGTH [chips/ms][10]	N/A / ~1 week	1023/1		10230/10		N/A		N/A/~1 week		10230/20	767250/1500	N/A		10230/1			
SECONDARY CODE LENGTH [chips]	-	-		-	1800	N/A		-		-		N/A		10	20		
DATA RATE [bps/sps][11]	50/50	50/50		50/100	-	N/A		50/50		IIF/IIR-M: 25/50	-	N/A		100/50	-		
MIN. RECEIVED POWER (dBW)[12]	IIA/IIR/IIR-M/IIRF/IIIc: -161.5	IIA/IIR/IIR-M/IIRF/IIIc: -158.5		IIIc: -157		-157[13,14]		IIA/IIR: -164.5, IIR-M: -161.5		IIA/IIR: -164.5, IIR-M/IIF: -160.0, IIIc: -158.5		N/A[14]		IIE: -157.9	IIE: -157.9		
POWER DISTRIBUTION[15]	1	1		10/11	1/11	1		1		0.5	0.5	100		1	1		
REF. ELEVATION [deg]	5	5		5		N/A		5		5		N/A		5			
MODULATION BW (RF) [MHz][16]	20.46	2.046		4.092	14.322	30.69		20.46		10.23		30.69		20.46			

Table A.2: GLONASS main parameters summary.

GNSS	GLONASS									
BAND	L1			L2			L3			
CARRIER FREQ. (Fc) [MHz]	1602 + k·0.5625			1246+k·0.4375			1202.025			
Wavelength (λ) [cm]	18.73			24.07			24.96			
TX BW (RF) [MHz][18]	18.6575	18.6575		18.6575	18.6575		20			
ITU BW (RF) [MHz][17]	16.4075	16.4075		16.4075	16.4075		-			
I/Q[6]	I	Q		I	Q		I	Q		
SERVICES[7,19]	C/A Code (L1OF)	P Code (L1SF)		C/A Code (L2OF)	P Code (L2SF)		L3I	L3Q		
COMPONENT	Data			Data			Pilot	Data		
MODULATION	BPSK	BPSK		BPSK	BPSK		BPSK	BPSK		
CODE FREQ. (fc) [MHz]	0.511	5.11		0.511	5.11		10	10		
SUB-CARRIER FREQ. (fs) [MHz]	-	-		-	-		-	-		
PRIMARY CODE FAMILY	PRN M-Sequence	-		PRN M-Sequence	-		PRN M-Sequence	PRN M-Sequence		
PRIMARY CODE LENGTH [chips/ms][10]	511/1	-		511/1	-		10000	10000		
SECONDARY CODE LENGTH [chips]	Meander	-		-	-		-	-		
DATA RATE [bps/sps][11]	50/50	-		50/50	-		-	-		
MIN. RECEIVED POWER [dBW][12]	-161	-		-167	-		-	-		
POWER DISTRIBUTION[15]	-	-		-	-		1	1		
REF. ELEVATION [deg]	5	-		5	-		5	5		
MODULATION BW (RF) [MHz][16]	1.022	10.22		1.022	10.22		20	20		

Table A.3: Galileo main parameters summary.

GNSS	GALILEO[1]													
BAND	E1			E6			E5[3]							
CARRIER FREQ. (Fc) [MHz]	1575.42			1278.75			Fc = 1191.795 Fca = 1176.45 Fcb = 1207.14							
Wavelength (λ) [cm]	19.0			23.4			λa = 25.5 λb = 24.8							
TX BW (RF) [MHz][18]	24.552			40.92			BW = 51.15 BWa = BWb = 20.46							
ITU BW (RF) [MHz][17]	32.0			40.9			BW_{ITU} = 51.2 BWa_{ITU} = BWb_{ITU} = 24.0							
I/Q[4]	I	I	Q	I	I	Q	I	Q	I	Q				
SERVICES[7,19]	PRS	OS, SoL, CS		PRS	CS		OS, CS			OS, SoL, CS				
COMPONENT	DATA (E1A)	DATA (E1B)	PILOT (E1C)	DATA (E6A)	DATA (E6B)	PILOT (E6C)	DATA (E5aI)	PILOT (E5aQ)		DATA (E5bI)		PILOT (E5bQ)		
MODULATION	BOCc(15,2,5)	CBOC(6,1,1/11)[9]		BOCc(10,5)	BPSK-R5	BPSK-R5	AltBOCs(15,10) + constant envelope							
		BOCs(1,1)	BOCs(6,1)											
CODE FREQ. (fc) [MHz]	25.575	1.023		5,115	5,115	5.115	10.23							
SUB-CARRIER FREQ. (fs) [MHz]	15.345	1.023	6.138	10.23	-	-	15.345							
PRIMARY CODE FAMILY	N/A	Random		N/A	Memory		short cycled + m-Sequence							
PRIMARY CODE LENGTH [ch/ps/ms][10]	N/A	4092/4		N/A	5115/1		10230/1							
SECONDARY CODE LENGTH [ch/ps]	N/A	-	25	N/A	-	100	20	100	4	100				
DATA RATE [bps/sps][11]	50/100	125/250	-	50/100	500/1000	-	25/50	-	125/250	-				
MIN. RECEIVED POWER [dBW][12]	-157	-157		-155	-155		-155		-155					
POWER DISTRIBUTION[15]	1	10/11	1/11	1	0.5	0.5	0.5	0.5	0.5	0.5				
REF. ELEVATION [deg]	N/A	10		N/A	10		10							
MODULATION BW (RF) [MHz][16]	35.805	4.092	14.32	30.69	10.23		51.15							

Table A.4: BeiDou main parameters summary.

GNSS	Beidou-2											
BAND	B1		B1-2		B2		B3					
CARRIER FREQ. (Fc) [MHz]	1561.098		1589.742		1207.14		1268.52					
Wavelength (λ) [cm]	19.22		18.87		24.85		23.65					
TX BW (RF) [MHz][18]	16		16		36		?	?				
ITU BW (RF) [MHz][17]	?	?	?	?	?	?	?	?	?	?		
I/Q[6]	I	Q	I	Q	I	Q	I	Q				
SERVICES[7,19]	B1		B1-2		B2-I	B2-Q	B3					
COMPONENT	-	Data	Data	Data	-	Data	-	Data				
MODULATION	QPSK-R2		QPSK-R2		BPSK-R10	BPSK-R2	QPSK-R10					
CODE FREQ. (fc) [MHz]	2.046		2.046		10.23	2.046	10.23					
SUB-CARRIER FREQ. (fs) [MHz]	-	-	-	-	-	-	-	-				
PRIMARY CODE FAMILY	?	?			?	?	?	?				
PRIMARY CODE LENGTH [chips/ms][10]	?/>400 ms	2046/1	?/>400 ms	2046/1	?/160	2046/1	?/>160	10230/1				
SECONDARY CODE LENGTH [chips]	-	20/20	-	20/20	-	20/20	-	20/20				
DATA RATE [bps/sps][11]	-	50/50	-	50/50	-	50/50	-	50/50				
MIN. RECEIVED POWER [dBW][12]	-163		-163	-163	-163	-163	-163					
POWER DISTRIBUTION[13]	1		1		1	1	1					
REF. ELEVATION [deg]	5		5		5	5	5					
MODULATION BW (RF) [MHz][16]	4.092		4.092		20.46	4.092	20.46					

B

Appendix B

Fresnel reflection coefficients and IPT

This Appendix aims at complementing Chapter 3, with more detailed mathematical developments of the simplifications made there. It starts detailing the mathematical operations on the Fresnel reflection coefficients, starting from the general expression using the medium impedance and both transmitted and incident angles, until they are expressed as a function of the incidence angle only and the dielectric constant. It continues with the Brewster angle derivation. Using the notation from Chapter 2, the IPT coherent model is derived. The Appendix finishes with the limitations of the IPT due to the codes chip length.

B.1 Fresnel Reflection Coefficients Mathematical Manipulations

B.1.1 H-Pol

The Fresnel reflection coefficient for the perpendicular or horizontal polarization is given by Eqn. (3.4):

$$r_{\perp} = \frac{Z_2 \cos(\theta_{inc}) - Z_1 \cos(\theta_{trans})}{Z_2 \cos(\theta_{inc}) + Z_1 \cos(\theta_{trans})}, \tag{B.1}$$

where Z_i is the characteristic impedance of medium i, θ_{inc} the incidence angle, and θ_{trans} the transmitted angle. Taking into account that the characteristic or intrinsic impedance is defined as:

$$Z_i = \frac{|E|}{|H|} = \sqrt{\frac{\mu_i}{\varepsilon_i}} = Z_0 \sqrt{\frac{\mu_{ri}}{\varepsilon_{ri}}}, \tag{B.2}$$

and Z_0 is the free space characteristic impedance and it is normally approximated by 120π. Then, Eqn. (3.4) becomes:

$$r_{\perp} = \frac{Z_0 \sqrt{\frac{\mu_{r2}}{\varepsilon_{r2}}} \cos(\theta_{inc}) - Z_0 \sqrt{\frac{\mu_{r1}}{\varepsilon_{r1}}} \cos(\theta_{trans})}{Z_0 \sqrt{\frac{\mu_{r2}}{\varepsilon_{r2}}} \cos(\theta_{inc}) + Z_0 \sqrt{\frac{\mu_{r1}}{\varepsilon_{r1}}} \cos(\theta_{trans})}, \tag{B.3}$$

and assuming a non-magnetic medium ($\mu_{r1} = 0$ and $\mu_{r2} = 0$):

$$r_{\perp} = \frac{\sqrt{\frac{1}{\varepsilon_{r2}}} \cos(\theta_{inc}) - \sqrt{\frac{1}{\varepsilon_{r1}}} \cos(\theta_{trans})}{\sqrt{\frac{1}{\varepsilon_{r2}}} \cos(\theta_{inc}) + \sqrt{\frac{1}{\varepsilon_{r1}}} \cos(\theta_{trans})}, \tag{B.4}$$

Using Snell's law it is possible to express the transmitted angle as a function of the incidence one:

$$\sin(\theta_{trans}) = \sqrt{\frac{\varepsilon_{r1}}{\varepsilon_{r2}}} \sin(\theta_{inc}), \tag{B.5}$$

and using the trigonometric relation $\cos(\theta) = \sqrt{1 - \sin^2(\theta)}$:

$$r_{\perp} = \frac{\sqrt{\frac{1}{\varepsilon_{r2}}} \sqrt{1 - \sin^2(\theta inc)} - \sqrt{\frac{1}{\varepsilon_{r1}}} \sqrt{1 - \frac{\varepsilon_{r1}}{\varepsilon_{r2}} \sin^2(\theta inc)}}{\sqrt{\frac{1}{\varepsilon_{r2}}} \sqrt{1 - \sin^2(\theta inc)} + \sqrt{\frac{1}{\varepsilon_{r1}}} \sqrt{1 - \frac{\varepsilon_{r1}}{\varepsilon_{r2}} \sin^2(\theta inc)}}, \tag{B.6}$$

and simplifying it becomes:

$$r_{\perp} = \frac{\sqrt{\varepsilon_{r1} - \varepsilon_{r1} \sin^2(\theta inc)} - \sqrt{\varepsilon_{r2} - \varepsilon_{r1} \sin^2(\theta inc)}}{\sqrt{\varepsilon_{r1} - \varepsilon_{r1} \sin^2(\theta inc)} + \sqrt{\varepsilon_{r2} - \varepsilon_{r1} \sin^2(\theta inc)}}, \tag{B.7}$$

which resembles Eqn. (3.6) considering $i = 1$ and $i + 1 = 2$.

B.1.2 V-Pol

In the same way that the reflection coefficient for the perpendicular polarization has been treated, the one from the parallel polarization will be treated. The parallel polarization Fresnel reflection coefficient is given by:

$$r_{\parallel} = \frac{Z_2 \cos(\theta_{trans}) - Z_1 \cos(\theta_{inc})}{Z_2 \cos(\theta_{trans}) + Z_1 \cos(\theta_{inc})}, \tag{B.8}$$

then:

$$r_{\parallel} = \frac{Z_0\sqrt{\frac{\mu_{r2}}{\varepsilon_{r2}}} \cos(\theta_{trans}) - Z_0\sqrt{\frac{\mu_{r1}}{\varepsilon_{r1}}} \cos(\theta_{inc})}{Z_0\sqrt{\frac{\mu_{r2}}{\varepsilon_{r2}}} \cos(\theta_{trans}) + Z_0\sqrt{\frac{\mu_{r1}}{\varepsilon_{r1}}} \cos(\theta_{inc})}, \tag{B.9}$$

$$r_{\parallel} = \frac{\sqrt{\frac{1}{\varepsilon_{r2}}} \cos(\theta_{trans}) - \sqrt{\frac{1}{\varepsilon_{r1}}} \cos(\theta_{inc})}{\sqrt{\frac{1}{\varepsilon_{r2}}} \cos(\theta_{trans}) + \sqrt{\frac{1}{\varepsilon_{r1}}} \cos(\theta_{inc})}, \tag{B.10}$$

$$r_{\parallel} = \frac{\sqrt{\frac{1}{\varepsilon_{r2}}}\sqrt{1 - \sin^2(\theta_{trans})} - \sqrt{\frac{1}{\varepsilon_{r1}}}\sqrt{1 - \sin^2(\theta_{inc})}}{\sqrt{\frac{1}{\varepsilon_{r2}}}\sqrt{1 - \sin^2(\theta_{trans})} + \sqrt{\frac{1}{\varepsilon_{r1}}}\sqrt{1 - \sin^2(\theta_{inc})}}, \tag{B.11}$$

$$r_{\parallel} = \frac{\sqrt{\varepsilon_{r1} - \varepsilon_{r1} \sin^2(\theta_{trans})} - \sqrt{\varepsilon_{r2} - \varepsilon_{r2} \sin^2(\theta_{inc})}}{\sqrt{\varepsilon_{r1} - \varepsilon_{r1} \sin^2(\theta_{trans})} + \sqrt{\varepsilon_{r2} - \varepsilon_{r2} \sin^2(\theta_{inc})}}, \tag{B.12}$$

$$r_{\parallel} = \frac{\sqrt{\varepsilon_{r1} - \varepsilon_{r1}\frac{\varepsilon_{r1}}{\varepsilon_{r2}} \sin^2(\theta_{inc})} - \sqrt{\varepsilon_{r2} - \varepsilon_{r2} \sin^2(\theta_{inc})}}{\sqrt{\varepsilon_{r1} - \varepsilon_{r1}\frac{\varepsilon_{r1}}{\varepsilon_{r2}} \sin^2(\theta_{inc})} + \sqrt{\varepsilon_{r2} - \varepsilon_{r2} \sin^2(\theta_{inc})}}, \tag{B.13}$$

$$r_{\parallel} = \frac{\varepsilon_{r1}\sqrt{\varepsilon_{r2} - \varepsilon_{r1} \sin^2(\theta_{inc})} - \varepsilon_{r2}\sqrt{\varepsilon_{r1} - \varepsilon_{r1} \sin^2(\theta_{inc})}}{\varepsilon_{r1}\sqrt{\varepsilon_{r2} - \varepsilon_{r1} \sin^2(\theta_{inc})} + \varepsilon_{r2}\sqrt{\varepsilon_{r1} - \varepsilon_{r1} \sin^2(\theta_{inc})}}, \tag{B.14}$$

which again resembles to Eqn. (3.7) considering $i = 1$ and $i + 1 = 2$.

B.2 Brewster Angle

The Brewster angle occurs when all the energy is transmitted to the medium and no wave is reflected. For the horizontal or perpendicular polarization it occurs when:

$$Z_2 \cos(\theta_{inc}) - Z_1 \cos(\theta_{trans}) = 0, \tag{B.15}$$

$$\frac{Z_2}{Z_1} \cos(\theta_{inc}) = \cos(\theta_{trans}), \tag{B.16}$$

$$\frac{\varepsilon_{r1}}{\varepsilon_{r2}} \cos^2(\theta_{inc}) = 1 - \sin^2(\theta_{inc}), \tag{B.17}$$

$$\frac{\varepsilon_{r1}}{\varepsilon_{r2}} \cos^2(\theta_{inc}) + \sin^2(\theta_{inc}) = 1, \tag{B.18}$$

and this equation is never accomplished unless $\varepsilon_{r1} = \varepsilon_{r2}$, which means that there is no change of medium and consequently no reflection.

However, for parallel or vertical polarization things are different:

$$Z_2 \cos(\theta_{trans}) - Z_1 \cos(\theta_{inc}) = 0, \tag{B.19}$$

$$\cos(\theta_{trans}) = \frac{Z_1}{Z_2} \cos(\theta_{inc}), \tag{B.20}$$

$$1 - \frac{\varepsilon_{r1}}{\varepsilon_{r2}} \sin^2(\theta_{inc}) = \frac{\varepsilon_{r2}}{\varepsilon_{r1}} \cos^2(\theta_{inc}), \tag{B.21}$$

$$\left(\frac{\varepsilon_{r2}}{\varepsilon_{r1}} - \frac{\varepsilon_{r1}}{\varepsilon_{r2}} \right) \sin^2(\theta_{inc}) = \frac{\varepsilon_{r2}}{\varepsilon_{r1}} - 1, \tag{B.22}$$

$$\left(\varepsilon_{r2}^2 - \varepsilon_{r2}^2 \right) \sin^2(\theta_{inc}) = \varepsilon_{r2} \left(\varepsilon_{r2} - \varepsilon_{r1} \right), \tag{B.23}$$

$$\theta_{inc} = \theta_B = \arcsin \left(\sqrt{\frac{\varepsilon_{r2}}{\varepsilon_{r2} + \varepsilon_{r1}}} \right). \tag{B.24}$$

Also, taking into account:

$$1 - \frac{\varepsilon_{r1}}{\varepsilon_{r2}} \sin^2(\theta_{inc}) = \frac{\varepsilon_{r2}}{\varepsilon_{r1}} \cos^2(\theta_{inc}), \tag{B.25}$$

and using the trigonometric identity $\cos^2\theta + \sin^2\theta = 1$ leads to:

$$\frac{\varepsilon_{r2} - \varepsilon_{r1}}{\varepsilon_{r2}} \sin^2(\theta_{inc}) = \frac{\varepsilon_{r2} - \varepsilon_{r1}}{\varepsilon_{r1}} \cos^2(\theta_{inc}), \tag{B.26}$$

$$\theta_{inc} = \theta_B = \arctan \left(\sqrt{\frac{\varepsilon_{r2}}{\varepsilon_{r1}}} \right) \tag{B.27}$$

which is the normal way the Brewster angle is expressed.

B.3 IPT Coherent Model

In Sec. 2.3 the direct GNSS signal is defined as:

$$U_d \left(\vec{R}_r, t \right) = \alpha \cdot a(t - R_d(t)/c) \frac{e^{-jkR_d(t)}}{4\pi R_d(t)} e^{-j2\pi(f_c + f_{D\,d}(t))t}. \tag{B.28}$$

Therein, the coherent reflected signal it is defined as:

$$U_{r\,coh} \left(\vec{R}_r, t \right) = \alpha \cdot a \left(t - \frac{|\vec{R}_t| + |\vec{R}_r|}{c} \right) r_{pq} \frac{e^{-jk\left(|\vec{R}_t| + |\vec{R}_r|\right)}}{4\pi \left(|\vec{R}_t| + |\vec{R}_r| \right)} e^{-j2\pi(f_c + f_{D\,r}(t))t}, \tag{B.29}$$

so, assuming a receiving linear polarized antenna, and considering a flat surface (no incoherent component), the IPT is:

$$U_{IPT} \left(\vec{R}_r, t \right) = U_d \left(\vec{R}_r, t \right) + U_{r\,coh} \left(\vec{R}_r, t \right), \tag{B.30}$$

assuming a low antenna height which implies ($R_d \approx |\vec{R}_t| + |\vec{R}_r|$)

$$U_{IPT}\left(\vec{R}_r, t\right) = \alpha \cdot a\left(t - \frac{R_d(t)}{c}\right)\frac{e^{-j2\pi f_c t}}{4\pi R_d(t)} e^{-j2\pi f_D(t)t} e^{-jkR_d(t)} \left(F_n(\theta_{elev}) + F_n(-\theta_{elev}) r_{pq} e^{-j2\pi(f_{Dr}(t) - f_D(t))t} e^{-jk\left(|\vec{R}_t| + |\vec{R}_r| - R_d(t)\right)}\right), \tag{B.31}$$

assuming that both antenna and surface can be considered frozen for the coherent integration time, then $f_{Dr}(t) = f_D(t)$, and $e^{-j2\pi(f_{Dr}(t) - f_D(t))t} = 1$. Also assuming that the antenna is pointing to the horizon and has a rotationally symmetric pattern, $F_n(\theta_{elev}) = F_n(-\theta_{elev})$. Then:

$$U_{IPT}\left(\vec{R}_r, t\right) = \alpha \cdot a\left(t - \frac{R_d(t)}{c}\right)\frac{e^{-j2\pi f_c t}}{4\pi R_d(t)} e^{-j2\pi f_D(t)t} e^{-jkR_d(t)} F_n(\theta_{elev}) \left(1 + r_{pq} e^{-jk\left(|\vec{R}_t| + |\vec{R}_r| - R_d(t)\right)}\right), \tag{B.32}$$

with the help of Fig. B.1, it is possible to deduce that $|\vec{R}_t| + |\vec{R}_r| - R_d(t) = 2H \sin\theta_{elev}$. So:

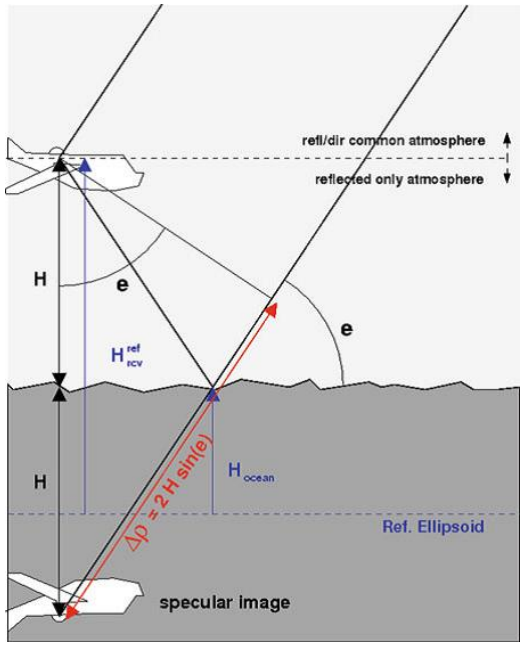

Figure B.1: Path length difference between direct and reflected signals [249].

$$P_R = |U_{IPT}|^2 = \alpha^2 \cdot a^2\left(t - \frac{R_d(t)}{c}\right)\left(\frac{1}{4\pi R_d(t)}\right)^2 |F_n(\theta_{elev})|^2 \left|1 + |r_{pq}(\theta_{elev})| e^{-jk2H\sin(\theta_{elev}) + \phi_{r_{pq}}(\theta_{elev})}\right|^2, \tag{B.33}$$

and considering

$$|U_{d0}| = \alpha^2 \cdot a^2 \left(t - \frac{R_d(t)}{c} \right) \left(\frac{1}{4\pi R_d(t)} \right)^2, \tag{B.34}$$

prior equation resembles Eqn. (3.16) shown in Sec. 3.2.1, which represents the coherent IPT model.

B.4 Codes Limitation

One required condition for the IPT or the SNR-analysis is the in-phase coherent addition of the direct and reflected signal codes. In other words, the delay between the direct and reflected signals has to be less than half of the codes chips. Moreover, one has to take also into account the BOC modulation in those codes that it is used over the DSSS or PRN modulation. Generalizing, the base-band signal bandwidth taking into account all the codes used is the limiting factor. Considering that the path difference between direct and reflected signals is given by:

$$\Delta r = r_{reflected} - r_{direct} = 2H \sin(\theta_{elev}) = 2H \sin(90 - \theta_{inc}), \tag{B.35}$$

and this distance must be smaller than $c/(2B)$, where B is the baseband signal bandwidth. So,

$$\Delta r < \frac{c}{2B} \Rightarrow H < \frac{c}{4B \sin(90 - \theta_{inc})}. \tag{B.36}$$

Figure B.2 shows the maximum antenna height that ensures that the direct and reflected signals will arrive with the same chip code as a function of the satellite elevation angle. It has been done as an example for three different codes taking the bandwidth values shown in App. A. This can be expanded to any code just by knowing their base-band bandwidth. It is interesting to remark that whereas for positioning, the larger the bandwidth, the sharper the ACF, and the better the accuracy of the position estimation. However, this is the contrary for the IPT or the SNR-analysis, since they rely on multipath, and the sharper the ACF the lower the multipath effect.

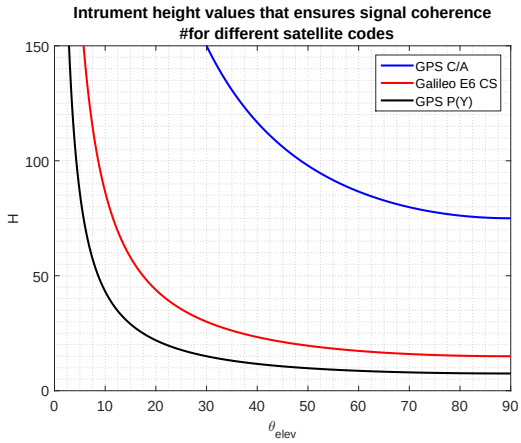

Figure B.2: Maximum antenna height with respect to the surface for three different codes.

C

Appendix C

Statistics of the coherent, incoherent, and thermal noise components

This Appendix describes all the mathematical computations that aid to the final formulations shown in Chapter 4. It starts describing the signal model used for both the cGNSS-R and iGNSS-R techniques. It computes the first order correlation function of the coherent reflected component, of the incoherent component, and of the thermal noise. It also determines the second order coherence functions of the same components. It computes the overall $\mathrm{SNR}_{\mathrm{nc,in/out}}$ with detailed mathematical developments of the simplifications made. It ends with an scatterometric error budget for different scenarios.

C.1 Signal Model

As has been seen along the entire dissertation, two different approaches are used to process GNSS reflected signals, cGNSS-R and iGNSS-R. The cGNSS-R consists of the correlation of the digitized received signal with a clean replica of the satellite code. The iGNSS-R consists of the correlation of the digitized received signal with a digitized version of the direct signal. Even though the iGNSS-R technique was proposed earlier (Martin-Neira 1993 [48]), in this section the cGNSS-R signal model is presented prior to the iGNSS-R one, because the iGNSS-R can be seen as the cGNSS-R with the addition of two extra noise terms.

C.1.1 cGNSS-R

The voltage signal after the correlation with a clean replica of the satellite code has three main different components:

$$y_c(t,\tau) = \frac{1}{T_c}\int_{-\frac{T_c}{2}}^{+\frac{T_c}{2}} \left[u_r(t+t'+\tau) + n_{r_t}(t+t'+\tau)\right] a(t+t')dt' = \rho_0(\tau)+n_S(t,\tau)+n_{T,c}(t,\tau), \tag{C.1}$$

where u_r stands for the received reflected (r) signal, n_{r_t} for the reflected thermal (t) noise signal, a for the satellite spreading code, T_c for the coherent integration time, subscript c for cGNSS-R, $\rho_0(\tau)$ is a deterministic value and stands for the coherent component of the signal, $n_S(t,\tau)$ is a complex Gaussian random variable with zero mean and power/variance $2\sigma_s^2(\tau)$ representing the incoherent reflected power or speckle noise [74, 75], and $n_{T,c}(t,\tau)$ is also a complex Gaussian random variable with zero mean and power/variance $2\sigma_{t,c}^2(\tau)$, which represents the thermal noise in the cGNSS-R. The real and imaginary parts of both thermal and speckle are uncorrelated by definition.

The signal part of the computed waveform can be expressed as a function of the system parameters [52]:

$$\begin{aligned} y_s(t,\tau) =& \frac{1}{T_c}\int_{-\frac{T_c}{2}}^{+\frac{T_c}{2}} u_r(t+t'+\tau)a(t+t')dt' = \rho_0(\tau) + n_S(t,\tau) = \\ =& \int \sqrt{EIRP_T}D(\vec{\rho})ACF\left[\delta t\,(t,\vec{\rho})\right] S\left[\delta f\,(t,\vec{\rho})\right] g(\vec{\rho},t)d\vec{\rho}, \end{aligned} \tag{C.2}$$

where $\sqrt{EIRP_T}$ is the square root of the EIRP of the transmitting satellite, $D(\vec{\rho})$ is the voltage antenna pattern projected on ground, ACF stands for the ACF shape of the GNSS signals [250], S is a *sinc* function expressing the Doppler behavior of the spreading function [131], $\vec{\rho}$ is a vector from the specular reflection position to the surface scattering point, and $g(\vec{\rho},t)$ is defined as a solution for the scattered field in the KA [52]:

$$g(\vec{\rho},t) = r\frac{exp(-j2\pi ft)}{j4\pi R_0 R}exp\left[jk(R_0+R)\right]\frac{q^2}{q_z}, \tag{C.3}$$

where r stands for the Fresnel reflection coefficient, f is the GNSS carrier frequency, k stands for the wavenumber, R_0 is the distance from some surface point to the transmitter,

R is the distance from the same surface point to the receiver, $\vec{q} = -k(\vec{n} - \vec{m}) = (q_z, \vec{q}_\perp)$, $\vec{m}$ is the unitary vector of the incident wave, and $\vec{n}$ is the unitary vector of the scattered wave.

For a perfectly flat surface, a purely coherent scattering reflection takes place. Then, Eqn. (C.2) tends to [52]:

$$y_s(t,\tau) \sim \sqrt{EIRP_T} D(0) \Lambda[\tau] S[0] \frac{e^{\left(j2\pi\left(\frac{R_{0,sp}+R_{sp}}{\lambda}\right)-ft\right)}}{j4\pi(R_{0,sp}+R_{sp})} r e^{-2k^2\sigma_h^2\cos^2(\theta_{inc})}, \tag{C.4}$$

where σ_h^2 stands for the variance of surface heights, θ_{inc} for the incidence angle, and the factor $e^{-2k^2\sigma_h^2\cos^2(\theta_{inc})}$ corresponds to the reflected field attenuation under the PO approximation [71]. Equation (C.4) is equivalent to the case when the receiver is located under the surface, and the incident field is multiplied by the rough surface Fresnel reflection coefficient. This is in agreement with [70], where the specular reflected power in a bistatic configuration is defined. However, for very rough surfaces ($k\sigma_h \sin(\theta_{inc}) \gg 1$), the coherently reflected component vanishes ($e^{-2k^2\sigma_h^2\cos^2(\theta_{inc})} \to 0$). As a result, the received scattered field becomes normally distributed (as described in Chapter 4), and its expression is given in [52], which represents a so-called *speckle* or self-noise.

The thermal noise part of the reflected waveform is expressed by:

$$y_{r_t}(t,\tau) = \frac{1}{T_c}\int_{-\frac{T_c}{2}}^{+\frac{T_c}{2}} n_{r_t}(t+t'+\tau)a(t+t')dt' = n_{T,c}(t,\tau), \tag{C.5}$$

C.1.2 iGNSS-R

For this case, the complex voltage signal after the correlation with the direct signal has also three distinct components, which are similar to those in the cGNSS-R case, taking into account the addition of some terms to the thermal noise component:

$$y_i(t,\tau) = \frac{1}{T_c}\int_{-\frac{T_c}{2}}^{+\frac{T_c}{2}} \left[u_r(t+t'+\tau) + n_{r_t}(t+t'+\tau)\right] s_d(t+t')dt' = \rho_0(\tau) + n_S(t,\tau) + n_{T,i}(t,\tau), \tag{C.6}$$

where s_d stands for the direct sampled signal, and $n_{T,i}(t,\tau)$ for the iGNSS-R equivalent thermal noise term. If the direct signal is under the LOS conditions, it can be expressed as a sum of the coherent term which represents the spreading code, and the thermal noise component for the direct signal. Consequently, the iGNSS-R waveform can be expressed as a function of the cGNSS-R waveform as follows:

$$y_i(t,\tau) = y_c(t,\tau) + \frac{1}{\sqrt{SNR_d}}\left[y_{u_r,d_t}(t,\tau) + y_{r_t,d_t}(t,\tau)\right], \tag{C.7}$$

where $y_c(t,\tau)$ is given by Eqn. (C.1), $1/\sqrt{SNR_d}$ is a normalizing factor that appears due to normalizing the spreading code direct signal part to unit energy, SNR_d is the pre-correlation thermal SNR for the direct signal or $\mathrm{SNR_{c,in}}$ as expressed in Fig. 4.4, $y_{u_r,d_t}(t,\tau)$ is the correlation of the reflected signal component with the normalized direct channel thermal noise, and $y_{r_t,d_t}(t,\tau)$ is the correlation between the normalized direct thermal noise and the reflected thermal noise components.

C.2 Correlation Functions of the Different Terms

C.2.1 cGNSS-R Thermal Noise

The correlation function of $n_{T,c}(t,\tau)$ is:

$$\begin{aligned}\mathrm{E}\{n_{T,c}(t_1,\tau_1)n^*_{T,c}(t_2,\tau_2)\} =&\frac{1}{T_c^2}\mathrm{E}\Bigg\{\int_{-\frac{T_c}{2}}^{+\frac{T_c}{2}} n_{r_t}(t_1+t'+\tau_1)a(t_1+t')dt'\times \\ &\int_{-\frac{T_c}{2}}^{+\frac{T_c}{2}} n^*_{r_t}(t_2+t''+\tau_2)a(t_2+t'')dt''\Bigg\},\end{aligned} \tag{C.8}$$

$$\begin{aligned}\mathrm{E}\{n_{T,c}(t_1,\tau_1)n^*_{T,c}(t_2,\tau_2)\} =&\frac{1}{T_c^2}\int_{-\frac{T_c}{2}}^{+\frac{T_c}{2}} dt'\int_{-\frac{T_c}{2}}^{+\frac{T_c}{2}} dt''a(t_1+t')a(t_2+t'')\times \\ &\mathrm{E}\{n_{r_t}(t_1+t'+\tau_1)n^*_{r_t}(t_2+t''+\tau_2)\}.\end{aligned} \tag{C.9}$$

Note that t_1, t_2 stand for different times, and τ_1, τ_2 for different delays. The term $\mathrm{E}\{n_{r_t}(t_1+t'+\tau_1)n^*_{r_t}(t_2+t''+\tau_2)\}$ stands for the correlation function of the incident thermal noise, which is $R_{n_{r_t},n_{r_t}}(t_1-t_2+\tau_1-\tau_2+t'-t'')$. It can be obtained assuming a band-limited white noise spectrum (square pulse in the frequency domain) and computing its inverse Fourier transform. Therefore:

$$\begin{aligned}\mathrm{E}\{n_{T,c}(t_1,\tau_1)n^*_{T,c}(t_2,\tau_2)\} =&\frac{1}{T_c^2}\int_{-\frac{T_c}{2}}^{+\frac{T_c}{2}} dt'\int_{-\frac{T_c}{2}}^{+\frac{T_c}{2}} dt''a(t_1+t')a(t_2+t'')\times \\ &kT_{Nr}\frac{\sin\left[\pi B(t_1-t_2+\tau_1-\tau_2+t'-t'')\right]}{\pi(t_1-t_2+\tau_1-\tau_2+t'-t'')},\end{aligned} \tag{C.10}$$

where B is the RF bandwidth of the system, and kT_{Nr} the reflected thermal noise spectral density. Also, assuming that $1/B \ll T_c$ the sinc function can be approximated by a delta function in the integral. Therefore:

$$\begin{aligned}\mathrm{E}\{n_{T,c}(t_1,\tau_1)n^*_{T,c}(t_2,\tau_2)\} =&\frac{kT_{Nr}}{T_c^2}\int_{-\frac{T_c}{2}}^{+\frac{T_c}{2}} dt'\int_{-\infty}^{+\infty} dt''a(t_1+t')a(t_2+t'')\Pi\left(\frac{t''}{T_c}\right)\times \\ &\delta(t_1-t_2+\tau_1-\tau_2+t'-t''),\end{aligned} \tag{C.11}$$

$$\begin{aligned}\mathrm{E}\{n_{T,c}(t_1,\tau_1)n^*_{T,c}(t_2,\tau_2)\} =&\frac{kT_{Nr}}{T_c^2}\int_{-\frac{T_c}{2}}^{+\frac{T_c}{2}} a(t_1+t')a(t_1+t'+\tau_1-\tau_2)\times \\ &\Pi\left(\frac{t_1+t'+\tau_1-\tau_2-t_2}{T_c}\right)dt',\end{aligned} \tag{C.12}$$

and if this correlation is analyzed for the same delay ($\tau=\tau_1-\tau_2=0$), then:

$$\mathrm{E}\{n_{T,c}(t_1,\tau)n^*_{T,c}(t_2,\tau)\} = \frac{kT_{Nr}}{T_c}\Lambda\left(\frac{t_1-t_2}{T_c}\right) = 2\sigma^2_{t,c}(\tau)\gamma_{n_{Tc},n_{Tc}}(t_1-t_2,0), \tag{C.13}$$

where $\gamma_{n_{Tc},n_{Tc}}(t_1 - t_2, 0)$ is the normalized correlation function of the thermal noise after the correlation with a clean replica of the satellite code, and Λ refers to the triangle function which is defined as:

$$\Lambda\left(\frac{\xi}{T}\right) = \begin{cases} 1 - \frac{|\xi|}{T} & |\xi| \leq T \\ 0 & elsewhere \end{cases}. \tag{C.14}$$

If it is analyzed at different delays ($\tau \neq 0$) the general expression of the correlation function becomes:

$$\mathrm{E}\{n_{Tc}(t_1,\tau_1)n^*_{Tc}(t_2,\tau_2)\} = \frac{kT_{Nr}}{T_c}\Lambda\left(\frac{t_1 - t_2}{T_c}\right)R_{a,a}(\tau_1 - \tau_2), \tag{C.15}$$

where

$$R_{a,a}(\tau_1 - \tau_2) \approx \Lambda\left(\frac{\tau_1 - \tau_2}{\tau_{chip}}\right), \tag{C.16}$$

and it is an approximation of the code auto-correlation function [250], which is described by the Λ function in the GPS case, where τ_{chip} is the chip length (977 ns for the GPS C/A code). Note that white thermal noise is by definition uncorrelated, but due to the coherent integration process it becomes partially correlated for the same delay ($\tau = 0$). Also note that by the properties of the Fourier transform, when $t_1 = t_2$ the thermal noise power for the cGNSS-R case can be obtained from (C.15):

$$\mathrm{P}_{\mathrm{T}_c}(\tau) = \frac{kT_{Nr}}{T_c}. \tag{C.17}$$

This expression demonstrates a reduction of the noise equivalent bandwidth due to the coherent integration process.

C.2.2 Coherent Component

The correlation function of $\rho_0(\tau)$ (deterministic) is:

$$\begin{aligned}\mathrm{E}\{\rho_0(\tau_1)\rho_0^*(\tau_2)\} = \mathrm{P}_{\mathrm{coh}}(\tau) = &\frac{E_T G_R D_R^2(0)\Lambda^2\left(\tau_1 - \tau_2 - \frac{R_{0,sp}+R_{sp}}{c}\right)|S(0)|^2\lambda^2}{(4\pi)^2(R_{0,sp}+R_{sp})^2}\times \\ &|r(\theta)|^2 e^{-4k^2\sigma_h^2\cos^2(\theta_{inc})},\end{aligned} \tag{C.18}$$

where G_R stands for the receiving antenna gain, and has assumed that the coherent reflected power does not vary with time. It also shows that this only exists when the signal correlation is maximal (for a determined value of τ). In other words, it is only defined for

$$\tau = \tau_1 - \tau_2 = \frac{R_{0,sp} + R_{sp}}{c}. \tag{C.19}$$

C.2.3 Incoherent Component or Speckle Noise

The correlation of $n_S(t,\tau)$ has been studied in several works in the literature for the sea surface (in the absence of a coherent component), [55, 72, 76, 251–253]. A dedicated study

is required to analyze this term in detail. For instance, [72] assumes that between 1 ms waveforms the correlation function is a Kronecker delta function. This fact occurs, for instance, with the thermal noise correlation function as $\gamma_{n_{Tc},n_{Tc}}(t_1-t_2,\tau)$ sampled at $t_1-t_2 \propto$ 1ms is equivalent to a Kronecker delta function too. In this appendix it has been decided to use a Gaussian correlation function whose correlation time is computed based on the Van Cittert-Zernike theorem [252]. Therefore:

$$\begin{aligned}\mathrm{E}\{n_S(t_1,\tau_1)n_S^*(t_2,\tau_2)\} =&\mathrm{E}\left\{\frac{1}{T_c}\int_{-\frac{T_c}{2}}^{+\frac{T_c}{2}} u_{r_{inc}}(t_1+t'+\tau_1)a(t_1+t')dt'\times\right.\\ &\left.\frac{1}{T_c}\int_{-\frac{T_c}{2}}^{+\frac{T_c}{2}} u^*_{r_{inc}}(t_2+t''+\tau_2)a(t_2+t'')dt''\right\},\end{aligned} \tag{C.20}$$

$$\begin{aligned}\mathrm{E}\{n_S(t_1,\tau_1)n_S^*(t_2,\tau_2)\} =&\frac{1}{T_c^2}\int_{-\frac{T_c}{2}}^{+\frac{T_c}{2}} dt'\int_{-\frac{T_c}{2}}^{+\frac{T_c}{2}} dt''a(t_1+t')a(t_2+t'')\times\\ &\mathrm{E}\{u_{r_{inc}}(t_1+t'+\tau_1)u^*_{r_{inc}}(t_2+t''+\tau_2)\}.\end{aligned} \tag{C.21}$$

Taking into account that:

$$u_{r_{inc}}\left(\vec{R}_r,t\right)=\iint D(\vec{r})a[t-(R_0-R)/c]g_{inc}(\vec{r},t)d\vec{r}, \tag{C.22}$$

then:

$$\begin{aligned}\mathrm{E}\{n_S(t_1,\tau_1)n_S^*(t_2,\tau_2)\} =& \iint \frac{1}{T_c^2}\int_{-\frac{T_c}{2}}^{+\frac{T_c}{2}} dt'\int_{-\frac{T_c}{2}}^{+\frac{T_c}{2}} dt''a(t_1+t')a(t_2+t'')\times\\ &a\left(t_1+t'+\tau_1-(R_0-R)/c\right)a\left(t_2+t''+\tau_2-(R_0-R)/c\right)\times\\ &\rho_{u_{r_{inc}},u_{r_{inc}}}(t_1-t_2+\tau_1-\tau_2+t'-t'')d\vec{r}d\vec{r}',\end{aligned} \tag{C.23}$$

where it has been assumed that the surface remains frozen for the coherent integration time, and $\rho_{u_{r_{inc}},u_{r_{inc}}}(t_1-t_2+\tau_1-\tau_2+t'-t'')$ is the correlation function of the $g_{inc}(\vec{r},t)$ function multiplied by some scaling parameters. Recall that its value must be the reflected power at its origin. Then:

$$\begin{aligned}&\mathrm{E}\{n_S(t_1,\tau_1)n_S^*(t_2,\tau_2)\} =\\ &=\iint \frac{1}{2T_c^2}\int_{-T_c}^{0} d\xi\rho_{u_{r_{inc}},u_{r_{inc}}}(t_1-t_2+\tau_1-\tau_2+\xi)\int_{-\xi-T_c}^{\xi+T_c} a\left(t_1+\frac{\eta}{2}+\frac{\xi}{2}\right)a\left(t_2+\frac{\eta}{2}-\frac{\xi}{2}\right)\times\\ &\quad a\left(t_1+\frac{\eta}{2}+\frac{\xi}{2}+\tau_1-(R_0-R)/c\right)a\left(t_2+\frac{\eta}{2}-\frac{\xi}{2}+\tau_2-(R_0-R)/c\right)d\eta d\vec{r}d\vec{r}'+\\ &+\iint \frac{1}{2T_c^2}\int_{0}^{T_c} d\xi\rho_{u_{r_{inc}},u_{r_{inc}}}(t_1-t_2+\tau_1-\tau_2+\xi)\int_{\xi-T_c}^{-\xi+T_c} a\left(t_1+\frac{\eta}{2}+\frac{\xi}{2}\right)a\left(t_2+\frac{\eta}{2}-\frac{\xi}{2}\right)\times\\ &\quad a\left(t_1+\frac{\eta}{2}+\frac{\xi}{2}+\tau_1-(R_0-R)/c\right)a\left(t_2+\frac{\eta}{2}-\frac{\xi}{2}+\tau_2-(R_0-R)/c\right)d\eta d\vec{r}d\vec{r}',\end{aligned} \tag{C.24}$$

$$\mathrm{E}\{n_S(t_1,\tau_1)n_S^*(t_2,\tau_2)\} \approx \iint \frac{1}{T_c}\int_{-T_c}^{T_c} \rho_{u_{r_{inc}},u_{r_{inc}}}(t_1-t_2+\tau_1-\tau_2+\xi)\Lambda\left(\frac{\xi}{T_c}\right)\times \Lambda\left(\frac{\tau_1-\frac{R_0-R}{c}}{\tau_{chips}}\right)\Lambda\left(\frac{\tau_2-\frac{R_0-R}{c}}{\tau_{chips}}\right)d\xi d\vec{r}d\vec{r}'. \tag{C.25}$$

This equation can be rearranged into two different integrals as the convolution of two different functions, the surface correlation function and the Λ function. Then:

$$\mathrm{E}\{n_S(t_1,\tau_1)n_S^*(t_2,\tau_2)\} = \frac{1}{T_c}\left(R_{u_{r_{inc}},u_{r_{inc}}} * \Lambda_{T_c}\right)(t_1-t_2+\tau_1-\tau_2), \tag{C.26}$$

where

$$R_{u_{r_{inc}},u_{r_{inc}}}(t_1-t_2+\tau_1-\tau_2) = \iint \Lambda\left(\frac{\tau_1-\frac{R_0-R}{c}}{\tau_{chips}}\right)\Lambda\left(\frac{\tau_2-\frac{R_0-R}{c}}{\tau_{chips}}\right)\times \rho_{u_{r_{inc}},u_{r_{inc}}}(t_1-t_2+\tau_1-\tau_2)d\vec{r}d\vec{r}', \tag{C.27}$$

and it stands for the surface correlation function, and takes into account the modulation of the codes used. Assuming that $\tau_1=\tau_2=(R_0-R)/c$, then Λ function inside the surface integral is equal to one in the entire correlation integral, and therefore:

$$\mathrm{E}\{n_S(t_1,\tau)n_S^*(t_2,\tau)\} = \mathrm{P}_{\mathrm{incoh}}(\tau)\gamma_{s,s}(t_1-t_2,\tau) = \frac{1}{T_c}\left[\rho_{u_{r_{inc}},u_{r_{inc}}}(t_1-t_2) * \Lambda\left(\frac{t_1-t_2}{T_c}\right)\right]. \tag{C.28}$$

If a Gaussian correlation function is assumed, then:

$$\rho_{u_{r_{inc}},u_{r_{inc}}}(t_1-t_2,\tau=0) = \mathrm{P}_{\mathrm{incoh}}(\tau)e^{-\left(\frac{t_1-t_2}{t_c}\right)^2}, \tag{C.29}$$

where $\mathrm{P}_{\mathrm{incoh}}(\tau)$ is the incoherent received power at a given delay which is given by [70]:

$$\mathrm{P}_{\mathrm{incoh}}(\tau) = \frac{EIRP_T G_R}{(4\pi)^2} I_{A_{illpq}}(\tau), \tag{C.30}$$

$$I_{A_{illpq}}(\tau) = \lambda^2 \int_{A_{ill}} \frac{\sigma^0(\vec{\rho})D_T^2(\vec{\rho})D_R^2(\vec{\rho})\Lambda^2(\tau,\vec{\rho})|S(\tau,\vec{\rho})|^2}{4\pi R_0^2(\vec{\rho})R^2(\vec{\rho})}d^2\rho, \tag{C.31}$$

and

$$t_c \approx 2\cdot\frac{\lambda}{2v_r}\sqrt{\frac{R}{c\tau_{chip}}}, \tag{C.32}$$

where v_r is the platform's speed, and the initial 2 has been added because the surface is illuminated with a triangular pulse instead of a square one due to the ACF function shape of the satellite codes. A reference to compute the equivalent ACF for PRN codes different from the C/A is [250]. The $\gamma_{s,s}(t_1-t_2,\tau=0)$ becomes:

$$\gamma_{s,s}(t_1-t_2,\tau=0) = \frac{1}{T_c}\left[e^{-\left(\frac{t_1-t_2}{t_c}\right)^2} * \Lambda\left(\frac{t_1-t_2}{T_c}\right)\right]. \tag{C.33}$$

C.2.4 iGNSS-R Thermal Noise

As it was seen in Chapter 4 and in the first section of this Appendix, the iGNSS-R can be expressed as a function of the cGNSS-R and plus the addition of some terms. This subsection describes the remaining term for the iGNSS-R, which is $\mathrm{E}\{n_{T,i}(t_1,\tau)n^*_{T,i}(t_2,\tau)\}$, and it will be related to $\mathrm{E}\{n_{T,c}(t_1,\tau)n^*_{T,c}(t_2,\tau)\}$ described in C.2.1. Recall that the $n_{T,i}(t,\tau)$ is:

$$n_{T,i}(t,\tau) = n_{T,c}(t,\tau) + \sqrt{\frac{1}{SNR_d}}\left[y_{u_r,d_t}(t,\tau) + y_{r_t,d_t}(t,\tau)\right] \tag{C.34}$$

Hence, taking into account that all the terms are mutually independent, and that their respective mean value is 0, it is obtained that:

$$\begin{aligned}\mathrm{E}\{n_{T,i}(t_1,\tau_1)n^*_{T,i}(t_2,\tau_2)\} =& \mathrm{E}\{n_{T,c}(t_1,\tau_1)n^*_{T,c}(t_2,\tau_2)\}+\\ &+\frac{1}{SNR_d}\Big(\mathrm{E}\{y_{u_r,d_t}(t_1,\tau_1)y^*_{u_r,d_t}(t_2,\tau_2)\}+\\ &+\mathrm{E}\{y_{d_t,r_t}(t_1,\tau_1)y^*_{d_t,r_t}(t_2,\tau_2)\}\Big),\end{aligned} \tag{C.35}$$

where:

$$\mathrm{E}\{n_{T,c}(t_1,\tau)n^*_{T,c}(t_2,\tau)\} = \frac{kT_{Nr}}{T_c}\Lambda\left(\frac{t_1-t_2}{T_c}\right)R_{a,a}(\tau_1-\tau_2), \tag{C.36}$$

as was seen in section C.2.1,

$$\begin{aligned}\mathrm{E}\{y_{u_r,d_t}(t_1,\tau_1)y^*_{u_r,d_t}(t_2,\tau_2)\} =& \int_{-\frac{T_c}{2}}^{+\frac{T_c}{2}}dt'\int_{-\frac{T_c}{2}}^{+\frac{T_c}{2}}dt''\mathrm{E}\{u_r(t_1+t'+\tau_1)u^*_r(t_2+t''+\tau_2)\}\times\\ &\mathrm{E}\{\bar{n}_{d_t}(t_1+t'+\tau_1)\bar{n}^*_{d_t}(t_2+t''+\tau_2)\}\frac{1}{T_c^2},\end{aligned} \tag{C.37}$$

where $\bar{n}_{d_t}$ is the normalized thermal noise power (recall that by definition the direct noise signal has been normalized by the power of the clean direct signal). Assuming the same band-limited noise properties, Eqn. (C.37) becomes:

$$\begin{aligned}\mathrm{E}\{y_{u_r,d_t}(t_1,\tau_1)y^*_{u_r,d_t}(t_2,\tau_2)\} =& \int_{-\frac{T_c}{2}}^{+\frac{T_c}{2}}dt'\int_{-\infty}^{+\infty}dt''\mathrm{E}\{u_r(t_1+t'+\tau_1)u^*_r(t_2+t''+\tau_2)\}\times\\ &\Pi\left(\frac{t''}{T_c}\right)\frac{\sin\left[\pi B(t_1+t'\tau_1-t_2-t''-\tau_2)\right]}{\pi(t_1+t'\tau_1-t_2-t''-\tau_2)}\frac{1}{BT_c^2},\end{aligned} \tag{C.38}$$

and by approximating the *sinc* function by a delta function, therefore:

$$\begin{aligned}\mathrm{E}\{y_{u_r,d_t}(t_1,\tau_1)y^*_{u_r,d_t}(t_2,\tau_2)\} =& \frac{1}{BT_c^2}\int_{-\frac{T_c}{2}}^{+\frac{T_c}{2}}dt'\mathrm{E}\{|u_r(t_1+t'+\tau_1)|^2\}\times\\ &\Pi\left(\frac{t_1-t_2+\tau_1-\tau_2+t'}{T_c}\right).\end{aligned} \tag{C.39}$$

The term $\mathrm{E}\{|u_r(t_1+t'+\tau)|^2\}$ stands for the total reflected signal power $(\mathrm{P_{coh}}(\tau)+\mathrm{P_{incoh}}(\tau))$, and due to stationarity it can be taken out of the integral. Therefore:

$$\mathrm{E}\{y_{u_r,d_t}(t_1,\tau_1)y^*_{u_r,d_t}(t_2,\tau_2)\}=\frac{\mathrm{P_{coh}}(\tau)+\mathrm{P_{incoh}}(\tau)}{BT_c^2}\int_{-\frac{T_c}{2}}^{+\frac{T_c}{2}}\Pi\left(\frac{t_1-t_2+\tau_1-\tau_2+t'}{T_c}\right)dt', \tag{C.40}$$

and solving the integral,

$$\mathrm{E}\{y_{u_r,d_t}(t_1,\tau_1)y^*_{u_r,d_t}(t_2,\tau_2)\}=\frac{\mathrm{P_{coh}}(\tau)+\mathrm{P_{incoh}}(\tau)}{BT_c}\Lambda\left(\frac{t_1-t_2+\tau_1-\tau_2}{T_c}\right). \tag{C.41}$$

If considering the same delay ($\tau=0$), then:

$$\mathrm{E}\{y_{u_r,t_d}(t_1,\tau)y^*_{u_r,t_d}(t_2,\tau)\}=\frac{\mathrm{P_{coh}}(\tau)+\mathrm{P_{incoh}}(\tau)}{BT_c}\Lambda\left(\frac{t_1-t_2}{T_c}\right). \tag{C.42}$$

The last term ($\mathrm{E}\{y_{r_t,d_t}(t_1,\tau_1)y^*_{r_t,d_t}(t_2,\tau_2)\}$) is given by:

$$\begin{aligned}\mathrm{E}\{y_{r_t,d_t}(t_1,\tau_1)y^*_{r_t,d_t}(t_2,\tau_2)\}=&\int_{-\frac{T_c}{2}}^{+\frac{T_c}{2}}dt'\int_{-\frac{T_c}{2}}^{+\frac{T_c}{2}}dt''\mathrm{E}\{n_{r_t}(t_1+t'+\tau_1)n^*_{r_t}(t_2+t''+\tau_2)\}\times\\&\mathrm{E}\{\bar{n}_{d_t}(t_1+t'+\tau_1)\bar{n}^*_{d_t}(t_2+t''+\tau_2)\}\frac{1}{T_c^2},\end{aligned} \tag{C.43}$$

$$\begin{aligned}\mathrm{E}\{y_{r_t,d_t}(t_1,\tau_1)y^*_{r_t,d_t}(t_2,\tau_2)\}=&\frac{kT_{Nr}}{T_c}\frac{1}{BT_c}\times\\&\int_{-\frac{T_c}{2}}^{+\frac{T_c}{2}}dt'\int_{-\frac{T_c}{2}}^{+\frac{T_c}{2}}dt''\frac{\sin^2\left[\pi B(t_1+t'+\tau_1-t_2-t''-\tau_2)\right]}{\left[\pi(t_1+t'-t_2-t'')\right]^2},\end{aligned} \tag{C.44}$$

and this integral can be solved by changing the variables, $\xi=t'-t''$, $\eta=t'+t''$, and considering that the Jacobian of the transformation is 1/2. Hence:

$$\mathrm{E}\{y_{r_t,d_t}(t_1,\tau)y^*_{r_t,d_t}(t_2,\tau)\}=\frac{kT_{Nr}}{T_c}\frac{1}{B}\int_{-T_c}^{+T_c}\Lambda\left(\frac{x}{T_c}\right)\frac{\sin^2\left[\pi B(t_1-t_2+\tau_1-\tau_2+x)\right]}{\left[\pi(t_1-t_2+\tau_1-\tau_2+x)\right]^2}dx. \tag{C.45}$$

If $1/B\ll T_c$, which always occurs since there is a minimum of 3 orders of magnitude difference between them, the $sinc^2$ function is much more narrower than the Λ function. This results in being able to take the Λ function out of the integral. Therefore:

$$\begin{aligned}\mathrm{E}\{y_{r_t,d_t}(t_1,\tau)y^*_{r_t,d_t}(t_2,\tau)\}=&\frac{kT_{Nr}}{T_c}\frac{1}{B}\Lambda\left(\frac{t_1-t_2+\tau_1-\tau_2}{T_c}\right)\times\\&\int_{-T_c}^{+T_c}\frac{\sin^2\left[\pi B(t_1-t_2+\tau_1-\tau_2+x)\right]}{\left[\pi(t_1-t_2+\tau_1-\tau_2+x)\right]^2}dx,\end{aligned} \tag{C.46}$$

$$\mathrm{E}\{y_{r_t,d_t}(t_1,\tau)y^*_{r_t,d_t}(t_2,\tau)\}=\frac{kT_{Nr}}{T_c}\Lambda\left(\frac{t_1-t_2+\tau_1-\tau_2}{T_c}\right), \tag{C.47}$$

where the symmetry property of the Λ function has been used. If, for all cases $\tau_1 = \tau_2$, then the correlation function of the equivalent iGNSS-R thermal noise becomes:

$$\mathrm{E}\{n_{T,i}(t_1,\tau)n^*_{T,i}(t_2,\tau)\} = \Lambda\left(\frac{t_1-t_2}{T_c}\right)\left[\frac{kT_{Nr}}{T_c} + \frac{1}{SNR_d}\left(\frac{\mathrm{P}_{\mathrm{coh}}(\tau)+\mathrm{P}_{\mathrm{incoh}}(\tau)}{BT_c} + \frac{kT_{Nr}}{T_c}\right)\right], \tag{C.48}$$

and simplifying:

$$\mathrm{E}\{n_{T,i}(t_1,\tau)n^*_{T,i}(t_2,\tau)\} = \Lambda\left(\frac{t_1-t_2}{T_c}\right)2\sigma^2_{t,c}(\tau)\cdot\left(1+\frac{1}{SNR_d}\left(SNR_r+1\right)\right), \tag{C.49}$$

where SNR_r refers to the pre-correlation SNR for the reflected signal:

$$SNR_r = \frac{\mathrm{P}_{\mathrm{coh}}(\tau)+\mathrm{P}_{\mathrm{incoh}}(\tau)}{kT_{Nr}B}, \tag{C.50}$$

and

$$\gamma_{n_{Ti},n_{Ti}}(t_1-t_2,\tau) = \gamma_{n_{Tc},n_{Tc}}(t_1-t_2,\tau), \tag{C.51}$$

which indicates that the correlation functions for the thermal noise in the cGNSS-R case, and the equivalent thermal noise for the iGNSS-R case are the same. Differently, their powers are different as shown by Eqn. (C.49), where the thermal noise in the iGNSS-R case is equivalent to the cGNSS-R case multiplied by the coefficient $1+\frac{1}{SNR_d}\left(SNR_r+1\right)$.

C.3 Fourth Order Correlation Functions

Assuming that the above mentioned processes are circular complex Gaussian processes, the fourth order correlation functions or second order coherence functions can be expressed as a function of the second order correlation functions [131, 254]:

$$\Gamma_{x,x}(t_1-t_2,\tau) = \left[2\sigma^2(\tau)\right]^2\left(1+\left|\gamma_{x,x}(t_1-t_2,\tau)\right|^2\right). \tag{C.52}$$

Therefore:

$$\begin{aligned}\mathrm{E}\{n_S(t_1,\tau)n^*_S(t_1,\tau)n_S(t_2,\tau)n^*_S(t_2,\tau)\} =& \mathrm{P}^2_{\mathrm{incoh}}(\tau)\left(1+\left|\frac{1}{T_c}\left[e^{\left(\frac{t_1-t_2}{t_c}\right)^2} * \Lambda\left(\frac{t_1-t_2}{T_c}\right)\right]\right|^2\right) = \\ =& \Gamma_{S,S}(t_1-t_2,\tau),\end{aligned} \tag{C.53}$$

$$\begin{aligned}\mathrm{E}\{n_{T,c}(t_1,\tau)n^*_{T,c}(t_1,\tau)n_{T,c}(t_2,\tau)n^*_{T,c}(t_2,\tau)\} =& \mathrm{P}^2_{\mathrm{T_c}}(\tau)\left(1+\left|\Lambda\left(\frac{t_1-t_2}{T_c}\right)\right|^2\right) = \\ =& \Gamma_{n_{Tc},n_{Tc}}(t_1-t_2,\tau),\end{aligned} \tag{C.54}$$

$$\begin{aligned}\mathrm{E}\{n_{T,i}(t_1,\tau)n^*_{T,i}(t_1,\tau)n_{T,i}(t_2,\tau)n^*_{T,i}(t_2,\tau)\} =& \mathrm{P}^2_{\mathrm{T_i}}(\tau)\left(1+\left|\Lambda\left(\frac{t_1-t_2}{T_c}\right)\right|^2\right) = \\ =& \Gamma_{n_{Ti},n_{Ti}}(t_1-t_2,\tau).\end{aligned} \tag{C.55}$$

C.4 Detectability Criteria for the Different Cases

This section details the computation of the detectability criteria to the power waveforms for the $\mathrm{SNR}_{\mathrm{nc,in}}$ when no incoherent integration has been applied. Let us show here again Fig. 4.4, where the SNRs are defined.

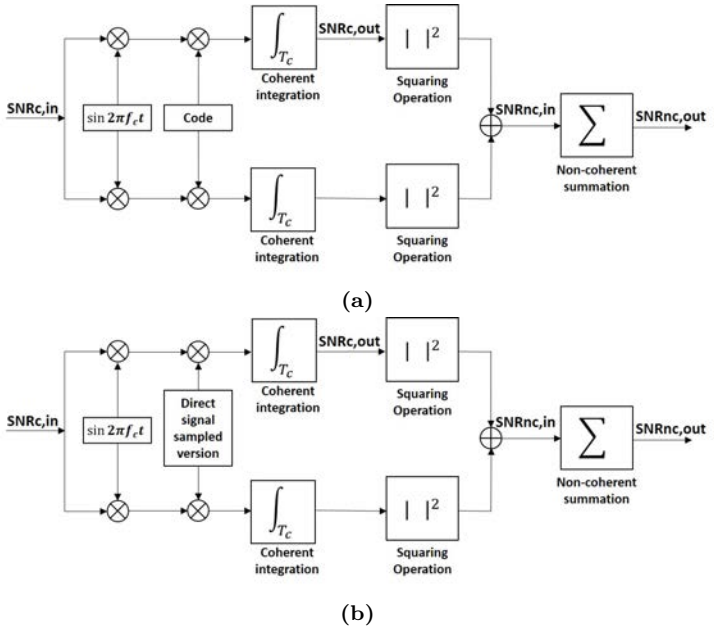

Figure C.1: (a) Typical GNSS/cGNSS-R receiver block diagram, (b) Simplified iGNSS-R receiver block diagram.

To compute each detectability criterion the following assumptions must be considered, which are related to the power waveform definition, and it is the waveform observed at the time of computing $\mathrm{SNR}_{\mathrm{nc,in}}$. For the cGNSS-R:

$$f_{S+N} = Y_c(t,\tau) = |y_c(t,\tau)|^2, \tag{C.56}$$

$$f_N = |n_{T,c}(t,\tau)|^2, \tag{C.57}$$

and for the iGNSS-R:

$$f_{S+N} = Y_i(t,\tau) = |y_i(t,\tau)|^2, \tag{C.58}$$

$$f_N = \left| n_{T,c}(t,\tau) + \sqrt{\frac{1}{SNR_d}} y_{r_t,d_t}(t,\tau) \right|^2. \tag{C.59}$$

Note that in the absence of signal power $y_{u_r,d_t}(t,\tau) = 0$, which is why it does not appear in the f_N expression for the iGNSS-R.

C.4.1 Derivation of d_c

The detectability criterion d_c is:

$$d_c = \frac{\mathrm{E}\{f_{S+N}\} - \mathrm{E}\{f_N\}}{\sqrt{\mathrm{E}\{f_N^2\} - \mathrm{E}\{f_N\}^2}} = \frac{\mathrm{P}_{\mathrm{coh}}(\tau) + \mathrm{P}_{\mathrm{incoh}}(\tau) + \mathrm{P}_{\mathrm{T}_c}(\tau) - \mathrm{P}_{\mathrm{T}_c}(\tau)}{\sqrt{2\mathrm{P}_{\mathrm{T}_c}^2(\tau) - \mathrm{P}_{\mathrm{T}_c}^2(\tau)}} = \frac{\mathrm{P}_{\mathrm{coh}}(\tau) + \mathrm{P}_{\mathrm{incoh}}(\tau)}{\mathrm{P}_{\mathrm{T}_c}(\tau)}, \tag{C.60}$$

where:

$$\begin{aligned} Y_c(t,\tau) =& y_c(t,\tau)y_c(t,\tau)^* = |\rho_0(t,\tau)|^2 + \rho_0(t,\tau)n_S^*(t,\tau) + \rho_0(t,\tau)n_{T,c}^*(t,\tau) + \\ &+ \rho_0^*(t,\tau)n_S(t,\tau) + |n_S(t,\tau)|^2 + n_S(t,\tau)n_{T,c}^*(t,\tau) + \rho_0^*(t,\tau)n_{T,c}(t,\tau) + \\ &+ n_{T,c}(t,\tau)n_S^*(t,\tau) + |n_{T,c}(t,\tau)|^2, \end{aligned} \tag{C.61}$$

$$\begin{aligned} \mathrm{E}\{f_{S+N}\} =& \mathrm{E}\{|\rho_0(t,\tau)|^2 + |n_S(t,\tau)|^2 + |n_{T,c}(t,\tau)|^2\} = \\ =& \mathrm{P}_{\mathrm{coh}}(\tau) + \mathrm{P}_{\mathrm{incoh}}(\tau)\gamma_{s,s}(0,\tau) + \mathrm{P}_{\mathrm{T}_c}(\tau)\gamma_{n_{Tc},n_{Tc}}(0,\tau) = \\ =& \mathrm{P}_{\mathrm{coh}}(\tau) + \mathrm{P}_{\mathrm{incoh}}(\tau) + \mathrm{P}_{\mathrm{T}_c}(\tau), \end{aligned} \tag{C.62}$$

$$\mathrm{E}\{f_N\} = \mathrm{E}\{|n_{T,c}(t,\tau)|^2\} = \mathrm{P}_{\mathrm{T}_c}(\tau)\gamma_{n_{Tc},n_{Tc}}(0,\tau) = \mathrm{P}_{\mathrm{T}_c}(\tau), \tag{C.63}$$

and using the properties of Gaussian processes:

$$\mathrm{E}\{{f_N}^2\} = \mathrm{E}\{|n_{T,c}(t,\tau)|^4\} = \Gamma_{n_{Tc},n_{Tc}}(0,\tau) = \mathrm{P}_{\mathrm{T}_c}^2(\tau)\left(1 + |\gamma_{n_{Tc},n_{Tc}}(0,\tau)|^2\right) = 2\mathrm{P}_{\mathrm{T}_c}^2(\tau). \tag{C.64}$$

C.4.2 Derivation of d_c'

The detectability criterion d_c' is:

$$\begin{aligned} d_c' =& \frac{\mathrm{E}\{f_{S+N}\} - \mathrm{E}\{f_N\}}{\sqrt{\mathrm{E}\{f_{S+N}^2\} - \mathrm{E}\{f_{S+N}\}^2}} = \\ =& \frac{\mathrm{P}_{\mathrm{coh}}(\tau) + \mathrm{P}_{\mathrm{incoh}}(\tau) + \mathrm{P}_{\mathrm{T}_c}(\tau) - \mathrm{P}_{\mathrm{T}_c}(\tau)}{\sqrt{2(\mathrm{P}_{\mathrm{coh}}(\tau) + \mathrm{P}_{\mathrm{incoh}}(\tau) + \mathrm{P}_{\mathrm{T}_c}(\tau))^2 - \mathrm{P}_{\mathrm{coh}}^2(\tau) - (\mathrm{P}_{\mathrm{coh}}(\tau) + \mathrm{P}_{\mathrm{incoh}}(\tau) + \mathrm{P}_{\mathrm{T}_c}(\tau))^2}} = \\ =& \frac{\mathrm{P}_{\mathrm{coh}}(\tau) + \mathrm{P}_{\mathrm{incoh}}(\tau)}{\sqrt{(\mathrm{P}_{\mathrm{coh}}(\tau) + \mathrm{P}_{\mathrm{incoh}}(\tau) + \mathrm{P}_{\mathrm{T}_c}(\tau))^2 - \mathrm{P}_{\mathrm{coh}}^2(\tau)}} = \frac{1}{\sqrt{\left(1 + \frac{1}{\mathrm{SNR}_{\mathrm{TH}_c}}\right)^2 - \left(1 - \frac{1}{\mathrm{SNR}_{\mathrm{SP}}}\right)^2}}, \end{aligned} \tag{C.65}$$

where:

$$\begin{aligned} \mathrm{E}\{{f_{S+N}}^2\} =& \mathrm{E}\{Y_c^2(t,\tau)\} = \mathrm{E}\{Y_c(t,\tau)Y_c(t,\tau)\} = \\ =& \mathrm{E}\{|\rho_0(t,\tau)|^4\} + \mathrm{E}\{|n_S(t,\tau)|^4\} + \mathrm{E}\{|n_{T,c}(t,\tau)|^4\} + 4\mathrm{E}\{|\rho_0(t,\tau)|^2|n_S(t,\tau)|^2\} + \\ &+ 4\mathrm{E}\{|\rho_0(t,\tau)|^2|n_{T,c}(t,\tau)|^2\} + 4\mathrm{E}\{|n_S(t,\tau)|^2|n_{T,c}(t,\tau)|^2\} = \\ =& 2(\mathrm{P}_{\mathrm{coh}}(\tau) + \mathrm{P}_{\mathrm{incoh}}(\tau) + \mathrm{P}_{\mathrm{T}_c}(\tau))^2 - \mathrm{P}_{\mathrm{coh}}^2(\tau), \end{aligned} \tag{C.66}$$

$$\mathrm{SNR}_{\mathrm{TH}_c} = \frac{\mathrm{P}_{\mathrm{coh}}(\tau) + \mathrm{P}_{\mathrm{incoh}}(\tau)}{\mathrm{P}_{\mathrm{T}_c}(\tau)}, \tag{C.67}$$

$$\mathrm{SNR}_{\mathrm{SP}} = \frac{\mathrm{P}_{\mathrm{coh}}(\tau) + \mathrm{P}_{\mathrm{incoh}}(\tau)}{\mathrm{P}_{\mathrm{incoh}}(\tau)}, \tag{C.68}$$

and the other terms are described in the previous subsection.

C.4.3 Derivation of d_i

The detectability criterion d_i is:

$$\begin{aligned} d_i =& \frac{\mathrm{E}\{f_{S+N}\} - \mathrm{E}\{f_N\}}{\sqrt{\mathrm{E}\{f_N^2\} - \mathrm{E}\{f_N\}^2}} = \\ =& \frac{\mathrm{P}_{\mathrm{coh}}(\tau) + \mathrm{P}_{\mathrm{incoh}}(\tau) + \mathrm{P}_{\mathrm{T}_c}(\tau)\left(1 + \frac{1}{SNR_d}\left(SNR_r + 1\right)\right) - \mathrm{P}_{\mathrm{T}_c}(\tau)\left(1 + \frac{1}{SNR_d}\right)}{\sqrt{2\mathrm{P}^2_{\mathrm{T}_c(\tau)}\left(1 + \frac{1}{SNR_d}\right)^2 - \mathrm{P}^2_{\mathrm{T}_c}(\tau)\left(1 + \frac{1}{SNR_d}\right)^2}} = \\ =& \frac{\mathrm{P}_{\mathrm{coh}}(\tau) + \mathrm{P}_{\mathrm{incoh}}(\tau) + \mathrm{P}_{\mathrm{T}_c}(\tau)\frac{SNR_r}{SNR_d}}{\mathrm{P}_{\mathrm{T}_c(\tau)}\left(1 + \frac{1}{SNR_d}\right)} = \frac{1 + \frac{1}{d_c}\frac{SNR_r}{SNR_d}}{\frac{1}{d_c}\left(1 + \frac{1}{SNR_d}\right)}, \end{aligned} \tag{C.69}$$

where:

$$Y_i(t,\tau) = y_i(t,\tau)y_i(t,\tau)^* =$$

$$\begin{aligned} Y_i(t,\tau) =& |y_c(t,\tau)|^2 + \sqrt{\frac{1}{SNR_d}}y_c(t,\tau)y^*_{u_r,d_t}(t,\tau) + \sqrt{\frac{1}{SNR_d}}y_c(t,\tau)y^*_{r_t,d_t}(t,\tau) + \\ &+ \sqrt{\frac{1}{SNR_d}}y_{u_r,d_t}(t,\tau)y^*_c(t,\tau) + \frac{1}{SNR_d}|y_{u_r,d_t}(t,\tau)|^2 + \\ &+ \sqrt{\frac{1}{SNR_d}}y_{u_r,d_t}(t,\tau)y^*_{r_t,d_t}(t,\tau) + \sqrt{\frac{1}{SNR_d}}y_{r_t,d_t}(t,\tau)y^*_c(t,\tau) + \\ &+ \sqrt{\frac{1}{SNR_d}}y_{r_t,d_t}(t,\tau)y^*_{u_r,d_t}(t,\tau) + \frac{1}{SNR_d}|y_{r_t,d_t}(t,\tau)|^2, \end{aligned} \tag{C.70}$$

$$\begin{aligned} \mathrm{E}\{f_{S+N}\} =& \mathrm{E}\Big\{|y_c(t,\tau)|^2 + \frac{1}{SNR_d}|y_{u_r,d_t}(t,\tau)|^2 + \frac{1}{SNR_d}|y_{r_t,d_t}(t,\tau)|^2\Big\} = \\ &= \mathrm{P}_{\mathrm{coh}}(\tau) + \mathrm{P}_{\mathrm{incoh}}(\tau) + \mathrm{P}_{\mathrm{T}_c}(\tau)\left(1 + \frac{1}{SNR_d}\left(SNR_r + 1\right)\right), \end{aligned} \tag{C.71}$$

$$\mathrm{E}\{f_N\} = \mathrm{E}\Big\{\Big|n_{T,c}(t,\tau) + \sqrt{\frac{1}{SNR_d}}y_{r_t,d_t}(t,\tau)\Big|^2\Big\} = \mathrm{P}_{\mathrm{T}_c}(\tau)\left(1 + \frac{1}{SNR_d}\right), \tag{C.72}$$

and

$$\mathrm{E}\{{f_N}^2\} = \mathrm{E}\Big\{\Big|n_{T,c}(t,\tau) + \sqrt{\frac{1}{SNR_d}}y_{r_t,d_t}(t,\tau)\Big|^4\Big\},$$

$$\begin{aligned}\mathrm{E}\{{f_N}^2\} =&\mathrm{E}\Big\{\Big(|n_{T,c}(t,\tau)|^2+\frac{1}{SNR_d}|y_{r_t,d_t}(t,\tau)|^2+\sqrt{\frac{1}{SNR_d}}n_{T,c}(t,\tau)y^*_{r_t,d_t}(t,\tau)+\\&+\sqrt{\frac{1}{SNR_d}}n^*_{T,c}(t,\tau)y_{r_t,d_t}(t,\tau)\Big)\Big(|n_{T,c}(t,\tau)|^2+\frac{1}{SNR_d}|y_{r_t,d_t}(t,\tau)|^2+\\&+\sqrt{\frac{1}{SNR_d}}n^*_{T,c}(t,\tau)y_{r_t,d_t}(t,\tau)+\sqrt{\frac{1}{SNR_d}}n_{T,c}(t,\tau)y^*_{r_t,d_t}(t,\tau)\Big)\Big\}.\end{aligned} \tag{C.73}$$

To solve these moments, the results from Appendix C.3 can be used. Therefore:

$$\Gamma_{n_{Tc},n_{Tc}}(t_1-t_2,\tau)=[2\sigma^2_{t,c}(\tau)]^2\left(1+|\gamma_{n_{Tc},n_{Tc}}(t_1-t_2,\tau)|^2\right)=\mathrm{P}^2_{\mathrm{T}_c}(\tau)\left[1+\Lambda^2\left(\frac{t_1-t_2}{T_c}\right)\right], \tag{C.74}$$

$$\Gamma_{y_{r_t,d_t},y_{r_t,d_t}}(t_1-t_2,\tau)=\mathrm{P}^2_{\mathrm{T}_c}(\tau)\left[1+\Lambda^2\left(\frac{t_1-t_2}{T_c}\right)\right]. \tag{C.75}$$

Hence:

$$\begin{aligned}\mathrm{E}\{{f_N}^2\} =&\mathrm{E}\{|n_{Tc}(t,\tau)|^4\}+\frac{4}{SNR_d}\mathrm{E}\{|n_{T,c}(t,\tau)|^2|y_{r_t,d_t}(t,\tau)|^2\}+\frac{1}{SNR_d^2}\mathrm{E}\{|y_{r_t,d_t}(t,\tau)|^4\}=\\&=2\mathrm{P}^2_{\mathrm{T}_c(\tau)}\left(1+\frac{1}{SNR_d}\right)^2.\end{aligned} \tag{C.76}$$

C.4.4 Derivation of d'_i

The detectability criterion d'_i is:

$$\begin{aligned}k_i =&\frac{\mathrm{E}\{f_{S+N}\}-\mathrm{E}\{f_N\}}{\sqrt{\mathrm{E}\{f^2_{S+N}\}-\mathrm{E}\{f_{S+N}\}^2}}=\\&=\frac{\mathrm{P}_{\mathrm{coh}}(\tau)+\mathrm{P}_{\mathrm{incoh}}(\tau)+\mathrm{P}_{\mathrm{T}_c}(\tau)\frac{SNR_r}{SNR_d}}{\sqrt{2(\mathrm{P}_{\mathrm{coh}}(\tau)+\mathrm{P}_{\mathrm{incoh}}(\tau)+\mathrm{P}_{\mathrm{T}_i}(\tau))^2-\mathrm{P}^2_{\mathrm{coh}}(\tau)-(\mathrm{P}_{\mathrm{coh}}(\tau)+\mathrm{P}_{\mathrm{incoh}}(\tau)+\mathrm{P}_{\mathrm{T}_i}(\tau))^2}}=\\&=\frac{\mathrm{P}_{\mathrm{coh}}(\tau)+\mathrm{P}_{\mathrm{incoh}}(\tau)+\mathrm{P}_{\mathrm{T}_c}(\tau)\frac{SNR_r}{SNR_d}}{\sqrt{(\mathrm{P}_{\mathrm{coh}}(\tau)+\mathrm{P}_{\mathrm{incoh}}(\tau)+\mathrm{P}_{\mathrm{T}_i}(\tau))^2-\mathrm{P}^2_{\mathrm{coh}}(\tau)}}=\frac{1+\frac{1}{d_c}\frac{SNR_r}{SNR_d}}{\sqrt{\left(1+\frac{1}{\mathrm{SNR}_{\mathrm{TH}_i}}\right)^2-\left(1-\frac{1}{\mathrm{SNR}_{\mathrm{SP}}}\right)^2}}.\end{aligned} \tag{C.77}$$

In this case, the term $\mathrm{E}\{{f_{S+N}}^2\}$ can be computed similarly to the previous computation of the k'_c parameter, but considering the noise term as $n_{T_i}(t,\tau)$ instead of $n_{T_c}(t,\tau)$. Therefore:

$$\mathrm{E}\{{f_{S+N}}^2\}=2(\mathrm{P}_{\mathrm{coh}}(\tau)+\mathrm{P}_{\mathrm{incoh}}(\tau)+\mathrm{P}_{\mathrm{T}_i}(\tau))^2-\mathrm{P}^2_{\mathrm{coh}}(\tau), \tag{C.78}$$

$$\mathrm{P}_{\mathrm{T}_i}(\tau)=\mathrm{P}_{\mathrm{T}_c}(\tau)\left[1+\frac{1}{SNR_d}\left(SNR_r+1\right)\right], \tag{C.79}$$

$$\begin{aligned}\mathrm{SNR}_{\mathrm{TH}_i} =& \frac{\mathrm{P}_{\mathrm{coh}}(\tau)+\mathrm{P}_{\mathrm{incoh}}(\tau)}{\mathrm{P}_{\mathrm{T}_i}(\tau)} = \frac{\mathrm{P}_{\mathrm{coh}}(\tau)+\mathrm{P}_{\mathrm{incoh}}(\tau)}{\mathrm{P}_{\mathrm{T}_c}(\tau)\left(1+\frac{1}{SNR_d}\left(SNR_r+1\right)\right)} = \\ =& \frac{\mathrm{SNR}_{\mathrm{TH}_c}}{1+\frac{1}{SNR_d}\left(SNR_r+1\right)}.\end{aligned} \tag{C.80}$$

C.5 Incoherent Averaging Implementation

Due to the low power, and consequently low SNR, of GNSS reflected signals, averaging or non-coherent summations of consecutive power waveforms is needed to improve the quality/SNR of the data retrieved. This is also known as non-coherent integration, and it is also the same procedure performed in conventional GNSS receivers as was remarked in the last step of the signal processing flow chart in Fig. 4.4. Mathematically, conventional non-coherent averaging of consecutive power waveforms is modeled as:

$$W(t,\tau) = \frac{1}{N}\sum_{n=1}^{N} Y_{na}(t,\tau), \tag{C.81}$$

where $Y_{na}(t,\tau)$ stands for the power waveform, n for the waveform index, and N is the number of waveforms used in the summation. When non-coherent integration is applied, the variability of the signal is highly reduced, which helps to detect the waveform. However, a more general mathematical expression of the non-coherent integration can be used, expressed by:

$$Z(t,\tau) = \frac{1}{T}\int_0^T Y_a(t+t',\tau)dt', \tag{C.82}$$

which is the averaging definition of a random process when $T \to \infty$, being T the non-coherent integration time.

The main differences between Eqns. (C.81)–(C.82) are depicted in Fig. C.2. If 1 ms waveforms are highly correlated, the use of partially overlapped data, Eqn. (C.82), will not provide any improvement because the addition is made with data whose correlation coefficient is nearly 1.

The effect on the detectability criterion or $\mathrm{SNR}_{\mathrm{nc,out}}$ after non-coherent integration will be evaluated using the general formulation, Eqn. (C.82).

C.6 Detectability Criteria for the Different Cases After Incoherent Integration

This section details the computation of the detectability criteria shown in Chapter 4 when incoherent integration has been applied. To derive each detectability criterion the following assumptions must be considered.

For the cGNSS-R:

$$f_{S+N} = \frac{1}{T}\int_0^T Y_c(t+t',\tau)dt', \tag{C.83}$$

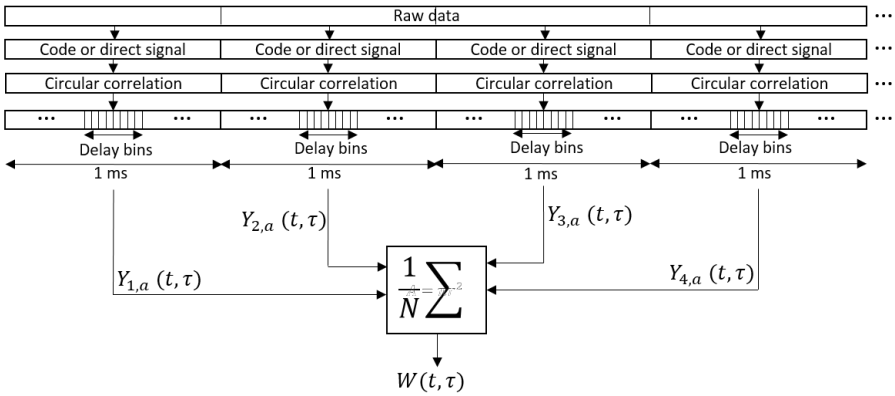

(a)

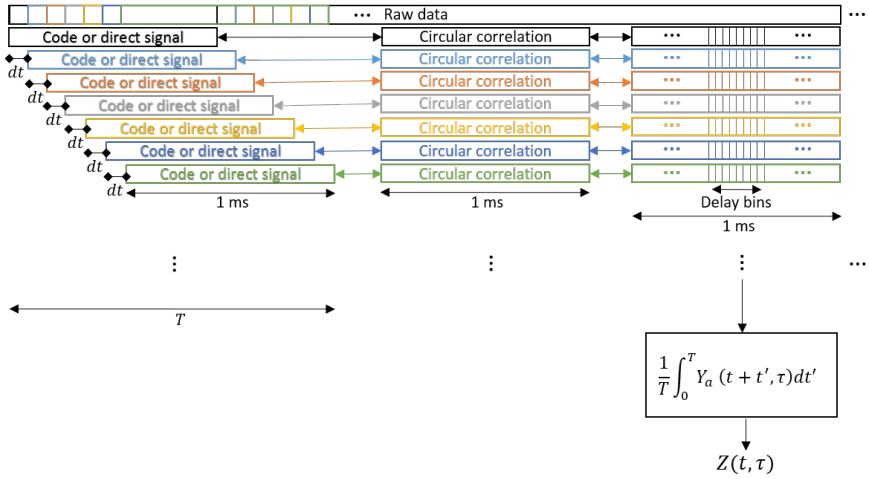

(b)

Figure C.2: (a) Conventional non-coherent integration scheme, (b) General non-coherent integration definition.

$$f_N = \frac{1}{T}\int_0^T |n_{T,c}(t+t',\tau)|^2 dt', \tag{C.84}$$

and for the iGNSS-R:

$$f_{S+N} = \frac{1}{T}\int_0^T Y_i(t+t',\tau)dt', \tag{C.85}$$

$$f_N = \frac{1}{T}\int_0^T \left| n_{T,c}(t+t',\tau) + \sqrt{\frac{1}{SNR_d}} y_{r_t,d_t}(t+t',\tau) \right|^2 dt'. \tag{C.86}$$

C.6.1 Derivation of d_{nc}

The d_{nc} is given by:

$$\begin{aligned} d_{nc} =& \frac{\mathrm{E}\{f_{S+N}\} - \mathrm{E}\{f_N\}}{\sqrt{\mathrm{E}\{f_N^2\} - \mathrm{E}\{f_N\}^2}} = \frac{\mathrm{P}_{\mathrm{coh}}(\tau) + \mathrm{P}_{\mathrm{incoh}}(\tau) + \mathrm{P}_{\mathrm{T}_c}(\tau) - \mathrm{P}_{\mathrm{T}_c}(\tau)}{\sqrt{\mathrm{P}_{\mathrm{T}_c}^2(\tau)\left(1 + \frac{1}{\overline{T}_n}\right) - \mathrm{P}_{\mathrm{T}_c}^2(\tau)}} = \\ =& \sqrt{\frac{1}{\overline{T}_n}} \frac{\mathrm{P}_{\mathrm{coh}}(\tau) + \mathrm{P}_{\mathrm{incoh}}(\tau)}{\mathrm{P}_{\mathrm{T}_c}(\tau)} = \sqrt{\frac{1}{\overline{T}_n}} d_c, \end{aligned} \tag{C.87}$$

where:

$$\overline{T}_n = \frac{2}{3}\frac{Tc}{T}, \tag{C.88}$$

$$\begin{aligned} \mathrm{E}\{f_{S+N}\} =& \mathrm{E}\Big\{\frac{1}{T}\int_0^T Y_c(t+t',\tau)dt'\Big\} = \frac{1}{T}\int_0^T \mathrm{E}\{Y_c(t+t',\tau)\}dt' = \\ =& \mathrm{P}_{\mathrm{coh}}(\tau) + \mathrm{P}_{\mathrm{incoh}}(\tau) + \mathrm{P}_{\mathrm{T}_c}(\tau), \end{aligned} \tag{C.89}$$

$$\mathrm{E}\{f_N\} = \mathrm{E}\Big\{\frac{1}{T}\int_0^T |n_{T,c}(t+t',\tau)|^2 dt'\Big\} = \frac{1}{T}\int_0^T \mathrm{E}\{|n_{T,c}(t+t',\tau)|^2\}dt' = \mathrm{P}_{\mathrm{T}_c}(\tau), \tag{C.90}$$

and using the properties of Gaussian processes and assuming $T \gg T_c$:

$$\mathrm{E}\{{f_N}^2\} = \mathrm{E}\Big\{\frac{1}{T}\int_0^T |n_{T,c}(t+t',\tau)|^2 dt' \frac{1}{T}\int_0^T |n_{T,c}(t+t'',\tau)|^2 dt''\Big\} = \tag{C.91}$$

$$\mathrm{E}\{{f_N}^2\} = \frac{1}{T^2}\int_0^T dt' \int_0^T dt'' \mathrm{E}\{|n_{T,c}(t+t',\tau)|^2 |n_{T,c}(t+t'',\tau)|^2\} = \tag{C.92}$$

$$\mathrm{E}\{{f_N}^2\} = \frac{1}{T^2}\int_0^T dt' \int_0^T dt'' \Gamma_{n_{Tc},n_{Tc}}(t'-t'',\tau) = \tag{C.93}$$

$$\mathrm{E}\{{f_N}^2\} = \frac{1}{T^2}\int_0^T dt' \int_0^T dt'' \mathrm{P}_{\mathrm{T}_c}^2(\tau)\left(1 + \Lambda^2\left(\frac{t'-t''}{T_c}\right)\right) = \tag{C.94}$$

$$\mathrm{E}\{{f_N}^2\} = \mathrm{P}_{\mathrm{T}_c}^2(\tau)\left(1 + \frac{1}{T^2}\int_0^T dt' \int_0^T dt'' \Lambda^2\left(\frac{t'-t''}{T_c}\right)\right) = \tag{C.95}$$

$$\mathrm{E}\{{f_N}^2\} = \mathrm{P}_{\mathrm{T}_c}^2(\tau)\left(1 + \frac{1}{T}\int_{-T}^T \Lambda\left(\frac{\xi}{T}\right)\Lambda^2\left(\frac{\xi}{T_c}\right)d\xi\right) \approx \mathrm{P}_{\mathrm{T}_c}^2(\tau)\left(1 + \overline{T}_n\right). \tag{C.96}$$

Note that the factor 2/3 appears because overlapped samples have been considered. This value is the best achievable value, and the more separated are the samples the less noise reduction will be produced. If non-overlapped samples are considered, the parameter $\frac{2}{3}\frac{T_{coh}}{T}$ becomes $\frac{T_{coh}}{T}$, and no improvement will be achieved.

C.6.2 Derivation of d'_{nc}

The d'_{nc} is given by:

$$d'_{nc} = \frac{\mathrm{E}\{f_{S+N}\} - \mathrm{E}\{f_N\}}{\sqrt{\mathrm{E}\{f_{S+N}^2\} - \mathrm{E}\{f_{S+N}\}^2}} = \\ = \frac{\mathrm{P}_{\mathrm{coh}}(\tau) + \mathrm{P}_{\mathrm{incoh}}(\tau)}{\sqrt{2\bar{t}_s \mathrm{P}_{\mathrm{coh}}(\tau)\mathrm{P}_{\mathrm{incoh}}(\tau) + 2\bar{t}_n \mathrm{P}_{\mathrm{coh}}(\tau)\mathrm{P}_{\mathrm{T}_c}(\tau) + 2\bar{t}_s\bar{t}_n \mathrm{P}_{\mathrm{incoh}}(\tau)\mathrm{P}_{\mathrm{T}_c}(\tau) + \overline{T}_n \mathrm{P}_{\mathrm{T}_c}^2(\tau) + \overline{T}_s \mathrm{P}_{\mathrm{incoh}}^2(\tau)}}, \tag{C.97}$$

where:

$$\mathrm{E}\{{f_{S+N}}^2\} = \mathrm{E}\Big\{\frac{1}{T}\int_0^T Y_c(t+t',\tau)dt' \frac{1}{T}\int_0^T Y_c(t+t'',\tau)dt''\Big\} = \tag{C.98}$$

$$\mathrm{E}\{{f_{S+N}}^2\} = \frac{1}{T^2}\int_0^T dt' \int_0^T dt'' \mathrm{E}\{Y_c(t+t',\tau)Y_c(t+t'',\tau)\} = \tag{C.99}$$

$$\begin{aligned}\mathrm{E}\{{f_{S+N}}^2\} =& \mathrm{P}_{\mathrm{coh}}^2(\tau) + 2\mathrm{P}_{\mathrm{coh}}(\tau)\mathrm{P}_{\mathrm{incoh}}(\tau) + 2\mathrm{P}_{\mathrm{coh}}(\tau)\mathrm{P}_{\mathrm{T}_c}(\tau) + 2\mathrm{P}_{\mathrm{incoh}}(\tau)\mathrm{P}_{\mathrm{T}_c}(\tau) + \\ &+ \frac{1}{T^2}\int_0^T\int_0^T 2\mathrm{P}_{\mathrm{coh}}(\tau)\mathrm{P}_{\mathrm{incoh}}(\tau)\gamma_{s,s}(t'-t'',\tau) + \\ &+ 2\mathrm{P}_{\mathrm{coh}}(\tau)\mathrm{P}_{\mathrm{T}_c}(\tau)\gamma_{n_{Tc},n_{Tc}}(t'-t'',\tau) + \\ &+ 2\mathrm{P}_{\mathrm{incoh}}(\tau)\gamma_{s,s}(t'-t'',\tau)\mathrm{P}_{\mathrm{T}_c}(\tau)\gamma_{n_{Tc},n_{Tc}}(t'-t'',\tau) + \Gamma_{s,s}(t'-t'',\tau) + \\ &+ \Gamma_{n_{Tc},n_{Tc}}(t'-t'',\tau)dt'dt'' =\end{aligned} \tag{C.100}$$

$$\begin{aligned}\mathrm{E}\{{f_{S+N}}^2\} =& \mathrm{P}_{\mathrm{coh}}^2(\tau) + 2\mathrm{P}_{\mathrm{coh}}(\tau)\mathrm{P}_{\mathrm{incoh}}(\tau) + 2\mathrm{P}_{\mathrm{coh}}(\tau)\mathrm{P}_{\mathrm{T}_c}(\tau) + 2\mathrm{P}_{\mathrm{incoh}}(\tau)\mathrm{P}_{\mathrm{T}_c}(\tau) + \\ &+ \frac{1}{T}\int_{-T}^T \Lambda\left(\frac{\xi}{T}\right)\Big(2\mathrm{P}_{\mathrm{coh}}(\tau)\mathrm{P}_{\mathrm{incoh}}(\tau)\gamma_{s,s}(\xi,\tau) + 2\mathrm{P}_{\mathrm{coh}}(\tau)\mathrm{P}_{\mathrm{T}_c}(\tau)\gamma_{n_{Tc},n_{Tc}}(\xi,\tau) + \\ &+ 2\mathrm{P}_{\mathrm{incoh}}(\tau)\gamma_{s,s}(\xi,\tau)\mathrm{P}_{\mathrm{T}_c}(\tau)\gamma_{n_{Tc},n_{Tc}}(\xi,\tau) + \Gamma_{s,s}(\xi,\tau) + \Gamma_{n_{Tc},n_{Tc}}(\xi,\tau)\Big)dt'dt'' =\end{aligned} \tag{C.101}$$

$$\begin{aligned}\mathrm{E}\{{f_{S+N}}^2\} =& \mathrm{P}_{\mathrm{coh}}^2(\tau) + 2\left(1+\bar{t}_s\right)\mathrm{P}_{\mathrm{coh}}(\tau)\mathrm{P}_{\mathrm{incoh}}(\tau) + 2\left(1+\bar{t}_n\right)\mathrm{P}_{\mathrm{coh}}(\tau)\mathrm{P}_{\mathrm{T}_c}(\tau) + \\ &+ 2\left(1+\bar{t}_s\bar{t}_n\right)\mathrm{P}_{\mathrm{incoh}}(\tau)\mathrm{P}_{\mathrm{T}_c}(\tau) + \mathrm{P}_{\mathrm{T}_c}^2(\tau)\left(1+\overline{T}_n\right) + \mathrm{P}_{\mathrm{incoh}}^2(\tau)\left(1+\overline{T}_s\right),\end{aligned} \tag{C.102}$$

which uses the following time definitions:

$$\begin{aligned}\bar{t}_s &= \frac{1}{T}\int_{-T}^T \Lambda\left(\frac{\xi}{T}\right)\gamma_{s,s}(\xi,\tau)d\xi, \\ \bar{t}_n &= \frac{1}{T}\int_{-T}^T \Lambda\left(\frac{\xi}{T}\right)\gamma_{n_{Tc},n_{Tc}}(\xi,\tau)d\xi = \frac{T_c}{T}, \\ \overline{T}_s &= \frac{1}{T}\int_{-T}^T \Lambda\left(\frac{\xi}{T}\right)|\gamma_{s,s}(\xi,\tau)|^2 d\xi, \\ \overline{T}_n &= \frac{1}{T}\int_{-T}^T \Lambda\left(\frac{\xi}{T}\right)|\gamma_{n_{Tc},n_{Tc}}(\xi,\tau)|^2 d\xi = \frac{2}{3}\frac{T_c}{T}.\end{aligned} \tag{C.103}$$

C.6.3 Derivation of d_{ni}

The d_{ni} is given by:

$$d_{ni} = \frac{\mathrm{E}\{f_{S+N}\} - \mathrm{E}\{f_N\}}{\sqrt{\mathrm{E}\{f_N^2\} - \mathrm{E}\{f_N\}^2}} = \frac{\mathrm{P}_{\mathrm{coh}}(\tau) + \mathrm{P}_{\mathrm{incoh}}(\tau) + \mathrm{P}_{\mathrm{T}_i}(\tau) - \mathrm{P}_{\mathrm{T}_c}(\tau)\left(1 + \frac{1}{SNR_d}\right)}{\sqrt{\mathrm{P}^2_{\mathrm{T}_c}(\tau)\left(1+\overline{T}_n\right)\left(1+\frac{1}{SNR_d}\right)^2 - \mathrm{P}^2_{\mathrm{T}_c}(\tau)\left(1+\frac{1}{SNR_d}\right)^2}} =$$
$$= \sqrt{\frac{1}{\overline{T}_n}} \frac{\mathrm{P}_{\mathrm{coh}}(\tau) + \mathrm{P}_{\mathrm{incoh}}(\tau) + \mathrm{P}_{\mathrm{T}_c}(\tau)\frac{SNR_r}{SNR_d}}{\mathrm{P}_{\mathrm{T}_c}(\tau)\left(1+\frac{1}{SNR_d}\right)} = \frac{d_{nc} + \sqrt{\frac{1}{\overline{T}_n}}\frac{SNR_r}{SNR_d}}{1+\frac{1}{SNR_d}}, \tag{C.104}$$

where:

$$\begin{aligned}\mathrm{E}\{f_{S+N}\} =& \mathrm{E}\Big\{\frac{1}{T}\int_0^T Y_i(t+t',\tau)dt'\Big\} = \frac{1}{T}\int_0^T \mathrm{E}\{Y_i(t+t',\tau)\}dt' = \\ =& \mathrm{P}_{\mathrm{coh}}(\tau) + \mathrm{P}_{\mathrm{incoh}}(\tau) + \mathrm{P}_{\mathrm{T}_i}(\tau),\end{aligned} \tag{C.105}$$

$$\mathrm{E}\{f_N\} = \mathrm{E}\Big\{\frac{1}{T}\int_0^T \Big|n_{T,c}(t+t',\tau) + \sqrt{\frac{1}{SNR_d}}y_{r_t,d_t}(t+t',\tau)\Big|^2 dt'\Big\} = \tag{C.106}$$

$$\mathrm{E}\{f_N\} = \frac{1}{T}\int_0^T \mathrm{E}\{|n_{T,c}(t+t',\tau)|^2\}dt' + \frac{1}{SNR_d}\frac{1}{T}\int_0^T \mathrm{E}\{|y_{r_t,d_t}(t+t',\tau)|^2\}dt' = \tag{C.107}$$

$$\mathrm{E}\{f_N\} = \mathrm{P}_{\mathrm{T}_c}(\tau)\left(1+\frac{1}{SNR_d}\right), \tag{C.108}$$

and using the properties of Gaussian processes, it is obtained:

$$\begin{aligned}\mathrm{E}\{{f_N}^2\} =& \mathrm{E}\Bigg\{\frac{1}{T}\int_0^T \Big|n_{T,c}(t+t',\tau) + \sqrt{\frac{1}{SNR_d}}y_{r_t,d_t}(t+t',\tau)\Big|^2 dt' \\ & \frac{1}{T}\int_0^T \Big|n_{T,c}(t+t'',\tau) + \sqrt{\frac{1}{SNR_d}}y_{r_t,d_t}(t+t'',\tau)\Big|^2 dt''\Bigg\} =\end{aligned} \tag{C.109}$$

$$\begin{aligned}\mathrm{E}\{{f_N}^2\} =& \frac{1}{T^2}\int_0^T\int_0^T \mathrm{E}\{|n_{T,c}(t+t',\tau)|^2|n_{T,c}(t+t'',\tau)|^2\} + \\ &+ \frac{1}{SNR_d}\mathrm{E}\{|n_{T,c}(t+t',\tau)|^2|y_{r_t,d_t}(t+t'',\tau)|^2\} + \\ &+ \frac{1}{SNR_d}\mathrm{E}\{n_{T,c}(t+t',\tau)n^*_{T,c}(t+t'',\tau)y_{r_t,d_t}(t+t',\tau)y^*_{r_t,d_t}(t+t'',\tau)\} + \\ &+ \frac{1}{SNR_d}\mathrm{E}\{n_{T,c}(t+t'',\tau)n^*_{T,c}(t+t',\tau)y_{r_t,d_t}(t+t'',\tau)y^*_{r_t,d_t}(t+t',\tau)\} + \\ &+ \frac{1}{SNR_d}\mathrm{E}\{|n_{T,c}(t+t'',\tau)|^2|y_{r_t,d_t}(t+t',\tau)|^2\} + \\ &+ \frac{1}{SNR_d^2}\mathrm{E}\{|y_{r_t,d_t}(t+t',\tau)|^2|y_{r_t,d_t}(t+t'',\tau)|^2\}dt'dt'' =\end{aligned} \tag{C.110}$$

$$\begin{aligned}\mathrm{E}\{{f_N}^2\} =& \frac{1}{T^2}\int_0^T\int_0^T \Gamma_{n_{Tc},n_{Tc}}(t'-t'',\tau) + \frac{2\mathrm{P}_{\mathrm{T}_c}^2(\tau)}{SNR_d}\gamma_{n_{Tc},n_{Tc}}(0,\tau)\gamma_{y_{r_t,d_t},y_{r_t,d_t}}(0,\tau)+\\ &+\Gamma_{y_{r_t,d_t},y_{r_t,d_t}}(t'-t'',\tau)+\\ &+\frac{2\mathrm{P}_{\mathrm{T}_c}^2(\tau)}{SNR_d}\gamma_{n_{Tc},n_{Tc}}(t'-t'',\tau)\gamma_{y_{r_t,d_t},y_{r_t,d_t}}(t'-t'',\tau)dt'dt'' =\end{aligned} \tag{C.111}$$

$$\mathrm{E}\{{f_N}^2\} = \mathrm{P}_{\mathrm{T}_c}^2(\tau)\left(1+\overline{T}_n\right)\left(1+\frac{1}{SNR_d}\right)^2. \tag{C.112}$$

C.6.4 Derivation of d'_{ni}

The d'_{ni} is given by:

$$\begin{aligned}d'_{ni} &= \frac{\mathrm{E}\{f_{S+N}\}-\mathrm{E}\{f_N\}}{\sqrt{\mathrm{E}\{f_{S+N}^2\}-\mathrm{E}\{f_{S+N}\}^2}} =\\ &= \frac{\mathrm{P}_{\mathrm{coh}}(\tau)+\mathrm{P}_{\mathrm{incoh}}(\tau)+\mathrm{P}_{\mathrm{T}_c}(\tau)\frac{SNR_r}{SNR_d}}{\sqrt{2\bar{t}_s\mathrm{P}_{\mathrm{coh}}(\tau)\mathrm{P}_{\mathrm{incoh}}(\tau)+2\bar{t}_n\mathrm{P}_{\mathrm{coh}}(\tau)\mathrm{P}_{\mathrm{T}_i}(\tau)+2\bar{t}_s\bar{t}_n\mathrm{P}_{\mathrm{incoh}}(\tau)\mathrm{P}_{\mathrm{T}_i}(\tau)+\overline{T}_n\mathrm{P}_{\mathrm{T}_i}^2(\tau)+\overline{T}_s\mathrm{P}_{\mathrm{incoh}}^2(\tau)}},\end{aligned} \tag{C.113}$$

where:

$$\begin{aligned}\mathrm{E}\{{f_{S+N}}^2\} =& \mathrm{P}_{\mathrm{coh}}^2(\tau)+2\left(1+\bar{t}_s\right)\mathrm{P}_{\mathrm{coh}}(\tau)\mathrm{P}_{\mathrm{incoh}}(\tau)+2\left(1+\bar{t}_n\right)\mathrm{P}_{\mathrm{coh}}(\tau)\mathrm{P}_{\mathrm{T}_i}(\tau)+\\ &+2\left(1+\bar{t}_s\bar{t}_n\right)\mathrm{P}_{\mathrm{incoh}}(\tau)\mathrm{P}_{\mathrm{T}_i}(\tau)+\mathrm{P}_{\mathrm{T}_i}^2(\tau)\left(1+\overline{T}_n\right)+\mathrm{P}_{\mathrm{incoh}}^2(\tau)\left(1+\overline{T}_s\right),\end{aligned} \tag{C.114}$$

which is obtained similarly to the case when d'_{nc} was computed, but substituting $\mathrm{P}_{\mathrm{T}_c}(\tau)$ by $\mathrm{P}_{\mathrm{T}_i}(\tau)$, which can be done because they have the same statistics and correlation functions, and only the scaling factor must be taken into account.

C.7 Correlation Peak Variability

The SNR has been defined with the help of the detectability criterion, which is basically the useful signal's mean value divided by its standard deviation. Using those defined SNRs, the correlation peak variability should be computed in order to estimate the minimum incoherent integration time to obtain a variability less than the accepted one, which indicates the system's accuracy. The useful signal can be estimated as:

$$\hat{S}_{use} = S_{meas,S+N} - S_{meas,N} \tag{C.115}$$

where *use* stands for useful, and its standard deviation is:

$$\sigma_{\hat{S}_{use}} = \sqrt{\mathrm{E}\left\{\hat{S}_{use}^2\right\}-\mathrm{E}\left\{\hat{S}_{use}\right\}^2} = \sqrt{var\{S_{meas,S+N}\}+var\{S_{meas,N}\}} \tag{C.116}$$

under the assumption that measurements of the signal + noise term ($S+N$) and the noise term (N) are uncorrelated, which is true since they are computed at different values of τ (different correlation lags), and the correlation functions derived in this Appendix demonstrate that. Therefore, the variability of the signal for the cGNSS-R technique is (the $var\{S_{meas,S+N}\}$ and $var\{S_{meas,N}\}$):

$$\sigma_{\hat{S}_{use},cGNSS-R} = \\ = \sqrt{2\bar{t}_s \mathrm{P}_{\mathrm{coh}}(\tau)\mathrm{P}_{\mathrm{incoh}}(\tau) + 2\mathrm{P}_{\mathrm{coh}}(\tau)\mathrm{P}_{\mathrm{T}_c}(\tau) + 2\bar{t}_s \mathrm{P}_{\mathrm{incoh}}(\tau)\mathrm{P}_{\mathrm{T}_c}(\tau) + 2\frac{2}{3}\mathrm{P}^2_{\mathrm{T}_c}(\tau) + \overline{T}_s \mathrm{P}^2_{\mathrm{incoh}}(\tau)}, \tag{C.117}$$

and normalized to the signal power ($\mathrm{P}_{\mathrm{coh}}(\tau) + \mathrm{P}_{\mathrm{incoh}}(\tau)$):

$$\overline{\sigma}_{\hat{S}_{use},cGNSS-R} = \\ = \sqrt{2\left(1 - \frac{1}{\mathrm{SNR}_{\mathrm{SP}}}\right)\left(\frac{\bar{t}_s}{\mathrm{SNR}_{\mathrm{SP}}} + \frac{1}{\mathrm{SNR}_{\mathrm{TH}_c}}\right) + 2\bar{t}_s \frac{1}{\mathrm{SNR}_{\mathrm{SP}}}\frac{1}{\mathrm{SNR}_{\mathrm{TH}_c}} + 2\frac{2}{3}\frac{1}{\mathrm{SNR}^2_{\mathrm{TH}_c}} + \overline{T}_s \frac{1}{\mathrm{SNR}^2_{\mathrm{SP}}}}. \tag{C.118}$$

For the iGNSS-R technique such variability, for the case $SNR_r \ll SNR_d$, can be approximated by:

$$\sigma_{\hat{S}_{use},iGNSS-R} \approx \\ \approx \sqrt{2\bar{t}_s \mathrm{P}_{\mathrm{coh}}(\tau)\mathrm{P}_{\mathrm{incoh}}(\tau) + 2\bar{t}_n \mathrm{P}_{\mathrm{coh}}(\tau)\mathrm{P}_{\mathrm{T}_i}(\tau) + 2\bar{t}_s\bar{t}_n \mathrm{P}_{\mathrm{incoh}}(\tau)\mathrm{P}_{\mathrm{T}_i}(\tau) + 2\overline{T}_n \mathrm{P}^2_{\mathrm{T}_i}(\tau) + \overline{T}_s \mathrm{P}^2_{\mathrm{incoh}}(\tau)}. \tag{C.119}$$

If it is normalized by the signal power, it turns into:

$$\overline{\sigma}_{\hat{S}_{use},iGNSS-R} \approx \\ \approx \sqrt{2\left(1 - \frac{1}{\mathrm{SNR}_{\mathrm{SP}}}\right)\left(\frac{\bar{t}_s}{\mathrm{SNR}_{\mathrm{SP}}} + \frac{1}{\mathrm{SNR}_{\mathrm{TH}_i}}\right) + 2\bar{t}_s \frac{1}{\mathrm{SNR}_{\mathrm{SP}}}\frac{1}{\mathrm{SNR}_{\mathrm{TH}_i}} + 2\frac{2}{3}\frac{1}{\mathrm{SNR}^2_{\mathrm{TH}_i}} + \overline{T}_s \frac{1}{\mathrm{SNR}^2_{\mathrm{SP}}}}. \tag{C.120}$$

C.8 Estimation of the SNR and Signal's Peak Variability for the UK TDS-1 and GEROS-ISS Missions

In this section the theoretical values derived above are applied to specific scenarios considering the lag (τ) where the signal is maximal in order to estimate both the best achievable SNR and the variability of the measured reflectivity or radar-cross section at that point. With those estimations the scatterometric accuracy of the cGNSS-R and iGNSS-R techniques could be assessed. For the first scenario it is considered the UK TDS-1 mission, launched in 2014 with a GPS bistatic payload. For the second scenario the future GEROS-ISS mission is considered, which is analyzed for both the cGNSS-R and iGNSS-R cases. For all these scenarios, it is assumed that only incoherent sea surface scattering

takes place, so the coherent component is negligible. In such situations a widely accepted scattering model to simulate the incoherent reflected signal power is used [52], in which the radar cross-section is given by:

$$\sigma_0(\vec{\rho}) = \frac{\pi |r|^2 q^4}{q_z^4} P\left(-\frac{\vec{q}_\perp}{q_z}\right). \tag{C.121}$$

The theoretical results presented in previous sections have been extended to situations when there is a coherent component, and in those situations a different radar cross section model must be used. Also they have been extended for other lags using the appropriate correlation functions derived in the Appendices.

C.8.1 cGNSS-R

C.8.1.1 UK TDS-1 Scenario

The main parameters of the simulation are shown in Tab. C.1. For this scenario two different values of the received power at the Earth surface are considered, from which the EIRP of the GPS satellites is estimated. One is -158.5 dBW which is the minimum received power at the Earth's surface defined by the GPS ICD [255], and the other one is -153 dBW, which is the maximum received power at the Earth's surface in the same document [255]. Both can be considered as pessimistic and optimistic cases, respectively. Also, all simulation results shown here consider 1 ms coherent integration time.

Table C.1: UK TDS-1 scenario simulation parameters.

Sensor Parameter	**Magnitude**
Orbit Height	635 [km]
Ground speed	6864 [m/s]
Minimum Rx Power on Earth	-158.5 [dBW]
Maximum Rx Power on Earth	-153 [dBW]
Incidence angle	15°
Frequency Band	L1 (C/A Code)
Sea Water Dielectric Constant	72.6 + j58.5
Down-Looking Antenna Gain	13 [dBiC]
Noise Figure	3.5 [dB]

Figure C.3 shows a summary of the estimated SNRs as a function of the incoherent integration time for the two proposed scenarios: a pessimistic one (a), and an optimistic one (b). This examples truncated to 1 s of incoherent averaging could be referred to the level 1b of the data provided by UK TDS-1 MERRByS research team. Figure C.4 shows the estimated normalized peak variability or accuracy of the σ_0 retrieval for the scenario described in Table C.1 and the estimated SNRs shown in Fig. C.3.

C.8.1.2 GEROS-ISS Scenario

The main parameters of the simulation are shown in Tab. C.2. For this scenario the same parameters as for the UK TDS-1 scenario have been considered only changing the

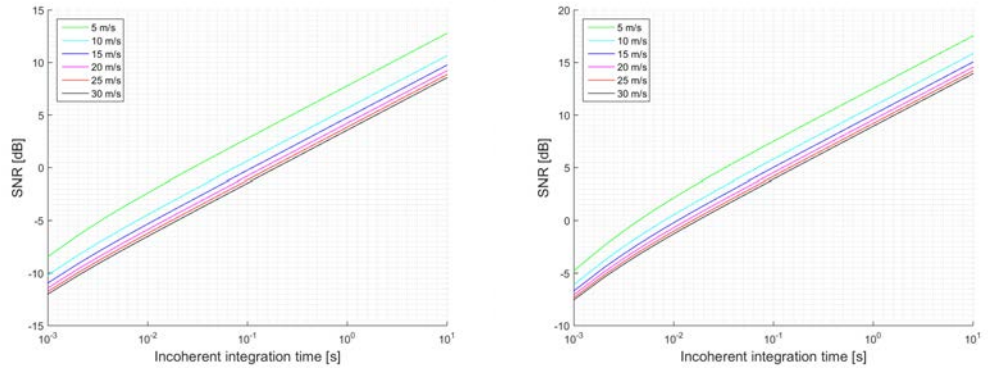

(a) **(b)**

Figure C.3: Simulations SNR for the TDS-1 scenario and cGNSS-R: (a) Minimum received power on ground of -158.5 dBW, (b) Minimum received power on ground of -153 dBW.

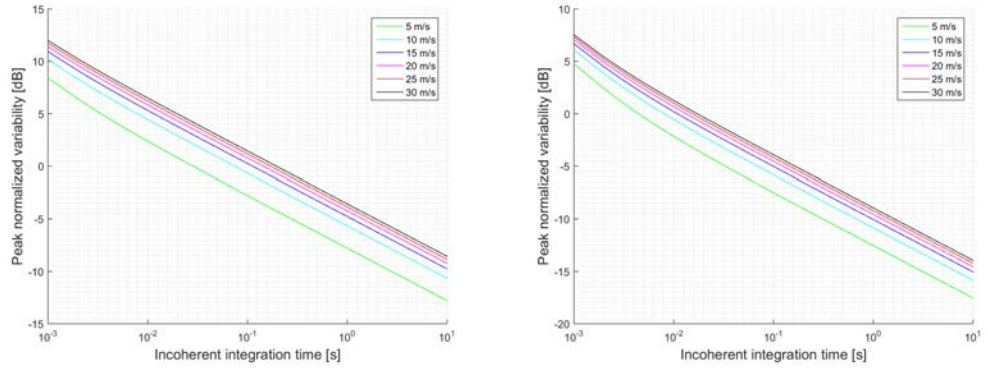

(a) **(b)**

Figure C.4: Simulations of the normalized peak variability for the TDS-1 scenario and cGNSS-R: (a) Minimum received power on ground of -158.5 dBW, (b) Minimum received power on ground of -153 dBW.

antenna directivity, and the platform's height and speed, which will change the $\overline{t}_s$ and $\overline{T}_s$ parameters. Also, all simulation results shown here use 1 ms coherent integration time.

Figure C.5 shows another summary of the estimated SNRs for the GEROS-ISS mission as a function of the incoherent integration time for the two different values of received power. These simulations can be used to estimate the expected SNR and better define the parameters of the cGNSS-R scatterometric operation mode. Figure C.6 shows the estimated normalized peak variability for the estimated SNRs shown in Fig. C.5. It is seen that for the most optimistic case, the expected performance does not depend on the sea state, because it is largely determined by the speckle noise.

Table C.2: GEROS-ISS scenario simulation parameters.

Sensor Parameter	Magnitude
Orbit Height	400 [km]
Ground speed	7214 [m/s]
Minimum Rx Power on Earth	-158.5 [dBW]
Maximum Rx Power on Earth	-153 [dBW]
Incidence angle	15°
Frequency Band	L1 (C/A Code)
Sea Water Dielectric Constant	72.6 + j58.5
Down-Looking Antenna Gain	22 [dBiC]
Noise Figure	3.5 [dB]

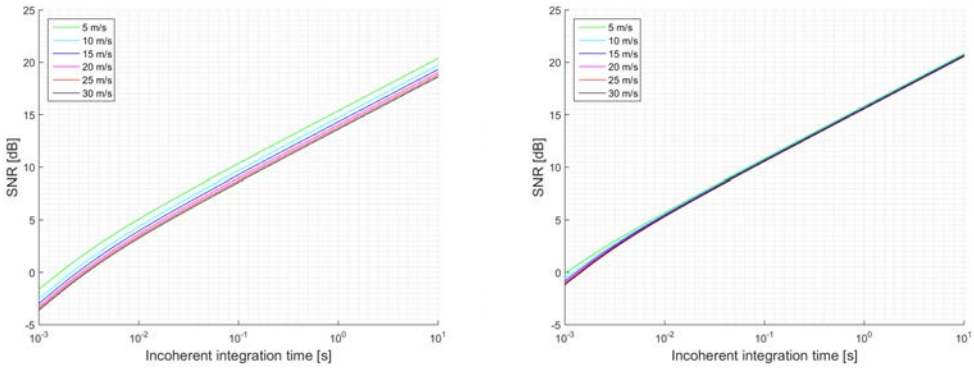

Figure C.5: Simulations SNR for the GEROS-ISS scenario and cGNSS-R: (a) Minimum received power on ground of -158.5 dBW, (b) Minimum received power on ground of -153 dBW.

C.8.2 iGNSS-R

C.8.2.1 GEROS-ISS Scenario

The main parameters of the simulation are shown in Tabs. C.3–C.4 for the pessimistic and optimistic cases, respectively. For the iGNSS-R technique the same parameters as for the GEROS-ISS scenario have been considered while only changing the traditional waveform (C/A code) to the full-composite model (C/A- , P-, and M-codes), which will change the $\overline{t}_s$ and $\overline{T}_s$ parameters. Note that each signal term for each code will result in a different correlation time (the chip size determines the footprint size at the reflecting surface), and the correlation function can be expressed as a weighted linear combination of each code correlation function. Consequently, the EIRPs have been changed and separated by the code under use, to finally add them up and obtain the total EIRP. Furthermore, in the iGNSS-R the bandwidth is a critical parameter, since it determines the SNR_d and SNR_r, which at the same time determines the scatterometric accuracy. They do not depend on the coherent integration time because they refer to the pre-correlation SNR. Results for

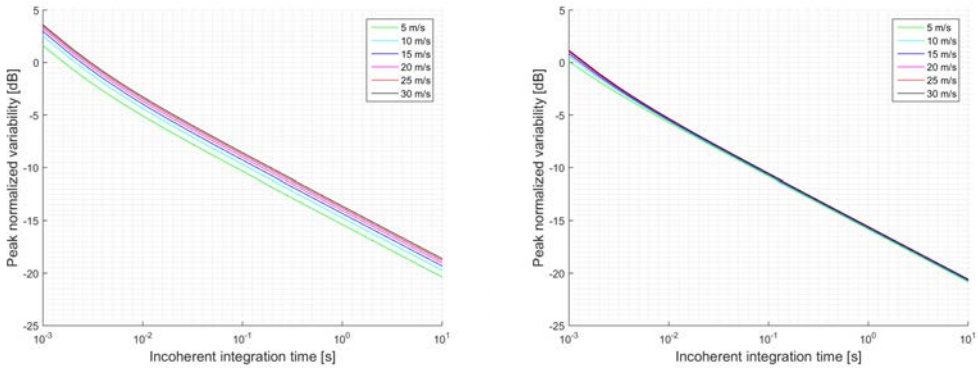

Figure C.6: Simulations of the normalized peak variability for the GEROS-ISS scenario and cGNSS-R: (a) Minimum received power on ground of -158.5 dBW, (b) Minimum received power on ground of -153 dBW.

this simulations are shown in Fig. C.7 for the SNR, and in Fig. C.8 for the normalized peak variability.

Table C.3: GEROS-ISS scenario simulation parameters for the iGNSS-R pessimistic case.

Sensor Parameter	**Magnitude**
EIRP C/A	24 [dBW]
EIRP M	25.5 [dBW]
EIRP P	21 [dBW]
EIRP Total	28.64 [dBW]
Orbit Height	400 [km]
Ground speed	7214 [m/s]
Incidence angle	15°
Frequency Band	L1 (Composite)
Sea Water Dielectric Constant	72.6 + j58.5
Up-Looking Antenna Gain	22 [dBiC]
Down-Looking Antenna Gain	22 [dBiC]
Noise Figure	3.5 [dB]
Bandwidth	40 [MHz]

C.8.3 Discussion

Firstly, it can be concluded that when the antenna directivity is relatively low, which is the case of the UK TDS-1 scenario, the signal power is an important parameter, since it increases the SNR, and decreases the signal's variability. This effect can be observed by comparing Fig. C.3(a) with Fig. C.3(b), and Fig. C.4(a) with Fig. C.4(b). This indicates that for those scenarios the thermal SNR is the limiting factor.

Table C.4: GEROS-ISS scenario simulation parameters changes for the iGNSS-R optimistic case.

Parameter	Magnitude
EIRP C/A	29.5 [dBW]
EIRP M	31 [dBW]
EIRP P	27 [dBW]
EIRP Total	34.23 [dBW]

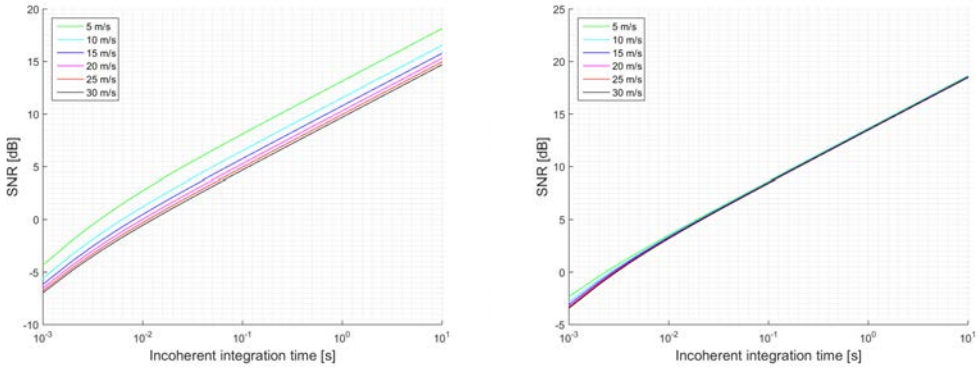

(a) **(b)**

Figure C.7: Simulations SNR for the GEROS-ISS scenario and iGNSS-R: (a) Total EIRP of 28.64 dBW (pessimistic), (b) Total EIRP of 34.23 dBW (optimistic).

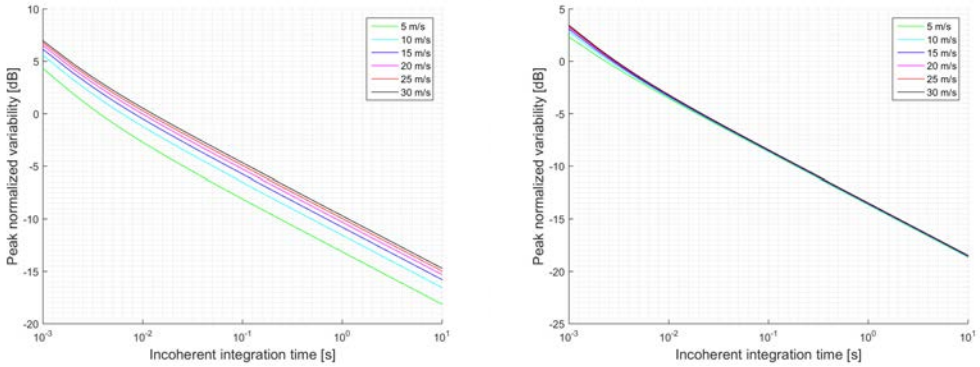

(a) **(b)**

Figure C.8: Simulations of the normalized peak variability for the GEROS-ISS scenario and iGNSS-R: (a) Total EIRP of 28.64 dBW (pessimistic), (b) EIRP of 34.23 dBW (optimistic).

When the antenna directivity is large enough, which is in the case of the proposed antenna for the GEROS-ISS mission, the transmitted power is not that important, and the expected performance does not depend significantly on the wind speed. This can

be seen by comparing Fig. C.5(a) with Fig. C.5(b), and Fig. C.6(a) with Fig. C.6(b). Furthermore, an increase on the transmitted power by the GPS satellites results in a retrieval performance independent from the wind speed.

When comparing the cGNSS-R and the iGNSS-R techniques, the results of the expected SNR and the peak variability are at least 3 dB better for the cGNSS-R for the same simulation conditions. This occurs mainly because the thermal SNR for the iGNSS-R is degraded as compared to the cGNSS-R one. Also, there is another aspect to be analyzed: the wider bandwidth codes used in the iGNSS-R translate into smaller footprints, resulting in a larger correlation time between waveforms, and a reduction of the improvement by incoherent averaging is expected as compared to the cGNSS-R approach. Note that the incoherent averaging considered here includes partially overlapped waveforms, and in the case when they are not partially overlapped, the simulations presented are an overestimation of the expected performance. In that situation, $\overline{T}_n$ would increase, resulting in a degradation of the expected SNR and an increase of the peak's variability (the factor 3/2 would become 1). However, if the antenna directivity is as large as the one in the GEROS-ISS mission, the limiting factor is the speckle noise rather than the thermal noise, and experimental results will be closer to the theoretical ones.

Note that all equations derived in this Appendix can be applied to any lag different from the specular one, taking into account that the coherent component in those cases will be negligible. All the necessary correlation functions are available in sections C.2–C.3, and the correlation times should be accordingly recomputed for the appropriate lag. If the surface region under analysis falls into the Delay-Doppler ambiguity free zone, the Van Cittert-Zernike theorem can be used to compute the correlation times. However, if Delay-Doppler ambiguity exists, it should be computed taking into account two different areas contributing to the same Delay-Doppler cell.

D

Appendix D
NMEA Protocol

This Appendix shows a summary of the NMEA protocol of the GPS receiver used in the Dual-Polarization SMIGOL and in the McGiverinstruments. Herein, only the most important ones and used by the GPS receiver in those instruments are shown, and further information can be found in `http://www.gpsinformation.org/dale/nmea.htm`. As those instruments only rely on power measurements of the prompt correlator, the C/N0 parameter can be used as a measurement of the received signal power compared to the noise power. Consequently, no more information than the one provided by this protocol is necessary for the techniques used by those two instruments. In particular the most important packets are the GSV and the RMC.

D.1 GGA - Global Positioning System Fix Data

The GGA package provides information about the time, latitude, longitude, altitude, and the number of satellites used to retrieve the navigation solution. It has the following structure:

```
GPGGA,hhmmss.sss,ddmm.mmmm,a,dddmm.mmmm,a,x,xx,x.x,x.x,M,,,,xxxx*hh
```

where the fields are listed as follows:

```
GPGGA,1,2,3,4,5,6,7,8,9,M,10,M,,11*12
```

and an example:

```
GPGGA,111636.932,2447.0949,N,12100.5223,E,1,11,0.8,118.2,M,46.9,M,,0000*02
```

Table D.1 shows detailed information of each possible field content and relates them to the example proposed.

Table D.1: GGA Message information.

Field	Name	Example	Description
1	UTC Time	111636.932	UTC of position in hhmmss.sss format, (000000.000 - 235959.999).
2	Latitude	2447.0949	Latitude in ddmm.mmmm format. Leading zeros transmitted.
3	N/S Indicator	N	Latitude hemisphere indicator: N = North. S = South.
4	Longitude	12100.5223	Longitude in dddmm.mmmm format. Leading zeros transmitted.
5	E/W Indicator	E	Longitude hemisphere indicator: E = East. W = West.
6	GPS quality indicator	1	0: Position fix unavailable. 1: Valid position fix. SPS mode. 2: Valid position fix. Differential GPS mode. 3: GPS PPS Mode. Fix valid. 4: Real Time Kinematic. System used in RTK mode with fixed integers. 5: Float RTK. Satellite system used in RTK mode. Floating integers. 6: Estimated (dead reckoning) Mode. 7: Manual Input Mode. 8: Simulator Mode.
7	Satellites Used	11	Number of satellites in use, (00 - 12)-.
8	HDOP	0.8	Horizontal dilution of precision, (00.0 - 99.9).
9	Altitude	108.2	With respect to the mean sea level (geoid), (-9999.9 - 17999.9)
10	Height of Geoid	46.9	Height of Geoid (mean sea level) above WGS84 ellipsoid.
-	-	-	Time in seconds since last DGPS update.
11	DGPS Station ID	0000	Differential reference station ID, 0000 - 1023, NULL when DGPS not used.
12	Checksum	02	Checksum

D.2 GLL - Latitude Longitude

The GLL package provides information about the time, latitude, and longitude where the GPS receiver is located. It has the following structure:

`GPGLL,ddmm.mmmm,a,dddmm.mmmm,a,hhmmss.sss,a,a*hh`

where the fields are listed as follows:

`GPGLL,1,2,3,4,5,6,7*8`

and an example:

`GPGLL,2447.0944,N,12100.5213,E,112609.932,A,A*57`

Table D.2 shows detailed information of each possible field content and relates them to the example proposed.

Table D.2: GLL Message information.

Field	Name	Example	Description
1	Latitude	2447.0944	Latitude in ddmm.mmmm format Leading zeros transmitted.
2	N/S Indicator	N	Latitude hemisphere indicator: N = North. S = South.
3	Longitude	12100.5213	Longitude in dddmm.mmmm format Leading zeros transmitted.
4	E /W Indicator	E	Longitude hemisphere indicator: E = East. W = West.
5	UTC Time	112609.932	UTC time in hhmmss.sss format (000000.000 - 235959.999).
6	Status	A	A = Data valid. V = Data not valid.
7	Mode Indicator	A	N = Data not valid. A = Autonomous mode. D = Differential mode. E = Estimated (dead reckoning) mode. M = Manual input mode. S = Simulator mode.
8	Checksum	57	Checksum

D.3 GSA – GNSS DOP and Active Satellites

The GSA package provides information about the GPS operating mode and the number of satellites used in the navigation solution. It has the following structure:

`GPGSA,A,x,xx,xx,xx,xx,xx,xx,xx,xx,xx,xx,xx,xx,x.x,x.x,x.x*hh`

where the fields are listed as follows:

`GPGSA,1,2,3,3,3,3,3,3,3,3,3,3,3,4,5,6*7`

and an example:

`GPGSA,A,3,05,12,21,22,30,09,18,06,14,01,31,,1.2,0.8,0.9*36`

Table D.3 shows detailed information of each possible field content and relates them to the example proposed.

Table D.3: GSA Message information.

Field	Name	Example	Description
1	Mode	A	M = Manual, forced to operate in 2D or 3D mode. A = Automatic, allowed to automatically switch 2D/3D.
2	Fix type	3	1 = Fix not available. 2 = 2D. 3 = 3D.
3	Satellites used 1-12	05,12,...,31„	Satellite ID number, 01 to 32, of satellite used in solution, up to 12 transmitted.
4	PDOP	1.2	Position dilution of precision (00.0 to 99.9).
5	HDOP	0.8	Horizontal dilution of precision (00.0 to 99.9).
6	VDOP	0.9	Vertical dilution of precision (00.0 to 99.9).
7	Checksum	36	Checksum.

D.4 GSV – GNSS Satellites in View

The GSV package provides information about the GPS satellites in view together with the azimuth, elevation and C/N0. It has the following structure:

`GPGSV,x,x,xx,xx,xx,xxx,xx,...,xx,xx,xxx,xx*hh`

where the fields are listed as follows:

`GPGSV,1,2,3,4,5,6,7,...,4,5,6,7*8`

and an example:

`GPGSV,3,1,12,05,54,069,45,12,44,061,44,21,07,184,46,22,78,289,47*72`

`GPGSV,3,2,12,30,65,118,45,09,12,047,37,18,62,157,47,06,08,144,45*7C`

`GPGSV,3,3,12,14,39,330,42,01,06,299,38,31,30,256,44,32,36,320,47*7B`

Table D.4 shows detailed information of each possible field content and relates them to the example proposed.

Table D.4: GSV Message information.

Field	Name	Example	Description
1	Number of message	3	Total number of GSV messages to be transmitted (1-3).
2	Sequence number	1	Sequence number of current GSV message.
3	Satellites in view	12	Total number of satellites in view (00 - 12).
4	Satellite ID	05	Satellite ID number, GPS: 01 - 32, SBAS: 33 - 64 (33 = PRN120).
5	Elevation	54	Satellite elevation in degrees, (00 - 90).
6	Azimuth	069	Satellite azimuth angle in degrees, (000 - 359).
7	SNR	45	C/N0 in dB/Hz (00 - 99). Null when not tracking.
8	Checksum	72	Checksum.

D.5 RMC – Recommended Minimum Specific GNSS Data

The RMC package provides information about the time, date, latitude, longitude, course, and speed of the GPS receiver. It has the following structure:

`GPRMC,hhmmss.sss,A,dddmm.mmmm,a,dddmm.mmmm,a,x.x,x.x,ddmmyy,ddd.d,a,a*hh`

where the fields are listed as follows:

`GPRMC,1,2,3,4,5,6,7,8,9,10,11,12*13`

and an example:

`GPRMC,111636.932,A,2447.0949,N,12100.5223,E,000.0,000.0,030407,003.1,W,A*61`

Table D.5 shows detailed information of each possible field content and relates them to the example proposed.

Table D.5: RMC Message information.

Field	Name	Example	Description
1	UTC time	0111636.932	UTC time in hhmmss.sss format (000000.00 - 235959.999).
2	Status	A	V = Navigation receiver warning. A = Data Valid.
3	Latitude	2447.0949	Latitude in dddmm.mmmm format. Leading zeros transmitted.
4	N/S indicator	N	Latitude hemisphere indicator: N = North. S = South.
5	Longitude	12100.5223	Longitude in dddmm.mmmm format. Leading zeros transmitted.
6	E/W Indicator	E	Longitude hemisphere indicator: E = East. W = West.
7	Speed over ground	000.0	Speed over ground in knots (000.0 - 999.9).
8	Course over ground	000.0	Course over ground in degrees (000.0 - 359.9).
9	UTC Date	030407	UTC date of position fix, ddmmyy format.
10	Magnetic Variation	003.1	Magnetic Variation.
11	E/W Indicator	W	Magnetic variation indicator: W = West. E = East.
12	Mode indicator	A	N = Data not valid. A = Autonomous mode. D = Differential mode E = Estimated (dead reckoning) mode. M = Manual input mode. S = Simulator mode.
13	Checksum	61	Checksum.

D.6 VTG – Course Over Ground and Ground Speed

The VTG package provides information about the course and speed relative to the ground. It has the following structure:

```
GPVTG,x.x,T,,M,x.x,N,x.x,K,a*hh
```

where the fields are listed as follows:

```
GPVTG,1,T,,M,2,N,3,K,4*5
```

and an example:

```
GPVTG, 000.0,T,,M,000.0,N,0000.0,K,A*3D
```

Table D.6 shows detailed information of each possible field content and relates them to the example proposed.

Table D.6: VTG Message information.

Field	Name	Example	Description
1	Course	000.0	True course over ground in degrees (000.0 - 359.9).
2	Speed	000.0	Speed over ground in knots (000.0 - 999.9).
3	Speed	0000.0	Speed over ground in kilometers per hour (0000.0 - 1800.0).
4	Mode indicator	A	N= not valid. A = Autonomous mode. D = Differential mode. E = Estimated (dead reckoning) mode. M = Manual input mode. S = Simulator mode.
5	Checksum	3D	Checksum.

E

Appendix E

Basics of Microwave Radiometry

This Appendix details the basics of microwave radiometry used in the first part of Chapter 8 in order to compare the relation between microwave radiometry and microwave reflectometry.

E.1 Basics of Microwave Radiometry

The other passive microwave technique mentioned and used in this PhD Thesis dissertation is microwave radiometry. It is used in Chapter 8 to inter-compare radiometric and reflectometric measurements, and as a source of ground-truth to infer the soil water content. Differently from GNSS-R, microwave radiometry is based on the spontaneous emission of radiation instead of scattering. However, as it is seen here and in Chapter 8, they are strongly related.

All matter at a temperature above 0 K emits EM radiation in the whole EM spectrum. A black-body is an object that absorbs all the EM energy coming from all directions indistinctly from its polarization, and re-emits it iso-tropically when the thermal equilibrium is reached. This re-emission is explained by Planck's radiation law [256]:

$$B_{bb}(f) = \frac{2hf^3}{c^2} \frac{1}{e^{\frac{hf}{kT}} - 1} \left[\frac{W}{m^2 sr Hz} \right], \tag{E.1}$$

where $h = 6.63 \cdot 10^{-34}$ [J·s] is the Planck's constant, c is the speed of the light in [m/s], $k = 1.38 \cdot 10^{-23}$ [J/K], f is the frequency in [Hz], and T is the absolute physical temperature in [K].

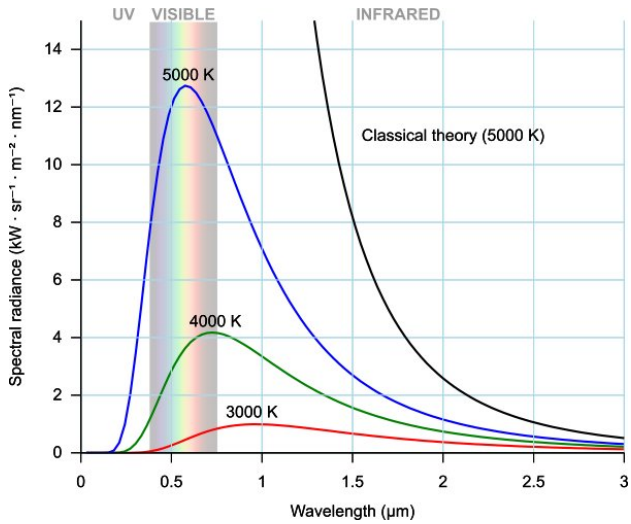

Figure E.1: Plank's radiation law representation. [Source: `https://en.wikipedia.org/wiki/Planck%27s_law`]

Figure E.1 shows the representation of Plank's law for different body temperatures. For instance, it has an important meaning in the radioastronomy field, which indicates how a star radiates and its brighter wavelength. As seen in Fig. E.1, the radiation emitted has a maximum that depends on the physical temperature. At ambient temperature $\sim$ 300 K, the maximum is close to the near-infrared, and consequently invisible for the human eye. Conversely, stars have a temperature ranging from 2.000 K to 10.000 K, falling in the visible band of the spectrum, and consequently being visible for the human eye. In the case of stars, their radiation peak determines their apparent "color". Also, the power of the radiation depends on the temperature, which is another factor related to the visibility of this radiation.

At microwave frequencies such as L-band, the term hf/kT is very small, and the exponential function can be approximated by its first order Taylor polynomial, which is $1 + hf/kT$. After

substituting in Eqn. (E.1) the Plank's thermal radiation becomes:

$$B_{bb}(f) \approx \frac{2kT}{\lambda^2}\left[\frac{W}{m^2 srHz}\right], \tag{E.2}$$

which is the so-called Rayleigh-Jeans approximation. Equation (E.2) shows that the radiance of a black-body has a linear dependence on its physical temperature. However, a black-body is an idealized object which does not exist in reality.

Natural bodies are known as gray-bodies, and they neither absorb, nor re-emit all incident EM radiation. Gray-bodies in thermal equilibrium re-emit all the radiation they have absorbed, which leads to the concept of brightness temperature. The brightness temperature is the apparent temperature of a gray-body at which it works as a black-body radiator, and it is defined as:

$$T_{BP} = e_P(\varepsilon_r(f,\theta,\phi),\sigma)T, \tag{E.3}$$

where e stands for the emissivity, and it depends on dielectric constant (ε_r), incidence and azimuth angles (θ, ϕ), surface roughness (σ), frequency (f), and polarization(P). Emissivity is modeled as $1 - R_P$, where R_P is the terrain's reflectivity, since the incoming EM radiation that has not been absorbed by the object has been reflected. Note that reflectivity depends on the same parameters than emissivity. Consequently, the radiance emitted by a gray-body is:

$$B_{gb}(f) \approx \frac{2kT_{BP}}{\lambda^2}\left[\frac{W}{m^2 srHz}\right]. \tag{E.4}$$

A microwave radiometer is a very sensitive instrument that measures the power emitted by a gray-body [257]. Assuming an ideal isotropical antenna, and a system bandwidth (B) sufficiently narrow where radiance, and consequently emissivity, can be considered constant, the power collected by its antenna is:

$$P_{gb} \approx kT_{BP}B[W]. \tag{E.5}$$

The measurement of the power collected by the antenna and the determination of the object's T_{BP}, and consequently the measurement of emissivity, is the basic observable of passive microwave radiometry. From there, all Earth Observation geophysical radiometric products are obtained. The ones used in this PhD Thesis dissertation, which are related to the soil moisture measurement, are seen in Chap. 8.

F

Appendix F

Coordinate systems and Antenna Pattern Compensation

This Appendix shows a summary of the coordinate systems used in the antenna pattern compensation algorithm, and it also describes the developed compensation algorithm.

F.1 Coordinate Systems

Four different coordinate systems are used for the antenna pattern compensation algorithm derived in Chapter 8:

- GCS (Fig. F.1(a)) is centered in the platform and has the x axis pointing towards the North, the y axis towards the East and the z axis towards the center of the Earth, or Nadir. It does not depend on how the platform is oriented, tilted or rolled: wherever the platform is located on the space, this system maintains its precise orientation. Since each reflection point has to be processed singularly and for each of them the platform assumes a fixed orientation in the space, it is convenient to center the global system in the platform itself. This reference system is used because the IMU installed onto the platform also adopts this convention for its axes' definition and it is easier to use the same reference frame for further computations. It can be simply described as follows:

$$\begin{cases} \hat{\mathbf{x}}_G \rightarrow \text{North} \\ \hat{\mathbf{y}}_G \rightarrow \text{East} \\ \hat{\mathbf{z}}_G \rightarrow \text{center of the Earth} \end{cases} \tag{F.1}$$

- Local Cartesian System (LCS) (Fig. F.1(b)) is the system integral with the platform; the x axis is oriented towards the front of the platform, the y axis towards the right side and the z axis toward the bottom side. If the platform is pointing towards the North in a flat position, the GCS and the LCS coincide. It can be simply described as follows:

$$\begin{cases} \hat{\mathbf{x}}_L \rightarrow \text{platform direction of movement} \\ \hat{\mathbf{y}}_L \rightarrow \text{platform right side} \\ \hat{\mathbf{z}}_L \rightarrow \text{platform nadir looking} \end{cases} \tag{F.2}$$

- The RHCP and LHCP LCS (Fig. F.1(c),(d) respectively) are systems integral with the up-looking and down-looking antennas respectively, and therefore with the entire platform. If the antennas are horizontally leveled when installed on the platform, they can be summarized as follows:

$$\begin{cases} \hat{\mathbf{x}}_{RHCP} = \hat{\mathbf{y}}_L \\ \hat{\mathbf{y}}_{RHCP} = \hat{\mathbf{x}}_L \\ \hat{\mathbf{z}}_{RHCP} = -\hat{\mathbf{z}}_L \end{cases} \qquad \begin{cases} \hat{\mathbf{x}}_{LHCP} = -\hat{\mathbf{y}}_L \\ \hat{\mathbf{y}}_{LHCP} = \hat{\mathbf{x}}_L \\ \hat{\mathbf{z}}_{LHCP} = \hat{\mathbf{z}}_L \end{cases} \tag{F.3}$$

F.2 Antenna Pattern Coordinates

It has been shown in Fig. F.1(c)–(d) that the coordinates for the antenna pattern on the plane are expressed generally in the LCS format. However, when an antenna is measured in an anechoic chamber, it is measured in spherical coordinates. In particular the UPC anechoic chamber uses the azimuth over elevation coordinate system definition, and it is depicted in Fig. F.2.

The spherical coordinate systems resulting from the antenna pattern measurement is also represented in Fig. F.3. If a Cartesian system is defined, a point $Q = (x_q, y_q, z_q)$ in the space can be defined by the spherical coordinates (r, θ, φ) where:

- r is the radius, or radial distance between the origin and the point Q;
- θ is the inclination, or polar angle, and denotes the angle between the z axis and the straight line connecting Q and the origin;

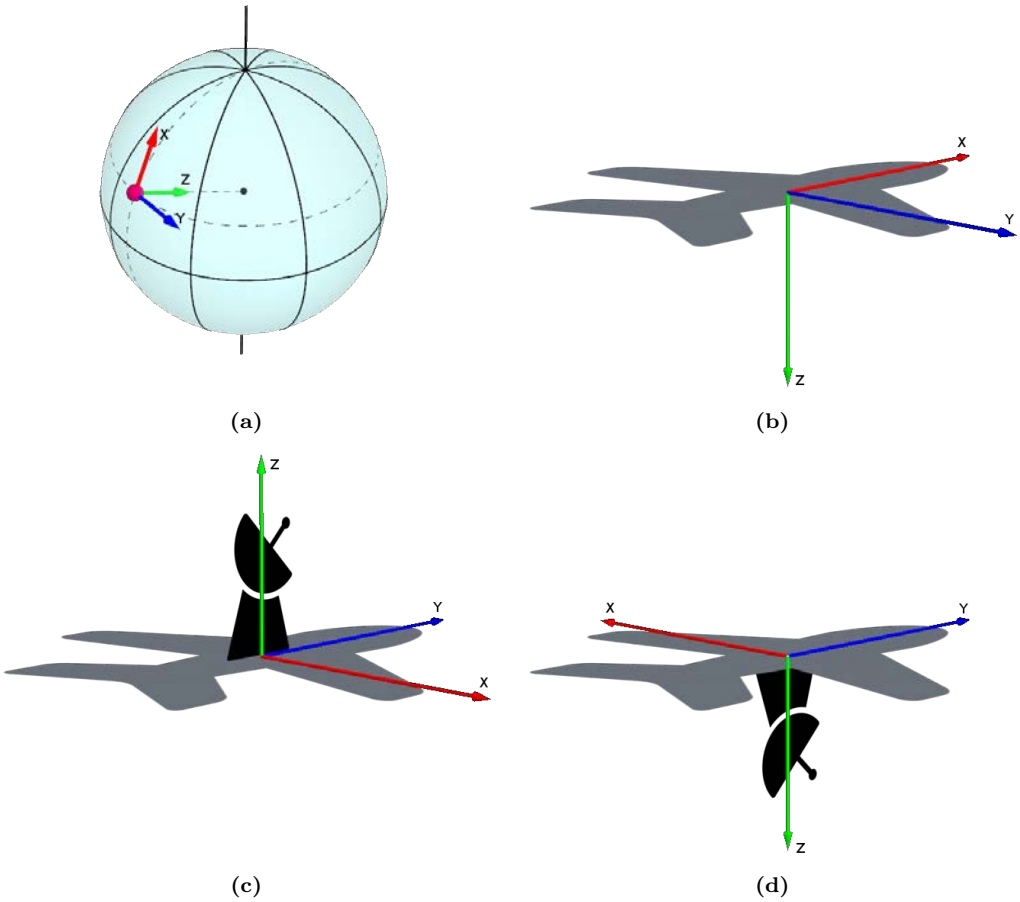

Figure F.1: Representation of the coordinate systems used: (a) Global Cartesian System, (b) Local Cartesian System, (c) RHCP Cartesian System, (d) LHCP Cartesian System.

- φ is the azimuth and denotes the right-handed angle between the x axis and the straight line connecting the origin to the projection of Q on the x-y plane.

Therefore, the relationship between the RHCP and LHCP LCS is determined by:

$$\begin{cases} r = \sqrt{x^2+y^2+z^2} \\ \theta = \arctan \frac{\sqrt{x^2+y^2}}{z} \\ \varphi = \arctan \frac{y}{x} \end{cases} \qquad \begin{cases} x = r \sin\theta \cos\varphi \\ y = r \sin\theta \sin\varphi \\ z = r \cos\theta \end{cases} \tag{F.4}$$

Note that the coordinates needed to retrieve the compensation parameters for the two antennas will be expressed in the RHCP and LHCP spherical systems for each antenna, which will correspond to $(\theta_{up}, \varphi_{up})$ and $(\theta_{down}, \varphi_{down})$.

In this Appendix the symbol θ is used to indicate inclination and no more the GPS satellite elevation angle, as it has been done in the entire dissertation. Therefore, for the sake of simplicity, from now on the GPS satellite elevation in a horizontal coordinate system will be expressed by

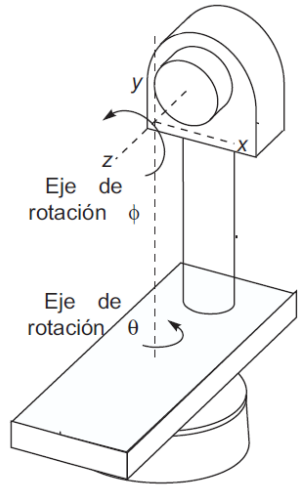

Figure F.2: Antenna measurement coordinate system: θ represents the rotation with respect to the z axis or main propagation direction, and ϕ the azimuth rotation direction (x towards y) [258].

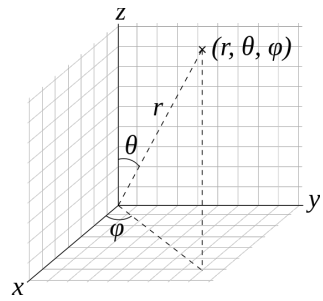

Figure F.3: Spherical coordinate system.

the symbol γ.

Now that all the coordinate systems are properly defined, it is necessary to use the IMU information to track the platform's movements. Those platforms movements are transformed into rotations in the RHCP and LHCP LCS, which will correspond to different $(\theta_{up}, \varphi_{up})$ and $(\theta_{down}, \varphi_{down})$ values, from which the antenna gain seen by the direct and reflected waves is computed and compensated for.

F.3 Platform's Attitude and Coordinate Transformation

As aforementioned, the LARGO instrument includes an IMU to monitor the platform's movements at any time. The IMU is sampled 20 times per second. The IMU measurement notation describes the device attitude as it was first rotated around axis z by ψ_Y degrees (yaw), then

around the new y' axis by θ_P degrees (pitch), and eventually around the new x'' axis by ϕ_R degrees (roll), through intrinsic rotations. Equivalently, if extrinsic rotations are employed, in other words, if rotations are performed only with respect to one fixed reference system such as the GCS, the order must be inverted and it should be first rolled around the x axis, then pitched around the y axis, and eventually yawed around the z axis. For the antenna pattern compensation algorithm, the new position of a generic point Q after the platform rotations must be expressed in the fixed reference system's coordinates GCS. Assuming extrinsic rotations results to be more easily writable in matrix notation; as a matter of fact, if the yaw-pitch-roll triple is $(\psi_Y, \theta_P, \phi_R)$ and point Q has initial coordinates (x_q, y_q, z_q) in the GCS reference system, after rotation, its new coordinates in the GCS reference system will be (x'_q, y'_q, z'_q) are:

$$\underbrace{\begin{bmatrix} x'_q \\ y'_q \\ z'_q \end{bmatrix}}_{Q'} = \underbrace{\begin{bmatrix} \cos\psi_Y & -\sin\psi_Y & 0 \\ \sin\psi_Y & \cos\psi_Y & 0 \\ 0 & 0 & 1 \end{bmatrix}}_{\text{yaw}} \underbrace{\begin{bmatrix} \cos\theta_P & 0 & \sin\theta_P \\ 0 & 1 & 0 \\ -\sin\theta_P & 0 & \cos\theta_P \end{bmatrix}}_{\text{pitch}} \underbrace{\begin{bmatrix} 1 & 0 & 0 \\ 0 & \cos\phi_R & -\sin\phi_R \\ 0 & \sin\phi_R & \cos\phi_R \end{bmatrix}}_{\text{roll}} \underbrace{\begin{bmatrix} x_q \\ y_q \\ z_q \end{bmatrix}}_{Q}, \quad \text{(F.5)}$$

Those angles are also known as the Tayt-Bryan angles.

So, the axes of the platform in the LCS can be described in the GCS as a triple of unitary vectors pointing towards the local axes' directions and, if the platform lies in its starting position where GCS and LCS coincide, then:

$$\hat{x}_L = \begin{bmatrix} 1 \\ 0 \\ 0 \end{bmatrix} \quad \hat{y}_L = \begin{bmatrix} 0 \\ 1 \\ 0 \end{bmatrix} \quad \hat{z}_L = \begin{bmatrix} 0 \\ 0 \\ 1 \end{bmatrix}, \quad \text{(F.6)}$$

If the platform rotates, vectors describing the LCS axes will rotate integrally with it and the movement of each can be computed using equation F.5. Therefore, since yaw-pitch-roll triple $(\psi_Y, \theta_P, \phi_R)$ refers to the starting position of the platform, LCS axes' orientation can be expressed through the following equality:

$$\begin{bmatrix} \mathbf{x}' & \mathbf{y}' & \mathbf{z}' \end{bmatrix} = \mathbf{YPR} \cdot \mathbf{I}, \quad \text{(F.7)}$$

where $\mathbf{x}'$, $\mathbf{y}'$ and $\mathbf{z}'$ are the column vectors representing the GCS axes, $\mathbf{Y}$, $\mathbf{P}$ and $\mathbf{R}$ are the yaw, pitch and roll rotation matrices respectively as indicated in Eqn. F.5 and $\mathbf{I}$, identity matrix, represents the LCS axes in the starting position. For instance in the case of the RHCP and LHCP LCS, the equivalent GCS become:

$$\begin{bmatrix} \mathbf{x_{RHCP}}' & \mathbf{y_{RHCP}}' & \mathbf{z_{RHCP}}' \end{bmatrix} = \mathbf{YPR} \cdot \begin{bmatrix} 0 & 1 & 0 \\ 1 & 0 & 0 \\ 0 & 0 & -1 \end{bmatrix}, \quad \text{(F.8)}$$

$$\begin{bmatrix} \mathbf{x_{LHCP}}' & \mathbf{y_{LHCP}}' & \mathbf{z_{LHCP}}' \end{bmatrix} = \mathbf{YPR} \cdot \begin{bmatrix} 0 & 1 & 0 \\ -1 & 0 & 0 \\ 0 & 0 & 1 \end{bmatrix}. \quad \text{(F.9)}$$

To retrieve the gain compensation value, the signals' incoming direction must be expressed in the antennas reference systems, which are integral with the LCS. Therefore, after rotating the antennas LCS using Eqn. (F.7), Eqns. (F.8)–(F.9) provide the formulations of the new RHCP and LHCP Cartesian Systems. To find the polar angles in the LCS, from which it will be easy to find the RHCP and LHCP spherical coordinates, the satellite's position has to be first expressed in Cartesian form, so that local inclination and azimuth (θ_L, φ_L) can be deduced by evaluating angles between vectors. Since the real distance between the platform and the satellite does not

matter, but only the sight direction, the vector pointing from the platform to the satellite is assumed to have unitary length and therefore it can be expressed as:

$$\mathbf{s} = \begin{cases} x_{sat} = \sin\theta\cos\varphi \\ y_{sat} = \sin\theta\sin\varphi \\ z_{sat} = \cos\theta \end{cases} . \tag{F.10}$$

The direct GPS signal coming from the satellite can also be expressed by Cartesian coordinates:

$$\mathbf{s}_{up} = \begin{cases} x_{up} = x_{sat} = \sin\theta\cos\varphi \\ y_{up} = y_{sat} = \sin\theta\sin\varphi \\ z_{up} = z_{sat} = \cos\theta \end{cases} . \tag{F.11}$$

The reflected signal is located at the specular position to the real satellite with respect to the x–y plane and therefore the GPS ray is expressed by:

$$\mathbf{s}_{down}^{simple} = \begin{cases} x_{dwon} = x_{sat} = \sin\theta\cos\varphi \\ y_{down} = y_{sat} = \sin\theta\sin\varphi \\ z_{down} = -z_{sat} = -\cos\theta \end{cases} . \tag{F.12}$$

Then, the spherical coordinates on the antenna reference frame to compute where the radiation comes from can be computed.

The inclination is the angle between axis z and unitary vector $\mathbf{s}$. Recalling the vector scalar product properties, then:

$$\mathbf{z}_{up} \cdot \mathbf{s}_{up} = \|\mathbf{z}_{up}\|\|\mathbf{s}_{up}\|\cos\theta_{up} = \cos\theta_{up}, \tag{F.13}$$

θ_{up} evaluation is straightforward:

$$\theta_{up} = \arccos(\mathbf{z}_{up} \cdot \mathbf{s}_{up}). \tag{F.14}$$

Since inclination is defined in the interval $[0, 180°]$, the $\arccos(\cdot)$ function gives the real angle value.

The azimuth φ_{up} is the right-handed angle between the $\mathbf{x}_{up}$ axis and the $\mathbf{s}_{up}$ projection, $\mathbf{u}$, onto the x_{up}-y_{up} plane. To compute such an angle a little more calculations are needed and Fig. F.4 may help in visualizing the geometry of the problem. If the cross product is performed between vector $\mathbf{s}_{up}$ and axis vector z_{up}, the resulting unitary vector $\mathbf{w}$ lies in the x_{up}–y_{up} plane, because it must be orthogonal to the z axis, which is orthogonal to such plane. Moreover, being $\mathbf{w}$ orthogonal to the plane defined by $\mathbf{s}_{up}$ and z_{up}, it is also orthogonal to $\mathbf{u}$, because the projection of $\mathbf{s}_{up}$ must belong to this plane. If only right-handed angles are considered, that is those whose amplitudes increase opening from x axis to y axis, it is easy to see that rotating $\mathbf{w}$ by 90° it comes to superimpose to $\mathbf{u}$, no matter what $\mathbf{s}_{up}$ is. Defining β as the right-handed angle between x_{up} and $\mathbf{w}$, the following always holds:

$$\varphi_{up} = \beta + 90°. \tag{F.15}$$

Differently than the inclination angle, azimuth spans the entire $[0°, 360°]$ range and thus the $\arccos(\cdot)$ function is not enough to compute it, because it may exclude one solution. If angle ψ between $\mathbf{w}$ and $\mathbf{y}_{up}$ is introduced:

$$\psi = \arccos(\mathbf{w} \cdot \mathbf{y}_{up}), \tag{F.16}$$

it is possible to know the real amplitude of β by the following expression:

$$\beta = \begin{cases} +\arccos(\mathbf{w} \cdot \mathbf{x}_{up}) & \text{if } \psi \in [0°, 90°] \\ -\arccos(\mathbf{w} \cdot \mathbf{x}_{up}) & \text{if } \psi \in (90°, 180°] \end{cases} , \tag{F.17}$$

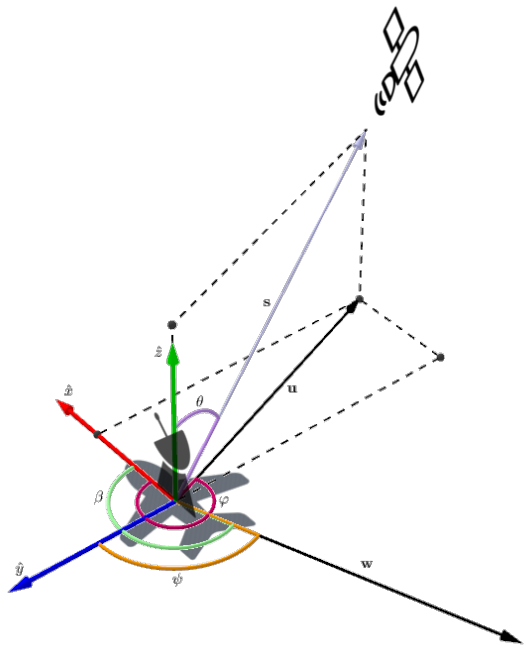

Figure F.4: RHCP reference system, direct signal and azimuth computation.

The computation of the reflected signal incoming direction in the down-looking antenna reference frame is exactly the same, so that, in general form, spherical coordinates for the signal direction can be found as:

$$\begin{cases} \theta = \arccos(\mathbf{z} \cdot \mathbf{s}) \\ \varphi = 90^\circ + \begin{cases} +\arccos(\mathbf{w} \cdot \mathbf{x}) & \text{if } \psi \in [0^\circ, 90^\circ] \\ -\arccos(\mathbf{w} \cdot \mathbf{x}) & \text{if } \psi \in (90^\circ, 180^\circ] \end{cases} \end{cases}, \tag{F.18}$$

where:

$$\mathbf{w} = \mathbf{s} \times \mathbf{z} \quad \text{and} \tag{F.19}$$

$$\psi = \arccos(\mathbf{w} \cdot \mathbf{y}). \tag{F.20}$$

Once the spherical coordinates are obtained, the Antenna Pattern Compensation coefficients $(APC_{up}(\theta_{up}, \varphi_{up}))$ and $(APC_{down}(\theta_{down}, \varphi_{down}))$ can be retrieved from the proper functions, or tables, and the antenna pattern compensated reflectivity yields:

$$\Gamma = SNR_L - SNR_R - k_{calib} + APC_{up}(\theta_{up}, \varphi_{up}) - APC_{down}(\theta_{down}, \varphi_{down}), \tag{F.21}$$

where k_{calib} is a compensation term that can be estimated during the calibration phase.

G

Appendix G

Geo-location: Ray-tracing and specular reflection conditions

This Appendix shows the two different methodologies applied for geolocating the surface specular reflection points. The first one is very simple and it is based on ray-tracing. The second one is a little bit more tedious and it is based on applying the specular reflection conditions for each surface point.

G.1 Ray-tracing

The first implemented geolocation method is the simplest one and assumes that the ground can be approximated with an infinitely wide and perfectly smooth plane. It also assumes that the height of the platform is very small, and that paraxial approximation of rays can be used. The last assumption is a flat Earth model, which works properly if the flight height is lower than 1000 m. In the reference system used the platform is the origin, how it is oriented does not matter, and only the position of the satellite relative to the geometrical point occupied by the center of the platform is needed. Figure G.1 schematizes this approach remarking the direct and reflected rays. To avoid confusion with reference systems, in Fig. G.1 the platform is represented by a big light-blue sphere. The x axis (in red) points towards the real North, the y axis (in blue) towards the East and the z axis (in green) towards the center of the Earth. This is coincident with the GCS system described in Appendix F. The two purple arrows represent the directions from where the direct and reflected signals are coming.

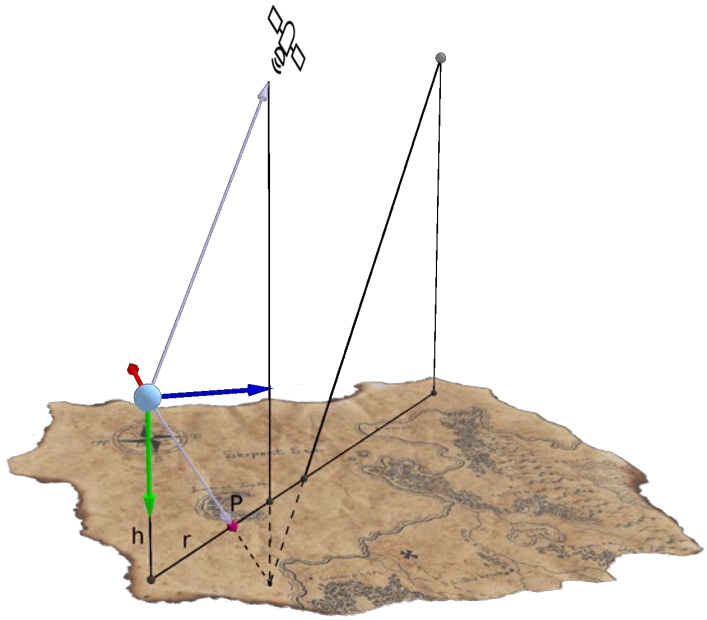

Figure G.1: Simple geolocation using a ray-tracing approach.

Information collected by the GPS back-end receivers in the LARGO instrument provide the elevation (θ) and the azimuth (ϕ) angles of each satellite in view with respect to the receiver itself. This information is provided by the GSV NMEA packet described in Appendix D. The azimuth is defined as the angle in degrees from the North to the projection of the satellite on the horizontal plane where the platform lies (azimuth increases towards the East), while elevation is the angle between such plane and the satellite itself (elevation increases towards the zenith). These two horizontal coordinates are sufficient to compute a vector representing the direct signal direction. The distance between the satellite and the platform is not relevant, and only its direction matters. This is acceptable because one of the assumptions is that the satellite is very far away as compared to the platform's height. So, the normalized distance ρ between the

platform and the satellite projection on the plane is:

$$\rho = \cos\theta, \tag{G.1}$$

Through ρ, the direction of the satellite can be expressed in GCS Cartesian coordinates centered at the platform position:

$$\begin{cases} x_{sat} = \rho\cos\phi = \cos\theta\cos\phi \\ y_{sat} = \rho\sin\phi = \cos\theta\sin\phi \\ z_{sat} = -\sin\theta \end{cases}, \tag{G.2}$$

where the z coordinate is negative because the z axis points towards the center of the Earth (nadir direction).

In the Cartesian reference system, locating the reflection point is very simple. The ground plane is the infinite plane parallel to both the x and y axes and its z coordinate can be defined using information about the platform's height. The distance between the platform and the WGS84 geodetic model is known thanks to the altitude parameter in the GPS GGA message. Also the distance between the Earth's surface (geoid) and the WGS84 geodetic model is given in the same NMEA packet. Therefore, the true height h of the platform is:

$$h = \text{altitude} - \text{geoidal separation}, \tag{G.3}$$

and thus the ground plane is defined as:

$$z = h. \tag{G.4}$$

Due to the paraxial approximation, the spherical wave transmitted by the GPS satellite can be assumed to be a plane wave and all its rays have the same incidence angle when impinging on the soil surface. Under those approximations and assumptions, the reflected ray is seen as a direct ray generated by the specular image of the satellite, having the Cartesian coordinates:

$$\begin{cases} x'_{sat} = x_{sat} = \cos\theta\cos\phi \\ y'_{sat} = y_{sat} = \cos\theta\sin\phi \\ z'_{sat} = -z_{sat} = \sin\theta \end{cases}, \tag{G.5}$$

and horizontal coordinates:

$$\begin{cases} \theta' = -\theta \\ \phi' = \phi \end{cases}, \tag{G.6}$$

To find the precise location of the reflection point on space the distance r between the platform projection and the reflection point, which is the red dot on the ground in Fig. G.1, must be computed and by noticing that:

$$\tan\theta' = \frac{h}{r}, \tag{G.7}$$

from which:

$$r = \frac{h}{\tan\theta}. \tag{G.8}$$

Using the azimuth angle it is easy to find also the x and the y coordinates of the reflection point P, whose z coordinate is necessarily h:

$$\begin{cases} x_P = r\cos\phi \\ y_P = r\sin\phi \\ z_P = h \end{cases}. \tag{G.9}$$

Currently the reflection point location with respect to the platform's position has been obtained. As all the computations were performed in meters, the (x_P, y_P, z_P) are also given in those

units. Now the only remaining part is to obtain the geographic coordinates of the platform in meters, which is achieved by converting the Lat/Lon coordinates on the GGA or RMC NMEA packets to UTM coordinates. The UTM is a conformal projection whose coordinates are expressed in meters and play an important role in the first developed geolocation algorithms [259]. First, the local reflection point coordinates are added to the platform's UTM coordinates computed. Second, the resulting UTM coordinates of the reflection point are converted back into Lat/Lon coordinates and the reflection point is geolocated.

G.2 Topography-based Geo-location

The second geo-location technique, which is based on the topographic model, aims to be more precise by not assuming that ground is a perfectly flat surface: hills and valleys are often present and affect the reflection direction of the incident rays, which was the case of the *Salamanca* field experiment test site. For this approach, information about the ground topography is needed. If a DEM or DSM are available from the field test site that would be optimum. However, in a more general way Google Earth's terrain elevation data can be used. Because the latter is a more general approach and it will work for any test site, it is the one used here.

The first step of the algorithm is to download the elevation data from Google Earth (GE). To do it, the area under interest is first discretized (entire field campaign test site). For each point the elevation data is queried to Google using the GE API. In this phase it is convenient to use UTM coordinates, so that a Cartesian reference system can be built. It is worth to mention that the denser the grid is, the more accurate the ground approximation will be. However, as a drawback, the larger the number of surface points, the larger the processing time will be. Once the surface points have been geometrically defined, a surface can be drawn by interpolating the samples. Figure G.2 shows an example of a surface obtained by sampling the data from a test flight held in *Ripollet*, Spain. Black dots denote the platform position during the test flight.

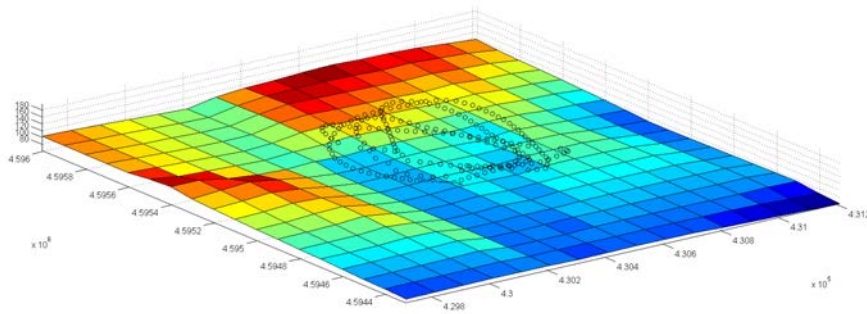

Figure G.2: Surface approximation of the area under interest.

After interpolating a surface from the topography data, the surface normal vectors can be computed for each surface point, and they are shown in red in Fig. G.3.

At each instant of time the platform used occupies a well-known position in the space due to its GPS back-end receiver. The satellite can also be located onto a line of sight by means of the elevation and azimuth information provided by the GSV NMEA packet of the back-end receivers. If the Cartesian reference system is centered in the UTM zone origin, the platform

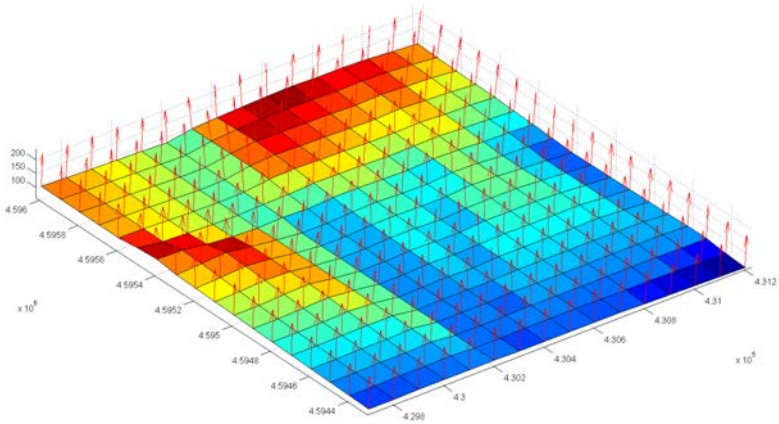

Figure G.3: Surface approximation of the covered area and surface normal vectors.

position $\mathbf{v}$ is defined as:

$$\begin{cases} x_v = \text{northing}_v \\ y_v = \text{easting}_v \\ z_v = -\text{height}_v \end{cases} . \tag{G.10}$$

Assuming that the satellite is very far away, the distance between the transmitting satellite and the platform is approximately the distance between the Earth's surface and the satellite. This distance, from now on called R, is approximately 20200 km long. Therefore the transmitting GPS satellite position $\mathbf{s}$ becomes:

$$\begin{cases} x_s = x_v + R\cos\theta\cos\phi \\ y_s = y_v + R\cos\theta\sin\phi \\ z_s = z_v - R\sin\theta \end{cases} . \tag{G.11}$$

Finally, the ith discretized surface point is represented by the following coordinates $\mathbf{p}_i$:

$$\begin{cases} x_{p,i} = \text{northing}_{p,i} \\ y_{p,i} = \text{easting}_{p,i} \\ z_{p,i} = -\text{height}_{p,i} \end{cases} . \tag{G.12}$$

The GPS signal impinges every point of the discretized surface. The incidence vector for the ith surface point is:

$$\mathbf{r}_{s,p_i} = \mathbf{p}_i - \mathbf{s}. \tag{G.13}$$

For sake of simplicity, it will be easier for future computations to use the opposite vector, that is the one going from the soil sample to the satellite which is:

$$\mathbf{r}_{p_i,s} = \mathbf{s} - \mathbf{p}_i. \tag{G.14}$$

Once all the incidence vectors are obtained, it is time to compute the scattering vectors, which are the vectors between the platform position and the discretized surface points, and for the ith point it is given by:

$$\mathbf{r}_{p_i,v} = \mathbf{v} - \mathbf{p}_i. \tag{G.15}$$

If $\mathbf{r}_{p_i,s}$ and $\mathbf{r}_{p_i,v}$ (respectively the blue and red vectors in Fig. G.4) are specular with respect to the surface normal (black vector) of the ith surface point they are impinging on, they must accomplish the specular reflection conditions which are:

- Incident and reflected rays must lie on the same plane, the incidence plane. The incidence plane must also contain the surface normal vector and therefore it will be orthogonal to the surface.
- Angles between incident vector and surface normal and between reflected/scattering vector and surface normal must be equal.
- In a forward scattering geometry, such as the one found in GNSS-R, the incidence and scattering vectors must follow a different direction.

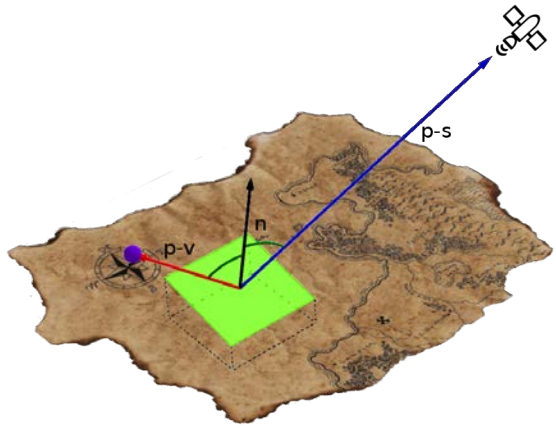

Figure G.4: Topography-based geolocation geometry.

If the triple of vectors $(\mathbf{v}, \mathbf{s}, \mathbf{p}_i)$ satisfy these conditions, then $\mathbf{p}_i$ is considered a specular reflection point. The mathematical specular reflection conditions are given by:

1.
$$(\hat{\mathbf{r}}_{p_i,s} \times \hat{\mathbf{r}}_{p_i,v}) \cdot \hat{\mathbf{n}}_i = 0, \tag{G.16}$$
where $\hat{\mathbf{r}}_{p_i,s}$ and $\hat{\mathbf{r}}_{p_i,v}$ denote the unitary vectors of $\mathbf{r}_{p_i,s}$ and $\mathbf{r}_{p_i,v}$ respectively. The vector product $\hat{\mathbf{r}}_{p_i,s} \times \hat{\mathbf{r}}_{p_i,v}$ gives a vector $\hat{\mathbf{k}}$ orthogonal to both $\mathbf{r}_{p_i,s}$ and $\mathbf{r}_{p_i,v}$, and therefore to the plane defined by them. If the surface normal $(\hat{\mathbf{n}}_i)$ also belongs to the this plane, then it must be orthogonal to vector $\hat{\mathbf{k}}$, that is $\hat{\mathbf{k}} \cdot \hat{\mathbf{n}}_i = 0$, which defines the specular incidence plane.

2.
$$(\hat{\mathbf{r}}_{p_i,s} - \hat{\mathbf{r}}_{p_i,v}) \cdot \hat{\mathbf{n}}_i = 0. \tag{G.17}$$
Equality $\mathbf{a} \cdot \mathbf{b} = \|\mathbf{a}\|\|\mathbf{b}\| \cos\alpha$, where α is the angle between vectors $\mathbf{a}$ and $\mathbf{b}$, is a known rule. Applying this equality to the vectors incidence, normal, and reflected vector leads to:
$$\hat{\mathbf{r}}_{p_i,v} \cdot \hat{\mathbf{n}}_i = \cos\alpha_v, \tag{G.18}$$
$$\hat{\mathbf{r}}_{p_i,s} \cdot \hat{\mathbf{n}}_i = \cos\alpha_s, \tag{G.19}$$

where, for the geometry of the problem, angles α_v and α_s are necessarily included in the interval $[0°, 90°]$ and thus are unequivocally identified by their cosine function. If the angles are equal, so must be their cosine, and therefore:

$$\hat{\mathbf{r}}_{p_i,v} \cdot \hat{\mathbf{n}}_i = \hat{\mathbf{r}}_{p_i,s} \cdot \hat{\mathbf{n}}_i, \tag{G.20}$$

which is equivalent to Eqn. (G.17).

3.
$$\hat{\mathbf{r}}_{p_i,s} \cdot \hat{\mathbf{r}}_{p_i,v} < 1. \tag{G.21}$$

If vectors $\hat{\mathbf{r}}_{p_i,s}$ and $\hat{\mathbf{r}}_{p_i,v}$ have the same direction, then their scalar product is ± 1. If they do not have the same direction as required by the forward scattering geometry, their scalar product will be smaller than 1.

Those conditions are evaluated numerically on a computer, and have been programmed in Matlab under the following definition:

$$|(\hat{\mathbf{r}}_{p_i,s} \times \hat{\mathbf{r}}_{p_i,v}) \cdot \hat{\mathbf{n}}_i| < \epsilon, \tag{G.22}$$
$$|(\hat{\mathbf{r}}_{p_i,s} - \hat{\mathbf{r}}_{p_i,v}) \cdot \hat{\mathbf{n}}_i| < \epsilon, \tag{G.23}$$
$$|\hat{\mathbf{r}}_{p_i,s} \cdot \hat{\mathbf{r}}_{p_i,v}| < 1 - \epsilon, \tag{G.24}$$

with ϵ a conveniently small value.

After verifying the three conditions for all the surface points some candidate specular reflection points, or possibly none, are found for each platform position. Note that this algorithm must be executed anytime the platform is at a different position. If more than one soil sample satisfies the conditions and those points are largely spatially separated, they should be discarded, because this is an indication of a multiple reflection environment and there is not any a priori information of how the addition of electric fields from each region will be (constructive or destructive). On the other hand, if one surface point or several ones very close to each other which define a region satisfy the specular reflection conditions, that point/area is assumed to be the specular reflection area and its location is directly given by its coordinates $(x_{p,i}, y_{p,i}, z_{p,i})$. Figure G.5 shows the topography-based geolocation principle after filtering all candidate reflection points and saving the ones that match the specular reflection conditions. That figure employs again data collected from the test flight performed in *Ripollet*. in Fig. G.5, black vectors are surface normal vectors, blue ones represent the incidence vectors and point towards the satellite, and red ones denote the reflected/scattering vectors and denote signal's trajectory after ground reflection; the black dot represents the platform position in this particular case. This algorithm is applied in Chapter 8 for geolocating the reflection points in the *Salamanca* field experiment due to the severe topography conditions faced. Also, in Chapter 8 another example of how this algorithm works is given.

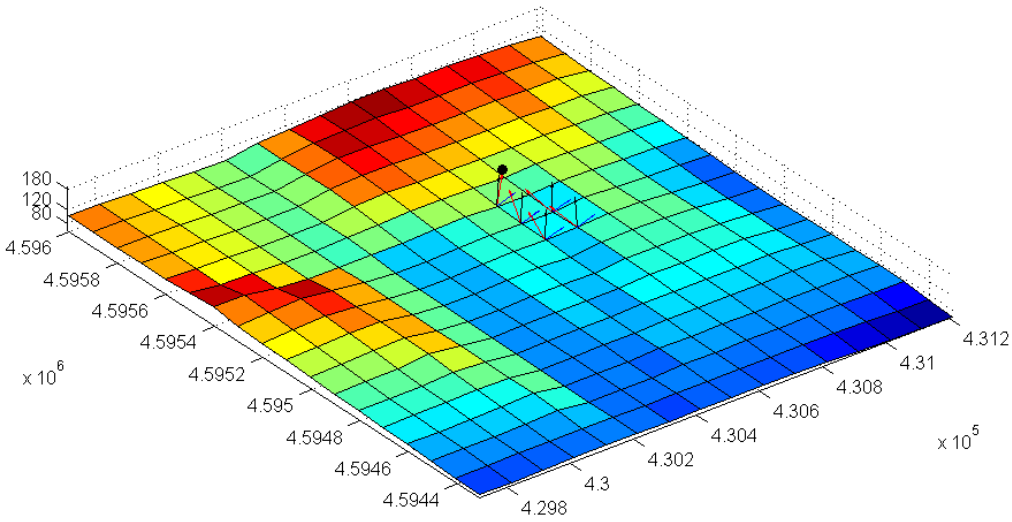

Figure G.5: Topography-based geolocation: black vectors are surface normals, blue ones point towards the transmitting satellite (incidence vectors) and red ones point towards the platform (reflection/scattering vectors) and denote signal's trajectory after ground reflection. The black dot represents the platform position.

H

Appendix H

Polar stereographic coordinates

This Appendix details the polar stereographic projection used by Chapter 10 in the representation of the ice detection maps. As it name indicates, it is a projection specifically designed for the Polar regions, since projections such as the Mercator projection deform excessively the data represented.

H.1 Definition

A Polar stereographic projection specifies a projection plane or grid tangent to the Earth's surface. In Polar stereographic projections it is common to set the plane or grid tangent to the Earth's surface at the Poles. In that case, the grid has minimum distortion at the Poles and it increases as latitude becomes more separated. In Chapter 10 it has been decided to use the polar stereographic projection defined by National Sea & Ice Data Center (NSIDC), which centers the grid at 70° latitude. All ground-truth used in Chapter 10 was already defined in that projection, which is the main reason in order to chose that one. In the selected projection, the no distortion area is centered around ±70°, for the North and South Poles respectively, and it increases as latitude becomes separated from the center value. However, since sea ice maps are normally represented up to ±50° latitude, centering the projection at ±70° helps to minimize the distortion of the overall map. Differently, if a Mercator projection would be used, distortion at the Poles would be maximum.

The area covered by the projection is generally defined in the x-y plane with the properties described by Table H.1. Therein, it is seen that the spatial resolution is 6.25 km x 6.25 km, and that the grid is described in a matrix version with a limited number of columns and rows. The corners of the matrix defined by the grid are given in Table H.2 for the Northern Hemisphere, and in Table H.3 for the Southern one. In order to better understand the meaning of those tables Fig. H.1 has been added, where visually the size of the matrix in Lat/Lon coordinates can be appreciated. The mathematical operation to convert between Lat/Lon coordinates and Polar stereographic coordinates (x,y) such as the ones presented in this Appendix or other ones centered at a latitude different from ±70° can be found in [260].

Table H.1: Grid dimension of the Polar stereographic projection selected.

Region	Nominal Gridded Resolution [km]	Columns	Rows
North	6.25	1216	1792
South	6.25	1264	1328

Table H.2: Grid coordinates for the Northern Hemisphere.

X [km]	Y [km]	Latitude [deg]	Longitude [deg]
-3850	5850	30.98	168.35
3750	5850	31.37	102.34
3750	-5350	34.35	350.03
-3850	-5350	33.92	279.26

Table H.3: Grid coordinates for the Southern Hemisphere.

X [km]	Y [km]	Latitude [deg]	Longitude [deg]
-3950	4350	-39.23	317.76
3950	4350	-39.23	42.24
3950	-3950	-41.45	135.00
-3950	-3950	-41.45	225.00

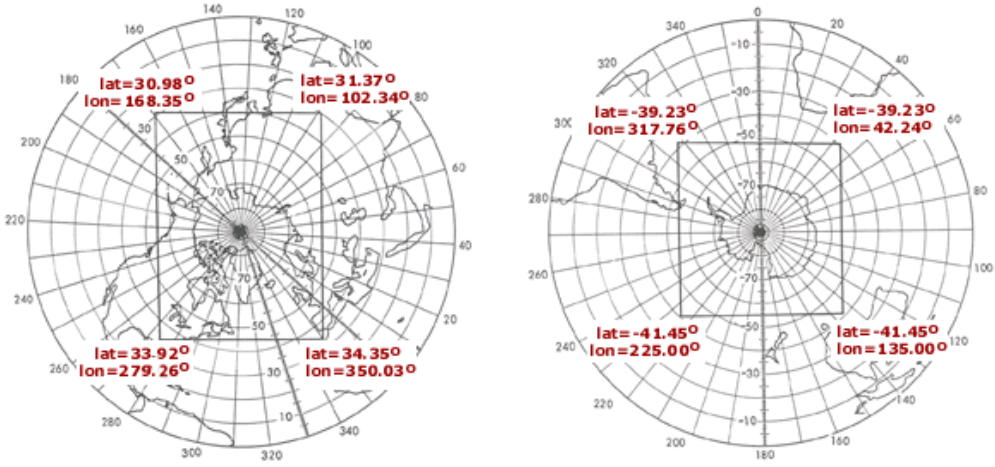

(a) **(b)**

Figure H.1: Polar stereographic projection highlighting the Lat/Lon limits of the sea ice maps shown in Chapter 10. (a) Northern Hemisphere, (b) Southern Hemisphere. Source: `https://nsidc.org/data/polar-stereo/ps_grids.html`.

Bibliography

[1] "IEEE Standard Letter Designations for Radar-Frequency Bands," *IEEE Std 521-2002 (Revision IEEE Std 521-1984)*, pp. 0_1–3, 2003. (Cited on page 4.)

[2] S. Buckreuss, U. Steinbrecher, and B. Schattler, "The TerraSAR-X mission status," in *2015 IEEE 5th Asia-Pacific Conf. Synth. Aperture Radar*. IEEE, sep 2015, pp. 357–361. (Cited on page 6.)

[3] R. Gehrels, "Rising Sea Levels as an Indicator of Global Change," in *Clim. Chang. Obs. Impacts Planet Earth*, 1st ed. Elsevier B.V., 2009, ch. 18, pp. 325–336. [Online]. Available: http://dx.doi.org/10.1016/B978-0-444-53301-2.00018-X (Cited on page 6.)

[4] S. I. Seneviratne, T. Corti, E. L. Davin, M. Hirschi, E. B. Jaeger, I. Lehner, B. Orlowsky, and A. J. Teuling, "Investigating soil moisture–climate interactions in a changing climate: A review," *Earth-Science Rev.*, vol. 99, no. 3-4, pp. 125–161, may 2010. (Cited on page 7.)

[5] Y. Kerr, P. Waldteufel, J.-P. Wigneron, J. Martinuzzi, J. Font, and M. Berger, "Soil moisture retrieval from space: the Soil Moisture and Ocean Salinity (SMOS) mission," *IEEE Trans. Geosci. Remote Sens.*, vol. 39, no. 8, pp. 1729–1735, 2001. (Cited on page 7.)

[6] J. Font, A. Camps, A. Borges, M. Martin-Neira, J. Boutin, N. Reul, Y. H. Kerr, A. Hahne, and S. Mecklenburg, "SMOS: The Challenging Sea Surface Salinity Measurement From Space," *Proc. IEEE*, vol. 98, no. 5, pp. 649–665, may 2010. (Cited on page 7.)

[7] Y. H. Kerr, P. Waldteufel, J.-P. Wigneron, S. Delwart, F. Cabot, J. Boutin, M.-J. Escorihuela, J. Font, N. Reul, C. Gruhier, S. E. Juglea, M. R. Drinkwater, A. Hahne, M. Martin-Neira, and S. Mecklenburg, "The SMOS Mission: New Tool for Monitoring Key Elements ofthe Global Water Cycle," *Proc. IEEE*, vol. 98, no. 5, pp. 666–687, may 2010. (Cited on pages 7 and 8.)

[8] D. Le Vine, G. Lagerloef, C. Ruf, F. Wentz, S. Yueh, J. Piepmeier, E. Lindstrom, and E. Dinnat, "Aquarius: The instrument and initial results," in *2012 12th Spec. Meet. Microw. Radiom. Remote Sens. Environ.* IEEE, mar 2012, pp. 1–3. (Cited on page 7.)

[9] D. Entekhabi, E. Njoku, P. O'Neill, M. Spencer, T. Jackson, J. Entin, E. Im, and K. Kellogg, "The Soil Moisture Active/Passive Mission (SMAP)," in *IGARSS 2008 - 2008 IEEE Int. Geosci. Remote Sens. Symp.* IEEE, 2008, pp. III – 1–III – 4. (Cited on page 7.)

[10] D. Entekhabi, E. Njoku, and P. O'Neill, "The Soil Moisture Active and Passive Mission (SMAP): Science and applications," in *2009 IEEE Radar Conf.* IEEE, 2009, pp. 1–3. (Cited on page 7.)

[11] D. Entekhabi, E. G. Njoku, P. E. O'Neill, K. H. Kellogg, W. T. Crow, W. N. Edelstein, J. K. Entin, S. D. Goodman, T. J. Jackson, J. Johnson, J. Kimball, J. R. Piepmeier, R. D. Koster, N. Martin, K. C. McDonald, M. Moghaddam, S. Moran, R. Reichle, J. C. Shi, M. W. Spencer, S. W. Thurman, L. Tsang, and J. Van Zyl, "The Soil Moisture Active Passive (SMAP) Mission," *Proc. IEEE*, vol. 98, no. 5, pp. 704–716, may 2010. (Cited on page 7.)

[12] W. Bannoura, A. Wade, and D. Srinivas, "NOAA Ocean Surface Topography Mission Jason-2 Project Overview," in *Proc. Ocean. 2005 MTS/IEEE.* IEEE, pp. 1–5. (Cited on page 7.)

[13] C. Donlon, B. Berruti, S. Mecklenberg, J. Nieke, H. Rebhan, U. Klein, A. Buongiorno, C. Mavrocordatos, J. Frerick, B. Seitz, P. Goryl, P. Femenias, J. Stroede, and R. Sciarra, "The Sentinel-3 Mission: Overview and status," in *2012 IEEE Int. Geosci. Remote Sens. Symp.* IEEE, jul 2012, pp. 1711–1714. (Cited on page 7.)

[14] G. C. Topp, J. L. Davis, and A. P. Annan, "Electromagnetic determination of soil water content: Measurements in coaxial transmission lines," *Water Resour. Res.*, vol. 16, no. 3, pp. 574–582, jun 1980. (Cited on page 7.)

[15] O. Nogues, A. Sumpsi, A. Camps, and A. Rius, "A 3 GPS-channels Doppler-delay receiver for remote sensing applications," in *IGARSS 2003. 2003 IEEE Int. Geosci. Remote Sens. Symp. Proc. (IEEE Cat. No.03CH37477)*, vol. 7. IEEE, pp. 4483–4485. (Cited on page 8.)

[16] I. Ramos-Perez, G. F. Forte, A. Camps, X. Bosch-Lluis, E. Valencia, N. Rodriguez-Alvarez, H. Park, and M. Vall-llosera, "Calibration, Performance, and Imaging Tests of a Fully Digital Synthetic Aperture Interferometer Radiometer," *IEEE J. Sel. Top. Appl. Earth Obs. Remote Sens.*, vol. 5, no. 3, pp. 723–734, jun 2012. (Cited on page 8.)

[17] X. Bosch-Lluis, I. Ramos-Perez, A. Camps, N. Rodriguez-Alvarez, J. Marchan-Hernandez, E. Valencia, J. Nieto, and M. Guerrero, "Digital beamforming analysis and performance for a digital L-band Pseudo-correlation radiometer," in *2009 IEEE Int. Geosci. Remote Sens. Symp.* IEEE, 2009, pp. V–184–V–187. (Cited on page 8.)

[18] E. Valencia, A. Camps, J. Marchan-Hernandez, X. Bosch-Lluis, N. Rodriguez-Alvarez, and I. Ramos-Perez, "Advanced architectures for real-time Delay-Doppler Map GNSS-reflectometers: The GPS reflectometer instrument for PAU (griPAU)," *Adv. Sp. Res.*, vol. 46, no. 2, pp. 196–207, jul 2010. (Cited on pages 8, 103, and 122.)

[19] J. M. Tarongi and A. Camps, "Multifrequency experimental radiometer with interference tracking for experiments over land and littoral: Meritxell," in *2009 IEEE Int. Geosci. Remote Sens. Symp.* IEEE, 2009, pp. IV–653–IV–656. (Cited on page 8.)

[20] Sparkfun, "SiGe GN3S Sampler v3." [Online]. Available: https://www.sparkfun.com/products/retired/10981 (Cited on pages 8 and 220.)

[21] N. Rodriguez-Alvarez, X. Bosch-Lluis, A. Camps, M. Vall-llossera, E. Valencia, J. Marchan-Hernandez, and I. Ramos-Perez, "Soil Moisture Retrieval Using GNSS-R Techniques: Experimental Results Over a Bare Soil Field," *IEEE Trans. Geosci. Remote Sens.*, vol. 47, no. 11, pp. 3616–3624, nov 2009. (Cited on pages xx, 8, 47, 50, 56, 139, 142, 170, 173, 174, 178, and 179.)

[22] A. Camps, N. Rodriguez-Alvarez, X. Bosch-Lluis, J. Marchan, I. Ramos-Perez, M. Segarra, L. Sagues, D. Tarrago, O. Cunado, R. Vilaseca, A. Tomas, J. Mas, and J. Guillamon, "PAU in SeoSAT: A proposed hybrid L-band microwave radiometer/GPS reflectometer to improve Sea Surface Salinity estimates from space," in *2008 Microw. Radiom. Remote Sens. Environ.* IEEE, mar 2008, pp. 1–4. (Cited on pages 8 and 122.)

[23] A. Camps, J. Marchan, E. Valencia, I. Ramos, X. Bosch-Lluis, N. Rodriguez, H. Park, A. Alcayde, A. Mollfulleda, J. Galindo, P. Martinez, S. Chavero, M. Angulo, and A. Rius, "PAU instrument aboard INTA MicroSat-1: A GNSS-R demonstration mission for sea state correction in L-band radiometry," in *2011 IEEE Int. Geosci. Remote Sens. Symp.* IEEE, jul 2011, pp. 4126–4129. (Cited on pages 8 and 122.)

[24] A. Alonso, A. Camps, D. Pascual, H. Park, A. Alcayde, S. Chavero, P. Martinez, L. Crespo, M. Angulo, and A. Rius, "PAU instrument aboard INTA MicroSat-1: Flight model tests," in *2012 IEEE Int. Geosci. Remote Sens. Symp.* IEEE, jul 2012, pp. 1038–1041. (Cited on page 8.)

[25] A. Alonso-Arroyo, A. Camps, D. Pascual, H. Park, A. Alcayde, S. Chavero, P. Martinez, L. Crespo, M. Angulo, and A. Rius, "PAU Instrument aboard INTA MicroSAT-1: Initial results of the FM model from an airborne experiment," in *2012 Work. Reflectometry Using GNSS Other Signals Oppor.* IEEE, oct 2012, pp. 1–5. (Cited on pages 8 and 227.)

[26] A. Camps, X. Bosch-Lluis, I. Ramos-Perez, J. F. Marchán-Hernández, N. Rodríguez, E. Valencia, J. M. Tarongi, A. Aguasca, and R. Acevo, "New Passive Instruments Developed for Ocean Monitoring at the Remote Sensing Lab—Universitat Politècnica de Catalunya," *Sensors*, vol. 9, no. 12, pp. 10 171–10 189, dec 2009. (Cited on page 8.)

[27] A. Camps, J. F. Marchan-Hernandez, X. Bosch-Lluis, N. Rodriguez-Alvarez, I. Ramos-Perez, E. Valencia, J. M. Tarongi, H. Park, H. Carreno-Luengo, A. Alonso-Arroyo, D. Pascual, R. Onrubia, G. Forte, and J. Querol, "Review of GNSS-R instruments and tools developed at the Universitat Politecnica de Catalunya-Barcelona tech," in *2014 IEEE Geosci. Remote Sens. Symp.* IEEE, jul 2014, pp. 3826–3829. (Cited on pages 8 and 102.)

[28] N. Rodriguez-Alvarez, "Contributions to earth observation using gnss-r opportunity signals," Ph.D. dissertation, Universitat piltecnica de Catalunya, 2011. [Online]. Available: http://tdx.cat/handle/10803/53636 (Cited on pages 9, 10, 11, 55, 71, 104, 170, 272, 296, and 297.)

[29] H. Carreno-Luengo, A. Camps, I. Perez-Ramos, and A. Rius, "Pycaro's instrument proof of concept," in *2012 Work. Reflectometry Using GNSS Other Signals Oppor. GNSS+R 2012*, 2012. (Cited on pages 9, 31, and 220.)

[30] R. Onrubia, D. Pascual, A. Camps, A. Alonso-Arroy, and H. Park, "MIR: The microwave interferometric reflectometer, a new airborne sensor for GNSS-R advanced research," in *2013 IEEE Int. Geosci. Remote Sens. Symp. - IGARSS.* IEEE, jul 2013, pp. 109–112. (Cited on page 9.)

[31] R. Onrubia, D. Pascual, A. Camps, A. Alonso-Arroyo, and H. Park, "The Microwave Interferometric Reflectometer. Part I: Front-end and beamforming description," in *2014 IEEE Geosci. Remote Sens. Symp.* IEEE, jul 2014, pp. 4046–4049. (Cited on page 9.)

[32] D. Pascual, R. Onrubia, A. Alonso-Arroyo, H. Park, and A. Camps, "The microwave interferometric reflectometer. Part II: Back-end and processor descriptions," in *2014 IEEE Geosci. Remote Sens. Symp.* IEEE, jul 2014, pp. 3782–3785. (Cited on page 9.)

[33] R. Onrubia, L. Garrucho, D. Pascual, H. Park, J. Querol, A. Alonso-Arroyo, and A. Camps, "Advances in the MIR instrument: Integration, control subsystem and analysis of the flight dynamics for beamsteering purposes," in *2015 IEEE Int. Geosci. Remote Sens. Symp.* IEEE, jul 2015, pp. 4765–4768. (Cited on page 9.)

[34] A. Alonso Arroyo, A. Camps, A. Aguasca, G. F. Forte, A. Monerris, C. Rüdiger, J. P. Walker, H. Park, D. Pascual, and R. Onrubia, "Dual-Polarization GNSS-R Interference Pattern Technique for Soil Moisture Mapping," *IEEE J. Sel. Top. Appl. Earth Obs. Remote Sens.*, vol. 7, no. 5, pp. 1533–1544, may 2014. (Cited on pages 9 and 71.)

[35] A. Alonso-Arroyo, A. Camps, A. Aguasca, G. Forte, A. Monerris, C. Rüdiger, J. P. Walker, H. Park, D. Pascual, and R. Onrubia, "Improving the Accuracy of Soil Moisture Retrievals Using the Phase Difference of the Dual-Polarization GNSS-R Interference Patterns," *IEEE Geosci. Remote Sens. Lett.*, vol. 11, no. 12, pp. 2090–2094, dec 2014. (Cited on pages 9, 71, and 192.)

[36] A. Alonso-Arroyo, G. Forte, A. Monerris, A. Camps, H. Park, D. Pascual, and R. Onrubia, "The Light Airborne Reflectometer for GNSS-R Observations (LARGO) instrument: Towards Soil Moisture retrievals," in *URSI Com. F Microw. Signatures 2013*, Espoo, 2013, p. 56. (Cited on page 9.)

[37] A. Alonso-Arroyo, A. Camps, A. Monerris, C. Rüdiger, J. P. Walker, G. Forte, D. Pascual, H. Park, and R. Onrubia, "The light airborne reflectometer for GNSS-R observations (LARGO) instrument: Initial results from airborne and Rover field campaigns," in *2014 IEEE Geosci. Remote Sens. Symp.* IEEE, jul 2014, pp. 4054–4057. (Cited on pages 9, 193, and 207.)

[38] A. Alonso-Arroyo, G. Forte, A. Camps, H. Park, D. Pascual, R. Onrubia, and R. Jove-Casulleras, "Soil Moisture mapping using forward scattered GPS L1 signals," in *2013 IEEE Int. Geosci. Remote Sens. Symp. - IGARSS*. IEEE, jul 2013, pp. 354–357. (Cited on page 9.)

[39] A. Alonso-Arroyo, S. Torrecilla, J. Querol, A. Camps, D. Pascual, H. Park, and R. Onrubia, "Two dedicated soil moisture experiments using the scatterometric properties of GNSS-reflectometry," in *2015 IEEE Int. Geosci. Remote Sens. Symp.* IEEE, jul 2015, pp. 3921–3924. (Cited on page 9.)

[40] N. Rodriguez-Alvarez, X. Bosch-Lluis, A. Camps, I. Ramos-Perez, E. Valencia, H. Park, and M. Vall-llossera, "Water level monitoring using the interference pattern GNSS-R technique," in *2011 IEEE Int. Geosci. Remote Sens. Symp.* IEEE, jul 2011, pp. 2334–2337. (Cited on pages xx, 11, 47, 56, 59, 170, 173, and 174.)

[41] Wikipedia, "Radio navigation." [Online]. Available: http://en.wikipedia.org/wiki/Radio{_}navigation (Cited on page 16.)

[42] P. B. Morris, R. R. Gupta, R. S. Warren, and P. M. Creamer, *Omega Navigation System Course Book Vol 1*, 1st ed., Alexandria, 1994. (Cited on page 16.)

[43] ——, *Omega Navigation System Course Book Vol 2*, 1st ed., Alexandria, 1994. (Cited on page 16.)

[44] B. Parkingson and J. Spilker, *Global Positioning System: Theory and Applications*, 3rd ed., P. Axelrad and P. Enge, Eds. American Institute of Aeronautics and Astronautics, Inc, 1996. (Cited on pages 16, 17, 20, 62, and 114.)

[45] P. Misra and P. Enge, *The Global Positioning System: Signals, measurements, and performance*, 2nd ed., 2011. (Cited on pages 17 and 20.)

[46] S. Gleason, *GNSS Applications and Methods*, first edit ed., S. Gleason and D. Gebre-Egziabher, Eds. Artech House Publishers, 2009. (Cited on pages 20, 21, 22, 23, and 197.)

[47] C. Hall and R. Cordey, "Multistatic Scatterometry," in *Int. Geosci. Remote Sens. Symp. 'Remote Sens. Mov. Towar. 21st Century'.* IEEE, 1988, pp. 561–562. (Cited on pages 22 and 198.)

[48] M. Martín-Neira, "A passive reflectometry and interferometry system(PARIS): Application to ocean altimetry," *ESA J.*, vol. 17, pp. 331–355, 1993. (Cited on pages 22, 26, 28, and 318.)

[49] J.-C. Auber, A. Bibaut, and J.-M. Rigal, "Characterization of Multipath on Land and Sea at GPS Frequencies," in *Proc. 7th Int. Tech. Meet. Satell. Div. Inst. Navig. (ION GPS 1994)*, Salt Lake City, 1994, pp. 1155–1171. (Cited on page 22.)

[50] S. J. Katzberg and J. L. Garrison, "Utilizing GPS to Determine Ionospheric Delay over the Ocean," Tech. Rep., 1996. [Online]. Available: http://ntrs.nasa.gov/archive/nasa/casi.ntrs.nasa.gov/19970005019.pdf (Cited on pages 22, 25, and 102.)

[51] J. Garrison and S. Katzberg, "Detection of ocean reflected GPS signals: theory and experiment," in *Proc. IEEE SOUTHEASTCON '97. 'Engineering New Century'.* IEEE, 1997, pp. 290–294. (Cited on pages 22 and 91.)

[52] V. Zavorotny and A. Voronovich, "Scattering of GPS signals from the ocean with wind remote sensing application," *IEEE Trans. Geosci. Remote Sens.*, vol. 38, no. 2, pp. 951–964, mar 2000. (Cited on pages 22, 23, 24, 25, 28, 62, 77, 78, 91, 207, 250, 251, 253, 255, 318, 319, and 338.)

[53] A. Komjathy, M. Armatys, D. Masters, P. Axelrad, V. Zavorotny, and S. Katzberg, "Retrieval of Ocean Surface Wind Speed and Wind Direction Using Reflected GPS Signals," *J. Atmos. Ocean. Technol.*, vol. 21, no. 3, pp. 515–526, mar 2004. (Cited on pages 23 and 255.)

[54] S. Lowe, P. Kroger, G. Franklin, J. LaBrecque, J. Lerma, M. Lough, M. Marcin, R. Muellerschoen, D. Spitzmesser, and L. Young, "A delay/Doppler-mapping receiver system for GPS-reflection remote sensing," *IEEE Trans. Geosci. Remote Sens.*, vol. 40, no. 5, pp. 1150–1163, may 2002. (Cited on page 23.)

[55] C. Zuffada, T. Elfouhaily, and S. Lowe, "Sensitivity analysis of wind vector measurements from ocean reflected GPS signals," *Remote Sens. Environ.*, vol. 88, no. 3, pp. 341–350, dec 2003. (Cited on pages 23 and 321.)

[56] T. Elfouhaily, D. Thompson, and L. Linstrom, "Delay-Doppler analysis of bistatically reflected signals from the ocean surface: theory and application," *IEEE Trans. Geosci. Remote Sens.*, vol. 40, no. 3, pp. 560–573, mar 2002. (Cited on pages 23, 79, and 251.)

[57] S. Gleason, S. Hodgart, Yiping Sun, C. Gommenginger, S. Mackin, M. Adjrad, and M. Unwin, "Detection and Processing of bistatically reflected GPS signals from low Earth orbit for the purpose of ocean remote sensing," *IEEE Trans. Geosci. Remote Sens.*, vol. 43, no. 6, pp. 1229–1241, jun 2005. (Cited on pages xix, 23, 29, and 255.)

[58] V. U. Zavorotny, S. Gleason, E. Cardellach, and A. Camps, "Tutorial on Remote Sensing Using GNSS Bistatic Radar of Opportunity," *IEEE Geosci. Remote Sens. Mag.*, vol. 2, no. 4, pp. 8–45, 2014. (Cited on pages 23, 26, 207, 252, and 263.)

[59] G. Ruffini and F. Soulat, "On the GNSS-R Interferometric Complex Field Coherence Time," 2004. (Cited on page 23.)

[60] M. Martin-Neira, M. Caparrini, J. Font-Rossello, S. Lannelongue, and C. Vallmitjana, "The PARIS concept: an experimental demonstration of sea surface altimetry using GPS reflected signals," *IEEE Trans. Geosci. Remote Sens.*, vol. 39, no. 1, pp. 142–150, 2001. (Cited on pages 23 and 28.)

[61] E. Cardellach, F. Fabra, O. Nogués-Correig, S. Oliveras, S. Ribó, and A. Rius, "GNSS-R ground-based and airborne campaigns for ocean, land, ice, and snow techniques: Application to the GOLD-RTR data sets," *Radio Sci.*, vol. 46, no. 6, pp. n/a–n/a, dec 2011. (Cited on pages 23 and 102.)

[62] A. Rius, E. Cardellach, and M. Martin-Neira, "Altimetric Analysis of the Sea-Surface GPS-Reflected Signals," *IEEE Trans. Geosci. Remote Sens.*, vol. 48, no. 4, pp. 2119–2127, apr 2010. (Cited on pages 23 and 228.)

[63] E. Cardellach, G. Ruffini, D. Pino, A. Rius, A. Komjathy, and J. L. Garrison, "Mediterranean Balloon Experiment: ocean wind speed sensing from the stratosphere, using GPS reflections," *Remote Sens. Environ.*, vol. 88, no. 3, pp. 351–362, dec 2003. (Cited on pages 23 and 255.)

[64] V. Zavorotny and A. Voronovich, "Bistatic GPS signal reflections at various polarizations from rough land surface with moisture content," in *IGARSS 2000. IEEE 2000 Int. Geosci. Remote Sens. Symp. Tak. Pulse Planet Role Remote Sens. Manag. Environ. Proc. (Cat. No.00CH37120)*, vol. 7, no. 303. IEEE, 2000, pp. 2852–2854. (Cited on pages 23 and 92.)

[65] D. Masters, V. Zavorotny, S. Katzberg, and W. Emery, "GPS signal scattering from land for moisture content determination," *IGARSS 2000. IEEE 2000 Int. Geosci. Remote Sens. Symp. Tak. Pulse Planet Role Remote Sens. Manag. Environ. Proc. (Cat. No.00CH37120)*, vol. 7, 2000. (Cited on pages 23 and 92.)

[66] A. Kavak, W. Vogel, and G. Xu, "Using GPS to measure ground complex permittivity," *Electron. Lett.*, vol. 34, no. 3, p. 254, 1998. (Cited on pages 23, 54, and 61.)

[67] K. D. Anderson, "Method for remotely determining sea surface roughness and wind speed at a water surface," pp. 1–13, 1998. [Online]. Available: http://www.google.com.ar/patents/US5808741 (Cited on pages 23 and 54.)

[68] ——, "Determination of water level and tides using interferometric observations of GPS signals," *J. Atmos. Ocean. Technol.*, vol. 17, no. 8, pp. 1118–1127, aug 2000. (Cited on page 23.)

[69] P. Beckmann and A. Spizzichino, *The Scattering of Electromagnetic Waves From Rough Surfaces*, artech hou ed. Artech Print on Demand, 1987. (Cited on pages 23, 25, 48, 76, 79, 80, 171, 172, 173, 250, 252, and 253.)

[70] R. De Roo and F. Ulaby, "Bistatic specular scattering from rough dielectric surfaces," *IEEE Trans. Antennas Propag.*, vol. 42, no. 2, pp. 220–231, 1994. (Cited on pages 23, 78, 252, 319, and 323.)

[71] ——, "A modified physical optics model of the rough surface reflection coefficient," in *IEEE Antennas Propag. Soc. Int. Symp. 1996 Dig.*, vol. 3. IEEE, pp. 1772–1775. (Cited on pages 23, 53, 77, and 319.)

[72] M. Martin-Neira, S. D'Addio, C. Buck, N. Floury, and R. Prieto-Cerdeira, "The PARIS Ocean Altimeter In-Orbit Demonstrator," *IEEE Trans. Geosci. Remote Sens.*, vol. 49, no. 6, pp. 2209–2237, jun 2011. (Cited on pages xx, 27, 28, 35, 90, 91, 321, and 322.)

[73] F. Martin, "Interferometric GNSS-R processing : modeling and analysis of advanced processing concepts for altimetry," Ph.D. dissertation, Universitat Politècnica de Catalunya - BarcelonaTech, 2015. [Online]. Available: http://tdx.cat/handle/10803/316583 (Cited on pages 27 and 28.)

[74] J. W. Goodman, "Some fundamental properties of speckle*," *J. Opt. Soc. Am.*, vol. 66, no. 11, p. 1145, nov 1976. (Cited on pages 27, 79, 81, and 318.)

[75] D. L. Fried, "Statistics of the laser radar cross section of a randomly rough targe," *J. Opt. Soc. Am.*, vol. 66, no. 11, p. 1150, nov 1976. (Cited on pages 27 and 318.)

[76] F. Martin, A. Camps, H. Park, S. DaAddio, M. Martin-Neira, and D. Pascual, "Cross-Correlation Waveform Analysis for Conventional and Interferometric GNSS-R Approaches," *IEEE J. Sel. Top. Appl. Earth Obs. Remote Sens.*, vol. 7, no. 5, pp. 1560–1572, may 2014. (Cited on pages 28 and 321.)

[77] S. T. Lowe, J. L. LaBrecque, C. Zuffada, L. J. Romans, L. E. Young, and G. A. Hajj, "First spaceborne observation of an Earth-reflected GPS signal," *Radio Sci.*, vol. 37, no. 1, pp. 7–1–7–28, jan 2002. (Cited on page 28.)

[78] S. Gleason, "Remote Sensing of Ocean, Ice and Land Surfaces Using Bistatically Scattered GNSS Signals From Low Earth Orbit," Ph.D. dissertation, University of Surrey, 2006. (Cited on pages xix, xxxiii, 29, 250, 252, and 255.)

[79] M. Unwin, "The SGR-ReSI Experiment on the TechDemoSat-1 Mission," in *TechDemoSat-1 User Consult. Work.*, 2015. (Cited on pages xix, xxxiii, 30, 31, and 207.)

[80] H. Carreno-Luengo, A. Camps, J. Munoz, D. Vidal, P. Vila, A. Amezaga, A. Bolet, J. Jane, R. Olive, J. Carola, N. Catarino, M. Hagenfeldt, P. Palomo, and S. Cornara, "3CAT-2; AN EXPERIMENTAL NANO-SATELLITE FOR GNSS-R EARTH OBSERVATION: MISSION CONCEPT AND ANALYSIS," 2016. (Cited on pages xxxiii, 30, and 32.)

[81] H. Carreno-Luengo, A. Camps, I. Perez-Ramos, G. Forte, R. Onrubia, and R. Diez, "3Cat-2: A P(Y) and C/A GNSS-R experimental nano-satellite mission," in *2013 IEEE Int. Geosci. Remote Sens. Symp. - IGARSS*. IEEE, jul 2013, pp. 843–846. (Cited on pages xxxiii, 30, and 32.)

[82] H. Carreno-Luengo, A. Amezaga, A. Bolet, D. Vidal, J. Jane, J. Munoz, R. Olive, A. Camps, J. Carola, N. Catarino, M. Hagenfeldt, P. Palomo, and S. Cornara, "3CAT-2: A 6U CubeSat-based multi-constellation, dual-polarization, and dual-frequency GNSS-R and GNSS-RO experimental mission," in *2015 IEEE Int. Geosci. Remote Sens. Symp.* IEEE, jul 2015, pp. 5115–5118. (Cited on pages xxxiii, 30, and 32.)

[83] A. Camps, R. Jove-Casulleras, and H. Carreno-Luengo, "UPC NanoSat Lab," 2013. [Online]. Available: http://www.tsc.upc.edu/nanosatlab/ (Cited on page 31.)

[84] H. Carreno-Luengo, A. Camps, J. Querol, G. Forte, R. Onrubia, and R. Diez, "A stratospheric balloon GNSS-R experiment: The 3Cat-2 project in DLR/SNSB BEXUS," in *2014 IEEE Geosci. Remote Sens. Symp.* IEEE, jul 2014, pp. 3626–3629. (Cited on pages xxxiii, 31, and 32.)

[85] H. Carreno-Luengo, A. Amezaga, A. Bolet, D. Vidal, J. Jane, J. Munoz, R. Olive, and A. Camps, "Multi-constellation, dual-polarization, and dual-frequency GNSS-R stratospheric balloon experiment over boreal forests," in *2015 IEEE Int. Geosci. Remote Sens. Symp.* IEEE, jul 2015, pp. 5107–5110. (Cited on pages xxxiii, 31, and 32.)

[86] H. Carreno-Luengo and A. Camps, "First Dual-Band Multiconstellation GNSS-R Scatterometry Experiment Over Boreal Forests From a Stratospheric Balloon," *IEEE J. Sel. Top. Appl. Earth Obs. Remote Sens.*, pp. 1–1, 2015. (Cited on pages xxxiii, 31, and 32.)

[87] H. Carreno-Luengo, A. Camps, J. Querol, and G. Forte, "First Results of a GNSS-R Experiment From a Stratospheric Balloon Over Boreal Forests," *IEEE Trans. Geosci. Remote Sens.*, vol. 54, no. 5, pp. 2652–2663, may 2016. (Cited on pages xxxiii, 31, and 32.)

[88] National Aeronautics and Space Administration, "Cyclone Global Navigation Satellite System," Tech. Rep., 2015. [Online]. Available: file:///C:/Users/aalonso/Desktop/PhD{_}Thesis{_}Dissertation/02{_}Chapter{_}2/figures/cygnss-fs-2015-05-230-larc.pdf (Cited on pages xx, xxxiii, 33, and 34.)

[89] R. Rose, C. Ruf, D. Rose, M. Brummitt, and A. Ridley, "The CYGNSS flight segment; A major NASA science mission enabled by micro-satellite technology," in *2013 IEEE Aerosp. Conf.* IEEE, mar 2013, pp. 1–13. (Cited on pages xxxiii and 33.)

[90] ESA, "GEROS overview." [Online]. Available: http://www.esa.int/Our{_}Activities/Observing{_}the{_}Earth/Mapping{_}sea{_}surface{_}from{_}the{_}Space{_}Station (Cited on page 32.)

[91] ——, "GEROS Mission Requirements Document," European Space Agency, Tech. Rep., 2013. [Online]. Available: http://esamultimedia.esa.int/docs/EarthObservation/GEROS{_}MRD.pdf (Cited on page 32.)

[92] J. H. Poynting, "On the Transfer of Energy in the Electromagnetic Field," *Philos. Trans. R. Soc. London*, vol. 175, pp. 343–361, jan 1884. (Cited on page 40.)

[93] V. U. Zavorotny, K. M. Larson, J. J. Braun, E. E. Small, E. D. Gutmann, and A. L. Bilich, "A Physical Model for GPS Multipath Caused by Land Reflections: Toward Bare Soil Moisture Retrievals," *IEEE J. Sel. Top. Appl. Earth Obs. Remote Sens.*, vol. 3, no. 1, pp. 100–110, mar 2010. (Cited on pages xx, 41, 61, 62, 64, 67, 70, 182, and 207.)

[94] J. R. Wang and T. J. Schmugge, "An Empirical Model for the Complex Dielectric Permittivity of Soils as a Function of Water Content," *IEEE Trans. Geosci. Remote Sens.*, vol. GE-18, no. 4, pp. 288–295, oct 1980. (Cited on pages xxxiii, 42, 43, 138, and 192.)

[95] G. Lerondel and R. Romestain, "Fresnel coefficients of a rough interface," *Appl. Phys. Lett.*, vol. 74, no. 19, p. 2740, 1999. (Cited on page 43.)

[96] W. Gordon, "Far-field approximations to the Kirchoff-Helmholtz representations of scattered fields," *IEEE Trans. Antennas Propag.*, vol. 23, no. 4, pp. 590–592, jul 1975. (Cited on page 44.)

[97] A. Alonso-Arroyo, A. Camps, H. Park, D. Pascual, R. Onrubia, and F. Martin, "Retrieval of Significant Wave Height and Mean Sea Surface Level Using the GNSS-R Interference Pattern Technique: Results From a Three-Month Field Campaign," *IEEE Trans. Geosci. Remote Sens.*, vol. 53, no. 6, pp. 3198–3209, jun 2015. (Cited on pages 47, 72, and 207.)

[98] N. Rodriguez-Alvarez, X. Bosch-Lluis, A. Camps, A. Aguasca, M. Vall-llossera, E. Valencia, I. Ramos-Perez, and H. Park, "Review of crop growth and soil moisture monitoring from a ground-based instrument implementing the Interference Pattern GNSS-R Technique," *Radio Sci.*, vol. 46, no. 6, pp. n/a–n/a, dec 2011. (Cited on pages xx, 47, 56, 58, 173, and 174.)

[99] O. Landron, M. Feuerstein, and T. Rappaport, "A comparison of theoretical and empirical reflection coefficients for typical exterior wall surfaces in a mobile radio environment," *IEEE Trans. Antennas Propag.*, vol. 44, no. 3, pp. 341–351, mar 1996. (Cited on page 53.)

[100] V. Zavorotny and A. Voronovich, "Two-scale model and ocean radar Doppler spectra at moderate- and low-grazing angles," *IEEE Trans. Antennas Propag.*, vol. 46, no. 1, pp. 84–92, 1998. (Cited on pages 53 and 256.)

[101] Newport Corporation, "Theory of Lloyd's Mirror Interferometer (DS-091201)," Newport Corporation, Tech. Rep., 2012. [Online]. Available: http://assets.newport.com/webdocuments-en/images/app{_}note{_}49{_}lloyds{_}mirror{_}interf.pdf (Cited on page 54.)

[102] A. Kavak, G. Xu, and W. Vogel, "GPS Multipath Fade Measurements to Determine L-Band Ground Reflectivity Properties," in *Proc. Twent. NASA Propag. Exp. Meet. (NAPEX 20) Adv. Commun. Technol. Satell. Propag. Stud. Miniworkshop; 257-263; (JPL-Publ-96-20); (SEE 19970004346)*, Texas, 1996, pp. 257–263. (Cited on pages 54 and 61.)

[103] N. Rodriguez-Alvarez, J. F. Marchan-Hernandez, A. Camps, X. Bosch-Lluis, E. Valencia, I. Ramos-Perez, M. Valf-Llossera, A. Monern, J. Martinez-Fernandez, C. Perez-Gmerrez, G. BaroncM-Jurncch, N. Sanchez-Martin, and J. M. Nieto, "Topographic profile retrieval using the Interference Pattern GNSS-R technique," in *2009 IEEE Int. Geosci. Remote Sens. Symp.* IEEE, jul 2009, pp. III–420–III–423. (Cited on page 55.)

[104] N. Rodriguez-Alvarez, A. Monerris, X. Bosch-Lluis, A. Camps, M. Vall-Llossera, J. F. Marchan-Hernandez, I. Ramos-Perez, E. Valencia, J. Martinez-Fernandez, N. Sanchez-Martin, G. Baroncini-Turricchid, and C. Perez-Gutierrez, "Soil moisture and vegetation height retrieval using GNSS-R techniques," in *2009 IEEE Int. Geosci. Remote Sens. Symp.* IEEE, 2009, pp. III–869–III–872. (Cited on page 56.)

[105] N. Rodriguez-Alvarez, A. Camps, M. Vall-llossera, X. Bosch-Lluis, A. Monerris, I. Ramos-Perez, E. Valencia, J. F. Marchan-Hernandez, J. Martinez-Fernandez, G. Baroncini-Turricchia, C. Perez-Gutierrez, and N. Sanchez, "Land Geophysical Parameters Retrieval Using the Interference Pattern GNSS-R Technique," *IEEE Trans. Geosci. Remote Sens.*, vol. 49, no. 1, pp. 71–84, jan 2011. (Cited on pages xx, 56, 57, 58, 170, 173, 174, and 207.)

[106] N. Rodriguez-Alvarez, A. Aguasca, E. Valencia, X. Bosch-Lluis, A. Camps, I. Ramos-Perez, H. Park, and M. Vall-llossera, "Snow Thickness Monitoring Using GNSS Measurements," *IEEE Geosci. Remote Sens. Lett.*, vol. 9, no. 6, pp. 1109–1113, nov 2012. (Cited on pages xx, 59, 60, and 170.)

[107] K. M. Larson, E. E. Small, E. Gutmann, A. Bilich, P. Axelrad, and J. Braun, "Using GPS multipath to measure soil moisture fluctuations: initial results," *GPS Solut.*, vol. 12, no. 3, pp. 173–177, jul 2008. (Cited on pages 64 and 65.)

[108] K. M. Larson, E. E. Small, E. D. Gutmann, A. L. Bilich, J. J. Braun, and V. U. Zavorotny, "Use of GPS receivers as a soil moisture network for water cycle studies," *Geophys. Res. Lett.*, vol. 35, no. 24, p. L24405, dec 2008. (Cited on page 64.)

[109] E. G. Njoku and D. Entekhabi, "Passive microwave remote sensing of soil moisture," pp. 101–129, 1996. (Cited on page 64.)

[110] K. M. Larson, J. J. Braun, E. E. Small, V. U. Zavorotny, E. D. Gutmann, and A. L. Bilich, "GPS Multipath and Its Relation to Near-Surface Soil Moisture Content," *IEEE J. Sel. Top. Appl. Earth Obs. Remote Sens.*, vol. 3, no. 1, pp. 91–99, mar 2010. (Cited on pages 64, 65, and 207.)

[111] C. C. Chew, E. E. Small, K. M. Larson, and V. U. Zavorotny, "Effects of Near-Surface Soil Moisture on GPS SNR Data: Development of a Retrieval Algorithm for Soil Moisture," *IEEE Trans. Geosci. Remote Sens.*, vol. 52, no. 1, pp. 537–543, jan 2014. (Cited on page 64.)

[112] E. E. Small, K. M. Larson, and J. J. Braun, "Sensing vegetation growth with reflected GPS signals," *Geophys. Res. Lett.*, vol. 37, no. 12, pp. n/a–n/a, jun 2010. (Cited on page 65.)

[113] K. M. Larson and E. E. Small, "Normalized Microwave Reflection Index: A Vegetation Measurement Derived From GPS Networks," *IEEE J. Sel. Top. Appl. Earth Obs. Remote Sens.*, vol. 7, no. 5, pp. 1501–1511, may 2014. (Cited on page 65.)

[114] E. E. Small, K. M. Larson, and W. K. Smith, "Normalized Microwave Reflection Index: Validation of Vegetation Water Content Estimates From Montana Grasslands," *IEEE J. Sel. Top. Appl. Earth Obs. Remote Sens.*, vol. 7, no. 5, pp. 1512–1521, may 2014. (Cited on page 65.)

[115] C. C. Chew, E. E. Small, K. M. Larson, and V. U. Zavorotny, "Vegetation Sensing Using GPS-Interferometric Reflectometry: Theoretical Effects of Canopy Parameters on Signal-to-Noise Ratio Data," *IEEE Trans. Geosci. Remote Sens.*, vol. 53, no. 5, pp. 2755–2764, may 2015. (Cited on page 66.)

[116] C. Chew, E. E. Small, and K. M. Larson, "An algorithm for soil moisture estimation using GPS-interferometric reflectometry for bare and vegetated soil," *GPS Solut.*, may 2015. (Cited on page 66.)

[117] K. M. Larson, E. D. Gutmann, V. U. Zavorotny, J. J. Braun, M. W. Williams, and F. G. Nievinski, "Can we measure snow depth with GPS receivers?" *Geophys. Res. Lett.*, vol. 36, no. 17, p. L17502, sep 2009. (Cited on pages xxi, 66, and 67.)

[118] N. R. Lomb, "Least-squares frequency analysis of unequally spaced data," *Astrophys. Space Sci.*, vol. 39, no. 2, pp. 447–462, feb 1976. (Cited on pages 66 and 183.)

[119] E. D. Gutmann, K. M. Larson, M. W. Williams, F. G. Nievinski, and V. Zavorotny, "Snow measurement by GPS interferometric reflectometry: an evaluation at Niwot Ridge, Colorado," *Hydrol. Process.*, vol. 26, no. 19, pp. 2951–2961, sep 2012. (Cited on page 67.)

[120] K. M. Larson and F. G. Nievinski, "GPS snow sensing: results from the EarthScope Plate Boundary Observatory," *GPS Solut.*, vol. 17, no. 1, pp. 41–52, jan 2013. (Cited on page 67.)

[121] F. G. Nievinski and K. M. Larson, "Inverse Modeling of GPS Multipath for Snow Depth Estimation—Part I: Formulation and Simulations," *IEEE Trans. Geosci. Remote Sens.*, vol. 52, no. 10, pp. 6555–6563, oct 2014. (Cited on page 67.)

[122] ——, "Inverse Modeling of GPS Multipath for Snow Depth Estimation—Part II: Application and Validation," *IEEE Trans. Geosci. Remote Sens.*, vol. 52, no. 10, pp. 6564–6573, oct 2014. (Cited on page 68.)

[123] J. S. Löfgren, R. Haas, and J. M. Johansson, "Monitoring coastal sea level using reflected GNSS signals," *Adv. Sp. Res.*, vol. 47, no. 2, pp. 213–220, jan 2011. (Cited on pages 68 and 170.)

[124] K. M. Larson, J. S. Löfgren, and R. Haas, "Coastal sea level measurements using a single geodetic GPS receiver," *Adv. Sp. Res.*, vol. 51, no. 8, pp. 1301–1310, apr 2013. (Cited on pages xxi, 68, 69, and 170.)

[125] K. M. Larson, R. D. Ray, F. G. Nievinski, and J. T. Freymueller, "The Accidental Tide Gauge: A GPS Reflection Case Study From Kachemak Bay, Alaska," *IEEE Geosci. Remote Sens. Lett.*, vol. 10, no. 5, pp. 1200–1204, sep 2013. (Cited on pages 68, 70, and 170.)

[126] J. S. Löfgren, R. Haas, and H.-G. Scherneck, "Sea level time series and ocean tide analysis from multipath signals at five GPS sites in different parts of the world," *J. Geodyn.*, vol. 80, pp. 66–80, oct 2014. (Cited on pages 69, 170, and 188.)

[127] J. S. Löfgren and R. Haas, "Sea level measurements using multi-frequency GPS and GLONASS observations," *EURASIP J. Adv. Signal Process.*, vol. 2014, no. 1, p. 50, 2014. (Cited on pages 69, 70, and 170.)

[128] T. Hobiger, R. Haas, and J. S. Löfgren, "GLONASS-R: GNSS reflectometry with a Frequency Division Multiple Access-based satellite navigation system," *Radio Sci.*, vol. 49, no. 4, pp. 271–282, apr 2014. (Cited on page 70.)

[129] N. Roussel, G. Ramillien, F. Frappart, J. Darrozes, A. Gay, R. Biancale, N. Striebig, V. Hanquiez, X. Bertin, and D. Allain, "Sea level monitoring and sea state estimate using a single geodetic receiver," *Remote Sens. Environ.*, vol. 171, pp. 261–277, dec 2015. (Cited on pages 70 and 170.)

[130] F. Martin, A. Camps, F. Fabra, A. Rius, M. Martin-Neira, S. D'Addio, and A. Alonso, "Mitigation of Direct Signal Cross-Talk and Study of the Coherent Component in GNSS-R," *IEEE Geosci. Remote Sens. Lett.*, vol. 12, no. 2, pp. 279–283, feb 2015. (Cited on page 77.)

[131] P. Woodward, "Radar ambiguity analysis, Technical Note No. 731," Tech. Rep., 1967. (Cited on pages 78, 251, 318, and 326.)

[132] J. Marchan-Hernandez, A. Camps, N. Rodriguez-Alvarez, E. Valencia, X. Bosch-Lluis, and I. Ramos-Perez, "An Efficient Algorithm to the Simulation of Delay–Doppler Maps of Reflected Global Navigation Satellite System Signals," *IEEE Trans. Geosci. Remote Sens.*, vol. 47, no. 8, pp. 2733–2740, aug 2009. (Cited on pages 79 and 251.)

[133] D. Pascual, A. Camps, F. Martin, H. Park, A. A. Arroyo, and R. Onrubia, "Precision Bounds in GNSS-R Ocean Altimetry," *IEEE J. Sel. Top. Appl. Earth Obs. Remote Sens.*, vol. 7, no. 5, pp. 1416–1423, may 2014. (Cited on pages 79 and 251.)

[134] A. Abdi, C. Tepedelenlioglu, M. Kaveh, and G. Giannakis, "On the estimation of the K parameter for the Rice fading distribution," *IEEE Commun. Lett.*, vol. 5, no. 3, pp. 92–94, mar 2001. (Cited on pages 84, 85, and 86.)

[135] K. K. Talukdar, "Estimation of the parameters of the Rice distribution," *J. Acoust. Soc. Am.*, vol. 89, no. 3, p. 1193, 1991. (Cited on page 85.)

[136] C. Tepedelenlioglu, A. Abdi, and G. Giannakis, "The ricean K factor: Estimation and performance analysis," *IEEE Trans. Wirel. Commun.*, vol. 24, no. 5, pp. 799–810, may 2003. (Cited on pages 85 and 86.)

[137] Y. Chen and N. Beaulieu, "Estimation of Ricean and Nakagami distribution parameters using noisy samples," in *2004 IEEE Int. Conf. Commun. (IEEE Cat. No.04CH37577)*. IEEE, 2004, pp. 562–566 Vol.1. (Cited on page 85.)

[138] A. Morabito, D. Percival, J. Sahr, Z. Berkowitz, and L. Vertatschitsch, "Ricean parameter estimation using phase information in low SNR environments," *IEEE Commun. Lett.*, vol. 12, no. 4, pp. 244–246, apr 2008. (Cited on pages 86 and 87.)

[139] C. Strassle, D. Megnet, H. Mathis, and C. Burgi, "The Squaring-Loss Paradox," in *Proc. 20th Int. Tech. Meet. Satell. Div. Inst. Navig. (ION GNSS 2007)*, 2007, pp. 2715–2722. (Cited on page 88.)

[140] J. L. Lawson and G. E. Ulhenbeck, *Threshold signals*, 1st ed., L. N. Ridenour and G. B. Collins, Eds. McGraw-Hill, 1950. (Cited on page 88.)

[141] S. Lowe, "Voltage Signal-to-Noise Ratio (SNR) Nonlinearity Resulting From Incoherent Summations (TMO 42-137)," Tech. Rep., 1999. [Online]. Available: http://ipnpr.jpl.nasa.gov/progress{_}report/42-137/137E.pdf (Cited on page 88.)

[142] R. Thompson, J. M. Moran, and G. W. Swenson, *Interferometry and Synthesis in Radio Astronomy*, 2nd ed., 2001. (Cited on page 89.)

[143] E. Cardellach, "Sea Surface Determination Using GNSS Reflected Signals," Ph.D. dissertation, Universitat Politècnica de Catalunya, 2001. [Online]. Available: http://www.ice.csic.es/es/view{_}theses.php?TID=2 (Cited on page 89.)

[144] J. Garrison, A. Komjathy, V. Zavorotny, and S. Katzberg, "Wind speed measurement using forward scattered GPS signals," *IEEE Trans. Geosci. Remote Sens.*, vol. 40, no. 1, pp. 50–65, 2002. (Cited on pages 91 and 255.)

[145] D. Masters, P. Axelrad, and S. Katzberg, "Initial results of land-reflected GPS bistatic radar measurements in SMEX02," *Remote Sens. Environ.*, vol. 92, no. 4, pp. 507–520, sep 2004. (Cited on pages xxi, 92, 93, 113, and 268.)

[146] S. J. Katzberg, O. Torres, M. S. Grant, and D. Masters, "Utilizing calibrated GPS reflected signals to estimate soil reflectivity and dielectric constant: Results from SMEX02," *Remote Sens. Environ.*, vol. 100, no. 1, pp. 17–28, jan 2006. (Cited on pages xxi, 92, 93, 113, and 268.)

[147] A. Egido, M. Caparrini, G. Ruffini, S. Paloscia, E. Santi, L. Guerriero, N. Pierdicca, and N. Floury, "Global Navigation Satellite Systems Reflectometry as a Remote Sensing Tool for Agriculture," *Remote Sens.*, vol. 4, no. 12, pp. 2356–2372, aug 2012. (Cited on pages xxi, 93, 94, 95, 96, and 113.)

[148] A. Egido, S. Paloscia, E. Motte, L. Guerriero, N. Pierdicca, M. Caparrini, E. Santi, G. Fontanelli, and N. Floury, "Airborne GNSS-R Polarimetric Measurements for Soil Moisture and Above-Ground Biomass Estimation," *IEEE J. Sel. Top. Appl. Earth Obs. Remote Sens.*, vol. 7, no. 5, pp. 1522–1532, may 2014. (Cited on pages xxi, 94, 96, 97, 113, and 207.)

[149] A. Egido, "GNSS Reflectometry for Land Remote Sensing Applications," Ph.D. dissertation, Universitat Politècnica de Catalunya, 2013. (Cited on pages 98, 102, 207, and 300.)

[150] A. Rius, F. Fabra, S. Ribo, J. C. Arco, S. Oliveras, E. Cardellach, A. Camps, O. Nogues-Correig, J. Kainulainen, E. Rohue, and M. Martin-Neira, "PARIS Interferometric Technique proof of concept: Sea surface altimetry measurements," in *2012 IEEE Int. Geosci. Remote Sens. Symp.* IEEE, jul 2012, pp. 7067–7070. (Cited on page 102.)

[151] E. Cardellach, A. Rius, M. Martin-Neira, F. Fabra, O. Nogues-Correig, S. Ribo, J. Kainulainen, A. Camps, and S. D'Addio, "Consolidating the Precision of Interferometric GNSS-R Ocean Altimetry Using Airborne Experimental Data," *IEEE Trans. Geosci. Remote Sens.*, vol. 52, no. 8, pp. 4992–5004, aug 2014. (Cited on page 102.)

[152] E. Research, "USRP," 2016. [Online]. Available: https://www.ettus.com/product (Cited on page 102.)

[153] C. A. Balanis, *ANTENNA THEORY: ANALYSIS AND DESIGN*, third edit ed. John Wiley & Sons Inc., 2005. (Cited on pages xxi and 106.)

[154] D. M. Pozar, *Microwave Engineering, 3rd*, 2005. (Cited on pages 105 and 137.)

[155] AntennaLab, "Anechoic Chamber," 2015. [Online]. Available: http://www.tsc.upc.edu/antennalab/ (Cited on pages 108, 114, 212, and 276.)

[156] Sparkfun, "Venus GPS receiver," 2016. [Online]. Available: https://www.sparkfun.com/products/11058 (Cited on page 108.)

[157] E. Valencia, A. Camps, X. Bosch-Lluis, N. Rodriguez-Alvarez, I. Ramos-Perez, F. Eugenio, and J. Marcello, "On the Use of GNSS-R Data to Correct L-Band Brightness Temperatures for Sea-State Effects: Results of the ALBATROSS Field Experiments," *IEEE Trans. Geosci. Remote Sens.*, vol. 49, no. 9, pp. 3225–3235, sep 2011. (Cited on pages 122 and 255.)

[158] N. Rodriguez-Alvarez, X. Bosch-Lluis, A. Camps, I. Ramos-Perez, E. Valencia, H. Park, and M. Vall-llossera, "Vegetation Water Content Estimation Using GNSS Measurements," *IEEE Geosci. Remote Sens. Lett.*, vol. 9, no. 2, pp. 282–286, mar 2012. (Cited on pages xxix, 128, 272, 273, 274, 275, and 292.)

[159] A. B. Smith, J. P. Walker, A. W. Western, R. I. Young, K. M. Ellett, R. C. Pipunic, R. B. Grayson, L. Siriwardena, F. H. S. Chiew, and H. Richter, "The Murrumbidgee soil moisture monitoring network data set," *Water Resour. Res.*, vol. 48, no. 7, pp. n/a–n/a, jul 2012. (Cited on page 136.)

[160] A. Hawdon, D. McJannet, and J. Wallace, "Calibration and correction procedures for cosmic-ray neutron soil moisture probes located across Australia," *Water Resour. Res.*, vol. 50, no. 6, pp. 5029–5043, jun 2014. (Cited on page 136.)

[161] "SDI-12 on OzNet network." [Online]. Available: http://www.oznet.org.au/SDI-12.html (Cited on page 144.)

[162] R. Hamdesign, "Big Ras Motor," 2016. [Online]. Available: http://www.rfhamdesign.com/products/spid-hr-antenna-rotators/bigrashr/index.php (Cited on page 151.)

[163] G. F. Forte Véliz, "Contributions to radio frequency interference detection and mitigation in Earth observation," PhD Thesis, Universitat Politècnica de Catalunya, 2013. [Online]. Available: http://www.tdx.cat/handle/10803/285320 (Cited on page 153.)

[164] D. Devices, "ECH-5 Soil Moisture Probes," 2016. [Online]. Available: https://www.decagon.com/en/soils/volumetric-water-content-sensors/ec-5-lowest-cost-vwc/ (Cited on pages xxiv and 158.)

[165] S. Torrecilla Miguel del Corral, "GNSS Reflectometer implementation and data processing software development to Monitor Soil Moisture," Degree, Universitat Politècnica de Catalunya, 2015. [Online]. Available: http://hdl.handle.net/2099.1/26321 (Cited on page 161.)

[166] J. S. Löfgren, R. Haas, H.-G. Scherneck, and M. S. Bos, "Three months of local sea level derived from reflected GNSS signals," *Radio Sci.*, vol. 46, no. 6, pp. n/a–n/a, dec 2011. (Cited on page 170.)

[167] B. Kinsman, *Wind Waves: Their Generation and Propagation on the Ocean Surface*, 1st ed. Mineola, New York: Dover Phoenix Editions, 1984. (Cited on pages 171 and 173.)

[168] Y. Karasawa and T. Shiokawa, "Characteristics of L-band multipath fading due to sea surface reflection," *IEEE Trans. Antennas Propag.*, vol. 32, no. 6, pp. 618–623, jun 1984. (Cited on page 172.)

[169] a.T. Manninen, "Multiscale Surface Roughness and Backscattering - Summary," *J. Electromagn. Waves Appl.*, vol. 11, no. 4, pp. 471–475, jan 1997. (Cited on page 173.)

[170] F. Hogben, N.; Lumb, *Ocean Wave Statistics: A Statistical Survey of Wave Characteristics Estimated Usually from Voluntary Observing Ships Sailing Along the Shipping Routes of the World*. H.M. Stationery Office, 1967. (Cited on page 173.)

[171] Vega, "Radar VEGAPULS62," 2016. [Online]. Available: https://www.vega.com/en/Products/Product-catalog/Level/Radar/VEGAPULS-62 (Cited on page 174.)

[172] L. Cohen, "Time-frequency distributions-a review," *Proc. IEEE*, vol. 77, no. 7, pp. 941–981, jul 1989. (Cited on page 177.)

[173] P. Stoica, "Spectral Analysis of Nonuniformly Sampled Data: A New Approach Versus the Periodogram," *IEEE Trans. Signal Process.*, vol. 57, no. 3, pp. 843–858, mar 2009. (Cited on pages 183, 184, and 299.)

[174] J. D. Scargle, "Studies in astronomical time series analysis. II - Statistical aspects of spectral analysis of unevenly spaced data," *Astrophys. J.*, vol. 263, p. 835, dec 1982. (Cited on page 183.)

[175] M. Zechmeister and M. Kürster, "The generalised Lomb-Scargle periodogram," *Astron. Astrophys.*, vol. 496, no. 2, pp. 577–584, mar 2009. (Cited on page 183.)

[176] P. Stoica and N. Sandgren, "Spectral analysis of irregularly-sampled data: Paralleling the regularly-sampled data approaches," *Digit. Signal Process.*, vol. 16, no. 6, pp. 712–734, nov 2006. (Cited on pages 183 and 184.)

[177] V. Zavorotny, A. Gasiewski, R. Zamora, E. McIntyre, V. Leuski, and V. Irisov, "Stationary L-Band Radiometry for Seasonal Measurements of Soil Moisture," in *2006 IEEE Int. Symp. Geosci. Remote Sens.* IEEE, jul 2006, pp. 2028–2031. (Cited on page 192.)

[178] O. Merlin, A. Chehbouni, J. Walker, R. Panciera, and Y. Kerr, "A Simple Method to Disaggregate Passive Microwave-Based Soil Moisture," *IEEE Trans. Geosci. Remote Sens.*, vol. 46, no. 3, pp. 786–796, mar 2008. (Cited on pages 192, 209, and 215.)

[179] O. Merlin, J. Walker, A. Chehbouni, and Y. Kerr, "Towards deterministic downscaling of SMOS soil moisture using MODIS derived soil evaporative efficiency," *Remote Sens. Environ.*, vol. 112, no. 10, pp. 3935–3946, oct 2008. (Cited on pages 192, 209, and 215.)

[180] M. Piles, A. Camps, M. Vall-llossera, I. Corbella, R. Panciera, C. Rudiger, Y. H. Kerr, and J. Walker, "Downscaling SMOS-Derived Soil Moisture Using MODIS Visible/Infrared Data," *IEEE Trans. Geosci. Remote Sens.*, vol. 49, no. 9, pp. 3156–3166, sep 2011. (Cited on pages 192, 209, and 215.)

[181] M. Hallikainen, F. Ulaby, M. Dobson, M. El-rayes, and L.-k. Wu, "Microwave Dielectric Behavior of Wet Soil-Part 1: Empirical Models and Experimental Observations," *IEEE Trans. Geosci. Remote Sens.*, vol. GE-23, no. 1, pp. 25–34, jan 1985. (Cited on page 192.)

[182] M. Dobson, F. Ulaby, M. Hallikainen, and M. El-rayes, "Microwave Dielectric Behavior of Wet Soil-Part II: Dielectric Mixing Models," *IEEE Trans. Geosci. Remote Sens.*, vol. GE-23, no. 1, pp. 35–46, jan 1985. (Cited on page 192.)

[183] V. Mironov, M. Dobson, V. Kaupp, S. Komarov, and V. Kleshchenko, "Generalized refractive mixing dielectric model for moist soils," *IEEE Trans. Geosci. Remote Sens.*, vol. 42, no. 4, pp. 773–785, apr 2004. (Cited on page 192.)

[184] S. Paloscia and P. Pampaloni, "Microwave polarization index for monitoring vegetation growth," *IEEE Trans. Geosci. Remote Sens.*, vol. 26, no. 5, pp. 617–621, 1988. (Cited on page 193.)

[185] J.-P. Wigneron, J.-C. Calvet, T. Pellarin, A. Van de Griend, M. Berger, and P. Ferrazzoli, "Retrieving near-surface soil moisture from microwave radiometric observations: current status and future plans," *Remote Sens. Environ.*, vol. 85, no. 4, pp. 489–506, jun 2003. (Cited on page 193.)

[186] W. H. McMaster, "Polarization and the Stokes Parameters," *Am. J. Phys.*, vol. 22, no. 6, p. 351, 1954. (Cited on page 193.)

[187] ——, "Matrix Representation of Polarization," *Rev. Mod. Phys.*, vol. 33, no. 1, pp. 8–28, jan 1961. (Cited on page 193.)

[188] J. P. Randa, J. Lahtinen, A. Camps, A. Gasiewski, M. Hallikainen, D. Leine V, M. Martin-Neira, J. Piepmeier, P. Rosenkranz, C. Ruf, J. Shiue, and N. Skou, "Recommended Terminology For Microwave Radiometry," National Institute of Standards and Technology (NIST), Boulder, Tech. Rep., 2008. [Online]. Available: http://www.nist.gov/customcf/get{_}pdf.cfm?pub{_}id=33079 (Cited on page 193.)

[189] R. Panciera, J. Walker, J. Kalma, E. Kim, J. Hacker, O. Merlin, M. Berger, and N. Skou, "The NAFE'05/CoSMOS Data Set: Toward SMOS Soil Moisture Retrieval, Downscaling, and Assimilation," *IEEE Trans. Geosci. Remote Sens.*, vol. 46, no. 3, pp. 736–745, mar 2008. (Cited on pages 193 and 195.)

[190] "Polarimetric L-Band Microwave Radiometer (PLMR)," 2015. [Online]. Available: http://www.prosensing.com/sensors/radiometers/soilmoisture/plmr/ (Cited on page 195.)

[191] N. Sánchez, A. Alonso-Arroyo, J. Martínez-Fernández, M. Piles, Á. González-Zamora, A. Camps, and M. Vall-llosera, "On the Synergy of Airborne GNSS-R and Landsat 8 for Soil Moisture Estimation," *Remote Sens.*, vol. 7, no. 8, pp. 9954–9974, aug 2015. (Cited on pages xxvi, 200, 209, 210, 215, and 216.)

[192] "UK Tech-DemoSAT." [Online]. Available: http://www.sstl.co.uk/Missions/TechDemoSat-1-Launched-2014 (Cited on page 207.)

[193] "UK Tech-DemoSAT data." [Online]. Available: http://www.merrbys.co.uk/ (Cited on page 207.)

[194] "Cyclone Global Navigation Satellite System (CYGNSS)." [Online]. Available: http://aoss-research.engin.umich.edu/missions/cygnss/ (Cited on page 207.)

[195] "Cyclone Global Navigation Satellite System (CYGNSS)." [Online]. Available: http://science.nasa.gov/missions/cygnss/ (Cited on page 207.)

[196] A. Camps, H. Park, A. Ghavidel, J. M. Rius, and I. Sekulic, "GEROS-ISS, a demonstration mission of GNSS remote sensing capabilities to derive geophysical parameters of the earth surfaces: Altimetry performance evaluation," in *2015 IEEE Int. Geosci. Remote Sens. Symp.* IEEE, jul 2015, pp. 3917–3920. (Cited on page 207.)

[197] S. T. Lowe, S. Chan, S. Esterhuizen, A. Freedman, S. Oveisgharan, and L. Young, "GNSS-Reflectometry with NASA's Soil Moisture Active/Passive Mission," in *Usn. Natl. Radio Sci. Meet.*, Boulder, 2016. (Cited on page 209.)

[198] G. Johnston and G. Morgan-Owen, "Differential GPS positioning," *Electron. Commun. Eng. J.*, vol. 7, no. 1, pp. 11–21, feb 1995. (Cited on page 210.)

[199] D. Masters, "Surface Remote Sensing Applications of GNSS Bistatic Radar: Soil Moisture and Aircraft Altimetry," Ph.D. dissertation, University of Colorado, 2004. (Cited on pages 213 and 215.)

[200] N. Sanchez, A. Alonso-Arroyo, A. Gonzalez-Zamora, J. Martinez-Fernandez, A. Camps, M. Vall-llosera, M. Pablos, and C. M. Herrero-Jimenez, "Airborne GNSS-R, thermal and optical data relationships for soil moisture retrievals," in *2015 IEEE Int. Geosci. Remote Sens. Symp.* IEEE, jul 2015, pp. 4785–4788. (Cited on page 215.)

[201] N. Sánchez, A. Alonso-Arroyo, J. Martínez-Fernández, A. Camps, A. González-Zamora, M. Pablos, C. M. Herrero-Jiménez, and A. Gumuzzio, "MULTISENSOR EXPERIMENTS OVER VINEYARD: NEW CHALLENGES FOR THE GNSS-R TECHNIQUE," *ISPRS - Int. Arch. Photogramm. Remote Sens. Spat. Inf. Sci.*, vol. XL-7/W3, pp. 1299–1303, apr 2015. (Cited on page 215.)

[202] H. Carreno-Luengo, A. Camps, I. Ramos-Perez, and A. Rius, "Experimental Evaluation of GNSS-Reflectometry Altimetric Precision Using the P(Y) and C/A Signals," *IEEE J. Sel. Top. Appl. Earth Obs. Remote Sens.*, vol. 7, no. 5, pp. 1493–1500, may 2014. (Cited on page 220.)

[203] G. Spreen, L. Kaleschke, and G. Heygster, "Sea ice remote sensing using AMSR-E 89-GHz channels," *J. Geophys. Res.*, vol. 113, no. C2, p. C02S03, jan 2008. (Cited on pages 250 and 257.)

[204] S. Andersen, L.-A. Breivik, S. Eastwood, G. Oysten, T. Lavergne, M. Lind, and M. Porcires, "Ocean & Sea Ice SAF: Sea Ice Product User's Manual, OSI-401-a, OSI-402-a, OSI-403-a." Meteo France, Ifremer, EUMETSAT, DMI, Norwegian Meteorological Institute, Tech. Rep., 2014. (Cited on pages 250, 257, and 258.)

[205] C. Rapley and A. P. Cooper, "A Study of Satellite Radar Altimeter Operations Over Ice-covered Surfaces," University College London, Tech. Rep., 1983. (Cited on page 250.)

[206] A. Komjathy, J. Maslanik, V. Zavorotny, P. Axelrad, and S. Katzberg, "Sea ice remote sensing using surface reflected GPS signals," in *IGARSS 2000. IEEE 2000 Int. Geosci. Remote Sens. Symp. Tak. Pulse Planet Role Remote Sens. Manag. Environ. Proc. (Cat. No.00CH37120)*, vol. 7. IEEE, 2000, pp. 2855–2857. (Cited on page 250.)

[207] M. Wiehl, B. Legrésy, and R. Dietrich, "Potential of Reflected GNSS Signals for Ice Sheet Remote Sensing," *Prog. Electromagn. Res.*, vol. 40, pp. 177–205, 2003. (Cited on pages 250 and 251.)

[208] S. Gleason, "Towards Sea Ice Remote Sensing with Space Detected GPS Signals: Demonstration of Technical Feasibility and Initial Consistency Check Using Low Resolution Sea Ice Information," *Remote Sens.*, vol. 2, no. 8, pp. 2017–2039, aug 2010. (Cited on page 250.)

[209] M. Rivas, J. Maslanik, and P. Axelrad, "Bistatic Scattering of GPS Signals Off Arctic Sea Ice," *IEEE Trans. Geosci. Remote Sens.*, vol. 48, no. 3, pp. 1548–1553, mar 2010. (Cited on page 250.)

[210] G. Brown, "The average impulse response of a rough surface and its applications," *IEEE Trans. Antennas Propag.*, vol. 25, no. 1, pp. 67–74, jan 1977. (Cited on page 250.)

[211] G. S. Brown, "A theory for near-normal incidence microwave scattering from first-year sea ice," *Radio Sci.*, vol. 17, no. 1, pp. 233–243, jan 1982. (Cited on pages 250, 252, and 266.)

[212] C. Rapley and A. P. Cooper, "Applications and Scientific Uses of ERS-1 Radar Altimeter Data," University College London, Tech. Rep., 1985. (Cited on page 250.)

[213] M. R. Drinkwater, "K u band airborne radar altimeter observations of marginal sea ice during the 1984 Marginal Ice Zone Experiment," *J. Geophys. Res.*, vol. 96, no. C3, p. 4555, 1991. (Cited on page 250.)

[214] F. Fabra, "GNSS-R as a source of opportunity for remote sensing of the cryosphere," Ph.D. dissertation, Universitat Politècnica de Catalunya - BarcelonaTech, 2013. [Online]. Available: http://www.tdx.cat/handle/10803/117605 (Cited on page 251.)

[215] T. W. K. Armitage and M. W. J. Davidson, "Using the Interferometric Capabilities of the ESA CryoSat-2 Mission to Improve the Accuracy of Sea Ice Freeboard Retrievals," *IEEE Trans. Geosci. Remote Sens.*, vol. 52, no. 1, pp. 529–536, jan 2014. (Cited on page 253.)

[216] G. Foti, C. Gommenginger, P. Jales, M. Unwin, A. Shaw, C. Robertson, and J. Roselló, "Spaceborne GNSS reflectometry for ocean winds: First results from the UK TechDemoSat-1 mission," *Geophys. Res. Lett.*, vol. 42, no. 13, pp. 5435–5441, jul 2015. (Cited on pages 255 and 258.)

[217] N. Pierdicca, L. Guerriero, R. Giusto, M. Brogioni, and A. Egido, "SAVERS: A Simulator of GNSS Reflections From Bare and Vegetated Soils," *IEEE Trans. Geosci. Remote Sens.*, vol. 52, no. 10, pp. 6542–6554, oct 2014. (Cited on page 255.)

[218] A. K. Fung, "Coherent scattering of a spherical wave from an irregular surface," 1983. (Cited on page 255.)

[219] M. P. Clarizia, C. S. Ruf, P. Jales, and C. Gommenginger, "Spaceborne GNSS-R Minimum Variance Wind Speed Estimator," *IEEE Trans. Geosci. Remote Sens.*, vol. 52, no. 11, pp. 6829–6843, nov 2014. (Cited on page 255.)

[220] M. P. Clarizia, C. S. Ruf, A. O'Brien, and S. Gleason, "A level 2 wind speed retrieval algorithm for the CYGNSS mission," in *EGU Gen. Assem. Conf. Abstr.*, Vienna, 2014, p. 15776. (Cited on page 256.)

[221] M. P. Clarizia and C. S. Ruf, "An Improved Wind Speed Retrieval Algorithm For The CYGNSS Mission," in *AGU Fall Meet.*, San Francisco, 2015. (Cited on page 256.)

[222] F. M. Fetterer, M. R. Drinkwater, K. C. Jezek, S. W. C. Laxon, R. G. Onstott, and L. M. H. Ulander, "Sea ice altimetry," ser. Geophysical Monograph Series, F. D. Carsey, Ed. Washington, D. C.: American Geophysical Union, 1992, vol. 68, pp. 111–135. [Online]. Available: http://doi.wiley.com/10.1029/GM068http://doi.wiley.com/10.1029/GM068p0111 (Cited on page 256.)

[223] S. Laxon and C. Rapley, "Radar altimeter data quality flagging," *Adv. Sp. Res.*, vol. 7, no. 11, pp. 315–318, jan 1987. (Cited on page 256.)

[224] S. Laxon, "Seasonal and inter-annual variations in Antarctic sea ice extent as mapped by radar altimetry," *Geophys. Res. Lett.*, vol. 17, no. 10, pp. 1553–1556, sep 1990. (Cited on pages 256 and 258.)

[225] N. R. Peacock and S. Laxon, "Sea surface height determination in the Arctic Ocean from ERS altimetry," *J. Geophys. Res.*, vol. 109, no. C7, p. C07001, 2004. (Cited on pages 256 and 258.)

[226] "Sea Ice Concentration Maps from AMSR2 data." [Online]. Available: http://www.meereisportal.de (Cited on page 257.)

[227] NSIDC, "Special Sensor Microwave Imager/Sounder (SSMIS)," 2016. [Online]. Available: https://nsidc.org/data/docs/daac/ssmis{_}instrument/ (Cited on page 257.)

[228] "Ocean & Sea Ice SAF: Sea Ice Concentration Maps." [Online]. Available: http://osisaf.met.no/p/ice/ (Cited on page 258.)

[229] P. Jales, "TDS-1 GNSS-R data products & access," in *TechDemoSat-1 User Consult. Work.*, 2015. (Cited on page 258.)

[230] S. M. Kay, *Fundamentals of Statistical Signal Processing. Volume II: Detection Theory.*, 1st ed. Prentice Hall, 1998. (Cited on page 259.)

[231] F. T. Ulaby, R. K. Moore, and A. K. Fung, *Microwave Remote Sensing: Active and Passive Volume II: Radar Remote Sensing and Surface Scattering and Emission Theory*, 1982, vol. 2. (Cited on page 266.)

[232] ——, *Microwave remote sensing: Active and passive. Volume 1 - Microwave remote sensing fundamentals and radiometry*, 1981, vol. 1, no. 1. (Cited on page 269.)

[233] E. Valencia, A. Camps, N. Rodriguez-Alvarez, H. Park, and I. Ramos-Perez, "Using GNSS-R Imaging of the Ocean Surface for Oil Slick Detection," *IEEE J. Sel. Top. Appl. Earth Obs. Remote Sens.*, vol. 6, no. 1, pp. 217–223, feb 2013. (Cited on page 269.)

[234] J.-P. Wigneron, A. Chanzy, J.-C. Calvet, and N. Bruguier, "A simple algorithm to retrieve soil moisture and vegetation biomass using passive microwave measurements over crop fields," *Remote Sens. Environ.*, vol. 51, no. 3, pp. 331–341, mar 1995. (Cited on pages 272 and 273.)

[235] J.-P. Wigneron, M. Parde, P. Waldteufel, A. Chanzy, Y. Kerr, S. Schmidl, and N. Skou, "Characterizing the Dependence of Vegetation Model Parameters on Crop Structure, Incidence Angle, and Polarization at L-Band," *IEEE Trans. Geosci. Remote Sens.*, vol. 42, no. 2, pp. 416–425, feb 2004. (Cited on pages 272, 273, and 289.)

[236] Array Systems Computing Inc., "Algorithm Theoretical Basis Document (ATBD) for the SMOS Level 2 Soil Moisture Processor Development Continuation Project. Code: SO-TN-ARR-L2PP-0037," European Space Agency, Tech. Rep., 2011. [Online]. Available: https://earth.esa.int/c/document{_}library/get{_}file?folderId=127856{&}name=DLFE-1506.pdf (Cited on page 272.)

[237] T. Jackson and T. Schmugge, "Vegetation effects on the microwave emission of soils," *Remote Sens. Environ.*, vol. 36, no. 3, pp. 203–212, jun 1991. (Cited on pages 272 and 273.)

[238] C. Laymon, P. Meyer, and J. Braun, "Biomass Characterization from Microwave Attenuation Using Ground-based GPS Receivers," Tech. Rep., 2008. [Online]. Available: https://www.unavco.org/community/publications{_}and{_}reports/proposals/2007/facility2007/section3/UNV-GRID-SPREAD-R{_}2.pdf (Cited on pages xxix, 273, and 275.)

[239] T. H. Meyer, J. E. Bean, C. R. Ferguson, and J. M. Naismith, "The Effect of Broadleaf Canopies on Survey-grade Horizontal GPS/GLONASS Measurements," *Surv. L. Inf. Sci.*, vol. 62, no. 4, pp. 215–224, 2002. (Cited on pages 273 and 274.)

[240] H. Hasegawa and T. Yoshimura, "Application of dual-frequency GPS receivers for static surveying under tree canopies," *J. For. Res.*, vol. 8, no. 2, pp. 103–110, 2003. (Cited on page 274.)

[241] I. Sawaguchi, Y. Saitoh, and S. Tatsukawa, "A study of the effects of stems and canopies on the signal to noise ratio of GPS signals," *J. For. Res.*, vol. 10, no. 5, pp. 395–401, sep 2005. (Cited on page 274.)

[242] I. Sawaguchi, Y. Nemoto, and S. Tatsukawa, "Effects of moisture in wood materials on the SNR of GPS signals," *J. For. Res.*, vol. 14, no. 2, pp. 63–72, apr 2009. (Cited on page 274.)

[243] NASA, "LAI and NDVI maps," 2016. [Online]. Available: http://neo.sci.gsfc.nasa.gov/ (Cited on page 280.)

[244] MeteOlot, "MeteOlot," 2016. [Online]. Available: www.meteolot.com (Cited on page 280.)

[245] Y. Zhang, J. M. Chen, and J. R. Miller, "Determining digital hemispherical photograph exposure for leaf area index estimation," *Agric. For. Meteorol.*, vol. 133, no. 1-4, pp. 166–181, nov 2005. (Cited on page 286.)

[246] A. E. Goodenough and A. S. Goodenough, "Development of a Rapid and Precise Method of Digital Image Analysis to Quantify Canopy Density and Structural Complexity," *ISRN Ecol.*, vol. 2012, pp. 1–11, 2012. (Cited on page 286.)

[247] E. Burke, W. Shuttleworth, and A. French, "Using vegetation indices for soil-moisture retrievals from passive microwave radiometry," *Hydrol. Earth Syst. Sci.*, vol. 5, no. 4, pp. 671–678, 2001. (Cited on page 291.)

[248] J.-P. Wigneron, Y. Kerr, P. Waldteufel, K. Saleh, M.-J. Escorihuela, P. Richaume, P. Ferrazzoli, P. de Rosnay, R. Gurney, J.-C. Calvet, J. Grant, M. Guglielmetti, B. Hornbuckle, C. Mätzler, T. Pellarin, and M. Schwank, "L-band Microwave Emission of the Biosphere (L-MEB) Model: Description and calibration against experimental data sets

over crop fields," *Remote Sens. Environ.*, vol. 107, no. 4, pp. 639–655, apr 2007. (Cited on page 300.)

[249] S. Jin, E. Cardellach, and F. Xie, *GNSS Remote Sensing*, ser. Remote Sensing and Digital Image Processing. Dordrecht: Springer Netherlands, 2014, vol. 19. (Cited on pages xxx and 313.)

[250] D. Pascual, H. Park, A. Camps, A. A. Arroyo, and R. Onrubia, "Simulation and Analysis of GNSS-R Composite Waveforms Using GPS and Galileo Signals," *IEEE J. Sel. Top. Appl. Earth Obs. Remote Sens.*, vol. 7, no. 5, pp. 1461–1468, may 2014. (Cited on pages 318, 321, and 323.)

[251] C. Zuffada and V. Zavorotny, "Coherence time and statistical properties of the GPS signal scattered off the ocean surface and their impact on the accuracy of remote sensing of sea surface topography and winds," in *IGARSS 2001. Scanning Present Resolv. Futur. Proceedings. IEEE 2001 Int. Geosci. Remote Sens. Symp. (Cat. No.01CH37217)*, vol. 7. IEEE, 2001, pp. 3332–3334. (Cited on page 321.)

[252] H. You, J. L. Garrison, G. Heckler, and V. U. Zavorotny, "Stochastic voltage model and experimental measurement of ocean-scattered GPS signal statistics," in *IEEE Trans. Geosci. Remote Sens.*, vol. 42, 2004, pp. 2160–2169. (Cited on pages 321 and 322.)

[253] H. You, J. Garrison, G. Heckler, and D. Smajlovic, "The Autocorrelation of Waveforms Generated From Ocean-Scattered GPS Signals," *IEEE Geosci. Remote Sens. Lett.*, vol. 3, no. 1, pp. 78–82, jan 2006. (Cited on page 321.)

[254] L. Isserlis, "On a Formula for the product-moment coefficient of any order of a normal frequency distribution in any number of variables," *Biometrika*, vol. 12, no. 1-2, pp. 134–139, nov 1918. (Cited on page 326.)

[255] Global positioning Systems Directorate, "Global positioning Systems Directorate System Engineering & Integration, Interface Specification (IS-GPS-200H)," Tech. Rep., 2013. [Online]. Available: http://www.gps.gov/technical/icwg/IS-GPS-200H.pdf (Cited on page 338.)

[256] M. Plank, *The theory of heat radiation.* P. Blakiston's Son & Co., 1914. (Cited on page 354.)

[257] R. H. Dicke, "The Measurement of Thermal Radiation at Microwave Frequencies," *Rev. Sci. Instrum.*, vol. 17, no. 7, p. 268, 1946. (Cited on page 355.)

[258] Á. Cardama Aznar, L. Jofre Roca, J. M. Manuel Rius, J. Romeu Robert, S. Blanch Boris, and M. Ferrando Bataller, *Antenas*, segunda ed., E. UPC, Ed. Edicions UPC, 1988. (Cited on pages xxxi and 360.)

[259] Wikipedia, "Universal Transverse Mercator coordinate system," 2016. [Online]. Available: https://en.wikipedia.org/wiki/Universal{_}Transverse{_}Mercator{_}coordinate{_}system (Cited on page 368.)

[260] J. P. Snyder, *Map Projections - A Working Manual.* Washington, D. C.: Series: Geological Survey professional paper; 1395., 1987. (Cited on page 374.)

List of Publications

Journal Articles

[JA1] A. Alonso Arroyo, A. Camps, A. Aguasca, G. F. Forte, A. Monerris, C. Rüdiger, J. P. Walker, H. Park, D. Pascual, and R. Onrubia, "Dual-Polarization GNSS-R Interference Pattern Technique for Soil Moisture Mapping," *IEEE J. Sel. Top. Appl. Earth Obs. Remote Sens.*, vol. 7, no. 5, pp. 1533–1544, may 2014.

[JA2] A. Alonso-Arroyo, A. Camps, A. Aguasca, G. Forte, A. Monerris, C. Rüdiger, J. P. Walker, H. Park, D. Pascual, and R. Onrubia, "Improving the Accuracy of Soil Moisture Retrievals Using the Phase Difference of the Dual-Polarization GNSS-R Interference Patterns," *IEEE Geosci. Remote Sens. Lett.*, vol. 11, no. 12, pp. 2090–2094, dec 2014.

[JA3] A. Alonso-Arroyo, A. Camps, H. Park, D. Pascual, R. Onrubia, and F. Martin, "Retrieval of Significant Wave Height and Mean Sea Surface Level Using the GNSS-R Interference Pattern Technique: Results From a Three-Month Field Campaign," *IEEE Trans. Geosci. Remote Sens.*, vol. 53, no. 6, pp. 3198–3209, jun 2015.

[JA4] A. Alonso-Arroyo, A. Camps, A. Monerris, C. Rudiger, J. P. Walker, R. Onrubia, J. Querol, H. Park, and D. Pascual, "On the Correlation Between GNSS-R Reflectivity and L-Band Microwave Radiometry," *IEEE J. Sel. Top. Appl. Earth Obs. Remote Sens.*, pp. 1–18, 2016.

[JA5] A. Alonso-Arroyo, V. U. Zavorotny, and A. Camps, "Sea Ice Detection Using UK TDS-1 SNR Data," *IEEE Trans. Geosci. Remote Sens. (Under Review)*, 2016.

[JA6] A. Alonso-Arroyo, J. Querol, C. Lopez-Martinez, V. U. Zavorotny, H. Park, D. Pascual, R. Onrubia, and A. Camps, "SNR and Standard Deviation of cGNSS-R and iGNSS-R Scatterometric Measurements," *IEEE Trans. Geosci. Remote Sens. (Submitted)*, 2016.

[JA7] D. Pascual, H. Park, A. Camps, A. A. Arroyo, and R. Onrubia, "Simulation and Analysis of GNSS-R Composite Waveforms Using GPS and Galileo Signals," *IEEE Journal of Selected Topics in Applied Earth Observations and Remote Sensing*, vol. 7, no. 5, pp. 1461–1468, may 2014.

[JA8] D. Pascual, A. Camps, F. Martin, H. Park, A. A. Arroyo, and R. Onrubia, "Precision Bounds in GNSS-R Ocean Altimetry," *IEEE Journal of Selected Topics in Applied Earth Observations and Remote Sensing*, vol. 7, no. 5, pp. 1416–1423, may 2014.

[JA9] H. Park, D. Pascual, A. Camps, F. Martin, A. Alonso-Arroyo, and H. Carreno-Luengo, "Analysis of spaceborne GNSS-R delay-doppler tracking," *IEEE Journal of Selected Topics in Applied Earth Observations and Remote Sensing*, vol. 7, no. 5, pp. 1481–1492, 2014.

[JA10] F. Martin, A. Camps, F. Fabra, A. Rius, M. Martin-Neira, S. D'Addio, and A. Alonso, "Mitigation of Direct Signal Cross-Talk and Study of the Coherent Component in GNSS-R," *IEEE Geoscience and Remote Sensing Letters*, vol. 12, no. 2, pp. 279–283, feb 2015.

[JA11] N. Sánchez, A. Alonso-Arroyo, J. Martínez-Fernández, M. Piles, Á. González-Zamora, A. Camps, and M. Vall-llosera, "On the Synergy of Airborne GNSS-R and Landsat 8 for Soil Moisture Estimation," *Remote Sensing*, vol. 7, no. 8, pp. 9954–9974, aug 2015.

[JA12] R. Onrubia, J. Querol, D. Pascual, A. Alonso-Arroyo, H. Park, and A. Camps, "DME/TACAN Impact Analysis on GNSS Reflectometry," *IEEE Journal of Selected Topics in Applied Earth Observations and Remote Sensing*, pp. 1–10, 2016.

[JA13] D. Pascual, H. Park, R. Onrubia, A. A. Arroyo, J. Querol, and A. Camps, "Crosstalk Statistics and Impact in Interferometric GNSS-R," *IEEE J. Sel. Top. Appl. Earth Obs. Remote Sens.*, pp. 1–10, 2016.

[JA14] J. Querol, A. Alonso-Arroyo, R. Onrubia, D. Pascual, H. Park, and A. Camps, "SNR Degradation in GNSS-R Measurements Under the Effects of Radio-Frequency Interference," *IEEE J. Sel. Top. Appl. Earth Obs. Remote Sens.*, pp. 1–14, 2016.

[JA15] J. Querol, R. Onrubia, A. Alonso-Arroyo, D. Pascual, H. Park, and A. Camps, "Performance Assessment of Time-Frequency RFI Mitigation Techniques in Microwave Radiometry," *IEEE J. Sel. Top. Appl. Earth Obs. Remote Sens. (Under Review)*, 2016.

Conference Articles

[CA1] A. Alonso, A. Camps, D. Pascual, H. Park, A. Alcayde, S. Chavero, P. Martinez, L. Crespo, M. Angulo, and A. Rius, "PAU instrument aboard INTA MicroSat-1: Flight model tests," in *2012 IEEE International Geoscience and Remote Sensing Symposium*. IEEE, jul 2012, pp. 1038–1041.

[CA2] A. Alonso-Arroyo, A. Camps, D. Pascual, H. Park, A. Alcayde, S. Chavero, P. Martinez, L. Crespo, M. Angulo, and A. Rius, "PAU Instrument aboard INTA MicroSAT-1: Initial results of the FM model from an airborne experiment," in *2012 Workshop on Reflectometry Using GNSS and Other Signals of Opportunity (GNSS+R)*. IEEE, oct 2012, pp. 1–5.

[CA3] A. Alonso-Arroyo, G. Forte, A. Camps, H. Park, D. Pascual, R. Onrubia, and R. Jove-Casulleras, "Soil Moisture mapping using forward scattered GPS L1 signals," in *2013 IEEE International Geoscience and Remote Sensing Symposium - IGARSS*. IEEE, jul 2013, pp. 354–357.

[CA4] A. Alonso-Arroyo, G. Forte, A. Monerris, A. Camps, H. Park, D. Pascual, and R. Onrubia, "The Light Airborne Reflectometer for GNSS-R Observations (LARGO) instrument: Towards Soil Moisture retrievals," in *URSI Comission F Microwave Signatures 2013*, Espoo, 2013, p. 56.

[CA5] A. Alonso-Arroyo, A. Camps, A. Monerris, C. Ruudiger, J. P. Walker, G. Forte, D. Pascual, H. Park, and R. Onrubia, "The dual polarization GNSS-R interference pattern technique," in *2014 IEEE Geoscience and Remote Sensing Symposium*. IEEE, jul 2014, pp. 4058–4061.

[CA6] A. Alonso-Arroyo, A. Camps, A. Monerris, C. Rüdiger, J. P. Walker, G. Forte, D. Pascual, H. Park, and R. Onrubia, "The light airborne reflectometer for GNSS-R observations (LARGO) instrument: Initial results from airborne and Rover field campaigns," in *2014 IEEE Geoscience and Remote Sensing Symposium*. IEEE, jul 2014, pp. 4054–4057.

[CA7] A. Alonso-Arroyo, J. Querol, C. López-Martínez, A. Camps, H. Park, D. Pascual, and R. Onrubia, "GNSS-R CORRELATION PEAK STATISTICS, SNR ESTIMATION AND ITS RELATION TO GEOPHYSICAL PARAMETERS," in *2015 Workshop on Reflectometry Using GNSS and Other Signals of Opportunity (GNSS+R)*, 2015.

[CA8] A. Alonso-Arroyo, S. Torrecilla, J. Querol, A. Camps, D. Pascual, H. Park, and R. Onrubia, "Two dedicated soil moisture experiments using the scatterometric properties of GNSS-reflectometry," in *2015 IEEE International Geoscience and Remote Sensing Symposium (IGARSS)*. IEEE, jul 2015, pp. 3921–3924.

[CA9] A. Alonso-Arroyo, A. Camps, N. Sanchez, M. Pablos, A. Gonzalez-Zamora, J. Martinez-Fernandez, M. Vall-llosera, and D. Pascual, "An airborne GNSS-R field experiment over a vineyard for soil moisture estimation and monitoring," in *2015 IEEE International Geoscience and Remote Sensing Symposium (IGARSS)*. IEEE, jul 2015, pp. 4761–4764.

[CA10] A. Alonso-Arroyo, A. Camps, A. Monerris, C. Rüdiger, J. Walker, Y. Gao, H. Park, J. Querol, D. Pascual, and R. Onrubia, "On the Comparison of Airborne L-Band Brightness Temperatures and GNSS-Reflectivities: A case study in Australia," in *2016 14th Spec. Meet. Microw. Radiom. Remote Sens. Environ.*, 2016.

[CA11] A. Alonso-Arroyo, J. Querol, A. Camps, R. Onrubia, H. Park, and D. Pascual, "CAN WE MEASURE VEGETATION WATER CONTENT AND VEGETATION OPACITY AT L-BAND WITH A SINGLE GPS RECEIVER?" in *2016 IEEE Int. Geosci. Remote Sens. Symp.*, 2016.

[CA12] A. Alonso-Arroyo, V. Zavorotny, and A. Camps, "SEA ICE DETECTION USING GNSS-R DATA FROM UK TDS-1," in *2016 IEEE Int. Geosci. Remote Sens. Symp.*, 2016.

[CA13] A. Camps, G. Forte, I. Ramos, A. Alonso, P. Martinez, L. Crespo, and A. Alcayde, "Recent advances in land monitoring using GNSS-R techniques," in *2012 Workshop on Reflectometry Using GNSS and Other Signals of Opportunity (GNSS+R)*. IEEE, oct 2012, pp. 1–4.

[CA14] H. Park, A. Camps, E. Valencia, H. Carreno-Luengo, F. Martin, A. Alonso, and D. Pascual, "Analysis of GNSS-R delay and Doppler tracking errors," in *2012 Workshop on Reflectometry Using GNSS and Other Signals of Opportunity (GNSS+R)*. IEEE, oct 2012, pp. 1–4.

[CA15] A. Camps, H. Park, and A. Alonso-Arroyo, "Wind speed maping from the ISS using GNSS-R? A simulation study," in *2013 IEEE Int. Geosci. Remote Sens. Symp.* IEEE, jul 2013, pp. 382–385.

[CA16] H. Park, A. Camps, D. Pascual, A. Alonso, F. Martin, and H. Carreno-Luengo, "Improvement of the PAU/PARIS End-to-end Performance Simulator (P2EPS) in preparation for upcoming GNSS-R missions," in *2013 IEEE Int. Geosci. Remote Sens. Symp.* IEEE, jul 2013, pp. 362–365.

[CA17] D. Pascual, H. Park, A. Camps, A. Alonso, and R. Onrubia, "Comparison of GPS L1 and Galileo E1 signals for GNSS-R ocean altimetry," in *2013 IEEE Int. Geosci. Remote Sens. Symp.* IEEE, jul 2013, pp. 358–361.

[CA18] R. Onrubia, D. Pascual, A. Camps, A. Alonso-Arroy, and H. Park, "MIR: The microwave interferometric reflectometer, a new airborne sensor for GNSS-R advanced research," in *2013 IEEE Int. Geosci. Remote Sens. Symp.* IEEE, jul 2013, pp. 109–112.

[CA19] A. Camps, N. Rodriguez-Alvarez, E. Valencia, G. Forte, I. Ramos, A. Alonso-Arroyo, and X. Bosch-Lluis, "Land monitoring using GNSS-R techniques: A review of recent advances," in *2013 IEEE Int. Geosci. Remote Sens. Symp.* IEEE, jul 2013, pp. 4026–4029.

[CA20] R. Jove-Casulleras, A. Camps, M. Vall-llossera, E. Bou Balust, J. J. Ramos Castro, E. J. Alarcon Cot, and A. Alonso-Arroyo, "UPCSAT-1, demostrador CubeSat para observación terrestre," in *Sistemas operacionales de observación de la tierra : XV congreso de la Asociacion Española de Teledetección, INTA*, Madrid, 2013, pp. 49–52.

[CA21] R. Onrubia, D. Pascual, A. Camps, A. Alonso-Arroyo, and H. Park, "The Microwave Interferometric Reflectometer. Part I: Front-end and beamforming description," in *2014 IEEE Int. Geosci. Remote Sens. Symp.* IEEE, jul 2014, pp. 4046–4049.

[CA22] D. Pascual, R. Onrubia, A. Alonso-Arroyo, H. Park, and A. Camps, "The microwave interferometric reflectometer. Part II: Back-end and processor descriptions," in *2014 IEEE Int. Geosci. Remote Sens. Symp.* IEEE, jul 2014, pp. 3782–3785.

[CA23] A. Camps, J. F. Marchan-Hernandez, X. Bosch-Lluis, N. Rodriguez-Alvarez, I. Ramos-Perez, E. Valencia, J. M. Tarongi, H. Park, H. Carreno-Luengo, A. Alonso-Arroyo, D. Pascual, R. Onrubia, G. Forte, and J. Querol, "Review of GNSS-R instruments and tools developed at the Universitat Politecnica de Catalunya-Barcelona tech," in *2014 IEEE Int. Geosci. Remote Sens. Symp.* IEEE, jul 2014, pp. 3826–3829.

[CA24] Hyuk Park, A. Camps, D. Pascual, A. Alonso-Arroyo, F. Martin, H. Carreno-Luengo, and R. Onrubia, "Simulation study on tropicial cyclone tracking from the ISS using GNSS-R measurements," in *2014 IEEE Geosci. Remote Sens. Symp.* IEEE, jul 2014, pp. 4062–4065.

[CA25] H. Carreno-Luengo, A. Camps, R. Jove-Casulleras, A. Alonso-Arroyo, R. Olive, A. Amezaga, D. Vidal, and J. Munoz, "The 3Cat-2 Project: GNSS-R In-Orbit Demonstrator for Earth Observation," in *The 4S Symposium: Small Satellites Systems and Services*, Mallorca, 2014.

[CA26] D. Pascual, H. Park, A. Camps, A. Alonso-Arroyo, R. Onrubia, and J. Querol, "Advances in the MIR instrument: Integration, control subsystem and analysis of the flight dynamics for beamsteering purposes," in *8th Workshop on GNSS Reflectrometry, GNSS+R 2015 Workshop: May 11-13, 2015, GFZ, Potsdam, Germany*, 2015.

[CA27] R. Onrubia, J. Querol, D. Pascual, A. Alonso-Arroyo, H. Park, and A. Camps, "DME/TACAN interference impact in interferometric GNSS-R," in *8th Workshop on GNSS Reflectrometry, GNSS+R 2015 Workshop: May 11-13, 2015, GFZ, Potsdam, Germany*, 2015.

[CA28] J. Querol, A. Alonso-Arroyo, R. Onrubia, D. Pascual, and A. Camps, "SNR degradation in conventional GNSS-R measurements under the effects of radio frequency interference," in *8th Workshop on GNSS Reflectrometry, GNSS+R 2015 Workshop: May 11-13, 2015, GFZ, Potsdam, Germany*, 2015.

[CA29] H. Park, D. Pascual, A. Camps, A. Alonso-Arroyo, R. Onrubia, F. Martin, and J. Querol, "Antenna beam impact on GEROS-ISSinstrument observables," in *8th Workshop on GNSS Reflectrometry, GNSS+R 2015 Workshop: May 11-13, 2015, GFZ, Potsdam, Germany*, 2015.

[CA30] ——, "GEROS instrument simulator built by using P2EPS," in *8th Workshop on GNSS Reflectrometry, GNSS+R 2015 Workshop: May 11-13, 2015, GFZ, Potsdam, Germany*, 2015.

[CA31] N. Sánchez, A. Alonso-Arroyo, J. Martínez-Fernández, A. Camps, A. González-Zamora, M. Pablos, C. M. Herrero-Jiménez, and A. Gumuzzio, "MULTISENSOR EXPERIMENTS OVER VINEYARD: NEW CHALLENGES FOR THE GNSS-R TECHNIQUE," *ISPRS - International Archives of the Photogrammetry, Remote Sensing and Spatial Information Sciences*, vol. XL-7/W3, pp. 1299–1303, apr 2015.

[CA32] R. Onrubia, L. Garrucho, D. Pascual, H. Park, J. Querol, A. Alonso-Arroyo, and A. Camps, "Advances in the MIR instrument: Integration, control subsystem and analysis of the flight dynamics for beamsteering purposes," in *2015 IEEE Int. Geosci. Remote Sens. Symp.* IEEE, jul 2015, pp. 4765–4768.

[CA33] N. Sanchez, A. Alonso-Arroyo, A. Gonzalez-Zamora, J. Martinez-Fernandez, A. Camps, M. Vall-llosera, M. Pablos, and C. M. Herrero-Jimenez, "Airborne GNSS-R, thermal and optical data relationships for soil moisture retrievals," in *2015 IEEE Int. Geosci. Remote Sens. Symp.* IEEE, jul 2015, pp. 4785–4788.

[CA34] H. Park, A. Camps, D. Pascual, R. Onrubia, A. Alonso-Arroyo, and F. Martin, "Evolution of PAU/PARIS End-to-end Performance Simulator (P2EPS) towards GNSS reflectometry, radio occulation and Scatterometry simulator (GEROS-SIM)," in *2015 IEEE Int. Geosci. Remote Sens. Symp.* IEEE, jul 2015, pp. 4757–4760.

[CA35] J. Querol, A. Alonso-Arroyo, R. Onrubia, D. Pascual, and A. Camps, "Assessment of back-end RFI mitigation techniques in passive remote sensing," in *2015 IEEE Int. Geosci. Remote Sens. Symp.* IEEE, jul 2015, pp. 4746–4749.

[CA36] J. Querol, R. Onrubia, D. Pascual, A. Alonso-Arroyo, H. Park, and A. Camps, "Comparison of real-time time-frequency RFI mitigation techniques in microwave radiometry," in *2016 14th Spec. Meet. Microw. Radiom. Remote Sens. Environ.* IEEE, apr 2016, pp. 68–70.

[CA37] D. Pascual, R. Onrubia, J. Querol, A. Alonso-Arroyo, H. Park, and A. Camps, "FIRST DELAY DOPPLER MAPS OBTAINED WITH THE MICROWAVE INTEFEROMETRIC REFLECTOMETER (MIR)," in *2016 IEEE Int. Geosci. Remote Sens. Symp.*, 2016.

[CA38] R. Onrubia, J. Querol, D. Pascual, H. Park, A. Alonso-Arroyo, and A. Camps, "ASSESSMENT OF DME/TACAN RFI MITIGATION TECHNIQUES IN GNSS-R," in *2016 IEEE Int. Geosci. Remote Sens. Symp.*, 2016.

[CA39] J. Querol, E. M. Julian, R. Onrubia, A. Alonso-Arroyo, D. Pascual, and A. Camps, "PRELIMINARY RESULTS OF FENIX: FRONT-END GNSS INTERFERENCE EXCISOR," in *2016 IEEE Int. Geosci. Remote Sens. Symp.*, 2016.

[CA40] H. Park, A. Camps, I. Sekulic, J. Rius, D. Pascual, A. Alonso-Arroyo, J. Querol, and R. Onrubia, "IMPACT OF MULTI-PATH BY ISS STRUCTURE ON GEROS-ISS MEASURED WAVEFORMS," in *2016 IEEE Int. Geosci. Remote Sens. Symp.*, 2016.

[CA41] H. Park, A. Camps, D. Pascual, A. Alonso-Arroyo, J. Querol, and R. Onrubia, "IMPROVEMENT OF PAU/PARIS END-TO-END PERFORMANCE SIMULATOR (P2EPS): LAND SCATTERING INCLUDING TOPOGRAPHY," in *2016 IEEE Int. Geosci. Remote Sens. Symp.*, 2016.

[CA42] A. Camps, H. Park, R. Onrubia, D. Pascual, J. Querol, A. Alonso-Arroyo, J. Benito, A. Andres-Beivide, S. Moreno, X. Ballesteros, M. Segarra, V. R., A. Rius, and M. Neira, "ALTIMETRIC PERFORMANCE OF THE GEROS EXPERIMENT AT THE ISS," in *2016 IEEE Int. Geosci. Remote Sens. Symp.*, 2016.